rapy Solutions

by MicroVention®

HydroFrame®
HydroCoil® Embolic System

HydroFill®
HydroCoil® Embolic System

HydroSoft®
HydroCoil® Embolic System

HYDROGEL ADVANCED COILS

The clinical benefits of **hydrogel** NOW engineered with the softness of bare platinum on the **V-Trak® Advanced Coil System**.

- CLINICALLY STUDIED HYDROGEL
- EFFECTIVE[1,2,3]
- ESTABLISHED SAFETY PROFILE[4]
- SOFTER DESIGN[5]

For more information or a product demonstration, contact your local MicroVention representative:

MicroVention® TERUMO

MicroVention, Inc.
Worldwide Headquarters PH +1.714.247.8000
1311 Valencia Avenue
Tustin, CA 92780 USA
MicroVention UK Limited PH +44 (0) 191 258 6777
MicroVention Europe, S.A.R.L. PH +33 (1) 39 21 77 46
MicroVention Deutschland GmbH PH +49 211 210 798-0
microvention.com

References
1. Speirs, Burke, Lee, and Ala. The next generation HydroCoil: initial clinical experience with the HydroFill embolic coil. J NeuroIntervent Surg, 2013.
2. Brinjikiji et al. Abstract 112. Presented at: International Stroke Conference 2015, Nashville, Tennessee, February 11-13, 2015.
3. Lee, Seo, Less, Cho, Kang and Han. Mid-term outcome of intracranial aneurysms treated with HydroSoft coils compared to historical controls treated with bare platinum coils: a single-center experience. Acta Neurochir, 156:1687-1694, 2014.
4. Laymond et al. Patients prone to recurrence after endovascular treatment: periprocedural results of the PRET randomized trial on large and recurrent aneurysms, AJNR AM J Neuroradiol, 2014.
5. Data on file at MicroVention, Inc.

Target®
DETACHABLE COILS

Smooth and Stable

Whether you are framing, filling or finishing, Target Detachable Coils deliver consistently smooth deployment and exceptional microcatheter stability. Focused on design, Target Coils feature a host of advantages to ensure the high-powered performance you demand.

For more information, please visit www.strykerneurovascular.com/Target or contact your local Stryker Neurovascular sales representative.

stryker® Neurovascular

Stroke: *Our Only Focus. Our Ongoing Promise.*

ASNR 2016
Washington, DC

ASFNR • ASHNR • ASPNR • ASSR • SNIS

THE FOUNDATION OF THE ASNR

THE FOUNDATION OF THE ASNR SYMPOSIUM 2016: EMERGENCY NEURORADIOLOGY
MAY 21-22

ASNR 54TH ANNUAL MEETING
MAY 23-26

Howard A. Rowley, MD, ASNR 2016 Program Chair/President-Elect
Programming developed in cooperation with …

American Society of Functional Neuroradiology (ASFNR)
Christopher G. Filippi, MD

American Society of Head and Neck Radiology (ASHNR)
Lindell R. Gentry, MD

American Society of Pediatric Neuroradiology (ASPNR)
Erin Simon Schwartz, MD

American Society of Spine Radiology (ASSR)
Gregory J. Lawler, MD

Society of NeuroInterventional Surgery (SNIS)
Charles J. Prestigiacomo, MD

American Society of Neuroradiology (ASNR) Committee Programming:
Health Policy Committee
Robert M. Barr, MD, FACR

Computer Science and Informatics (CSI) Committee
John L. Go, MD, FACR

Research Scientists Committee
Dikoma C. Shungu, PhD

ABSTRACT DEADLINE:
Friday, December 11, 2015
Please visit www.asnr.org/2016
for more information

ASNR 54TH ANNUAL MEETING
c/o American Society of Neuroradiology
800 Enterprise Drive, Suite 205
Oak Brook, Illinois 60523-4216
Phone: 630-574-0220
Fax: 630 574-0661
www.asnr.org/2016

SCAN NOW
TO VISIT
OUR WEBSITE

SAVE THE DATE... MAY 21-26, 2016
WASHINGTON MARRIOTT WARDMAN PARK • WASHINGTON, DC

PHYSICIANS BOOST THE ECONOMY.

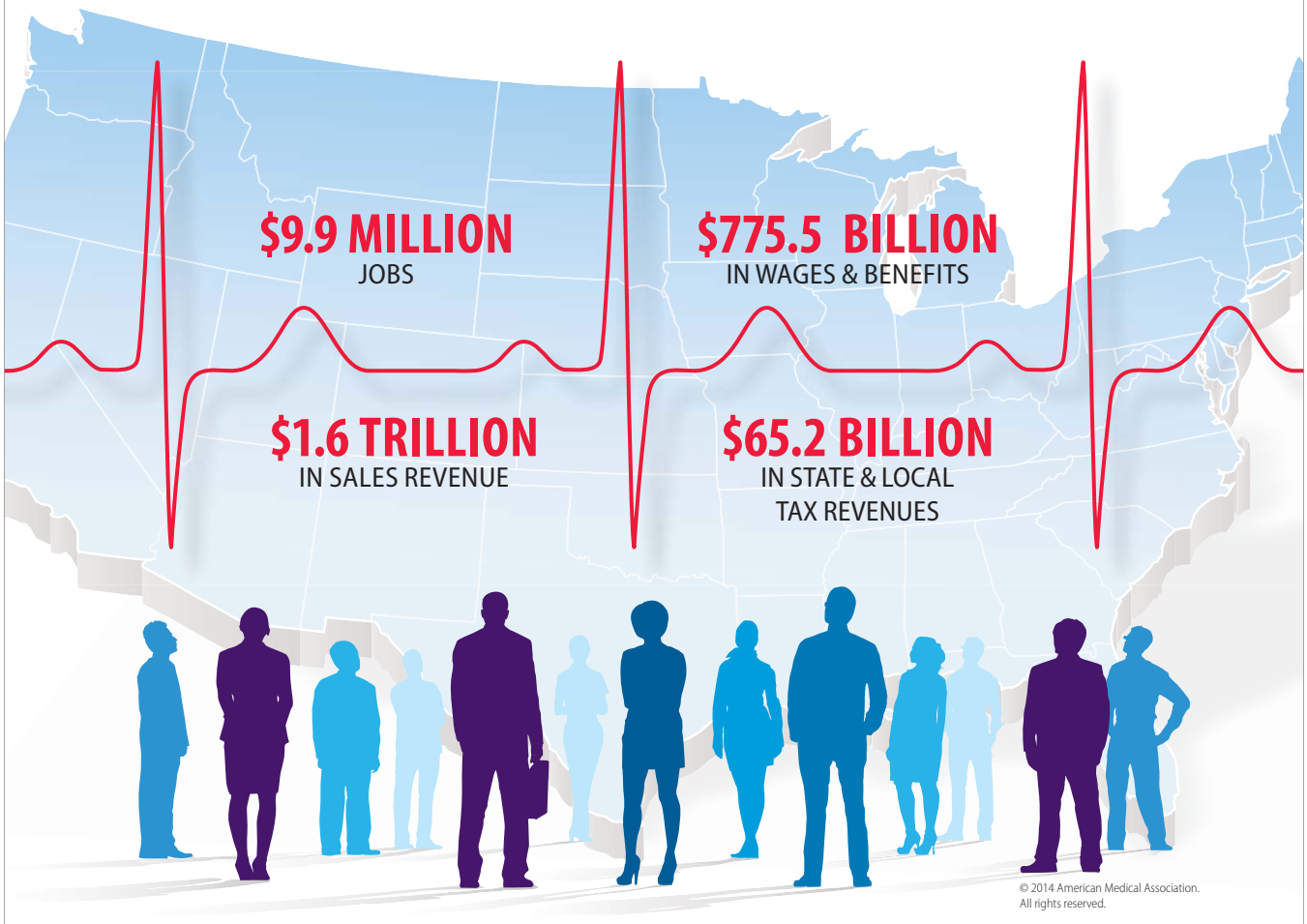

See the effects across the nation.

The American Medical Association 2014 Economic Impact Study shows how much physicians add to the economic health of our nation.

Check the effect physicians have on the U.S. economy by viewing the entire national report from the AMA Advocacy Resource Center at **ama-assn.org/go/eis**.

AMA
AMERICAN MEDICAL ASSOCIATION

Please activate your 2015 AMA membership by calling (800) 262-3211 or visit ama-assn.org/go/join.

AJNR

CALL FOR AJNR EDITORIAL FELLOWSHIP CANDIDATES

ASNR and AJNR are pleased once again to join efforts with other imaging-related journals that have training programs on editorial aspects of publishing for trainees or junior staff (3–5 years after training), including Radiology (Olmsted fellowship), AJR (Figley and Rogers fellowships), JACR (Bruce J. Hillman fellowship), and Radiologia.

2016 Candidate Information and Requirements

GOALS

- Increase interest in "editorial" and publication-related activities in younger individuals.
- Increase understanding and participation in the AJNR review process.
- Incorporate into AJNR's Editorial Board younger individuals who have previous experience in the review and publication process.
- Fill a specific need in neuroradiology not offered by other similar fellowships.
- Increase the relationship between "new" generation of neuroradiologists and more established individuals.
- Increase visibility of AJNR among younger neuroradiologists.

ACTIVITIES OF THE FELLOWSHIP

- Serve as Editorial Fellow for one year. This individual will be listed on the masthead as such.
- Review at least one manuscript per month for 12 months. Evaluate all review articles submitted to AJNR.
- Access to our electronic manuscript review system will be granted so that the candidate can learn how these systems work.
- Be involved in the final decision of selected manuscripts together with the Editor-in-Chief.
- Participate in all monthly Senior Editor telephone conference calls.
- Participate in all meetings of the Editors and Publications Committee during the annual meetings of ASNR and RSNA as per candidate's availability. The Foundation of the ASNR will provide $2000 funding for this activity.
- Evaluate progress and adjust program to specific needs in annual meeting or telephone conference with the Editor-in-Chief.
- Write at least one editorial for AJNR.
- Embark on an editorial scientific or bibliometric project that will lead to the submission of an article to AJNR or another appropriate journal as determined by the Editor-in-Chief. This project will be presented by the Editorial Fellow at the ASNR annual meeting.
- Serve as liaison between AJNR and ASNR's Young Professionals Network and the 3 YPs appointed to AJNR as special consultants. Participate in meetings and telephone calls with this group. Design one electronic survey/year polling the group regarding readership attitudes and wishes.
- Recruit trainees as reviewers as determined by the Editor-in-Chief.
- Participate in Web improvement projects.
- Invite Guest Editors for AJNR's News Digest to cover a variety of timely topics.

QUALIFICATIONS

- Be a fellow in neuroradiology from North America, including Canada (this may be extended to include other countries).
- Be a junior faculty neuroradiology member (< 3 years) in either an academic or private environment.
- Be an "in-training" or member of ASNR in any other category.

APPLICATION

- Include a short letter of intent with statement of goals and desired research project. CV must be included.
- Include a letter of recommendation from the Division Chief or fellowship program director. A statement of protected time to perform the functions outlined is desirable.
- Applications will be evaluated by AJNR's Senior Editors and the Chair of the Publications Committee prior to the ASNR meeting. The name of the selected individual will be announced at the meeting.
- Applications should be received by March 4, 2016 and sent to Ms. Karen Halm, AJNR Managing Editor, electronically at khalm@asnr.org.

American Society of Spine Radiology

2016 Annual Symposium • February 18-21, 2016

Hyatt Regency Coconut Point • Bonita Springs, FL

- Stillwater Spa with 18 treatment rooms, Watsu pool, and beauty salon
- Big Hickory Island Beach
- Spectacular waterfalls and pool features, as well as a spacious sundeck
- Family pool with 140-foot corkscrew water slide and hot tub, heated adult pool with hot tub, cold-plunge pool with waterfall
- 18-hole Raymond Floyd designed Raptor Bay golf course and club
- 24-hour Hyatt StayFit gym with cardio theater
- Bicycle and kayak rentals
- Dolphin watch eco-tours and sunset cruises
- Video arcade
- Har-Tru clay tennis courts
- Camp Hyatt®

A tropical paradise centrally located between Fort Myers and Naples, Florida in the upscale community of Bonita Springs. With stunning views of the Gulf Coast, Hyatt Regency Coconut Point Resort and Spa offers casual elegance and southern style hospitality, personalized service and attention to detail at every turn.

SAVE THE DATE

AJNR

AMERICAN JOURNAL OF NEURORADIOLOGY

Publication Preview at www.ajnr.org features articles released in advance of print. Visit www.ajnrblog.org to comment on AJNR content and chat with colleagues and AJNR's News Digest at http://ajnrdigest.org to read the stories behind the latest research in neuroimaging.

NOVEMBER 2015 • VOLUME 36 • NUMBER 11 • WWW.AJNR.ORG

Official Journal:
American Society of Neuroradiology
American Society of Functional Neuroradiology
American Society of Head and Neck Radiology
American Society of Pediatric Neuroradiology
American Society of Spine Radiology

AJNR (Am J Neuroradiol ISSN 0195–6108) is a journal published monthly, owned and published by the American Society of Neuroradiology (ASNR), 800 Enterprise Drive, Suite 205, Oak Brook, IL 60523. Annual dues for the ASNR include $170.00 for journal subscription. The journal is printed by Cadmus Journal Services, 5457 Twin Knolls Road, Suite 200, Columbia, MD 21045; Periodicals postage paid at Oak Brook, IL and additional mailing offices. Printed in the U.S.A. POSTMASTER: Please send address changes to American Journal of Neuroradiology, P.O. Box 3000, Denville, NJ 07834, U.S.A. Subscription rates: nonmember $380 ($450 foreign) print and online, $305 online only; institutions $440 ($510 foreign) print and basic online, $875 ($940 foreign) print and extended online, $365 online only (basic), extended online $790; single copies are $35 each ($40 foreign). Indexed by PubMed/Medline, BIOSIS Previews, Current Contents (Clinical Medicine and Life Sciences), EMBASE, Google Scholar, HighWire Press, Q-Sensei, RefSeek, Science Citation Index, and SCI Expanded.

UNITED STATES POSTAL SERVICE® **Statement of Ownership, Management, and Circulation (All Periodicals Publications Except Requester Publications)**

1. Publication Title	2. Publication Number	3. Filing Date
American Journal of Neuroradiology	0 1 9 5 - 6 1 0 8	10/14/2015
4. Issue Frequency	**5. Number of Issues Published Annually**	**6. Annual Subscription Price**
Monthly	12	$380.00

7. Complete Mailing Address of Known Office of Publication *(Not printer) (Street, city, county, state, and ZIP+4®)*
800 Enterprise Drive, Suite 205, Oak Brook, IL 60523
Contact Person: Karen Halm
Telephone *(Include area code)*: 630/574-1487 x 238

8. Complete Mailing Address of Headquarters or General Business Office of Publisher *(Not printer)*
800 Enterprise Drive, Suite 205, Oak Brook, IL 60523

9. Full Names and Complete Mailing Addresses of Publisher, Editor, and Managing Editor *(Do not leave blank)*

Publisher *(Name and complete mailing address)*
American Society of Neuroradiology

Editor *(Name and complete mailing address)*
Jeffrey S. Ross

Managing Editor *(Name and complete mailing address)*
Karen E. Halm

10. Owner *(Do not leave blank. If the publication is owned by a corporation, give the name and address of the corporation immediately followed by the names and addresses of all stockholders owning or holding 1 percent or more of the total amount of stock. If not owned by a corporation, give the names and addresses of the individual owners. If owned by a partnership or other unincorporated firm, give its name and address as well as those of each individual owner. If the publication is published by a nonprofit organization, give its name and address.)*

Full Name	Complete Mailing Address
American Society of Neuroradiology	800 Enterprise Drive, Suite 205, Oak Brook, IL 60523

11. Known Bondholders, Mortgagees, and Other Security Holders Owning or Holding 1 Percent or More of Total Amount of Bonds, Mortgages, or Other Securities. If none, check box → ☒ None

Full Name	Complete Mailing Address

12. Tax Status *(For completion by nonprofit organizations authorized to mail at nonprofit rates) (Check one)*
The purpose, function, and nonprofit status of this organization and the exempt status for federal income tax purposes:
☒ Has Not Changed During Preceding 12 Months
☐ Has Changed During Preceding 12 Months *(Publisher must submit explanation of change with this statement)*

PS Form **3526**, July 2014 *[Page 1 of 4 (see instructions page 4)]* PSN: 7530-01-000-9931 **PRIVACY NOTICE:** See our privacy policy on *www.usps.com*

13. Publication Title	14. Issue Date for Circulation Data Below
American Journal of Neuroradiology	9/10/2015

15. Extent and Nature of Circulation			Average No. Copies Each Issue During Preceding 12 Months	No. Copies of Single Issue Published Nearest to Filing Date
a. Total Number of Copies *(Net press run)*			4188	4132
b. Paid Circulation *(By Mail and Outside the Mail)*	(1)	Mailed Outside-County Paid Subscriptions Stated on PS Form 3541 (Include paid distribution above nominal rate, advertiser's proof copies, and exchange copies)	3211	2847
	(2)	Mailed In-County Paid Subscriptions Stated on PS Form 3541 *(Include paid distribution above nominal rate, advertiser's proof copies, and exchange copies)*	0	0
	(3)	Paid Distribution Outside the Mails Including Sales Through Dealers and Carriers, Street Vendors, Counter Sales, and Other Paid Distribution Outside USPS®	577	560
	(4)	Paid Distribution by Other Classes of Mail Through the USPS (e.g., First-Class Mail®)	0	0
c. Total Paid Distribution *[Sum of 15b (1), (2), (3), and (4)]* ▶			3788	3407
d. Free or Nominal Rate Distribution *(By Mail and Outside the Mail)*	(1)	Free or Nominal Rate Outside-County Copies included on PS Form 3541	0	0
	(2)	Free or Nominal Rate In-County Copies Included on PS Form 3541	0	0
	(3)	Free or Nominal Rate Copies Mailed at Other Classes Through the USPS (e.g., First-Class Mail)	0	0
	(4)	Free or Nominal Rate Distribution Outside the Mail *(Carriers or other means)*	70	25
e. Total Free or Nominal Rate Distribution *(Sum of 15d (1), (2), (3) and (4))*			70	25
f. Total Distribution *(Sum of 15c and 15e)* ▶			3858	3432
g. Copies not Distributed *(See Instructions to Publishers #4 (page #3))* ▶			330	700
h. Total *(Sum of 15f and g)*			4188	4132
i. Percent Paid *(15c divided by 15f times 100)* ▶			98.2	99.2

* If you are claiming electronic copies, go to line 16 on page 3. If you are not claiming electronic copies, skip to line 17 on page 3.

16. Electronic Copy Circulation	Average No. Copies Each Issue During Preceding 12 Months	No. Copies of Single Issue Published Nearest to Filing Date
a. Paid Electronic Copies ▶		
b. Total Paid Print Copies (Line 15c) + Paid Electronic Copies (Line 16a) ▶		
c. Total Print Distribution (Line 15f) + Paid Electronic Copies (Line 16a) ▶		
d. Percent Paid (Both Print & Electronic Copies) (16b divided by 16c × 100) ▶		

☒ I certify that 50% of all my distributed copies (electronic and print) are paid above a nominal price.

17. Publication of Statement of Ownership
☒ If the publication is a general publication, publication of this statement is required. Will be printed in the November issue of this publication. ☐ Publication not required.

18. Signature and Title of Editor, Publisher, Business Manager, or Owner — Date: 10/15/2015

Karen E. Halm

I certify that all information furnished on this form is true and complete. I understand that anyone who furnishes false or misleading information on this form or who omits material or information requested on the form may be subject to criminal sanctions (including fines and imprisonment) and/or civil sanctions (including civil penalties).

Target® Detachable Coil

See package insert for complete indications, contraindications, warnings and instructions for use.

INTENDED USE / INDICATIONS FOR USE
Target Detachable Coils are intended to endovascularly obstruct or occlude blood flow in vascular abnormalities of the neurovascular and peripheral vessels.

Target Detachable Coils are indicated for endovascular embolization of:
- Intracranial aneurysms
- Other neurovascular abnormalities such as arteriovenous malformations and arteriovenous fistulae
- Arterial and venous embolizations in the peripheral vasculature

CONTRAINDICATIONS
None known.

POTENTIAL ADVERSE EVENTS
Potential complications include, but are not limited to: allergic reaction, aneurysm perforation and rupture, arrhythmia, death, edema, embolus, headache, hemorrhage, infection, ischemia, neurological/intracranial sequelae, post-embolization syndrome (fever, increased white blood cell count, discomfort), TIA/stroke, vasospasm, vessel occlusion or closure, vessel perforation, dissection, trauma or damage, vessel rupture, vessel thrombosis. Other procedural complications including but not limited to: anesthetic and contrast media risks, hypotension, hypertension, access site complications.

WARNINGS
- Contents supplied STERILE using an ethylene oxide (EO) process. Do not use if sterile barrier is damaged. If damage is found, call your Stryker Neurovascular representative.
- For single use only. Do not reuse, reprocess or resterilize. Reuse, reprocessing or resterilization may compromise the structural integrity of the device and/or lead to device failure which, in turn, may result in patient injury, illness or death. Reuse, reprocessing or resterilization may also create a risk of contamination of the device and/or cause patient infection or cross-infection, including, but not limited to, the transmission of infectious disease(s) from one patient to another. Contamination of the device may lead to injury, illness or death of the patient.
- After use, dispose of product and packaging in accordance with hospital, administrative and/or local government policy.
- **This device should only be used by physicians who have received appropriate training in interventional neuroradiology or interventional radiology and preclinical training on the use of this device as established by Stryker Neurovascular.**
- Patients with hypersensitivity to 316LVM stainless steel may suffer an allergic reaction to this implant.
- MR temperature testing was not conducted in peripheral vasculature, arteriovenous malformations or fistulae models.
- The safety and performance characteristics of the Target Detachable Coil System (Target Detachable Coils, InZone Detachment Systems, delivery systems and accessories) have not been demonstrated with other manufacturer's devices (whether coils, coil delivery devices, coil detachment systems, catheters, guidewires, and/or other accessories). Due to the potential incompatibility of non Stryker Neurovascular devices with the Target Detachable Coil System, the use of other manufacturer's device(s) with the Target Detachable Coil System is not recommended.
- To reduce risk of coil migration, the diameter of the first and second coil should never be less than the width of the ostium.
- In order to achieve optimal performance of the Target Detachable Coil System and to reduce the risk of thromboembolic complications, it is critical that a continuous infusion of appropriate flush solution be maintained between a) the femoral sheath and guiding catheter, b) the 2-tip microcatheter and guiding catheters, and c) the 2-tip microcatheter and Stryker Neurovascular guidewire and delivery wire. Continuous flush also reduces the potential for thrombus formation on, and crystallization of infusate around, the detachment zone of the Target Detachable Coil.
- Do not use the product after the "Use By" date specified on the package.
- Reuse of the flush port/dispenser coil or use with any coil other than the original coil may result in contamination of, or damage to, the coil.
- Utilization of damaged coils may affect coil delivery to, and stability inside, the vessel or aneurysm, possibly resulting in coil migration and/or stretching.
- The fluoro-saver marker is designed for use with a Rotating Hemostatic Valve (RHV). If used without an RHV, the distal end of the coil may be beyond the alignment marker when the fluoro-saver marker reaches the microcatheter hub.
- If the fluoro-saver marker is not visible, do not advance the coil without fluoroscopy.
- Do not rotate delivery wire during or after delivery of the coil. Rotating the Target Detachable Coil delivery wire may result in a stretched coil or premature detachment of the coil from the delivery wire, which could result in coil migration.
- Verify there is no coil loop protrusion into the parent vessel after coil placement and prior to coil detachment. Coil loop protrusion after coil placement may result in thromboembolic events if the coil is detached.
- Verify there is no movement of the coil after coil placement and prior to coil detachment. Movement of the coil after coil placement may indicate that the coil could migrate once it is detached.
- Failure to properly close the RHV compression fitting over the delivery wire before attaching the InZone® Detachment System could result in coil movement, aneurysm rupture or vessel perforation.
- Verify repeatedly that the distal shaft of the catheter is not under stress before detaching the Target Detachable Coil. Axial compression or tension forces could be stored in the 2-tip microcatheter causing the tip to move during coil delivery. Microcatheter tip movement could cause the aneurysm or vessel to rupture.
- Advancing the delivery wire beyond the microcatheter tip once the coil has been detached involves risk of aneurysm or vessel perforation.
- The long term effect of this product on extravascular tissues has not been established so care should be taken to retain this device in the intravascular space.

Damaged delivery wires may cause detachment failures, vessel injury or unpredictable distal tip response during coil deployment. If a delivery wire is damaged at any point during the procedure, do not attempt to straighten or otherwise repair it. Do not proceed with deployment or detachment. Remove the entire coil and replace with undamaged product.

- After use, dispose of product and packaging in accordance with hospital, administrative and/or local government policy.

CAUTIONS / PRECAUTIONS
- Federal Law (USA) restricts this device to sale by or on the order of a physician.
- Besides the number of InZone Detachment System units needed to complete the case, there must be an extra InZone Detachment System unit as back up.
- Removing the delivery wire without grasping the introducer sheath and delivery wire together may result in the detachable coil sliding out of the introducer sheath.
- Failure to remove the introducer sheath after inserting the delivery wire into the RHV of the microcatheter will interrupt normal infusion of flush solution and allow back flow of blood into the microcatheter.
- Some low level overhead light near or adjacent to the patient is required to visualize the fluoro-saver marker; monitor light alone will not allow sufficient visualization of the fluoro-saver marker.
- Advance and retract the Target Detachable Coil carefully and smoothly without excessive force. If unusual friction is noticed, slowly withdraw the Target Detachable Coil and examine for damage. If damage is present, remove and use a new Target Detachable Coil. If friction or resistance is still noted, carefully remove the Target Detachable Coil and microcatheter and examine the microcatheter for damage.
- If it is necessary to reposition the Target Detachable Coil, verify under fluoroscopy that the coil moves with a one-to-one motion. If the coil does not move with a one-to-one motion or movement is difficult, the coil may have stretched and could possibly migrate or break. Gently remove both the coil and microcatheter and replace with new devices.
- Increased detachment times may occur when:
  - Other embolic agents are present.
  - Delivery wire and microcatheter markers are not properly aligned.
  - Thrombus is present on the coil detachment zone.
- Do not use detachment systems other than the InZone Detachment System.
- Increased detachment times may occur when delivery wire and microcatheter markers are not properly aligned.
- Do not use detachment systems other than the InZone Detachment System.

Stryker Neurovascular
47900 Bayside Parkway
Fremont, CA 94538-6515

stryker.com/neurovascular

Date of Release: FEB/2014

EX_EN_US

Trevo® XP ProVue Retrievers

See package insert for complete indications, complications, warnings, and instructions for use.

INDICATIONS FOR USE
The Trevo Retriever is intended to restore blood flow in the neurovasculature by removing thrombus in patients experiencing ischemic stroke within 8 hours of symptom onset. Patients who are ineligible for intravenous tissue plasminogen activator (IV t-PA) or who fail IV t-PA therapy are candidates for treatment.

COMPLICATIONS
Procedures requiring percutaneous catheter introduction should not be attempted by physicians unfamiliar with possible complications which may occur during or after the procedure. Possible complications include, but are not limited to, the following: air embolism; hematoma or hemorrhage at puncture site; infection; distal embolization; pain/headache; vessel spasm, thrombosis, dissection, or perforation; emboli; acute occlusion; ischemia; intracranial hemorrhage; false aneurysm formation; neurological deficits including stroke; and death.

COMPATIBILITY
3x20 mm retrievers are compatible with Trevo® Pro 14 Microcatheters (REF 90231) and Trevo® Pro 18 Microcatheters (REF 90238). 4x20 mm retrievers are compatible with Trevo® Pro 18 Microcatheters (REF 90238). Compatibility of the Retriever with other microcatheters has not been established. Performance of the Retriever device may be impacted if a different microcatheter is used. The Merci® Balloon Guide Catheters are recommended for use during thrombus removal procedures. Retrievers are compatible with the Abbott Vascular DOC® Guide Wire Extension (REF 22260).

WARNINGS
- Contents supplied STERILE, using an ethylene oxide (EO) process. Nonpyrogenic.
- To reduce risk of vessel damage, adhere to the following recommendations:
  - Take care to appropriately size Retriever to vessel diameter at intended site of deployment.
  - Do not perform more than six (6) retrieval attempts in same vessel using Retriever devices.
  - Maintain Retriever position in vessel when removing or exchanging Microcatheter.
- To reduce risk of kinking/fracture, adhere to the following recommendations:
  - Immediately after unsheathing Retriever, position Microcatheter tip marker just proximal to shaped section. Maintain Microcatheter tip marker just proximal to shaped section of Retriever during manipulation and withdrawal.
  - Do not rotate or torque Retriever.
  - Use caution when passing Retriever through stented arteries.
- Do not resterilize and reuse. Structural integrity and/or function may be impaired by reuse or cleaning.
- The Retriever is a delicate instrument and should be handled carefully. Before use and when possible during procedure, inspect device carefully for damage. Do not use a device that shows signs of damage. Damage may prevent device from functioning and may cause complications.
- Do not advance or withdraw Retriever against resistance or significant vasospasm. Moving or torquing device against resistance or significant vasospasm may result in damage to vessel or device. Assess cause of resistance using fluoroscopy and if needed resheath the device to withdraw.
- If Retriever is difficult to withdraw from the vessel, do not torque Retriever. Advance Microcatheter distally, gently pull Retriever back into Microcatheter, and remove Retriever and Microcatheter as a unit. If undue resistance is met when withdrawing the Retriever into the Microcatheter, consider extending the Retriever using the Abbott Vascular DOC guidewire extension (REF 22260) so that the Microcatheter can be exchanged for a larger diameter catheter such as a DAC® catheter. Gently withdraw the Retriever into the larger diameter catheter.
- Administer anti-coagulation and anti-platelet medications per standard institutional guidelines.

PRECAUTIONS
- Prescription only – device restricted to use by or on order of a physician.
- Store in cool, dry, dark place.
- Do not use open or damaged packages.
- Use by "Use By" date.
- Exposure to temperatures above 54°C (130°F) may damage device and accessories. Do not autoclave.
- Do not expose Retriever to solvents.
- Use Retriever in conjunction with fluoroscopic visualization and proper anti-coagulation agents.
- To prevent thrombus formation and contrast media crystal formation, maintain a constant infusion of appropriate flush solution between guide catheter and Microcatheter and between Microcatheter and Retriever or guidewire.
- Do not attach a torque device to the shaped proximal end of DOC® Compatible Retriever. Damage may occur, preventing ability to attach DOC® Guide Wire Extension.

Concentric Medical
301 East Evelyn
Mountain View, CA 94041

Stryker Neurovascular
47900 Bayside Parkway
Fremont, CA 94538-6515

stryker.com/neurovascular
stryker.com/emea/neurovascular

EC REP

EMERGO Europe
Molenstraat 15
2513 BH, The Hague
The Netherlands

Date of Release: JUN/2014

EX_EN_GL

CE 0459

Aneurysm The

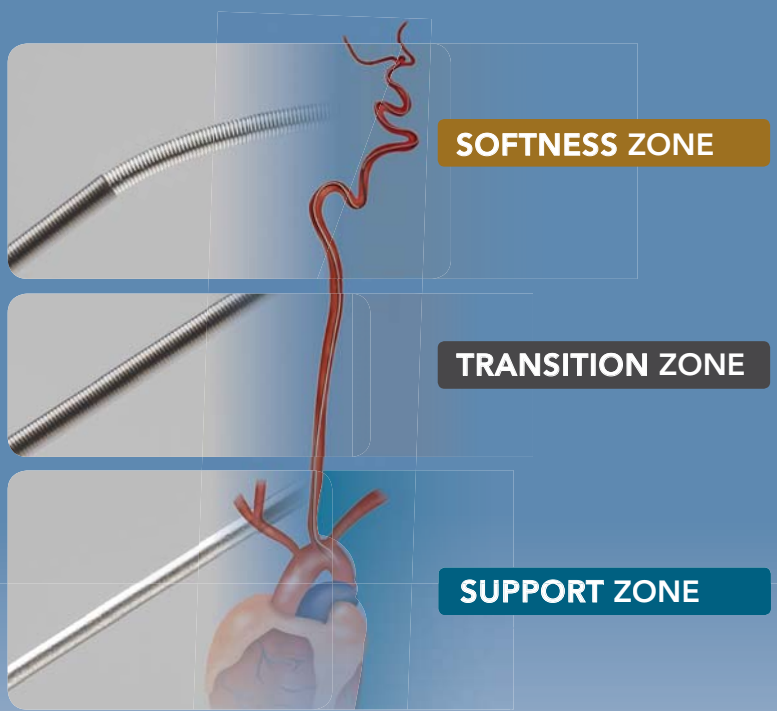

V-Trak® Advanced Coil System

ENHANCED CONTROL TO MAXIMIZE COIL PERFORMANCE

The **V-Trak® Advanced Coil System**, the next generation to power the performance of our most technically advanced line of coils. Offering the optimal combination of support and flexibility.

INDICATIONS FOR USE:
The HydroCoil® Embolic System (HES) is intended for the endovascular embolization of intracranial aneurysms and other neurovascular abnormalities such as arteriovenous malformations and arteriovenous fistulae. The HES is also intended for vascular occlusion of blood vessels within the neurovascular system to permanently obstruct blood flow to an aneurysm or other vascular malformation and for arterial and venous embolizations in the peripheral vasculature. The device should only be used by physicians who have undergone pre-clinical training in all aspects of HES procedures as prescribed by MicroVention.

CE 0297

66%

of Patients in MR CLEAN Were Treated with a Trevo® Stent Retriever

stryker® Neurovascular

Trevo®
PROVUE RETRIEVER

MR CLEAN[1]

First clinical evidence for intra-arterial treatment with stent retrievers

- **Largest** of the randomized AIS trials[2], with over 500 patients enrolled
- The Trevo Retriever was the **#1** device used in the **MR CLEAN** Trial

[1] O.A. Berkhemer et al. A Randomized Trial for Intra-arterial Treatment for Acute Ischemic Stroke. *N Eng J Med* December 2014.
[2] MR CLEAN is the largest AIS Trial in which stent retrievers were used.
http://www.mrclean-trial.org/

Stroke: *Our Only Focus. Our Ongoing Promise.*

COILING OPTIMIZED

NOW AVAILABLE

BARRICADE COMPLEX FINISHING COIL

- Extremely soft profile of The Barricade Finishing coil now in a complex shape
- Excellent microcatheter stability for confident coil placement
- Available in a size range of 1mm-5mm

BARRICADE™ COIL SYSTEM

MADE IN AMERICA

The Barricade Coil System is intended for the endovascular embolization of intracranial aneurysms and other neurovascular abnormalities such as arteriovenous malformations and arteriovenous fistulae. The System is also intended for vascular occlusion of blood vessels within the neurovascular system to permanently obstruct blood flow to an aneurysm or other vascular malformation and for arterial and venous embolizations in the peripheral vasculature. Refer to the instructions for use for complete product information.

18 TECHNOLOGY DRIVE #169, IRVINE CA 92618
p: 949.788.1443 | f: 949.788.1444

WWW.BLOCKADEMEDICAL.COM

MKTG-031 Rev. A

BLOCKADE MEDICAL

AJNR
AMERICAN JOURNAL OF NEURORADIOLOGY

NOVEMBER 2015
VOLUME 36
NUMBER 11
WWW.AJNR.ORG

THE JOURNAL OF DIAGNOSTIC AND INTERVENTIONAL NEURORADIOLOGY

Nigrosome 1 detection at 3T in Parkinson disease

Carotid webs and recurrent ischemic stroke

Contrast enhancement in anaplastic glioma with *IDH1* mutation

Official Journal ASNR • ASFNR • ASHNR • ASPNR • ASSR

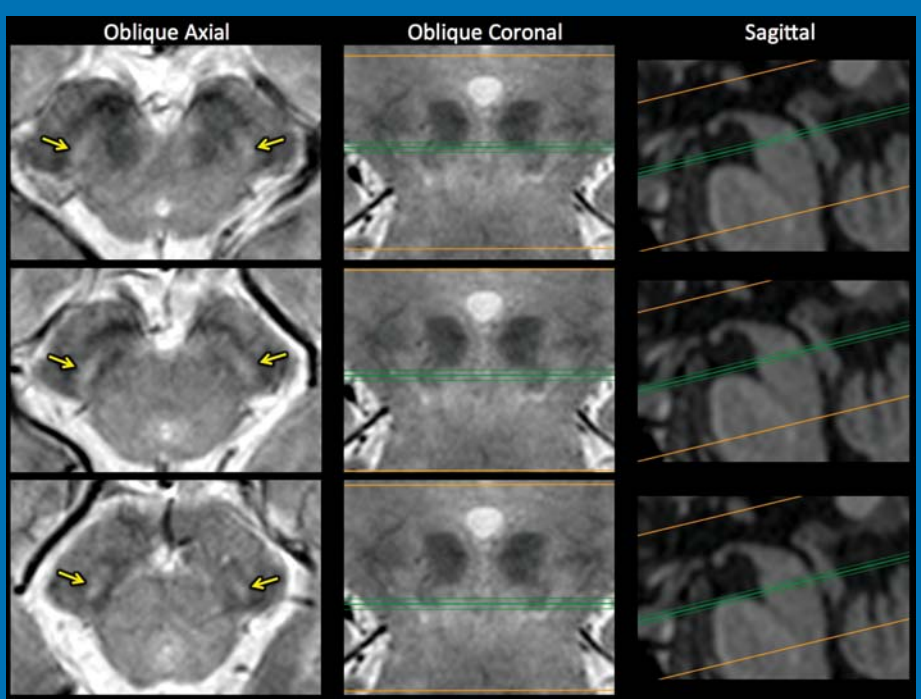

AJNR

AMERICAN JOURNAL OF NEURORADIOLOGY

NOVEMBER 2015
VOLUME 36
NUMBER 11
WWW.AJNR.ORG

Publication Preview at www.ajnr.org features articles released in advance of print. Visit www.ajnrblog.org to comment on AJNR content and chat with colleagues and AJNR's News Digest at http://ajnrdigest.org to read the stories behind the latest research in neuroimaging.

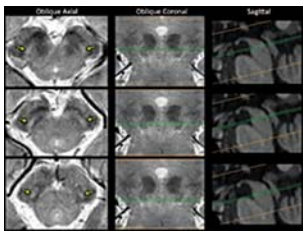

Oblique axial MEDIC imaging of the substantia nigra pars compacta area shows normal nigrosome 1 regions.

Indicates Editor's Choices selection
Indicates Fellows' Journal Club selection
Indicates open access to non-subscribers at www.ajnr.org
Indicates article with supplemental on-line table
Indicates article with supplemental on-line photo
Indicates article with supplemental on-line video
Evidence-Based Medicine Level 1
Evidence-Based Medicine Level 2

The Fall Carpet. Photographed in Palo Alto, California, in November 2012. More of the Dr. Pauranik's work can be seen at: http://anvitapauranik.weebly.com/.

Anvita Pauranik, MD, Calgary, Alberta, Canada

MRI of Acute Stroke: What Went Wrong?

K.-O. Lövblad and V.M. Pereira

The news of the recently published trials about the efficacy of intra-arterial interventions for stroke lifted the spirits of all neuroradiologists and the vascular neurology community.[1-4] Finally, these trials proved our personal experience: Effective early reperfusion of proximal occlusions can save brain parenchyma and improve patient outcomes. Studies were focused on patient selection and fast-treatment workflow to perform interventions as early as possible. In most hospitals, the preferred imaging technique to select patients is CT with CTA and/or CT perfusion, based more on local logistics than on imaging quality or predefined standards. While we are no longer in the era of the early stroke trials, in which imaging with negative findings (ie, CT without hemorrhage) was the indicator for thrombolysis, we are still early in the use of advanced imaging in acute stroke interventions. It seems that just by identifying proximal occlusions, we have improved the selection of patients despite the limitations of CT to demonstrate early definitive lesions in acute stroke. While CT has made great strides in recent years, with perfusion, dual-energy, and other techniques improving and becoming a clear standard, MR imaging techniques seem to have "lost it," at least, in acute stroke.

Despite the potential of MR imaging, such as the extreme sensitivity of diffusion techniques,[5,6] its capacity to image the whole brain, and a whole armamentarium of techniques (FLAIR, SWI, MRA, perfusion, and so forth), this potential did not convince most centers to invest in or adapt their workflow to the use of MR imaging over CT. CT evaluation criteria and scores for acute stroke are undisputed. However, their assessment requires experience and can vary considerably among operators. MR imaging is vastly superior in delineating lesion extent, making the differential diagnosis of other conditions, measuring the clot length, and detecting potential "risky" lesions like microbleeds. DWI with or without FLAIR can still demonstrate an early ischemic lesion much better than CT.

So, what went wrong with MR imaging in stroke? In the era of the new-generation devices and early and effective reperfusion, has the clear identification of the stroke core lost its importance? One opinion is that use of MR imaging in an emergency setting disturbs the workflow, inhibiting effective treatment. Others might say that without a clear benefit from MR imaging, it is not worth the sacrifice in time to get better image quality. Recent studies have revolutionized the field of acute stroke treatment, but a significant proportion of patients have inadequate reperfusion.[1-4] How can we reduce or eliminate the inadequate reperfusion? Can MR imaging–based patient selection be a solution in addition to the improvement of health care systems, prehospital transportation, societal awareness, and hospital workflow improvements?

We think that MR imaging can add more information on patient selection for acute stroke and should be the ultimate goal for acute stroke triage imaging. DWI can define the early lesions, though reversible DWI lesions have been described also.[7,8] A recent study described DWI-FLAIR mismatch as a potential parameter to consider in stroke selection, but its relevancy and validity are still to be evaluated and proved.[9] SWI may be helpful in identifying potential lesions preventing hemorrhagic transformation and can precisely measure the clot length. MRA and MR perfusion have already demonstrated their benefits in recent trials (Extending the Time for Thrombolysis in Emergency Neurological Deficits–Intra-Arterial and Solitaire With the Intention For Thrombectomy as PRIMary Endovascular Treatment [SWIFT PRIME]).[2] MR imaging allows better contrast with additional sequences such as SWI for bleeding, FLAIR for lesion identification, and arterial spin-labeling for collateral flow analysis. All these techniques would make MR imaging the ideal for acute imaging.

CT with all its advantages of being quick, easy to interpret, and widely available produces much less valuable information for acute stroke diagnosis than MR imaging at any stage of stroke onset. Except for imaging time, there is no major advantage of CT over MR imaging. This even extends to the determination of the collateral circulation. CT is a great contributor to radiation exposure during hospitalization, and given that these patients will require repeat imaging (at least ≥2 after the event), it is incomprehensible why MR imaging has not had a more important role in the acute phase.

Will this be enough to justify the investment in MR imaging for acute stroke? In addition to the practical aspects of patient throughput and imaging time, MR imaging adds complexity to the interpretation of images, especially in the differential diagnosis of stroke. While the literature tells us that hemorrhage can be demonstrated very early, very often in untrained hands, CT is preferred because the hematoma is clearly seen as a hyperdense mass which is easily detected and recognizable.[10]

In the end, there will always be a balance between imaging quality and treatment workflow. We cannot add too many sequences and have examinations that are long or slow down the process of getting the brain reperfused. However, with a careful selection of sequences, we should be able to better select patients for treatment, reducing reperfusion and hemorrhagic complications and increasing effectiveness.

The major step of creating evidence for mechanical thrombectomy in acute stroke is done. Now, we need to move forward and look for how can we make treatment for acute stroke even better and more cost-effective. Improving patient selection is an essential step in this direction. While MR imaging–derived techniques seem to be more sensitive and safer than CT in acute stroke, there is not a demonstrated benefit suggesting a change in stroke workflow in the centers using CT. We think this change needs to be reconsidered for the acute management of patients with cerebro-

http://dx.doi.org/10.3174/ajnr.A4546

vascular diseases, given the potential tremendous benefit possible with MR imaging.

Disclosures: V.M. Pereira—*UNRELATED*: *Consultancy*: Principal Investigator for Study of Tamoxifen and Raloxifene and SWIFT PRIME trials.* *Money paid to the institution.

REFERENCES

1. Jovin TG, Chamorro A, Cobo E, et al; REVASCAT Trial Investigators. **Thrombectomy within 8 hours after symptom onset in ischemic stroke.** *N Engl J Med* 2015;372:2296–306 CrossRef Medline
2. Saver JL, Goyal M, Bonafe A, et al; SWIFT PRIME Investigators. **Stent-retriever thrombectomy after intravenous t-PA vs. t-PA alone in stroke.** *N Engl J Med* 2015;372:2285–95 CrossRef Medline
3. Goyal M, Demchuk AM, Menon BK, et al; ESCAPE Trial Investigators. **Randomized assessment of rapid endovascular treatment of ischemic stroke.** *N Engl J Med* 2015;372:1019–30 CrossRef Medline
4. Berkhemer OA, Fransen PS, Beumer D, et al; MR CLEAN Investigators. **A randomized trial of intraarterial treatment for acute ischemic stroke.** *N Engl J Med* 2015;372:11–20 CrossRef Medline
5. Lövblad KO, Laubach HJ, Baird AE, et al. **Clinical experience with diffusion-weighted MR in patients with acute stroke.** *AJNR Am J Neuroradiol* 1998;19:1061–66 Medline
6. González RG, Schaefer PW, Buonanno FS, et al. **Diffusion-weighted MR imaging: diagnostic accuracy in patients imaged within 6 hours of stroke symptom onset.** *Radiology* 1999;210:155–62 CrossRef Medline
7. Tortora F, Cirillo M, Ferrara M, et al. **DWI reversibility after intra-arterial thrombolysis: a case report and literature review.** *Neuroradiol J* 2010;23:752–62 CrossRef Medline
8. Taleb M, Lövblad KO, El-Koussy M, et al. **Reperfusion demonstrated by apparent diffusion coefficient mapping after local intra-arterial thrombolysis for ischaemic stroke.** *Neuroradiology* 2001;43:591–94 CrossRef Medline
9. Legrand L, Tisserand M, Turc G, et al. **Do FLAIR vascular hyperintensities beyond the DWI lesion represent the ischemic penumbra?** *AJNR Am J Neuroradiol* 2015;36:269–74 CrossRef Medline
10. Kidwell CS, Chalela JA, Saver JL, et al. **Comparison of MRI and CT for detection of acute intracerebral hemorrhage.** *JAMA* 2004;292:1823–30 CrossRef Medline

Current Applications of MRI-Guided Laser Interstitial Thermal Therapy in the Treatment of Brain Neoplasms and Epilepsy: A Radiologic and Neurosurgical Overview

R. Medvid, A. Ruiz, R.J. Komotar, J.R. Jagid, M.E. Ivan, R.M. Quencer, and M.B. Desai

ABSTRACT

SUMMARY: Minimally invasive stereotactic tumor ablation is a viable option for the treatment of benign and malignant intracranial lesions. Although surgical excision constitutes first-line therapy for various brain pathologies, it can cause irreversible neurologic deficits. Additionally, many patients who may benefit from surgery do not qualify as surgical candidates due to multiple comorbidities. Recent advancements in laser interstitial thermal therapy, namely the ability to monitor ablation in real-time under MR imaging, have improved the safety and efficacy of the procedure. MRI-guided laser interstitial thermal therapy is currently used as a minimally invasive treatment for brain metastases, radiation necrosis, glioma, and epilepsy. This article will discuss the principles, suggested indications, complications, and imaging characteristics of MRI-guided laser interstitial thermal therapy as they pertain to the treatment of brain pathology.

ABBREVIATIONS: GBM = glioblastoma multiforme; LITT = laser interstitial thermal therapy; MRgLITT = MRI-guided laser interstitial thermal therapy; MRTI = MRI thermal imaging; RN = delayed radiation necrosis; SRS = stereotactic radiosurgery

Laser interstitial thermal therapy (LITT) is a stereotactically guided percutaneous minimally invasive procedure, which delivers light energy to target tissue via a fiberoptic catheter, resulting in selective thermal ablation of malignant and benign lesions. LITT was described in 1983 by Bown[1] and was first applied in the treatment of brain lesions in 1990 by Sugiyama et al.[2] Acceptance of the procedure has been slow due to initial technologic shortcomings, which resulted in low efficacy and an unacceptably high risk of thermal damage to the surrounding normal brain parenchyma. Recent improvements have led to the development of percutaneous MRI-guided laser interstitial thermal therapy (MRgLITT), which enables monitoring of tissue ablation in real-time. Multiple academic centers are now using MRgLITT as a minimally invasive treatment for brain metastases, radiation necrosis, gliomas, and epilepsy. Successful management of patients undergoing MRgLITT requires interdisciplinary collaboration among neurosurgeons, neuroradiologists, neurologists, anesthesiologists, radiation oncologists, and neuro-oncologists. This article will discuss the principles, suggested indications, complications, and imaging characteristics of MRgLITT as they pertain to the treatment of brain pathology.

From the Department of Radiology (R.M., A.R., R.M.Q., M.B.D.), Division of Neuroradiology, and Department of Neurological Surgery (J.R.J., R.J.K., M.E.I.), Jackson Memorial Hospital/University of Miami Hospital, Miami, Florida.

Please address correspondence to Rostislav Medvid, MD, Jackson Memorial Hospital, Department of Radiology, 1611 NW 12th Ave, West Wing 279, Miami, FL 33136; e-mail: rostislav.medvid@jhsmiami.org

Indicates open access to non-subscribers at www.ajnr.org

http://dx.doi.org/10.3174/ajnr.A4362

Background

Minimally invasive stereotactic tumor ablation is a viable option for the treatment of benign and malignant intracranial lesions. Surgical excision constitutes first-line therapy for many malignant brain tumors followed by chemotherapy and/or radiation therapy. Aggressive complete resection or surgical debulking of newly diagnosed glioblastoma (GBM) improves survival,[3] compared with chemotherapy and radiation therapy alone.[4,5] A problem arises when patients do not qualify for surgical resection due to the presence of deep-seated lesions, low functional scores, comorbidities, or an inability to tolerate general anesthesia. In such cases, survival is limited; this outcome underscores the need for minimally invasive alternatives. In the case of inoperable brain metastases, stereotactic radiosurgery (SRS) presents a viable minimally invasive option. SRS achieves an 80%–90% local control rate over metastatic lesions[6,7] but plays a limited role in the treatment of glioma or medically intractable seizures. Metastatic recurrence after SRS and whole-body radiation therapy is common, with estimates of up to 46.8% at 1-year follow-up.[8] Repeat use of radiation therapy after recurrence is limited due to concerns about cumulative adverse radiation effects, such as radiation necrosis.

Delayed radiation necrosis (RN) is a known complication of SRS, with reported rates ranging from 5% to 50%.[9] The true incidence of RN in the setting of prior SRS is unknown because of

diagnostic difficulties in distinguishing RN and recurrence. Imaging-wise, radiation necrosis and tumor recurrence can both appear as enlarging previously treated lesions with a variable increase in internal enhancement or as a new thickening and/or irregularity of a peripherally enhancing rim with surrounding edema.[10] Although commonly used modalities such as MR perfusion imaging, MR imaging spectroscopy, SPECT, and PET may provide useful clues about the identity of a previously treated enlarging lesion, their utility is limited. Current MR imaging and MR spectroscopy concepts under investigation include lesion quotient,[11] T1/T2 mismatch,[12] percentage signal recovery,[13] relative cerebral blood volume,[14] and multivoxel proton MR spectroscopy,[15] but specificities and sensitivities are variable. Unfortunately, the specificity of biopsy can also be low due to sampling error.[16] Definitive diagnosis is further limited because up to 33% of enlarging lesions after treatment with SRS represent a combination of RN and recurrence rather than a pure form of either entity.[17] Given the common coexistence of RN and recurrence, Rao et al[18] postulated that an ablation technique such as LITT, which treats both RN and recurrent metastatic lesions, may circumvent diagnostic difficulties by providing the same standardized treatment for both types of lesions.

Another entity that could benefit from minimally invasive treatment is epilepsy. One-third of seizures are refractory to pharmacologic therapy. The success rate of additional pharmacologic therapy after 2 failed regimens is $\leq$3%.[19] In the setting of medically intractable seizures, open resection of well-defined epileptic foci has been shown to achieve a control rate of up to 75%–80%.[20] However, many of the lesions are deep-seated, requiring excessive dissection during resection, thus increasing the risk of iatrogenic complications and residual permanent neurologic deficits. Minimally invasive procedures such as SRS and radiofrequency ablation are currently of limited utility in the treatment of epilepsy due to the inability to visualize ablation in real-time.

The ideal minimally invasive procedure should reduce intra- and postoperative morbidity and mortality, shorten hospital stays, decrease health care costs, and offer effective treatment options to patients who are otherwise not eligible for open surgery or other debulking treatments. To date, multiple modalities have been used for stereotactic lesion ablation, including cryoablation, radiofrequency, sonography, microwave, ionizing radiation, and laser. Recent technologic advances in laser ablation have significantly improved safety and efficacy by providing the ability to monitor ablation in real-time. Other advantages include shorter ablation times and sharper ablation zone boundaries. Both SRS and LITT can treat difficult-to-access lesions, can be performed with the patient under minimal sedation, and do not require discontinuation of ongoing systemic therapy. Although MRgLITT is an invasive intracranial procedure, which requires a burr-hole and possible general anesthesia, it provides a potential benefit over the noninvasive SRS: MRgLITT delivers nonionizing radiation to target lesions, thus avoiding long-term adverse radiation effects and theoretically allowing retreatment of the same lesion. However, the long-term effects of thermal necrosis have not yet been clearly elucidated.

Physics of MRgLITT

During LITT, photons emitted from a fiberoptic laser are absorbed by tumor chromophores, organic molecules that absorb, transmit, and reflect light. Light absorption leads to molecular excitation and subsequent release of thermal energy within the target tissue. Thermally induced irreversible cell damage occurs between temperatures of 46°C and 60°C.[21] Temperatures above 60°C result in instantaneous coagulation necrosis.[22] The absorption coefficient determines the extent of photon absorption within a target tissue. In general, the absorption coefficient of pathologic lesions and coagulation necrosis is higher than that in normal brain parenchyma, leading to preferential ablation of the target tissue.[23] There is a sharp temperature fall-off at the border of the ablation zone,[24] creating a sharp margin between viable and nonviable tissue, which can be monitored with real-time MRI thermal imaging (MRTI).

Proton resonance frequency is the most widely used temperature-sensitive MR imaging parameter for real-time MRTI.[25] Proton resonance frequency–based MRTI is the basis of MRgLITT. The physical mechanism of proton resonance frequency–based MRTI depends on the presence of hydrogen bonds within a tissue.[26-28] As the temperature increases, the number of hydrogen bonds decreases. This decrease leads to a more uniform distribution of electron clouds within a molecule. The more evenly distributed electron clouds are better able to shield the ^{1}H nuclei from the full force of the external magnetic field supplied by the MR imaging machine. Thus, as the temperature increases, the local magnetic field experienced by a ^{1}H nucleus decreases due to increased shielding by the surrounding electrons. The decrease in the local magnetic field decreases the Larmour precession frequency of the ^{1}H nucleus, which, in turn, alters the phase of gradient recalled-echo phase images.[25] Measurements are obtained by subtracting "thermal" fast-spoiled gradient recalled phase images (obtained after administration of thermal energy) from a "reference" fast-spoiled gradient recalled phase image (obtained at body temperature before any energy pulse is delivered).[26,27] The phase difference, or phase shift, between the 2 images is proportional to the overall temperature change. As such, proton resonance frequency–based MRTI does not measure the absolute temperature of a sample, but simply measures the temperature difference between the sample and a designated reference temperature image.[25,28] Temperature information and time of ablation can be incorporated into a mathematic model of thermal tissue destruction (Arrhenius model) to provide a real-time quantitative estimate of tissue necrosis,[29] displayed in real-time as an orange "damage zone" (Fig 1).

LITT Setup and Procedure

Two major LITT platforms are in use today. NeuroBlate (Monteris Medical Corporation, Minneapolis, Minnesota), which received 510(k) FDA clearance in May 2009, uses a 12-W 1064-nm neodymium-doped yttrium aluminium garnet laser with a CO_2 cooled side-firing probe.[30] Visualase (Medtronic, Minneapolis, Minnesota), which received FDA clearance in 2007, is the platform used in our institution. The major components of the Visualase system include a 15-W 980-nm diode laser, a disposable saline-cooled diffusing laser applicator probe with a 1-cm-long

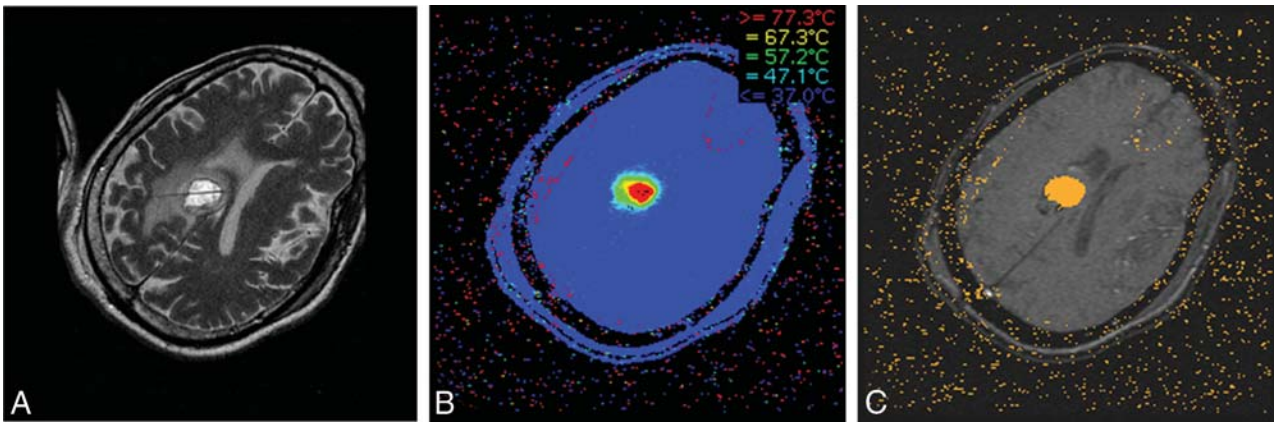

FIG 1. Once the location of the laser probe is confirmed, ablation can proceed. *A*, T2 image demonstrates a properly positioned laser probe within a metastatic melanoma lesion. *B*, Heat map: during ablation, temperatures surrounding the laser tip are continuously updated and depicted with various colors. *C*, Damage zone images: orange color depicts the area of tissue that has been successfully ablated (damage zone) on the basis of the Arrhenius model of thermal tissue ablation.

1.65-mm diameter outer cooling catheter, and a computer workstation, which communicates with MR imaging. MRTI generates "thermal" images, which are then used to generate "damage" images (Fig 1). Treatment concludes when the "damage zone" in a damage image covers the entire target area. The software allows the programming of temperature limit points near the tip of the probe and in the periphery of the lesion. If temperatures exceed the programmed thresholds, the laser shuts down automatically. Recommended temperature limit points are 90°C near the tip of the probe as a safeguard against overheating, carbonization, and vaporization and 50°C at the periphery to prevent damage to adjacent normal brain tissue.[31]

The procedure can be performed with the patient under light sedation or general anesthesia, depending on patient positioning and preference. The preoperative MR imaging examination identifies the target lesion and entry site. Using intraoperative neuronavigation, we make a small burr-hole by using a twist drill. A bone anchor is then placed into the skull in the exact target trajectory identified by neuronavigation. The cooling catheter is advanced through the anchor to the desired target and fixed to the bone anchor. The laser probe is then inserted into the cooling catheter and locked into place. T2 imaging is performed to confirm the exact placement of the probe (Fig 1*A*). Fast-spoiled gradient recalled phase images are obtained at the patient's body temperature to serve as a baseline for all intraprocedural thermal measurements. Once the cooling system begins to circulate, a test pulse of 3–4 W for 30–60 seconds is administered to determine the exact location of the distal 1-cm segment of the laser probe. This is important because thermal energy is emitted from the distal-most 1- cm segment of the laser fiber, and knowing its exact location within the target lesion is crucial to ensuring the accuracy of ablation. Ablation is performed by applying treatment doses of 10–15 W for 30–180 seconds until the damage zone covers the entire area of the target lesion. After completion of the procedure, we remove the probe, catheter, and anchor and close the small skin puncture site with a running Monocryl stitch (Ethicon, Cincinnati, Ohio). The reported average hospital stay varies, but most studies report 24–48 hours for cases without complications.[29,31-33]

Imaging Protocol

On the day before the procedure, a contrast-enhanced T1WI fiducial study is performed for neuronavigation purposes and to provide a map of the surrounding vasculature. The neuroradiologist assesses change in lesion size, appearance, and enhancement. Gradient recalled echo or susceptibility sequences are used to assess acute intracranial hemorrhage, which may be confirmed on follow-up CT. Acute intracranial hemorrhage is a contraindication to MRgLITT because of the risk of increased postprocedural hemorrhage, edema, and the resultant increase in intracranial pressure. Additionally, the presence of blood products can lead to suboptimal lesion ablation due to the propensity of blood to absorb heat emitted from the laser probe.

On the day of the procedure, the patient is taken to the operating room, where the probe is surgically advanced into the lesion as described above. The patient is then transferred to the MR imaging suite, where probe tip placement is confirmed. Intraoperative imaging and ablation are performed using a head coil capable of accommodating the MR imaging calvarial bone anchor, cooling catheter, and laser probe. Intraprocedural MRTI allows the neurosurgeon to visualize ablation in real-time. This is particularly useful for lesions located adjacent to fluid-filled structures with internal flow, such as vessels or ventricles. Structures with internal flow are potential sources of heat loss via a flow-induced heat sink effect, which can lead to asymmetric ablation of adjacent target lesions. MRTI can detect suboptimal heating within a segment of the lesion, thus prompting the neurosurgeon to apply additional energy until ablation throughout the entire lesion is achieved.

Immediate postprocedural contrast-enhanced T1WI is performed to evaluate the effectiveness of ablation. An additional contrast-enhanced study is performed 24 hours after the procedure to better characterize the ablated lesion. Additionally, because MRgLITT-treated lesions evolve in a somewhat predictable manner (discussed below), this study serves as a baseline for all follow-up imaging. The role of the neuroradiologist is to be able to recognize the normal temporal radiographic evolution of a treated lesion and to differentiate it from disease recurrence. Specific imaging pearls are discussed in the following sections.

MRTI Artifacts

The accuracy of MRTI can be hindered by the following: 1) susceptibility artifacts from calcifications or pre-existing surgical hardware, 2) the presence of fat, 3) misregistration artifacts due to motion, and 4) magnetic field inhomogeneities. In general, if a lesion cannot be adequately visualized, then ablation should not be attempted. Large amounts of susceptibility artifacts adjacent to a lesion are a relative contraindication to MRgLITT, though no publications exist in support of this claim, to our knowledge. The presence of intralesional calcifications has not been addressed in the literature, but we have verbal confirmation from Visualase representatives of successful treatment of partially calcified lesions at other institutions (in conversation with David Simon, PhD, January 22, 2015). The presence of fat is a potential source of susceptibility in proton resonance frequency–based MRTI because fat does not contain hydrogen bonds.[27] The lack of hydrogen bonds in fat makes proton resonance frequency less susceptible to temperature change, thus leading to inaccurate temperature measurements and susceptibility effects.[26,27] This characteristic implies that ablation of fat-containing lesions cannot be accurately monitored with proton resonance frequency–based MRTI. To our knowledge, there are no published reports on the use of MRgLITT in the treatment of fat-containing lesions. Misregistration artifacts from motion can be prevented with mechanical immobilization of the cranium, proper sedation, and stabilization of the laser tip with a bone anchor. Magnetic field inhomogeneities can be eliminated by subtracting baseline reference images from thermal images.[25]

Imaging and Radiologic-Pathologic Correlation of Lesions Treated with LITT

Ablated lesions demonstrate a thin peripheral rim of enhancement, variable T1 and T2 central signal due to presence of blood and protein products and surrounding edema on T1WI contrast-enhanced images obtained 24 hours after treatment. At the microscopic level, these changes correspond to 5 histologically separate concentric zones (Fig 2).[34] At the core is the probe track, which may be filled with CSF or blood. The probe track is surrounded by the central zone of coagulation necrosis, which contains damaged cell membranes and stains positive for markers of apoptosis. On 24-hour follow-up, the central zone may appear hyperintense on T1 and hypointense on T2 because of the presence of subacute blood products and protein coagulation. Alternatively, it may appear hypointense on T1 and hyperintense on T2, depending on the age of the blood products and relative concentration of protein.

The peripheral zone makes up the next concentric layer, which contains thrombosed vessels and distended cell bodies. This area undergoes delayed liquefaction necrosis and tends to enlarge during the first 1–40 days, followed by a continuous reduction in size thereafter.[35] On MR imaging, this layer appears hypointense on T1 and hyperintense on T2 due to edema. The peripheral zone contains a thin peripherally enhancing rim on T1-weighted contrast-enhanced images, secondary to blood-brain barrier damage. The peripheral rim gradually changes in circumference and enhancement in accordance with changes in the entire peripheral zone. It generally decreases with time or may remain stable (Fig 3). Residual enhancement persists on long-term-follow-up, likely due to reactive inflammatory/granulation tissue. According to Rao et al,[18] most lesions re-

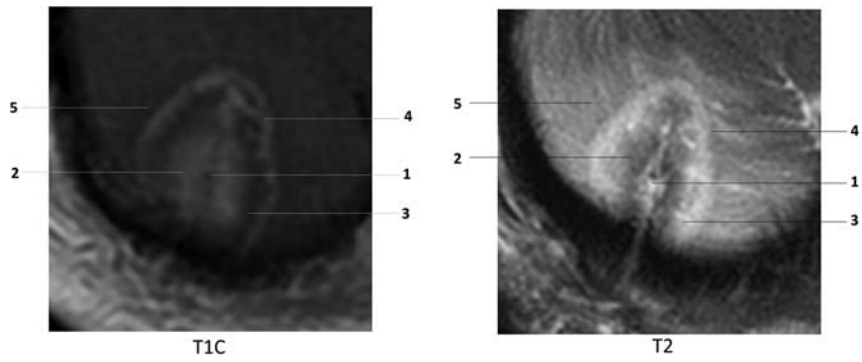

FIG 2. Concentric zones: T1 contrast-enhanced (T1C) and T2WI 24 hours after laser ablation of a recurrent right cerebellar metastatic lesion in a 71-year-old female patient with history of breast carcinoma: 1) probe track, 2) central zone, 3) peripheral zone, 4) peripherally enhancing rim, 5) marginal zone. Note that the concentric zones appear as inverse images on T1C and T2 images.

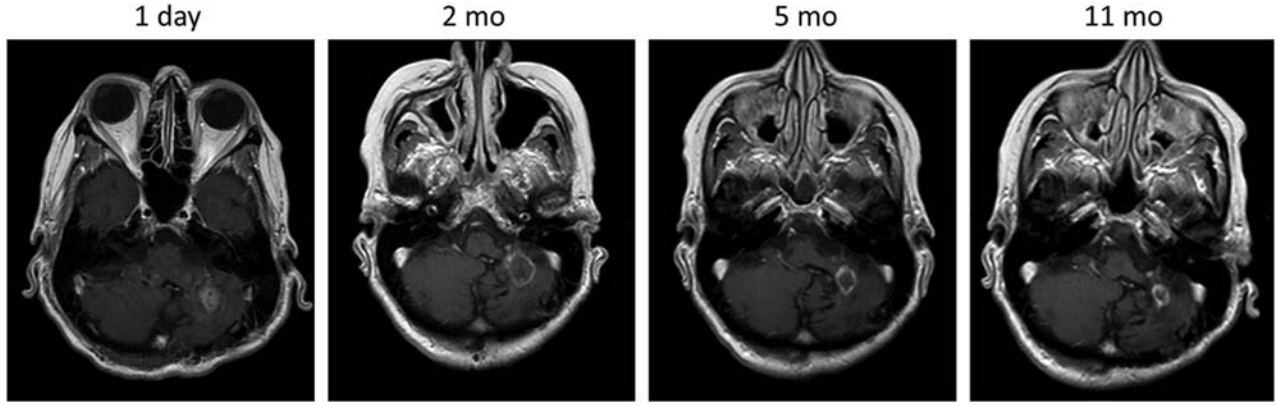

FIG 3. T1 contrast-enhanced images demonstrating the normal evolution of a LITT-treated metastatic left cerebellar lesion, which recurred after SRS in a 70-year-old female patient with history of ovarian adenocarcinoma. Note the expected increase in the size of the treated lesion at 2-month follow-up and a steady decrease in size on subsequent follow-up.

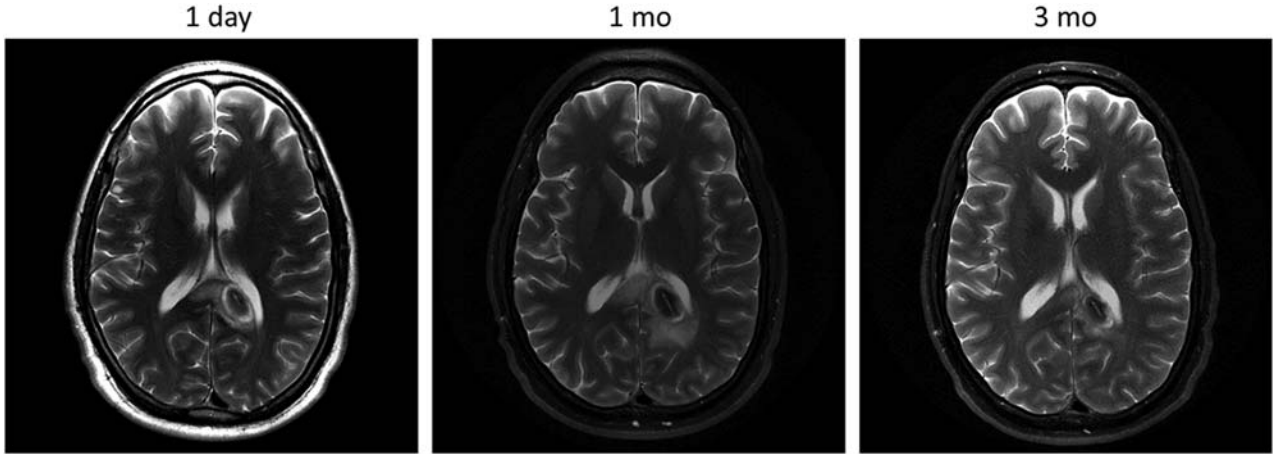

FIG 4. T2WI demonstrating the normal evolution of an LITT-treated left splenial low-grade astrocytoma in a 30-year-old male patient with a history of type 1 neurofibromatosis. Note the expected increase in the size of the lesion and marginal zone at 1-month follow-up and subsequent decrease at 3 months.

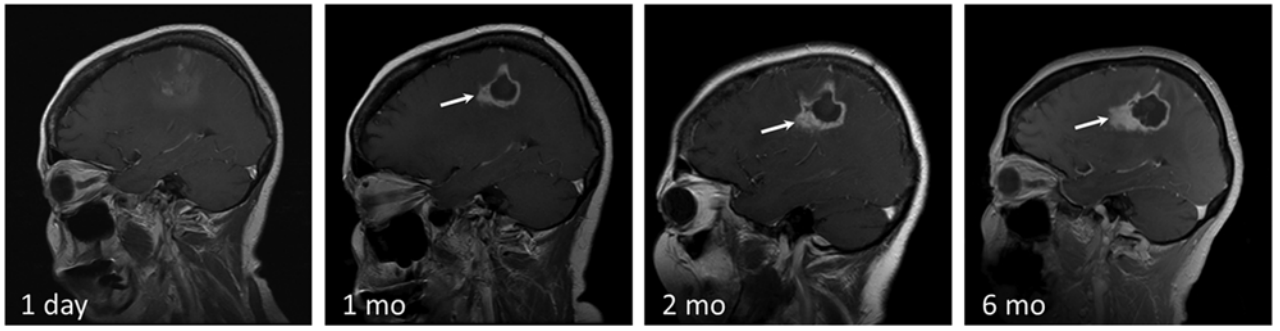

FIG 5. Disease recurrence after treatment with LITT. T1 contrast-enhanced images in a 58-year-old man with GBM status post surgical excision, chemoradiation, and SRS for a recurrent left parietal lobe lesion. The second recurrence was treated with LITT. Note irregular peripheral nodular enhancement at 1-month follow-up (*white arrow*), which progressively increases in size at 2 and 6 months. Findings are consistent with disease recurrence.

turn to pretreatment size within 16 weeks. The outermost layer of the LITT lesion is the marginal zone, an area of reversible post-surgical perifocal edema, which appears hypointense on T1 and hyperintense on T2. This layer contains viable edematous tissue and demonstrates axonal swelling without thrombosis. It increases in size, reaching maximum dimensions at 1–3 days and gradually decreases in size during the course of 15 days to 2 months (Fig 4). In some cases, the marginal zone may demonstrate high T1 signal without corresponding susceptibility artifacts, likely due to the presence of myelin breakdown products. Patients are instructed to return for follow-up 1 month after ablation. Depending on imaging findings, clinical presentation, and type of disease, subsequent follow-up may be performed on a monthly basis or may be extended to longer intervals. There are no official follow-up recommendations.

Recurrence

Serial follow-up performed >40 days after the procedure should demonstrate a continuous decrease in the size of the ablated lesion and stable or decreased enhancement (Fig 3). Overall, the entire ablated lesion decreases to 50% of its original size within 93 days of treatment[35] and continues to decrease in size for 6–15 months, becoming more homogeneous in appearance. Peripheral enhancement that persists or gradually decreases in size is a sign of the normal evolution of the ablated lesion. Any interval increase in lesion size, heterogeneity, peripheral nodular enhancement, restricted diffusion, CBF/CBV, and surrounding edema in a lesion treated >40–60 days prior should raise suspicion for recurrence (Fig 5).[36,37] Recurrence usually occurs within the peripheral rim of enhancement and presents as new or enlarging peripheral enhancing nodularity (Figs 5) or simply as thickening of the rim of enhancement (Fig 6). Comparison with prior images is vital in monitoring tumor recurrence because normally evolving lesions can demonstrate asymmetric enhancement similar to that of recurring lesions. Therefore, irregularly enhancing lesions require close-interval follow-up. Any increase in size, enhancement, or surrounding edema should be further assessed with adjunctive techniques such as MR spectroscopy, perfusion imaging, or PET.

Clinical Applications

Studies during the past 20 years report the use of LITT to treat a variety of brain lesions. The most studied lesions include glioma[2,30,31,33,38-48] and metastases.[2,18,29,32,40,41,44,49-51] Epilepsy[51-55] and radiation necrosis[50,56] represent a much smaller subset of treated lesions reported in the literature. Additionally, MRgLITT has been used to treat refractory cerebral edema[57] and tumors such as ependymoma, meningioma, primitive neuroectodermal tumor, hemangioblastoma, and chordoma.[31,58] The sur-

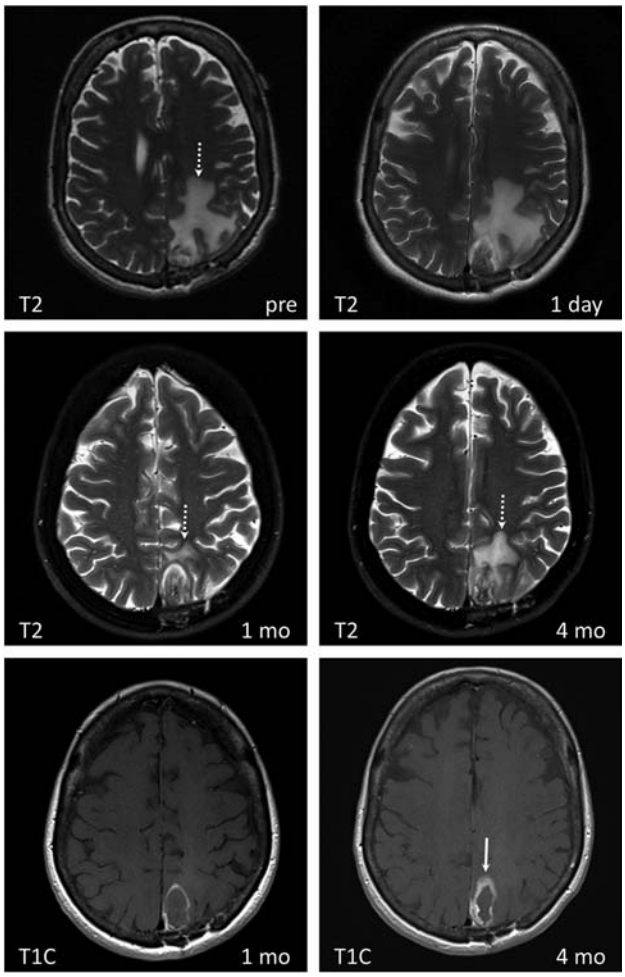

FIG 6. LITT of radiation necrosis with subsequent disease recurrence in a 68-year-old female patient with lung squamous cell carcinoma status post surgical excision and SRS of a metastatic brain lesion in the left parietal lobe, which subsequently resulted in radiation necrosis. Medically intractable radiation necrosis was treated with LITT. Pre-LITT imaging demonstrated an enhancing lesion in the left parietal lobe on T1 contrast-enhanced (not shown) with significant vasogenic edema on T2 images (*dashed white arrow* on T2 image labeled "pre"). Dynamic imaging pre-LITT (not shown) did not demonstrate a significant increase in CBF or CBV. The patient was not treated with bevacizumab, and RN was favored over recurrence. Note a significant decrease in vasogenic edema 1 month after treatment (*dashed white arrow*), coinciding with symptomatic improvement. T2 images obtained at 4-month follow-up demonstrate a significant increase in peritumoral vasogenic edema. There is significant thickening of the peripheral zone of enhancement (*white arrow*) on T1 contrast-enhanced images at 4 months compared with 1 month. Findings are concerning for tumor recurrence within a treated RN lesion, which was corroborated on PET CT (not shown).

vival benefits of LITT after treatment of various brain lesions vary from favorable to statistically insignificant. Evidence is limited because to date, all studies consist of noncontrolled, nonrandomized retrospective reports, case series, or case reports, thus predisposing to selection bias. Many of the studies mix multiple disease entities to increase the number of enrolled subjects; this mixture makes the evaluation of survival benefits for a given disease entity difficult. Another major limitation is the use of variable inclusion criteria by selecting patients with either recurrent, newly diagnosed, previously treated, or untreated tumors or a mixture of any of the above. However, the above studies offer a plethora of evidence on the safety profile of the procedure. The variable complications of MRgLITT will be addressed below after a brief discussion of the 4 most common indications for the procedure: gliomas, metastatic lesions, radiation necrosis, and medically intractable epilepsy.

Gliomas

Gliomas are subdivided into multiple subtypes, of which GBM is the most common primary brain neoplasm in adults. Median survival of newly diagnosed patients after treatment with maximal safe resection, radiation therapy, and adjuvant chemotherapy is 12–15 months.[59] Survival decreases with inoperable deep-seated lesions. GBM poses multiple treatment challenges due to its diffusely infiltrative nature and strong resistance to therapy. As a result, all GBMs recur, and median survival after recurrence is 3–5 months.[60] Surgical resection increases survival but is not feasible in cases of difficult-to-access tumors, thus the need for minimally invasive surgical procedures. The use of SRS in newly diagnosed GBM demonstrated no survival benefit,[61] while data on MRgLITT are inconclusive. Local therapies, such as MRgLITT, SRS, or open surgical resection, do not address the infiltrative component of GBM and can only be used for palliative/salvage therapy. Examples of MRgLITT-treated gliomas are provided in Figs 4 and 5.

Metastatic Brain Tumors

Metastatic brain tumors are 10 times more prevalent than primary brain tumors, accounting for approximately 200,000 cases of the total of 225,000 cases of brain tumors per year.[32] The incidence of brain metastases is increasing due to effective oncologic treatments of primary malignancies, resulting in longer survival. The first-line treatment for new brain metastatic lesions is radiation therapy (with SRS, whole-brain radiation therapy, or both) and surgical resection.[29] Local recurrence within 1 year of treatment is approximately 10% after resection and radiation therapy, compared with 46% after surgical resection alone.[62] Similar to GBM, no consensus exists on the treatment of recurrent metastatic brain lesions, and repeat use of radiation therapy is limited due to concerns over adverse cumulative radiation effects. To date, studies have shown that MRgLITT is a safe, minimally invasive alternative. Further evidence is needed to determine whether there are definitive survival benefits over currently accepted treatments. Examples of treated metastatic lesions are provided in Figs 1–3 and 6.

Radiation Necrosis

Radiation necrosis is a common entity in neuro-oncology. Estimated incidence varies between 5% and 10% for all radiation therapy modalities, but the risk may be as high as 50% in the setting of prior SRS, particularly at treatment doses between 16 and 22 Gy.[9] RN, also known as delayed neurotoxicity, represents a specific type of radiation injury and occurs at least 3 months after radiation therapy. The process is irreversible, and approximately 85% of cases occur within 2 years of treatment.[10] Histologically, RN consists of a central zone of necrosis surrounded by a peripheral zone of altered astrocytes, which release large quantities of proinflammatory factors such as hypoxia-inducing factor 1α and

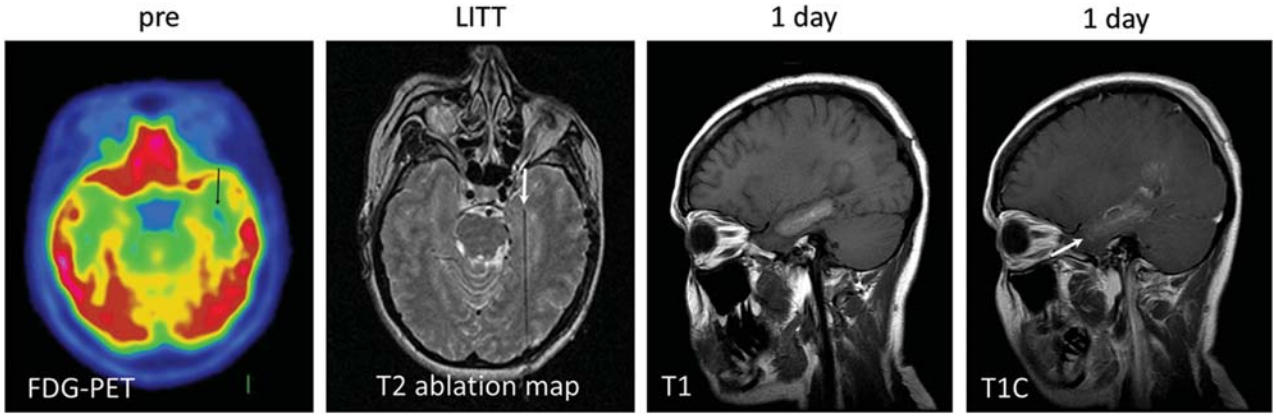

FIG 7. Mesial temporal sclerosis confirmed on preprocedural FDG-PET (*black arrow*), which showed decreased FDG uptake in the left hippocampal/parahippocampal region. The lesion was not noted on prior contrast-enhanced MR imaging and did not demonstrate enhancement (not shown). Intraprocedural T2 ablation map demonstrates the laser probe tip within the left medial temporal lobe (*white arrow*). TI and TI contrast-enhanced images 24 hours after LITT demonstrate an oval, rather than round, postablation lesion with signal characteristics similar to those of contrast-enhancing lesions (see Fig 2). The elongated shape is due to sequential probe retraction during ablation to cover the entire left hippocampo-amygdalar area.

vascular endothelial growth factor, inducing severe inflammation and edema.[63] First-line treatment is steroids to decrease inflammation. A new effective non-FDA-approved treatment is bevacizumab, a humanized mouse monoclonal vascular endothelial growth factor antibody acting as vascular endothelial growth factor inhibitor, though its use is limited due to high cost, increased risk of deep venous thrombosis and pulmonary emboli, and the need to stop other concurrent systemic therapy.[9] Surgical resection is reserved for medically refractory RN, but its role is limited in the setting of deep or difficult-to-access lesions and in patients with multiple comorbidities who are unable to tolerate general anesthesia. LITT induces resolution of RN,[50,56] but long-term data are limited due to low numbers and lack of sufficient long-term follow-up. The postulated mechanism of action of LITT in the setting of RN is ablation of the peripheral zone of altered astrocytes, thus terminating the proinflammatory signaling cascade induced by vascular endothelial growth factor.[9] Figure 6 demonstrates an example of MRgLITT-treated RN in which metastatic disease subsequently recurred.

Epilepsy

Medically intractable focal epilepsy is generally treated with surgical resection of epileptic foci. Given the deep location of many seizure foci, surgical resection can be difficult and can leave patients with persistent neurologic and cognitive deficits secondary to collateral tissue damage. Available minimally invasive treatment options such as SRS[64,65] and RF ablation[65] offer the potential benefit of decreasing iatrogenic complications, but the inability to monitor ablation in real-time diminishes their margin of safety. A pilot study by Curry et al[52] first demonstrated the feasibility of MRgLITT in the successful treatment of medically intractable epileptic foci. To date, studies report laser ablation of tuberous sclerosis, hypothalamic hamartoma, mesial temporal sclerosis, cortical dysplasia, and periventricular nodular hyperplasia with follow-up ranging from 2 to 13 months.[51-54] Seven of a total of 9 patients remained seizure-free at 6- to 13-month follow-up, depending on the study. The remaining 2 patients experienced seizure recurrence at 2 and 3 months after LITT and underwent subsequent definitive open surgical treatment.[52,54] This result suggests that MRgLITT does not preclude future invasive therapy. Given these findings, Esquenazi et al[54] postulated that laser ablation could be used as a first-line treatment for deep-seated medically intractable epileptic foci and that surgical resection be reserved for patients who fail therapy with LITT. More recently, a report by Willie et al[55] showed that seizure-free rates for mesiotemporal epilepsy by using MRgLITT closely approximate those of open temporal lobectomies while potentially improving postprocedural neurocognitive outcomes. Figure 7 provides an imaging example of ablation of the left hippocampo-amygdalar area to treat mesial temporal sclerosis.

Complications

Although the survival benefits and clinical outcomes of MRgLITT are difficult to estimate on the basis of the currently available studies, enough data are available to evaluate the safety profile of the procedure. We performed an analysis of all LITT studies conducted on human subjects to date with complications as an end point. We tallied the different complications and calculated their rates. The most common reported complication of LITT is transient neurologic deficit, accounting for 13% of all complications. Reported symptoms include dysphagia, weakness, hemianopsia, or minor seizures. The symptoms either resolved spontaneously or responded to steroid administration within days to weeks.

The next most common complications include new progressive or permanent neurologic symptoms (3%), intracranial hemorrhage (2.5%), infection (2.5%), and deep venous thrombosis (2.5%). Life-threatening complications include intracranial hemorrhage, ventriculitis, meningitis, and 1 case of refractory intracranial hypertension after simultaneous use of multiple probes to treat a large irregular lesion.[31,33,48,51] Two deaths have been reported, both in patients with GBM, one from intractable intracranial hemorrhage and the other from meningitis.[48,51] Sloan et al[33] suggested that pretreatment MRA or CTA and fiber-tract imaging with DTI may be useful modalities in presurgical planning to identify and potentially avoid critical vascular and white matter structures. Jethwa et al[58] recommended that LITT treatment of lesions of >3 cm

should be staged. Administration of high-dose preprocedural steroids should be considered.[31]

CONCLUSIONS

LITT appears to be a safe palliative alternative for the treatment of malignant high-grade gliomas and recurrent metastatic lesions. While several life-threatening complications have been reported in the setting of GBM, preliminary data suggest that their overall incidence is acceptably low. Furthermore, the incidence of such complications may be decreased with appropriate preoperative imaging and as neurosurgeons overcome the steep learning curve associated with the procedure. Because research on the use of MRgLITT is in its infancy, indications and contraindications are relative and are still being worked out. The most common post-procedural complications of MRgLITT are non-life-threatening and transient. LITT may also provide a safe curative option in cases of radiation necrosis and in certain types of medically intractable epilepsy.

REFERENCES

1. Bown S. **Phototherapy in tumors.** *World J Surg* 1983;7:700–09
2. Sugiyama K, Sakai T, Fujishima I, et al. **Stereotactic interstitial laser-hyperthermia using Nd-YAG laser.** *Stereotact Funct Neurosurg* 1990;54:501–05
3. Sanai N, Polley MY, McDermott MW, et al. **An extent of resection threshold for newly diagnosed glioblastomas.** *J Neurosurg* 2011;115:3–8
4. Simpson JR, Horton J, Scott C, et al. **Influence of location and extent of surgical resection on survival of patients with glioblastoma multiforme: results of three consecutive Radiation Therapy Oncology Group (RTOG) clinical trials.** *Int J Radiat Oncol Biol Phys* 1993;26:239–44
5. Vuorinen V, Hinkka S, Färkkilä M, et al. **Debulking or biopsy of malignant glioma in elderly people—a randomised study.** *Acta Neurochir (Wien)* 2003;145:5–10
6. Loeffler JS, Barker FG, Chapman PH. **Role of radiosurgery in the management of central nervous system metastases.** *Cancer Chemother Pharmacol* 1999;43(suppl):S11–14
7. Young RF. **Radiosurgery for the treatment of brain metastases.** *Semin Surg Oncol* 1998;14:70–78
8. Aoyama H, Shirato H, Tago M, et al. **Stereotactic radiosurgery plus whole-brain radiation therapy vs stereotactic radiosurgery alone for treatment of brain metastases: a randomized controlled trial.** *JAMA* 2006;295:2483–91
9. Rahmathulla G, Marko NF, Weil RJ. **Cerebral radiation necrosis: a review of the pathobiology, diagnosis and management considerations.** *J Clin Neurosci* 2013;20:485–502
10. Shah R, Vattoth S, Jacob R, et al. **Radiation necrosis in the brain: imaging features and differentiation from tumor recurrence.** *Radiographics* 2012;32:1343–59
11. Dequesada IM, Quisling RG, Yachnis A, et al. **Can standard magnetic resonance imaging reliably distinguish recurrent tumor from radiation necrosis after radiosurgery for brain metastases? A radiographic-pathological study.** *Neurosurgery* 2008;63:898–903; discussion 904
12. Kano H, Kondziolka D, Lobato-Polo J, et al. **T1/T2 matching to differentiate tumor growth from radiation effects after stereotactic radiosurgery.** *Neurosurgery* 2010;66:486–91; discussion 491–92
13. Barajas RF, Chang JS, Sneed PK, et al. **Distinguishing recurrent intra-axial metastatic tumor from radiation necrosis following gamma knife radiosurgery using dynamic susceptibility-weighted contrast-enhanced perfusion MR imaging.** *AJNR Am J Neuroradiol* 2009;30:367–72
14. Mitsuya K, Nakasu Y, Horiguchi S, et al. **Perfusion weighted magnetic resonance imaging to distinguish the recurrence of metastatic brain tumors from radiation necrosis after stereotactic radiosurgery.** *J Neurooncol* 2010;99:81–88
15. Chernov M, Hayashi M, Izawa M, et al. **Differentiation of the radiation-induced necrosis and tumor recurrence after gamma knife radiosurgery for brain metastases: importance of multi-voxel proton MRS.** *Minim Invasive Neurosurg* 2005;48:228–34
16. Mullins ME, Barest GD, Schaefer PW, et al. **Radiation necrosis versus glioma recurrence: conventional MR imaging clues to diagnosis.** *AJNR Am J Neuroradiol* 2005;26:1967–72
17. Forsyth PA, Kelly PJ, Cascino TL, et al. **Radiation necrosis or glioma recurrence: is computer-assisted stereotactic biopsy useful?** *J Neurosurg* 1995;82:436–44
18. Rao MS, Hargreaves EL, Khan AJ, et al. **Magnetic resonance-guided laser ablation improves local control for postradiosurgery recurrence and/or radiation necrosis.** *Neurosurgery* 2014;74:658–67
19. Kwan P, Brodie MJ. **Early identification of refractory epilepsy.** *N Engl J Med* 2000;342:314–19
20. Téllez-Zenteno JF, Hernández Ronquillo L, Moien-Afshari F, et al. **Surgical outcomes in lesional and non-lesional epilepsy: a systematic review and meta-analysis.** *Epilepsy Res* 2010;89:310–18
21. Larson TR, Bostwick DG, Corica A. **Temperature-correlated histopathologic changes following microwave thermoablation of obstructive tissue in patients with benign prostatic hyperplasia.** *Urology* 1996;47:463–69
22. Goldberg SN, Gazelle GS, Mueller PR. **Thermal ablation therapy for focal malignancy: a unified approach to underlying principles, techniques, and diagnostic imaging guidance.** *AJR Am J Roentgenol* 2000;174:323–31
23. Yaroslavsky AN, Schulze PC, Yaroslavsky IV, et al. **Optical properties of selected native and coagulated human brain tissues in vitro in the visible and near infrared spectral range.** *Phys Med Biol* 2002;47:2059–73
24. McNichols RJ, Gowda A, Kangasniemi M, et al. **MR thermometry-based feedback control of laser interstitial thermal therapy at 980 nm.** *Lasers Surg Med* 2004;34:48–55
25. Rieke V, Butts Pauly K. **MR thermometry.** *J Magn Reson Imaging* 2008;27:376–90
26. De Poorter J, De Wagter C, De Deene Y, et al. **Noninvasive MRI thermometry with the proton resonance frequency (PRF) method: in vivo results in human muscle.** *Magn Reson Med* 1995;33:74–81
27. De Poorter J. **Noninvasive MRI thermometry with the proton resonance frequency method: study of susceptibility effects.** *Magn Reson Med* 1995;34:359–67
28. Quesson B, de Zwart JA, Moonen CT. **Magnetic resonance temperature imaging for guidance of thermotherapy.** *J Magn Reson Imaging* 2000;12:525–33
29. Carpentier A, McNichols RJ, Stafford RJ, et al. **Real-time magnetic resonance-guided laser thermal therapy for focal metastatic brain tumors.** *Neurosurgery* 2008;63(1 suppl 1):ONS21–28; discussion ONS28–29
30. Mohammadi AM, Schroeder JL. **Laser interstitial thermal therapy in treatment of brain tumors–the NeuroBlate system.** *Expert Rev Med Devices* 2014;11:109–19
31. Jethwa PR, Barrese JC, Gowda A, et al. **Magnetic resonance thermometry-guided laser-induced thermal therapy for intracranial neoplasms: initial experience.** *Neurosurgery* 2012;71(1 suppl operative):133–44; 144–45
32. Carpentier A, McNichols RJ, Stafford RJ, et al. **Laser thermal therapy: real-time MRI-guided and computer-controlled procedures for metastatic brain tumors.** *Lasers Surg Med* 2011;43:943–50
33. Sloan AE, Ahluwalia MS, Valerio-Pascua J, et al. **Results of the NeuroBlate System first-in-humans phase I clinical trial for recurrent glioblastoma: clinical article.** *J Neurosurg* 2013;118:1202–19
34. Schober R, Bettag M, Sabel M, et al. **Fine structure of zonal changes in experimental Nd:YAG laser-induced interstitial hyperthermia.** *Lasers Surg Med* 1993;13:234–41
35. Schwabe B, Kahn T, Harth T, et al. **Laser-induced thermal lesions in**

the human brain: short- and long-term appearance on MRI. *J Comput Assist Tomogr* 1997;21:818–25
36. Tracz RA, Wyman DR, Little PB, et al. **Magnetic resonance imaging of interstitial laser photocoagulation in brain.** *Lasers Surg Med* 1992;12:165–73
37. Tracz RA, Wyman DR, Little PB, et al. **Comparison of magnetic resonance images and the histopathological findings of lesions induced by interstitial laser photocoagulation in the brain.** *Lasers Surg Med* 1993;13:45–54
38. Bettag M, Ulrich F, Schober R, et al. **Stereotactic laser therapy in cerebral gliomas.** *Acta Neurochirurgica* 1992;52:81–83
39. Ascher P, Justich E, Schröttner O. **A new surgical but less invasive treatment of central brain tumours preliminary report.** *Acta Neurochirurgica* 1992;52:78–80
40. Roux FX, Merienne L, Fallet-Bianco C, et al. **Stereotaxic laser interstitial thermotherapy: a new alternative in the therapeutic management of some brain tumors** [in French]. *Neurochirurgie* 1992; 38:238–44
41. Kahn T, Bettag M, Ulrich F, et al. **MRI-guided laser-induced interstitial thermotherapy of cerebral neoplasms.** *J Comput Assist Tomogr* 1994;18:519–32
42. Leonardi MA, Lumenta CB, Gumprecht HK, et al. **Stereotactic guided laser-induced interstitial thermotherapy (SLITT) in gliomas with intraoperative morphologic monitoring in an open MR-unit.** *Minim Invasive Neurosurg* 2001;44:37–42
43. Leonardi MA, Lumenta CB. **Stereotactic guided laser-induced interstitial thermotherapy (SLITT) in gliomas with intraoperative morphologic monitoring in an open MR: clinical experience.** *Minim Invasive Neurosurg* 2002;45:201–07
44. Schulze P, Vitzthum H, Goldammer A, et al. **Laser-induced thermotherapy of neoplastic lesions in the brain– underlying tissue alterations, MRI-monitoring and clinical applicability.** *Acta Neurochir (Wein)* 2004;146:803–12
45. Schwarzmaier HJ, Eickmeyer F, von Tempelhoff W, et al. **MR-guided laser irradiation of recurrent glioblastomas.** *J Magn Reson Imaging* 2005;22:799–803
46. Schwarzmaier HJ, Eickmeyer F, von Tempelhoff W, et al. **MR-guided laser-induced interstitial thermotherapy of recurrent glioblastoma multiforme: preliminary results in 16 patients.** *Eur J Radiol* 2006;59:208–15
47. Carpentier A, Chauvet D, Reina V, et al. **MR-guided laser-induced thermal therapy (LITT) for recurrent glioblastomas.** *Lasers Surg Med* 2012;44:361–68
48. Mohammadi AM, Hawasli AH, Rodriguez A, et al. **The role of laser interstitial thermal therapy in enhancing progression-free survival of difficult-to-access high-grade gliomas: a multicenter study.** *Cancer Med* 2014;3:971–79
49. Hawasli AH, Ray WZ, Murphy RK, et al. **Magnetic resonance imaging-guided focused laser interstitial thermal therapy for subinsular metastatic adenocarcinoma: technical case report.** *Neurosurgery* 2012;70(2 suppl operative):332–37; discussion 338
50. Rahmathulla G, Recinos PF, Valerio JE, et al. **Laser interstitial thermal therapy for focal cerebral radiation necrosis: a case report and literature review.** *Stereotact Funct Neurosurg* 2012;90:192–200
51. Hawasli AH, Bagade S, Shimony JS, et al. **Magnetic resonance imaging-guided focused laser interstitial thermal therapy for intracranial lesions: single-institution series.** *Neurosurgery* 2013;73:1007–17
52. Curry DJ, Gowda A, McNichols RJ, et al. **MR-guided stereotactic laser ablation of epileptogenic foci in children.** *Epilepsy Behav* 2012;24:408–14
53. Tovar-Spinoza Z, Carter D, Ferrone D, et al. **The use of MRI-guided laser-induced thermal ablation for epilepsy.** *Childs Nerv Syst* 2013;29:2089–94
54. Esquenazi Y, Kalamangalam GP, Slater JD, et al. **Stereotactic laser ablation of epileptogenic periventricular nodular heterotopia.** *Epilepsy Res* 2014;108:547–54
55. Willie JT, Laxpati NG, Drane DL, et al. **Real-time magnetic resonance-guided stereotactic laser amygdalohippocampotomy for mesial temporal lobe epilepsy.** *Neurosurgery* 2014;74:569–84; discussion 584–85
56. Torres-Reveron J, Tomasiewicz HC, Shetty A, et al. **Stereotactic laser induced thermotherapy (LITT): a novel treatment for brain lesions regrowing after radiosurgery.** *J Neurooncol* 2013;113:495–503
57. Fabiano AJ, Alberico RA**. Laser-interstitial thermal therapy for refractory cerebral edema from post-radiosurgery metastasis.** *World Neurosurg* 2014;81:652.e1–4
58. Jethwa PR, Lee JH, Assina R, et al. **Treatment of a supratentorial primitive neuroectodermal tumor using magnetic resonance-guided laser-induced thermal therapy.** *J Neurosurg Pediatr* 2011;8:468–75
59. Stupp R, Mason WP, van den Bent MJ, et al. **Radiotherapy plus concomitant and adjuvant temozolomide for glioblastoma.** *N Engl J Med* 2005;352:987–96
60. Barker FG 2nd, Chang SM, Gutin PH, et al. **Survival and functional status after resection of recurrent glioblastoma multiforme.** *Neurosurgery* 1998;42:709–20; discussion 720–23
61. Souhami L, Seiferheld W, Brachman D, et al. **Randomized comparison of stereotactic radiosurgery followed by conventional radiotherapy with carmustine to conventional radiotherapy with carmustine for patients with glioblastoma multiforme: report of Radiation Therapy Oncology Group 93-05 protocol.** *Int J Radiat Oncol Biol Phys* 2004;60:853–60
62. Patchell RA, Tibbs PA, Regine WF, et al. **Postoperative radiotherapy in the treatment of single metastases to the brain: a randomized trial.** *JAMA* 1998;280:1485–89
63. Nonoguchi N, Miyatake S, Fukumoto M, et al. **The distribution of vascular endothelial growth factor-producing cells in clinical radiation necrosis of the brain: pathological consideration of their potential roles.** *J Neurooncol* 2011;105:423–31
64. Quigg M, Barbaro NM. **Stereotactic radiosurgery for treatment of epilepsy.** *Arch Neurol* 2008;65:177–83
65. Liscak R, Malikova H, Kalina M, et al. **Stereotactic radiofrequency amygdalohippocampectomy in the treatment of mesial temporal lobe epilepsy.** *Acta Neurochir (Wien)* 2010;152:1291–98

Multiple Procedure Payment Reduction: Health Policy Update

B. Rehani, J.A. Hirsch, W.P. Dillon, R.G. González, M.H. Lev, and P.W. Schaefer

ABSTRACT

SUMMARY: Multiple Procedure Payment Reduction currently applies to multiple diagnostic imaging services administered to the same patient during the same day and entails a 50% decrease in the technical component and a 25% decrease in the professional component reimbursement. This might change with time due to further legislation, so it is important to be up-to-date on these health policy developments.

ABBREVIATION: MPPR = Multiple Procedure Payment Reduction

The Multiple Procedure Payment Reduction (MPPR) has been a major challenge for radiology practice. Despite its criticality, there is a continued need to increase awareness regarding its implementation and resultant impact. This Health Care Reform Vignette aims to outline, in comprehensible terms, the effect of the MPPR on neuroradiologists and the specialty of radiology at large.

WHAT IS THE MULTIPLE PROCEDURE PAYMENT REDUCTION?

MPPR is a per-day Centers for Medicare and Medicaid Services reimbursement policy that applies across disciplines and across different practice settings. Imaging MPPRs apply to multiple diagnostic imaging services administered to the same patient on a single day. With an MPPR, Medicare fully reimburses the most expensive procedure; however, the second and all subsequent procedures are reduced by a specific percentage. Imaging-specific MPPRs are traditionally applied to advanced diagnostic imaging services, which the federal government defines as CT, MR imaging, and sonography.

As a result of the Balanced Budget Act of 2005,[1] the Centers for Medicare and Medicaid Services, through the 2006 Medicare Physician Fee Schedule Final Rule,[2] first applied an MPPR to the technical component of advanced diagnostic imaging services. The technical component of advanced diagnostic imaging represents reimbursement from Medicare for the cost of equipment, nonphysician personnel, and medical supplies in the office setting. In addition, the initial structure of the technical component MPPR policy applied to contiguous body parts within specific families of codes.

Congress and the Centers for Medicare and Medicaid Services continued to expand the scope of the technical component MPPR policy in subsequent years. In fact, the passage of the Patient Protection and Affordable Care Act[3] commonly referred to as "Health Care Reform," resulted in an increase in the technical component MPPR from 25% to 50%. In addition, the 2011 Medicare Physician Fee Schedule Final Rule expanded the scope of the technical component MPPR policy so that it applied to noncontiguous body parts, across different modalities. Although a small amount of efficiencies exist within the technical component when a single patient receives multiple advanced diagnostic imaging services, during the same session, on the same day, this amount is nowhere near 25%, to say nothing of 50%. The decision of the Supreme Court to uphold the constitutionality of the Patient Protection and Affordable Care Act ensured that the 50% technical component MPPR would remain in effect for multiple CT, MR imaging, and sonography procedures, including those services delivered on noncontiguous body parts across different modalities.

The concept of applying an MPPR to the professional component of advanced diagnostic imaging did not come under serious consideration by the federal government until 2011. The Medicare Payment Advisory Commission recommended that Congress apply a professional component MPPR to advanced diagnostic imaging services. The Medicare Payment Advisory Commission unanimously voted in favor of including the profes-

From the Departments of Neuroradiology (B.R., W.P.D.) and Radiology and Biomedical Imaging (B.R., W.P.D.), University of California, San Francisco, San Francisco, California; and Departments of Neuroradiology (J.A.H., R.G.G., M.H.L., P.W.S.) and Radiology (J.A.H., R.G.G., M.H.L., P.W.S.), Massachusetts General Hospital, Boston, Massachusetts.

Please address correspondence to Bhavya Rehani, MD, Neuroradiology, Dept of Radiology and Biomedical Imaging, UCSF, 1001 Poterero Avenue, SFGH 5, San Francisco, CA 94110; e-mail: bhavya.rehani@ucsf.edu

http://dx.doi.org/10.3174/ajnr.A4523

sional component MPPR recommendation within the June 2011 Annual Report to Congress.[4]

In July 2011, the Centers for Medicare and Medicaid Services, citing the June 2011 Medicare Payment Advisory Commission recommendation, included provisions in the 2011 Medicare Physician Fee Schedule Proposed Rule to apply a 50% multiple-procedure payment reduction to the professional component of advanced diagnostic imaging services. As a result of the effort of organized radiology, the Centers for Medicare and Medicaid Services elected to lower the professional component MPPR reduction to 25% in the Medicare Physician Fee Schedule Final Rule.[5]

Although the Final Rule included a cut of 25% rather than 50%, the policy was expanded in January 2013 so that it now applied to 2 different physicians interpreting multiple images from the same patient, during the same session, on the same day.[6,7] The progression is noteworthy. The Balanced Budget Act of 2005 introduced the technical MPPR to address perceived efficiencies in obtaining imaging of contiguous body parts. These perceived efficiencies are likely overstated. The interpretive component of advanced imaging enjoys very limited efficiencies when a single reader provides these services[8] as described above. It is difficult to posit even a perceived efficiency when 2 different physicians, potentially in separate locations, interpret images of contiguous body parts in the same patient.

WHAT IS A PRACTICAL EXAMPLE OF APPLICATION OF MPPR?

As an example, a hypothetic patient presents to the emergency department with symptoms of a stroke. With an imaging strategy that helps to illustrate the MPPR point, a CT of the head/CT angiography of the neck and head followed perhaps by an MR imaging of the brain are performed on the same day. The MR imaging of the brain, which is the most expensive procedure, will be reimbursed at 100%; however, under the MPPR, the reimbursement of both the CTA and CT of the head will be decreased, the technical component by 50% and the professional component by 25%.

WHAT IS THE OBJECTIVE BASIS FOR MPPR?

It has been suggested that there is no scientific rationale behind the application of a professional component MPPR, especially because the radiologist is morally and professionally obliged to spend an equal amount of time, energy, and expertise interpreting multiple patient images, irrespective of technique or section of the body under review. On a more objective basis, a June 2011 peer-reviewed study published in *Journal of the American College of Radiology*[8] found that the gained efficiency in professional component interpretations under the MPPR rules only ranged from a minimum of 2.96% for CT to a maximum of 5.45% for sonography.[9]

The patients who undergo multiple imaging studies in a single session are often those with the most complex conditions seen by radiologists. These include patients with stroke, severe trauma, or suspicion of metastatic cancer. The effort required by radiologists when interpreting multiple imaging studies on the same patient, during the same session, on the same day, is often more intense, rather than less. Per above, it is difficult to comprehend what argument could be advanced to explain supposed efficiencies obtained by different radiologists interpreting contiguous body parts on the same day.

WHAT IS HR 4302?

HR 4302, the Protecting Access to Medicare Act, signed into law in April 2014, included provisions specifically addressing the 25% professional component Multiple Procedure Payment Reduction. HR 4302/S. 1020, the Diagnostic Imaging Services Access Protection Act, was bipartisan, bicameral legislation, which temporarily prevented the impending 24% cut associated with the flawed sustainable growth rate formula from going into effect for 12 months. With respect to the professional component MPPR, language was included in HR 4302 mandating that the Centers for Medicare and Medicaid Services disclose the specific data that were used in the 2012 Medicare Physician Fee Schedule Final Rule when the 25% reimbursement decrease was initially proposed.[9] Despite this being established law, the specific data have not been shared with organized radiology or the public yet. More recently, HR 6, the 21st Century Cures Act (Section 4003), unanimously passed out of the House Energy and Commerce Committee to repeal the professional component payment reduction of MPPR.

ACKNOWLEDGMENTS

We thank the American College of Radiology Government Relations Department: Chris Sherin, Josh Cooper, and Ted Burnes.

Disclosures: Joshua A. Hirsch—*UNRELATED*: *Consultancy*: Medtronic, CareFusion, *Comments*: Medtronic, ongoing consultancy related to interventional spine; CareFusion, single, non-Continuing Medical Education course; *Stock/Stock Options:* InNeurCo, Intratech, *Comments*: development-stage companies in which I have invested or for which I have consulted. Ramon Gilberto González—*UNRELATED*: *Expert Testimony*: Hill, Adams, Hall & Schieffelin, PA; Gross, Minsky & Mogul, PA; *Royalties*: Springer.

REFERENCES

1. Balanced Act of 2005 and Deficit Reduction Act. 2006. http://www.gpo.gov/fdsys/pkg/PLAW-109publ171/pdf/PLAW-109publ171.pdf. Accessed March 1, 2015.
2. Federal Register. Medicare Physician Fee Schedule Final Rule Text. 2006. http://www.gpo.gov/fdsys/pkg/FR-2005-11-21/pdf/05-22160.pdf. Accessed March 1, 2015.
3. MPPR Provisions in the Patient Protection and Affordable Care Act. 2010. http://www.gpo.gov/fdsys/pkg/PLAW-111publ148/pdf/PLAW-111publ148.pdf. Accessed March 1, 2015.
4. Medicare Payment Advisory Commission's Report to Congress. 2011. http://www.medpac.gov/documents/reports/Jun11_Ch02.pdf?sfvrsn=0 Accessed March 1, 2015.
5. Rehani B, Basu P, Ellenbogen PH, et al. **The threat to radiologists from the multiple-procedure payment reduction.** *J Am Coll Radiol* 2013;10:237–38 CrossRef Medline
6. Department of Health and Human Services. Centers for Medicare & Medicaid Services. Application of the Multiple Procedure Payment Reduction (MPPR) on Imaging Services to Physicians in the Same Group Practice. http://www.cms.gov/Outreach-and-Education/Medicare-Learning-Network-MLN/MLNMattersArticles/downloads/MM7747.pdf. Accessed March 1, 2015
7. American College of Radiology. ACR Radiology Coding Source for January-February 2012. Medicare's MPPR Policy and Professional

Component Reporting. http://www.acr.org/Advocacy/Economics-Health-Policy/Billing-Coding/Coding-Source-List/2012/Jan-Feb-2012/Medicares-MPPR-Policy-and-Professional-Component-Reporting. Accessed March 1, 2015

8. Duszak R Jr, Silva E 3rd, Kim AJ, et al. **Professional efficiencies for diagnostic imaging services rendered by different physicians: analysis of recent Medicare Multiple Procedure Payment Reduction Policy.** *J Am Coll Radiol* 2013;10:682–88 CrossRef Medline
9. American College of Radiology. Multiple Procedure Payment Reduction and H.R. 2043/S. 1020, the Diagnostic Imaging Services Access Protection Act. http://www.acr.org/Advocacy/Legislative-Issues/MPPR. Accessed March 2, 2015

Nigrosome 1 Detection at 3T MRI for the Diagnosis of Early-Stage Idiopathic Parkinson Disease: Assessment of Diagnostic Accuracy and Agreement on Imaging Asymmetry and Clinical Laterality

Y. Noh, Y.H. Sung, J. Lee, and E.Y. Kim

ABSTRACT

BACKGROUND AND PURPOSE: In the early stages of idiopathic Parkinson disease, motor symptoms are usually asymmetric. We aimed to assess the feasibility of nigrosome 1 detection at 3T MR imaging to analyze the agreement of its asymmetry and clinical laterality.

MATERIALS AND METHODS: High-resolution 3D multiecho imaging was performed at 3T MR imaging in 13 healthy subjects and 24 patients with idiopathic Parkinson disease confirmed by N-3-fluoropropyl-2-β-carbomethoxy-3-β-(4-iodophenyl) nortropane (^{18}F-FP-CIT) PET. The nigrosome 1 detection findings by using the MR imaging data were rated as "normal," "possibly abnormal," and "abnormal" by 2 independent reviewers. The degree of ^{18}F-FP-CIT binding was visually assessed in the caudate nucleus and putamen on PET images. Clinical laterality was evaluated by scores of the Unified Parkinson Disease Rating Scale, Part III. Asymmetry of the affected nigrosome 1 and the degree of ^{18}F-FP-CIT binding were analyzed for agreement with clinical laterality.

RESULTS: The diagnostic sensitivity, specificity, and accuracy of the nigrosome 1 detection at 3T MR imaging was 100%, 84.6%, and 94.6%, respectively. Interrater agreements for the abnormality and asymmetry of nigrosome 1 were excellent ($\kappa = 0.863$ and 0.835, respectively). In patients with idiopathic Parkinson disease, the agreement of asymmetry between clinical laterality and nigrosome 1 detection was good ($\kappa = 0.724$). The degree of the ^{18}F-FP-CIT PET binding showed fair agreement ($\kappa = 0.235$) with clinical laterality.

CONCLUSIONS: The abnormality involving nigrosome 1 can be detected at 3T MR imaging with an accuracy of 94.6%. The clinical laterality is in high concordance with the laterality of the nigrosome 1 detection at 3T ($\kappa = 0.724$).

ABBREVIATIONS: DAT = dopamine transporter; ^{18}F-FP-CIT = N-3-fluoropropyl-2-β-carbomethoxy-3-β-(4-iodophenyl) nortropane; H&Y = Hoehn and Yahr stage; IPD = idiopathic Parkinson disease; MEDIC = multiecho data image combination; UPDRS III = Unified Parkinson Disease Rating Scale, Part III

Nigrosomes are calbindin-poor zones within the substantia nigra pars compacta.[1] The nigrosomes are primary subregions of the substantia nigra pars compacta where dopaminergic cells are lost in idiopathic Parkinson disease (IPD). Within the nigrosomes, the maximal cell loss occurs in nigrosome 1, which is the largest subgroup of the nigrosomes.[2]

Recently, a few researchers have tried to visualize the nigrosome 1 area with 7T MR imaging and demonstrated its feasibility as an imaging biomarker for the diagnosis of IPD.[3-6] The results, however, had a limited clinical utility because of low availability of 7T MR imaging. Hence, several studies have tried to translate nigrosome 1 detection to 3T MR imaging, which is widely available.[7-9] In the previous studies at 3T, however, patients were confirmed as having IPD by clinical assessment, not by dopamine-transporter (DAT) imaging such as N-3-fluoropropyl-2-β-carbomethoxy-3-β-(4-iodophenyl) nortropane (^{18}F-FP-CIT) PET or SPECT, which is commonly used for an early diagnosis of IPD.

In clinical practice, it is more difficult to diagnose an early stage of parkinsonism than an advanced stage. Therefore, a confirmation by an imaging biomarker would be desirable in the diagnosis of a patient in an early stage. If the nigrosome 1 detection at 3T MR imaging is available for the diagnosis of early-stage IPD, it can minimize the need for the DAT PET or SPECT.

In early stages of IPD, motor symptoms are usually asymmetric.[10] Unilateral or asymmetric symptoms have been suggested to

Received November 24, 2014; accepted after revision April 12, 2015.

From the Departments of Neurology (Y.N., Y.H.S.) and Radiology (E.Y.K.), Gachon University Gil Medical Center, Incheon, Korea; and Department of Electrical and Computer Engineering (Jongho Lee), Seoul National University, Seoul, Korea.

This research was supported by a grant of the Korea Health Technology R&D Project through the Korea Health Industry Development Institute, funded by the Ministry of Health and Welfare, Republic of Korea (grant No. HI14C1135) and by the Gachon University Gil Medical Center (2013-06).

Paper previously presented at: Annual Meeting of International Society for Magnetic Resonance in Medicine, May 30 to June 5, 2015; Toronto, Ontario, Canada.

Please address correspondence to: Eung Yeop Kim, MD, Department of Radiology, Gachon University Gil Medical Center, 21, Namdong-daero 774 beon-gil, Namdong-gu, Incheon, 21565, South Korea; e-mail: neuroradkim@gmail.com

Indicates open access to non-subscribers at www.ajnr.org

Evidence-Based Medicine Level 2.

http://dx.doi.org/10.3174/ajnr.A4412

correspond to nigrostriatal degeneration in the contralateral hemisphere.[11] On the basis of this observation, we hypothesized that the asymmetric dopaminergic cell loss in the substantia nigra pars compacta reflects the contralateral symptoms in early-stage IPD, and the cell loss can be visualized by the signal change in the nigrosome 1 area at 3T MR imaging.

In this study, we investigated the feasibility of the nigrosome 1 detection at 3T MR imaging for the diagnosis of patients with early-stage IPD with abnormal findings on DAT PET imaging.[12] Additionally, we assessed the agreement of asymmetry between the nigrosome 1 detection and patient symptoms, and the asymmetry between the DAT PET imaging and patient symptoms.

MATERIALS AND METHODS

This study was approved by the institutional review board of the Gachon University, Gil Medical Center. All patients and healthy subjects gave written informed consent.

Participants

Twenty-four patients with IPD were recruited from the movement disorder clinic at Gachon University Gil Medical Center from March 2013 to July 2014 (mean age, 63.6 ± 10.97 years; 14 men and 10 women). The clinical diagnosis was based on UK Parkinson's Disease Society Brain Bank Clinical Diagnostic Criteria.[13] All patients underwent ^{18}F- FP-CIT PET for the initial diagnosis. The severity of motor symptoms was evaluated by the Hoehn and Yahr (H&Y) stages[14] and Unified Parkinson Disease Rating Scale, Part III (UPDRS III). We enrolled only patients with IPD with H&Y stages between 1 and 2 (stages 1 and 1.5, 2 patients each; stage 2, 20 patients). The UPDRS III ranged from 6 to 25 (mean, 13.5 ± 6.19). The exclusion criteria included the following: 1) atypical Parkinson disease (progressive supranuclear palsy, multiple systemic atrophy, and corticobasal degeneration); 2) patients with dementia; 3) neurologic diseases other than Parkinson disease; 4) other potential causes of parkinsonism such as structural lesions or metabolic derangement; 5) patients with infarction, hemorrhage, tumors, trauma, or severe white matter hyperintensity (deep white matter lesion of >25 mm and caps or bands of >10 mm)[15]; 6) history of taking drugs that are known to cause parkinsonism: antipsychotics, antiemetic drugs such as metoclopramide, calcium-channel blockers such as flunarizine, amiodarone, sodium valproate, lithium; and selective serotonin reuptake inhibitors such as fluoxetine; and 7) MR imaging contraindication due to metal foreign bodies/implants or claustrophobia.

Thirteen age-matched healthy subjects were recruited (mean age, 61.6 ± 12.29 years; 4 men and 9 women). They were recruited with the following inclusion criteria: 1) age older than 40 years; 2) no history of neurologic or psychiatric diseases; 3) no family history of movement disorders; and 4) normal cognition without subjective memory impairment (Mini-Mental State Examination score of >26). All participants underwent the Mini-Mental State Examination. The patients were assessed and scanned while medicated. Demographic and clinical characteristics of the participants are summarized in Table 1.

Table 1: Demographic characteristics and imaging findings in study population[a]

	IPD (*n* = 24)	Healthy Control (*n* = 13)	*P* Value
Age (yr)	63.6 ± 10.97	61.6 ± 12.29	.620
Female sex (%)	10 (41.7%)	9 (69.2%)	.170
MMSE	27.5 (25.0–29.0)	29.0 (28.0–29.5)	.036
Onset age (yr)	62.4 ± 11.59	–	
Disease duration (mo)	9.0 (3.0–12.0)	–	
H&Y scale (1/1.5/2)	2/2/20	–	
UPDRS I	1.0 (0–2.0)	–	
UPDRS II	6.75 ± 2.85	–	
UPDRS III	13.5 ± 6.19	–	

Note:—MMSE indicates Mini-Mental State Examination; UPDRS, Unified Parkinson Disease Rating Scale, –, not applicable.

[a] Data are presented as mean ± SD for normally distributed variables and median (interquartile ranges) for non-normally distributed variables. The χ^2 test with Yates continuity correction was used.

MR Image Acquisition

All participants underwent MR imaging on a 3T scanner with a 32-channel coil (Magnetom Skyra; Siemens, Erlangen, Germany). Whole-brain sagittal 3D MPRAGE imaging was performed first with the following parameters: TR, 1750 ms; TE, 4.32 ms; TI, 920 ms; matrix, 224 × 222; FOV, 307 × 309; acceleration factor, 2; acquisition time, 3 minutes 35 seconds. Oblique axial 3D multi-echo data image combination (MEDIC; proprietary sequence; Siemens) imaging (multi-echo gradient-echo imaging that combines each TE magnitude by the sum of squares) was performed vertical to the longitudinal axis of the midbrain (Fig 1*A*). The parameters for MEDIC were as follows: TR, 88 ms; minimum and maximum TE, 11.1 and 66.9 ms, respectively (the number of combined echoes, 6; echo spacing, 11.1 ms); flip angle, 10°; echo-train length, 6; thickness, 1.5 mm; section number, 20; matrix, 384 × 384; FOV, 192 × 192 (in-plane resolution, 0.5 × 0.5 mm); acceleration factor, 2; acquisition time, 4 minutes 45 seconds. Additionally, oblique coronal 3D MEDIC data were acquired parallel to the longitudinal axis of the midbrain (Fig 1*B*) by using the same parameters as in oblique axial imaging (Fig 1*A*).

Visual Rating of Nigrosome 1

The nigrosome 1 area on the MEDIC images was defined according to the location that was described in the previous pathologic study.[2] In healthy subjects, the structure appeared symmetrically with slight hyperintensity compared with the adjacent crus cerebri on the MEDIC images (Fig 1). On the oblique axial MEDIC data, evaluation of the nigrosome 1 was performed on 3 sections: an upper section at the lower tip of red nucleus and 2 successive lower sections (Fig 1*A*). The oblique coronal MEDIC images were also assessed on 3 sections: an anterior section at the anterior tip of red nucleus and the other 2 successive sections posteriorly (Fig 1*B*). Both oblique axial and coronal images were displayed side by side by using OsiriX Imaging Software (Version 5.9, http://www.osirix-viewer.com). A neuroradiologist with 11 years' experience (E.Y.K.) and a neurologist (Y.N.) with 4 years' experience independently reviewed anonymized images without any clinical information. We compared the signal intensity of the central portion of nigrosome 1 with that of the white matter lateral to the decussation of the superior cerebellar peduncles. The nigrosome 1

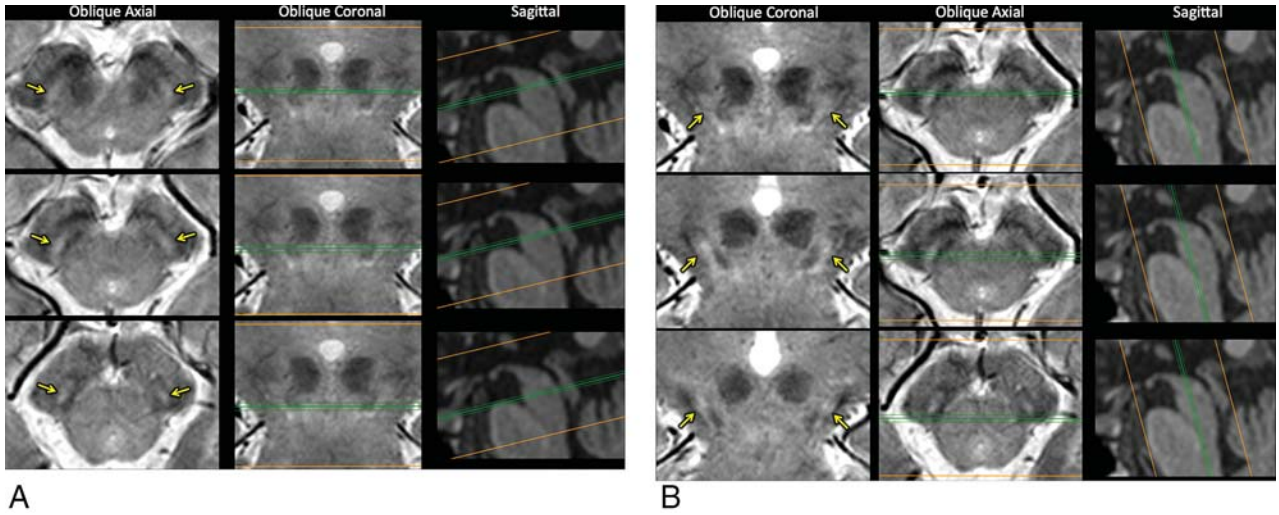

FIG 1. Visual assessment of nigrosome 1 in MR imaging. On the oblique axial MEDIC imaging, the evaluation of nigrosome 1 (*arrows*) was performed on 3 sections: an upper section at the lower tip of the red nucleus and the 2 successive sections (*A*). The oblique coronal MEDIC imaging was also assessed on 3 sections: an anterior section at the anterior tip of the red nucleus and the 2 consecutive sections (*B*). In this particular 71-year-old woman, the nigrosome 1 appears normal on both sides.

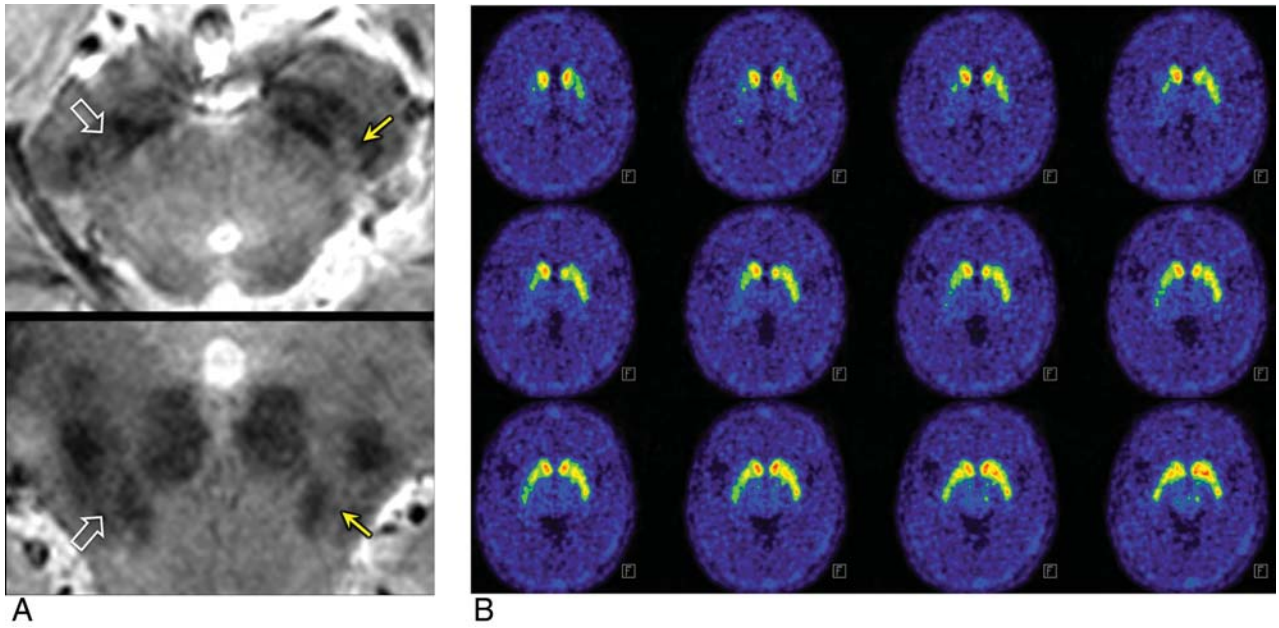

FIG 2. Degree of abnormality on MR imaging. Possibly abnormal and definitely abnormal were rated in the left (*arrows*) and right (*open arrows*) nigrosome 1, respectively (*A*). Similar asymmetry was observed on ^{18}F-FP-CIT PET. This 53-year-old woman has H&Y stage 2 and UPDRS Part III (motor score) of 4 and 1 on the left and right, respectively, which is in concordance with asymmetry on both MR imaging and ^{18}F-FP-CIT PET.

images from the MEDIC imaging were classified into 3 grades: "normal" (iso- or hyperintensity in the central portion of the presumed nigrosome 1) (Fig 1), "possibly abnormal'" (hypointensity in <50% of the presumed nigrosome 1) (left nigrosome 1 on Fig 2), and "definitely abnormal" (hypointensity in ≥50% of the presumed nigrosome 1) (right nigrosome 1 on Fig 2). Each side was rated separately. Asymmetry was determined once any difference was rated between the right and left nigrosome 1. For a simplified statistical analysis, the subjects' images were reclassified as abnormal if any abnormality was determined on either side of the nigrosome 1 area; a subject's image was classified as normal when the bilateral nigrosome 1 was determined to be normal. Any discrepancy between the 2 readers was resolved by consensus.

^{18}F-FP-CIT PET Image Acquisition

All patients with IPD underwent ^{18}F-FP-CIT PET imaging of the brain 120 minutes after injection of 5-mCi (185 MBq) ^{18}F-FP-CIT at a PET/CT scanner (Biograph-6; Siemens, Erlangen, Germany). Data were collected in a 3D scanning mode that examined 35 sections (thickness, 4.25 mm). Levodopa, dopamine agonist, catechol-O-methyltransferase inhibitors, and monoamine oxidase type B inhibitors were allowed because they are known to have no significant influence on the DAT imaging.[16] The median

Table 2: Interpretation of nigrosome 1 by 2 reviewers

	Reviewer 1		Reviewer 2	
	Right	Left	Right	Left
Normal (No.)	10	13	12	11
Possibly abnormal (No.)	7	5	2	3
Definitely abnormal (No.)	20	19	23	23

duration between MR imaging and PET was 4.5 months (interquartile range, 2.25–10.75 months).

Visual Rating of ^{18}F-FP-CIT PET

Visual analysis of ^{18}F-FP-CIT binding to the caudate nucleus and putamen was performed by a neurologist (Y.H.S.). No clinical information was provided. Each side was rated separately. The degree of DAT reduction was evaluated by dividing the putamen into anterior and posterior halves along its longitudinal axis.[17] "Normal" was defined as no discernible reduction of DAT availability in the striatal region (caudate nucleus and putamen). If the reduction of DAT availability was limited in the posterior putamen, the availability was classified as "mild" reduction. When it showed a decrease or absence up to the anterior putamen, it was classified as "moderate" reduction. It was classified as "severe" if the caudate nucleus was involved.[18] Any difference between right and left DAT availability indicated the presence of asymmetry. No patients with IPD showed normal DAT availability in this study.

Quantification of the Laterality of Symptoms

The clinical laterality of motor symptoms was evaluated by using the scores of UPDRS III, which was tested bilaterally. Scores of resting tremor, rigidity, finger tapping, hand movement, and rapid alternative movements of hand and leg agility were summed in the right and left sides separately. When the score of one side was higher than that of the other side by 2 points, the symptom was defined as asymmetric.

Statistical Analysis

Comparisons of demographic and clinical data between patients with IPD and healthy subjects were conducted by the Student *t* test for normally distributed continuous variables and the Mann-Whitney *U* test for non-normally distributed continuous variables. Categoric variables were evaluated by using a χ^2 test. Interrater agreement was assessed by using κ statistics: weighted k test for the ratings and the Cohen κ test for the 2 groups (normal or abnormal findings). Agreement on the symmetry of MR imaging or PET and clinical laterality was examined by using the Cohen κ test. Statistical significance was set at $P < .05$. Statistical analyses were conducted by PASW Statistics 18 (IBM, Armonk, New York) software.

RESULTS

Diagnostic Accuracy of IPD by Using Nigrosome 1 Detection in MR Imaging

No scan showed poor image quality or motion artifacts. When the participants were dichotomized as having normal and abnormal findings, 2 of 37 participants were rated differently by the 2 raters. Of the 35 subjects, 26 were rated as having abnormal findings, and 9 subjects were rated as having normal findings (Table 2).

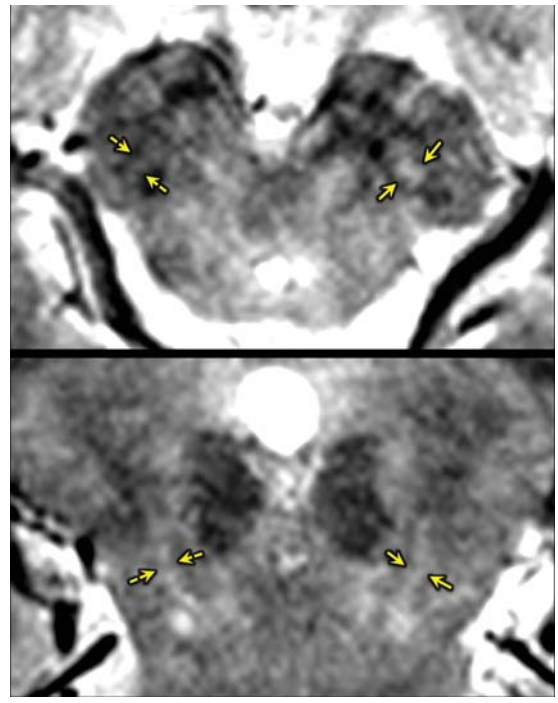

FIG 3. False-positive on MR imaging. In this 64-year-old healthy female subject, both reviewers interpreted the left nigrosome (*arrows*) was as normal, whereas they called the right one (*broken arrows*) abnormal.

The interrater agreement on the abnormality of nigrosome 1 findings was excellent ($\kappa = 0.863$). After consensus agreement, the 2 subjects with the rater discrepancies were classified as having normal findings. With the 37 participants, the sensitivity and specificity were 100% and 84.6%, respectively. The positive predictive value was 92.3% (24/26). The negative predictive value was 100% (11/11). Two of 13 healthy controls were misclassified to the abnormal group (Fig 3). Diagnostic accuracy was 94.6%.

Interrater Agreement on the Laterality of Nigrosome 1

The interrater agreement on the laterality was excellent ($\kappa = 0.835$; 95% CI, 0.673–0.997). For the grading system (normal, possibly abnormal, and definitely abnormal findings), the weighted κ value for interrater agreement on the abnormality of the left side was 0.711 (95% CI, 0.537–0.886), while that of the right side was 0.792 (95% CI, 0.648–0.936) (Table 2). Interrater agreement of the affected side was slightly improved when patients were dichotomized (normal or abnormal findings): left side, $\kappa = 0.754$, and right side, $\kappa = 0.871$.

Agreement on the Asymmetry of Nigrosome 1 and Clinical Laterality

Of 24 patients with IPD, 4 showed no clinical asymmetry, whereas the other 20 patients demonstrated asymmetry (left- and right-side-dominant symptoms in 10 patients each). MR imaging showed symmetric nigrosome 1 findings in 2 patients, whereas 22 patients had asymmetric nigrosome 1. The asymmetry in the affected nigrosome 1 at MR imaging and clinical laterality were in agreement in 19 of 24 patients ($\kappa = 0.724$). Of 20 patients with clinical asymmetry, the agreement of the asymmetry in the af-

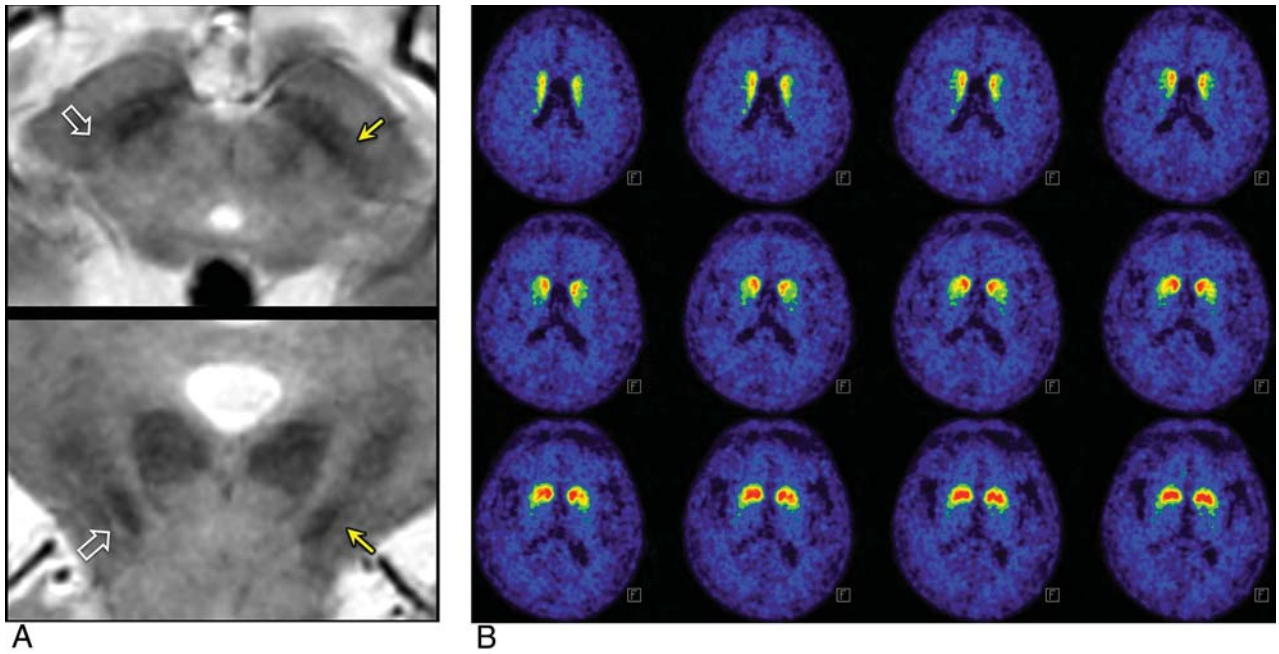

FIG 4. Asymmetry on MR imaging but not on ^{18}F-FP-CIT in a 78-year-old woman with H&Y stage 2 and UPDRS of 4 and 2 on the right and left shows that the left nigrosome 1 is more affected (*arrows*) than the right one (*open arrows*) (*A*), whereas ^{18}F-FP-CIT PET shows relatively symmetric findings (*B*).

fected nigrosome 1 at MR imaging and clinical laterality increased ($\kappa = 0.800$). In the ^{18}F-FP-CIT PET data, no asymmetry was observed in 10 patients. The agreement of the asymmetry on the ^{18}F-FP-CIT PET imaging and clinical laterality was fair ($\kappa = 0.235$) (Fig 4). The agreement between the asymmetry in the nigrosome 1 MR imaging and that in the ^{18}F- FP-CIT PET imaging was fair ($\kappa = 0.304$).

DISCUSSION

Our primary findings were as follows: First, we achieved a high accuracy in the diagnosis of IPD by the detection of abnormality in nigrosome 1 at 3T MR imaging. Second, we demonstrated that the asymmetry of the affected nigrosome 1 and clinical laterality evaluated with UPDRS III had good agreement.

By using 7T[3-6] and 3T MR imaging,[7,8] recent studies demonstrated that nigrosome 1 can serve as a surrogate biomarker for IPD. Schwarz et al[7] obtained high-resolution 3D gradient recalled-echo imaging (voxel size, 0.55 × 0.55 × 0.7 mm) in an imaging plane parallel to the splenium-genu line at 3T. To improve diagnostic confidence, we acquired both oblique axial and coronal images by using 3D MEDIC imaging (voxel size, 0.5 × 0.5 × 1.5 mm) vertical and parallel to the longitudinal axis of the midbrain on sagittal MPRAGE, respectively. SWI is well-known for its higher sensitivity in delineating iron-containing pathology. Its SNR, however, is relatively low. We tested SWI in healthy elderly subjects before conducting this study and found that both higher SNR and higher spatial resolution are necessary to determine pathology involving nigrosome 1. These 2 factors are conflicting in MR imaging. To address this challenge, we acquired data by using the MEDIC imaging with a relatively larger section thickness. To minimize potential complications from the thicker sections, we acquired coronal images. Using this technique, we obtained the diagnostic accuracy of 94.6%. This result is between the diagnostic accuracy of a prospective case-control study (84%) and a retrospective cross-sectional study (96%) in the report by Schwarz et al[7] and is higher than that in the study by Cosottini et al (86%).[8]

It is difficult to compare the diagnostic accuracy with that in the previous studies because each study used its own imaging sequence with different image thickness (PRinciples of Echo Shifting by using a Train of Observations by Schwarz et al[7] and Susceptibility-Weighted ANgiography by Cosottini et al[8]) and enrolled patients had different severities: in our study, H&Y stage range, 1–2, UPDRS III mean, 13.5. In the prospective study by Schwarz et al, the severities were H&Y stage 1–3, UPDRS III, 32.5[7]; in the study by Cosottini et al, they were H & Y stage 1–3, UPDRS III, 18.3.[8] Although our study subjects were in relatively earlier stages, patients with H&Y stage 2 were the most numerous. Thus, further studies are needed to determine the best imaging method for nigrosome 1, with more patients with very early stages or clinical suspicion of parkinsonism.

Our second finding was that the laterality of the nigrosome 1 (more affected on either the left or right) was in concordance with the clinical laterality. This finding supports unilateral IPD corresponding to neuronal nigrostriatal degeneration in the contralateral hemisphere. As a previous study reported, abnormal findings of nigrosome 1 in IPD do not imply that the nigrosome 1 was completely lost.[7] We observed that the nigrosome 1 in each hemisphere often had different appearances. This observation agrees with the finding that asymmetry of clinical features is common in the patients with IPD. Many patients have unilateral motor deficits at the time of onset of the IPD symptoms.[14] Clinical asymmetry may continue in late stages of the disease, with more marked extrapyramidal symptoms on the initially affected body side.[19]

Although it has been reported that nigrosome 1 detection at

3T MR imaging may serve as a surrogate biomarker for the diagnosis of IPD in previous studies,[7,8] and in our study, it may still be challenging to determine the presence of subtle abnormalities of nigrosome 1 by directly looking at structures. Instead, one may compare the agreement between nigrosome 1 images and clinical laterality to improve the diagnostic confidence. To further consolidate the usefulness of the nigrosome 1 detection for the early diagnosis of IPD, however, a prospective study is needed.

In our study, the agreement on the laterality between ^{18}F-FP-CIT binding and clinical symptoms was fair. This finding may suggest that ^{18}F-FP-CIT PET shows nigrostriatal functional changes that are earlier than structural changes observed in the nigrosome 1 detection and may also support the dying-back phenomenon. Alternatively, the nigrosome 1 detection might be more sensitive for neuronal degeneration. One potential complication on the laterality results is the time delay (interquartile range, 2.25–10.75 months) between the 2 imaging sessions. The earlier imaging of ^{18}F-FP-CIT PET may have resulted a lower agreement on the laterality, though the delay was relatively short considering the slow progression of the disease.

Although DAT PET or SPECT has been considered a criterion standard for the diagnosis of IPD, such imaging studies increase the medical costs and result in radiation exposure. In addition, in the very early stages, the DAT PET technique could have limitations in diagnosing Parkinson disease. A previous study reported that compensatory upregulation of presynaptic dopaminergic nerve terminals in the early stages of Parkinson disease could cause false-negative results and that dopaminergic medications might increase radiotracer uptake.[20] Hence, a diagnostic marker using MR imaging (especially the more widely available 3T MR imaging rather than 7T MR imaging) will be beneficial to patients. As we have demonstrated in this study, the nigrosome 1 detection at 3T MR imaging can serve as a surrogate marker for IPD in its early stage and may negate the need for ^{18}F-FP-CIT PET imaging, particularly when there is definite asymmetric abnormality in nigrosome 1 at MR imaging and the patient shows clinical laterality on the corresponding side.

A few limitations exist in this study. The number of study subjects is small. Further study with more participants will be needed to confirm the effectiveness of the nigrosome 1 detection in routine clinical diagnosis. Another limitation is a relatively large false-positive. Two participants (64 and 72 years of age) showed false-positive results. According to a previous study, nigrosome 1 was not observed in 2% of the patients without IPD older than 50 years of age, a finding that was similar to the rate of prevalence of IPD in the elderly, indicating the possibility of undiagnosed IPD.[7] We could not completely exclude the possibility that the 2 healthy control subjects had presymptomatic Parkinson disease because ^{18}F-FP-CIT PET was not performed in healthy control subjects. However, no preclinical symptom such as rapid eye movement, sleep behavior disorders, anosmia, or autonomic dysfunction was observed in these subjects. An alternative explanation is that normal aging may also show changes in nigrosome 1. Further study with a large number of healthy elderly subjects is needed to elucidate this question. Last, the optimization and standardization of a sequence for the visualization of nigrosome 1 should be sought to improve diagnostic accuracy. Although we enrolled only patients with clinically well-established IPD, the specificity of our study was lower (84.6%) than that in the studies with 7T MR imaging (87.5%–96.2%).[5,6,9] Thus, a more specific imaging biomarker that could give confirmation to patients with clinical suspicion of parkinsonism is still needed.[21,22] On the basis of our results of a relatively lower specificity than that of previous studies, nigrosome 1 detection at 3T MR imaging should be further improved to serve as a confirmatory test of IPD. The higher specificity of 7T MR imaging in the diagnosis of IPD may be due to its higher SNR and superb spatial resolution. It is difficult to improve spatial resolution substantially at 3T. However, we could improve the susceptibility effect without compromising SNR by susceptibility weighting of each TE image, followed by combining images afterward, which can be applicable to all 3T scanners without dependence on vendor-specific sequences. In addition, assessment of agreement on clinical laterality and imaging asymmetry may help improve specificity. With such an effort, a more specific and sensitive surrogate marker to detect the disease in the preclinical stages could be developed.

CONCLUSIONS

Our study showed that abnormality involving nigrosome 1 can be detected at 3T MR imaging with an accuracy of 94.6%, and its asymmetry shows a high concordance with clinical laterality.

REFERENCES

1. Damier P, Hirsch EC, Agid Y, et al. **The substantia nigra of the human brain, I: nigrosomes and the nigral matrix, a compartmental organization based on calbindin D(28K) immunohistochemistry.** *Brain* 1999;122(pt 8):1421–36 CrossRef Medline
2. Damier P, Hirsch EC, Agid Y, et al. **The substantia nigra of the human brain, II: patterns of loss of dopamine-containing neurons in Parkinson's disease.** *Brain* 1999;122(pt 8):1437–48 CrossRef Medline
3. Kwon DH, Kim JM, Oh SH, et al. **Seven-Tesla magnetic resonance images of the substantia nigra in Parkinson disease.** *Ann Neurol* 2012;71:267–77 CrossRef Medline
4. Lotfipour AK, Wharton S, Schwarz ST, et al. **High resolution magnetic susceptibility mapping of the substantia nigra in Parkinson's disease.** *J Magn Reson Imaging* 2012;35:48–55 CrossRef Medline
5. Blazejewska AI, Schwarz ST, Pitiot A, et al. **Visualization of nigrosome 1 and its loss in PD: pathoanatomical correlation and in vivo 7 T MRI.** *Neurology* 2013;81:534–40 CrossRef Medline
6. Cosottini M, Frosini D, Pesaresi I, et al. **MR imaging of the substantia nigra at 7 T enables diagnosis of Parkinson disease.** *Radiology* 2014; 271:831–38 CrossRef Medline
7. Schwarz ST, Afzal M, Morgan PS, et al. **The 'swallow tail' appearance of the healthy nigrosome: a new accurate test of Parkinson's disease—a case-control and retrospective cross-sectional MRI study at 3T.** *PLoS One* 2014;9:e93814 CrossRef Medline
8. Cosottini M, Frosini D, Pesaresi I, et al. **Comparison of 3T and 7T susceptibility-weighted angiography of the substantia nigra in diagnosing Parkinson disease.** *AJNR Am J Neuroradiol* 2015;36: 461–66 CrossRef Medline
9. Mueller C, Pinter B, Reiter E, et al. **Visualization of nigrosome 1 and its loss in PD: pathoanatomical correlation and in vivo 7T MRI.** *Neurology* 2014;82:1752 CrossRef Medline
10. Fahn S. **Description of Parkinson's disease as a clinical syndrome.** *Ann N Y Acad Sci* 2003;991:1–14 CrossRef Medline
11. van der Hoorn A, Bartels AL, Leenders KL, et al. **Handedness and dominant side of symptoms in Parkinson's disease.** *Parkinsonism Relat Disord* 2011;17:58–60 CrossRef Medline
12. Jin S, Oh M, Oh SJ, et al. **Differential diagnosis of parkinsonism**

using dual-phase F-18 FP-CIT PET imaging. *Nucl Med Mol Imaging* 2013;47:44–51 CrossRef Medline
13. Hughes AJ, Daniel SE, Kilford L, et al. **Accuracy of clinical diagnosis of idiopathic Parkinson's disease: a clinico-pathological study of 100 cases.** *J Neurol Neurosurg Psychiatry* 1992;55:181–84 CrossRef Medline
14. Hoehn MM, Yahr MD. **Parkinsonism: onset, progression and mortality.** *Neurology* 1967;17:427–42 CrossRef Medline
15. Scheltens P, Barkhof F, Leys D, et al. **A semiquantative rating scale for the assessment of signal hyperintensities on magnetic resonance imaging.** *J Neurol Sci* 1993;114:7–12 CrossRef Medline
16. Booij J, Kemp P. **Dopamine transporter imaging with [(123)I]FP-CIT SPECT: potential effects of drugs.** *Eur J Nucl Med Mol Imaging* 2008;35:424–38 CrossRef Medline
17. Wang J, Zuo CT, Jiang YP, et al. **18F-FP-CIT PET imaging and SPM analysis of dopamine transporters in Parkinson's disease in various Hoehn & Yahr stages.** *J Neurol* 2007;254:185–90 CrossRef Medline
18. Park E, Hwang YM, Lee CN, et al. **Differential diagnosis of patients with inconclusive Parkinsonian features using [(18)F]FP-CIT PET/CT.** *Nucl Med Mol Imaging* 2014;48:106–13 CrossRef Medline
19. Kempster PA, Gibb WR, Stern GM, et al. **Asymmetry of substantia nigra neuronal loss in Parkinson's disease and its relevance to the mechanism of levodopa related motor fluctuations.** *J Neurol Neurosurg Psychiatry* 1989;52:72–76 CrossRef Medline
20. Lee CS, Samii A, Sossi V, et al. **In vivo positron emission tomographic evidence for compensatory changes in presynaptic dopaminergic nerve terminals in Parkinson's disease.** *Ann Neurol* 2000; 47:493–503 CrossRef Medline
21. Schwarz ST, Bajaj N, Gowland PA, et al. **MR imaging of the substantia nigra for the diagnosis of Parkinson disease.** *Radiology* 2014;273: 627–28 CrossRef Medline
22. Cosottini M, Frosini D, Pesaresi I, et al. **Response.** *Radiology* 2014; 273:628–29 Medline

Comparison of the Diagnostic Accuracy of DSC- and Dynamic Contrast-Enhanced MRI in the Preoperative Grading of Astrocytomas

T.B. Nguyen, G.O. Cron, K. Perdrizet, K. Bezzina, C.H. Torres, S. Chakraborty, J. Woulfe, G.H. Jansen, J. Sinclair, R.E. Thornhill, C. Foottit, B. Zanette, and I.G. Cameron

ABSTRACT

BACKGROUND AND PURPOSE: Dynamic contrast-enhanced MR imaging parameters can be biased by poor measurement of the vascular input function. We have compared the diagnostic accuracy of dynamic contrast-enhanced MR imaging by using a phase-derived vascular input function and "bookend" T1 measurements with DSC MR imaging for preoperative grading of astrocytomas.

MATERIALS AND METHODS: This prospective study included 48 patients with a new pathologic diagnosis of an astrocytoma. Preoperative MR imaging was performed at 3T, which included 2 injections of 5-mL gadobutrol for dynamic contrast-enhanced and DSC MR imaging. During dynamic contrast-enhanced MR imaging, both magnitude and phase images were acquired to estimate plasma volume obtained from phase-derived vascular input function (Vp_Φ) and volume transfer constant obtained from phase-derived vascular input function (K^{trans}_Φ) as well as plasma volume obtained from magnitude-derived vascular input function (Vp_SI) and volume transfer constant obtained from magnitude-derived vascular input function (K^{trans}_SI). From DSC MR imaging, corrected relative CBV was computed. Four ROIs were placed over the solid part of the tumor, and the highest value among the ROIs was recorded. A Mann-Whitney *U* test was used to test for difference between grades. Diagnostic accuracy was assessed by using receiver operating characteristic analysis.

RESULTS: Vp_ Φ and K^{trans}_Φ values were lower for grade II compared with grade III astrocytomas ($P < .05$). Vp_SI and K^{trans}_SI were not significantly different between grade II and grade III astrocytomas ($P = .08–0.15$). Relative CBV and dynamic contrast-enhanced MR imaging parameters except for K^{trans}_SI were lower for grade III compared with grade IV ($P \leq .05$). In differentiating low- and high-grade astrocytomas, we found no statistically significant difference in diagnostic accuracy between relative CBV and dynamic contrast-enhanced MR imaging parameters.

CONCLUSIONS: In the preoperative grading of astrocytomas, the diagnostic accuracy of dynamic contrast-enhanced MR imaging parameters is similar to that of relative CBV.

ABBREVIATIONS: DCE = dynamic contrast-enhanced; K^{trans}_Φ = volume transfer constant obtained from phase-derived vascular input function; K^{trans}_SI = volume transfer constant obtained from magnitude-derived vascular input function; rCBV = relative CBV; SI = signal intensity; VIF = vascular input function; Vp = plasma volume; Vp_Φ = plasma volume obtained from phase-derived vascular input function; Vp_SI = plasma volume obtained from magnitude-derived vascular input function

Conventional MR imaging by using gadolinium contrast enhancement has been reported to have high sensitivity but low specificity in the preoperative grading of gliomas.[1-4] The accuracy of conventional imaging might be improved by adding perfusion-weighted imaging. In clinical practice, DSC imaging remains the most commonly used perfusion technique and provides semiquantitative measurements such as relative CBV (rCBV), which can be influenced by the presence of susceptibility artifacts and contrast leakage from tumor vessels.[5,6]

Dynamic contrast-enhanced (DCE)-MR imaging is an alternate technique that can potentially provide absolute values of plasma volume (Vp) and a measurement of vascular permeability referred to as the volume transfer constant (K^{trans}). This technique generally involves additional measurements and postprocessing steps. Measurements of precontrast tissue T1 and the vascular input function (VIF) in the brain are usually needed for proper quantification of DCE-MR imaging.[7,8] Recently, some au-

Received November 14, 2014; accepted after revision March 24, 2015.

From the Departments of Radiology (T.B.N., G.O.C., C.H.T., R.E.T., I.G.C., S.C.), Medical Physics (C.F., I.G.C.), Pathology (G.H.J., J.W.), Surgery, Division of Neurosurgery (J.S.), Internal Medicine (K.P.), and Faculty of Medicine (K.B.), Ottawa Hospital, University of Ottawa, Ottawa, Ontario, Canada; and Department of Medical Biophysics (B.Z.), University of Toronto, Toronto, Ontario, Canada.

This work was supported by an investigator-initiated research grant from Bayer HealthCare, who did not have any input in the formulation of this paper.

Paper previously presented as an abstract at: American Society of Neuroradiology Annual Meeting and the Foundation of the ASNR Symposium, May 17–22, 2014; Montreal, Quebec, Canada.

Please address correspondence to Thanh Binh Nguyen, MD, Department of Radiology, Ottawa Hospital, 1053 Carling Ave, Ottawa, Ontario K1Y 4E9, Canada; e-mail: thnguyen@toh.on.ca

Indicates article with supplemental on-line table.

http://dx.doi.org/10.3174/ajnr.A4398

thors have suggested that measuring changes in the phase of the MR signal rather than its magnitude following gadolinium injection might provide a more accurate VIF because phase change inside the vessel is linearly related to the concentration of contrast agent.[9-12] While measurement of precontrast tissue T1 is typically included in DCE-MR imaging studies, an additional measurement of tissue T1 postinjection ("bookend" method) might also improve the reproducibility of perfusion values in gliomas.[13,14]

To our knowledge, there have been few comparative studies between DCE and DSC imaging in patients with gliomas.[15,16] The main objective of our study was to compare the diagnostic accuracy of DCE-MR imaging with DSC-MR imaging in the preoperative grading of astrocytomas at 3T by using a high-relaxivity agent. For DCE-MR imaging analysis, we performed 2 different methods: 1) using phase-derived VIF with bookend T1 measurements; and 2) using magnitude-derived VIF without T1 mapping.

MATERIALS AND METHODS

Patient Population

All examinations were conducted in accordance with the guidelines for human research of The Ottawa Hospital, and written informed consent was obtained from all participating subjects. From March 1, 2011, to December 31, 2013, 70 consecutive patients presenting to our institution with a newly diagnosed brain lesion compatible with a glioma were asked to participate in this study. Following surgical resection or biopsy, histopathologic diagnosis was provided by an experienced neuropathologist by using the 2007 World Health Organization classification. Thirteen patients were excluded due to the absence of a histopathologic diagnosis or the presence of an alternate histopathologic diagnosis: no biopsy ($n = 2$), inconclusive biopsy ($n = 1$), oligodendrogliomas ($n = 2$), metastatic disease ($n = 2$), lymphomas ($n = 2$), glioneuronal tumors ($n = 2$), meningioma ($n = 1$), and neurosarcoidosis ($n = 1$). Nine patients with astrocytomas were subsequently excluded for technical reasons: inadequate bolus injection of contrast ($n = 4$), hemorrhage within glioblastoma causing extensive susceptibility artifacts ($n = 3$), dynamic acquisition not centered over the tumor ($n = 1$), and inadequate VIF for the DCE acquisition ($n = 1$).

MR Imaging Acquisition Protocols

Conventional MR imaging was performed on a 3T scanner (TimTrio; Siemens, Erlangen, Germany) by using axial T1 precontrast (TR = 280 ms, TE = 2.51 ms, thickness = 3 mm), axial FLAIR (TR = 9710 ms, TE = 93 ms, TI = 2580 ms, thickness = 3 mm), axial T2 (TR = 6910 ms, TE = 97 ms, thickness = 3 mm), axial T1 Volume Interpolated Breathhold Examination (VIBE) postcontrast (TR = 8.48 ms, TE = 3.21 ms, flip angle = 12°, thickness = 1 mm), and coronal T1 postcontrast (TR = 280 ms, TE = 2.51 ms, thickness = 4 mm) images.

DCE-MR imaging was performed by using a 3D FLASH sequence (TR = 6.5 ms, TE = 1.7/3.9 ms, flip angle = 30°, thickness = 5 mm, 18 sections, temporal resolution = 3.5 seconds, duration = 440 seconds). This pulse sequence generated phase images in addition to the standard magnitude images. Both before and after the dynamic scan, two 3D Volume Interpolated Breathhold Examination (VIBE) sequences with different flip angles (TR = 20 ms, TE = 1.22 ms, flip angle = 4° and 25°, thickness = 5 mm, 18 sections) were acquired, which enabled calculation of T1 maps.

In patients weighing between 50 and 100 kg, a fixed preloaded dose of 0.05 mmol (equivalent to 5 mL) of gadobutrol (Gadavist 1.0; Bayer Schering Pharma, Berlin, Germany) was injected at 2 mL/s for DCE imaging. This also served to decrease the T1 effects before a second injection of 0.05 mmol of contrast was performed for the DSC perfusion imaging. In patients weighing <50 kg or >100 kg, we used a dose of 0.05 mmol/kg.

The second injection of contrast agent was given 10 minutes after the first injection at 4 mL/s. DSC imaging was performed by using a T2* EPI gradient recalled-echo sequence (TR = 2380 ms, TE = 54 ms, flip angle = 90°, thickness = 5 mm, 18 sections, temporal resolution = 2.5 seconds, duration = 125 seconds).

Postprocessing of DCE Images

Two methods were used to process the DCE images.

Phase-Derived Vascular Input Function with Bookend T1 Correction. Voxelwise maps of tissue contrast concentration with time were calculated by using pre- and post-DCE T1 maps combined with the tissue signal intensity-versus-time curve.[14] Phase analysis was used to estimate the arterial input function from 1 section where the superior sagittal sinus ran approximately parallel with the main magnetic field and perpendicular to the section. A small ROI (2–4 pixels) was drawn at the center of the superior sagittal sinus, and the mean phase was measured as a function of time. The phase-versus-time curve was converted to a gadolinium-versus-time curve, which was then saved in a text file. This step was performed off-line by using in-house software written in IDL (Exelis Visual Information Solutions, Boulder, Colorado) and is described in previous articles.[10,13] The gadolinium-versus-time curve was imported as the arterial input function in kinetic modeling analysis software (nordicICE software, Version 2; NordicNeuroLab, Bergen, Norway) for a voxel-by-voxel estimation of plasma volume obtained from the phase-derived vascular input function (Vp_Φ) and the volume transfer constant obtained from phase-derived vascular input function (K^{trans}_Φ). Postprocessing parameters were the following: noise level = 0, spatial smoothing = off, vascular deconvolution = on, normalize kinetic parameters = on, auto-detect arterial input function tissue delay = on, hematocrit correction factor = 0.45.

Magnitude-Derived Vascular Input Function with No T1 Correction. DCE magnitude images were processed directly in nordicICE to generate maps of plasma volume obtained from magnitude-derived vascular input function (Vp_SI) and volume transfer constant obtained from magnitude-derived vascular input function (K^{trans}_SI). The signal intensity (SI) was converted to percentage change in signal intensity (relSI) by using the expression: $\text{relSI}(t) = 100 \times (S(t) - S_o)/S_o$, where S is the SI at time t and S_o is the baseline SI. The relative change in 1/T1 was estimated from this relative change in signal intensity, which is assumed to be linearly related to 1/T1 changes. The VIF was selected from a small ROI placed in the superior sagittal sinus directly from the DCE images. Signal conversion was set as SI to relSI(%). Remaining postprocessing parameters were similar as for the

analysis with phase-derived vascular input function and bookend T1 correction.

Postprocessing of DSC Images

DSC images were processed by using singular value decomposition and deconvolution as implemented in nordicICE. MR signal intensity was converted to a T2 relaxation rate. An automated algorithm selected the most suitable pixels for VIF in a manually defined ROI covering the middle cerebral artery contralateral to the tumor. The SI was converted to relative change in R2 (ie, $R2^* = 1/T2^*$) by using the standard expression: $delR2(t) = -\ln(S(t)/S_o)/TE$, where S is the SI at time t and S_o is the baseline SI. Corrected rCBV maps were generated. Correction for leakage in rCBV calculations was done by using preinjection of contrast agent and linear fitting to estimate the T1 contamination caused by extravasation of contrast agent.[5] Postprocessing parameters were set in nordicICE as the following: noise level = 0, spatial smoothing = min, temporal smoothing = min, signal conversion SI to delR2, vascular deconvolution = on, apply contrast agent leakage correction = checked, detect both T1 and T2 leakage values = checked.

Image Interpretation

Two fellowship-trained neuroradiologists blinded to the histopathologic diagnosis examined the structural images to determine the preoperative grade of the tumor. We used radiologic criteria described by Asari et al[17] for grade II (nonenhancing mass, no central necrosis, absent or mild edema), grade III (enhancing mass, no central necrosis, mild or moderate edema), and grade IV gliomas (enhancing mass, with cyst or necrosis, moderate or severe edema). Axial T1-weighted postcontrast images were coregistered to the parametric maps. Because areas of highest values could vary between different parametric maps, a medical student traced 2 sets of ROIs: 1) 1 large "large tumor" ROI over the solid component of the tumor for the section where the tumor was largest (identical ROIs for all maps); and 2) 4 small "hot spot" ROIs (35 mm^2) over the areas of highest values, which could vary in location between maps. For each parametric map, the mean pixel value inside each of the 5 ROIs was calculated. For the 4 small hot spot ROIs, the 3 ROIs with the smallest values were discarded. Thus, for each parametric map, we recorded 2 values: 1 large tumor value and 1 hot spot value. All ROIs were verified by a neuroradiologist to ensure that inadvertent placement on an adjacent vessel or on hemorrhage was avoided. For DSC images, corrected rCBV values in tumors were normalized to the contralateral white matter.

Statistical Analysis

All data were analyzed by using MedCalc for Windows (Version 12; MedCalc Software, Mariakerke, Belgium). There were 5 components to the statistical analysis: 1) calculation of sensitivity and specificity for each reader by using the conventional, nondynamic contrast-enhanced MR images to grade gliomas; 2) assessment of interreader reliability by using the κ statistic; 3) tests for differences in hot spot DSC- and DCE-derived parameters, according to grades by using Kruskal-Wallis and Mann-Whitney U tests; 4) assessment of the diagnostic accuracy for each parameter in grading gliomas by using receiver operating characteristic analysis; and 5) correlation analysis between large tumor DSC- and DCE-derived parameters by using a Spearman rank correlation coefficient.

RESULTS

Participants

From March 2011 to December 2013, we prospectively recruited 70 patients with a mass suspicious for glioma. Forty-eight patients (25 men, 23 women) with a new histopathologic diagnosis of astrocytomas and adequate DCE and DSC images were included in the study. The mean age was 57 years (95% CI, 53–62 years). There were 9 patients with grade II astrocytomas, 11 patients with grade III (including 3 oligoastrocytomas), and 28 patients with grade IV. Thirty-two patients (5 grade II, 8 grade III, and 19 grade IV) received steroids before MR imaging. The median time between imaging and surgery was 6 days. Thirteen patients underwent a surgical biopsy (5 grade II, 3 grade III, and 5 grade IV), and 35 patients underwent a surgical resection.

Accuracy of Conventional Imaging for Distinguishing Low- from High-Grade Gliomas

For the differentiation of low- (grade II) and high-grade gliomas (grades III and IV), the sensitivity of contrast-enhanced MR imaging (95% for both readers) was higher than the specificity (56% for reader 1 and 67% for reader 2). The interreader agreement was moderate (weighted $\kappa = 0.56$; 95% CI, 0.37–0.75).

DSC- and DCE-Derived Parameters according to Tumor Grades

Tumor grade is a factor influencing DSC- and DCE-derived parameters according to the Kruskal-Wallis test of independent samples ($P < .05$). Post hoc pair-wise comparisons according to the Mann-Whitney U test showed that median Vp_Φ and K^{trans}_Φ parameters were lower for grade II compared with grade III astrocytomas ($P < .05$, On-line Table, Figure 1). Median rCBV, Vp_SI, and K^{trans}_SI values for grade II were not significantly different from those of grade III astrocytomas ($P = .08$, $P = .15$, and $P = .11$ respectively; On-line Table, Figure 1).

Among grade III astrocytomas, median Vp_Φ, K^{trans}_Φ, and K^{trans}_SI values were lower for the 7 pure astrocytomas than for the 4 astrocytomas with an oligoastrocytic component ($P < .05$). No statistically significant difference was found for median rCBV and Vp_SI values between the 2 groups ($P = .07$).

When comparing grade III with grade IV astrocytomas, median Vp_Φ, Vp_SI, rCBV, and K^{trans}_Φ values were significantly lower for grade III compared with grade IV ($P < .05$), while K^{trans}_SI values were not significantly different between the 2 groups ($P = .056$).

Accuracy of DSC- and DCE-Derived Parameters for Distinguishing Astrocytoma Grades

In differentiating low- from high-grade astrocytomas, the accuracy of Vp_Φ, Vp_SI, and K^{trans}_Φ (area under the curve = 0.88, 0.81, and 0.84, respectively) seems to be a higher than that of K^{trans}_SI and rCBV (area under the curve = 0.77 and 0.78), but this did not reach a statistically significant difference (Table 1). When we excluded patients with grade III oligoastrocytomas, the accuracy of various parameters was not affected. In differentiating grade III from grade IV gliomas, there was no significant differ-

ence in the accuracy among parameters (Table 2). When we excluded patients with grade III oligoastrocytomas, the specificity of each parameter was increased.

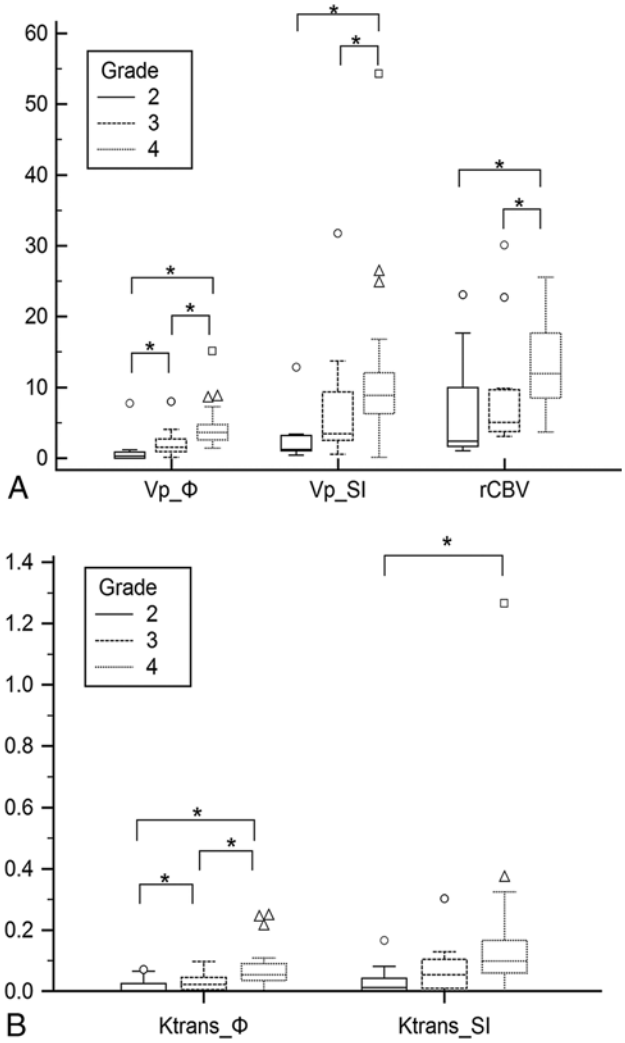

FIG 1. *A*, Boxplot graph of parameters Vp_Φ (milliliters/100 g), Vp_SI (milliliters/100 g), and rCBV (unitless) according to grades. *B*, Boxplot graph of parameters K^{trans}_Φ (minute^{-1}) and K^{trans}_SI (minute^{-1}) according to grades. The asterisk indicates $P < .05$.

Correlation Analysis between DSC- and DCE-Derived Parameters

There was a moderate correlation between rCBV and Vp_Φ mean values obtained from large tumor ROI ($r = 0.54$, $P < .05$, Table 3). There was a weaker correlation between rCBV and Vp_SI ($r = 0.44$, $P < .05$). There was a good correlation between Vp_Φ and Vp_SI ($r = 0.77$, $P < .05$) and between K^{trans} Φ and K^{trans}_SI ($r = 0.82$, $P < .05$).

DISCUSSION

Conventional imaging is not always accurate in differentiating low- from high-grade gliomas, particularly in the presence of a nonenhancing or poorly enhancing tumor.

DSC and DCE perfusion imaging have been reported to help in the preoperative grading of gliomas. In the differentiation between low- (2) and high-grade (III and IV) astrocytomas and between grade III and IV astrocytomas, we have found that the diagnostic accuracies of DCE-derived Vp and K^{trans} were similar to those of DSC-derived rCBV regardless of the choice of the VIF from magnitude or phase images. The diagnostic accuracies of DCE-derived parameters in this study were in the range of previously published data from 2 studies, 1 by using a hot spot method and 1 by using histogram analysis.[13,18] The accuracy of DSC-derived rCBV in this study was also similar to that in previous studies using hot spot analysis.[1,19]

Using the bookend T1 mapping and phase-derived VIF, we also found that DCE-derived Vp and K^{trans} were lower for grade II than for grade III astrocytomas. This difference could not be observed when we used a simpler DCE method by using MR signal intensity only. In our study, this difference was due to the presence of oligoastrocytomas among grade II tumors because no difference was found when comparing grade II with grade III pure astrocytomas. To our knowledge, the higher K^{trans} and Vp values seen in oligoastrocytomas relative to pure astrocytomas have not been previously reported with DCE imaging. It is known that DSC-derived rCBV is higher for oligoastrocytic and oligodendroglial tumors than for grade II and III astrocytic tumors.[20,21] This finding can be explained by the cortical location and the presence of a "chicken wire" type of vascularity in oligodendrogliomas.[21]

In our study, the correlation between DSC-derived rCBV and DCE-derived Vp was weak by using magnitude-derived VIF and moderate by using phase-derived VIF. It is possible that DCE-derived Vp and DSC-derived Vp are measuring slightly different vascular processes. Because we used a T2*-weighted DSC imag-

Table 1: Diagnostic accuracy of DSC- and DCE-derived parameters in differentiating high- and low-grade astrocytomas using hot spot ROIs[a]

	AUC	95% CI	Cutoff Value	Sensitivity (%)	Specificity (%)	Oligoastrocytomas
Vp_Φ	0.88	0.68–1	1.15	90	89	Including
Vp_Φ	0.87	0.68–1	1.16	89	89	Excluding
Vp_SI	0.81	0.64–0.98	3.38	79	89	Including
Vp_SI	0.80	0.62–0.98	3.39	83	89	Excluding
rCBV	0.78	0.54–1	3.31	97	67	Including
rCBV	0.78	0.54–1	3.31	97	67	Excluding
K^{trans}_Φ	0.84	0.66–1	0.0006	100	67	Including
K^{trans}_Φ	0.84	0.66–1	0.0006	100	67	Excluding
K^{trans}_SI	0.77	0.58–0.95	0.030	79	78	Including
K^{trans}_SI	0.76	0.57–0.94	0.030	76	78	Excluding

[a] No statistically significant difference ($P > .05$) was found between area under the curve of different parameters.

Table 2: Diagnostic accuracy of DSC- and DCE-derived parameters in differentiating between grade III and grade IV astrocytomas using hot spot ROIs[a]

	AUC	95% CI	Cutoff Value	Sensitivity %	Specificity %	Oligoastrocytomas
Vp_Φ	0.79	0.60–0.97	1.88	86	73	Including
Vp_Φ	0.95	0.89–1	1.88	86	100	Excluding
Vp_SI	0.71	0.49–0.93	4.21	89	73	Including
Vp_SI	0.91	0.81–1	4.21	89	100	Excluding
rCBV	0.73	0.51–0.95	5.04	93	55	Including
rCBV	0.83	0.56–1	5.04	93	86	Excluding
K^{trans}_Φ	0.75	0.57–0.94	0.023	86	64	Including
K^{trans}_Φ	0.85	0.66–1	0.024	86	86	Excluding
K^{trans}_SI	0.70	0.50–0.90	0.056	79	64	Including
K^{trans}_SI	0.76	0.69–1	0.046	79	71	Excluding

[a] No statistically significant difference ($P > .05$) was between area under the curve of different parameters.

Table 3: Spearman coefficients of rank correlation (ρ) between DSC- and DCE-derived parameters obtained from identical large tumor ROIs[a]

	Vp_Φ	Vp_SI	rCBV	K^{trans}_Φ	K^{trans}_SI
Vp_Φ (95% CI)	–	0.77 (0.63–0.87)	0.54 (0.27–0.70)	0.73 (0.56–0.84)	0.68 (0.49–0.81)
Vp_SI (95% CI)	0.77 (0.63–0.87)	–	0.44 (0.17–0.64)	0.62 (0.45–0.79)	0.75 (0.59–0.85)
rCBV (95% CI)	0.54 (0.27–0.70)	0.44 (0.17–0.64)	–	0.51 (0.26–0.69)	0.47 (0.22–0.67)
K^{trans}_Φ (95% CI)	0.73 (0.56–0.84)	0.62 (0.45–0.79)	0.51 (0.26–0.69)	–	0.82 (0.70–0.90)
K^{trans}_SI (95% CI)	0.68 (0.49–0.81)	0.76 (0.59–0.85)	0.47 (0.22–0.67)	0.82 (0.70–0.90)	–

[a] All correlations were statistically significant ($P < .05$).

ing, rCBV is probably more sensitive than Vp to the presence of large blood vessels in tumor. Further studies with histopathologic correlation are needed. Measurement bias is another possible factor that could explain a weak correlation between the 2 methods. For DSC-MR imaging, although we used a prebolus injection and performed a linear fitting to reduce T1 and residual T2 effects, this process might not completely overcome the decreased T2* effect from contrast leakage into the extravascular compartment. For DCE-MR imaging, Vp values have lower coefficients of variation by using the phase method with bookend T1 measurements than values obtained with magnitude-derived VIF. This could explain why a better correlation was found between Vp and CBV by using the phase method. Ludemann et al[16] compared DCE- and DSC-derived CBV values in intra-axial tumors with no baseline T1 measurements and found a borderline correlation (P value between 0.1 and 0.05). Haroon and al[15] found a good correlation ($r = 0.667$, $P < .05$) between DSC- and DCE-derived CBV in intra-axial tumors by using a method with baseline T1 calculation.

Both DSC and DCE techniques provide similar measurements of angiogenesis, which can help in the preoperative grading of gliomas. There are certain advantages and disadvantages for each technique. DSC perfusion imaging can provide semiquantitative measurements of rCBV from the whole brain with high temporal resolution and a short acquisition time (<2 minutes). The single-shot gradient-echo EPI sequence, which is the standard sequence for DSC perfusion, can have susceptibility artifacts at tissue interfaces. Three patients in our study had to be excluded due to the presence of significant intratumoral hemorrhage causing susceptibility artifacts and obscuring adjacent enhancing tumor tissue. Tumors located in the brain stem and near the skull base might also be obscured. Susceptibility artifacts are more important at 3T but can be reduced by the use of a spin-echo EPI sequence, which we did not use in our study. Another limitation is that rCBV is dependent on field strength, sequence parameters, and relaxivity of the contrast agent used.[22,23] A preinjection of contrast is also desirable to decrease T1 effects that could arise from contrast extravasation and could cause an underestimation of rCBV.[5]

DCE imaging can provide absolute measurements of plasma volume and K^{trans}, which could be useful as biomarkers for angiogenesis. However, it cannot provide the same spatial coverage and temporal resolution compared with DSC imaging. There is usually a compromise to be made between sufficient temporal resolution and adequate spatial coverage for DCE acquisition protocols. Another common limitation of DCE imaging is the difficulty in obtaining an accurate VIF. This limitation can be overcome by using phase images to derive the VIF.[9-13] Phase measurements are less biased by intensity changes from inflow and relaxation effects. Magnitude-derived vascular input functions can underestimate the contrast concentration measurement during the first pass (if >5 mmol/L), especially when a high-relaxivity agent is used.[9]

One limitation of our study is the estimation of the precontrast T1 map by using a variable flip angle technique with only 2 flip angles. This approach is sensitive to B1 variation and could introduce errors in the conversion of DCE signal to concentration. However, the estimation of both pre- and postcontrast T1 maps can reduce errors in the conversion of signal-to-contrast concentration.[24] A modified look-locker inversion recovery technique would have improved T1 mapping (data not shown), but this sequence was not available at the beginning of our study. Another limitation of the study is the small sample size, which might not provide enough power to reveal a statistically significant difference in the diagnostic accuracies between DSC and DCE parameters in differentiating low- from high-grade gliomas. The initial sample size calculation for our study was based on the recruitment of 35 patients with high-grade and 15 patients with low-grade gliomas. However, we could only enroll 9 patients with biopsy-proved low-grade gliomas, decreasing the power of our study. A third limitation is the possibility of inaccurate histo-

pathologic grading due to sampling error in the 13 patients who had a only biopsy and not a surgical resection.

CONCLUSIONS

In differentiating between low- and high-grade astrocytomas and grade III and IV astrocytomas, we found that DCE-derived K^{trans} and Vp parameters have the same diagnostic accuracy as DSC-derived rCBV.

ACKNOWLEDGMENTS

We acknowledge William Petrcich, MS, and Betty Anne Schwarz, MS, RN, who provided statistical and administrative support for this study.

Disclosures: Thanh Binh Nguyen—*RELATED*: *Grant*: Bayer HealthCare,* *Comments*: investigator-initiated research grant; *Consulting Fee or Honorarium*: Bayer HealthCare, *Comments*: for attendance of advisory panel; *Support for Travel to Meetings for the Study or Other Purposes*: Bayer HealthCare, *Comments*: reimbursement for travel expenses; *UNRELATED*: *Grants/Grants Pending*: Brain Tumour Foundation of Canada*; *Payment for Development of Educational Presentations*: Bayer HealthCare. Kirstin Perdrizet—*RELATED*: *Grant*: Mach-Gaensslen Research award, *Comments*: research award granted to me during the summer as an undergraduate research student. Kathryn Bezzina—*RELATED*: *Grant*: Mach-Gaensslen of Canada, *Comments*: 2013 grant recipient as part of Summer Studentship Program. Carlos H. Torres—*RELATED*: Bayer HealthCare,* *Comments*: researcher-initiated grant. Santanu Chakraborty—*RELATED*: *Grant*: Bayer HealthCare*; *UNRELATED*: *Grants/Grants Pending*: GE Healthcare.* Brandon Zanette—*RELATED*: *Grant*: Bayer HealthCare, *Comments*: Part of my graduate student stipend was paid for from an investigator-initiated research grant from Bayer HealthCare. *Money paid to the institution.

REFERENCES

1. Law M, Yang S, Wang H, et al. **Glioma grading: sensitivity, specificity, and predictive values of perfusion MR imaging and proton MR spectroscopic imaging compared with conventional MR imaging.** *AJNR Am J Neuroradiol* 2003;24:1989–98
2. Ellika SK, Jain R, Patel SC, et al. **Role of perfusion CT in glioma grading and comparison with conventional MR imaging features.** *AJNR Am J Neuroradiol* 2007;28:1981–87
3. Fan GG, Deng QL, Wu ZH, et al. **Usefulness of diffusion/perfusion-weighted MRI in patients with non-enhancing supratentorial brain gliomas: a valuable tool to predict tumour grading?** *Br J Radiol* 2006;79:652–58
4. Liu X, Tian W, Kolar B, et al. **MR diffusion tensor and perfusion-weighted imaging in preoperative grading of supratentorial nonenhancing gliomas.** *Neuro Oncol* 2011;13:447–55
5. Boxerman JL, Schmainda KM, Weisskoff RM. **Relative cerebral blood volume maps corrected for contrast agent extravasation significantly correlate with glioma tumor grade, whereas uncorrected maps do not.** *AJNR Am J Neuroradiol* 2006;27:859–67
6. Boxerman JL, Prah DE, Paulson ES, et al. **The role of preload and leakage correction in gadolinium-based cerebral blood volume estimation determined by comparison with MION as a criterion standard.** *AJNR Am J Neuroradiol* 2012;33:1081–87
7. Sourbron S, Ingrisch M, Siefert A, et al. **Quantification of cerebral blood flow, cerebral blood volume, and blood-brain-barrier leakage with DCE-MRI.** *Magn Reson Med* 2009;62:205–17
8. Patankar TF, Haroon HA, Mills SJ, et al. **Is volume transfer coefficient (Ktrans) related to histologic grade in human gliomas?** *AJNR Am J Neuroradiol* 2005;26:2455–65
9. de Rochefort L, Nguyen T, Brown R, et al. **In vivo quantification of contrast agent concentration using the induced magnetic field for time-resolved arterial input function measurement with MRI.** *Med Phys* 2008;35:5328–39
10. Foottit C, Cron GO, Hogan MJ, et al. **Determination of the venous output function from MR signal phase: feasibility for quantitative DCE-MRI in human brain.** *Magn Reson Med* 2010;63:772–81
11. Bleeker EJ, van Buchem MA, Webb AG, et al. **Phase-based arterial input function measurements for dynamic susceptibility contrast MRI.** *Magn Reson Med* 2010;64:358–68
12. Garpebring A, Wirestam R, Yu J, et al. **Phase-based arterial input functions in humans applied to dynamic contrast-enhanced MRI: potential usefulness and limitations.** *MAGMA* 2011;24:233–45
13. Nguyen TB, Cron GO, Mercier JF, et al. **Diagnostic accuracy of dynamic contrast-enhanced MR imaging using a phase-derived vascular input function in the preoperative grading of gliomas.** *AJNR Am J Neuroradiol* 2012;33:1539–45
14. Cron GO, Kelcz F, Santyr GE. **Improvement in breast lesion characterization with dynamic contrast-enhanced MRI using pharmacokinetic modeling and bookend T(1) measurements.** *Magn Reson Med* 2004;51:1066–70
15. Haroon HA, Patankar TF, Zhu XP, et al. **Comparison of cerebral blood volume maps generated from T2* and T1 weighted MRI data in intra-axial cerebral tumours.** *Br J Radiol* 2007;80:161–68
16. Lüdemann L, Warmuth C, Plotkin M, et al. **Brain tumor perfusion: comparison of dynamic contrast enhanced magnetic resonance imaging using T1, T2 and T2* contrast, pulsed arterial spin labeling, and $H_2(15)O$ positron emission tomography.** *Eur J Radiol* 2009;70:465–74
17. Asari S, Makabe T, Katayama S, et al. **Assessment of the pathological grade of astrocytic gliomas using an MRI score.** *Neuroradiology* 1994;36:308–10
18. Jung SC, Yeom JA, Kim JH, et al. **Glioma: application of histogram analysis of pharmacokinetic parameters from T1-weighted dynamic contrast-enhanced MR imaging to tumor grading.** *AJNR Am J Neuroradiol* 2014;35:1103–10
19. Emblem KE, Nedregaard B, Nome T, et al. **Glioma grading by using histogram analysis of blood volume heterogeneity from MR-derived cerebral blood volume maps.** *Radiology* 2008;247:808–17
20. Saito T, Yamasaki F, Kajiwara Y, et al. **Role of perfusion-weighted imaging at 3T in the histopathological differentiation between astrocytic and oligodendroglial tumors.** *Eur J Radiol* 2012;81:1863–69
21. Cha S, Tihan T, Crawford F, et al. **Differentiation of low-grade oligodendrogliomas from low-grade astrocytomas by using quantitative blood-volume measurements derived from dynamic susceptibility contrast-enhanced MR imaging.** *AJNR Am J Neuroradiol* 2005;26:266–73
22. Mauz N, Krainik A, Tropres I, et al. **Perfusion magnetic resonance imaging: comparison of semiologic characteristics in first-pass perfusion of brain tumors at 1.5 and 3 Tesla.** J *Neuroradiol* 2012;39:308–16
23. Giesel FL, Mehndiratta A, Risse F, et al. **Intraindividual comparison between gadopentetate dimeglumine and gadobutrol for magnetic resonance perfusion in normal brain and intracranial tumors at 3 Tesla.** *Acta Radiol* 2009;50:521–30
24. Zanette B, Cron GO, Nguyen TB, et al. **Accuracy of quantitative 3D DCE-MRI using variable flip angle T1 mapping, B1 correction, and the bookend method.** In: *Proceedings of the 21st Annual Meeting of the International Society of Magnetic Resonance Imaging in Medicine,* Salt Lake City, Utah. April 20–26, 2013.

Patterns of Tumor Contrast Enhancement Predict the Prognosis of Anaplastic Gliomas with *IDH1* Mutation

Y.Y. Wang, K. Wang, S.W. Li, J.F. Wang, J. Ma, T. Jiang, and J.P. Dai

ABSTRACT

BACKGROUND AND PURPOSE: It is proposed that *isocitrate dehydrogenase 1* (*IDH1*) mutation predicts the outcome in patients with high-grade glioma. In addition, contrast enhancement on preoperative MR imaging reflects tumor biologic features. Patients with anaplastic glioma with the *IDH1* mutation were evaluated by using MR imaging to determine whether tumor enhancement is a prognostic factor and can be used to predict survival.

MATERIALS AND METHODS: A cohort of 216 patients with histologically confirmed anaplastic glioma was reviewed retrospectively. Tumor contrast-enhancement patterns were classified on the basis of preoperative T1 contrast MR images. Tumor *IDH1* status was examined by using RNA sequencing. We used univariate analysis and the multivariate Cox model to evaluate the prognostic value of the *IDH1* mutation and tumor contrast-enhancement pattern for progression-free survival and overall survival.

RESULTS: In all 216 patients, *IDH1* mutation was associated with longer progression-free survival ($P = .004$, hazard ratio = 0.439) and overall survival ($P = .002$, hazard ratio = 0.406). For patients with *IDH1* mutant anaplastic glioma, the absence of contrast enhancement was associated with longer progression-free survival ($P = .038$, hazard ratio = 0.473) and overall survival ($P = .043$, hazard ratio = 0.436). Furthermore, we were able to stratify the progression-free survival and overall survival of patients with *IDH1* mutation by using the tumor contrast-enhancement patterns ($P = .022$ and 0.029, respectively; log-rank).

CONCLUSIONS: Tumor enhancement on postcontrast MR imaging is a valuable prognostic factor for patients with anaplastic glioma and *IDH1* mutation. Furthermore, the contrast-enhancement patterns could potentially be used to stratify the survival outcome of such patients.

ABBREVIATIONS: AG = anaplastic glioma; GTR = gross total resection; <GTR = residual tumor; HR = hazard ratio; *IDH1* = *isocitrate dehydrogenase 1*; KPS = Karnofsky Performance Status Scale; PFS = progression-free survival; OS = overall survival

Anaplastic gliomas (AGs), classified as World Health Organization grade III, are aggressive brain tumors. They exhibit morphometric heterogeneity on radiologic imaging, and their clinical course varies substantially so that some patients succumb to progressive disease within weeks while others survive for a decade or more. The clinical characteristics, radiologic features, genetic changes, and extent of resection all play important roles in determining the prognosis of patients with AG.[1-9] Interaction and synergy may exist among these factors.

The presence of contrast enhancement on MR images, which is based on pathophysiologic changes indicating the destruction of the blood-brain barrier, is considered a specific radiologic feature of high-grade gliomas. Previous studies have revealed the prognostic role of contrast enhancement in patients with AG.[5,8,10-12] Additionally, radiologic features such as enhancement and multifocality correlate with the molecular characteristics of malignant glioma.[13]

Mutation in the *isocitrate dehydrogenase 1* (*IDH1*) gene at R132 is an important molecular event and plays a significant role in gliomagenesis. This genetic change is detected in approximately 50%–70% of anaplastic astrocytomas[1,14,15] and in 70% of anaplastic oligodendrogliomas.[14-16] Furthermore, the presence of

Received January 26, 2015; accepted after revision March 21.

From the Departments of Neurosurgery (Y.Y.W., J.F.W., T.J.) and Neuroradiology (K.W., S.W.L., J.M., J.P.D.), Beijing Tian Tan Hospital, and Beijing Neurosurgical Institute (Y.Y.W., T.J., J.P.D.), Capital Medical University, Beijing, China; and Center for Brain Tumor (T.J.), Beijing Institute for Brain Disorders, Beijing, China.

Yinyan Wang and Kai Wang contributed equally to this article.

The authors declare that they have no conflict of interest.

This work was supported by the National High Technology Research and Development Program No. 2011CB707804 and No. 2015CB755500 (T.J.) and the National Natural Science Foundation of China No. 81271541 (J.P.D.).

Please address correspondence to Tao Jiang, PhD, Beijing Neurosurgical Institute, Capital Medical University, 6, Tiantanxili, Beijing, 100050, China; e-mail: taojiang1964@163.com; and Jianping Dai, PhD, Beijing Neurosurgical Institute, Capital Medical University, 6, Tiantanxili, Beijing, 100050, China; e-mail: djpbeijing@hotmail.com; @taojiang1964

Indicates open access to non-subscribers at www.ajnr.org

http://dx.doi.org/10.3174/ajnr.A4407

IDH1 mutations distinguishes tumors with markedly different clinical presentations, concurrent molecular genetic alterations, and overall natural history.[1] For patients with AG, the occurrence of *IDH1* mutation is associated with gross total resection (GTR) and longer overall survival (OS).[17]

Previous studies have demonstrated the correlation between *IDH1* status and the radiologic features of glioma, in that tumors with *IDH1* mutation are more likely to be larger, and cyst, edema, and contrast enhancement are present.[18] However, investigations of the interactive and synergistic role of *IDH1* mutation and tumor contrast enhancement in predicting the survival of patients with AG are rare. By classifying tumor contrast enhancement according to the patterns observed, patients with anaplastic glioma with *IDH1* mutation were evaluated by using MR imaging to determine whether tumor enhancement is a prognostic factor and can be used to predict outcome survival stratification.

MATERIALS AND METHODS

Patients

In total, 216 adult patients diagnosed with AG who had undergone surgical treatment at our institution from February 2007 to June 2010 were reviewed retrospectively. Patients were included on the basis of the following criteria: 1) age 18 years or older, 2) presurgical structural MR imaging scan available (T1-weighted, T2-weighted, postcontrast T1-weighted), 3) pathology-confirmed AG based on the modified World Health Organization grading system, and 4) no previous diagnosis of any brain tumor. The histopathologic diagnosis was evaluated and confirmed by 2 independent neuropathologists blinded to the patients' clinical and radiologic information. According to the Response Assessment in Neuro-Oncology criteria,[19] GTR was defined as no visible contrast enhancement on postoperative MR images within 72 hours after the operation in contrast-enhanced tumors or absence of all abnormal hyperintense changes on preoperative MR images for tumors not demonstrating contrast enhancement. In this study, resections that were not GTR were considered residual tumor (<GTR). The overall follow-up duration was 85 months, which spanned March 2007 to April 2014. This study was approved by our institutional review board, and written consent was obtained from all enrolled patients.

Imaging Acquisition

MR imaging was performed on Trio 3T scanners (Siemens, Erlangen, Germany). It typically included axial T1-weighted (TR, 450 ms; TE, 15 ms; section thickness, 5 mm), T2-weighted fast spin-echo (TR, 6000 ms; TE, 140 ms; section thickness, 5 mm), and Gd-DTPA injection- enhanced (Beijing Beilu Pharmaceutical, Beijing, China; 0.1 mmol/kg) axial T1-weighted images (TR, 450 ms; TE, 15 ms; section thickness, 5 mm), with a 24-cm FOV and 256 × 256 matrix size. Postcontrast images were acquired immediately following injection of the contrast agent. The interval between contrast injection and the beginning of the contrast-enhanced T1-weighted image acquisition was maintained between 75 and 85 seconds. Postoperative MR images for determining the extent of resection were obtained within 72 hours after resection, and the radiologic parameters were maintained in accordance with the preoperative scans.

Identification of Imaging Features

Tumor contrast enhancement was assessed by 2 experienced neuroradiologists (Q.C. and X.C., who have 14 and 12 years of experience, respectively, in diagnosis using brain MR imaging) blinded to the patient clinical information. In cases in which the types of enhancement identified by the first 2 neuroradiologists were inconsistent, a third senior neuroradiologist (J.M., 25 years of experience in brain disease diagnosis) re-examined the images and determined the image to be used. "Contrast enhancement" was defined as newly emerged unequivocal increased signal intensity on the T1-weighted image following intravenous contrast administration compared with noncontrast T1 images. "Nonenhancement" was defined as no apparent hyperintensity on postcontrast T1-weighted images. Three contrast-enhancement patterns were identified on the basis of the size and morphologic features of the largest enhanced area on contrast-enhanced MR images regardless of whether it was single or multifocal: nodular, with the largest focal diameter of ≤1.5 cm; patchy, tumors with a maximum diameter of enhancement of >1.5 cm; and ringlike, cystic necrosis with peripheral enhancement (Fig 1). Multifocal tumor enhancement was defined as >1 area of tumor enhancement separated from the others on the postcontrast T1-weighted image.

DNA Sequencing for IDH1 Mutation

IDH1 mutation was determined by using DNA pyrosequencing, which we have described previously.[20] Briefly, a QIAamp DNA Mini Kit (QIAGEN, Hilden, Germany) was used to isolate genomic DNA from frozen tumor tissue samples. We then analyzed the genomic region spanning the wild type R132 of *IDH1* by using pyrophosphate sequencing with 5′-GCTTGTGAGTGGATGGGTAAAAC-3′ and 5′-biotin-TTGCCAACATGACTTACTTGATC-3′ primers. Duplicate polymerase chain reaction analyses were performed in 40-μL reaction volumes containing 1-μL of each 10-μmol/L forward and reverse primer, 4 μL of 10× buffer, 3.21 μL of 2.5-mmol/L deoxynucleotide triphosphates, 2.5-U HotStar *Taq* (Takara, Shiga, Japan), and 2 μL of 10 μmol/L DNA. The polymerase chain reaction conditions were as follows: 95°C for 3 minutes; 50 cycles of 95°C for 15 seconds, 56°C for 20 seconds, 72°C for 30 seconds; and 72°C for 5 minutes (Applied Biosystems GeneAmp PCR System 9700; Applied Biosystems, Foster City, California). Single-stranded DNA was purified from the polymerase chain reaction products and pyrosequenced with a PyroMark Q96 ID System (QIAGEN) by using a 5′-TGGATGGGTAAAACCT-3′ primer and an EpiTect Bisulfite Kit (QIAGEN).

Statistical Analysis

We used the χ^2 test for categoric variables to compare each clinical and imaging feature between the *IDH1* mutant and wild type groups. The agreement between judgments of the enhancement patterns assessed by the 2 radiologists was evaluated by using the κ consistency test. A κ value of ≥0.81, 0.61–0.80, and ≤0.60 was considered excellent, good, and poor agreement, respectively. Additionally, log-rank analysis of Kaplan-Meier data was performed to compare the progression-free survival (PFS) and OS of the cohort. Factors that were significant ($P < .05$) in univariate anal-

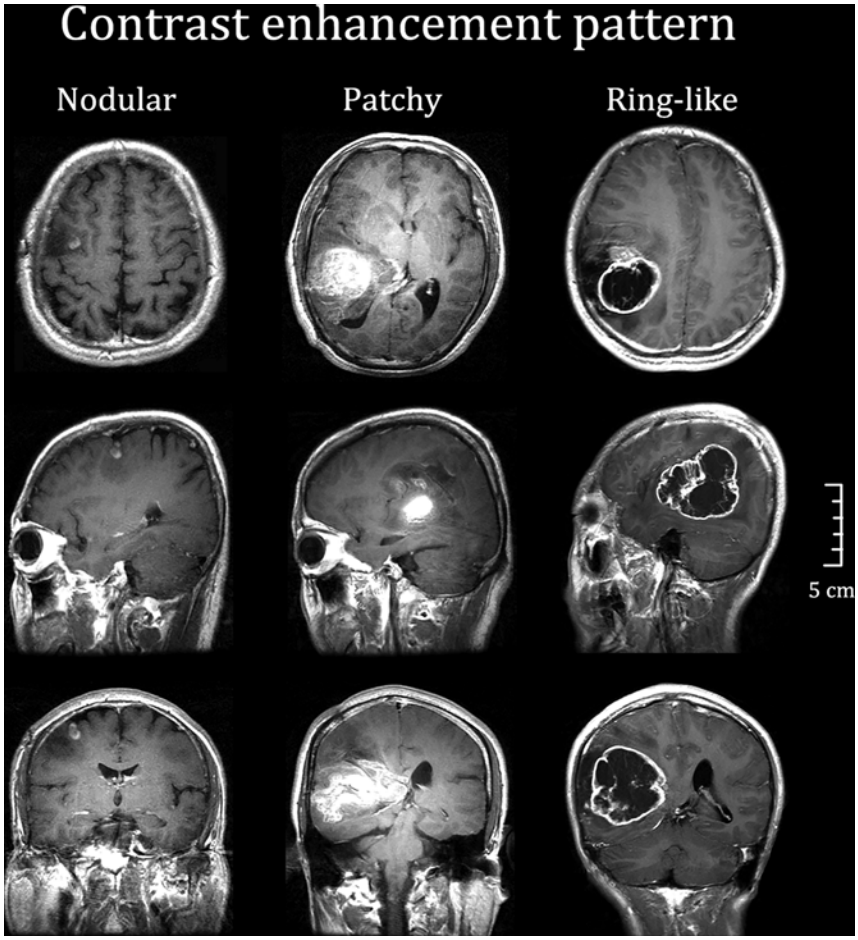

FIG 1. Tumor contrast-enhancement patterns in AG. Postcontrast T1-weighted images depict the nodular (largest focal diameter of ≤1.5 cm), patchy (largest focal diameter of >1.5 cm), and ringlike (cystic necrosis with peripheral enhancement) enhancement patterns.

Table 1: *IDH1* mutation status of patients with AG

Characteristics	*IDH1* Status			
	Total (*n* = 216)	Mutant (*n* = 84)	Wild Type (*n* = 132)	*P* Value[a]
Age (yr)				
Median (range)	44 (18–87)	43 (18–71)	45 (18–87)	
50 or older/50 or younger	77:139	23:61	54:78	.043
Sex				
Male/female	135:81	49:35	86/46	.313
KPS				
≥80/<80	181/35	78/6	103/29	.004
Contrast enhancement				
Yes/no	173/43	57/27	116/16	<.001
Pattern of enhancement				
Nodular/patchy/ringlike	26/62/85	9/14/34	17/48/51	.084
Extent of resection				
GTR/<GTR	123/93	56/28	67/65	.021
Histopathology				
AA/AO/AOA	57/44/115	16/20/48	41/24/67	.135

Note:—AA indicates anaplastic astrocytomas; AO, anaplastic oligodendrogliomas; AOA, anaplastic oligoastrocytomas.
[a] Results of the χ^2 test.

ysis were entered into multivariate survival analysis on the basis of the Cox proportional hazard ratio (HR) model. To identify the prognostic value of *IDH1* status and tumor contrast-enhancement pattern in patients according to their interactive effects, we subdivided patients into 4 subgroups according to these 2 indicators. The respective prognostic values of the tumor contrast-enhancement pattern of the *IDH1* mutant and wild type groups were evaluated.

RESULTS

Patient Characteristics

The clinical and radiologic data of the 216 patients with AG were reviewed (Table 1). Among these patients, 57 (26.4%) had anaplastic astrocytoma, 44 (20.4%) had anaplastic oligodendroglioma, and 115 (53.2%) had anaplastic oligoastrocytoma. Age at diagnosis, preoperative Karnofsky Performance Status Scale (KPS), and extent of resection were significantly different between patients with mutant and wild type *IDH1* ($P < .001$, χ^2 test). A total of 123 (56.9%) patients underwent GTR, and 93 (43.1%) patients had residual tumor.

Association between IDH1 *Mutation and Tumor Enhancement*

There was post-T1 contrast enhancement in 173 (80.1%) tumors. Patients with *IDH1* mutation were less likely to have MR imaging tumor enhancement than patients with wild type *IDH1* (67.9% versus 87.9%, $P < .001$). In addition, tumor contrast-enhancement patterns were identified in the AGs with enhancement. The κ value for the agreement of judgment of enhancement patterns between the 2 evaluators was 0.96 ($P = .012$). Enhancement was nodular in 26 (15.0%) cases, patchy in 62 (35.9%) cases, and ringlike in 85 (49.1%) cases (Table 1). However, there was no significant difference between the proportion of contrast-enhancement patterns between tumors from patients with mutant and wild type *IDH1* ($P = .084$) (Fig 2).

Association between Surgical Resection and Tumor Enhancement

Of the tumors with contrast enhancement, those with ringlike enhancement patterns were more likely to undergo GTR than tumors without ringlike enhancement patterns, but the difference was not statistically significant (59.7% versus 46.9%, $P = .113$). Notably, patients with mutant *IDH1* and tumors with ringlike enhancement patterns were also more likely to undergo GTR than patients with mutant *IDH1* and tumors without ringlike enhancement patterns (65.3% versus 37.5%, $P = .004$). However, in patients with wild type *IDH1*, GTR between tumors with and without

ringlike enhancement patterns was not significantly different (47.8% versus 66.7%, $P = .157$).

Progression-Free Survival

There was tumor recurrence in 165 (76.4%) patients during the follow-up period; the median PFS was 16.9 months (range, 3.1–82.8 months). Univariate analysis showed that patients with mutant *IDH1* had significantly longer PFS than patients with wild type *IDH1* ($P = .002$, log-rank). Additionally, age at diagnosis ($P < .001$), preoperative KPS ($P = .004$), and GTR ($P = .001$) were significant prognostic factors for PFS (Table 2). In multivariate Cox regression analysis, wild type *IDH1* ($P = .004$, HR = 2.277; 95% confidence interval, 1.303–3.968), preoperative KPS < 80 ($P = .015$, HR = 2.158; 95% CI, 1.179–3.471), age at diagnosis older than 50 years ($P = .018$, HR = 1.857; 95% CI, 1.111–3.106), and <GTR ($P = .028$, HR = 1.598; 95% CI, 1.053–2.597) were associated with poor PFS (Table 3).

Overall Survival

At the time of analysis, 69 patients (whose follow-up data were available) were still alive; the median follow-up period was 22.9 months (range, 3.3–86.4 months). In univariate analysis, *IDH1* status ($P = .004$), age at diagnosis ($P = .007$), preoperative KPS ($P = .002$), and extent of resection ($P < .001$) were prognostic factors of OS (Table 2). These 4 factors remained significant in the multivariate Cox proportional hazards analysis: Wild type *IDH1* ($P = .002$, HR = 2.463; 95% CI, 1.389–4.386), age at diagnosis 50 years and older ($P = .016$, HR = 1.431; 95% CI, 1.342–2.434), preoperative KPS < 80 ($P = .026$, HR = 1.836; 95% CI, 1.087–3.402), and <GTR ($P = .023$, HR = 1.488; 95% CI, 1.210–2.432) were poor prognostic factors for OS (Table 3).

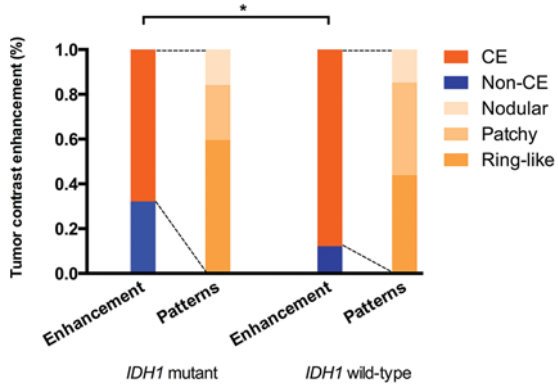

FIG 2. Constitution of tumor contrast enhancements between AG accompanied by mutant or wild type *IDH1*. The difference in contrast-enhancement rate (*asterisk*) between tumors from patients with mutant and wild type *IDH1* was significant ($P < .001$). There was no significant difference in enhancement-pattern distribution between tumors from patients with mutant and wild type *IDH1* ($P = .135$). CE indicates contrast enhancement.

Prognostic Role of Tumor Contrast-Enhancement Pattern for Patients with Mutant IDH1

In the mutant *IDH1* group, patients with contrast-enhanced tumors had significantly shorter PFS (median PFS, 15.9 months; range, 2.6–76.8 months) than those with nonenhanced tumors (median PFS, 26.3 months; range, 2.7–80.3 months) ($P = .038$, log-rank) (Fig 3). Furthermore, the tumor contrast-enhancement patterns allowed us to stratify the PFS of patients with mutant *IDH1*. Patients with nodular enhancement patterns had significantly longer PFS (median, 23.8 months) than those with patchy (median, 17.6 months) ($P = .042$, log-rank) or ringlike enhancement patterns (median, 14.7 months) ($P = .010$, log-rank). There were no significant differences between the PFS of patients with patchy or ringlike enhancement patterns ($P = .273$, log-rank) (Fig 4). In comparison, the tumor contrast enhancement patterns had no prognostic value in patients with wild type *IDH1* ($P = .896$, log-rank).

Patients were subdivided into 4 groups according to *IDH1* status and tumor contrast enhancement. Notably, among the 4 groups, patients with mutant *IDH1* and nonenhanced tumor had significantly longer OS than patients in the other groups ($P = .043$, Fig 3). Tumor contrast-enhancement pattern played a prognostic role in the OS of patients with mutant *IDH1*. In the mutant *IDH1* group, patients with nodular enhancement patterns had significantly longer OS (median, 31.8 months) than those with patchy (median, 27.1 months) ($P = .025$, log-rank) and ringlike enhancement patterns (median, 20.3 months) ($P = .012$, log-rank). There were no significant differences between the OS of patients with patchy enhancement patterns and those with ringlike enhancement patterns ($P = .441$, log-rank) (Fig 4). In comparison, tumor contrast enhancement patterns were not a prognostic factor in patients with wild type *IDH1* ($P = .842$, log-rank).

Prognostic Role of Extent of Resection for Patients with Mutant IDH1 and Contrast Enhancement

In the mutant *IDH1* and contrast-enhancement groups, patients with GTR had significantly longer PFS (median, 19.2 months; range, 2.1–75.8 months) than those with <GTR (median, 13.0 months; range, 3.0–73.7 months) ($P = .018$, log-rank). Similarly, for patients with mutant *IDH1* and contrast-enhanced tumors, GTR also predicted significantly longer OS than <GTR ($P = .030$,

Table 2: Univariate analysis of survival outcomes for patients with AG

Characteristic	PFS			OS		
	P Value	HR	95% CI	*P* Value	HR	95% CI
Age 50 yr or older	<.001	1.813	1.318–2.494	.007	1.729	1.134–2.421
Sex (male)	.215	0.873	0.695–1.064	.415	0.914	0.612–1.283
Preoperative KPS < 80	.004	2.603	1.154–3.548	.002	2.872	1.270–3.341
Enhancement	.570	1.200	0.641–2.247	.625	1.187	0.596–2.365
Enhancement pattern	.150	1.107	0.964–1.271	.247	1.902	0.941–1.266
<GTR/GTR	.001	1.734	1.237–2.429	<.001	1.926	1.346–2.758
Histopathology	.086	0.855	0.715–1.022	.054	0.789	0.654–1.002
IDH1 wild type	.002	2.364	1.362–4.098	.004	2.688	1.231–4.717

log-rank). Nevertheless, GTR did not have prognostic power for PFS and OS in the wild type *IDH1* and contrast-enhancement groups (PFS, $P = .224$; OS, $P = .141$, respectively; log-rank).

DISCUSSION

We combined clinical, radiologic, and specific genetic characteristics to investigate the prognostic factors for a large cohort of patients with AG, demonstrating that *IDH1* mutation was an independent prognostic factor for patients with AG. Furthermore, the tumor contrast-enhancement pattern identified from post-contrast MR imaging was associated with the survival outcomes of patients with mutant *IDH1*. To our knowledge, this is the first investigation of the prognostic role of combined *IDH1* mutation and tumor contrast-enhancement pattern for predicting survival in patients with AG.

Table 3: Multivariate analysis of survival outcomes

Predictor	*P* Value[a]	HR	95% CI
PFS			
Age 50 yr or older	.018	1.857	1.111–3.106
Preoperative KPS < 80	.015	2.158	1.179–3.471
<GTR	.028	1.598	1.053–2.597
IDH1 wild type	.004	2.277	1.303–3.968
OS			
Age 50 yr or older	.016	1.431	1.342–2.434
Preoperative KPS < 80	.026	1.836	1.087–3.402
<GTR	.023	1.488	1.210–2.432
IDH1 wild-type	.002	2.463	1.389–4.386

[a] Cox proportional hazard regression analyses. A *P* value of .05 denoted significance.

Previous studies have demonstrated the impact of *IDH1* mutation on the clinical prognosis of patients with malignant glioma.[1] In patients with AG, it has been demonstrated that *IDH1* mutation is a good prognostic marker and potential stratification factor for anaplastic astrocytoma and anaplastic oligodendroglioma.[20,21] Consistent with these findings, the present study showed that patients with mutant *IDH1* had significantly longer PFS and OS than those with wild type *IDH1*. The better prognosis of patients with mutant *IDH1* may be partly attributed to the effect of *IDH1* interaction with other clinical characteristics. First, *IDH1* mutation is frequent in diffuse low-grade gliomas but rare in primary glioblastomas, and the survival outcome of patients with low-grade glioma is generally better than that of patients with glioblastoma.[1,14,15,22] This variance of *IDH1* mutation incidence between low- and high-grade gliomas may contribute to the association of *IDH1* mutation with good prognosis. In addition, *IDH1* mutation is more common in younger than elder patients.[23] Because age is a widely reported significant prognostic factor,[2,4,6,18,24] the prognosis of patients with mutant *IDH1* might be good.

In this study, the frequency of *IDH1* mutation between the 2

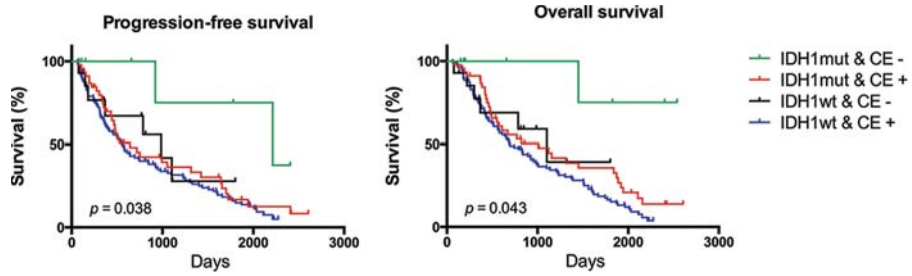

FIG 3. Kaplan-Meier plots of the series of 216 patients with AG showing the association between the PFS and OS according to combined *IDH1* status and tumor contrast enhancement. Mutant *IDH1* with no contrast enhancement predicts better survival (PFS, $P = .038$; OS, $P = .043$). mut indicates mutant; wt, wild type.

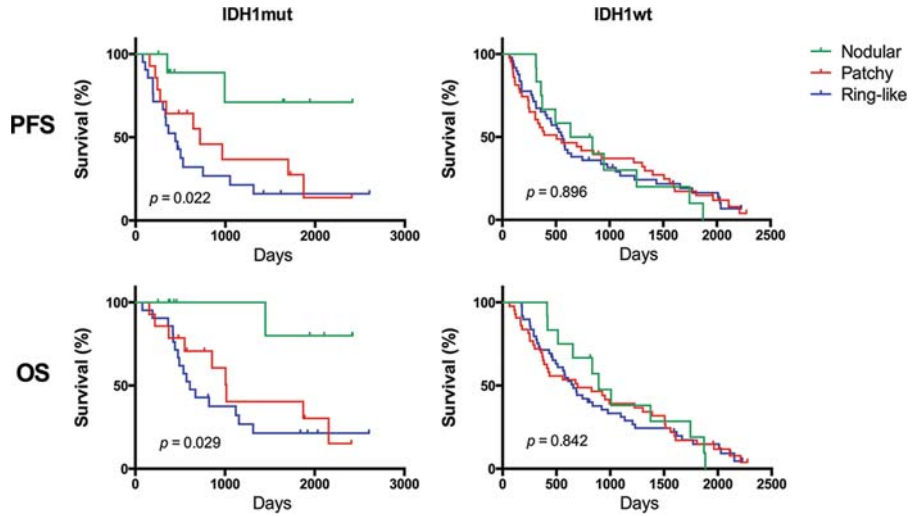

FIG 4. Kaplan-Meier plots showing that the tumor contrast enhancement pattern enabled stratification of the PFS and OS of patients with mutant *IDH1* (PFS, $P = .022$; OS, $P = .029$). Meanwhile, Kaplan-Meier plots show that the tumor contrast-enhancement pattern did not enable stratification of the PFS and OS of patients with wild type *IDH1* (PFS, $P = .896$; OS, $P = .842$).

age groups (50 years and older and younger than 50 years of age at diagnosis) was marginally significantly different ($P = .043$); these results agreed with the previous ones. Furthermore, this and a previous study[25] found that GTR was more likely to be achieved in AG with mutant *IDH1* than in AG with wild type *IDH1*. There was a higher rate of ringlike enhancement patterns in patients with mutant *IDH1*; in addition, these patients were more likely to undergo GTR than patients whose tumors did not have ringlike enhancement patterns, which could also have contributed to the difference in survival outcome between the 2 subgroups.

On the other hand, previous studies have suggested that the good prognosis of patients with mutant *IDH1* is primarily due to the less aggressive biologic behavior of tumors with mutant *IDH1* compared with tumors with wild type *IDH1*.[17,19,26] Because *IDH1* mutation is considered an early genetic event in tumorigenesis and may drive other genetic changes in tumor cells, tumors accompanied by *IDH1* mutation may consequently have different genetic characteristics compared with tumors unaccompanied by the mutation, which may lead to their varied biologic features. The intrinsic difference in the tumor biologic features may explain why the *IDH1* mutation, though associated with other clinical characteristics, was an independent prognostic factor for patients with AG. Other than *IDH1* mutation, however, the histopathologic subtypes in the present study did not have prognostic value, indicating that the variety of tumor components could not predict survival for patients with AG.

It has been reported that the radiologic features of glioma are associated with *IDH1* mutation. A recent study showed that *IDH1* mutation status in glioblastoma can be predicted from the radiologic features derived from MR images.[18] The study identified 4 subjective tumor characteristics observable on MR images: tumor size, contrast enhancement, and the presence or absence of cyst and satellite lesions, which were associated with *IDH1* status; these characteristics predicted the presence of *IDH1* mutation with 94% accuracy (by receiver operating characteristic analysis). Another study demonstrated that *IDH1*-mutated gliomas were predominantly located in a single lobe and were more likely to have a unilateral growth pattern, sharp tumor margin, homogeneous signal intensity, and less contrast enhancement on MR imaging.[27] In the present study, we also found that tumor contrast enhancement was associated with *IDH1* status. Tumors accompanied by mutant *IDH1* were less likely to show contrast enhancement on MR images compared with tumors without *IDH1* mutation. Most interesting, although there was no significant difference in the contrast-enhancement patterns between tumors accompanied by mutant or wild type *IDH1*, multivariate Cox analysis identified the tumor contrast-enhancement pattern as an independent prognostic factor in patients with mutant *IDH1*. This result implies that the tumor contrast-enhancement pattern may be a particularly important factor reflecting the biologic features of tumors in the presence of *IDH1* mutation.

The prognostic value of *IDH1* status and tumor contrast enhancement was determined in patients with AG, considering their interactive effects. Notably, among the 4 classifications based on the 2 indicators, patients with mutant *IDH1* and nonenhanced tumor had significantly longer PFS and OS (Fig 3) than patients who did not; there was no difference in survival time among the other 3 groups. This indicates that *IDH1* mutation and the absence of contrast enhancement may have synergistic effects in reflecting tumor malignancy and predicting survival outcome.

Most interesting, tumor contrast-enhancement patterns were identified as a prognostic marker that could be used to stratify PFS and OS only for patients with mutant *IDH1*, but not for patients with wild type *IDH1*. Specifically, patients with mutant *IDH1* with nodular enhancement patterns had longer PFS and OS than those with mutant *IDH1* with patchy or ringlike enhancement patterns ($P = .022$). Tumor contrast enhancement reflects the degree of destruction of the blood-brain barrier, which is induced by tumor cell invasion. Therefore, the tumor contrast-enhancement pattern may be strongly associated with the biologic features of a tumor. A small area of tumor enhancement (nodular pattern) possibly indicates lower grade malignancy compared with a relatively large area of tumor enhancement (patchy or ringlike pattern), which explains the present findings. Why the tumor contrast-enhancement pattern plays a more important role in predicting the survival of patients with AG with mutant *IDH1* compared with those with wild-type *IDH1* remains to be investigated.

In addition, the extent of resection in the enhanced tumors could be used to stratify PFS and OS for patients with mutant *IDH1*—that is, patients with GTR had longer PFS and OS than patients with <GTR; but this finding was not true for patients with wild type *IDH1*. As discussed above, there was a higher rate of ringlike enhancement pattern in the tumors of patients with mutant *IDH1*. Compared with tumors with nodular or patchy enhancement patterns, tumors with ringlike enhancement patterns had a relatively clear border on postcontrast T1-weighted images, which might facilitate surgical resection of the tumor bulk. On the other hand, *IDH1* mutation is common in diffuse low-grade gliomas and is more common in younger patients; these findings indicate less aggressive behavior and contribute to effective resection of most of the tumor in patients with mutant *IDH1*.

Our study has some limitations. First, we retrospectively enrolled patients from a single institution; therefore, the prognostic role of tumor contrast-enhancement patterns and *IDH1* mutation requires confirmation by a prospective multicenter investigation. Second, due to the limited number of patients and the similar distribution of *IDH1* mutation in the 3 anaplastic glioma subtypes, we did not separate patients by pathology for further discussion. Third, due to the relatively suboptimal timing of the postoperative scans, the potential presence of granulation tissue is a confounder in the MR imaging. The interval from contrast agent administration to image acquisition could also have influenced the level of enhancement. Although the study was carefully controlled, a slight discrepancy in the interval between contrast injection and scanning may still have been present among individuals. Future studies should investigate the association between the radiologic characteristics and survival of patients with tumors with other gene mutations.

CONCLUSIONS

We retrospectively reviewed 216 patients with AG and identified *IDH1* mutation as a significant prognostic factor. In this study, we found that the tumor contrast-enhancement patterns were asso-

ciated with the survival outcome of patients with mutant *IDH1*. Our results imply that there may be a synergistic effect between radiologic morphology and the genetic features of a tumor in determining prognosis, and this effect should be considered in future investigations.

ACKNOWLEDGMENTS

We thank Drs Q. Chen and X. Chen for their effort in tumor segmentation.

Disclosures: Jun Ma—*UNRELATED*: *Grants/Grants Pending*: National Natural Science Foundation of China (No. 81371610).* Tao Jiang—*RELATED*: *Grant:* National Ministry of Science and Technology,* *Comments*: National High Technology Research and Development Program No. 2011CB707804 and No. 2015CB755500; Jianping Dai—*RELATED*: *Grant*: China Ministry of Science and Technology,* *Comments*: This work was supported by the National Natural Science Foundation of China No. 81271541. *Money paid to the institution.

REFERENCES

1. Hartmann C, Hentschel B, Wick W, et al. **Patients with IDH1 wild type anaplastic astrocytomas exhibit worse prognosis than IDH1-mutated glioblastomas, and IDH1 mutation status accounts for the unfavorable prognostic effect of higher age: implications for classification of gliomas.** *Acta Neuropathol* 2010;120:707–18 CrossRef Medline
2. Paleologos NA, Merrell RT. **Anaplastic glioma.** *Curr Treat Options Neurol* 2012;14:381–90 CrossRef Medline
3. DeAngelis LM. **Anaplastic glioma: how to prognosticate outcome and choose a treatment strategy. [corrected].** *J Clin Oncol* 2009;27:5861–62 CrossRef Medline
4. Reyes-Botero G, Dehais C, Idbaih A, et al; POLA Network. **Contrast enhancement in 1p/19q-codeleted anaplastic oligodendrogliomas is associated with 9p loss, genomic instability, and angiogenic gene expression.** *Neuro Oncol* 2014;16:662–70 CrossRef Medline
5. Laigle-Donadey F, Martin-Duverneuil N, Lejeune J, et al. **Correlations between molecular profile and radiologic pattern in oligodendroglial tumors.** *Neurology* 2004;63:2360–62 CrossRef Medline
6. Parkinson JF, Afaghi V, Payne CA, et al. **The impact of molecular and clinical factors on patient outcome in oligodendroglioma from 20 years' experience at a single centre.** *J Clin Neurosci* 2011;18:329–33 CrossRef Medline
7. Shirai K, Suzuki Y, Okamoto M, et al. **Influence of histological subtype on survival after combined therapy of surgery and radiation in WHO grade 3 glioma.** *J Radiat Res* 2010;51:589–94 CrossRef Medline
8. Tortosa A, Viñolas N, Villa S, et al. **Prognostic implication of clinical, radiologic, and pathologic features in patients with anaplastic gliomas.** *Cancer* 2003;97:1063–71 CrossRef Medline
9. Ramirez C, Bowman C, Maurage CA, et al. **Loss of 1p, 19q, and 10q heterozygosity prospectively predicts prognosis of oligodendroglial tumors–towards individualized tumor treatment?** *Neuro Oncol* 2010;12:490–99 CrossRef Medline
10. Chaichana KL, Kosztowski T, Niranjan A, et al. **Prognostic significance of contrast-enhancing anaplastic astrocytomas in adults.** *J Neurosurg* 2010;113:286–92 CrossRef Medline
11. Matar E, Cook RJ, Fowler AR, et al. **Post-contrast enhancement as a clinical indicator of prognosis in patients with anaplastic astrocytoma.** *J Clin Neurosci* 2010;17:993–96 CrossRef Medline
12. Mangla R, Ginat DT, Kamalian S, et al. **Correlation between progression free survival and dynamic susceptibility contrast MRI perfusion in WHO grade III glioma subtypes.** *J Neurooncol* 2014;116:325–31 CrossRef Medline
13. Pope WB, Sayre J, Perlina A, et al. **MR imaging correlates of survival in patients with high-grade gliomas.** *AJNR Am J Neuroradiol* 2005;26:2466–74 Medline
14. Balss J, Meyer J, Mueller W, et al. **Analysis of the IDH1 codon 132 mutation in brain tumors.** *Acta Neuropathol* 2008;116:597–602 CrossRef Medline
15. Hartmann C, Meyer J, Balss J, et al. **Type and frequency of IDH1 and IDH2 mutations are related to astrocytic and oligodendroglial differentiation and age: a study of 1,010 diffuse gliomas.** *Acta Neuropathol* 2009;118:469–74 CrossRef Medline
16. Jiao Y, Killela PJ, Reitman ZJ, et al. **Frequent ATRX, CIC, FUBP1 and IDH1 mutations refine the classification of malignant gliomas.** *Oncotarget* 2012;3:709–22 Medline
17. Ren X, Cui X, Lin S, et al. **Co-deletion of chromosome 1p/19q and IDH1/2 mutation in glioma subsets of brain tumors in Chinese patients.** *PLoS One* 2012;7:e32764 CrossRef Medline
18. Carrillo JA, Lai A, Nghiemphu PL, et al. **Relationship between tumor enhancement, edema, IDH1 mutational status, MGMT promoter methylation, and survival in glioblastoma.** *AJNR Am J Neuroradiol* 2012;33:1349–55 CrossRef Medline
19. Vogelbaum MA, Jost S, Aghi MK, et al. **Application of novel response/progression measures for surgically delivered therapies for gliomas: Response Assessment in Neuro-Oncology (RANO) Working Group.** *Neurosurgery* 2012;70:234–43; discussion 243–44 CrossRef Medline
20. Frenel JS, Leux C, Loussouarn D, et al. **Combining two biomarkers, IDH1/2 mutations and 1p/19q codeletion, to stratify anaplastic oligodendroglioma in three groups: a single-center experience.** *J Neurooncol* 2013;114:85–91 CrossRef Medline
21. Zhang CB, Bao ZS, Wang HJ, et al. **Correlation of IDH1/2 mutation with clinicopathologic factors and prognosis in anaplastic gliomas: a report of 203 patients from China.** *J Cancer Res Clin Oncol* 2014;140:45–51 CrossRef Medline
22. Sanson M, Marie Y, Paris S, et al. **Isocitrate dehydrogenase 1 codon 132 mutation is an important prognostic biomarker in gliomas.** *J Clin Oncol* 2009;27:4150–54 CrossRef Medline
23. Dunn GP, Andronesi OC, Cahill DP. **From genomics to the clinic: biological and translational insights of mutant IDH1/2 in glioma.** *Neurosurg Focus* 2013;34:E2 CrossRef Medline
24. Youland RS, Brown PD, Giannini C, et al. **Adult low-grade glioma: 19-year experience at a single institution.** *Am J Clin Oncol* 2013;36:612–19 CrossRef Medline
25. Beiko J, Suki D, Hess KR, et al. **IDH1 mutant malignant astrocytomas are more amenable to surgical resection and have a survival benefit associated with maximal surgical resection.** *Neuro Oncol* 2014;16:81–91 CrossRef Medline
26. Stancheva G, Goranova T, Laleva M, et al. **IDH1/IDH2 but not TP53 mutations predict prognosis in Bulgarian glioblastoma patients.** *BioMed Res Int* 2014;2014:654727 CrossRef Medline
27. Qi S, Yu L, Li H, et al. **Isocitrate dehydrogenase mutation is associated with tumor location and magnetic resonance imaging characteristics in astrocytic neoplasms.** *Oncol Lett* 2014;7:1895–902 CrossRef Medline

Glioma Angiogenesis and Perfusion Imaging: Understanding the Relationship between Tumor Blood Volume and Leakiness with Increasing Glioma Grade

R. Jain, B. Griffith, F. Alotaibi, D. Zagzag, H. Fine, J. Golfinos, and L. Schultz

ABSTRACT

BACKGROUND AND PURPOSE: The purpose of this study was to investigate imaging correlates to the changes occurring during angiogenesis in gliomas. This was accomplished through in vivo assessment of vascular parameters (relative CBV and permeability surface-area product) and their changing relationship with increasing glioma grade.

MATERIALS AND METHODS: Seventy-six patients with gliomas underwent preoperative perfusion CT and assessment of relative CBV and permeability surface-area product. Regression analyses were performed to assess the rate of change between relative CBV and permeability surface-area product and to test whether these differed for distinct glioma grades. The ratio of relative CBV to permeability surface-area product was also computed and compared among glioma grades by using analysis of variance methods.

RESULTS: The rate of change in relative CBV with respect to permeability surface-area product was highest for grade II gliomas followed by grade III and then grade IV (1.64 versus 0.91 versus 0.27, respectively). The difference in the rate of change was significant between grade III and IV ($P = .003$) and showed a trend for grades II and IV ($P = .098$). Relative CBV/permeability surface-area product ratios were the highest for grade II and lowest for grade IV. The pair-wise difference among all 3 groups was significant ($P < .001$).

CONCLUSIONS: There is an increase in relative CBV more than permeability surface-area product in lower grade gliomas, whereas in grade III and especially grade IV gliomas, permeability surface-area product increases much more than relative CBV. The rate of change of relative CBV with respect to permeability surface-area product and relative CBV/permeability surface-area product ratio can serve as an imaging correlate to changes occurring at the tumor microvasculature level.

ABBREVIATIONS: K^{trans} = forward transfer constant; PCT = perfusion CT; PS = permeability surface-area product; rCBV = relative CBV

Gliomas have a complex and heterogeneous vasculature, relying on angiogenesis to maintain an adequate blood supply.[1,2] Development of in vivo imaging methods capable of providing insight into this process is critical for better understanding of tumor biology and, more important, the changes occurring at the microvasculature level. Perfusion imaging is one noninvasive method that can provide information about tumor vasculature. Two of the most commonly measured vascular parameters by using perfusion imaging are tumor blood volume and tumor vascular leakiness. It has been shown that both tumor blood volume and leakiness correlate with different aspects of vascular histology[3] and, hence, may change at different rates as the tumor transforms to a higher grade.[4] Tumor blood volume (cerebral blood volume) is known to be a surrogate marker of microvascular attenuation and, hence, total tumor vascularity.[5-11] On the other hand, permeability surface-area product (PS) is a measure of leakage of contrast agent from the intravascular to extravascular compartment and is a measure of the leakiness of tumor vasculature. Another commonly stated parameter of vascular leakage is the forward transfer constant (K^{trans}); because blood flow is usually very fast in high-grade leaky brain tumors, K^{trans} approximates PS.[12] PS has been shown to correlate with microvascular cellular proliferation and, therefore, may be a surrogate marker for angiogenesis.[3,13] Both of these parameters have also been shown to correlate very well with glioma grading.[3,4,12,14,15] Low-grade gliomas start recruiting native vessels by co-option.[16-18] However, with increasing tumor growth and grade, metabolic demand increases, leading to tissue hypoxia, which, in turn, induces angiogenesis.[16,17,19-21] Angiogenesis is a multifactorial complex cascade of structural changes in native vessels and neovessels, which

Received January 16, 2015; accepted after revision February 28.

From the Departments of Radiology (R.J.), Pathology (F.A., D.Z.), Neurosurgery (D.Z., J.G.), and Medicine (H.F.), New York University School of Medicine, New York, New York; and Departments of Radiology (B.G.) and Public Health Sciences (L.S.), Henry Ford Hospital, Detroit, Michigan.

Please address correspondence to Rajan Jain, MD, Department of Radiology, NYU School of Medicine, 660 First Ave, 2nd Floor, New York, NY 10016; e-mail: rajan.jain@nyumc.org

http://dx.doi.org/10.3174/ajnr.A4405

is dependent on a number of pro- and antiangiogenic signaling pathways and molecules, the balance of which is tilted to proangiogenesis by a number of factors including hypoxia.[22-24]

The purpose of this retrospective analysis was to show how relative CBV (rCBV) and PS changes occurring in different World Health Organization grades of gliomas can provide an insight into the glioma angiogenesis and, hence, would support the histologic knowledge base already available through an in vivo imaging technique, such as perfusion imaging. We hypothesized that rCBV and PS changes occur at different rates in different grades of gliomas and that the ratio of rCBV/PS will replicate how the vasculature changes and the "angiogenic switch" occur at the microvascular level, which are in response to overexpression of proangiogenic stimuli as the gliomas transform from a lower grade to a higher grade neoplasm.

MATERIALS AND METHODS

Study Population

Our study is Health Insurance Portability and Accountability Act–compliant, and approval was obtained from the institutional review board. The first author had control of the data and all other information being submitted for publication. Seventy-six treatment-naïve patients with glioma who underwent perfusion CT (PCT) were included in this study (44 men and 32 women with an age range from 22 to 81 years; mean age, 53 years). Of those patients, 45 had World Health Organization grade IV, 18 had grade III, and 13 had grade II gliomas proved by histopathology. PCT was performed between 1 and 7 days before surgery (surgical resection, $n = 54$; biopsy, $n = 22$). Before the PCT was performed, 37.7% of the patients with grade IV and 27.7% of those with grade III were on a stable dose of steroids. All lesions were confirmed histologically according to World Health Organization criteria by a board-certified neuropathologist who was blinded to the PCT results. Subsets of this patient population have been published in the past with a research focus not presented in the current article.[3,14,15]

CT Perfusion Technique and Perfusion Map Analysis

The CT perfusion tracer kinetics theory has been described well in multiple previous publications.[12,25-29] A low-radiation-dose noncontrast CT head study was performed to localize the ROI before obtaining a perfusion scan. For the perfusion scan, 50 mL of nonionic contrast was injected at a rate of 4–5 mL/s through an IV line by using an automatic power injector. At 5 seconds into the injection, a cine (continuous) scan was initiated with the following technique: 80 kV(peak), 100–120 mA, and 1 second per rotation for a duration of 50 seconds by using a 64-section CT scanner (VCT; GE Healthcare, Milwaukee, Wisconsin). After the initial 50-second cine scan, 8 more axial images were acquired, 1 image every 15 seconds for an additional 2 minutes, thus giving a total acquisition time of 170 seconds to assess delayed permeability.[12] Eight 5-mm-thick axial sections were acquired, resulting in a total coverage area of 4 cm and a mean effective radiation dose of 2.8–3.5 mSv. The superior sagittal sinus was used as the venous output function, and the artery with the greatest peak and slope on time-attenuation curves, as the arterial input function. An ROI was drawn within the confines of a large vessel, and the automatic function of the software selects the pixels with greatest peak and slope on the time-attenuation curve for analysis. Perfusion maps of CBV and PS were generated by using a 2-compartment model (Advantage Windows workstation by using CT perfusion 3.0 software; GE Healthcare) in all patients by a neuroradiologist with at least 9 years of experience. ROIs were drawn manually on the PCT parametric maps, including the whole solid and enhancing lesion on multiple axial images covering the whole lesion. We drew ROIs, taking care to exclude necrotic/cystic parts or calcified portions of the lesion and to avoid any major cortical vessels.[3,14,15] Corresponding contrast-enhanced MR images were also reviewed in detail to avoid any necrotic/cystic regions while placing ROIs. A second ROI was placed over the normal-appearing white matter in the contralateral cerebral hemisphere and opposite pole as far away from the tumor as possible. Mean absolute values of PS and rCBV obtained by using normal-appearing white matter as the denominator in each case were used for final analysis.

Vascular Leakiness: Permeability Surface-Area Product

PS characterizes diffusion of the contrast agent from the intravascular compartment into the interstitial/extravascular space due to a deficient blood-brain barrier and is used as a means of quantifying the "leakiness" of the vasculature.[12] Permeability is related to the diffusion coefficient of contrast agent in the assumed water-filled pores of the capillary endothelium. The diffusion flux of contrast agent across the capillary endothelium is dependent on both the diffusion coefficient and total surface area of the pores. PS is computed from the impulse residue function, which decreases exponentially with time.

In physiologic terms, PS is the rate at which contrast agent flows into the extravascular tissues and has the same dimensions as flow (milliliters/100 g/minute). It is related to another commonly stated parameter of vascular leakage, K^{trans}, by the following:

$$K^{trans} = E \times F,$$

where K^{trans} is the transfer constant with, again, the same dimensions as flow (unit commonly used, minute^{-1}).[12]

Statistical Analysis

Correlations (Pearson correlation coefficients) between PS and rCBV were computed for patients within each of the World Health Organization glioma grades (II, III, and IV) to assess the association between the 2 measures. These individual correlations were then compared among the 3 groups of patients by using methods developed for testing independent correlation coefficients to investigate any potential differences in associations.[30] Beyond associations, we were interested in assessing a measure of the rate of change of rCBV with respect to PS within each of 3 glioma groups. Regression methods were used to assess these rates of change with a regression model computed for the each of the glioma groups by using rCBV as the dependent variable and PS as the independent model. Within the regression analyses, the slopes, which are a measure of the rate of change, for the 3 glioma groups were compared. In addition to the rate of change determined by regression methods, we considered the ratio of rCBV to PS as a measure of the relationship between the 2 imaging mea-

sures and a patient. This new measure was computed for each patient by dividing the rCBV measures by PS. The differences in these ratios for the 3 glioma groups were compared by using analysis of variance methods with pair-wise comparisons. All testing was done at the .05 level. Data analyses were conducted by using SAS, Version 9.2 (SAS Institute, Cary, North Carolina).

RESULTS

Correlation between rCBV and PS for Different Glioma Grades

rCBV was positively correlated with the PS for all 3 glioma groups ($P < .05$ for all, Table 1). The correlations were high for grade II and III glioma groups ($r = 0.71$ and $r = 0.822$, respectively) and moderate for the grade IV glioma group ($r = 0.467$). Comparisons of the correlations (associations) of PS with rCBV between grade III and IV was significantly higher than between grade II and III or grade II and grade IV. However, the differences in the correlations between grade II and grades III and IV (Table 1) were not significant ($P = .499$ and $P = .279$, respectively).

Table 1: Correlation with PS

Group	rCBV		
	No.	Corr	*P* Value
Grade II	13	0.710	.006
Grade III	18	0.822	<.001
Grade IV	45	0.467	.001
Comparisons		II vs III, $P = .499$	
		II vs IV, $P = .279$	
		III vs IV, $P = .029$	

Note:—Corr indicates correlation.

Table 2: Regression models

Group	Regression Model for rCBV[a]
Grade II	rCBV = 0.48 + 2.21 × PS
Grade III	rCBV = 0.91 + 1.32 × PS
Grade IV	rCBV = 2.59 + 0.38 × PS

[a] rCBV = Intercept + Slope × PS.

Table 3: *P* Value for comparing intercepts and slopes among glioma groups

Group Comparison	rCBV	
	P Value for Intercept	*P* Value for Slope
Grade II vs III	.565	.423
Grade II vs IV	.004	.095
Grade III vs IV	<.001	.001

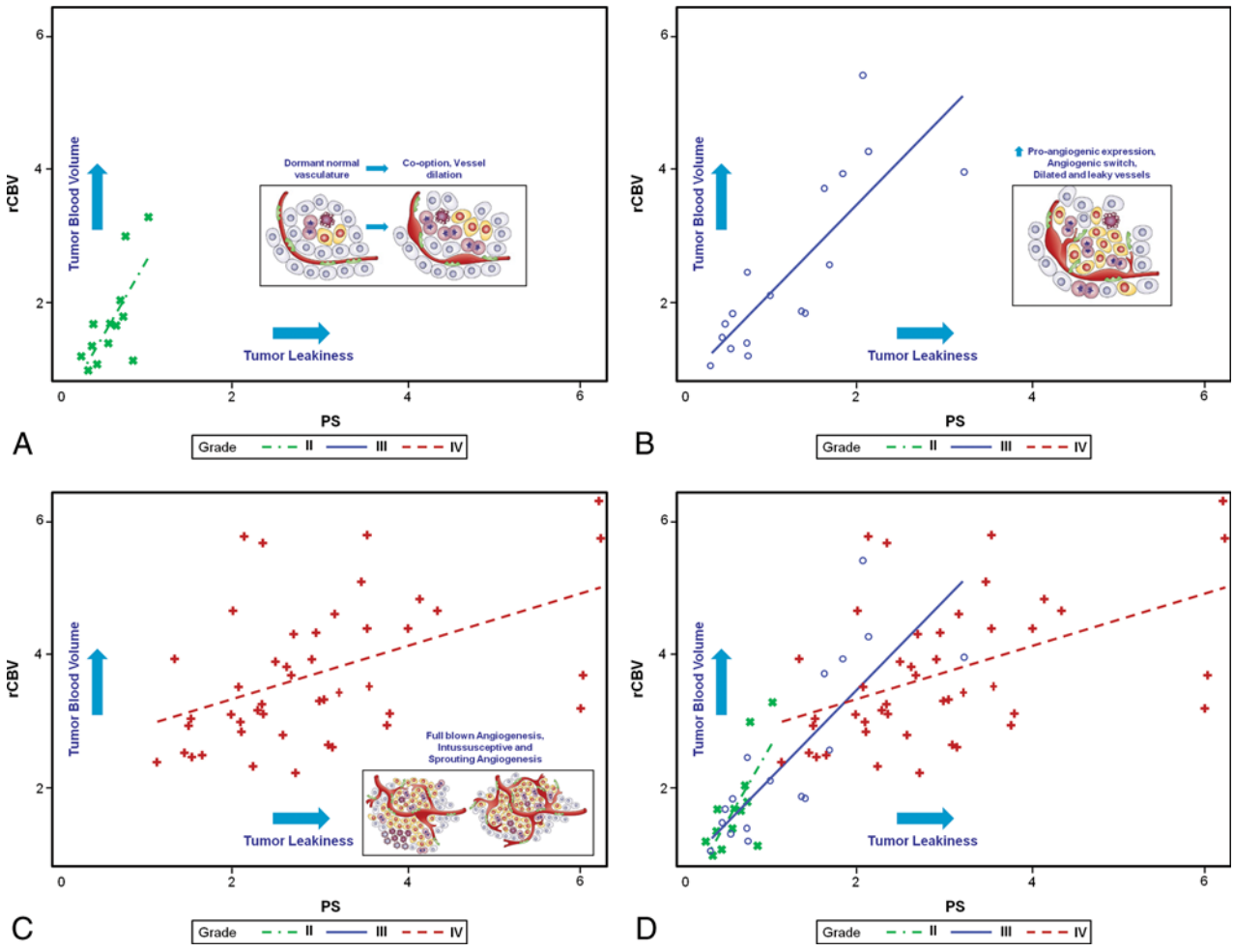

FIG 1. *A–C*, Scatterplots showing different rates of change of rCBV for PS with inset sketches showing how they correspond to different stages of angiogenesis for glioma grades II, III, and IV, respectively. *D*, A combined scatterplot for all glioma grades showing different rates of change of rCBV for PS. Inset sketches adapted with permission from *Nat Rev Cancer* 2003;3:401–10.

Rate of Change of rCBV with Respect to PS

The rate of change (ie, slopes) of rCBV with respect to PS (Fig 1) was highest for the grade II gliomas and lowest for the grade IV gliomas, with grade III gliomas falling between the other 2. The rate of change in rCBV with respect to PS was >2 for grade II gliomas and <0.5 for grade IV gliomas (Table 2). The rate of change of grade III gliomas was 1.3, and when we compared these rates of change, the difference between grades III and IV was significant ($P = .001$), while the difference between grades II and IV showed a trend ($P = .095$). The difference in the rate of change between grades II and III was not significant ($P = .423$) (Table 3).

rCBV/PS Ratios and Glioma Grade

As with the rate of change of rCBV with respect to PS, the average rCBV/PS ratio was highest for grade II gliomas followed by grade III and then grade IV gliomas (Fig 2). These averages ranged from 3.26 for grade II gliomas down to 1.41 for grade IV gliomas (Table 4). This linear decrease was significant between each adjacent glioma group and between grade II and IV glioma groups ($P < .001$ for all).

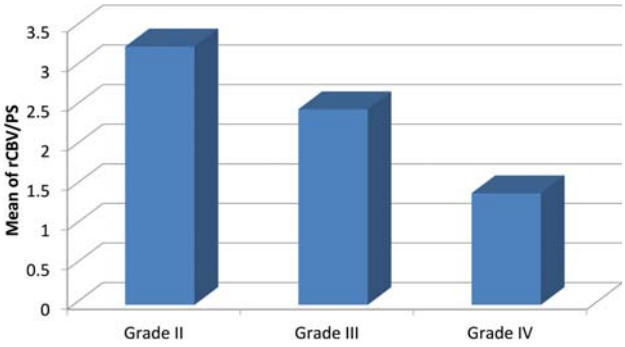

FIG 2. Bar chart showing the ratio of rCBV to PS (rCBV/PS).

Table 4: rCBV/PS ratio

		rCBV/PS	
Group	No.	Mean	SD
Grade II	13	3.26	0.98
Grade III	18	2.46	0.88
Grade IV	45	1.41	0.53

DISCUSSION

In this study, we demonstrated the interplay between the 2 most commonly measured tumor vascular imaging parameters (ie, tumor blood volume [rCBV] and tumor vascular leakiness [PS]) and how this could help improve our understanding of tumor angiogenesis and vascular phenotypes of different glioma grades. We demonstrated that these 2 parameters are correlated but do not necessarily increase in tandem with increasing glioma grade (Fig 3) and, therefore, correlate with different aspects of tumor vasculature and angiogenesis. Their relationship as assessed noninvasively by imaging in the current study demonstrates that in World Health Organization grade II gliomas, initially there is an increase in rCBV more than PS, suggestive of increasing microvascular density, but predominantly an increase in nonleaky vessels, most likely due to vessel co-option and intussusception. Whereas, in grade III and especially grade IV gliomas, PS increases much more than rCBV, this suggests that the increasing number of vessels now contains predominantly leaky vessels, which are reflective of increased proangiogenic expression due to tumor hypoxia. Grade III gliomas demonstrate an increase in both rCBV and PS compared with grade II gliomas, and this probably represents a stage corresponding to "angiogenic switch," in which lower grade tumors cannot simply continue growing by recruiting more native vessels and co-option and so also develop tissue hypoxia, which turns on angiogenesis by increased expression of proangiogenic stimuli and factors.

Interest in the concept of angiogenesis in tumor growth increased in the early 1960s and has continued to expand during the

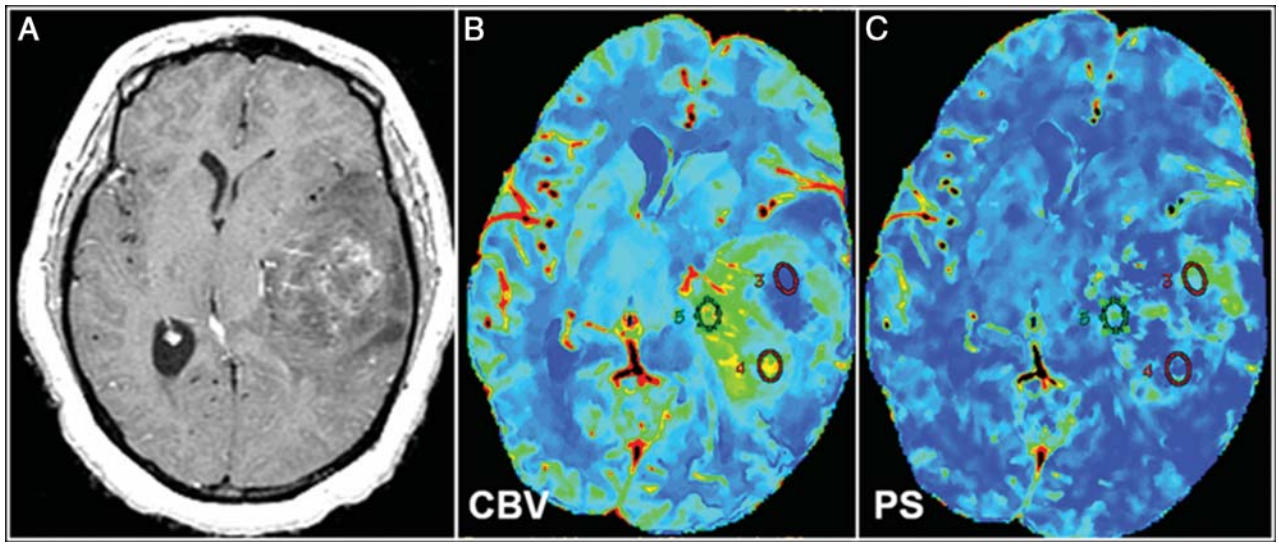

FIG 3. World Health Organization grade III glioma. *A*, Representative postcontrast T1-weighted axial MR image shows a large solid tumor with heterogeneous areas of enhancement. Corresponding CT perfusion CBV (*B*) and PS (*C*) maps show marked heterogeneity in different segments of the tumor (eg, ROI 5 shows markedly increased CBV) but not very high PS; and on the contrary, ROI 3 shows a marked increase of PS, but not very high CBV. This case is an example of a markedly heterogeneous tumor (as seen on postcontrast MR images), and this markedly heterogeneous imaging appearance could be due to the underlying complexity of angiogenesis. Some of this heterogeneity could be explained by a very complex interplay of CBV and PS, and these two parameters probably do not increase in perfect tandem.

past 5 decades, spearheaded by researchers such as Folkman[1] and Folkman et al.[2] It has been shown convincingly that growth of new capillary blood vessels or angiogenesis is required for growth of solid tumors and metastasis.[1,2,31-33] Tumor growth starts as an avascular mass, especially in well-perfused tissues like brain and lung.[34,35] Tumor cells can grow along existing vessels without invoking an angiogenic response. This process has been defined as vessel co-option. Initial co-opted vessels undergo dramatic regression as a host defense mechanism with tumor cell death in the center of the tumor.[16,17,20,36] However, the remaining tumor cells are rescued by robust angiogenesis at the periphery of the tumor. Angiogenesis has also been proposed to be required by in situ tumors to convert from low metastatic activity or a quiescent phenotype to an aggressive or invasive phenotype.[37,38] This conversion and acquisition of angiogenic properties have also been referred to as "angiogenic switch."[39,40]

Intussusceptive and sprouting angiogenesis are 2 known major types of angiogenesis based on how the new vessels are formed.[41] Intussusceptive angiogenesis, also known as "splitting angiogenesis," involves formation of blood vessels by a splitting process in which elements of interstitial tissues invade existing vessels, forming transvascular tissue pillars that expand. This process requires reorganization of existing endothelial cells and does not rely on immediate endothelial proliferation or migration. Sprouting angiogenesis is characterized by sprouts composed of endothelial cells, which usually grow toward an angiogenic stimulus such as vascular endothelial growth factor-A.[42] Sprouting angiogenesis can therefore add blood vessels to portions of tissues previously devoid of blood vessels, particularly in response to tissue hypoxia. It is probably difficult to differentiate these types of angiogenesis apart from a very detailed and high-resolution histologic assessment, and most likely these processes have a complex relationship. However, it appears that sprouting angiogenesis is most likely associated with more immature and leaky neovessels in response to tissue hypoxia and increased production of vascular endothelial growth factor–related complexes.

This whole process of recruiting native vessels (co-option) to the formation of neovessels (intussusceptive and sprouting angiogenesis) is essential for tumor growth and can, in fact, occur as gliomas transform from low to higher grades. Perfusion imaging provides information about tumor vasculature noninvasively. Two of the important vascular parameters assessed by in vivo techniques include tumor blood volume and tumor vascular leakiness. Tumor blood volume has been shown to be a surrogate marker of microvascular attenuation in various kinds of cancers but is not able to differentiate native vessels and neovessels. Tumor vascular leakiness, on the other hand, is a marker of predominantly neovessels, which are leaky and immature and, therefore, probably represent sites of active angiogenesis. It has been shown to correlate with microvascular endothelial proliferation, increased vascular endothelial growth factor expression,[3] and also proangiogenic gene expression.[43] Tumor blood volume and leakiness measures are 2 different imaging parameters that have a specific physiologic basis but result from a very complex multistep process and, therefore to some degree, are interrelated.

One of the major limitations of the current study is its retrospective nature, apart from the small sample size, especially with respect to grade II and III gliomas. A prospective study with a larger sample size and ideally different histologic-grade tumor specimens obtained from the same patient or multiple imaging studies and tissue samples obtained with longitudinal analysis in patients who show lower to higher grade malignant transformation (during multiple years of follow-up) will be needed to confirm our results and interpretation.

CONCLUSIONS

We have demonstrated that vascular changes and angiogenesis occurring with increasing glioma grade can be evaluated noninvasively by using in vivo perfusion imaging techniques. This finding not only adds to our knowledge of angiogenesis but provides a much deeper understanding of the physiologic basis of the commonly used vascular imaging parameters. It could make better integration of these imaging parameters in routine clinical use easier and, hence, take them another step closer to being potential biomarkers, which would provide not only important diagnostic and prognostic information but also useful predictive biomarkers, especially with the emergence of antiangiogenic therapy regimens.

Disclosures: John Golfinos—*UNRELATED*: *Board Membership*: Children's Tumor Foundation, *Comments*: board member for Children's Tumor Foundation, a not-for-profit organization supporting research in neurofibromatosis type 1 and neurofibromatosis type 2; no compensation received; *Consultancy*: Major League Baseball Players Association, *Comments*: head injury consultant; paid a fee directly by Major League Baseball Players Association.

REFERENCES

1. Folkman J. **Tumor angiogenesis: therapeutic implications.** *N Engl J Med* 1971;285:1182–86
2. Folkman J, Cole P, Zimmerman S. **Tumor behavior in isolated perfused organs: in vitro growth and metastases of biopsy material in rabbit thyroid and canine intestinal segment.** *Ann Surg* 1966;164:491–502
3. Jain R, Gutierrez J, Narang J, et al. **In vivo correlation of tumor blood volume and permeability with histologic and molecular angiogenic markers in gliomas.** *AJNR Am J Neuroradiol* 2011;32:388–94
4. Law M, Yang S, Babb JS, et al. **Comparison of cerebral blood volume and vascular permeability from dynamic susceptibility contrast-enhanced perfusion MR imaging with glioma grade.** *AJNR Am J Neuroradiol* 2004;25:746–55
5. Aronen HJ, Gazit IE, Louis DN, et al. **Cerebral blood volume maps of gliomas: comparison with tumor grade and histologic findings.** *Radiology* 1994;191:41–51
6. Aronen HJ, Glass J, Pardo FS, et al. **Echo-planar MR cerebral blood volume mapping of gliomas: clinical utility.** *Acta Radiol* 1995;36:520–28
7. Jackson A, Kassner A, Annesley-Williams D, et al. **Abnormalities in the recirculation phase of contrast agent bolus passage in cerebral gliomas: comparison with relative blood volume and tumor grade.** *AJNR Am J Neuroradiol* 2002;23:7–14
8. Sugahara T, Korogi Y, Kochi M, et al. **Correlation of MR imaging-determined cerebral blood volume maps with histologic and angiographic determination of vascularity of gliomas.** *AJR Am J Roentgenol* 1998;171:1479–86
9. Sugahara T, Korogi Y, Shigematsu Y, et al. **Value of dynamic susceptibility contrast magnetic resonance imaging in the evaluation of intracranial tumors.** *Top Magn Reson Imaging* 1999;10:114–24
10. Wong JC, Provenzale JM, Petrella JR. **Perfusion MR imaging of brain neoplasms.** *AJR Am J Roentgenol* 2000;174:1147–57
11. Shin JH, Lee HK, Kwun BD, et al. **Using relative cerebral blood flow**

and volume to evaluate the histopathologic grade of cerebral gliomas: preliminary results. *AJR Am J Roentgenol* 2002;179:783–89
12. Jain R, Ellika SK, Scarpace L, et al. **Quantitative estimation of permeability surface-area product in astroglial brain tumors using perfusion CT and correlation with histopathologic grade.** *AJNR Am J Neuroradiol* 2008;29:694–700
13. Roberts HC, Roberts TP, Ley S, et al. **Quantitative estimation of microvascular permeability in human brain tumors: correlation of dynamic Gd-DTPA-enhanced MR imaging with histopathologic grading.** *Acad Radiol* 2002;9(suppl 1):S151–55
14. Jain R, Narang J, Gutierrez J, et al. **Correlation of immunohistologic and perfusion vascular parameters with MR contrast enhancement using image-guided biopsy specimens in gliomas.** *Acad Radiol* 2011;18:955–62
15. Jain R, Narang J, Griffith B, et al. **Prognostic vascular imaging biomarkers in high-grade gliomas: tumor permeability as an adjunct to blood volume estimates.** *Acad Radiol* 2013;20:478–85
16. Hardee ME, Zagzag D. **Mechanisms of glioma-associated neovascularization.** *Am J Pathol* 2012;181:1126–41
17. Zagzag D, Amirnovin R, Greco MA, et al. **Vascular apoptosis and involution in gliomas precede neovascularization: a novel concept for glioma growth and angiogenesis.** *Lab Invest* 2000;80:837–49
18. Winkler F, Kienast Y, Fuhrmann M, et al. **Imaging glioma cell invasion in vivo reveals mechanisms of dissemination and peritumoral angiogenesis.** *Glia* 2009;57:1306–15
19. Rong Y, Durden DL, Van Meir EG, et al. **'Pseudopalisading' necrosis in glioblastoma: a familiar morphologic feature that links vascular pathology, hypoxia, and angiogenesis.** *J Neuropathol Exp Neurol* 2006;65:529–39
20. Holash J, Maisonpierre PC, Compton D, et al. **Vessel cooption, regression, and growth in tumors mediated by angiopoietins and VEGF.** *Science* 1999;284:1994–98
21. Reiss Y, Machein MR, Plate KH. **The role of angiopoietins during angiogenesis in gliomas.** *Brain Pathol* 2005;15:311–17
22. Fischer I, Gagner JP, Law M, et al. **Angiogenesis in gliomas: biology and molecular pathophysiology.** *Brain Pathol* 2005;15:297–310
23. Du R, Lu KV, Petritsch C, et al. **HIF1alpha induces the recruitment of bone marrow-derived vascular modulatory cells to regulate tumor angiogenesis and invasion.** *Cancer Cell* 2008;13:206–20
24. Aghi M, Cohen KS, Klein RJ, et al. **Tumor stromal-derived factor-1 recruits vascular progenitors to mitotic neovasculature, where microenvironment influences their differentiated phenotypes.** *Cancer Res* 2006;66:9054–64
25. Johnson JA, Wilson TA. **A model for capillary exchange.** *Am J Physiol* 1966;210:1299–303
26. Purdie TG, Henderson E, Lee TY. **Functional CT imaging of angiogenesis in rabbit VX2 soft-tissue tumour.** *Phys Med Biol* 2001; 46:3161–75
27. Lee TY, Purdie TG, Stewart E. **CT imaging of angiogenesis.** *Q J Nucl Med* 2003;47:171–87
28. St Lawrence KS, Lee TY. **An adiabatic approximation to the tissue homogeneity model for water exchange in the brain, I: theoretical derivation.** *J Cereb Blood Flow Metab* 1998;18:1365–77
29. Jain R. **Perfusion CT imaging of brain tumors: an overview.** *AJNR Am J Neuroradiol* 2011;32:1570–77
30. Wilcox RR. *New Statistical Procedures for the Social Sciences: Modern Solutions to Basic Problems*. Hillsdale, NJ: Lawrence Erlbaum Associates; 1987:258
31. Ribatti D, Vacca A, Dammacco F. **The role of the vascular phase in solid tumor growth: a historical review.** *Neoplasia* 1999;1:293–302
32. Liotta LA, Kleinerman J, Saidel GM. **Quantitative relationships of intravascular tumor cells, tumor vessels, and pulmonary metastases following tumor implantation.** *Cancer Res* 1974;34:997–1004
33. Zetter BR. **Angiogenesis and tumor metastasis.** *Annu Rev Med* 1998;49:407–24
34. Kunz-Schughart LA, Kreutz M, Knuechel R. **Multicellular spheroids: a three-dimensional in vitro culture system to study tumour biology.** *Int J Exp Pathol* 1998;79:1–23
35. Jiang Y, Pjesivac-Grbovic J, Cantrell C, et al. **A multiscale model for avascular tumor growth.** *Biophys J* 2005;89:3884–94
36. Holash J, Wiegand SJ, Yancopoulos GD. **New model of tumor angiogenesis: dynamic balance between vessel regression and growth mediated by angiopoietins and VEGF.** *Oncogene* 1999;18: 5356–62
37. Folkman J. **The role of angiogenesis in tumor growth.** *Semin Cancer Biol* 1992;3:65–71
38. Folkman J. **Role of angiogenesis in tumor growth and metastasis.** *Semin Oncol* 2002;29(6 suppl 16):15–18
39. Baeriswyl V, Christofori G. **The angiogenic switch in carcinogenesis.** *Semin Cancer Biol* 2009;19:329–37
40. Ribatti D, Nico B, Crivellato E, et al. **The history of the angiogenic switch concept.** *Leukemia* 2007;21:44–52
41. Ribatti D. **Genetic and epigenetic mechanisms in the early development of the vascular system.** *J Anat* 2006;208:139–52
42. Ribatti D, Crivellato E. **"Sprouting angiogenesis": a reappraisal.** *Dev Biol* 2012;372:157–65
43. Jain R, Poisson L, Narang J, et al. **Correlation of perfusion parameters with genes related to angiogenesis regulation in glioblastoma: a feasibility study.** *AJNR Am J Neuroradiol* 2012;33:1343–48

Identification of the Corticobulbar Tracts of the Tongue and Face Using Deterministic and Probabilistic DTI Fiber Tracking in Patients with Brain Tumor

M. Jenabi, K.K. Peck, R.J. Young, N. Brennan, and A.I. Holodny

ABSTRACT

BACKGROUND AND PURPOSE: The corticobulbar tract of the face and tongue, a critical white matter tract connecting the primary motor cortex and the pons, is rarely detected by deterministic DTI fiber tractography. Detection becomes even more difficult in the presence of a tumor. The purpose of this study was to compare identification of the corticobulbar tract by using deterministic and probabilistic tractography in patients with brain tumor.

MATERIALS AND METHODS: Fifty patients with brain tumor who underwent DTI were studied. Deterministic tractography was performed by using the fiber assignment by continuous tractography algorithm. Probabilistic tractography was performed by using a Monte Carlo simulation method. ROIs were drawn of the face and tongue motor homunculi and the pons in both hemispheres.

RESULTS: In all subjects, fiber assignment by continuous tractography was ineffectual in visualizing the entire course of the corticobulbar tract between the face and tongue motor cortices and the pons on either side. However, probabilistic tractography successfully visualized the corticobulbar tract from the face and tongue motor cortices in all patients on both sides. No significant difference ($P < .08$) was found between both sides in terms of the number of voxels or degree of connectivity. The fractional anisotropy of both the face and tongue was significantly lower on the tumor side ($P < .03$). When stratified by tumor type, primary-versus-metastatic tumors, no differences were observed between tracts in terms of the fractional anisotropy and connectivity values ($P > .5$).

CONCLUSIONS: Probabilistic tractography successfully reconstructs the face- and tongue-associated corticobulbar tracts from the lateral primary motor cortex to the pons in both hemispheres.

ABBREVIATIONS: CBT = corticobulbar tract; FA = fractional anisotropy; FACT = fiber assignment by continuous tractography

Precise localization of white matter fibers adjacent to brain tumors, such as the corticospinal tracts, is important for presurgical planning to maximize resection of brain lesions and minimize iatrogenic complications.[1,2] Diffusion tensor imaging is a rapidly growing technique to visualize the connectivity of white matter networks insufficiently evaluated by other imaging modalities.[2-4] The DTI technique is based on the anisotropic diffusion of water that preferentially occurs along the longitudinal axis of axons, which allows the delineation of white matter from the diffusion patterns of water molecules.[4,5]

The DTI data can be reconstructed via tractography algorithms to display the anatomic localization of the entire white matter.[4,6-13] The algorithms have been classified into 2 types: deterministic (streamline) and probabilistic. The fiber assignment by continuous tractography (FACT) algorithm is a popular deterministic method in which the propagation of tracking is primarily determined by the principal eigenvector of fractional anisotropy (FA) of each voxel. The measurement of FA is highly dependent on the distributions and intactness of axonal membranes and myelin. However, FACT is unable to solve fiber-crossing problems. The FA decreases in axonal regions with complex architecture due to crossing fibers, intricate branching configurations, and modified tissue organization due to nearby tumors.[1,3,12,14] One method to overcome these problems is the probabilistic tracking algorithms.[6,9] The probabilistic approach considers multiple fiber connectivity from large numbers of potential pathways to generate a connectivity map with the most probable connected voxels between seed points.

Visualizing the corticobulbar tract (CBT) associated with the

Received December 5, 2014; accepted after revision March 26, 2015.

From the Departments of Radiology (M.J., K.K.P., R.J.Y., N.B., A.I.H.) and Medical Physics (K.K.P.) and Brain Tumor Center (R.J.Y., A.I.H.), Memorial Sloan-Kettering Cancer Center, New York, New York; and Department of Radiology (R.J.Y., A.I.H.), Weill Medical College of Cornell University, New York, New York.

Please address correspondence to Andrei I. Holodny, MD, Department of Radiology, Memorial Sloan-Kettering Cancer Center, 1275 York Ave, NY, NY 10021; e-mail: holodnya@mskcc.org

Indicates article with supplemental on-line table.

http://dx.doi.org/10.3174/ajnr.A4430

face and tongue by using FACT is a special challenge because of the relatively small size of the CBT and the presence of prominent crossing fibers—the longitudinal fasciculus.[4,6,8] The CBT forms part of the descending pyramidal tract, in conjunction with the corticospinal tract. It originates from the primary motor cortex and descends through the corona radiata and internal capsule into the cerebral peduncles. The CBT then innervates the motor cranial nerve nuclei in the brain stem to control the muscles of the face, head, and neck. Studies based on single tensor deterministic tractography have failed to identify the CBT fibers associated with the face and tongue.[12,15-18] There have been a few, relatively sophisticated, high-angular-resolution diffusion imaging–based multitensor techniques with some success in extracting fibers from wider areas of the primary motor cortex, including the face and tongue areas[15,17,18]; however, high-angular-resolution diffusion imaging–based techniques have not been applied to large cohorts of patients with brain tumors. Multitensor techniques also require long acquisition times, which are a limiting factor in patients with brain tumors and neurologic deficits.

The purpose of this study was to compare the detection of the CBT fibers associated with the face and tongue by using both deterministic and probabilistic tractography in patients with brain tumors. Given that the probabilistic approach allows the visualization of a distribution of multiple fiber connectivity, we hypothesized that probabilistic tractography will outperform deterministic tractography.

MATERIALS AND METHODS

Patients

This retrospective study was approved by the local institutional review board. Fifty consecutive patients 7–80 years of age (20 males; mean age, 56.2 years; 30 females, mean age, 57.1 years), with single unilateral tumors, who underwent DTI as part of their standard of care during a 12-month period were studied. DTI was performed whenever the margin of the enhancing tumor or peritumoral FLAIR/T2 abnormality or both were within 2 cm of the face and/or tongue motor cortex and/or descending CBT on anatomic images. In none of the cases did the tumor (defined as abnormal enhancement or abnormal findings on FLAIR/T2) involve the contralateral side. The tumors consisted of glioblastomas ($n = 17$), metastases ($n = 19$), astrocytomas ($n = 6$), anaplastic astrocytomas ($n = 3$), oligoastrocytomas ($n = 3$), oligodendroglioma ($n = 1$), and hemangiopericytoma ($n = 1$). Among the 50 patients, only 6 received treatments before DTI. Five had chemotherapy and radiation therapy, and 1 had chemotherapy only.

MR Imaging Acquisition and Analysis

DTI was performed on 3T magnets (Signa Excite, Signa HDx, and Discovery 750HD; GE Healthcare, Milwaukee, Wisconsin) by using an 8-channel head coil. Data were acquired by using a single-shot spin-echo echo-planar imaging sequence (TR/TE = 11,000 and 13,500/60 and 100 ms, matrix = 128 × 128 mm, section thickness = 3 mm, b-value = 1000 s/mm^2, FOV = 240 mm, in-plane resolution = 1.8 × 1.8 × 3 mm with 25 noncollinear gradient directions). Head motion and eddy current corrections were applied to minimize artifacts; DTI&FiberTools (University Hospital, Freiburg, Germany) DTI analysis software implemented in Matlab (MathWorks, Natick, Massachusetts), was used to analyze DTI data. Routine anatomic images including axial 3D T1-weighted images by using a spoiled gradient-recalled-echo sequence (TR/TE = 22/4 ms, matrix = 256 × 256, flip angle = 30°, section thickness = 1.5 mm, FOV = 240 mm), T2-weighted images (TR/TE = 4000 ms/minimum full), and fluid-attenuated inversion recovery images (TR/TE = 6000/140 ms, matrix = 256 × 256, section thickness = 1 mm, FOV = 240 mm) were obtained.

ROIs for CBT

The ROIs (mean number of voxels in the ROI = 28 ± 9) were manually drawn under the direct supervision of a board-certified radiologist holding a Certificate of Added Qualification in Neuroradiology on the B0 images after inspection of the anatomic images, FA maps, and color FA maps. First, the "hand knob" of the primary motor cortex was identified.[19] Next, an ROI for the face was placed in the primary motor cortex lateral to the hand knob in the axial and sagittal planes.[16,19,20] The ROI for the tongue was then placed at the lowermost portion of the primary motor cortex just above the Sylvian fissure in the sagittal plane.[16,18] The ROI for the pons was placed at the ventral part of the midpons through which the CBT travels, as manifested by 2 symmetric blue circles on the color FA maps to represent descending tracts.[19] Anatomic images in the sagittal, coronal, and axial planes were used to confirm the final ROIs. The same seed ROIs were used for both deterministic and probabilistic tractography (Fig 1).

Deterministic Tractography

Deterministic tractography was performed by using the FACT[4] algorithm implemented in DTI&FiberTools. Whole-brain white matter masks were estimated and reconstructed by applying 2 thresholds to control the tracking area and minimize unwanted noise: a start and a stop mask. The start mask was set to FA > 0.25, and mean diffusivity $< 1.6 \times 10^{-3}$ mm^2/s, and the stop mask was set to FA > 0.1 and mean diffusivity $< 2 \times 10^{-3}$ mm^2/s. The maximum curvature of the tract was set to 60°. The whole-brain mask was then used to extract specific tracts between individual motor ROIs and the pons for each subject.

Probabilistic Tractography

Probabilistic tractography was performed by using DTI&FiberTools in an extended Monte Carlo simulation method similar to the probabilistic index of connectivity method.[6,7] Tracking areas were defined as regions with mean diffusivity $< 2 \times 10^{-3}$ mm^2 and FA > 0.1. The number of random walks was set to 100,000, and the maximum fiber length, to 150 voxels with no revisiting.[7,11] The tracts were reconstructed by extraction of the most probable connected voxels between 2 ROIs. First, the visiting connectivity maps were generated for each ROI.[7] For each visiting map, the frequency of a voxel reflects the degree of connectivity to the ROI. Second, the visiting maps from the 2 ROIs were combined to create a probability connectivity map that contains all voxels connecting to both ROIs. The probabilistic connectivity map represents the voxels with the highest likelihood of connecting any 2 selected ROIs. Visiting maps gener-

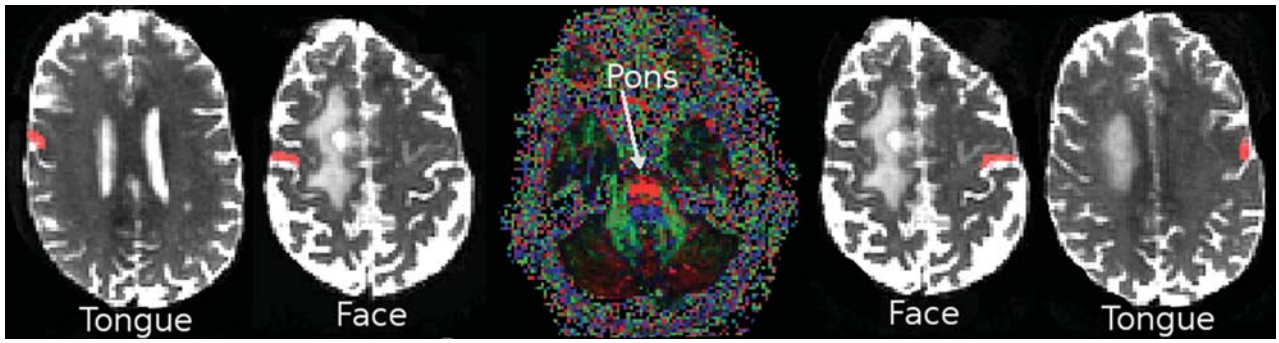

FIG 1. The location of ROIs for 1 patient with a right-handed tumor: Four seed ROIs in the precentral gyrus (primary motor cortex) of both hemispheres at the level of tongue and face homunculus and another in the pons were selected. Face and tongue ROIs are located in the ipsilateral and contralateral primary motor cortex associated with the face and tongue, respectively. The ipsilateral or contralateral sides are in reference to the location of the tumor.

ated from the motor ROIs were separately combined with visiting maps from the pons ROI to produce 4 "probabilistic connectivity maps" for each subject, named as the following probabilistic connectivity maps: face ipsilateral to tumor, face contralateral to tumor, tongue ipsilateral to tumor, and tongue contralateral to tumor.

Quantification of Probabilistic Connectivity

Within the connectivity probabilistic maps, the voxels with the most connectivity were extracted by generating histograms of the connectivity between seed regions and applying a threshold (0.001–0.5) to define the areas of highest connectivity.[11] The number of voxels was then determined by counting voxels within each probabilistic connectivity map and normalizing them to the sum of their corresponding ROIs as shown below:

Number of Voxels = Number of all Counted Voxels

in each Connectivity Map/(Motor ROI + Pons ROI).

The degree of connectivity of the probabilistic map or PIBI (probability index of forming part of the bundle of interest)[7] provides a measure of the strength of tract connectivity. It represents the probability that a voxel belongs to the white matter pathway connecting both ROIs.[7] For each map, the mean value of the PIBI has been used to determine the degree of connectivity.

Volumetric Measurements

An averaged FA value of each probabilistic connectivity map was measured on the tumor and contralateral sides of each patient. The enhancing tumor was manually segmented on the contrast T1-weighted images by a neuroradiologist (with >10 years of experience) and transferred to the FA and B0 maps. The volume of the enhancing tumor and volumes of the connectivity maps were used to generate 3D volume-rendering images. Determinations of possible displacement (deviation of the tract route) and disruption ($P < .05$; >95% decrease in the tract volume or interruption of tract route) were made by comparing the connectivity map on the tumor side with that of the normal side.

Statistical Analysis

Patients were stratified into 2 groups according to tumor distance from the primary motor cortex and/or CBT based on anatomic images. The margin of the enhancing tumor and/or peritumoral FLAIR/T2 abnormality ($n = 23$, ≤1 cm and $n = 27$, >1 cm and ≤2 cm; ≤1 cm versus >1 cm and ≤2 cm) comparisons were made for the number of voxels, degree of connectivity, and the FA value of each connectivity map for both sides within each patient and across patients by using groups consisting of tumor and contralateral sides. Comparisons were also made between primary and secondary tumor types, to examine the differences from which possible infiltrative growth patterns are known to occur in primary tumors. The data were analyzed by using independent paired *t* tests with statistical significance set at $P < .05$.

RESULTS

Deterministic Tractography

The entire course of the CBT between the face motor area and the pons or between the tongue motor area and the pons was not identified by using FACT tractography in any case on either the tumor or ipsilateral side. Instead, FACT tractography consistently terminated in regions adjacent to the tumor and/or areas with peritumoral abnormality with low FA (<0.25) as denoted by orange arrows (Fig 2*A*). Tracts from seeds placed in the primary motor cortex (terminated before the internal capsule) and tracts from seeds placed in the pons traveled through the internal capsules and terminated at the level of the corona radiata before the expected lateral curves toward the face and tongue seeds (Fig 2*A*).

Probabilistic Tractography

On the other hand, probabilistic tractography successfully identified the CBT pathways from the face and tongue motor to the pons in all patients on both tumor and normal sides. The results of probabilistic tractography for 2 patients with tumor on different sides are shown in Fig 2*B*, -*C*.

Patients with Tumors Located Less Than 1 Centimeter from the Anatomic Location of the Corticobulbar Tract

Within patients, although the tumor side trended toward an increased mean number of voxels (face, +16% and tongue, +2%) and mean connectivity values (face, +15% and tongue, +15%), as summarized in Table 1, no significant differences were observed between the tumor and normal sides in the number of

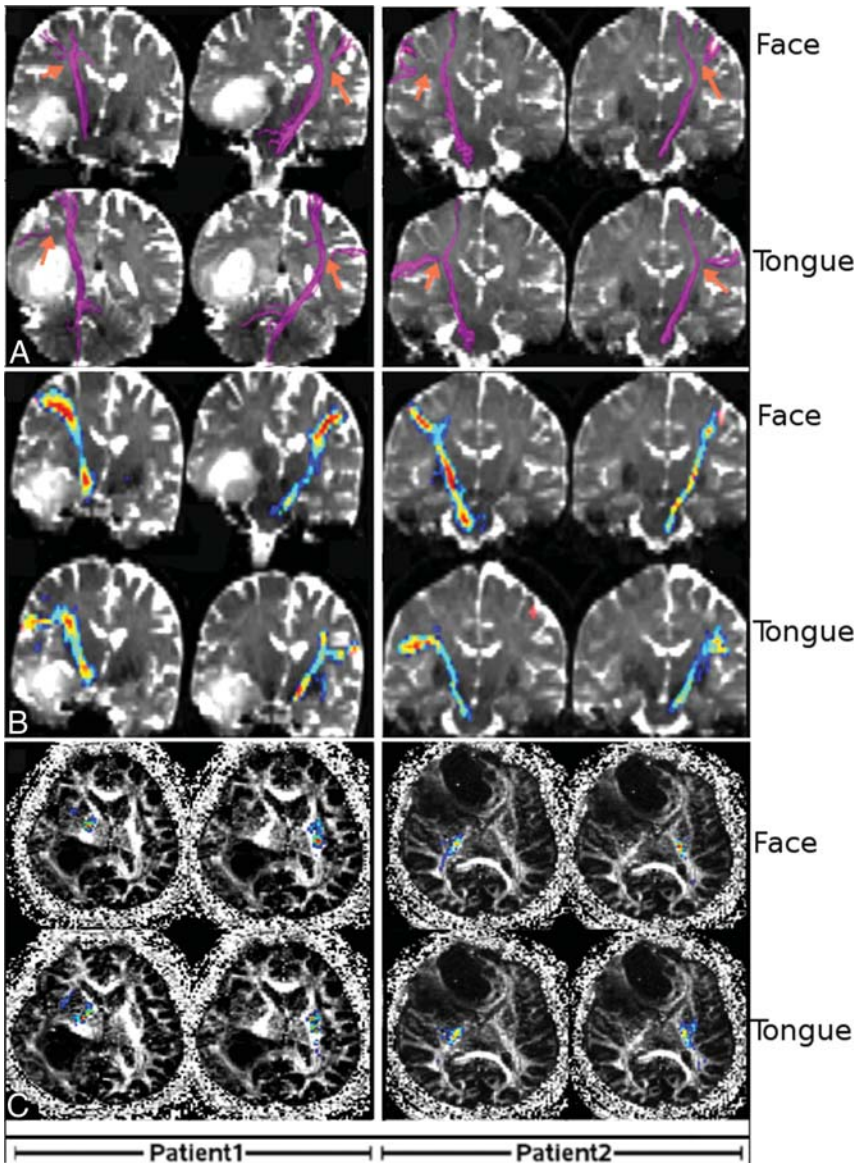

FIG 2. FACT and probabilistic fiber tractography results obtained from 2 patients: 1) a 56-year-old man with glioblastoma, and 2) a 63-year-old woman with brain metastasis (adenoid cystic carcinoma), *A*, The FACT algorithm was not capable of extracting fibers between the pons and face motor or pons and tongue motor. The FACT tracts were not continuous in areas where the CBT crosses the much more prominent superior longitudinal fasciculus (*orange arrow*). *B*, The probabilistic method was successful in identifying the CBT pathways from the face and tongue motor areas to the pons. *C*, The probabilistic connectivity of the face and tongue at the level of internal capsule. Colors represent the degree of connectivity: from 0.001 in blue to 0.5 in red.

voxels or degree of connectivity along each connectivity map ($P < .13$). For each patient, the tumor side showed significantly lower FA values of the probability maps of both face and tongue compared with the ipsilateral side ($P < .001$ and $P < .003$, respectively). The mean FA value across patients was also lower on the tumor side (face, −11% and tongue, −11%), as summarized in Table 1.

Patients with Tumors Located More Than 1 Centimeter and Equal to or Less Than 2 Centimeters from the Anatomic Location of the Corticobulbar Tract

Across patients, the tumor side showed a trend toward increased mean voxel number (face, +26% and tongue, +7%) (Table 2) and face connectivity values (+23%), but decreased tongue connectivity values (−6%) (Table 2); however, these differences were not significant ($P < .08$). In addition, the probabilistic connectivity map of the face and tongue on the tumor side had lower mean FA values of the connectivity maps (face, $P < .03$, and tongue, $P < .016$) (Table 2).

Types of Tumors

When tumor type was stratified as primary tumors ($n = 31$) versus secondary tumors ($n = 19$), no significant differences were observed among tracts in terms of the mean FA ($P < .6$), number of voxels ($P < .2$), or connectivity values ($P > .1$) (On-line Table).

Clinical Visualization

Visual inspection showed continuous connectivity maps for the face and tongue motor tracts from the primary

Table 1: Data for patients with tumor <1 cm from the corticobulbar tract

Averaged over Subjects ± SD	Connectivity Map of Face Motor				Connectivity Map of Tongue Motor			
	Tumor	Nontumor	*P* Value	% Change	Tumor	Nontumor	*P* Value	% Change
No. of voxels	10.8555 ± 4.3837	9.3350 ± 2.9498	.1300	+16%	12.0866 ± 5.8446	11.8514 ± 4.3694	.8500	+2%
Degree of connectivity	0.6768 ± 0.3906	0.5884 ± 0.3662	.3500	+15%	0.6367 ± 0.347	0.6357 ± 0.349	.9900	+0.15%
FA value	0.4615 ± 0.0664	0.5211 ± 0.0352	.0000	−11%	0.4557 ± 0.0701	0.5104 ± 0.045	.0003	−11%

Table 2: Data for patients with tumor >1 cm from the corticobulbar tract

Averaged over Subjects ± SD	Connectivity Map of Face Motor				Connectivity Map of Tongue Motor			
	Tumor	Nontumor	*P* Value	% Change	Tumor	Nontumor	*P* Value	% Change
No. of voxels	10.9157 ± 4.7361	8.6965 ± 3.3798	.0800	+26%	13.6748 ± 7.1344	12.7478 ± 6.8817	.3900	+7%
Degree of connectivity	0.59 ± 0.4437	0.4799 ± 0.2992	.3200	+23%	0.6267 ± 0.3798	0.6645 ± 0.3687	.6400	−6%
FA value	0.4924 ± 0.0567	0.5191 ± 0.0338	.0296	−5%	0.4765 ± 0.0650	0.5118 ± 0.0537	.0158	−7%

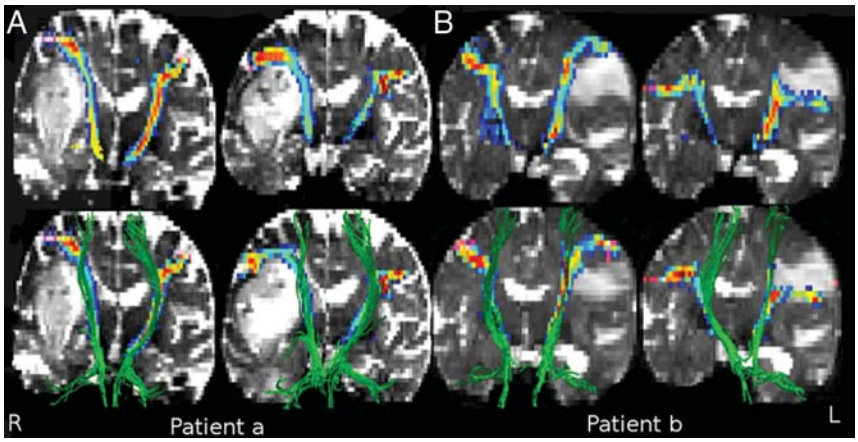

FIG 3. Probabilistic-versus-FACT tractography of 2 patients. *A*, A 69-year-old man with glioblastoma located <1 cm from the CBT. *B*, A 67-year-old woman with brain metastasis from lung carcinoma located >1 and ≤2 cm from the CBT. First row: probabilistic tractography results of the connectivity maps of the face and tongue motor areas. respectively. Second row: probabilistic-versus-FACT tractography. Probabilistic connectivity is shown as multicolored maps, and FACT is shown as green fiber projections. The FACT tract discontinuation is visible. Colors represent the degree of connectivity, from 0.001 in blue to 0.5 in red.

motor cortex to the pons. Separate pathways originating from face and tongue seeds consistently converged at the level of the internal capsule with decreasing connectivity values. Tumors along the path of the probabilistic maps resulted in mass effect and deflection of the maps, which appeared to wrap around the tumor, but remained continuous (Fig 3).

DISCUSSION

We demonstrate that the probabilistic tractography method of analysis of DTI data can successfully identify the CBT pathways from the face and tongue regions of the primary motor cortex to the pons in patients with brain tumors. This method is in contrast to deterministic tractography, in which the CBT pathways could not be identified, even on the side contralateral to the tumor. Our results suggest that probabilistic tractography can be used to visualize the CBT pathways, to guide neurosurgical planning, and to minimize the risk of white matter damage during the operation.

Preliminary effort to visualize the CBT motor pathways of the face and tongue has been described by a few groups, but their results were limited by the number of subjects studied. Akter et al[17] used multitensor tractography to detect face and tongue motor pathways in 5 healthy adults, but their techniques required complicated data processing and a longer postprocessing time compared with the usual single tensor tractography. A multitensor tractography study with high-angular-resolution diffusion imaging by Yamada et al[18] depicted face and tongue motor pathways; however, the CBT tracts of the face were identified in only 70% of their patients. Another study[15] described 2-tensor tractography as the preferred method for detecting hand and face fibers compared with single-tensor and probabilistic tractography in 2 controls and 1 patient. Kreher et al[7] showed that probabilistic fiber tracking could extract fibers of the entire motor cortex; however, they only demonstrated this in control adults and not in patients with tumors. In this study, we compared the ability of both the deterministic FACT and the probabilistic fiber tracking methods to extract CBT pathways associated with face and tongue motor in 50 patients with brain tumor. In addition, we also compared the results on the basis of the distance between the tumor margin and motor cortex.

We found that the number of voxels, a measure of the volume of the probabilistic map of connectivity, was increased on the side of the tumor (Tables 1 and 2). We postulate that this increase in volume was due to deflection and stretching of the CBTs by mass effect from the tumors and peritumoral abnormalities. Similar results have been described by Yeh et al,[1] who described altered morphology of the corticospinal tract with stretching of the tracts at the internal capsule. This deflection of the CBT was seen near the tumor in all cases.

The mean degree of connectivity of probabilistic maps was also slightly (15%) increased on the tumor side (Tables 1 and 2). Although this increase was not significant, it may be because of compression of the CBT due to mass effect, with subsequent increased fiber attenuation at tractography as discussed by Young et al.[21] Similar to that in other groups,[1-4] FA was decreased in tracts associated with brain tumors. This decrease in FA or increase in the degree of connectivity is a primary limitation of tractography techniques, which become less accurate due to uncertainties in determining the principal directionality of each voxel. The increases in the number of voxels occurred despite the decreased FA values; this finding suggests that probabilistic tractography may be reliable in visualizing important white matter tracts affected by brain tumors.

Visualization of the normal CBT pathways for the face and tongue shows a descending course from the lateral portions of the primary motor cortex into the medial portions of the pons. This is consistent with previous anatomic probabilistic tractography studies that demonstrated alterations in the orientation of the descending motor fibers.[15,16] In particular, a study by Pan et al[16] showed that the CBT fibers either cross or have crossed medial to the CST fibers at the level of the posterior limb of the internal capsule. These descending medial courses were also visible on the tumor sides, though there were additional deflections caused by tumor and peritumoral abnormalities.

This study may have the following limitations. First, we relied on anatomic markers for placing the seed ROIs for the face and tongue in the primary motor cortex. Although seed ROIs drawn from voxels activated by functional MR imaging can provide optimal localization of the correct locations, these data were not available in our retrospective cohort. Second, the probabilistic approach can sometimes introduce uncertainties, especially when measuring characteristics of the fiber bundle such as the length and degree of deflection by using the probabilistic map of connectivity of the face and tongue on the tumor side.[7]

CONCLUSIONS

Probabilistic tractography can successfully visualize the face- and tongue-associated CBT pathways in patients with brain tumors. By contrast, deterministic tractography was not successful in reconstructing the CBT on the tumor or contralateral sides. Probabilistic tractography may be useful to guide preoperative planning for patients with brain tumors affecting or adjacent to the CBT.

Disclosures: Robert J. Young—*RELATED*: *Grant*: Radiological Society of North America,* *Comments*: 2011 Fujifilm Medical Systems/Radiological Society of North America. Research Seed Grant. *Money paid to the institution.

REFERENCES

1. Yeh YY, Huang SC, Chiang WY, et al. **Effects of brain tumor on corticospinal tract and motor function: analysis of tract stretch using diffusion spectrum imaging tractography.** In: *Proceedings of the Annual Meeting of the International Society for Magnetic Resonance in Medicine*, Honolulu, Hawaii. April 18–24, 2009:17
2. Jellison BJ, Field AS, Medow J, et al. **Diffusion tensor imaging of cerebral white matter: a pictorial review of physics, fiber tract anatomy, and tumor imaging patterns.** *AJNR Am J Neuroradiol* 2004; 25:356–69
3. Parmar H, Sitoh YY, Yeo TT. **Combined magnetic resonance tractography and functional magnetic resonance imaging in evaluation of brain tumors involving the motor system.** *J Comput Assist Tomogr* 2004;28:551–56
4. Mori S, Crain BJ, Chacko VP, et al. **Three-dimensional tracking of axonal projections in the brain by magnetic resonance imaging.** *Ann Neurol* 1999;45:265–69
5. Basser PJ, Pajevic S, Pierpaoli C, et al. **In vivo fiber tractography using DT-MRI data.** *Magn Reson Med* 2000;44:625–32
6. Parker JG, Haroon HA, Wheeler-Kingshott CA. **A framework for a streamline-based probabilistic index of connectivity (PICo) using a structural interpretation of MRI diffusion measurements.** *J Magn Reson Imaging* 2003;18:242–54
7. Kreher BW, Schnell S, Mader I, et al. **Connecting and merging fibres: pathway extraction by combining probability maps.** *Neuroimage* 2008;43:81–89
8. Lazar M, Weinstein JS, Tsuruda KM, et al. **White matter tractography using diffusion tensor deflection.** *Hum Brain Mapp* 2003;18: 306–21
9. Parker GJ, Alexander DC. **Probabilistic Monte Carlo based mapping of cerebral connections utilising whole-brain crossing fibre information.** *Inf Process Med Imaging* 2003;18:684–95
10. Li Z, Peck KK, Brennan N, et al. **Diffusion tensor tractography of the arcuate fasciculus in patients with brain tumors: comparison between detrministic and probabilistic models.** *J Biomed Sci Eng* 2013;6:192–200q
11. Jenabi M, Peck KK, Young RJ, et al. **Probabilistic fiber tracking of the language and motor white matter pathways of the supplementary motor area (SMA) in patients with brain tumors.** *J Neuroradiol* 2014;41:342–49
12. Nguyen-Thanh T, Reisert M, Anastasopoulos C, et al. **Global tracking in human gliomas: a comparison with established tracking methods.** *Clin Neuroradiol* 2013;23:263–75
13. Behrens TE, Berg HJ, Jbabdi S, et al. **Probabilistic diffusion tractography with multiple fibre orientations: what can we gain?** *Neuroimage* 2007;34:144–55
14. Mader I, Nguyen Thanh T, Schnell S, et al. **Probability maps compared to face algorithm in human gliomas.** In: *Proceedings of the Annual Meeting of the International Society for Magnetic Resonance in Medicine*, Stockholm, Sweden. May 1–7, 2010:18
15. Qazi AA, Radmanesh A, O'Donnell L, et al. **Resolving crossings in the corticospinal tract by two-tensor streamline tractography: method and clinical assessment using fMRI.** *NeuroImage* 2009;47: T98–106
16. Pan C, Peck KK, Young RJ, et al. **Somatotopic organization of motor pathways in the internal capsule: a probabilistic diffusion tractography study.** *AJNR Am J Neuroradiol* 2012;33:1274–80
17. Akter M, Hirai T, Sasao A, et al. **Multi-tensor tractography of the motor pathway at 3T: a volunteer study.** *Magn Reson Med Sci* 2011;101:59–63
18. Yamada K, Sakai K, Hoogenraad FGC, et al. **Multitensor tractography enables better depiction of motor pathways: initial clinical experience using diffusion-weighted MR imaging with standard b-value.** *AJNR Am J Neuroradiol* 2007;28:1668–73
19. Yousry TA, Schmid UD, Alkadhi H, et al. **Localization of the motor hand area to a knob on the precentral gyrus: a new landmark.** *Brain* 1997;120:141–57
20. McCarthy G, Allison T, Spencer DD. **Localization of the face area of human sensorimotor cortex by intracranial recording of somatosensory evoked potentials.** *J Neurosurg* 1993;79:874–84
21. Young RJ, Lee V, Peck KK, et al. **Diffusion tensor imaging and tractography of the corticospinal tract in the presence of enlarged Virchow-Robin spaces.** *J Neuroimaging* 2014;24:79–82

Hyperintense Vessels on T2-PROPELLER-FLAIR in Patients with Acute MCA Stroke: Prediction of Arterial Stenosis and Perfusion Abnormality

S.J. Ahn, S.H. Suh, K.-Y. Lee, J.H. Kim, K.-D. Seo, and S. Lee

ABSTRACT

BACKGROUND AND PURPOSE: Fluid-attenuated inversion recovery hyperintense vessels in stroke represent leptomeningeal collateral flow. We presumed that FLAIR hyperintense vessels would be more closely associated with arterial stenosis and perfusion abnormality in ischemic stroke on T2-PROPELLER-FLAIR than on T2-FLAIR.

MATERIALS AND METHODS: We retrospectively reviewed 35 patients with middle cerebral territorial infarction who underwent MR imaging. FLAIR hyperintense vessel scores were graded according to the number of segments with FLAIR hyperintense vessels in the MCA ASPECTS areas. We compared the predictability of FLAIR hyperintense vessels between T2-PROPELLER-FLAIR and T2-FLAIR for large-artery stenosis. The interagreement between perfusion abnormality and FLAIR hyperintense vessels was assessed. In subgroup analysis (9 patients with MCA horizontal segment occlusion), the association of FLAIR hyperintense vessels with ischemic lesion volume and perfusion abnormality volume was evaluated.

RESULTS: FLAIR hyperintense vessel scores were significantly higher on T2-PROPELLER-FLAIR than on T2-FLAIR (3.50 ± 2.79 versus 1.21 ± 1.47, $P < .01$), and the sensitivity for large-artery stenosis was significantly improved on T2-PROPELLER-FLAIR (93% versus 68%, $P = .03$). FLAIR hyperintense vessels on T2-PROPELLER-FLAIR were more closely associated with perfusion abnormalities than they were on T2-FLAIR ($\kappa = 0.64$ and $\kappa = 0.27$, respectively). In subgroup analysis, FLAIR hyperintense vessels were positively correlated with ischemic lesion volume on T2-FLAIR, while the mismatch of FLAIR hyperintense vessels between the 2 sequences was negatively correlated with ischemic lesion volume ($P = .01$).

CONCLUSIONS: In MCA stroke, FLAIR hyperintense vessels were more prominent on T2-PROPELLER-FLAIR compared with T2-FLAIR. In addition, FLAIR hyperintense vessels on T2-PROPELLER-FLAIR have a significantly higher sensitivity for predicting large-artery stenosis than they do on T2-FLAIR. Moreover, the areas showing FLAIR hyperintense vessels on T2-PROPELLER-FLAIR were more closely associated with perfusion abnormality than those on T2-FLAIR.

ABBREVIATIONS: FHV = FLAIR hyperintense vessel; GRE = gradient-echo; T_{max} = time-to-maximum

FLAIR hyperintense vessels (FHVs) are frequently encountered in acute ischemic stroke. Two types of FHVs, proximal and distal, have different clinical implications.[1] Proximal FHVs, which are frequently observed proximal to or within the Sylvian fissure, can be used as a marker for arterial occlusion and are presumably the result of the thrombus or slow collateral flow.[2-4] Distal FHVs, which are present distal to the Sylvian fissure, may indicate collateral flow and salvageable brain parenchyma in acute stroke; angiography reveals that they are more related to retrograde collateral flow from arteries unaffected by occlusion.[1,5] Recently, distal FHVs have been studied more due to their clinical importance.[6,7]

Technically, in the setting of normal hemodynamics, the blood vessels show dark signal intensity on spin-echo sequences such as FLAIR because of the dephasing effect from mixed spin-echoes and stimulated echoes, as well as the disrupted spin-echo mechanism due to through-plane blood motion. The retrograde slow flow results in the loss of this flow void phenomenon, and vessels appear hyperintense against the dark CSF background.[8-10]

The PROPELLER technique has been implemented with conventional MR images to reduce motion-induced artifacts and increase

Received January 23, 2015; accepted after revision April 19.

From the Departments of Radiology (S.J.A., S.H.S.) and Neurology (K.-Y.L., J.H.K., K.-D.S.), Yonsei University College of Medicine, Seoul, Korea; Severance Institute for Vascular and Metabolic Research (S.H.S., K.-Y.L.), Yonsei University, Seoul, Korea; and Global Applications and Workflow (S.L.), GE Healthcare, Seoul, Korea.

Please address correspondence to Kyung-Yul Lee, MD, PhD, Department of Neurology, Gangnam Severance Hospital, Yonsei University, College of Medicine, 211 Eonju-ro, Gangnam-gu, Seoul 135–720, Korea; e-mail: kylee@yuhs.ac

 Indicates article with supplemental on-line photo.

http://dx.doi.org/10.3174/ajnr.A4423

image quality.[11-13] The PROPELLER technique may affect hyperintense vessels on T2-FLAIR.

We hypothesized that FHVs are assessed better on T2-PROPELLER-FLAIR than on T2-FLAIR and that FHVs are more closely associated with arterial stenosis and perfusion abnormality in ischemic stroke on T2-PROPELLER-FLAIR than on T2-FLAIR.

MATERIALS AND METHODS

Patients

We retrospectively screened consecutive patients who presented to our tertiary referral medical center. We included patients with acute middle cerebral artery territory ischemic stroke within 1 week of symptom onset. They underwent advanced MR imaging. All of the patients included in the study showed restricted diffusion in the MCA territory on diffusion-weighted imaging. We excluded patients with transient ischemic attack, multiple infarctions other than in MCA territories, or lacunar infarction. Our institutional review board approved this retrospective study.

MR Imaging Protocols

Patients were imaged with a 3T MR imaging unit (Discovery MR750; GE Healthcare, Milwaukee, Wisconsin). Our advanced MR imaging protocol for acute stroke included DWI, T2-FLAIR, T2-PROPELLER-FLAIR, gradient-echo (GRE), bolus-tracking perfusion-weighted imaging, intracranial and extracranial contrast-enhanced MR angiography, and intracranial time-of-flight MRA. FLAIR images were acquired with following parameters: TR/TE = 12,000/140 ms; TI = 2500 ms; flip angle = 110°; section thickness = 4 mm; gap = 1 mm; FOV = 210 × 210 mm; matrix = 352 × 353; and 30 contiguous sections for a total acquisition of 3 minutes 20 seconds. PROPELLER-T2-FLAIR images were also acquired with commercially available 2D sequences: TR/TE = 8800/120 ms; TI = 2200 ms; flip angle = 142°; and they matched resolution with T2-FLAIR. Total acquisition time for T2-PROPELLER-FLAIR was 3 minutes 30 seconds.

Table 1: Characteristics and MRA findings of study patients[a]

Features	
No. of patients	35
Age (yr) (mean)	65.1
Female sex	12/35 (34)
Hypertension	15/35 (42)
Diabetes mellitus	11/35 (31)
Median time interval from symptom onset to MRI (hr) (IQR)	23.4 (9.62–57.5)
MRA findings	
Large-artery stenosis or occlusion[b]	28/35 (80)
MCA horizontal segment	12 (34)
MCA insular segment	5 (15)
MCA cortical segment	1 (3)
Distal ICA	3 (8)
Proximal ICA	7 (20)
Negative	7 (20)

Note:—IQR indicates interquartile range.
[a] Unless otherwise specified, data are the number of patients, with percentages in parentheses.
[b] Represents ≥50% stenosis or occlusion of the large artery.

Table 2: Comparison of FHVs and parenchymal ischemic lesions between T2-FLAIR and T2-PROPELLER-FLAIR[a]

	T2-FLAIR	T2-PROPELLER-FLAIR	*P* Value
FHVs			
FHV score	1.21 ± 1.47	3.50 ± 2.79	<.01
Parenchymal ischemic lesions			
CNR	20.93 ± 8.61	8.43 ± 3.51	<.01
Sensitivity[b]	148/153 (96.7)	149/153 (97.4)	1.00

Note:—CNR indicates contrast-to-noise ratio: $(SI_{lesion} - SI_{WM}) / SD_n$.
[a] FHV scores were defined by counting the number of MCA-ASPECTS territories in which FHVs were present.
[b] Sensitivity for the detection of acute and old ischemic lesions. Data are the number of ischemic lesions and percentages.

Image Analysis

Two readers independently assessed either T2-FLAIR or T2-PROPELLER-FLAIR. The first review of images was randomly selected by the study coordinator; the remainder of the sequences were reviewed 1 week later. The reviewers were blinded to clinical history and imaging sequences and assessed FHVs and parenchymal ischemic lesions on both sequences.

To compare FHVs on both sequences, we used FHV scores, modifying a previous method.[6] In brief, images were scored from zero to 7 points by counting the number of MCA-Alberta Stroke Program Early CT Score territories in which FHVs were present.[14] FHVs were counted when they appeared as linear or serpentine hyperintensities corresponding to a typical arterial course on at least 2 consecutive axial sections. The MCA ASPECTS territories are composed of 7 territories: I and M1–M3 at the level of the basal ganglia and M4–M6 at the level of the ventricles immediately above the basal ganglia. I represents the insular ribbon. M1 represents the anterior MCA cortex corresponding to the frontal operculum, M2 represents the MCA cortex lateral to the insular ribbon corresponding to the anterior temporal lobe, and M3 represents the posterior MCA cortex corresponding to the posterior temporal lobe. M4, M5, and M6 represent the anterior, lateral, and posterior MCA territories immediately superior to M1, M2, and M3, respectively.

To compare the parenchymal ischemic lesions on both sequences, we calculated the contrast-to-noise ratio between the parenchymal ischemic lesion and adjacent white matter. The contrast-to-noise ratio was defined as $(SI_{lesion} - SI_{WM})/SD_n$, where SD_n is the SD of background noise. Signal intensities (*SIs*) of the lesion and WM were assessed by circular ROI measurements (area = 20 mm^2), which were placed identically on both sequences. For qualitative assessment, 2 readers recorded parenchymal ischemic lesions while evaluating FHVs. The diagnostic sensitivity for parenchymal ischemic lesions of both sequences was calculated. The standard reference was DWI.

A third experienced reader gauged the time-to-maximum (T_{max}) map of PWI with the same scoring system. A T_{max} map was generated by using perfusion-processing software (FuncTool; GE Healthcare). The number of MCA-ASPECTS territories with delayed perfusion was counted instead of the FHVs. The ischemic lesion volume and perfusion abnormality

volume were also measured by using DWI and the T_{max} map, respectively, with the reader blinded to the FHV scores. DICOM formats of DWI and the T_{max} map were imported into ImageJ software (National Institutes of Health, Bethesda, Maryland) by using a measurement stack plug-in to calculate volumes. ROIs were drawn along the borders of the high-signal area on DWI and the delayed perfusion area on the T_{max} map, compared with the contralateral area of each section. The arterial stenotic lesion was determined by MRA in conjunction with DWI, T_{max}, T2-FLAIR, and T2-PROPELLER-FLAIR.

Statistical Analysis

FHV scores and contrast-to-noise ratios for ischemic lesions between T2-FLAIR and T2-PROPELLER-FLAIR were compared by using a paired Student *t* test. The diagnostic sensitivities for parenchymal ischemic lesions were compared using the McNemar test. The interobserver agreement between the 2 readers was evaluated with κ statistics.

The sensitivity and specificity of T2-FLAIR and T2-PROPELLER-FLAIR for predicting large-artery stenosis (≥50%) and occlusion were also compared by using the McNemar test. The interagreement between both sequences and perfusion abnormality was assessed by κ statistics.

For the correlation with ischemic lesion volume and perfusion abnormality volume, subgroup analysis was performed. Due to the homogeneity of the occlusion site and the degree of stenosis, only 9 patients with horizontal segment occlusion were included. Spearman correlation analysis was used to explore the relationship among the FHV score on T2-FLAIR, FHV score on T2-PROPELLER-FLAIR, FHV mismatch, initial ischemic lesion volume, and initial perfusion abnormality volume. FHV mismatch was calculated by (FHV scores on T2-PROPELLER-FLAIR − FHV scores on T2-FLAIR) / FHV scores on T2-PROPELLER-FLAIR. Statistical analysis was performed by using commercial software (MedCalc, Version 10.1.2.0; MedCalc Software, Mariakerke, Belgium). A P value $< .05$ was statistically significant.

RESULTS

Thirty-five patients fulfilled the inclusion criteria (Table 1). The mean age was 65.1 years, and 34% of patients were women. The median time from symptom onset to MR imaging was 23.4 hours (interquartile range, 9.62–57.5 hours). Large-artery stenosis (≥50%) or occlusion was seen in 28/35 patients (80%) in the following areas: the MCA horizontal segment (12/35, 34%), the MCA insular segment (5/35, 15%), the MCA cortical segment (1/35, 3%), the distal internal carotid artery (3/35, 8%), and the proximal ICA (7/35, 20%). Mild stenosis or negative findings were observed in 7/35 patients (20%).

The FHV score of T2-PROPELLER-FLAIR was significantly higher than that of T2-FLAIR in patients with acute MCA territory infarction (3.50 ± 2.79 versus 1.21 ± 1.47, $P < .01$, Table 2). The contrast-to-noise ratio between parenchymal ischemic lesions and adjacent WM on T2-PROPELLER-FLAIR was significantly lower than that on T2-FLAIR (8.43 ± 3.51 versus 20.93 ± 8.61, $P < .01$). However, the diagnostic sensitivity for parenchymal ischemic lesions on both sequences was not significantly different ($P = 1.00$). Of 153 ischemic lesions, 148 ischemic lesions (96.7%) were detected on T2- FLAIR. Meanwhile, of 153 ischemic lesions, 149 (97.4%) were detected on T2-PROPELLR-FLAIR. The interobserver agreement between the 2 readers assessing FHVs and parenchymal lesions for T2-FLAIR and T2-PROPELLER-FLAIR was excellent ($\kappa = 0.83$ and 0.87 for the FHV score, $\kappa = 0.98$ and 0.98 for parenchymal ischemic lesions).

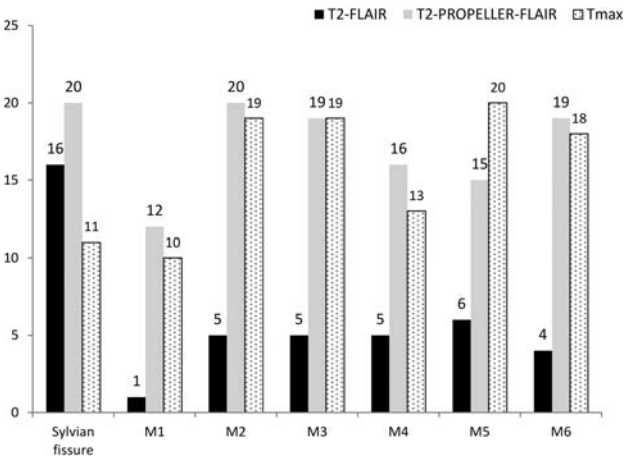

FIG 1. The distribution of FHVs and perfusion abnormality in each MCA-ASPECTS territory. The *black*, *gray*, and *dotted bars* represent the frequency of FHVs and perfusion abnormality for T2-FLAIR, T2-PROPELLER-FLAIR, and T_{max}, respectively.

Table 3: The predictability of FHVs for large-artery stenosis on T2-FLAIR and T2-PROPELLER-FLAIR[a]

	T2-FLAIR	T2-PROPELLER-FLAIR	*P* Value
Arterial stenosis or occlusion on MRA	28/35 (80%)		
Incidence of FHV	19/35 (54%)	26/35 (74%)	.06
Predictability[b]			
True-positive	19	26	
True-negative	7	7	
False-positive	0	0	
False-negative	9	2	
Sensitivity	68%	93%	.03
Specificity	100%	100%	

[a] Data are the number of patients and percentages.
[b] Represents the diagnostic value for the prediction of large-artery stenosis or occlusion.

The FHVs were most frequently present in the Sylvian fissure on T2-FLAIR (16/35, 45%, Fig 1). FHVs were also seen in M5 (6/35, 17%), M2, M3, M4 (5/35, 14% for each), M6 (4/35, 11%), and M1 (1/35, 3%). The FHVs were most frequently present in the Sylvian fissure and M2 on the T2-PROPELLER-FLAIR (20/35, 57% for each); FHVs were seen less frequently in M3 and M6 (19/35, 54% for each), M4 (16/35, 46%), M5 (15/35, 43%), and M1 (12/35, 34%). Perfusion abnormalities were observed in M5 (20/35, 57%), M2 (19/35, 54%), M3 (19/35, 54%), M6 (18/35, 51%), M4 (13/35, 37%), the Sylvian fissure (11/35, 31%), and M1 (10/35, 28%).

FHVs were depicted in 19/35 patients (54%) on T2-FLAIR and in 26/35 patients (74%) on T2-PROPELLER-FLAIR. The sensitivity of T2-PROPELLER-FLAIR for predicting large-artery stenosis or occlusion was 93%, which is significantly higher than that of T2-FLAIR, 68% ($P = .03$). However, the specificities of both sequences were 100% (Table 3).

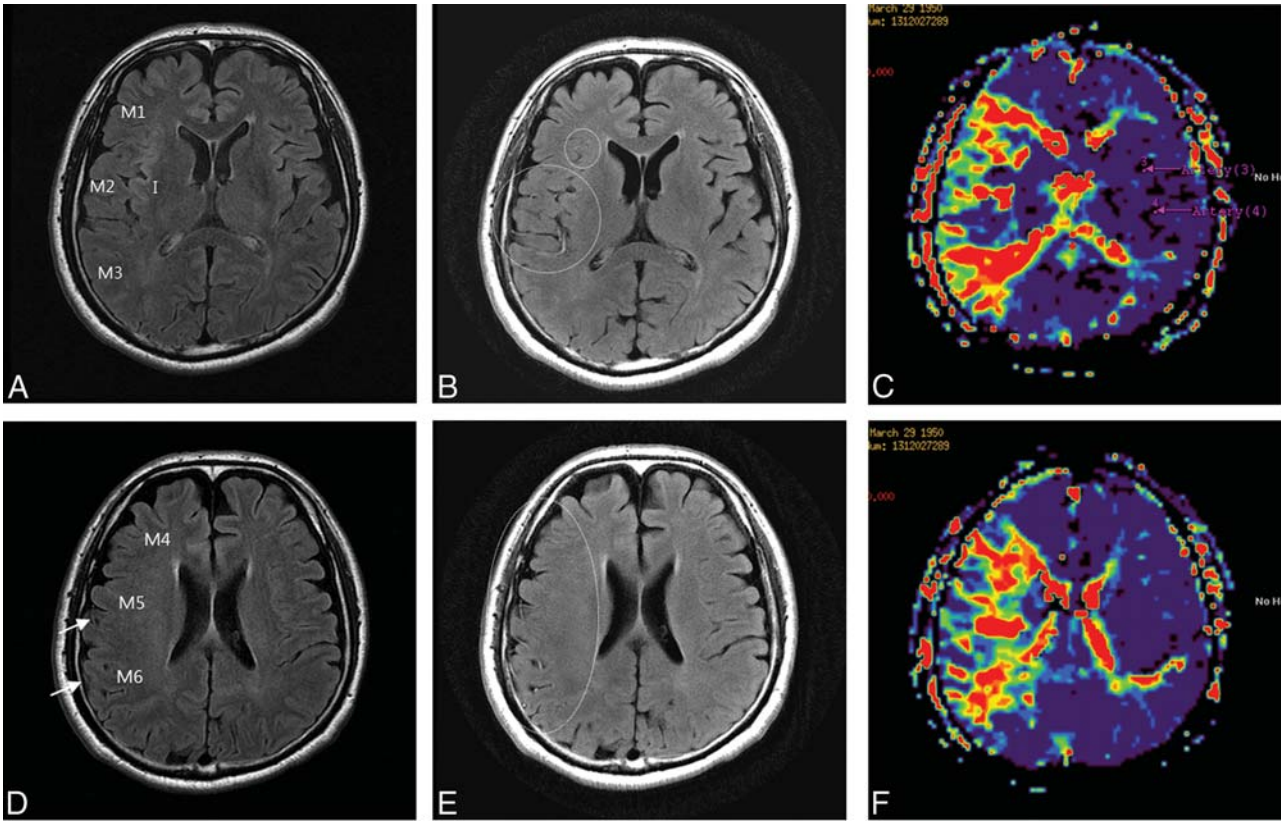

FIG 2. A 63-year-old man with right MCA territory infarction. FHVs on T2-FLAIR at the level of the basal ganglia (*A*) were not seen, whereas FHVs on T2-PROPELLER-FLAIR (*B*) were seen in the Sylvian fissure, M1, M2, and M3 (*dotted circle*). On the T_{max} map (*C*), FHVs were well-matched with perfusion abnormality. FHVs on T2-FLAIR at the level of the ventricle above the basal ganglia (*D*) were seen in the M5 and M6 territory (*arrow*), whereas FHVs on T2-PROPELLER-FLAIR (*E*) were seen in all territories (*dotted circle*). On T_{max} (*F*), FHVs on T2-PROPELLER-FLAIR were well-matched with perfusion abnormality.

Table 4: Associations among FHV scores, ischemic lesion volume, and perfusion abnormality volume in 9 patients with MCA horizontal segment occlusion

	Ischemic DWI Lesion Volume (*r*)[a]	Perfusion Abnormality Volume (*r*)[a]
Median (IQR) (mL)	4.74 (1.76–11.57)	64.91 (60.33–70.31)
FHV scores on T2-FLAIR	0.86, 0.01	0.28, 0.43
FHV scores on T2-PROPELLER-FLAIR	0.38, 0.34	0.79, 0.02
FHV mismatch[b]	−0.79, 0.01	0.33, 0.42

[a] *r* closer to 1 represents a positive correlation. *r* closer to −1 represents a negative correlation.
[b] Calculated by (FHV scores on T2-PROPELLER-FLAIR − FHV scores on T2-FLAIR) / FHV scores on T2-PROPELLER-FLAIR.

Territories in which FHVs were present on T2-PROPELLER-FLAIR were more closely associated with perfusion abnormality than on T2-FLAIR ($\kappa = 0.64$ and 0.27, respectively; Fig 2, On-line Fig 1).

In 9 patients with stroke with total occlusion of the MCA horizontal segment, FHV scores on T2-FLAIR showed a significant positive correlation with ischemic DWI lesion volume ($r = 0.86$, $P = .01$), while FHV scores on T2-FLAIR showed no significant relationship with perfusion abnormality volume ($r = 0.28$, $P = .43$). FHV scores on T2-PROPELLER-FLAIR did not show a significant relationship with ischemic lesion volume ($r = 0.38$, $P = .34$), whereas FHV scores on T2-PROPELLER-FLAIR showed a significant positive correlation with perfusion abnormality volume ($r = 0.79$, $P = .02$). FHV mismatch was significantly negatively correlated with ischemic DWI lesion volume ($r = -0.79$, $P = .01$). FHV mismatch did not show a significant relationship with perfusion abnormality volume ($r = 0.33$, $P = .42$, Table 4).

DISCUSSION

This study found that in patients with MCA stroke, FHVs were more prominent and observed in a wider territory on T2-PROPELLER-FLAIR than on T2-FLAIR. FHVs on T2-PROPELLER-FLAIR had significantly higher sensitivity for predicting large-artery stenosis or occlusion than on T2-FLAIR. The areas showing FHVs on T2-PROPELLER-FLAIR were associated with perfusion abnormality. Moreover, increased FHV mismatch between T2-FLAIR and T2-PROPELLER-FLAIR was associated with decreased infarct volume in patients with MCA horizontal segment occlusion.

These results have clinical impact. FHVs on T2-PROPELLER-FLAIR may be used as a second-look sequence in conjunction with MRA for detecting arterial stenosis in patients with MCA stroke. FHVs on T2-FLAIR and T2-PROPELLER-FLAIR may have the potential for use in evaluating collateral status and predicting prognosis in patients with MCA stroke.

FHVs on T2-PROPELLER-FLAIR were seen in a wider territory than those on T2-FLAIR. Previous studies reported that FHVs are prominent within the Sylvian fissure.[6-15] This might be because the larger arteries have a slower flow speed than the smaller distal arteries

under the same perfusion pressure. Hohenhaus et al[6] reported that FHVs were predominantly located in the distal central surface area (M2 and M5 region and the Sylvian fissure). However, we found fewer FHVs in the distal central surface areas (M2 and M5 regions) and other distal cortical regions (M1, M3, M4, and M6) on T2-FLAIR. On the other hand, FHVs were prominent even in distal cortical regions on T2-PROPELLER-FLAIR.

The prominence of FHVs on T2-PROPELLER-FLAIR could be explained by the following: Cerebral arteries exhibit pulsatile and anatomic positional changes.[16] This motion can lead to image blurring or signal loss and could affect the small-caliber distal cerebral artery in particular due to small voxel size.[17] PROPELLER corrects the motion of objects by repetitive sampling in the central *k*-space.[18] Thus, we speculate that PROPELLER could overcome the blurring or signal loss induced by cerebral artery motion.

Many institutions use limited, short MR imaging protocols that require <20 minutes of imaging. Because the optimal stroke protocol may include only 1 sequence, either conventional T2-FLAIR or T2-PROPELLER-FLAIR, the contrast-to-noise ratio between parenchymal ischemic lesions and adjacent WM is reduced on T2-PROPELLER-FLAIR images compared with T2-FLAIR. T2-FLAIR can estimate the onset time in patients with acute ischemic stroke and may be helpful in assessing wake-up strokes.[19] Although qualitative analysis showed that there was no significant difference between the 2 sequences for the detection of acute ischemic lesions, the contrast-to-noise ratio for parenchymal lesions on T2-PROPELLER-FLAIR could affect the estimation of onset time, resulting in a different treatment plan (On-line Fig 2).

Cosnard et al[20] reported that FHVs correspond to MRA evidence of stenosis or occlusion. The sensitivity and specificity were 65% and 85%, respectively. Kamran et al[15] reported that all 30 of their patients with FHVs had large-vessel occlusion or severe stenosis (≥90%), implying that the specificity of FHVs was 100%. Iancu-Gontard et al[21] reported that the concordance between FHV and stenosis on angiography was significantly higher for the MCA territory compared with the anterior cerebral artery territory. Schellinger et al[2] compared the vessel signs among CT, FLAIR, and GRE for the prediction of vessel status and found that FHVs were more sensitive than the other modalities (sensitivity for FLAIR, 65.9%; CT, 40%; GRE, 34.1%). The specificity of FHVs was 75%. On the basis of previous studies, FHVs on T2-FLAIR have high specificity but relatively low sensitivity for the prediction of large-artery stenosis; this finding is consistent with our results, which show a sensitivity of 68% and a specificity of 100%. However, we found that the sensitivity of FHVs is significantly increased (93%) when combined with the PROPELLER technique. T2-PROPELLER-FLAIR exhibited 2 false-negative cases in which collateral flows were too fast to show arterial hyperintensities. In one of the true-positive cases, arterial stenosis in the MCA cortical segment was difficult to detect, depending only on MRA. Nevertheless, occlusion of the distal arteries was detected in conjunction with FHVs on T2-PROPELLER-FLAIR (On-line Fig 3). Thus, FHVs on T2-PROPELLER-FLAIR may be used as a second-look sequence for the detection of arterial stenosis in patients with stroke. Moreover, the application of T2-PROPELLER-FLAIR might be extended to cohorts with brain tumor or neurodegenerative diseases in which MRA is not routinely performed.

Toyoda et al[22] reported that in 35 of 40 patients with acute ischemic stroke, areas of intra-arterial signal distribution were equal to the regions of abnormal perfusion. However, their detailed method for analysis was not explained. Gawlitza et al[23] reported that there was significant correlation between the degree of the FHV sign and PWI lesion volume, but they did not compare FHV signs with PWI territory by territory. Kwag et al[24] recently reported that MR imaging with a radial *k*-space filling (BLADE; Siemens, Erlangen, Germany), which is a similar technique provided by other MR imaging manufacturers, also improved hyperintense vessels on T2-FLAIR. They proposed that this technique may be helpful for detecting penumbra if it is used right after DWI. However, they did not compare FHVs with perfusion abnormalities. We analyzed the relationship between FHV signs and perfusion abnormalities territory by territory. Our results indicated that territories in which FHVs were present on T2-PROPELLER-FLAIR matched perfusion abnormalities better than those of T2-FLAIR. Perfusion abnormalities included the infarct core, penumbra, and benign oligemia. Currently, there is no threshold for differentiating the spectrum of perfusion abnormalities. Because FHVs exhibited a wider territory on T2-PROPELLER-FLAIR than on T2-FLAIR and a stronger association with perfusion abnormality, we presume that FHVs are closer to wide benign oligemia territory on T2-PROPELLER-FLAIR than they are on T2-FLAIR. Further studies are needed for validation of this assumption.

In our subgroup analysis, higher FHV scores on T2-FLAIR were related to larger ischemic DWI lesion volumes. The higher the FHV mismatch was between the 2 sequences, the smaller the ischemic DWI lesion volume was. This phenomenon might be explained by the following: FHVs on both sequences lie within the spectrum of poor and good collaterals. Because FHVs on T2-FLAIR reflect relatively slow collateral flows, they may represent "poor" collaterals,[25,26] while FHVs on T2-PROPELLER-FLAIR reflect relatively fast and slow collaterals, implying a mixture of "poor" and "good" collaterals. Thus, the mismatch in FHV scores between the 2 sequences may represent the "good" collaterals. However, our results should be cautiously interpreted. Previously, Lee et al[1] demonstrated the existence of FHVs on T2-FLAIR with smaller ischemic lesion volume, which was interpreted as "good" collaterals compared with the absence of FHVs. Therefore, it is difficult to simply define FHVs on T2-FLAIR as "poor" collaterals. In addition, as mentioned above, T2-PROPELLER-FLAIR may miss extremely fast and good collaterals, which can result in false-negative arterial stenosis results. Future studies with a larger and homogeneous population of patients with stroke are needed to investigate this issue. Moreover, considering that FHVs are free from the technical difficulties of PWI, such as arterial input function measurement and complicated deconvolution methods,[27] FHVs may be of value in ongoing research on leptomeningeal collateralization in stroke.

There were some limitations in this study. First, the number of cases was small and might not be sufficient to determine the exact diagnostic value for T2-PROPELLER-FLAIR. However, the diag-

nostic value of T2-FLAIR was consistent with that in previous studies and was thus presumed to be credible. Second, our cohort was heterogeneous, with patients representing both the acute and subacute stages of MCA stroke. The median time from onset to imaging was 23 hours, beyond the time window for IV or intra-arterial therapy. Thus, our results should be carefully applied in clinical practice. However, our results may serve as a cornerstone for future studies with a larger and more homogeneous population to validate and extend these results.

CONCLUSIONS

Our study showed that in patients with MCA stroke, FHVs were more prominent and observed across a wider territory on T2-PROPELLER-FLAIR than on T2-FLAIR. In addition, FHVs on T2-PROPELLER-FLAIR have a significantly higher sensitivity for predicting large-artery stenosis or occlusion than on T2-FLAIR. Moreover, the areas showing FHVs on T2-PROPELLER-FLAIR were more closely associated with perfusion abnormality than those on T2-FLAIR, reflecting leptomeningeal collateral circulation.

Disclosures: Sangwoo Lee—*UNRELATED*: *Employment*: GE Healthcare.

REFERENCES

1. Lee KY, Latour LL, Luby M, et al. **Distal hyperintense vessels on FLAIR: an MRI marker for collateral circulation in acute stroke?** *Neurology* 2009;72:1134-39 CrossRef Medline
2. Schellinger PD, Chalela JA, Kang DW, et al. **Diagnostic and prognostic value of early MR imaging vessel signs in hyperacute stroke patients imaged <3 hours and treated with recombinant tissue plasminogen activator.** *AJNR Am J Neuroradiol* 2005;26:618-24 Medline
3. Assouline E, Benziane K, Reizine D, et al. **Intra-arterial thrombus visualized on T2* gradient echo imaging in acute ischemic stroke.** *Cerebrovasc Dis* 2005;20:6-11 CrossRef Medline
4. Lee JY, Lee KY, Suh SH. **Different meaning of vessel signs in acute cerebral infarction.** *Neurology* 2010;75:668 CrossRef Medline
5. Sanossian N, Saver JL, Alger JR, et al. **Angiography reveals that fluid-attenuated inversion recovery vascular hyperintensities are due to slow flow, not thrombus.** *AJNR Am J Neuroradiol* 2009;30:564-68 CrossRef Medline
6. Hohenhaus M, Schmidt WU, Brunecker P, et al. **FLAIR vascular hyperintensities in acute ICA and MCA infarction: a marker for mismatch and stroke severity?** *Cerebrovasc Dis* 2012;34:63-69 CrossRef Medline
7. Haussen DC, Koch S, Saraf-Lavi E, et al. **FLAIR distal hyperintense vessels as a marker of perfusion-diffusion mismatch in acute stroke.** *J Neuroimaging* 2013;23:397-400 CrossRef Medline
8. Tsushima Y, Endo K. **Significance of hyperintense vessels on FLAIR MRI in acute stroke.** *Neurology* 2001;56:1248-49 CrossRef Medline
9. Storey P, Atanasova IP, Lim RP, et al. **Tailoring the flow sensitivity of fast spin-echo sequences for noncontrast peripheral MR angiography.** *Magn Reson Med* 2010;64:1098-108 CrossRef Medline
10. Park J, Kim EY. **Contrast-enhanced, three-dimensional, whole-brain, black-blood imaging: application to small brain metastases.** *Magn Reson Med* 2010;63:553-61 CrossRef Medline
11. Chen X, Xian J, Wang X, et al. **Role of periodically rotated overlapping parallel lines with enhanced reconstruction diffusion-weighted imaging in correcting distortion and evaluating head and neck masses using 3 T MRI.** *Clin Radiol* 2014;69:403-09 CrossRef Medline
12. Fries P, Runge VM, Kirchin MA, et al. **Diffusion-weighted imaging in patients with acute brain ischemia at 3 T: current possibilities and future perspectives comparing conventional echoplanar diffusion-weighted imaging and fast spin echo diffusion-weighted imaging sequences using BLADE (PROPELLER).** *Invest Radiol* 2009;44:351-59 CrossRef Medline
13. Forbes KP, Pipe JG, Karis JP, et al. **Improved image quality and detection of acute cerebral infarction with PROPELLER diffusion-weighted MR imaging.** *Radiology* 2002;225:551-55 CrossRef Medline
14. Pexman JH, Barber PA, Hill MD, et al. **Use of the Alberta Stroke Program Early CT Score (ASPECTS) for assessing CT scans in patients with acute stroke.** *AJNR Am J Neuroradiol* 2001;22:1534-42 Medline
15. Kamran S, Bates V, Bakshi R, et al. **Significance of hyperintense vessels on FLAIR MRI in acute stroke.** *Neurology* 2000;55:265-69 CrossRef Medline
16. Umeda Y, Ishida F, Hamada K, et al. **Novel dynamic four-dimensional CT angiography revealing 2-type motions of cerebral arteries.** *Stroke* 2011;42:815-18 CrossRef Medline
17. Gumus K, Keating B, Poser BA, et al. **Prevention of motion-induced signal loss in diffusion-weighted echo-planar imaging by dynamic restoration of gradient moments.** *Magn Reson Med* 2014;71:2006-13 CrossRef Medline
18. Pipe JG. **Motion correction with PROPELLER MRI: application to head motion and free-breathing cardiac imaging.** *Magn Reson Med* 1999;42:963-69 CrossRef Medline
19. Aoki J, Kimura K, Iguchi Y, et al. **FLAIR can estimate the onset time in acute ischemic stroke patients.** *J Neurol Sci* 2010;293:39-44 CrossRef Medline
20. Cosnard G, Duprez T, Grandin C, et al. **Fast FLAIR sequence for detecting major vascular abnormalities during the hyperacute phase of stroke: a comparison with MR angiography.** *Neuroradiology* 1999;41:342-46 CrossRef Medline
21. Iancu-Gontard D, Oppenheim C, Touzé E, et al. **Evaluation of hyperintense vessels on FLAIR MRI for the diagnosis of multiple intracerebral arterial stenoses.** *Stroke* 2003;34:1886-91 CrossRef Medline
22. Toyoda K, Ida M, Fukuda K. **Fluid-attenuated inversion recovery intraarterial signal: an early sign of hyperacute cerebral ischemia.** *AJNR Am J Neuroradiol* 2001;22:1021-29 Medline
23. Gawlitza M, Gragert J, Quäschling U, et al. **FLAIR-hyperintense vessel sign, diffusion-perfusion mismatch and infarct growth in acute ischemic stroke without vascular recanalisation therapy.** *J Neuroradiol* 2014;41:227-33 CrossRef Medline
24. Kwag E, Lim SM, Park JE, et al. **Arterial hyperintensity on BLADE fluid-attenuated inversion recovery images (FLAIR) in hyperacute territorial infarction: comparison with conventional FLAIR.** *Eur Radiol* 2014;24:2045-51 CrossRef Medline
25. Ebinger M, Kufner A, Galinovic I, et al. **Fluid-attenuated inversion recovery images and stroke outcome after thrombolysis.** *Stroke* 2012;43:539-42 CrossRef Medline
26. Girot M, Gauvrit JY, Cordonnier C, et al. **Prognostic value of hyperintense vessel signals on fluid-attenuated inversion recovery sequences in acute cerebral ischemia.** *Eur Neurol* 2007;57:75-79 CrossRef Medline
27. Latchaw RE, Yonas H, Hunter GJ, et al. **Guidelines and recommendations for perfusion imaging in cerebral ischemia: a scientific statement for healthcare professionals by the writing group on perfusion imaging, from the Council on Cardiovascular Radiology of the American Heart Association.** *Stroke* 2003;34:1084-104 CrossRef Medline

Structural Brain Changes following Long-Term 6° Head-Down Tilt Bed Rest as an Analog for Spaceflight

D.R. Roberts, X. Zhu, A. Tabesh, E.W. Duffy, D.A. Ramsey, and T.R. Brown

ABSTRACT

BACKGROUND AND PURPOSE: Following long-term spaceflight, a subset of the National Aeronautics and Space Administration astronauts present with visual impairment and increased intracranial pressure, known as visual impairment and intracranial pressure syndrome. We investigated structural brain changes following long-term head-down tilt bed rest as a spaceflight analog.

MATERIALS AND METHODS: Volumetric analysis was performed on structural pre- and post–bed rest brain MR images.

RESULTS: Comparing post–bed rest to pre–bed rest images, we found the following: 1) no significant group differences in GM, WM, CSF, or ventricular volumes; 2) shift of the center of mass of the brain upward and posterior rotation of the brain relative to the skull; 3) a significant correlation between posterior brain rotation and changes in ventricular volume; and 4) significant increases in brain tissue density in regions at the vertex, including the frontoparietal lobes, with contraction of adjacent extra-axial CSF spaces, and significant decreases in tissue density in areas along the base of the brain, including the orbitofrontal cortex.

CONCLUSIONS: We observed widespread morphologic changes with brain tissue redistribution in response to gravity changes; possible associated functional changes are unknown. The observation that ventricular change is correlated to posterior brain rotation suggests an alteration in CSF homeostasis. Ultimately, to elucidate any structural changes that may play a role in visual impairment and intracranial pressure syndrome, volumetric analysis of pre- and postflight structural scans of astronauts is needed.

ABBREVIATIONS: BR = bed rest; ICV = intracranial volume; IIH = idiopathic intracranial hypertension; NASA = National Aeronautics and Space Administration; VIIP = visual impairment and intracranial pressure

Following long-term missions aboard the International Space Station, increased intracranial pressure and papilledema have been documented in the National Aeronautics and Space Administration (NASA) astronauts. In 1 report[1] investigating 7 astronauts following 6 months of spaceflight, all astronauts demonstrated ophthalmologic findings, with disc edema in 5 astronauts and globe flattening in 5. Lumbar punctures were performed in 4 of these astronauts with opening pressures of 21–28.5 cm H_2O[1]. In the 1 astronaut who underwent repeated lumbar punctures, the opening pressure remained elevated 19 months following spaceflight at 22 cm H_2O[1]. The etiology of these findings is currently unclear; however, it has been hypothesized that they may result from loss of gravitational hydrostatic pressure gradients and large cephalad fluid shifts. NASA has coined the term "visual impairment and intracranial pressure [VIIP] syndrome" to describe this constellation of signs and symptoms in astronauts and has likened VIIP syndrome to Earth-based idiopathic intracranial hypertension (IIH) or pseudotumor cerebri.

A traditional ground-based analog used by NASA and other international space agencies to study physiologic changes associated with long-term spaceflight has been to place healthy subjects in 6° head-down tilt bed rest for varying periods.[2,3] Anecdotally, Russian scientists first devised the head-down-tilt protocol in the early 1970s on the basis of reports by Russian cosmonauts who had the sensation of slipping off the foot of the bed on return to Earth after long-duration missions.[3] The foot of the bed was

Received February 5, 2015; accepted after revision March 4.

From the Departments of Radiology and Radiological Sciences (D.R.R., X.Z., A.T., E.W.D., T.R.B.) and Neurosciences and Neuroscience Research (D.R.R., X.Z.), Medical University of South Carolina, Charleston, South Carolina; and Care Coordination Institute (D.A.R.), Department of Medicine, University of South Carolina School of Medicine, Greenville, South Carolina.

This work was funded by NASA, grant number NNJ04HF70G.

The authors wish to dedicate this article to Ali Tabesh, PhD.

Paper previously presented at: American Society of Neuroradiology and the Foundation of the ASNR Symposium, May 17–22, 2014; Montreal, Quebec, Canada.

Please address correspondence to Donna R. Roberts, MD, Department of Radiology and Radiological Sciences, 96 Jonathan Lucas St, MSC 323, Charleston, SC 29425-3230; e-mail: robertdr@musc.edu

Indicates open access to non-subscribers at www.ajnr.org

Indicates article with supplemental on-line tables.

Indicates article with supplemental on-line photos.

http://dx.doi.org/10.3174/ajnr.A4406

raised until it felt horizontal to help the cosmonauts sleep.[3] As an analog for spaceflight, the reduction in Gz gravitational stimuli during bed rest results in an upward shift of body fluids, unloading the upright weight of the body, reduced work against the force of gravity, and lower extremity inactivity.[3] As a result, many of the physiologic changes of spaceflight can be reproduced, including decreased cardiac output, orthostatic intolerance, muscle atrophy, and bone loss. This model has been applied extensively to investigate cardiovascular and musculoskeletal deconditioning, immunologic response, and cognitive functioning.[2,3]

We previously acquired structural MR imaging brain scans of subjects participating in a NASA-sponsored long-term bed rest study.[4] Given the recent interest in intracranial adaptation to spaceflight, we decided to perform a volumetric analysis of the structural MR imaging dataset to assess any potential alterations in brain structure or CSF distribution that may shed light on the spectrum of findings noted in VIIP syndrome. The results of this analysis are presented here.

MATERIALS AND METHODS

Bed Rest Study Protocol

Eight healthy volunteers (age, 33 ± 7.4 years; 3 women) underwent long-term bed rest at the NASA Flight Analogs Facility at the University of Texas Medical Branch, Galveston, as part of a multiinvestigator study.[2] Informed consent was obtained, and the study was approved by the appropriate institutional review boards. Subject recruitment included radio, television, and newspaper announcements and a Web site (www.bedreststudy.com). The study protocol has been described in detail elsewhere.[2] Before bed rest, subjects were admitted to the NASA Flight Analogs Facility and underwent a NASA-modified Air Force Class III physical examination and psychological assessment. Subjects then remained in the unit for 11–14 days before the start of bed rest for pre–bed rest data collection performed by other investigators and were free to ambulate normally. Male subjects were admitted into the study just after providing informed consent. Women were admitted so that the time of their next menses would occur 2 days before entering the bed rest phase of the study.[2] For ease of reference, study days during the pre–bed rest period are referred to as BR-x, with BR-1 being the last day before bed rest. The first day in BR is referred to as BR1. After bed rest following return to normal ambulation, subjects remained in the unit for 2 weeks to undergo reconditioning.

Throughout the bed rest portion of the study, the subjects' beds were placed in a 6° Trendelenburg position. Subjects were allowed to lift their heads on 1 elbow to eat. Otherwise, the head-down position was strictly maintained, though the subjects were free to move about in their beds and shift from supine to lateral or prone positions. Bedpans were used, and hygiene was maintained with overhead showers while remaining in the head-down position. To keep actively engaged, subjects participated in various cognitive tasks, completed a specified objective (such as learning a foreign language), and were provided with numerous entertainment opportunities (movies, video games, group social activities). The subjects were placed on a standardized diet so that all input and output were maintained to ensure balanced nutritional uptake and hydration with no net water gain or loss.[2] Monitors were present 24/7 to ensure subject compliance.

Initial plans were for all subjects to remain at bed rest for 90 days, and the first 4 subjects followed this protocol. The second group of subjects, unfortunately, was removed from the Flight Analogs Facility earlier than planned due to extreme weather. These subjects had undergone 42, 44, 49, and 52 days of bed rest at the time of the evacuation.

MR Imaging

Two brain MR imaging structural scans were obtained for each subject: one immediately before bed rest (pre–bed rest scan) and another toward the end of bed rest (referred to as the post–bed rest scan). On the first day of bed rest, BR1, the subjects walked to the MR imaging scanner facility and laid down on the MR imaging table for acquisition of the pre–bed rest scans. Immediately on completion of the MR imaging session, the subjects were moved from the scanner table while remaining supine and placed in a hospital bed in the 6° head-down-tilt position. Subjects then remained in this position throughout the bed rest period. For the 4 subjects who required emergent evacuation from the Flight Analogs Facility, end-of–bed rest imaging was performed on the day of evacuation, (ie, on days BR42, BR44, BR49, and BR52). On that day, while still in bed rest, the subjects were moved from their beds onto the MR imaging table, only shifting from head-down-tilt to supine. Structural scans were immediately acquired, and these were considered the post–bed rest scans. Following the scanning session, subjects were allowed to sit up and prepare for evacuation. For the 4 subjects who underwent 90 days of bed rest, MR imaging was performed on both day BR60, with the subjects remaining in the supine position only shifting from their bed to the scanner table after which they continued on bed rest for another 30 days, and day BR90. These subjects were not allowed to return to ambulation until BR90; however, given the shortened bed rest duration experienced by the evacuation subjects, for comparison purposes, in this report, the BR60 scans were considered the post–bed rest scans for these subjects. Therefore, considering all 8 subjects, the post–bed rest scans described in this report were obtained between days BR42 and BR60.

The structural MR images consisted of T1-weighted 3D echo-spoiled gradient-echo images acquired on a 1.5T scanner (GE Healthcare, Milwaukee, Wisconsin). Images were acquired in either transverse or coronal planes, at either 1.0- or 1.5-mm section thickness with FOVs of 250 or 260 mm. Scanning parameters were TR = 22 ms, TE = 8 ms, flip angle = 30°, and matrix = 256 × 256.

Physiologic Data

Because this study was part of a larger NASA-sponsored multiinvestigator study, extensive physiologic data were obtained. With institutional review board approval, other investigators provided the following parameters: daily water intake, daily urine output, plasma volume, blood volume, and urine cortisol levels. The acquisition of these data points are described by the relevant investigators.[2,5,6]

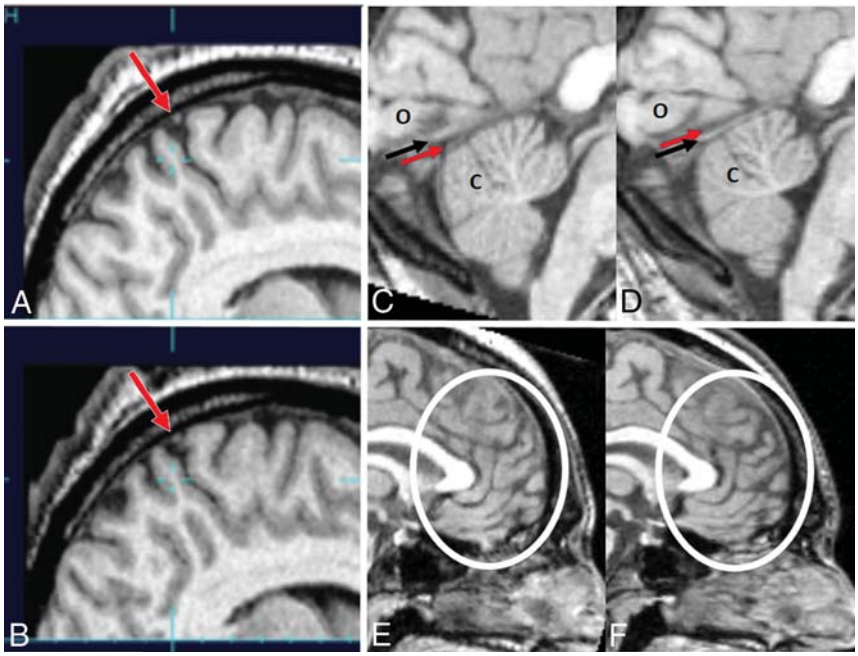

FIG 1. Structural images before and after bed rest. Sagittal images of the brain (subject H in On-line Tables 1–4) at the vertex before (*A*) and after (*B*) bed rest show a shift of the brain toward the vertex with contraction of the extra-axial spaces at the vertex and crowding of adjacent structures, including a cortical vein (*arrow*). Sagittal images of the posterior fossa before (*C*) and after (*D*) bed rest (subject A in On-line Tables 1–4). Before bed rest, the occipital lobes (o) lie against the tentorium cerebelli (*black arrow*). Below the tentorium, there is a thin layer of CSF (*red arrow*) between the tentorium and the upper aspect of the cerebellum (c). After bed rest, there is an upward shift of the occipital lobes away from the tentorium, now with a thin layer of CSF (*red arrow*) between the occipital lobes and the tentorium. In the posterior fossa, a layer of CSF is no longer visible between the tentorium and the cerebellum. Instead, the cerebellum now appears compressed against the tentorium. Sagittal images of the frontal lobes before (*E*) and after (*F*) bed rest show subtle expansion of the frontal lobe sulci after bed rest (subject A in On-line Tables 1–4).

MR Imaging Analysis

Voxel-Based Morphometry Analysis. Data preprocessing and analysis were performed with the VBM8 toolbox (http://dbm.neuro.uni-jena.de/vbm/) incorporated in the SPM8 software (http://www.fil.ion.ucl.ac.uk/spm/software/spm8) by using the default longitudinal preprocessing approach. We performed the following preprocessing steps: 1) registration of the post–bed rest scan to the pre–bed rest scan for each subject separately, 2) intrasubject bias correction, 3) segmentation of the different tissue classes, and 4) linear (ie, affine) and nonlinear (ie, Diffeomorphic Anatomical Registration Through Exponentiated Lie Algebra) registration. The segmentation procedure was refined by accounting for partial volume effects, applying adaptive maximum a posteriori estimations, and applying a hidden Markov random field model. The realigned and normalized GM and WM segments were smoothed with an 8-mm full width at half maximum Gaussian kernel. The images were then masked by a brain tissue mask defined by the probability of GM + WM > 80%.

Intracranial Volume Estimation. Manual measurements were performed on the T1-weighted images from the pre–bed rest and post–bed rest scans. Twelve delineations were performed by 1 tracer (E.W.D.), and the other 4, by a second tracer (X.Z.). Details of the measurement of intracranial volume (ICV) are described elsewhere.[7] In brief, the original sections were reformatted into the sagittal plane. Realigning the original sections to correct for head tilt was not necessary due to the large size of the intracranial cavity.[8] The brightness of the image was increased to improve the visual clarity of the boundary of the dura mater. Starting from the left-hand side of the head, we then estimated the ICV for each image by a hand-traced mask. The tracers were blinded as to which subject/time point the scans represented. The 2 tracers reviewed each other's ICV definitions for consistency, and no significant difference was found between the 2 tracers ($P = .25$).

Tissue-Specific Volumetric Analysis. GM, WM, and total intracranial CSF volume estimation was performed with the default "read raw volumes" function in the VBM8 toolbox. All images were segmented by using default templates (a modified version of the ICBM Tissue Probabilistic Atlas, http://www.bmap.ucla.edu/portfolio/atlases/ICBM_Probabilistic_Atlases/) and parameters. Specifically, these parameters included 2 Gaussians each for WM, GM, and CSF and 4 Gaussians for everything not fitting these categories; a warping regularization value of 1; a warp frequency cutoff of 25; very light regularization (0.0001); a 60-mm cutoff for the full width at half maximum of Gaussian smoothness of bias; and a sampling distance of 3. When generating masks, voxels with a probability of ≥0.5 were counted as members of that particular class.

Ventricular volumetric analysis was performed in a completely automated manner via FreeSurfer (http://surfer.nmr.mgh.harvard.edu). Standard reconstruction procedures, which delineate gross brain anatomy into a series of cortical and subcortical labels, were used. Structures are labeled by using a complex algorithm combining information on image intensity, probabilistic atlas location, and the local spatial relationships between subcortical structures by the FreeSurfer "recon-all" function.[9] Ventricular volume was defined as the sum of the lateral ventricles (including the choroid plexus) and the third and fourth ventricles. The GM, WM, total intracranial CSF, and ventricular volumes were compared pair-wise by using paired *t* tests.

Brain-Shift Analysis. To compare brain movement in reference to the skull, the skull was stripped from the images and used as a reference to calculate parameters for rotation and translation to estimate the difference before and after bed rest by using the FLIRT tool (FMRIB Linear Image Registration Tool, http://www.fmrib.ox.ac.uk/) of FSL. Because some of the images were originally acquired in the coronal plane, each pair of images (pre- and post–bed rest scans) was first resampled to the transverse plane. The skull image, obtained by using the ICV mask to remove all intracranial voxels, and the brain image, which included all voxels in the ICV mask, were then gener-

ated. The skull image of the pre–bed rest scan was then used as reference for a 6 *df* registration, to calculate the transformation matrix needed to align the post–bed rest skull to the reference. The same transformation matrix was then applied to the post–bed rest brain image to create the skull-aligned post–bed rest brains. Finally, the transformation matrix for aligning the post–bed rest brain to the pre–bed rest brain image was estimated on the basis of rigid-body assumptions, and the transformation/rotation parameters were calculated (On-line Fig 1).

RESULTS

On visual inspection by an experienced neuroradiologist (D.R.R.), comparing pre–bed rest with post–bed rest images, a clear change in brain structures was seen. The extra-axial CSF spaces near the vertex appeared more crowded, and the CSF spaces along the frontal lobes were more prominent on the post–bed rest images compared with the pre–bed rest images (Fig 1). The supravermian cistern appeared effaced on the post–bed rest images. Additionally, a noticeable change in ventricular size was seen in some individuals. Most interesting, these findings varied across individuals: In some subjects, the ventricles became visibly smaller, while in others the ventricles became larger (Fig 2). On the basis of the subjective findings and the fact that the subjects had been maintained in the head-down-tilt position, we hypothesized that there would be a global shift in brain tissue within the cranial vault toward the vertex.

Tissue-Specific Volumetric Analysis

On the group level, the GM, WM, CSF, and ventricular size did not demonstrate significant differences ($P > .1$) between pre- and post–bed rest (Table 1, See On-line Tables 1–4 for individual subject data). This held true for both the raw and normalized (tissue volume/estimated ICV) volumes. Although by visual inspection, a distinct change in ventricular volume was seen for some subjects between pre- and post–bed rest, on group analysis, this did not reach statistical significance due to the variability of responses across individuals (On-line Fig 2). No correlation was noted between sex and ventricular volume change.

Brain-Shift Analysis

After bed rest, the brain as a whole showed significant displacement in the inferior-to-superior direction (0.36 ± 0.15 mm, $t = 7.0$, $P < .01$), and marginally significant displacement in the anterior-to-posterior direction (0.21 ± 0.17 mm, $t = 3.4$, $P = .11$), with no significant effect in the left-right direction (0.01 ± 0.08 mm, $t = 0.4$, $P = .69$) (Fig 3). Rotation was found to be significant around the left-right axis ($0.28 \pm 0.34°$, $t = 2.3$, $P = .051$), but not around any other axis ($P = .27$ and 0.69). In other words, the center of mass of the brain was shifted upward, and the brain demonstrated posterior rotation relative to the skull. The change in ventricular size was found to correlate (Spearman correlation: $r = 0.893$, $P = .007$) with the degree of posterior rotation of the brain independent of subject variability (Fig 4).

Voxel-Based Morphometry

Paired *t* tests were used to estimate the possible changes of GM or WM between pre- and post–bed rest scans. The predictions were compared and thresholded at $P = .001$ ($t = 3.1$) and a cluster size of >296 voxels. Compared with pre–bed rest, the post–bed rest brains showed significant tissue (GM + WM) density increase in regions near the vertex, including the central frontoparietal lobes (Fig 5, See On-line Fig 3 for more detail). Other regions that also showed significant density increase included the posterior cingulate, cuneus, thalami, and cerebellum. Tissue-density decrease was found in the orbitofrontal cortex, brain stem, corpus callosum, striatum, anterior cingulate, and parietal operculum.

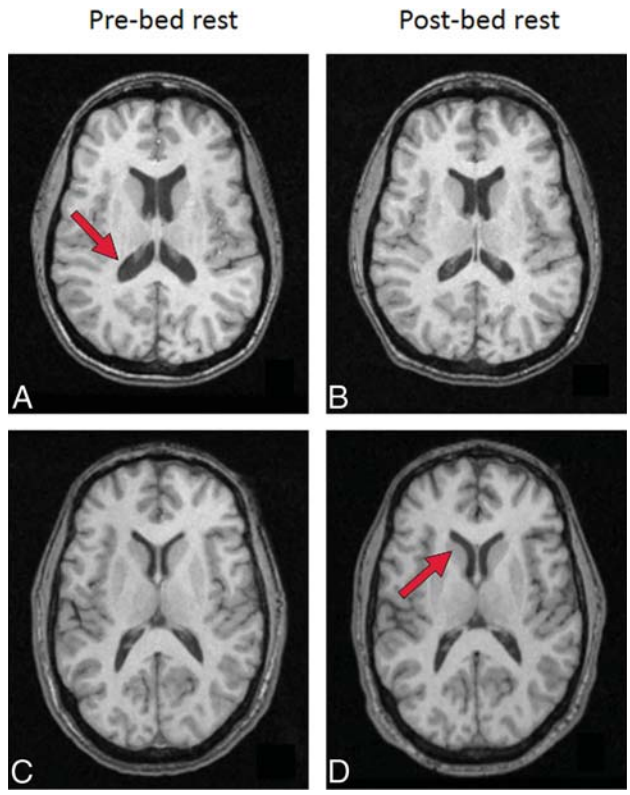

FIG 2. Changes in ventricular volume before and after bed rest. Axial images of the brain of the subject with the largest change in ventricular size on the post–bed rest scan (*B*) compared with the pre–bed rest scan (*A*). Compared with pre–bed rest, there was a 22.4% reduction in ventricular size post–bed rest in this subject, best appreciated at the level of the atrium of the lateral ventricles (*arrow*) (subject D in On-line Tables 1–4). Axial images of the brain of the subject with the largest increase in ventricular size on the post–bed rest scan (*D*) compared with the pre–bed rest scan (*C*). Compared with pre–bed rest, there was a 10.4% increase in ventricular size post–bed rest in this subject, best appreciated at the level of the frontal horns of the lateral ventricles (*arrow*) (subject C in On-line Tables 1–4).

Table 1: Pre- and post–bed rest volumetric MRI and physiologic measurements (group mean and SD)

Measurements	Pre-bed rest	Post-bed rest	*P* Value
ICV (mL)	1426 ± 105	1425 ± 105	.91
Gray matter (mL)	603.8 ± 40.8	615.1 ± 50.4	.18
White matter (mL)	546.0 ± 58.4	540.8 ± 51.5	.48
CSF (mL)	185.8 ± 15.0	186.6 ± 16.1	.83
Ventricle volume (mL)	15.45 ± 5.52	15.0 ± 4.31	.62
Plasma volume (mL)	2.63 ± 0.38	2.30 ± 0.46	.006
Blood volume (mL)	4.57 ± 1.02	4.08 ± 1.11	.004
Urine cortisol (μg/dL)	2.63 ± 0.97	3.58 ± 1.06	.14

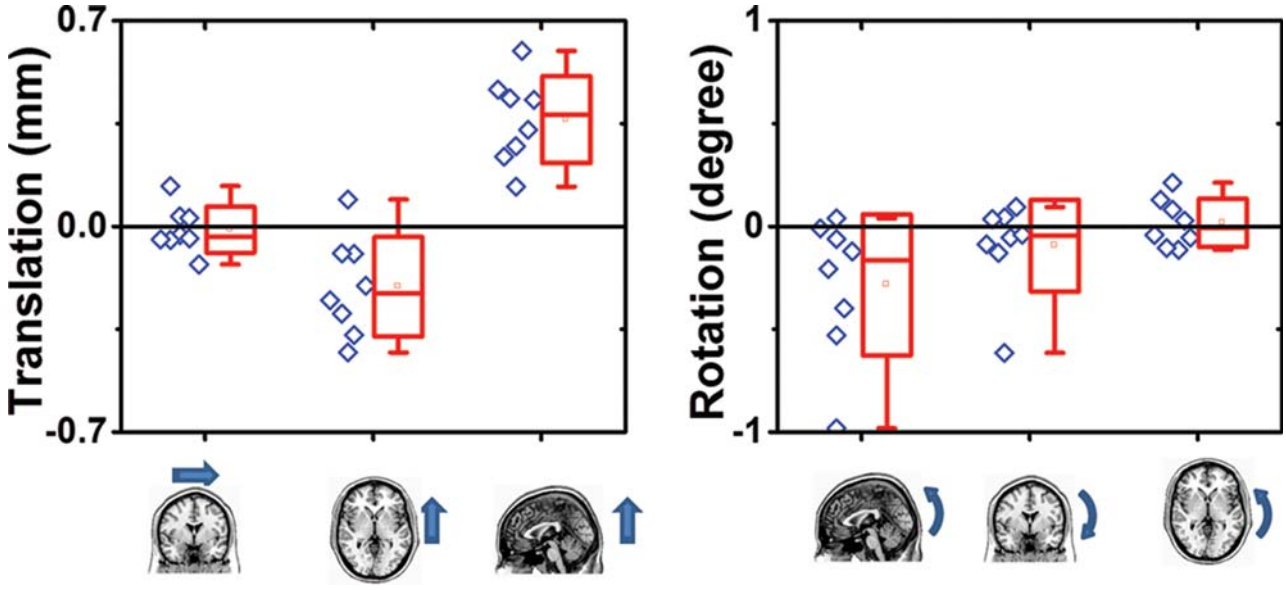

FIG 3. Brain translation and rotation in reference to the skull following bed rest. Parameters (translation and rotation on x, y, z-axes) were estimated on the basis of a rigid-body assumption. The *arrow* indicates the direction of movement that corresponds to positive values on the graph.

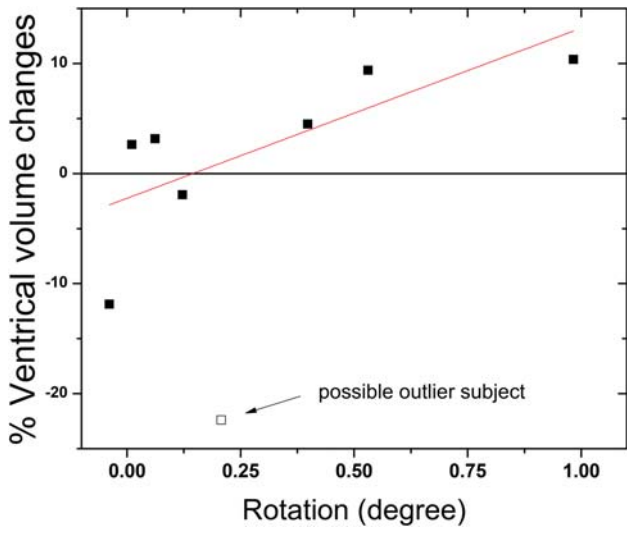

FIG 4. Correlation between brain rotation and ventricle volume changes. Without the potential outlier, which was the subject that demonstrated the largest ventricles before bed rest, the Spearman correlation is $r = 0.893$, $P = .007$. Including the outlier, the Spearman correlation is $r = 0.690$, $P = .058$.

Physiologic Data

The Spearman rank correlation was used to assess the association between physiologic data (fluid balance, plasma volume, blood volume, and cortisol levels provided by other investigators[5,6]) and MR imaging measures. No significant correlation was found (Table 1). See On-line Tables 1–4 for individual subject data.

DISCUSSION

NASA has recently described a constellation of findings, including visual decrement and elevated intracranial pressure, occurring in a subset of astronauts following long-term exposure to microgravity and the space environment, known as the VIIP syndrome. These are especially concerning given that plans for human spaceflight, such as a manned Mars mission, will be of even longer durations than current assignments on the International Space Station.

As a first step in elucidating the mechanisms underlying the development of the VIIP syndrome, we examined structural brain changes induced by long-term 6° head-down tilt bed rest, a traditional NASA model for studying physiologic changes associated with microgravity exposure. The consequences of long-term maintenance of a head-down body position on the brain are unknown; however, changes in body position and resultant changes in gravitational gradients have been found to impact brain physiology. For example, moving from the upright to the supine position alters venous outflow, with redirection of venous return from the vertebral venous plexuses to the internal jugular veins; decreases intracranial compliance; and increases intracranial pressure.[10] In this study, we found the following: 1) no significant group differences in GM, WM, CSF, or ventricular volumes between pre- and post–bed rest; 2) shift of the center of mass of the brain upward and posterior rotation of the brain relative to the skull; 3) significant correlation between posterior brain rotation and changes in ventricular volume; and 4) significant increases in brain tissue density in brain regions at the vertex, including the central frontoparietal lobes, with associated contraction of the adjacent extra-axial CSF spaces and significant decreases in tissue density in areas along the base of the brain, including the orbitofrontal cortex, with expansion of the basal extra-axial CSF spaces.

We hypothesize that these unique structural alterations occurring during bed rest and possibly during spaceflight due to altered gravity gradients may provide explanations for the findings of the VIIP syndrome. The extra-axial CSF effacement at the vertex found during bed rest may lead to changes in CSF flow dynamics, and an upward shift of the brain may result in compression of the dural venous sinuses along the vertex. This, in turn, may contribute to venous outflow obstruction and the spectrum of intraorbital and intracranial findings described in astronauts. This hypothesis is further supported by the observation that ventricular change is correlated to posterior brain rotation within the skull,

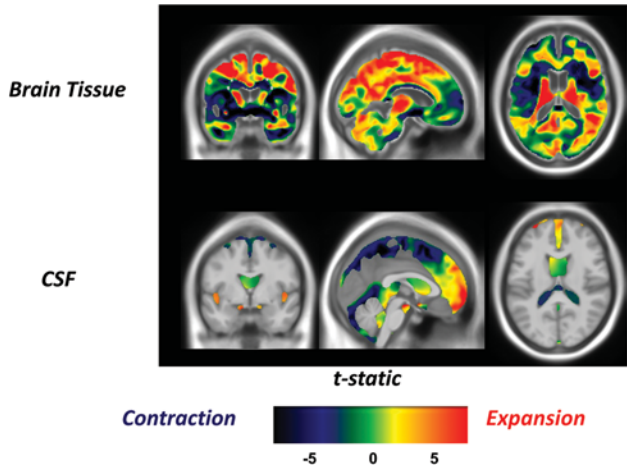

FIG 5. Regions of the brain most significantly affected by bed rest. There is increased brain tissue density (top row of images) at the vertex, particularly affecting the central frontoparietal lobes, with contraction of the adjacent CSF spaces (bottom row of images). There is decreased brain tissue density along the base of the brain, including the orbitofrontal cortex, with expansion of the adjacent CSF spaces.

Table 2: Comparison of typical clinical features in IIH and VIIP

	IIH	VIIP
Finding		
Increased intracranial pressure	√	Mildly elevated postflight; in-flight ICP unknown
Papilledema	√	√
Globe flattening	√	√
Choroidal folds	√	√
Hyperopic shifts	√	√
Chronic headaches	√	
Diplopia	√	
Transient visual obscurations	√	
Pulse-synchronous tinnitus	√	
Sixth cranial nerve palsy	√	
Patient characteristics		
Obesity	√	
Sex predominance	Female	Male
Imaging findings		
Optic nerve head protrusion	√	√
Flattened posterior globe	√	√
Enlarged optic nerve sheath	√	√
Optic nerve tortuosity	√	√
Empty sella	√	√

Note:—√ indicates clinical feature present.

suggesting altered CSF homeostasis. Future planned studies include advanced structural, functional, and venographic MR imaging of astronauts before and after spaceflight.

In some subjects in our study, the ventricular volume change is clearly visible without computer-aided analysis (Fig 2). The change in ventricular size ranged from a 10.4% increase to a 22.4% decrease post–bed rest compared with pre–bed rest values, an unexpected finding during the course of only 2 months in young, healthy subjects. For comparison, in elderly, healthy subjects, expansion of the ventricles has been reported to be 1.5%–3.0% per year and 5%–16% in patients with Alzheimer disease.[11] Ventricular volume can also be influenced by fluid balance, and the subjects with bed rest did undergo an initial diuresis, which stabilized within 3 days.[2] However, ventricular volume changes would be expected to be approximately 1%–3% during dehydration relative to normal hydration,[12] again less than the changes in ventricular size that we measured.

It has been suggested that the spectrum of intraorbital and intracranial findings of astronauts following spaceflight are similar to those in the Earth-based condition of IIH.[1,13] Increased intracranial pressure, papilledema, globe flattening, dilated optic nerve sheaths, and visual disturbances have been described in both conditions (Table 2).[1,13,14] Although the etiologies of both conditions are unknown, researchers speculate that venous insufficiency or hypertension caused by cephalad fluid shifts during spaceflight are possible mechanisms for the VIIP syndrome in astronauts. Similarly, the pathophysiology of IIH is thought to be related to decreased CSF absorption at the arachnoid villi possibly due to venous-outflow obstruction. However, there are important clinical differences between the VIIP syndrome and IIH. In the VIIP syndrome, none of the astronauts with ocular changes presented with clinical symptoms typical of IIH, including chronic headaches, diplopia, or transient visual obscurations.[1] Moreover, while IIH is typically a syndrome of female patients with obesity,[14] VIIP is more common in male astronauts.[1]

Similarly, in our study of structural brain changes associated with long-term bed rest, we found important structural differences in our subjects from those previously described in patients with IIH. For example, in a volumetric MR imaging study of patients with IIH,[15] a significant increase in extraventricular CSF volume was found, particularly along the vertex. Following bed rest, we found instead effacement of the extraventricular CSF spaces along the vertex and crowding of adjacent brain tissue, including the frontoparietal lobes. Other investigators have suggested an overlap in findings between patients with IIH and those with Chiari I malformation, with an incidence of 10%–21% of cerebellar tonsillar ectopia of >5 mm in patients with IIH.[16] In our study of subjects with bed rest, we demonstrated the opposite finding: a shift of the brain tissue upward in the skull with decreased crowding at the foramen magnum. If the head-down tilt bed rest model is an appropriate analog for the intracranial changes experienced by astronauts, then the Earth-based IIH syndrome may not be an appropriate model for VIIP syndrome. A volumetric analysis of the structural brain imaging data of astronauts would be informative in this respect.

Unrelated to VIIP symptoms and CSF homeostasis, morphologic changes were observed affecting widespread regions of the brain, with the frontal and parietal lobes (areas of the brain associated with sensorimotor and high-level cognitive functions) demonstrating the most prominent changes. The consequences of structural changes affecting functional brain areas is unknown but may be crucial given the involvement of these areas in adaptation to microgravity. For example, optimal performance in the microgravity environment requires re-interpretation of sensory input from peripheral receptors.[17] Because the lower extremities are used less for locomotion, new sensorimotor strategies emerge in spaceflight, requiring plasticity at higher cortical levels, including the sensorimotor cortices.[17] Disturbances in perceptual-motor task performance have been found during spaceflight, particularly while astronauts simultaneously engage in secondary

cognitive tasks.[17] These findings warrant further investigation, including planned and ongoing functional brain imaging studies of astronauts following long-term spaceflight.

Our study has several limitations. Definite conclusions concerning the VIIP syndrome cannot be made because this study was performed in subjects with bed rest and not the astronaut population. Most important, the MR imaging protocol was not initially designed to address structural changes in bed rest, and volumetric analysis was only undertaken much later after experiment completion to address the recent interest in intracranial adaptation to spaceflight. Therefore, the MR imaging protocol was not optimized for structural analysis with no datasets from control subjects to demonstrate between-session reproducibility. However, other investigators have demonstrated that volumes derived from automated segmentation of T1-weighted structural images are reliable measures when performed on the same scanner platform, finding the variability in volume across sessions to be <2.3% for subjects of a similar age group as in our study.[18] The influence of sex hormones and the menstrual cycle may also play a role in the structural brain changes seen in bed rest. Although, data concerning sex hormones were not available, the 3 female subjects in this study were admitted to bed rest in a standardized fashion related to the time of menses. Furthermore, no significant correlation was found between volumetric changes and sex, at odds with the male predominance in VIIP syndrome and the female predominance of IIH.

CONCLUSIONS

The consequences of long-term microgravity exposure on the brain are poorly understood but may include alterations in brain structure, vasculature, and function, leading to the VIIP syndrome experienced by some astronauts. In this study, we used long-term bed rest as an analog for spaceflight, to study structural changes of the human brain. Our results indicate that the brain as a whole can move within the skull in response to gravity changes, and in the head-down tilt bed rest model, the brain moved upward and rotated posteriorly in relation to the skull. There was a significant correlation between brain movement and changes in ventricular volume, suggesting altered CSF homeostasis and a possible explanation for the constellation of VIIP symptoms. Unrelated to the VIIP syndrome, widespread morphologic changes of the brain were observed as a result of brain tissue redistribution in response to gravity changes. These locally occurring morphologic changes may lead to possible brain function changes. For example, the frontal and parietal lobes were most affected, which could affect sensorimotor and high-level cognitive functions. Ultimately, to elucidate any structural changes that may play a role in VIIP syndrome, a volumetric analysis of the structural scans of astronauts before and following long-duration spaceflight is needed. The findings of this study may also be relevant to Earth-based, chronically ill patients who are confined to long-term bed rest.

ACKNOWLEDGMENTS

The authors wish to thank Dr Satish Mehta for providing cortisol data. Other physiological data was obtained from the NASA Life Sciences Data Archive.

Disclosures: Donna R. Roberts—*RELATED*: *Grant:* NASA*; *Support for Travel to Meetings for the Study or Other Purposes:* NASA; *UNRELATED*: *Grants/Grants Pending*: NASA, *Comments*: I am currently the Principal Investigator of a NASA grant separate from the one that funded the research described in the article. Edward W. Duffy—*RELATED*: *Grant*: Palmetto Academy. David A. Ramsey—*RELATED*: *Grant*: NASA,* *Comments*: NASA funded the study at MUSC who subcontracted my employer at the time (SCRA); *Support for Travel to Meetings for the Study or Other Purposes*: NASA,* *Comments*: As above. Truman R. Brown—*UNRELATED*: *Grants/Grants Pending*: NASA,* *Comments*: grant to study possible brain shifts after space flight. *Money paid to the institution.

REFERENCES

1. Mader TH, Gibson CR, Pass AF, et al. **Optic disc edema, globe flattening, choroidal folds, and hyperopic shifts observed in astronauts after long-duration space flight.** *Ophthalmology* 2011;118:2058–69
2. Meck JV, Dreyer SA, Warren LE. **Long-duration head-down bed rest: project overview, vital signs, and fluid balance.** *Aviat Space Environ Med* 2009;80(5 suppl):A1–8
3. Pavy-Le Traon A, Heer M, Narici MV, et al. **From space to Earth: advances in human physiology from 20 years of bed rest studies (1986–2006).** *Eur J Appl Physiol* 2007;101:143–94
4. Roberts DR, Ramsey D, Johnson K, et al. **Cerebral cortex plasticity after 90 days of bed rest: data from TMS and fMRI.** *Aviat Space Environ Med* 2010;81:30–40
5. Crucian BE, Stowe RP, Mehta SK, et al. **Immune status, latent viral reactivation, and stress during long-duration head-down bed rest.** *Aviat Space Environ Med* 2009;80:A37–44
6. Platts SH, Martin DS, Stenger MB, et al. **Cardiovascular adaptations to long-duration head-down bed rest.** *Aviat Space Environ Med* 2009;80:A29–36
7. Keihaninejad S, Heckemann RA, Fagiolo G, et al; Alzheimer's Disease Neuroimaging Initiative. **A robust method to estimate the intracranial volume across MRI field strengths (1.5T and 3T).** *Neuroimage* 2010;50:1427–37
8. Eritaia J, Wood SJ, Stuart GW, et al. **An optimized method for estimating intracranial volume from magnetic resonance images.** *Magn Reson Med* 2000;44:973–77
9. Fischl B, Salat DH, Busa E, et al. **Whole brain segmentation: automated labeling of neuroanatomical structures in the human brain.** *Neuron* 2002;33:341–55
10. Alperin N, Lee SH, Sivaramakrishnan A, et al. **Quantifying the effect of posture on intracranial physiology in humans by MRI flow studies.** *J Magn Reson Imaging* 2005;22:591–96
11. Frisoni GB, Fox NC, Jack CR Jr, et al. **The clinical use of structural MRI in Alzheimer disease**. *Nat Rev Neurol* 2010;6:67–77
12. Streitbürger DP, Möller HE, Tittgemeyer M, et al. **Investigating structural brain changes of dehydration using voxel-based morphometry.** *PLoS One* 2012;7:e44195
13. Kramer LA, Sargsyan AE, Hasan KM, et al. **Orbital and intracranial effects of microgravity: findings at 3-T MR imaging.** *Radiology* 2012;263:819–27
14. Degnan AJ, Levy LM. **Pseudotumor cerebri: brief review of clinical syndrome and imaging findings.** *AJNR Am J Neuroradiol* 2011;32:1986–93
15. Alperin N, Ranganathan S, Bagci AM, et al. **MRI evidence of impaired CSF homeostasis in obesity-associated idiopathic intracranial hypertension.** *AJNR Am J Neuroradiol* 2013;34:29–34
16. Aiken AH, Hoots JA, Saindane AM, et al. **Incidence of cerebellar tonsillar ectopia in idiopathic intracranial hypertension: a mimic of the Chiari I malformation.** *AJNR Am J Neuroradiol* 2012;33:1901–06
17. Clement G, Reschke MF. *Neuroscience in Space*. New York: Springer-Verlag; 2008
18. Jovicich J, Czanner S, Han X, et al. **MRI-derived measurements of human subcortical, ventricular and intracranial brain volumes: reliability effects of scan sessions, acquisition sequences, data analyses, scanner upgrade, scanner vendors and field strengths.** *Neuroimage* 2009;46:177–92

Whole-Brain *N*-Acetylaspartate Concentration Is Preserved during Mild Hypercapnia Challenge

S. Chawla, Y. Ge, H. Lu, O. Marshall, M.S. Davitz, G. Fatterpekar, B.J. Soher, and O. Gonen

ABSTRACT

BACKGROUND AND PURPOSE: Although NAA is often used as a marker of neuronal health and integrity in neurologic disorders, its normal response to physiologic challenge is not well-established and its changes are almost always attributed exclusively to brain pathology. The purpose of this study was to test the hypothesis that the neuronal cell marker NAA, often used to assess neuronal health and integrity in neurologic disorders, is not confounded by (possibly transient) physiologic changes. Therefore, its decline, when observed by using ^{1}H-MR spectroscopy, can almost always be attributed exclusively to brain pathology.

MATERIALS AND METHODS: Twelve healthy young male adults underwent a transient hypercapnia challenge (breathing 5% CO_2 air mixture), a potent vasodilator known to cause a substantial increase in CBF and venous oxygenation. We evaluated their whole-brain NAA by using nonlocalizing proton MR spectroscopy, venous oxygenation with T2-relaxation under spin-tagging MR imaging, CBF with pseudo-continuous arterial spin-labeling, and the cerebral metabolic rate of oxygen, during normocapnia (breathing room air) and hypercapnia.

RESULTS: There was insignificant whole-brain NAA change ($P = .88$) from normocapnia to hypercapnia and back to normocapnia in this cohort, as opposed to highly significant increases: 28.0 ± 10.3% in venous oxygenation and 49.7 ± 16.6% in global CBF ($P < 10^{-4}$); and a 6.4 ± 10.9% decrease in the global cerebral metabolic rate of oxygen ($P = .04$).

CONCLUSIONS: Stable whole-brain NAA during normocapnia and hypercapnia, despite significant global CBF and cerebral metabolic rate of oxygen changes, supports the hypothesis that global NAA changes are insensitive to transient physiology. Therefore, when observed, they most likely reflect underlying pathology resulting from neuronal cell integrity/viability changes, instead of a response to physiologic changes.

ABBREVIATIONS: $CMRO_2$ = cerebral metabolic rate of oxygen consumption; pCASL = pseudocontinuous arterial spin-labeling; TRUST = T2-relaxation under spin-tagging; WBNAA = whole-brain NAA; Yv = venous oxygenation

Proton MR spectroscopy (^{1}H-MR spectroscopy) allows noninvasive quantitative in vivo assessment of brain metabolites.[1,2] The most prominent metabolite in water-suppressed ^{1}H-MR spectroscopy is the amino acid derivative NAA, synthesized in neuronal mitochondria from acetyl coenzyme A and L-aspartate by a membrane-bound enzyme.[3] Although its precise function is still not fully known, possible roles include lipogenesis in myelination, ion balance, neuromodulation, and neuronal mitochondria energy metabolism.[4] Because it is almost exclusive to neurons and their processes (<10% contribution from glia and extracellular fluid),[5] NAA is considered a putative marker of their integrity.[4,6] Indeed, with the exception of Canavan disease,[7] nearly all brain pathologies show local or global NAA decline due to degeneration or metabolic impairment.[2,6,8]

Use of NAA as a marker of neuronal health, however, involves 2 implicit assumptions: 1) its concentration is insensitive to (possible) transient physiologic changes of normal physiologic fluctuation; and 2) detectable changes must, therefore, reflect only un-

Received February 10, 2015; accepted after revision April 1.

From the Department of Radiology (S.C., Y.G., O.M., M.S.D., G.F., O.G.), Center for Advanced Imaging Innovation and Research and Bernard and Irene Schwartz Center for Biomedical Imaging, New York University School of Medicine, New York, New York; The Russell H. Morgan Department of Radiology and Radiological Science (H.L.), Johns Hopkins University School of Medicine, Baltimore, Maryland; and Department of Radiology (B.J.S.), Center for Advanced MR Development, Duke University Medical Center, Durham, North Carolina.

This work was supported by National Institutes of Health grants NS076588, NS029029-S1, MH084021, NS067015, AG042753, EB01015 and EB008387 and by the Center for Advanced Imaging Innovation and Research (www.cai2r.net), a National Institute of Biomedical Imaging and Bioengineering Biomedical Technology Resource Center: P41 EB017183.

Please address correspondence to Yulin Ge, MD, and Oded Gonen, PhD, Department of Radiology, Center for Advanced Imaging Innovation and Research and Bernard and Irene Schwartz Center for Biomedical Imaging, NY University School of Medicine, 660 First Ave, 4th floor, NY, NY 10016; e-mail: yulin.ge@nyumc.org; oded.gonen@nyumc.org

Indicates open access to non-subscribers at www.ajnr.org

http://dx.doi.org/10.3174/ajnr.A4424

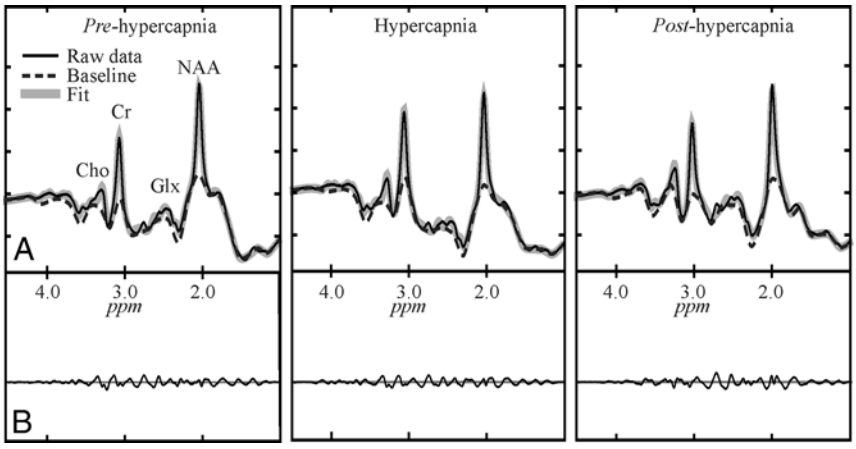

FIG 1. Automated spectral fitting of the pre- (*left*), during- (*center*), and posthypercapnia (*right*) WBNAA from 1 subject, all on the same intensity and chemical shift (parts per million [ppm]) scales. *Top, A,* Whole-head ^{1}H-spectrum (*thin black line*), estimated baseline (*dashed line*), and fitted (metabolites + baseline) estimate (*thick gray line*). *Bottom*: *B*, Residual signals (raw-fitted data). Note: 1) The similarity of the pre-, during, and posthypercapnia spectra, suggesting a minimal effect of this physiologic challenge on the brain NAA; 2) the quality of the fit on *A*; and 3) the consequent vanishing residuals in *B*; and 4) although other metabolites are also visible in the spectrum, only NAA is implicitly localized by its biochemistry to just the brain.

derlying pathology. Although stable NAA levels are reported in response to aerobic exercise,[9] verbal memory performance,[10] and caffeine ingestion[11] and alcohol consumption in healthy humans,[12] and prolonged hypoglycemia in the rat brain,[13] these 2 assumptions are made for expediency because little is known of the response of NAA to other physiologic challenges.[6,14]

Given its utility as a neuronal marker, our goal in the present study was to test the hypothesis that the global NAA concentration remains stable even under a substantial physiologic challenge that leads to otherwise easily detectable changes in other MR imaging metrics. We chose the mild hypercapnia paradigm (5% CO_2 by volume in inspired air) to test it for 5 reasons: First, it is a potent vasodilator, known to cause a dramatic, easily measurable 20%–50% increase in CBF.[15,16] Second, it has quick (~1 minute) onset and washout, making both states accessible within 1 MR imaging session. Third, its blood level can be reliably and instantly monitored by capnography. Fourth, animal studies have shown that NAA synthesis can be disrupted when O_2 consumption and adenosine triphosphate production are decreased by inhibitors of the mitochondrial respiratory chain.[17] Finally, it is also clinically and practically relevant for NAA quantification because patients with neurologic conditions often have irregular respiratory patterns during scans, which may lead to higher blood partial arterial CO_2 pressure.

To test the hypothesis and to quantify the hereto unknown effects of hypercapnia on NAA, we used whole-brain NAA (WBNAA) nonlocalizing ^{1}H-MR spectroscopy[18,19] and compared its changes with those observed with other MR imaging modalities: T2-relaxation under spin-tagging (TRUST) and pseudocontinuous arterial spin-labeling (pCASL) perfusion MR imaging, to quantify variations in venous oxygenation (Yv), CBF, and the cerebral metabolic rate of oxygen consumption ($CMRO_2$) in normocapnia (breathing room air) and during transient hypercapnia in healthy young adults.

MATERIALS AND METHODS

Participants

Twelve healthy young men (30.5 ± 9.2 years of age; range, 23–48 years) were prospectively enrolled in this study. Only young men were chosen to remove possible age and sex effects on the acquired metrics. None were smokers or had a history of asthma or neurologic or psychological disorders before the scan, and all had "unremarkable MR imaging" findings determined by a neuroradiologist afterward. All were also instructed to not drink coffee for 6 hours before the study. All participants provided institutional review board–approved written informed consent.

^{1}H-MR Spectroscopy WBNAA

The WBNAA ^{1}H-MR spectroscopy was acquired in a 3T whole-body MR imaging scanner (Tim Trio; Siemens, Erlangen, Germany) by using a circularly polarized transmit-receive head coil (TEM3000; MR Instruments, Minneapolis, Minnesota). After optimizing the magnetic field over the whole head with our proton chemical shift imaging–based automatic procedure,[20] we obtained the WBNAA with a nonlocalizing nonecho ^{1}H-MR spectroscopy sequence[18,19]: TR/TE/TI = 10000/5/940 ms, 16 averages, 90° flip angle, ±1 KHz acquisition bandwidth. The use of TR≫T1 and TE≈0 ensured insensitivity to (unknown) T1 and T2 variations, and whole-head volume of interest facilitates both a short, 2 minutes and 40 seconds, acquisition and an excellent signal-to-noise ratio, as seen in Fig 1.

MR Imaging Methods

All MR imaging examinations were performed in the same scanner by using a 12-channel array head coil. Clinical standard T1-weighted high-resolution (1 mm^3) 3D-MPRAGE and T2-weighted MR imaging were performed on every subject to exclude brain abnormalities. Subsequently, 2 advanced quantitative MR imaging sequences, TRUST and pCASL, were applied to estimate global Yv and CBF, from which the $CMRO_2$ was obtained.

TRUST uses spin-labeling to isolate pure venous blood signals and measures T2 value, which is converted to an O_2 saturation fraction (Yv) with a calibration plot.[21] TRUST MR imaging was performed with single-section EPI intersecting the lower superior sagittal sinus. Because this sinus drains most of the cerebrum, TRUST-obtained Yv is essentially a global metric. Acquisition parameters were 3.6 × 3.6 × 5 mm^3 voxels; TR = 8000 ms; TI = 1200 ms; 10-ms Carr Purcell Meiboom Gill sequence; 4 effective TEs = 0, 40, 80, and 160 ms; and 4:48-minute total acquisition time. The labeling slab was 50-mm-thick with a 25-mm gap between it and the imaging section.

CBF was obtained with perfusion imaging, by using the multisection pseudocontinuous arterial spin-labeling sequence covering the entire brain. This sequence was recently recommended by a white paper for clinical perfusion MR imaging.[22] It is based

on a single-shot gradient-echo EPI: TR/TE = 3900/17 ms; labeling duration = 1470 ms; postlabeling delay = 1230 ms; section thickness = 5 mm; 24 axial sections; 22 × 22 cm^2 FOV; 64 × 64 matrix (3.4 × 3.4 × 5 mm^3 voxels); integrated parallel acquisition technique factor of 2 and 52 measurements (26 pairs of label and control images) for a 3 minute and 35 second acquisition time. Arterial spin-labeling was performed 97 mm below the center-of-imaging volume approximately perpendicular to the internal carotid and vertebral arteries.

EXPERIMENTAL PROCEDURES

The participants underwent WBNAA, TRUST, and pCASL MR imaging under normocapnia and hypercapnia (5% CO_2, 21% O_2, and 74% N_2 mixture from a Douglas bag). Each was fitted with a nose clip, and the gas from each of the 2 sources was delivered through a 2-way nonrebreathing valve and mouthpiece combination (2600 series; Hans Rudolph, Shawnee, Kansas). Their end-tidal CO_2 values, the CO_2 concentration levels in the lung that approximate those in arterial blood (ie, partial arterial CO_2 pressure), were recorded throughout the experiment at 2-second intervals with an MR imaging–compatible 9500 Multigas Monitor (Medrad, Indianola, Pennsylvania). The averaged end-tidal CO_2 during each room air and hypercapnia scan was then calculated and reported.

The experimental paradigm comprised ^{1}H-MR spectroscopy WBNAA (2:40 minutes), pCASL (3:35 minutes), and TRUST (4:48 minutes) during normocapnia then hypercapnia and additional posthypercapnia normocapnia for WBNAA only, to test whether hypercapnia-induced WBNAA change, if present, recovers. The time interval needed to reach a new steady-state after switching the gas from one condition to another was monitored in each subject and usually took less <1 minute.

Data Processing and Analyses

WBNAA. Data processing and spectral fitting were performed by using the VeSPA software package (https://scion.duhs.duke.edu/vespa/project).[23] The VeSPA-Analysis application was extracted from the ^{1}H-MR spectroscopy data from the MR imaging scanner file format and applied a standard set of preset processing and spectral fitting parameters: Even time-signals were subtracted from the odd ones, the pairs were summed, and the spectral data were fitted parametrically by using the automated algorithm described previously.[19,24,25] The metabolite basis set for the parametric fit (synthesized with the VeSPA-Simulation application by using the radiofrequency pulses and timings from the actual WBNAA sequence) included the total-NAA (NAA + NAA-glutamate at a 7:1 ratio), glutamate, glutamine, total Cho, total Cr, and mIns. The latter 5 were included in the parametric model as known "nuisance signals" to simplify the use of wavelet filtering to account for nonparametric residual baseline signals. The inter- and intrasubject WBNAA signal area variability with this approach is ±12% and ±7%.[19] Because only within-subject changes from normocapnia to hypercapnia were sought for comparison, only percentage variations in WBNAA levels are reported in this study.

pCASL. The difference between the label and control images was calculated, and the CBF map produced normocapnia and hypercapnia by using a previously described perfusion kinetic model[22,26]:

$$1)\quad \mathrm{CBF(ml/100\ g/minute)} = \frac{60 \times 100 \times \Delta M \times \lambda}{2\alpha \times M_0 \times \mathrm{T}_1 \times (\mathrm{e}^{-w/T_1} - \mathrm{e}^{-(w+\tau)/T_1})},$$

where ΔM is the difference signal between control and labeling states; $\lambda = 0.9$ mL/g is the blood/tissue water partition coefficient; $\alpha = 0.86$ is the labeling efficiency of pCASL at 3T[22,26]; M_0 is the equilibrium magnetization of brain tissue during the nonlabeled condition, after accounting for blood T1 (1600 ms) at 3T[27]; w is the postlabeling delay, which is different for individual sections (1.23-second + section acquisition delay)[27]; and τ is the labeling duration (1.47 seconds in our data). To obtain the average CBF map for each breathing condition, we transformed each individual's images into the Montreal Neurological Institute template of 152 space-masking brain-only regions and spatially smoothed them by using a Gaussian kernel (8-mm full width at half maximum). GM CBF values were computed by overlaying the tissue mask (defined as 70% probability of being GM) on the normalized CBF maps. Global CBF was also computed by overlaying the whole-brain mask, excluding the CSF, on the normalized CBF maps, and it was obtained an averaged CBF over all sections including both GM and WM.

TRUST and $CMRO_2$. For Yv estimates, the TRUST data were processed by using in-house Matlab (MathWorks, Natick, Massachusetts) scripts based on a previously described algorithm.[21] Briefly, these images were motion-corrected and pair-wise subtracted (control-labeled images), resulting in a pure blood signal in the lower superior sagittal sinus. The averaged venous blood signal for each effective TE was fitted to a monoexponential model to obtain a blood T2, which was converted to Yv via a calibration plot established with in vitro blood by using subject-specific hematocrit values. $CMRO_2$ (micromole O_2/100 g tissue/minute) was then estimated by using the Kety-Schmidt method,[28]

$$2)\qquad \mathrm{CMRO_2} = CBF \times (Ya - Yv) \times Ca,$$

where CBF is expressed in milliliters/100 g/minute and is obtained from the pCASL data; Ya is the percentage of arterial oxygenation obtained by using finger pulse oximetry; and Ca the amount of oxygen a unit volume of blood can carry, assumed to be 856.2 μmol/100 mL. Note that because CBF and Yv are global metrics, so is the $CMRO_2$ from either the GM or whole brain.

Statistical Analyses

Kolmogorov-Smirnov tests were used to determine data distributions. Paired-samples t tests were performed to look for differences between hypercapnia and normocapnia in WBNAA, Yv, global CBF, GM CBF, global $CMRO_2$, and GM $CMRO_2$. $P < .05$ was considered significant. All analyses were performed with SPSS for Windows, Version 15.0 (IBM, Armonk, New York).

RESULTS

The end-tidal CO_2 and MR imaging/MR spectroscopy metrics for normocapnia and hypercapnia and their comparisons are sum-

Summary of $ETCO_2$ and MRI metrics (mean) for normocapnia and hypercapnia

MRI/MRS and Measures	Normocapnia	Hypercapnia	*P* Value
^{1}H-MRS[a]			
$ETCO_2$ (mm Hg)	44.40 ± 4.1	52.9 ± 2.4	$<10^{-4}$
WBNAA (arb. unit)	177.9 ± 40.5	178.8 ± 32.3	.88
pCASL MRI			
$ETCO_2$ (mm Hg)	40.6 ± 4.9	49.4 ± 3.9	$<10^{-4}$
CBF (mL/100 g/min)	33.9 ± 6.3	50.2 ± 6.9	$<10^{-4}$
TRUST MRI			
$ETCO_2$ (mm Hg)	43.3 ± 4.7	52.5 ± 2.9	$<10^{-4}$
Yv (%)	56.4 ± 5.6	71.9 ± 4.8	$<10^{-4}$
TRUST and pCASL			
$CMRO_2$ (μmol/100 g/min)	120.0 ± 23.9	111.2 ± 18.9	.04

Note:—Arb. indicates arbitrary; $ETCO_2$, end-tidal carbon dioxide.

[a] WBNAA values measured with ^{1}H-MRS of the posthypercapnic condition (the second normocapnia) are listed in the main text.

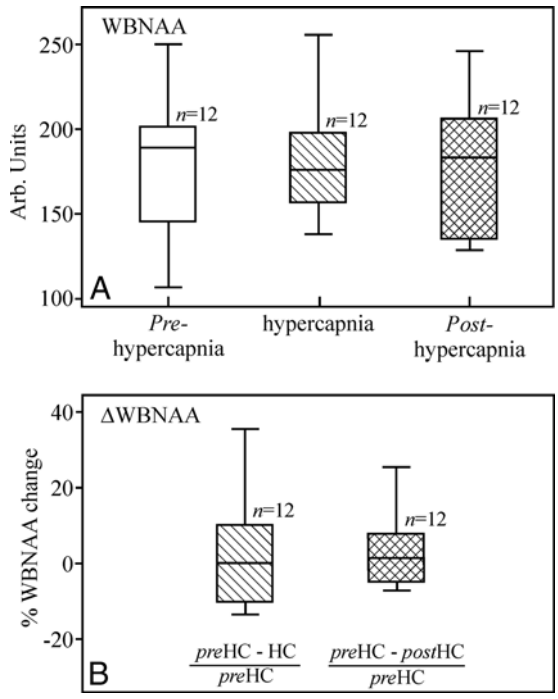

FIG 2. *A*, Boxplots showing the first, second (median), and third quartiles (*box*) and ±95% (*whiskers*) of the WBNAA distributions at normocapnia (white), hypercapnia (*hatched*), and posthypercapnia (*cross-hatched*). Note the insignificant WBNAA changes ($P = .676$). *B*, Boxplots show the percentage of NAA change from baseline normocapnia distribution of the 12 subjects. Note the ~0% change from normocapnia (preHC) to hypercapnia (HC) (*hatched*) and from the former to the posthypercapnia (postHC) normocapnia (*cross-hatched*), underscoring the negligible NAA change as a response to the physiologic CO_2 challenge. Arb indicates arbitrary.

marized in the Table. As expected, the end-tidal CO_2 increased significantly from normocapnia to hypercapnia: 44.4 ± 4.1 to 52.9 ± 2.4 mm Hg for WBNAA, 40.6 ± 4.9 to 49.4 ± 3.9 mm Hg for pCASL, and 43.3 ± 4.7 to 52.5 ± 2.9 mm Hg for TRUST ($P < 10^{-4}$ for all). The average range of end-tidal CO_2 changes during the 3 scans was tight: between 8 and 9 mm Hg.

WBNAA

Our automatic shimming yielded a 27 ± 4 Hz whole-head water line width in <5 minutes. Sample whole-head ^{1}H-MR spectroscopy during normocapnia, hypercapnia, and subsequent normocapnia are shown in Fig 1, and their distribution for all 12 subjects is shown in Fig 2*A*. On the basis of paired-samples *t* tests, there were insignificant 2.7 ± 15.1% changes from normocapnia to hypercapnia and 0.6 ± 18.2% from pre- to posthypercapnia normocapnia ($P = .88$), as shown in Fig 2*B*.

pCASL

The average global CBF maps during normocapnia and hypercapnia from all 12 subjects are shown in Fig 3. There was a highly significant 49.7 ± 16.6% increase in global CBF from 33.9 ± 6.3 mL/100 g/min in normocapnia to 50.2 ± 6.9 mL/100 g/min in hypercapnia ($P < 10^{-4}$), as shown in Fig 4*A*. Similarly, GM CBF increased a significant 40.0% from 45.3 ± 7.4 mL/100 g/min at normocapnia to 63.0 ± 8.6 mL/100 g/min at hypercapnia ($P < 10^{-4}$).

TRUST and $CMRO_2$

The lower superior sagittal sinus blood T2 increased from 54.6 ± 8.9 ms at normocapnia to 85.0 ± 11.8 ms at hypercapnia, and the corresponding Yv increased from 56.4 ± 5.6% to 71.9 ± 4.8% ($P < 10^{-4}$ for both). The global $CMRO_2$ declined a significant 6.4 ± 10.9%: from 120.0 ± 23.9 μmol/100 g/min at normocapnia to 111.2 ± 18.9 μmol/100 g/min at hypercapnia ($P = .04$), as shown in Fig 4*B*. GM $CMRO_2$ also decreased a significant 11.3 ± 11.6%, from 162.2 ± 40.1 μmol/100 g/min at normocapnia to 141.2 ± 24.7 μmol/100 g/min at hypercapnia ($P = .01$).

DISCUSSION

The findings substantiate the hypothesis that WBNAA is insensitive to a physiologic challenge that otherwise leads to significant variations in Yv, CBF, and $CMRO_2$. This finding suggests that neurons tolerate hypercapnia with unaltered structural or functional integrity. Consequently, blood partial arterial CO_2 pressure fluctuations (eg, due to irregular respiratory patterns during ^{1}H-MR spectroscopy scans) will likely have minimal effect on the NAA concentrations. Insensitivity to such an intense challenge suggests that NAA changes, when observed, most likely represent disease pathology and not physiology.

Hypercapnia is increasingly used to study cerebrovascular reactivity in clinical populations,[29,30] as well as to calibrate blood oxygen level–dependent signal.[31] Its well-known effect is a remarkable vasodilation leading to substantial CBF increase. Although the precise vasodilatory mechanism of CO_2 in humans is not well-known, it is believed that it activates potassium–adenosine triphosphate channels in vascular smooth muscle, causing dilation.[32] However, the effect of CO_2 inhalation on neural activity

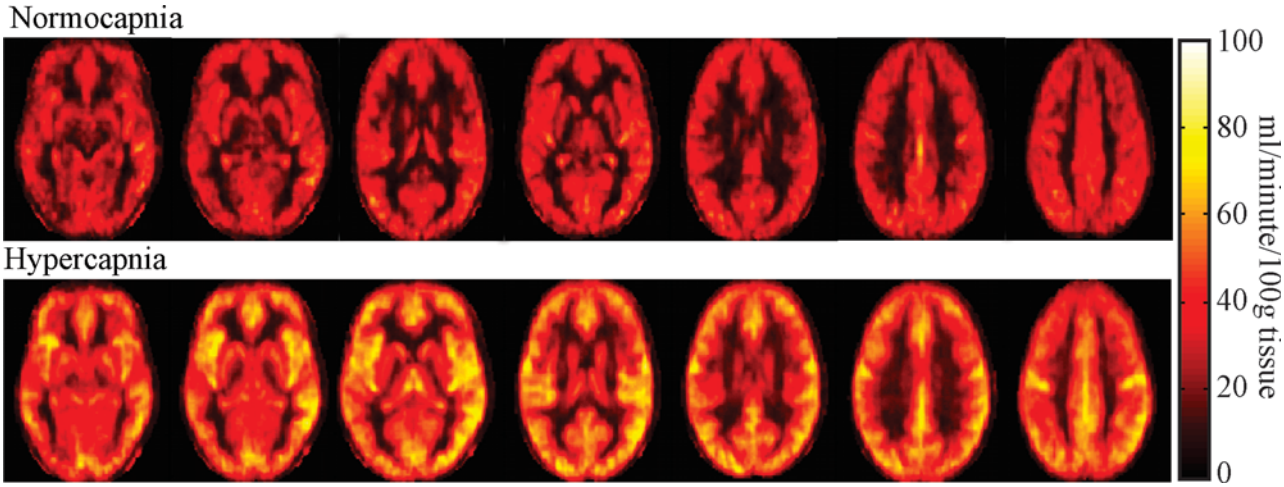

FIG 3. Average ($n = 12$) global CBF maps for 7 representative brain sections. Note the easily visible, ~50% increase ($P < 10^{-4}$) in CBF from normocapnia to hypercapnia.

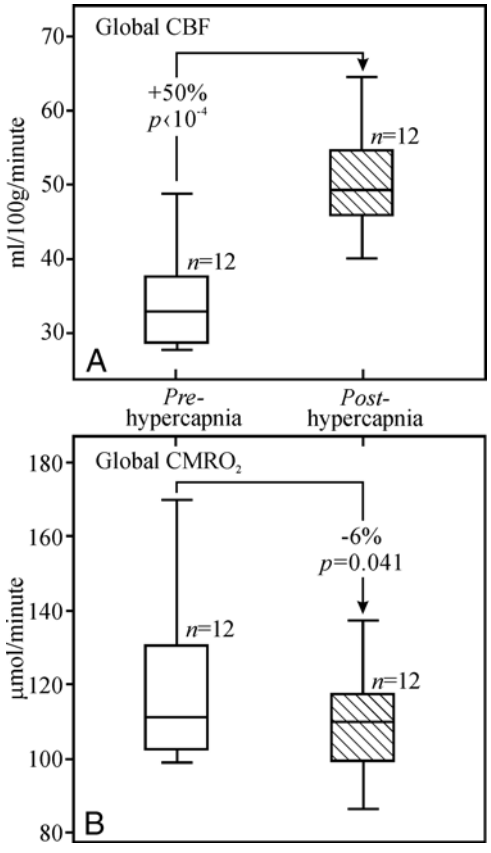

FIG 4. Boxplots of the distributions of global CBF (*A*) and $CMRO_2$ (*B*) at normocapnia (white) and hypercapnia (*hatched*). Note the significant ($P < 10^{-4}$) ~47% increases in global CBF and the 6.4% ($P = .04$) decrease in global $CMRO_2$ from normocapnia to hypercapnia.

or $CMRO_2$ is unclear, and its results are controversial. Earlier studies showed constant $CMRO_2$ at hypercapnia,[28] whereas others found that it decreased,[33,34] as in this study, or even increased.[35] These findings may be due to different methodologies (eg, strength and duration of CO_2 stimulus), use of anesthetic agents, and species studied. The large increase in CBF with mild reduction in $CMRO_2$ under hypercapnia observed here suggests uncoupling of these metrics due to increased partial pressure of carbon dioxide acting primarily on adenosine receptors to dilate blood vessels.

It is nevertheless intriguing why, despite significant CBF increase and likely neuronal activity ($CMRO_2$) decline, NAA levels remains constant, because it is known that under normal conditions, brain NAA level fluctuations are expected to link neuronal-to-mitochondrial activity.[3] Indeed, animal studies have shown that NAA synthesis can be disrupted when O_2 consumption and adenosine triphosphate production are decreased by inhibitors of the mitochondrial respiratory chain,[17] and a marked reduction in mitochondrial respiratory activities was observed in rodents exposed to intermittent hypoxia/hypercapnia for several days.[36] Together, these studies support the notion that relatively severe prolonged hypercapnia may have a detrimental effect on neuronal metabolism, leading to cell death, whereas in this study, the challenge was mild and its duration was short.

The above conjecture is also supported by the observed lack of NAA changes in the few other ^{1}H-MR spectroscopy studies involving short physiologic challenges (eg, in response to aerobic exercise,[9] verbal memory performance,[10] and caffeine ingestion[11] in healthy humans, and alcohol consumption[12] and prolonged hypoglycemia in the rat brain[13]) consistent with neuronal and mitochondrial integrity preservation. Furthermore, because NAA accounts only for a very small fraction, <0.05%, of the overall glucose metabolism, and its turnover rate is slow,[8] its concentration is also unaffected by extended hypoglycemia.[13] These findings lend further support to the notion that NAA is not an energy-buffering store (hence, requiring quick response) for neuronal activity in normal tasks.[13] At lower partial arterial CO_2 pressure, a recent study found that induced acidosis plays a role in maintaining mitochondrial function, regulating its metabolic pathway to preserve adenosine triphosphate production.[37] We believe that a relatively slower adaptive NAA metabolism may account for its preserved level despite a $CMRO_2$ decrease, suggesting that NAA is a cellular integrity index, (ie, sensitive to the number of neurons per unit volume and their overall viability), while $CMRO_2$ is a flux measure (ie, sensitive to instantaneous physiologic changes).

In the current study, we used WBNAA to assess the global variation in NAA during hypercapnia because of the global effect

of CO_2, which can be detected more reliably than single- or multivoxel MR spectroscopy methods, in particular when such an effect on NAA change is considered consistent among different regions. Our Yv and $CMRO_2$ measures are also global indices, by which WBNAA results are expected to be more comparable with $CMRO_2$ changes at the similar global level. Because most of the neurodegenerative diseases such as Alzheimer disease, amyotrophic lateral sclerosis, multiple sclerosis, and frontotemporal dementia are widespread in nature and involve more extended regions than previously understood, it is also more sensible to assess global variation in NAA levels following a physiologic challenge. Using a single-voxel technique, previous studies have reported no significant regional NAA change with other physiologic challenges, which is consistent with our whole-brain NAA findings.[9-12]

Admittedly, this study also has several limitations: First, the hypercapnia challenge lasted only several minutes. However, it is known that acute challenges (eg, partial hypoxia in stroke,[38]) may lead to NAA decline in a matter of minutes, suggesting that the duration of our paradigm may be appropriate to affect a change if there was one. Higher than normal partial arterial CO_2 pressure is common in subjects with chronic respiratory disorders, which may exist as comorbidities in patients with neurologic disorders during ^{1}H-MR spectroscopy. Our study, by its design, excludes the effect on brain NAA from both prolonged hypoxia and elevated partial arterial CO_2 pressure. Second, we restricted our study to young adult men, to remove (possible) age and sex differences in the metrics compared. However, the WBNAA insensitivity to hypercapnia in this cohort suggests that similar findings are expected in a more age- and sex-diverse group. Third, the whole-brain CBF values are slightly lower than those commonly reported because WM CBF is usually underestimated with arterial spin-labeling sequences. Because this study compared CBF between the 2 breathing conditions within a subject, however, its underestimation is expected to be similar between them.

CONCLUSIONS

Our study suggests that the NAA concentration is insensitive to even intensive transient physiologic challenges absent underlying pathology that affects the integrity or viability of these cells, meeting the requirement of a marker of neuronal cell integrity. The finding with this specific challenge paradigm is particularly germane to better understanding of NAA changes, specifically to NAA quantification when the subjects have an irregular breathing pattern during ^{1}H-MRS acquisition, in which elevated partial arterial CO_2 pressure can be seen.

Disclosures: Yulin Ge—*RELATED*: *Grant*: National Institutes of Health,* *Comments*: This work was supported by National Institutes of Health grants NS076588, NS029029-S1, MH084021, NS067015, AG042753, EB01015, and EB008387 and by the Center for Advanced Imaging Innovation and Research (www.cai2r.net), a National Institute of Biomedical Imaging and Bioengineering Biomedical Technology Resource Center: P41 EB017183. *Money paid to the institution.

REFERENCES

1. Oz G, Alger JR, Barker PB, et al; MRS Consensus Group. **Clinical proton MR spectroscopy in central nervous system disorders.** *Radiology* 2014;270:658–79 CrossRef Medline
2. Mountford CE, Stanwell P, Lin A, et al. **Neurospectroscopy: the past, present and future.** *Chem Rev* 2010;110:3060–86 CrossRef Medline
3. Moffett JR, Ross B, Arun P, et al. **N-Acetylaspartate in the CNS: from neurodiagnostics to neurobiology.** *Prog Neurobiol* 2007;81:89–131 CrossRef Medline
4. Baslow MH. **N-acetylaspartate in the vertebrate brain: metabolism and function.** *Neurochem Res* 2003;28:941–53 CrossRef Medline
5. Taylor DL, Davies SE, Obrenovitch TP, et al. **Extracellular N-acetylaspartate in the rat brain: in vivo determination of basal levels and changes evoked by high K+.** *J Neurochem* 1994;62:2349–55 Medline
6. Benarroch EE. **N-acetylaspartate and N-acetylaspartylglutamate: neurobiology and clinical significance.** *Neurology* 2008;70:1353–57 CrossRef Medline
7. Baslow MH, Guilfoyle DN. **Canavan disease, a rare early-onset human spongiform leukodystrophy: insights into its genesis and possible clinical interventions.** *Biochimie* 2013;95:946–56 CrossRef Medline
8. Choi IY, Gruetter R. **Dynamic or inert metabolism? Turnover of N-acetyl aspartate and glutathione from D-[1–13C]glucose in the rat brain in vivo.** *J Neurochem* 2004;91:778–87 CrossRef Medline
9. Caglar E, Sabuncuoğlu H, Keskin T, et al. **In vivo human brain biochemistry after aerobic exercise: preliminary report on functional magnetic resonance spectroscopy.** *Surg Neurol* 2005;64 (suppl 2): S53–56; discussion S56–67 Medline
10. Hagino H, Suzuki M, Mori K, et al. **Proton magnetic resonance spectroscopy of the inferior frontal gyrus and thalamus and its relationship to verbal learning task performance in patients with schizophrenia: a preliminary report.** *Psychiatry Clin Neurosci* 2002; 56:499–507 CrossRef Medline
11. Dager SR, Layton ME, Strauss W, et al. **Human brain metabolic response to caffeine and the effects of tolerance.** *Am J Psychiatry* 1999; 156:229–37 Medline
12. Liu H, Zheng W, Yan G, et al. **Acute ethanol-induced changes in edema and metabolite concentrations in rat brain.** *Biomed Res Int* 2014;2014:351903 CrossRef Medline
13. Rao R, Ennis K, Long JD, et al. **Neurochemical changes in the developing rat hippocampus during prolonged hypoglycemia.** *J Neurochem* 2010;114:728–38 CrossRef Medline
14. Rigotti DJ, Inglese M, Gonen O. **Whole-brain N-acetylaspartate as a surrogate marker of neuronal damage in diffuse neurologic disorders.** *AJNR Am J Neuroradiol* 2007;28:1843–9 CrossRef Medline
15. Marshall O, Lu H, Brisset JC, et al. **Impaired cerebrovascular reactivity in multiple sclerosis.** *JAMA Neurol* 2014;71:1275–81 CrossRef Medline
16. Pollock JM, Deibler AR, Whitlow CT, et al. **Hypercapnia-induced cerebral hyperperfusion: an underrecognized clinical entity.** *AJNR Am J Neuroradiol* 2009;30:378–85 CrossRef Medline
17. Bates TE, Strangward M, Keelan J, et al. **Inhibition of N-acetylaspartate production: implications for 1H MRS studies in vivo.** *Neuroreport* 1996;7:1397–400 CrossRef Medline
18. Gonen O, Viswanathan AK, Catalaa I, et al. **Total brain N-acetylaspartate concentration in normal, age-grouped females: quantitation with non-echo proton NMR spectroscopy.** *Magn Reson Med* 1998;40:684–89 CrossRef Medline
19. Soher BJ, Wu WE, Tal A, et al. **Automated whole-brain N-acetylaspartate proton MRS quantification.** *NMR Biomed* 2014;27:1275–84 CrossRef Medline
20. Hu J, Javaid T, Arias-Mendoza F, et al. **A fast, reliable, automatic shimming procedure using 1H chemical-shift-imaging spectroscopy.** *J Magn Reson B* 1995;108:213–19 CrossRef Medline
21. Lu H, Ge Y. **Quantitative evaluation of oxygenation in venous vessels using T2-relaxation-under-spin-tagging MRI.** *Magn Reson Med* 2008;60:357–63 CrossRef Medline
22. Wu WC, Fernández-Seara M, Detre JA, et al. **A theoretical and experimental investigation of the tagging efficiency of pseudocontinuous arterial spin labeling.** *Magn Reson Med* 2007;58:1020–27 CrossRef Medline
23. Soher BJ, Semanchuk P, Todd D, et al. **Vespa: Integrated applica-**

tions for RF pulse design, spectral simulation and MRS data analysis. In: *Proceedings of the Annual Meeting of the International Society for Magnetic Resonance in Medicine,* Montreal, Quebec, Canada. May 6–13, 2011:1410
24. Young K, Soher BJ, Maudsley AA. **Automated spectral analysis II: application of wavelet shrinkage for characterization of non-parameterized signals.** *Magn Reson Med* 1998;40:816–21 CrossRef Medline
25. Soher BJ, Young K, Govindaraju V, et al. **Automated spectral analysis III: application to in vivo proton MR spectroscopy and spectroscopic imaging.** *Magn Reson Med* 1998;40:822–31 CrossRef Medline
26. Aslan S, Xu F, Wang PL, et al. **Estimation of labeling efficiency in pseudocontinuous arterial spin labeling.** *Magn Reson Med* 2010;63:765–71 CrossRef Medline
27. Lu H, Clingman C, Golay X, et al. **Determining the longitudinal relaxation time (T1) of blood at 3.0 Tesla.** *Magn Reson Med* 2004;52:679–82 CrossRef Medline
28. Kety SS, Schmidt CF. **The nitrous oxide method for the quantitative determination of cerebral blood flow in man: theory, procedure and normal values.** *J Clin Invest* 1948;27:476–83 CrossRef Medline
29. Yezhuvath US, Uh J, Cheng Y, et al. **Forebrain-dominant deficit in cerebrovascular reactivity in Alzheimer's disease.** *Neurobiol Aging* 2012;33:75–82 CrossRef Medline
30. Donahue MJ, Strother MK, Hendrikse J. **Novel MRI approaches for assessing cerebral hemodynamics in ischemic cerebrovascular disease.** *Stroke* 2012;43:903–15 CrossRef Medline
31. Mark CI, Slessarev M, Ito S, et al. **Precise control of end-tidal carbon dioxide and oxygen improves BOLD and ASL cerebrovascular reactivity measures.** *Magn Reson Med* 2010;64:749–56 CrossRef Medline
32. Wang X, Wu J, Li L, et al. **Hypercapnic acidosis activates KATP channels in vascular smooth muscles.** *Circ Res* 2003;92:1225–32 CrossRef Medline
33. Sicard KM, Duong TQ. **Effects of hypoxia, hyperoxia, and hypercapnia on baseline and stimulus-evoked BOLD, CBF, and CMRO2 in spontaneously breathing animals.** *Neuroimage* 2005;25:850–58 CrossRef Medline
34. Xu F, Uh J, Brier MR, et al. **The influence of carbon dioxide on brain activity and metabolism in conscious humans.** *J Cereb Blood Flow Metab* 2011;31:58–67 CrossRef Medline
35. Jones M, Berwick J, Hewson-Stoate N, et al. **The effect of hypercapnia on the neural and hemodynamic responses to somatosensory stimulation.** *Neuroimage* 2005;27:609–23 CrossRef Medline
36. Douglas RM, Ryu J, Kanaan A, et al. **Neuronal death during combined intermittent hypoxia/hypercapnia is due to mitochondrial dysfunction.** *Am J Physiol Cell Physiol* 2010;298:C1594–602 CrossRef Medline
37. Khacho M, Tarabay M, Patten D, et al. **Acidosis overrides oxygen deprivation to maintain mitochondrial function and cell survival.** *Nat Commun* 2014;5:3550 Medline
38. Barker PB, Gillard JH, van Zijl PC, et al. **Acute stroke: evaluation with serial proton MR spectroscopic imaging.** *Radiology* 1994;192:723–32 CrossRef Medline

Ultra-High-Field MRI Visualization of Cortical Multiple Sclerosis Lesions with T2 and T2*: A Postmortem MRI and Histopathology Study

L.E. Jonkman, R. Klaver, L. Fleysher, M. Inglese, and J.J.G. Geurts

ABSTRACT

BACKGROUND AND PURPOSE: At 7T MR imaging, T2*-weighted gradient echo has been shown to provide high-resolution anatomic images of gray matter lesions. However, few studies have verified T2*WI lesions histopathologically or compared them with more standard techniques at ultra-high-field strength. This study aimed to determine the sensitivity of T2WI and T2*WI sequences for detecting cortical GM lesions in MS.

MATERIALS AND METHODS: At 7T, 2D multiecho spin-echo T2WI and 3D gradient-echo T2*WI were acquired from 27 formalin-fixed coronal hemispheric brain sections of 15 patients and 4 healthy controls. Proteolipid-stained tissue sections (8 μm) were matched to the corresponding MR images, and lesions were manually scored on both MR imaging sequences (blinded to histopathology) and tissue sections (blinded to MR imaging). The sensitivity of MR imaging sequences for GM lesion types and white matter lesions was calculated. An unblinded retrospective scoring was also performed.

RESULTS: If all cortical GM lesions were taken into account, the T2WI sequence detected slightly more lesions than the T2*WI sequence: 28% and 16%, respectively ($P = .054$). This difference disappeared when only intracortical lesions were considered. When histopathologic information (type, location) was revealed to the reader, the sensitivity went up to 84% (T2WI) and 85% (T2*WI) (not significant). Furthermore, the false-positive rate was 8.6% for the T2WI and 10.5% for the T2*WI sequence.

CONCLUSIONS: There is no strong advantage of the T2*WI sequence compared with a conventional T2WI sequence in the detection of cortical lesions at 7T. Retrospectively, a high percentage of lesions could be detected with both sequences. However, many lesions are still missed prospectively. This could possibly be minimized with better a priori observer training.

ABBREVIATIONS: CNR = contrast-to-noise ratio; DIR = double inversion recovery; GML = gray matter lesion; WML = white matter lesion

Multiple sclerosis is traditionally regarded as a chronic inflammatory demyelinating disease of the white matter with a variable clinical course; primary-progressive or relapsing-remitting with possible conversion to secondary-progressive. Pathologic, immunologic, and imaging studies have confirmed that tissue damage in the gray matter is also a key component of the disease process.[1-4] GM pathology occurs frequently, already early in the disease course, and explains cognitive and clinical disability better than white matter lesions.[5,6] Nevertheless, visualizing these GM abnormalities has been challenging due to their small size, absence of inflammation, and partial volume effect from adjacent CSF and WM. The introduction of ultra-high-field MR imaging scanners and specific MR imaging pulse sequences has improved the detection of GM lesions due to a higher signal-to-noise ratio and better spatial resolution.[7-9] 7T T2*-weighted gradient-echo MR imaging has been shown to provide high-resolution anatomic images of GM lesions, and it has even been suggested that this sequence be used as the new criterion standard for GM lesion detection.[10] It was reported to be 44% more sensitive than 1.5T MR imaging in detecting lesions with cortical involvement[11] and up to 69% more sensitive than 3T double inversion recovery (DIR) imaging in detecting subpial lesions.[10]

Few groups have had the opportunity to study GM lesions that were visualized with 7T T2*WI in terms of histopathology. There-

Received February 23, 2015; accepted after revision April 2.

From the Department of Anatomy and Neurosciences (L.E.J., R.K., J.J.G.G.), VU University Medical Center, Amsterdam, the Netherlands; Departments of Radiology (L.F., M.I.), Neurology (M.I.), and Neurosciences (M.I.), Mount Sinai School of Medicine, New York, New York; and Departments of Neuroscience, Rehabilitation, Ophthalmology, Genetics, Maternal and Child Health (M.I.), University of Genoa, Genoa, Italy.

This work was supported by the Dutch MS Research Foundation (grant No. 09-358b) and the US National MS Society (RG 4916A2/1) to M.I. and J.J.G.G. and the Noto Foundation to M.I.

Please address correspondence to L.E. Jonkman, VU University Medical Center, Department of Anatomy and Neurosciences, van der Boechorststraat 7, 1081 BT Amsterdam, the Netherlands; e-mail: le.jonkman@vumc.nl

http://dx.doi.org/10.3174/ajnr.A4418

Table 1: Demographic and neuropathologic data of subjects

Case No.	No[a]	Sex	Age (yr)	PMD (h:min)[b]	DD (yr)	MS Type	COD
MS							
1		M	80	6:05	45	SPMS	Pneumonia
2		F	81	3:30	27	PPMS	Pneumonia
3		M	75	10:10	50	NA	Pneumonia
4		F	66	7:30	17	NA	Pulmonary hypertension
5		M	71	4:00	15	SPMS	Pulmonary carcinoma
6		F	54	6:00	16	SPMS	Liver cancer
7		M	63	4:30	25	SPMS	Pneumonia
8		M	78	3:00	33	SPMS	Euthanasia
9		M	59	5:00	21	SPMS	Euthanasia
10		M	56	10:10	13	NA	Suicide
11		F	56	8:25	32	SPMS	Pneumonia
12		F	54	3:30	31	SPMS	Heart failure
13		M	58	4:00	27	SPMS	Pneumonia
14		F	95	6:30	55	SPMS	Unknown
15		F	81	6:30	21	SPMS	Heart failure
Mean			68.5 ± 12.7	5:56 ± 2:27	28.5 ± 12.9		
Control							
20	4	F	72	>24:00	–	–	Myocardial infarct
21	3	F	58	<24:00	–	–	Breast cancer
22	3	F	76	<24:00	–	–	Pneumonia
23	2	F	76	<8:00	–	–	Pneumonia
Mean			70.5 ± 8.5				

Note:—PMD indicates postmortem delay; DD, disease duration since diagnosis; SPMS, secondary-progressive MS; PPMS, primary-progressive MS; COD, cause of death; NA, unavailable/unknown; –, not applicable.

[a] The numbers indicate number of hemispheric sections included per case.

[b] Control cases are not part of the rapid postmortem examination program and therefore have a longer PMD.

fore, little information is available on the exact sensitivity of T2*WI and/or whether certain lesion types are more visible than others with this sequence. One postmortem study that did look at T2*WI sensitivity showed a 48% prospective sensitivity but made no distinction among lesion types.[12] Another 7T study found that 46% of cortical lesions could be prospectively detected by using T2*WI and a similar 43% could be detected by using a WM-attenuated turbo field echo.[13] However, the 2 sequences studied were suboptimally matched in terms of image resolution, which may explain the relative absence of differences between them. The current study aimed to determine the sensitivity of a standard T2WI and a T2*WI sequence, by using the same image resolution, for detecting MS GM lesion types in postmortem MS tissue.

MATERIALS AND METHODS

Patients and Postmortem Examination

Coronally cut, 10-mm-thick full-hemispheric brain sections of 15 patients with histopathologically confirmed MS (7 women) were selected after rapid postmortem examination (mean postmortem delay, 5 hours 56 minutes) and were formalin-fixed. Additionally, 12 control sections from 4 donors were obtained (recruited and evaluated by the pathology department of VU University Medical Center, Amsterdam, the Netherlands). Table 1 provides demographic and neuropathologic details of the donors. Before death, all donors were registered at the Netherlands Brain Bank, Amsterdam, the Netherlands. All donors gave written informed consent for the use of their tissue and medical records for research purposes. Permission for performing postmortem examinations, use of tissue, and access to medical records was granted by the institutional ethics review board.

MR Imaging

Imaging was performed by using a 7T BioSpec USR70/30 imager (Bruker BioSpin MRI, Ettlingen, Germany), and a vendor-provided 8.6-cm-diameter radiofrequency transmit/receive coil (model 1P T12053V3). Each formalin-fixed brain section was placed into a rectangular plastic tissue container and immersed in 10% buffered formalin. Particular care was devoted to sequence optimization due to the effect of tissue fixation on sequence parameters. The MR imaging protocol included a 2D multiecho spin-echo T2-weighted (TR/TE1/TE2/TE3 = 4000/19.1/38.2/57.3 ms; $\alpha = 90$ and 180; averages = 6) and a 3D gradient-echo T2*-weighted (TR/TE = 25/12 ms; $\alpha = 5$; averages = 16) sequence. All MR imaging sequences were acquired with an FOV of 100 × 80, matrix of 1000 × 800, and in-plane spatial resolution of 100 × 100 μm, with a section thickness of 1 mm.

Contrast-to-noise ratios (CNRs) were determined for the different MR image types in the MS samples on the basis of signal-intensity measurements in ROIs (ie, normal-appearing gray matter, GM lesions, normal-appearing white matter, WM lesions, formalin [noise]). The CNR between 2 tissue types was defined as $|SI1 - SI2|/SD\,(noise)$. For T2WI, the TE of 19.1 ms was used for lesion detection and CNR calculation.

Histology

After MR imaging, the brain sections were cut in half to reveal the imaged plane and were embedded in paraffin. Eight-micrometer-thick sections were cut, mounted onto glass slides (Superfrost; VWR International, Leuven, Belgium), and dried overnight at 37°C. Sections were deparaffinized in a series of xylene, 100% alcohol (ethanol), 96% alcohol, and 70% alcohol and rinsed with 0.01-mol/L tris-buffered saline (pH, 7.8–8.0). Endogenous per-

oxidase activity was blocked by incubating the sections in tris-buffered saline with 0.3% H_2O_2 for 30 minutes. After this, the sections were rinsed with 0.01-mol/L phosphate-buffered saline (pH, 7.4). Staining was performed with antibodies against proteolipid protein (AbD Serotec, Oxford, UK) diluted in tris-buffered saline (1:500) containing 1% normal goat serum (Dako, Glostrup, Denmark) and stored overnight at 6°C. Immunolabeling was detected by incubating the sections in biotinylated goat antimouse (1:400; Vector Laboratories, Burlingame, California) and in Vectastain ABC (horseradish peroxidase, 1:200; Vector Laboratories) for 60 minutes at room temperature. Afterward, the sections were washed in 0.05-mol/L tris-hydrochloric acid (pH, 7.6). Peroxidase activity was demonstrated with 0.5-mg/mL 3,3′ diaminobenzidine tetrahydrochloride (DAB; Sigma, St. Louis, Missouri) in 0.01-mol/L tris-hydrochloride containing 0.03% H_2O_2 for 5 minutes, which led to a brown reaction product. Sections were counterstained with hematoxylin (Sigma) and mounted (dePex; BDH Chemicals, Poole, UK).

Scoring, Classification, and Matching

MR imaging lesions were manually marked on all T2*WI, and all T2WI with TE = 19.1 which had contrast similar to that of clinically used T2WI sequences. The MIPAV (National Institutes of Health, Bethesda, Maryland) application was used for manual prospective and retrospective lesion scoring. The MR imaging reader scoring was blinded to clinical information and histopathologic results. Lesions were scored throughout all of the MR imaging slices to avoid bias toward scoring within the sampled areas. A subset of images ($n = 5$ for each sequence) was rated by a second independent reader to ascertain the quality of scoring and calculate an intraclass correlation coefficient for each sequence.

Histopathologically, lesions were defined as areas of complete demyelination (lack of proteolipid protein) and were scored by a histopathologic reader blinded to the clinical and MR imaging data. GM lesions were scored and classified according to criteria described in Bø et al,[14] in which a distinction among 4 cortical lesion types is made. Type I lesions involve the deeper layers of the GM and the adjacent WM; type II lesions are small demyelinated lesions, often centered around blood vessels and confined within the cortex; type III lesions extend from the pial surface into the cortex, most often reaching to cortical layers 3 or 4. When these lesions involve the entire span of the cortex without entering the subcortical white matter, they are defined as type IV lesions. After MR imaging and histopathologic scoring, hemispheric tissue sections were matched to the corresponding MR imaging planes by using WM lesions and as many cortical anatomic landmarks as possible. After the blinded prospective scoring of the postmortem MR imaging and the tissue-to–MR imaging matching, histopathology scores were made available to the MR imaging readers and a second, retrospective, unblinded scoring was performed in consensus between the raters.

Analysis of Data

Histopathologic lesion count was considered the criterion standard. Therefore, prospective and retrospective sensitivity of MR imaging sequences for detecting lesions was determined by dividing the number of lesions scored in the prospective or retrospective ratings by the number of lesions assessed on histopathology, times 100%. The sensitivity of T2WI and T2*WI MR images was statistically compared by using the Wilcoxon signed rank test in SPSS 20.0 (IBM, Armonk, New York). The specificity of MR imaging sequences was determined by dividing the number of false-positives by the number of lesions assessed on histopathology and subtracting this number from 100%. The interrater agreement for prospective lesion detection was expressed as an intraclass correlation coefficient for each sequence (T2WI and T2*WI) by using a 2-way random effects model in absolute agreement. Due to the small number of WM lesions, differences in WM CNRs were kept descriptive. For the difference between GM and gray matter lesion (GML) and between GM and WM (both normally distributed), a paired samples *t* test was performed.

RESULTS

Of the MR imaging–scanned and histopathologically processed samples, 1 section from 1 patient did not show any histopathologic abnormalities and was therefore excluded from analysis. The control sections did not show, apart from age-related frontal capping, any histopathologic abnormalities. The final dataset for analysis included 26 brain sections (from 14 patients and 4 controls). In the MS brain sections, we identified 105 lesions on MR imaging that were verified by histopathology: 7 WM and 98 cortical lesions. Of these cortical lesions, 14 were mixed GM-WM (type I) lesions and 84 were located entirely within the cortical GM (16 type II lesions, 43 type III lesions, and 25 type IV lesions). The intraclass correlation coefficient for the T2WI sequence was 0.972; the intraclass correlation coefficient for the T2*WI sequence was 0.968.

Comparison of Lesion Scoring between T2WI and T2*WI

Results of the histopathologic count and the proportion of lesions detected prospectively and retrospectively on T2WI and T2*WI sequences are shown in Table 2. When focusing on cortical GM lesions (I–IV), the T2WI sequence detected 69% more lesions than T2*WI (Table 2). This difference in GM I–IV lesion detection was not significant ($P = .054$). When only focusing on intracortical GM lesions (II–IV), the T2WI sequence detected 36% more lesions than the T2*WI sequence. This difference was also not significant ($P = .38$). On retrospective scoring, when lesion location was revealed to the MR imaging reader, 81 and 82 cortical lesions were found with the T2WI sequence and T2*WI sequence, respectively, an increase of 200% and 413% compared with prospective scoring. Figure 1 shows matched histologic, T2WI, and T2*WI with prospectively and retrospectively detected lesions. Aside from the detected lesions, we scored 19 false-positives (marked on MR imaging as a lesion but not confirmed by histopathology): 9 on the T2WI sequence and 10 on the T2*WI sequence. This resulted in a specificity of 91.4% for the T2WI and 90.5% for the T2WI sequence. After microscopic inspection of these false-positives, it appeared that many of the cases (89% for T2WI and 80% for the T2*WI sequence) were incompletely demyelinated/remyelinated lesions, which were not scored be-

Table 2: Lesion count and sensitivity of prospective and retrospective MRI scoring[a]

	Histology	Prospective MRI			Retrospective MRI		
Lesion Type	Count	T2WI	T2*WI	*P* Value	T2WI	T2*WI	*P* Value
I	14	8 (57)	2 (14)	–	14 (100)	13 (93)	–
II	16	3 (19)	5 (31)	–	13 (81)	10 (63)	–
III	43	5 (12)	5 (12)	–	32 (74)	36 (84)	–
IV	25	11 (44)	4 (16)	–	22 (88)	23 (92)	–
GML (I–IV)	98	27 (28)	16 (16)	.054	81 (83)	82 (84)	.803
GML (II–IV)	84	19 (23)	14 (17)	.380	67 (80)	69 (82)	0.608
WML	7	6 (86)	3 (43)	–	7 (100)	7 (100)	–
Total	105	33 (31)	19 (18)	.018[b]	88 (84)	89 (85)	.803

Note:— – indicates not statistically assessed.

[a] Sensitivity (in percentages between parentheses) was calculated by dividing the number of lesions scored in the prospective or retrospective ratings by the number of lesions assessed on histopathology, times 100%.

[b] Significant.

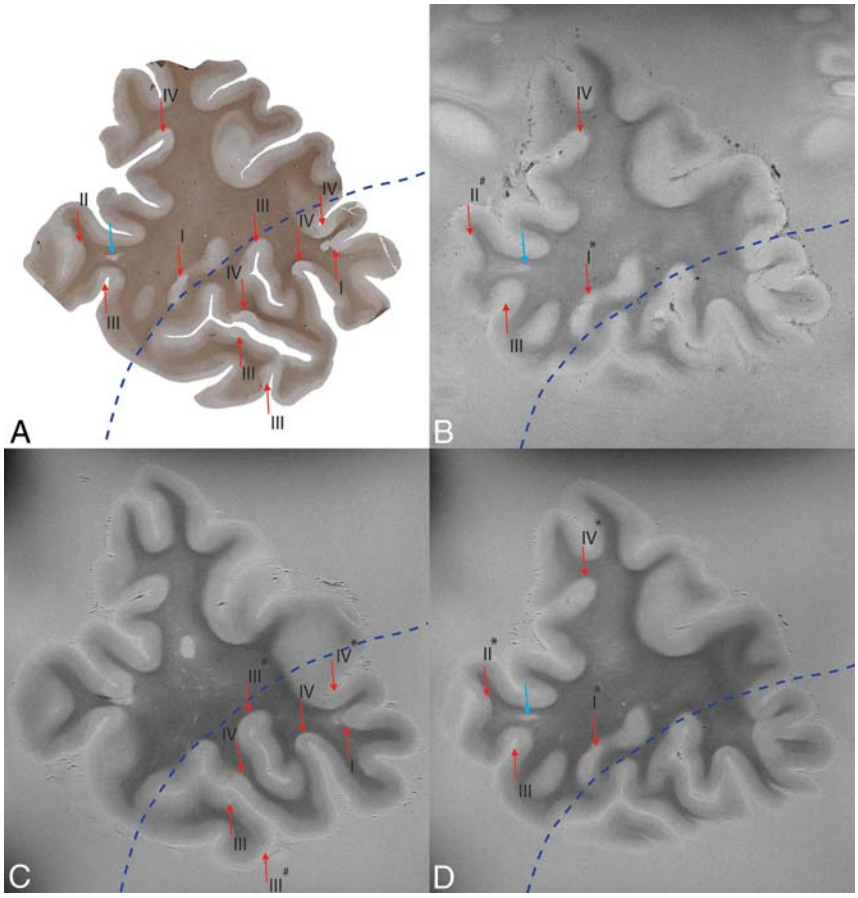

FIG 1. Section stained with anti-proteolipid protein antibodies (*A*), matched with T2*WI (*B*) and T2WI (*C* and *D*). Note that the histologic section corresponds with multiple slices of the MR image; the top part of image *B* and *D* corresponds to the top part of image *A*, and the bottom part of image *C* corresponds to the bottom part of image *A*. The border between successive MR imaging slices is depicted by the *blue dotted line*. Lesions are indicated with *arrows* (WML is blue; GML is red). The type of GM lesion is indicated by I–IV. Also indicated is whether histologic lesions were retrospectively seen on MR imaging (*asterisk*) or missed on MR imaging (*number sign*). All other histologic lesions were prospectively detected. Degree of magnification: 50×.

cause they did not fulfill the criterion of a "fully demyelinated lesion" (see "Materials and Methods").

Contrast-to-noise ratios for the various tissue types are shown in Table 3. Although only descriptive, the T2WI sequence showed higher WM to white matter lesion (WML) CNR, which could account for the higher prospective sensitivity than T2*WI sequence (Table 2). Regarding the T2WI and T2*WI sequences, a paired samples *t* test showed no significant difference between the comparably low GM-GML CNRs.

DISCUSSION

In the current study, we have demonstrated that prospectively (ie, without knowledge of histopathology [location and type of lesions]), the standard T2WI sequence detected more cortical lesions than the T2*WI sequence (ie, 28% versus 16%, respectively), though this difference was not statistically significant. When only intracortical lesions were taken into account, this difference between sequences vanished completely. It also vanished when lesion location was revealed to the reader (retrospective scoring). An explanation for this slight prospective difference could be that the T2*WI sequence is more susceptible to global inhomogeneities such as tissue-to-formalin boundaries, leading to local T2* signal decay,[15] which could hinder prospective lesion detection.

Retrospective detection of cortical lesions increased to 83% for the T2WI and 84% for the T2*WI sequence. When we focused on intracortical lesions, retrospective detection increased to 80% and 82%, respectively. This retrospective detection sensitivity is much higher than that in previous postmortem MR imaging studies at lower field strengths. Previous studies at 1.5T detected only 31%[3] or 56%[16] of intracortical lesions with a T2WI sequence and 29% with a DIR sequence.[17] With a FLAIR sequence, 9%,[17] 21%,[3] or 71%[18] of intracortical lesions were detected retrospectively. Compared with previous postmortem MR imaging studies at ultra-high-field (7T) strength, our T2WI and T2*WI retrospective detection rates are higher than the 67% found with R2* maps,[19] comparable with the 82% found with WM-attenuated turbo field echo, and slightly lower than the 93% detected with T2*WI.[13] However, prospective

Table 3: Contrast-to-noise ratio (±SD)

CNR	T2WI	T2*WI
WM-WML	12.07 (0.90)	5.03 (1.68)
GM-GML	2.01 (0.74)	1.7 (1.37)
GM-WM	7.5 (1.58)	4.96 (3.79)

Note:—WM-WML indicates white matter-to-white matter lesion CNR; GM-GML, gray matter-to-gray matter lesion CNR; GM-WM, gray matter-to-white matter CNR.

lesion detection in these studies varied between 42% and 48%,[13,19] which is higher than our cortical detection rate of up to 28%. One explanation for this higher detection rate in other studies could be the type of lesions identified; most lesions found by Yao et al[19] were the more easily detectable type I lesions, while most lesions in our sample were the more difficult detect type III lesions. Another explanation could be the higher CNR as found in the study by Pitt et al.[13] Their T2*WI sequence had a GML-GM CNR of 3.4, while our study only had an average CNR of 1.7, making distinction between GML and surrounding GM more difficult. These differences could have led to a more optimal sequence for lesion detection by Pitt et al. Future studies should be performed to see how lesion heterogeneity and within-sequence differences influence lesion detection. As shown by the high retrospective lesion count, 7T MR imaging has greatly improved the possibility of detecting cortical or intracortical lesions. However, the challenge remains to actually detect them *prospectively* and *in vivo*.

Regardless of 7T MR imaging with increased signal-to-noise ratio (SNR) and spatial resolution, the number of prospectively detected cortical lesions on MR images remains low; in our study, up to 84% of cortical or intracortical lesions remained undetected. In another study at 7T, up to 57% were still missed.[13] Lesion size has been found to affect the visibility of cortical lesions at both 1.5T[20] and 7T.[13] Furthermore, extensive cortical demyelination could hinder visibility of type IV lesions; when most of the cortex is affected, there is no normal-appearing gray matter present, making it difficult to differentiate areas of demyelination and normal-appearing gray matter (Fig 2). Perhaps quantitative MR imaging could provide additional information in these areas.[21] Automated segmentation could be another option to aid cortical lesion detection, though this could be extremely challenging due to a lack of contrast in the cortex, especially in the upper layers where most cortical lesions are located. Nevertheless, retrospective lesion detection shows that it is possible to find cortical lesions on MR imaging when lesion location is (histopathologically) known, indicating that observer training is important and could dramatically increase future prospective sensitivity.

There were only 7 WMLs observed during histopathologic analysis. This seems low, but the coronal sections were sampled from more frontal regions of the brain, a preferential area for cortical pathology,[22,23] but not far for WMLs, which are more frequently located periventricular.

Sequence parameters were optimized for the effect of fixation, SNR, and spatial resolution. Fixed tissue has a decrease in T2 signal,[24] which leads to lower contrast and requires an increase in averages to achieve a reasonable SNR. This results in an increase in acquisition time, a methodologic limitation when trying to compare the results from this study with the *in vivo* setting. The sequences used can be optimized for the 7T *in vivo* setting, but

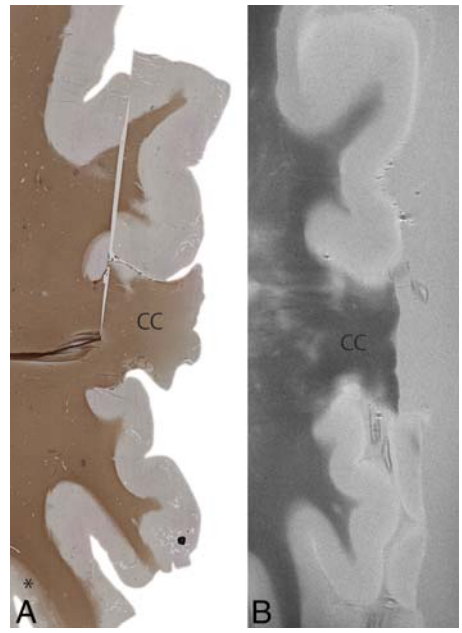

FIG 2. An example of extensive cortical demyelination in an MS case. Histologic section with anti-proteolipid protein antibody (*left*) and a matched T2WI (*right*). The histologic section shows extensive cortical demyelination (lack of proteolipid protein) in the cortex, except for a small section at the left bottom (*asterisk*). This extensive demyelination makes it difficult to differentiate lesions and normal-appearing gray matter on MR imaging (*right*). In this particular case, as a result, prospective MR imaging scoring was negative. CC indicates corpus callosum. Degree of magnification: 50×.

identifying cortical lesions will remain especially challenging for smaller sized lesions.[20] Another limitation in correlative studies between histopathology and MR imaging is matching tissue sections to MR images. Tissue sections were 8 μm, while MR images had a section thickness of 1 mm. However, accurate matching was made possible due to the many anatomic landmarks in the full-hemispheric sections used in this study.

Looking at the in vivo setting, DIR is reported to improve cortical lesion detection at 3T compared with 1.5T, while T2WI or FLAIR is not.[25] In turn, a 75% increase in cortical lesion detection was found with 7T T2WI versus 3T T2WI. For T1 and FLAIR, this was even 91% and 238%, respectively.[26] Another study found a 65% increase in cortical lesion detection with 7T T2*WI versus 3T DIR.[10] The same research group also investigated how various lesion types contributed to physical and cognitive performance. They found that type III–IV lesions had the strongest relationship to physical disability. In turn, type I lesions and, to a lesser extent, type III–IV lesions had a relationship with cognitive performance.[27] At 3T, DIR detected 538% more intracortical lesions than T2WI and 152% more intracortical lesions than FLAIR.[18] This finding was supported by another study in which DIR detected 43% more cortical lesions than FLAIR.[9] However, a study from Kilsdonk et al[28] at ultra-high-field strength (7T) showed that FLAIR detected 89% more cortical lesions than DIR, and that DIR and T2WI obtained nearly identical mean cortical lesion counts (115 versus 116). This finding indicates that a sequence that may be optimal at a lower field strength (DIR at 3T) may lose its benefit at a higher field strength (7T), and vice versa: A sequence suboptimal at a lower field strength may have an advan-

tage over other sequences at higher field strengths (FLAIR or T2* at 7T). It would be useful if future studies could elucidate which sequences have optimal lesion detection sensitivities at which field strength. Phase-sensitive inversion recovery looks promising at 3T with a 307% increase over DIR,[29] but how does it perform at 7T? How do FLAIR, T2WI, and T2*WI compare at 7T in 1 comparative study?

CONCLUSIONS

Our findings suggest that at 7T, T2WI and T2*WI sequences are equally capable of detecting up to 83%–84% of cortical lesions in postmortem MS samples. However, many lesions are still missed prospectively. With observer training, the expectation is that not only the "tip" but a large part of the proverbial "iceberg" of GM lesions may be uncovered.

Disclosures: Laura E. Jonkman—*RELATED*: *Grant*: Dutch MS Research Foundation (09–358b).* Roel Klaver—*RELATED*: Dutch MS Research Foundation.* Matilde Inglese—*RELATED*: *Grant*: National MS Society,* *Comments*: RG 4916A2/1; *UNRELATED*: *Grants/Grants Pending*: Novartis Pharmaceuticals.* Jeroen J.G. Geurts—*RELATED*: *Grant*: Dutch MS Research Foundation. *Money paid to the institution.

REFERENCES

1. Kidd D, Barkhof F, McConnell R, et al. **Cortical lesions in multiple sclerosis.** *Brain* 1999;122(pt 1):17–26 CrossRef Medline
2. Peterson JW, Bö L, Mörk S, et al. **Transected neurites, apoptotic neurons, and reduced inflammation in cortical multiple sclerosis lesions.** *Ann Neurol* 2001;50:389–400 CrossRef Medline
3. Geurts JJ, Blezer EL, Vrenken H, et al. **Does high-field MR imaging improve cortical lesion detection in multiple sclerosis?** *J Neurol* 2008;255:183–91 CrossRef Medline
4. Filippi M, Rocca MA, Calabrese M, et al. **Intracortical lesions: relevance for new MRI diagnostic criteria for multiple sclerosis.** *Neurology* 2010;75:1988–94 CrossRef Medline
5. Roosendaal SD, Moraal B, Pouwels PJ, et al. **Accumulation of cortical lesions in MS: relation with cognitive impairment.** *Mult Scler* 2009;15:708–14 CrossRef Medline
6. Nelson F, Datta S, Garcia N, et al. **Intracortical lesions by 3T magnetic resonance imaging and correlation with cognitive impairment in multiple sclerosis.** *Mult Scler* 2011;17:1122–29 CrossRef Medline
7. Vaughan JT, Garwood M, Collins CM, et al. **7T vs. 4T: RF power, homogeneity, and signal-to-noise comparison in head images.** *Magn Reson Med* 2001;46:24–30 CrossRef Medline
8. Metcalf M, Xu D, Okuda DT, et al. **High-resolution phased-array MRI of the human brain at 7 Tesla: initial experience in multiple sclerosis patients.** *J Neuroimaging* 2010;20:141–47 CrossRef Medline
9. Tallantyre EC, Morgan PS, Dixon JE, et al. **3 Tesla and 7 Tesla MRI of multiple sclerosis cortical lesions.** *J Magn Reson Imaging* 2010;32:971–77 CrossRef Medline
10. Nielsen AS, Kinkel RP, Tinelli E, et al. **Focal cortical lesion detection in multiple sclerosis: 3 Tesla DIR versus 7 Tesla FLASH-T2.** *J Magn Reson Imaging* 2012;35:537–42 CrossRef Medline
11. Kollia K, Maderwald S, Putzki N, et al. **First clinical study on ultra-high-field MR imaging in patients with multiple sclerosis: comparison of 1.5T and 7T.** *AJNR Am J Neuroradiol* 2009;30:699–702 CrossRef Medline
12. Yao B, Bagnato F, Matsuura E, et al. **Chronic multiple sclerosis lesions: characterization with high-field-strength MR imaging.** *Radiology* 2012;262:206–15 CrossRef Medline
13. Pitt D, Boster A, Pei W, et al. **Imaging cortical lesions in multiple sclerosis with ultra-high-field magnetic resonance imaging.** *Arch Neurol* 2010;67:812–18 CrossRef Medline
14. Bø L, Vedeler CA, Nyland HI, et al. **Subpial demyelination in the cerebral cortex of multiple sclerosis patients.** *J Neuropathol Exp Neurol* 2003;62:723–32 Medline
15. Bagnato F, Hametner S, Welch EB. **Visualizing iron in multiple sclerosis.** *Magn Reson Imaging* 2013;31:376–84 CrossRef Medline
16. Geurts JJ, Bö L, Pouwels PJ, et al. **Cortical lesions in multiple sclerosis: combined postmortem MR imaging and histopathology.** *AJNR Am J Neuroradiol* 2005;26:572–77 Medline
17. Seewann A, Kooi EJ, Roosendaal SD, et al. **Postmortem verification of MS cortical lesion detection with 3D DIR.** *Neurology* 2012;78:302–08 CrossRef Medline
18. Geurts JJ, Pouwels PJ, Uitdehaag BM, et al. **Intracortical lesions in multiple sclerosis: improved detection with 3D double inversion-recovery MR imaging.** *Radiology* 2005;236:254–60 CrossRef Medline
19. Yao B, Hametner S, van Gelderen P, et al. **7 Tesla magnetic resonance imaging to detect cortical pathology in multiple sclerosis.** *PLoS One* 2014;9:e108863 CrossRef Medline
20. Seewann A, Vrenken H, Kooi EJ, et al. **Imaging the tip of the iceberg: visualization of cortical lesions in multiple sclerosis.** *Mult Scler* 2011;17:1202–10 CrossRef Medline
21. Samson RS, Cardoso MJ, Muhlert N, et al. **Investigation of outer cortical magnetisation transfer ratio abnormalities in multiple sclerosis clinical subgroups.** *Mult Scler* 2014;20:1322–30 CrossRef Medline
22. Bö L, Geurts JJ, Ravid R, et al. **Magnetic resonance imaging as a tool to examine the neuropathology of multiple sclerosis.** *Neuropathol Appl Neurobiol* 2004;30:106–17 CrossRef Medline
23. Vercellino M, Plano F, Votta B, et al. **Grey matter pathology in multiple sclerosis.** *J Neuropathol Exp Neurol* 2005;64:1101–07 CrossRef Medline
24. Pfefferbaum A, Sullivan EV, Adalsteinsson E, et al. **Postmortem MR imaging of formalin-fixed human brain.** *Neuroimage* 2004;21:1585–95 CrossRef Medline
25. Simon B, Schmidt S, Lukas C, et al. **Improved in vivo detection of cortical lesions in multiple sclerosis using double inversion recovery MR imaging at 3 Tesla.** *Eur Radiol* 2010;20:1675–83 CrossRef Medline
26. de Graaf WL, Kilsdonk ID, Lopez-Soriano A, et al. **Clinical application of multi-contrast 7-T MR imaging in multiple sclerosis: increased lesion detection compared to 3 T confined to grey matter.** *Eur Radiol* 2013;23:528–40 CrossRef Medline
27. Nielsen AS, Kinkel RP, Madigan N, et al. **Contribution of cortical lesion subtypes at 7T MRI to physical and cognitive performance in MS.** *Neurology* 2013;81:641–49 CrossRef Medline
28. Kilsdonk ID, de Graaf WL, Soriano AL, et al. **Multicontrast MR imaging at 7T in multiple sclerosis: highest lesion detection in cortical gray matter with 3D-FLAIR.** *AJNR Am J Neuroradiol* 2013;34:791–96 CrossRef Medline
29. Sethi V, Yousry TA, Muhlert N, et al. **Improved detection of cortical MS lesions with phase-sensitive inversion recovery MRI.** *J Neurol Neurosurg Psychiatry* 2012;83:877–82 CrossRef Medline

The Contribution of Common Surgically Implanted Hardware to Functional MR Imaging Artifacts

A.A. Desai, M.K. Strother, C.C. Faraco, V.L. Morgan, T.R. Ladner, L.M. Dethrage, L.C. Jordan, and M.J. Donahue

ABSTRACT

BACKGROUND AND PURPOSE: Blood oxygenation level–dependent MR imaging is increasingly used clinically to noninvasively assess cerebrovascular reactivity and/or language and motor function. However, many patients have metallic implants, which will induce susceptibility artifacts, rendering the functional information uninformative. Here, we calculate and interpret blood oxygenation level–dependent MR imaging artifact impact arising from surgically implanted hardware.

MATERIALS AND METHODS: A retrospective analysis of all blood oxygenation level–dependent MRIs ($n = 343$; B0 = 3T; TE = 35 ms; gradient echo EPI) acquired clinically (year range = 2006–2014) at our hospital was performed. Blood oxygenation level–dependent MRIs were most commonly prescribed for patients with cerebrovascular disease ($n = 80$) or patients undergoing language or motor localization ($n = 263$). Artifact volume (cubic centimeters) and its impact on clinical interpretation were determined by a board-certified neuroradiologist.

RESULTS: Mean artifact volume associated with intracranial hardware was 4.3 ± 3.2 cm^3 (range = 1.1–9.4 cm^3). The mean artifact volume from extracranial hardware in patients with cerebrovascular disease was 28.4 ± 14.0 cm^3 (range = 6.1–61.7 cm^3), and in patients with noncerebrovascular disease undergoing visual or motor functional mapping, it was 39.9 ± 27.0 cm^3 (range = 6.9–77.1 cm^3). The mean artifact volume for ventriculoperitoneal shunts was 95.7 ± 39.3 cm^3 (range = 64.0–139.6 cm^3). Artifacts had no-to-mild effects on clinical interpretability in all patients with intracranial implants. Extracranial hardware artifacts had no-to-moderate impact on clinical interpretability, with the exception of 1 patient with 12 KLS-Martin maxDrive screws with severe artifacts precluding clinical interpretation. All examined ventriculoperitoneal shunts resulted in moderate-to-severe artifacts, limiting clinical interpretation.

CONCLUSIONS: Blood oxygenation level–dependent MR imaging yields interpretable functional maps in most patients beyond a small (30–40 cm^3) artifact surrounding the hardware. Exceptions were ventriculoperitoneal shunts, particularly those with programmable valves and siphon gauges, and large numbers of KLS-Martin maxDrive screws.

ABBREVIATIONS: BOLD = blood oxygenation level–dependent; CVR = cerebrovascular reactivity; VP = ventriculoperitoneal

Blood oxygenation level–dependent (BOLD) fMRI is becoming increasing used for presurgical mapping of eloquent cortex before resection of brain tumors[1] or epileptogenic foci[2] and to assess cerebrovascular reactivity (CVR) when combined with hypercapnic gas stimuli.[3,4] The main advantage of BOLD fMRI is the lack of ionizing radiation or exogenous contrast required, which makes it a particularly appealing approach for longitudinal monitoring of patients or for evaluating short-term responses to therapy in situations in which exogenous contrast agents may be dose-restricted.

A known limitation of BOLD fMRI over alternative approaches for assessing hemodynamics is the sensitivity of BOLD to magnetic field inhomogeneities, including those produced by implants. At clinical field strengths of 1.5T to 3T, BOLD fMRI requires a relatively long TE (30–55 ms) to sensitize the sequence to susceptibility differences between oxygenated (diamagnetic) and deoxygenated (paramagnetic) blood. However, this require-

Received October 22, 2014; accepted after revision March 26, 2015.

From the Departments of Radiology and Radiological Sciences (A.A.D., M.K.S., C.C.F., V.L.M., T.R.L., L.M.D., M.J.D.), Pediatrics (L.C.J.), Division of Pediatric Neurology, Psychiatry (M.J.D.), and Neurology (M.J.D.), Vanderbilt University School of Medicine, Nashville, Tennessee; and Department of Physics and Astronomy (M.J.D.), Vanderbilt University, Nashville, Tennessee.

This work was supported by the National Institutes of Health/National Institute of Neurological Disorders and Stroke (5R01NS078828) and the American Heart Association (14GRNT20150004).

Paper previously presented at: American Society of Neuroradiology Annual Meeting and the Foundation of the ASNR Symposium, May 17–22, 2014; Montreal, Quebec, Canada.

Please address correspondence to Aditi A. Desai, MD, Department of Radiology and Radiological Sciences, 1161 21st Ave South, Medical Center North, Suite CCC-1121, Nashville, TN 37232-2675; e-mail: aditi.desai@vanderbilt.edu

Indicates open access to non-subscribers at www.ajnr.org

Indicates article with supplemental on-line tables.

http://dx.doi.org/10.3174/ajnr.A4419

ment also sensitizes the sequence to susceptibility variations between implants and surrounding tissue. This feature adds variability to the static magnetic field (B0) and may manifest as distortion or signal voids.

The influence of implants on the quality of the diagnostic information has been historically defined as "MR imaging compatibility." Medical devices labeled "MR imaging compatible" were MR imaging–safe and did not affect the quality of the diagnostic information. However, due to ongoing confusion with medical labeling, in 2005, the US Food and Drug Administration recognized a new set of terms by the American Society for Testing and Materials international, which included the influence of implants on image quality, and requested manufacturers to use the terminology for new products. However, there remains a fundamental need to define the extent of image artifacts, because manufacturers frequently provide only general statements regarding the possible impact on image quality.[5] Furthermore, such MR imaging compatibility is most commonly considered in the context of conventional structural MR imaging sequences that use short TEs,[6-8] avoid single-shot echo-planar imaging readouts, and/or may not use parallel imaging, all of which are commonly used in BOLD fMRI. Thus, the impact of implants specifically on BOLD fMRI signal quality is not well-characterized.

For cerebral hemodynamic measurements derived from BOLD MR imaging to be reliable in routine clinical practice, susceptibility-induced influences of endovascular and surgical hardware on BOLD MR imaging must be characterized, particularly in studies that require imaging before and after implantation of surgical hardware. The purpose of this study was to review BOLD fMRI examinations performed clinically at 3T and to calculate the volume and artifact extent in patients with implants, as well as the degree to which the artifact impacts the clinical utility of the study. This information is intended to serve as an exemplar for when BOLD fMRI scans may remain interpretable, even in the presence of surgically implanted hardware.

MATERIALS AND METHODS

Patient Demographics and Ethical Considerations

This study was approved by our local institutional review board and conformed to the requirements of the United States Health Insurance Portability and Accountability Act. We conducted a retrospective analysis of all BOLD MRI acquired clinically (January 2006 to March 2014) at our institution as part of 2 separate institutional review board–approved studies. In one study, patients were prospectively recruited to undergo BOLD MR imaging by using a CVR protocol (institutional review board No. 110468, $n = 80$). Additionally, clinical BOLD MR imaging was performed by using a protocol with functional tasks for language or motor localization (functional localizer protocol, $n = 263$). An institutional review board exemption was obtained to retrospectively review data from the functional localizer protocol (institutional review board No. 150190).

Implant manufacturer and model were obtained when available in the electronic medical record, and all patients were screened per departmental policy to determine the MR imaging compatibility and safety of implants before scanning, following the American College of Radiology recommendations for safe MR imaging practices.[9]

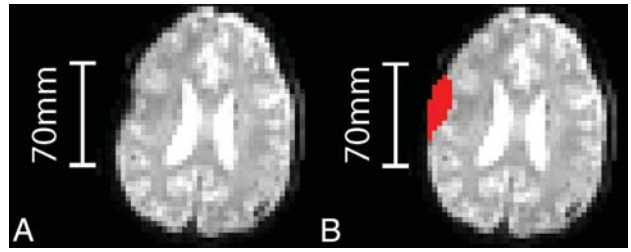

FIG 1. Representative images of artifact masks, which colocalize with areas of signal loss. *A*, A representative section from the magnitude gradient echo BOLD fMRI volume in a patient with right-sided surgical closure hardware. *B*, The artifact mask (red). The volume of the mask was summed over all sections to quantify the total artifact volume.

MR Imaging Parameters

All patients in the CVR protocol were scanned by using 3T MR imaging (Achieva; Phillips Healthcare, Best, the Netherlands) with body coil transmission and sensitivity encoding 8-array coil reception with a multimodal protocol, which included hypercarbic BOLD: spatial resolution = 3.4 × 3.4 × 5 mm^3, single-shot gradient-echo EPI, TR/TE = 2000/35 ms, flip angle = 80°, sensitivity encoding factor = 2, 30 sections; and a block paradigm of 3/3 minutes baseline (room air)/5% carbogen (5% CO_2, 95% O_2) breathing repeated twice. Patients undergoing the functional localizer protocol were scanned by using the same scanner with a slightly modified protocol: spatial resolution = 3.75 × 3.75 × 5.00 mm^3, single-shot gradient-echo EPI, TR/TE = 2000/35 ms, flip angle = 78°, sensitivity encoding factor = 1.8, 30 sections. The TE and readout type (single-shot gradient-echo EPI) were identical for both protocols; the total voxel volume (57.8 versus 52.7 mm^3) and parallel imaging factor (2.0 versus 1.8) were nearly identical between protocols and within the range of common fMRI acquisition parameters (see "Discussion").

Analysis

All fMRI data were corrected for motion and baseline drift and were coregistered to T1 and standard space (Montreal Neurological Institute, 2 mm) by using linear registration routines from the fMRI of the Brain Software Library (FSL; http://www.fmrib.ox.ac.uk/fsl).[10] Dephasing artifacts associated with metallic objects on BOLD MR imaging were overseen by a board-certified neuroradiologist (M.K.S. with 13 years' experience) and were quantified on all patients with implanted hardware by manually drawing ROIs demarcating areas of signal loss on each affected image section (Fig 1). These data were then summed to yield a total artifact volume (cubic centimeters). In patients with multiple ipsilateral implants, artifact volume per hemisphere was summated, because implant proximity precluded the ability to distinguish the extent of artifacts associated with each individual implant in subjects with bilateral implants. In patients with bilateral implants, right and left hemisphere artifacts were calculated separately. Additional analysis was performed to calculate the time course signal-to-noise ratio in each voxel by measuring the ratio of the mean baseline signal to the SD of the baseline signal with time.

All BOLD MRIs were reviewed by a fellowship-trained, board-certified neuroradiologist (M.K.S) and a MR imaging physicist (V.L.M. with 15 years' experience) to characterize the degree that artifact volume impacted clinical interpretability by using the following scale: none = no compromise of functional interpretation

Table 1: Intracranial implants

Patient, Location, and Implant Type	Model	Material	Total Volume (cm^3) from Artifacts	Impact on Clinical Interpretation
Patient 1			3.1	Mild
MCA stent	Wingspan stent[a]	Titanium, nickel alloy		
Patient 2A			9.4	None
ICA stent	Unknown	Unknown		
Anterior choroidal artery coils	Unknown	Unknown		
Patient 2B			8.7	None
ICA bifurcation aneurysm clip	Yasargil clip[b]	Titanium		
Patient 3			2.1	Mild
MCA stent	Pharos Vitesse stent	Titanium, nickel alloy		
Patient 4			4.7	Mild
Posterior communicating artery aneurysm coils	Matrix Soft coils[c]	Platinum		
	Matrix Ultrasoft coils[c]	Platinum		
	Guglielmi detachable coil–10 Soft coils[c]	Platinum		
	Sapphire Tension Safe coils[d]	Platinum		
ICA stent	Neuroform EZ stent[c]	Titanium, nickel alloy		
Patient 5			1.1	None
Anterior communicating artery aneurysm coils	Target 360 coils[c]	Platinum		

[a] Manufactured by Stryker, Kalamazoo, Michigan for Boston Scientific, Natick, Massachusetts.
[b] Aesculap, Center Valley, Pennsylvania.
[c] Stryker, Kalamazoo, Michigan.
[d] Micro Therapeutics, Irvine, California.

Table 2: Artifacts from surgically implanted hardware

Hardware Type	Average Artifact Volume (cm^3)	SD	Range (cm^3)
Intracranial hardware	4.3	3.2	1.1–9.4
Extracranial hardware (CVR protocol)	28.4	14.0	6.1–61.7
Extracranial hardware (functional localizer protocol)	39.9	27.0	6.9–77.1
Ventriculoperitoneal shunt	95.7	39.3	64.0–139.6

from hardware artifact (eg, hardware artifacts do not project onto the parenchyma); mild = hardware artifacts present but do not compromise clinical interpretation; moderate = hardware artifacts somewhat limit, but do not preclude, clinical interpretation; severe = hardware artifacts preclude clinical interpretation.

RESULTS

In patients in the CVR protocol, 26 of 80 (32.5%) had surgical hardware: intracranial implants ($n = 5$), extracranial hardware ($n = 19$), and ventriculoperitoneal (VP) shunts ($n = 2$). Intracranial implant characteristics are summarized in Table 1. Implanted extracranial hardware (On-line Table 1) primarily included closure hardware composed of titanium alloy and 1 patient with a polyethylene implant. Six of 19 patients had bilateral closure hardware with artifact sizes calculated separately by hemisphere, for a total of 25 hemispheres. Implanted VP shunts are described in On-line Table 2**.** Artifacts from surgically implanted hardware are shown in Table 2.

In patients in the functional localizer protocol, 14 of 263 (5.3%) had surgical hardware: extracranial hardware ($n = 13$) and VP shunt ($n = 1$). Extracranial hardware comprised surgical closure hardware, and implant records were not available for these patients. The implanted VP shunt is included in On-line Table 2.

Mean artifact volume associated with intracranial hardware in patients undergoing the CVR protocol was 4.3 ± 3.2 cm^3; range = 1.1–9.4 cm^3. As a point of reference, the average volume of the adult human brain is approximately 1380 cm^3.[11] The small artifact volume associated with implanted intracranial hardware did not compromise the functional interpretation of cerebral hemodynamic data, with intracranial implants considered to have no ($n = 3$) or mild ($n = 3$) effect on the clinical interpretability of the examination in the affected hemisphere. Figure 2 shows a representative image maximally affected by implanted intracranial hardware and hemodynamic data from a patient with a left MCA stent with in-stent restenosis, demonstrating the impact of the artifacts on the reactivity map.

Mean artifact volume of extracranial hardware in patients in the CVR protocol was 28.4 ± 14.0 cm^3; range = 6.1–61.7 cm^3; and in patients in the functional localizer protocol, it was 39.9 ± 27.0 cm^3 (range = 6.9–77.1 cm^3). Artifact volume associated with titanium closure hardware is typically small and peripheral, with 19 of the evaluated hemispheres (76%) considered to have mild artifacts, which did not compromise clinical interpretation of cerebral hemodynamics (Fig 3). Closure hardware artifacts in 5 of the evaluated hemispheres (20%) had a moderate effect on the clinical interpretation. However, in the patient (patient 10) with the largest number of maxDrive screws (KLS-Martin, Jacksonville, Florida),[12] artifact size (61.7 cm^3) was rated as severe and precluded ipsilateral CVR interpretation in the region of the indirect revascularization that underlay the closure hardware (Fig 4). These artifacts were larger than those in other patients with fewer KLS-Martin LP maxDrive screws (patient 20: 5 screws, artifact volume = 17.1 cm^3;

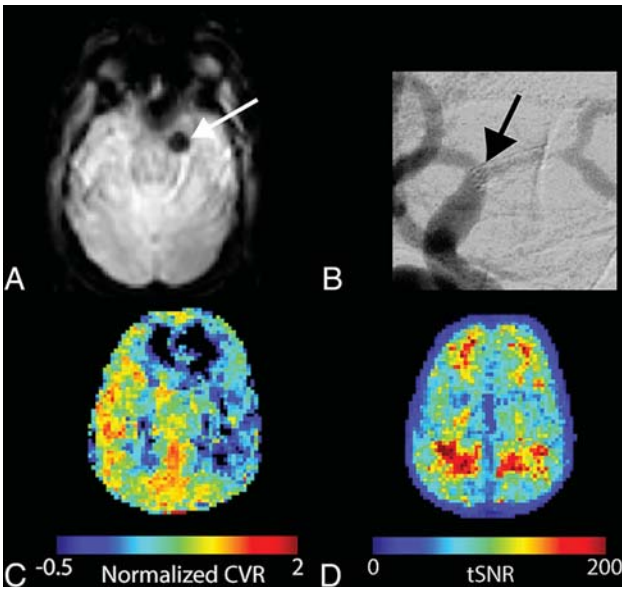

FIG 2. A representative patient (patient 3) with an intracranial implant. Signal drop-out from a left MCA Pharos Vitesse stent (Codman Neurovascular) is apparent on the magnitude BOLD fMRI image (*A*, *white arrow*), resulting in a total artifact volume of 2.1 cm^3, which only mildly affected clinical interpretation of the examination. The patient was evaluated 2 years following implantation of the Pharos Vitesse stent in a stenosed left MCA. DSA (*B*) shows in-stent restenosis (*black arrow*), with corresponding decreased cerebrovascular reactivity (normalized CVR: voxel CVR normalized to cerebellar CVR) in the left MCA territory (*C*). In contrast, there is relative symmetry of the temporal signal-to-noise ratio (tSNR) map (*D*), suggesting that the asymmetric hemodynamic findings are not attributable to artifacts.

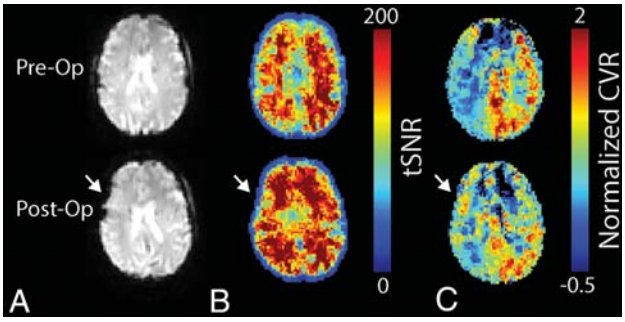

FIG 3. A patient with Moyamoya disease and asymmetric right-sided intracranial stenosis who underwent right encephaloduroanrteriosynangiosis. Comparison of pre- (Pre-Op) and postoperative (Post-Op) magnitude BOLD images (*A*) shows minimal artifacts (26.5 cm^3) associated with the closure hardware (LP Plate 0.6 × 15 mm, Low Profile Micro Plate, and Cross-Drive 1.5 × 4 mm screws; KLS-Martin) at the corresponding surgical site, which was determined to only mildly impact clinical interpretation of the study. Both pre- and postoperative temporal signal-to-noise ratio (tSNR) maps (*B*) demonstrate relatively symmetric tSNR, while pre- and postoperative CVR maps (*C*) show decreased CVR in the right hemisphere along the right frontal cortex, which improves following revascularization.

patient 21: 8 screws, artifact volume = 24.6 cm^3). The number of screws did not correlate directly with artifact volume across screw types, with up to 19 LP Cross-Drive screws (KLS-Martin) in 1 patient causing fewer artifacts (23.5 cm^3) than the 12 KLS-Martin maxDrive screws (61.7 cm^3).

The average artifacts associated with VP shunts were 95.7 ± 39.3 cm^3, range = 64.0–139.6 cm^3, and were rated as severe in 2 of

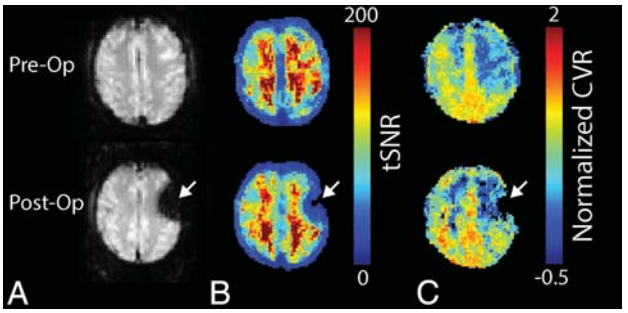

FIG 4. Pre- (Pre-Op) and postoperative (Post-Op) magnitude and hemodynamic images in a patient with left-sided idiopathic Moyamoya disease who underwent a left encephaloduroarteriosynangiosis with implantation of closure hardware. Magnitude images (*A*) demonstrate the large artifacts (61.7 cm^3) associated with surgical closure hardware, attributable to the large number of KLS-Martin maxDrive screws. Artifacts were thought to severely impact clinical interpretation of the study, and hemodynamic evaluation with temporal signal-to-noise ratio maps (*B*) and reactivity maps (*C*) shows that interpretable hemodynamic data were not obtainable near the closure hardware. tSNR indicates temporal signal-to-noise ratio.

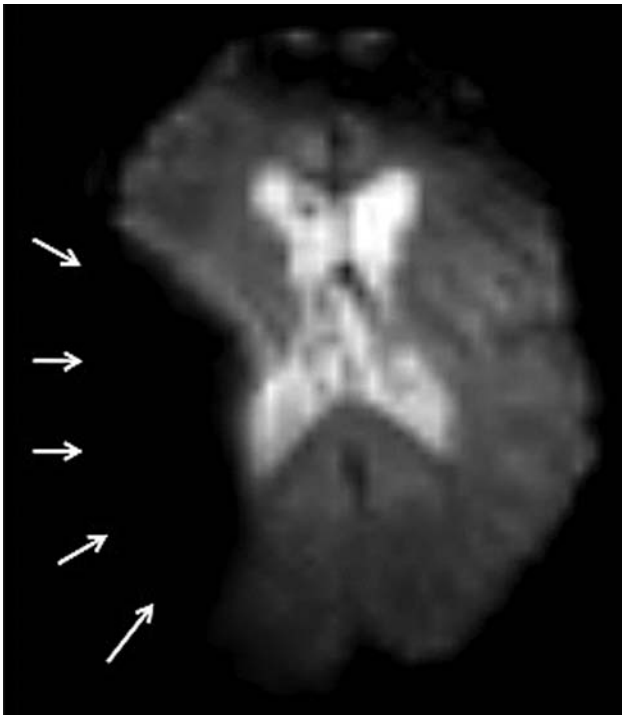

FIG 5. Artifacts (*white arrows*, volume = 139.6 cm^3) associated with a ventriculoperitoneal shunt with a Certas programmable valve and siphon gauge (Codman and Shurtleff).

3 patients (Fig 5, CVR protocol) and moderate in the remaining patient (functional localizer protocol).

DISCUSSION

Specificity of Different Implants on BOLD fMRI Artifact Volume

Dephasing artifacts on MR imaging associated with implanted devices are caused by perturbations in the magnetic field due to differences in magnetic susceptibility or the degree of magnetization of an object in the presence of a magnetic field between the implanted device and surrounding tissue. Larger differences in

magnetic susceptibility between an implanted device and surrounding tissue lead to larger perturbations of the magnetic field and greater spectral dispersion of spins within a voxel, resulting in more extensive dephasing artifacts. In BOLD fMRI, long-TE, T2*-weighted imaging is used to sensitize the sequence to susceptibility differences between oxygenated and deoxygenated blood, but these imaging parameters also render the sequence exquisitely sensitive to susceptibility variations from magnetic field inhomogeneities, exacerbating artifact extent.[6-8] The effect of increased dephasing artifacts associated with implants on the quality of data obtained specifically from BOLD MR imaging has not been previously well-documented, to our knowledge. Our results demonstrate that BOLD MR imaging is interpretable in the presence of most implants evaluated, except for VP shunts, particularly those with programmable valves and siphon gauges and 1 patient with multiple KLS-Martin maxDrive screws.

The intracranial implants and extracranial hardware analyzed are composed of materials with low magnetic susceptibilities, such as titanium, nickel, platinum, or their alloys. All intracranial implanted devices produced small artifacts that had no-to-mild effects on clinical interpretability, and closure hardware typically resulted in small, peripheral artifacts that did not preclude interpretation. The single notable exception was a patient with a large number of KLS-Martin maxDrive screws, which were associated with more artifacts than the KLS-Martin Cross-Drive screws. While both the maxDrive and Cross-Drive screws are made of a titanium and nickel alloy, the maxDrive screw has a larger head profile. The number of screws did not correlate directly with artifacts across screw types.

In contrast, VP shunts resulted in large artifacts that produced a moderate-to-severe impact on clinical interpretation, an effect attributable to the shunt valve composition. The valve portion of the VP shunt is composed of 316L stainless steel in addition to unalloyed titanium and tantalum in some models.[12,13] Stainless steel contains iron, a ferromagnetic substance. While 316L stainless steel contains a larger amount of nickel, which stabilizes iron in its nonmagnetic state and reduces its magnetic susceptibility, its magnetic susceptibility remains larger relative to titanium, resulting in larger perturbations of the magnetic field and more extensive artifacts.[14,15] In addition, the Certas programmable valve (Codman & Shurtleff, Raynham, Massachusetts) contains neodymium magnets, which caused extensive signal loss[13,16,17] and likely contributed to the large artifact volume (139.6 cm^3) relative to other VP shunts evaluated (64.0 and 83.5 cm^3).

Studies have described the effect of previously implanted surgical hardware on BOLD fMRI in the preoperative evaluation of brain tumor resection, demonstrating that language lateralization and primary motor cortex activation can be ascertained despite a reduction in total volume activation due to susceptibility artifacts.[18,19] Our study confirms the feasibility of obtaining data despite implants, which is particularly important in patients with cerebrovascular disease because longitudinal monitoring of patients before and after revascularization may be desired.

Imaging Parameters and Artifact Volume

Artifact volume will vary with imaging readout and scan parameters.[20] We have used scan parameters that are common for BOLD fMRI on all major vendor platforms, including single-shot gradient-echo EPI, voxel volume = 50–60 mm^3, and TE centered on the approximate 3T tissue T2* (eg, 35 ms).[21,22] We also used image-based parallel imaging (sensitivity encoding) with an acceleration factor of 1.8–2.0, which reduces the EPI readout train by an approximate factor of 2. Geometric distortions from off-resonant spins and signal drop-out are largely affected by susceptibility gradients, and parallel imaging can reduce these issues by increasing the per-voxel bandwidth in the phase-encoding direction,[23] thereby resulting in a shorter EPI readout (eg, approximately 36 ms without parallel imaging versus 18 ms with parallel imaging by using scan parameters in our sequences). While we used sensitivity encoding in our protocol, which is common on Philips scanners, *k*-space parallel imaging by using Generalized Autocalibrating Partial Parallel Acquisition or Autocalibrating Reconstruction for Cartesian sampling is more common on Siemens and GE Healthcare scanners, respectively, and performs comparably for reducing geometric distortions when similar acceleration factors are used. In the absence of parallel imaging, partial *k*-space acquisitions may also be used to reduce geometric distortions.

Limitations

First, information regarding implant manufacturer and type is not known for all implants considered, precluding a rigorous analysis in all patients. However, the composition of implants evaluated is similar to that in other commonly deployed implants; thus, results may generalize. Of the patients with intracranial implants analyzed, 1 (patient 2A) had incomplete information available regarding embolization coils and an ipsilateral stent, though this patient had an artifact size (9.4 cm^3) similar to that in another patient (patient 4A) with known platinum embolization coils and an ipsilateral titanium and nickel alloy stent (4.7 cm^3). Indeed, most embolization coils are composed of platinum, with only the earliest models containing stainless steel,[24,25] and most intracranial stents are composed of titanium, titanium alloys, or stainless steel.[24,26,27] Thus, our finding that the small artifacts produced by intracranial implants do not impact clinical interpretability of BOLD fMRI is likely generalizable, with the exception of those models of intracranial implants that contain stainless steel, which were not evaluated in our study population and may produce larger artifacts due to higher magnetic susceptibility.

Information regarding specific implant manufacturers and composition was not available for a subset of patients with extracranial implants (CVR protocol, $n = 2$; functional localizer protocol, $n = 13$). However, those patients with unknown closure hardware had artifact extent and clinical interpretability similar to those in patients with known extracranial hardware, which primarily included closure hardware composed of titanium alloy. Most implanted neurosurgical hardware is composed of titanium or titanium alloys similar to those evaluated in our study,[24,25] suggesting that results are likely generalizable. We did not evaluate any issues related to the safety of metallic devices; however, this topic has been studied extensively, and all patients were screened by using standard MR imaging safety screening procedures.[9]

Second, while BOLD fMRI is the most common noninvasive

fMRI application, additional methods such as arterial spin-labeling are being increasingly used.[28] We did not specifically evaluate the impact of artifacts on arterial spin-labeling image quality; however, arterial spin-labeling generally uses readouts similar to those in BOLD (eg, single-shot EPI with comparable spatial resolution), however with a shorter TE (eg, 10–20 ms). Thus, the impact of image distortion on similar data should be reduced relative to BOLD, and findings from this study could provide a conservative reference for guiding similar studies.

Third, this study focused on patients undergoing BOLD fMRI for clinical purposes, primarily those with cerebrovascular disease, epilepsy, and brain tumors. Thus, implants considered were specific to these populations, and a different population may have a higher fraction of implants not considered in this study. Therefore, while we hope that the findings of this study are useful for guiding imaging decisions in some of the most common types of patients undergoing BOLD fMRI, future studies incorporating a broader range of patients and implant types would be useful.

CONCLUSIONS

Three-Tesla single-shot gradient-echo EPI BOLD MR imaging performed on patients with a variety of implanted intracranial and extracranial hardware yields interpretable image quality in most patients beyond a small (30–40 cm^3) volume surrounding the hardware. Exceptions were VP shunts, particularly those with programmable valves and siphon gauges, and large numbers of KLS-Martin maxDrive screws.

Disclosures: Aditi A. Desai—*RELATED*: *Grant*: National Institutes of Health,* *Comments*: The study was funded by a National Institutes of Health grant. Megan K. Strother—*RELATED*: *Grant*: National Institutes of Health/National Institute of Neurological Disorders and Stroke R01 NS078828–01A1.* Carlos C. Faraco—*RELATED*: *Grant*: National Institutes of Health,* *Comments*: T-32 Postdoctoral Fellow Training Grant. Lori C. Jordan—*UNRELATED*: *Grants/Grants Pending*: American Heart Association Collaborative Science Award,* *Comments*: to study novel MRI techniques in sickle cell disease. Manus J. Donahue—*RELATED*: *Grant*: National Institutes of Health grants (National Institutes of Health/National Institute of Neurological Disorders and Stroke and National Institutes of Health/National Institute of Nursing Research).* *Money paid to the institution.

REFERENCES

1. Håberg A, Kvistad KA, Unsgård G, et al. **Preoperative blood oxygen level-dependent functional magnetic resonance imaging in patients with primary brain tumors: clinical application and outcome.** *Neurosurgery* 2004;54:902–14; discussion 914–15
2. Binder JR. **Functional MRI is a valid noninvasive alternative to Wada testing.** *Epilepsy Behav* 2011;20:214–22
3. Mandell DM, Han JS, Poublanc J, et al. **Mapping cerebrovascular reactivity using blood oxygen level-dependent MRI in patients with arterial steno-occlusive disease: comparison with arterial spin labeling MRI.** *Stroke* 2008;39:2021–28
4. Donahue MJ, Dethrage LM, Faraco CC, et al. **Routine clinical evaluation of cerebrovascular reserve capacity using carbogen in patients with intracranial stenosis.** *Stroke* 2014;45:2335–41
5. Shellock FG, Woods TO, Crues JV 3rd. **MR labeling information for implants and devices: explanation of terminology.** *Radiology* 2009;253:26–30
6. Schenck JF. **The role of magnetic susceptibility in magnetic resonance imaging: MRI magnetic compatibility of the first and second kinds.** *Med Phys* 1996;23:815–50
7. Port JD, Pomper MG. **Quantification and minimization of magnetic susceptibility artifacts on GRE images.** *J Comput Assist Tomogr* 2000;24:958–64
8. Koch KM, Hargreaves BA, Pauly KB, et al. **Magnetic resonance imaging near metal implants.** *J Magn Reson Imaging* 2010;32:773–87
9. Kanal E, Barkovich AJ, Bell C, et al; Expert Panel on MR Safety. **ACR guidance document on MR safe practices: 2013.** *J Magn Reson Imaging* 2013;37:501–30
10. Jenkinson M, Beckmann CF, Behrens TE, et al. **FSL.** *Neuroimage* 2012;62:782–90
11. Filipek PA, Richelme C, Kennedy DN, et al. **The young adult human brain: an MRI-based morphometric analysis.** *Cereb Cortex* 1994;4:344–60
12. Shellock FG, Bedwinek A, Oliver-Allen M, et al. **Assessment of MRI issues for a 3-T "immune" programmable CSF shunt valve.** *AJR Am J Roentgenol* 2011;197:202–07
13. Shellock FG, Wilson SF, Mauge CP. **Magnetically programmable shunt valve: MRI at 3-Tesla.** *Magn Reson Imaging* 2007;25:1116–21
14. Vaccaro AR, Chesnut RM, Scuderi G, et al. **Metallic spinal artifacts in magnetic resonance imaging.** *Spine (Phila Pa 1976)* 1994;19:1237–42
15. Khursheed F, Rohlffs F, Suzuki S, et al. **Artifact quantification and tractography from 3T MRI after placement of aneurysm clips in subarachnoid hemorrhage patients.** *BMC Med Imaging* 2011;11:19
16. Lavinio A, Harding S, Van Der Boogaard F, et al. **Magnetic field interactions in adjustable hydrocephalus shunts.** *J Neurosurg Pediatr* 2008;2:222–28
17. Toma AK, Tarnaris A, Grieve JP, et al. **Adjustable shunt valve-induced magnetic resonance imaging artifact: a comparative study.** *J Neurosurg* 2010;113:74–78
18. Kim MJ, Holodny AI, Hou BL, et al. **The effect of prior surgery on blood oxygen level-dependent functional MR imaging in the preoperative assessment of brain tumors.** *AJNR Am J Neuroradiol* 2005;26:1980–85
19. Peck KK, Bradbury M, Petrovich N, et al. **Presurgical evaluation of language using functional magnetic resonance imaging in brain tumor patients with previous surgery.** *Neurosurgery* 2009;64:644–52; discussion 652–53
20. Hargreaves BA, Worters PW, Pauly KB, et al. **Metal-induced artifacts in MRI.** *AJR Am J Roentgenol* 2011;197:547–55
21. Donahue MJ, Hoogduin H, van Zijl PC, et al. **Blood oxygenation level-dependent (BOLD) total and extravascular signal changes and ΔR2* in human visual cortex at 1.5, 3.0 and 7.0 T.** *NMR Biomed* 2011;24:25–34
22. Rane S, Mason E, Hussey E, et al. **The effect of echo time and post-processing procedure on blood oxygenation level-dependent (BOLD) functional connectivity analysis.** *Neuroimage* 2014;95:39–47
23. Schmiedeskamp H, Newbould RD, Pisani LJ, et al. **Improvements in parallel imaging accelerated functional MRI using multiecho echo-planar imaging.** *Magn Reson Med* 2010;63:959–69
24. Shellock FG. *Reference Manual for Magnetic Resonance Safety, Implants, and Devices: 2014 Edition.* Los Angeles: Biomedical Research Publishing Group; 2014
25. Shellock FG. **Metallic neurosurgical implants: evaluation of magnetic field interactions, heating, and artifacts at 1.5-Tesla.** *J Magn Reson Imaging* 2001;14:295–99
26. Lövblad KO, Yilmaz H, Chouiter A, et al. **Intracranial aneurysm stenting: follow-up with MR angiography.** *J Magn Reson Imaging* 2006;24:418–22
27. Choi JW, Roh HG, Moon WJ, et al. **Optimization of MR parameters of 3D TOF-MRA for various intracranial stents at 3.0T MRI.** *Neurointervention* 2011;6:71–77
28. Donahue MJ, Strother MK, Hendrikse J. **Novel MRI approaches for assessing cerebral hemodynamics in ischemic cerebrovascular disease.** *Stroke* 2012;43:903–15

Outcome Differences between Intra-Arterial Iso- and Low-Osmolality Iodinated Radiographic Contrast Media in the Interventional Management of Stroke III Trial

T.A. Tomsick, L.D. Foster, D.S. Liebeskind, M.D. Hill, J. Carrozella, M. Goyal, R. von Kummer, A.M. Demchuk, I. Dzialowski, V. Puetz, T. Jovin, H. Morales, Y.Y. Palesch, J. Broderick, P. Khatri, and S.D. Yeatts, for the IMS III Investigators

ABSTRACT

BACKGROUND AND PURPOSE: Intracarotid arterial infusion of nonionic, low-osmolal iohexol contrast medium has been associated with increased intracranial hemorrhage in a rat middle cerebral artery occlusion model compared with saline infusion. Iso-osmolal iodixanol (290 mOsm/kg H_2O) infusion demonstrated smaller infarcts and less intracranial hemorrhage compared with low-osmolal iopamidol and saline. No studies comparing iodinated radiographic contrast media in human stroke have been performed, to our knowledge. We hypothesized that low-osmolal contrast media may be associated with worse outcomes compared with iodixanol in the Interventional Management of Stroke III Trial (IMS III).

MATERIALS AND METHODS: We reviewed prospective iodinated radiographic contrast media data for 133 M1 occlusions treated with endovascular therapy. We compared 5 prespecified efficacy and safety end points (mRS 0–2 outcome, modified TICI 2b-3 reperfusion, asymptomatic and symptomatic intracranial hemorrhage, and mortality) between those receiving iodixanol (n = 31) or low-osmolal contrast media (n = 102). Variables imbalanced between iodinated radiographic contrast media types or associated with outcome were considered potential covariates for the adjusted models. In addition to the iodinated radiographic contrast media type, final covariates were those selected by using the stepwise method in a logistic regression model. Adjusted relative risks were then estimated by using a log-link regression model.

RESULTS: Of baseline or endovascular therapy variables potentially linked to outcome, prior antiplatelet agent use was more common and microcatheter iodinated radiographic contrast media injections were fewer with iodixanol. Relative risk point estimates are in favor of iodixanol for the 5 prespecified end points with M1 occlusion. The percentage of risk differences are numerically greater for microcatheter injections with iodixanol.

CONCLUSIONS: While data favoring the use of iso-osmolal iodixanol for reperfusion of M1 occlusion following IV rtPA are inconclusive, potential pathophysiologic mechanisms suggesting clinical benefit warrant further investigation.

ABBREVIATIONS: EVT = endovascular therapy; IA = intra-arterial; ICH = intracranial hemorrhage; IMS III = Interventional Management of Stroke III Trial; IRCM = iodinated radiographic contrast media; LOCM = low-osmolal contrast media; MCI = microcatheter injection; mTICI = modified TICI; SICH = symptomatic intracranial hemorrhage

Iodinated radiographic contrast media (IRCM) have variable antithrombotic, fibrinolytic, cytotoxic, hydrostatic, and vasoactive effects. In a rat middle cerebral artery reperfusion model, intracarotid arterial infusion of the nonionic low-osmolal contrast medium (LOCM) iohexol (672 mOsm/kg. H_2O) increased intracerebral hemorrhage (ICH) compared with saline infusion.[1] Iso-osmolal iodixanol (290 mOsm/kg H_2O) infusion led to

Received November 19, 2014; accepted after revision March 3, 2015.

From the Department of Radiology (T.A.T., J.C., H.M.), University of Cincinnati Academic Health Center, University Hospital, Cincinnati, Ohio; Department of Public Health Sciences (L.D.F., Y.Y.P., S.D.Y.), Medical University of South Carolina, Charleston, South Carolina; University of California, Los Angeles Stroke Center (D.S.L.), Los Angeles, California; Department of Radiology and Clinical Neurosciences (M.D.H., M.G.) and Calgary Stroke Program (A.M.D.), Department of Clinical Neurosciences/Medicine/Community Health Sciences, Hotchkiss Brain Institute, University of Calgary, Calgary, Alberta, Canada; Departments of Neuroradiology (R.v.K.) and Neurology (V.P.), Dresden University Stroke Center, Universitätsklinikum Carl Gustav Carus Technischen Universität Dresden, Dresden, Germany; Department of Neurology (I.D.), Elblandklinikum Meissen, Academic Teaching Hospital of Universitätsklinikum, Carl Gustav Carus Technische Universität Dresden, Meißen, Germany; Department of Neurology (J.B., P.K.), University of Cincinnati Academic Health Center, Cincinnati, Ohio; and The Stroke Institute (T.J.), University of Pittsburgh Medical Center, Pittsburgh. Pennsylvania.

This work was supported by grants from the National Institutes of Health and the National Institute of Neurological Disorders and Stroke (UC U01NS052220, MUSC U01NS054630, and U01NS077304) and by Genentech, EKOS, Concentric Medical, Cordis Neurovascular, and Boehringer Ingelheim.

Paper previously presented as a poster abstract at: International Stroke Conference, February 11–13, 2015 Nashville, Tennessee.

Please address correspondence to Thomas A. Tomsick, MD, University of Cincinnati Academic Health Center, UC Health, Department of Radiology, 234 Goodman St, Cincinnati, OH 45267-0761; e-mail: thomas.tomsick@uchealth.com

http://dx.doi.org/10.3174/ajnr.A4421

Table 1: Baseline clinical characteristics considered for adjusted analysis

	Iodixanol	LOCM[a]	*P* Value
Age[b] (median) (range) (yr)	73 (47–83)	68.5 (24–82)	.07
Baseline glucose[b] (mmol/L) (median) (range)	6.9 (5.2–18.3)	6.6 (3.8–21.5)	.33
Diabetes (%)	19.4	17.7	.83
Baseline SBP (mm Hg)[b] (median) (range)	145.5 (116–185)	146 (102–194)	.82
History of high BP (%)	74.2	73.5	.94
Atrial fibrillation (%)	48.4	35.3	.19
Coronary artery disease (%)	35.5	19.6	.07
ASPECTS 8–10[b] (%)	41.9	49.0	.49
Baseline NIHSS[b]			
≥20%	35.5	37.3	.86
≤19%	64.5	62.8	
Historical mRS (No. Sx)[b] (%)	90.3	86.3	.46
Antiplatelet agents (%)	67.7	44.1	.02
Presumptive stroke location right (%)	51.6	49.0	.80
Baseline CTA/MRA (%)	61.3	51.0	.31

Note:—Sx indicates symptoms; SBP, systolic blood pressure; BP, blood pressure.

[a] Four LOCM (mOsm/Kg H_2O): iohexol (672), iopamidol (616), ioversol (651), iopromide (607).[11]

[b] Baseline factors relevant to prespecified outcomes.

smaller infarcts and less ICH compared with both low-osmolal iopamidol and saline in a similar model.[2] Dzialowski et al[3] reported reduced odds of favorable outcome in patients receiving intravenous IRCM for CT angiography before IV thrombolysis.

Practical differences exist as well: IRCM differ in cost (ie, iodixanol is more expensive than LOCM) and ease of use (ie, iodixanol is more viscous and more difficult to inject). No study has prospectively and comprehensively compared outcomes according to intra-arterial (IA) IRCM use in endovascular therapy (EVT) of ischemic stroke in humans, to our knowledge. We report the efficacy and safety outcomes for subjects with EVT for MCA M1 occlusion in the Interventional Management of Stroke III Trial (IMS III) according to IRCM type and osmolality.

MATERIALS AND METHODS

Study eligibility/exclusion criteria, methods, and results have been previously reported.[4,5] Six hundred fifty-six subjects were randomized to either IV rtPA or IV rtPA plus endovascular therapy. CT angiography or MR angiography was not required but was allowed in centers where either was established as a local standard of evaluation and care. Five EVT methods were approved for use during the course of the trial (thrombolysis via standard microcatheter/guidewire rtPA infusion or the EkoSonic Endovascular System [EKOS, Bothell, Washington])[6]; clot removal via the Merci system (Concentric Medical, Mountain View, California),[7,8] Penumbra System (Penumbra, Alameda, California),[9] or Solitaire FR Retriever (Covidien, Irvine, California).[10] Intra-arterial rtPA infusion was also allowed as an adjuvant to mechanical thrombectomy. A 2000-U bolus of heparin was required per protocol for endovascular treatment procedures, followed by 500-U/h IV infusion.

The primary outcome measure was a modified Rankin Scale score of 0–2 at 90 days. Secondary EVT efficacy end points included revascularization, as measured by Modified Thrombolysis in Cerebral Infarction (mTICI) 2–3 and mTICI 2b–3 as ascribed by consensus of the Angiography Core Laboratory members (T.A.T., D.S.L.). Primary safety end points were 90-day mortality and symptomatic intracranial hemorrhage (SICH) within 30 hours of IV rtPA initiation, defined as an ICH temporally related to a decline in neurologic status and new or worsening neurologic symptoms in the judgment of the clinical investigator that may warrant medical intervention. Asymptomatic ICH within 30 hours of IV rtPA initiation was a secondary safety end point.

Investigators prospectively entered data on the IRCM compound type and volume for EVT subjects. The percentage of iodine concentration and/or specific IRCM osmolality was not consistently recorded. Clinical efficacy and safety end points were analyzed for subjects with EVT for M1 occlusion (defined as occlusion of the MCA trunk with 100% MCA distribution at risk, exclusive of a typical anterior temporal artery distribution), according to EVT use of either iso-osmolal iodixanol or any LOCM.

The 2 IRCM groups were initially compared for differences in prescribed outcomes that might warrant further comparative analysis. Baseline risk factors with a potential effect on clinical efficacy or safety outcome in revascularization therapy were then compared for balance between the 2 groups. Baseline variables imbalanced between IRCM types or associated with outcome ($P < .1$) were considered potential covariates for the adjusted models. Imbalance/association was measured by using the χ^2, Fisher, or Wilcoxon 2-sample test, as appropriate. The linearity in the logit assumption was checked for all continuous potential covariates. In addition to IRCM type, final covariates were those selected by using the stepwise method in a logistic regression model. Model fit was assessed via the Hosmer-Lemeshow test. For ease of interpretation, adjusted relative risks were then estimated by using a log-link regression model.

RESULTS

Thirty-one M1 occlusions were treated with iodixanol use during EVT, and 102, with LOCM of 4 different types. Differences in baseline characteristics known to be relevant in stroke efficacy or safety outcome with revascularization therapy and other relevant treatment-related variables are included in Tables 1 and 2.

Table 3 details relative and absolute efficacy and safety differences between the 2 IRCM groups.

Separate adjusted models were fit for each outcome (except SICH, due to an insufficient event rate). Variables imbalanced between IRCM types or associated with outcome ($P < .1$) were considered potential covariates for the adjusted models, including antiplatelet medication (67.7% iodixanol versus 44.1%, $P = .0212$), history of coronary artery disease (35.5% iodixanol versus 19.6%, $P = .0671$), age (iodixanol median, 73 versus 68.5 years, $P = .0698$), and microcatheter injection (MCI) (median, 1 iodixanol versus 2 LOCM; $P = .03$), varied according to IRCM type.

Adjusted relative risk point estimates were in favor of the iodixanol group for all outcomes (Table 4). No significant differences for specified outcomes were identified. Conclusions remained the same after sensitivity analyses were performed for asymptomatic ICH and

mRS 0–2 outcome models to include adjustments for variables known to be associated with these outcomes.

As a known variable affecting procedure outcome that was unequally distributed, MCIs were further analyzed. In bivariate analysis of MCI number compared with outcomes independent of the IRCM group, significant relationships were identified. Fewer MCIs were associated with greater mRS 0–2 outcome ($P = .029$) and better reperfusion ($P = .003$). MCI remained a significant predictor of reperfusion when adjusted for key baseline and treatment-related variables. MCIs were not significant predictors of mRS 0–2 or mortality when adjusted for other key variables. Ninety-one of 133 (68.5%) subjects had MCIs, including 16/31 (52%) with iodixanol and 75/102 (73.5%) with LOCM ($P = .022$). With MCI use, percentage risk differences in the measured end points were in favor of iodixanol for all end points. MCI use did not differ among device methods.

DISCUSSION

The potential risks and safety of IRCM use in the setting of acute stroke in humans have been discussed for a long time, with the advantages in diagnosis and treatment assumed to outweigh any theoretic, unproven risks.[11,12] However, with effective ischemic stroke therapies now available, investigation and deeper understanding of the theoretic effects of different media may assume greater practical significance.

Our analyses here disclose potential differences in outcomes from stroke treatment arising from the use of IA iso-osmolal iodixanol versus LOCM agents for EVT following IV rtPA in the setting of microcatheter use. Raw, unadjusted, and adjusted directions of effect were in favor of iodixanol for all prespecified efficacy and safety outcomes. Relatively greater age, blood glucose, percentage of atrial fibrillation, and CT hypoattenuation (as manifested by a lower ASPECT score), followed by relatively later IV rtPA administration, longer time to artery puncture, and more thrombolysis-only procedures, were present in the iodixanol group. Prior antiplatelet use, the only baseline variable significantly greater with iodixanol, has been associated with a small excess of SICH in systemic thrombolytic therapy.[13] While these factors should disadvantage iodixanol regarding mRS 0–2 outcome and ICH rate, point estimates from adjusted analyses remain in favor of iodixanol. MCIs were less common in the iodixanol group. Procedures with no MCI showed no benefit to iodixanol use. When MCIs were analyzed according to IRCM use, however, a greater relative benefit was suggested with MCI iodixanol use compared with LOCM for all end points.

IRCM effects may be collectively related to their ionic or nonionic properties, iso-osmolality, and their molecular structure and size as monomers or dimers. Osmolality is, in part, related to iodine concentration, generally recommended at 300-mg per cent for cerebral use. Multiple iodine concentrations of the same IRCM compound type were used in IMS III. Consensus that the use of ionic high-osmolal IRCM was associated with worse outcome after infarction in humans and animals has eliminated their use in this setting.[11,12,14] LOCM nonionic media may contribute to ICH in animals.[1] Differences in ICH number and infarct area effects might also exist between injection of iso-osmolal and LOCM.[2] It is reasonable to further hypothesize, then, that nonionic iso-osmolal IRCM may have a less harmful net effect in the setting of acute stroke than nonionic LOCM. No comparative data in IV or IA IRCM use in human stroke are available to refute that hypothesis.[3]

Mechanisms contributing to potential differences in IRCM efficacy and safety have been extensively analyzed under a variety of experimental conditions in vitro and in animal models, including coagulation, direct cytotoxic, neurotoxic, osmotic, hydrostatic, and direct vasomotor effects.

Table 2: Relevant treatment-related variables considered for adjusted analysis

	Iodixanol	LOCM[a]	*P* Value
Time to IV therapy (min) (median)	124	115	.25
Onset to puncture (min) (median)	215	205	.29
Proximal M1 (vs distal) (%)	45.2	52.0	.51
Thrombolysis only (%)	41.9	36.2	.57
No. microcatheter injections (median)	1	2	.03
Heparin volume (U) (median)	3185	2986.8	.59
New emboli (%)	16.1	11.8	.54
IRCM volume (mL) (median)	85	64	.34
Infarct volume 24 hr (mL)[a] (median)	61.0	50.2	.23

[a] Four LOCM (mOsm/Kg H2O): iohexol (672), iopamidol (616), ioversol (651), iopromide (607).[11]

Table 3: Efficacy and safety outcomes according to iodixanol versus LOCM use

	Iodixanol (No.) (%)	LOCM (No.) (%)	Absolute % Risk Difference	Relative % Difference
N	31	102	–	–
mTICI 2b/3	16 (51.6)	42 (41.2)	10.4	20.2
mRS 0–2	11 (35.5)	31 (30.4)	5.1	14.4
AICH	9 (29.0)	42 (41.2)	−12.1	−29.6
SICH	2 (6.5)	9 (8.8)	−2.4	−26.1
Mortality	6 (19.4)	26 (25.5)	−6.1	−23.9

Note:—AICH indicates asymptomatic ICH.

Table 4: Relative risk of specified outcomes for iodixanol versus LOCM

	Unadjusted			Adjusted		
	RR	99% CI		RR	99% CI	
mRS 0–2	1.1675	0.5606	2.4314	1.2002	0.6123	2.3528
mTICI 2b/3	1.2535	0.7291	2.1549	1.2829	0.7888	2.0864
AICH	0.7051	0.3216	1.5457	0.6596	0.3051	1.4260
SICH	0.7312	0.1048	5.1038		NA	
Mortality	0.7593	0.2683	2.1486	0.7538	0.2767	2.0537

Note:—RR indicates relative risk; AICH, asymptomatic ICH.

Coagulation

Platelet Activity Effects. Direct activation of platelets (ie, degranulation and release of the procoagulant content of attenuated bodies and α-granules) is induced in vitro by nonionic LOCM, with no activation by LOCM ionic (eg, ioxaglate) and nonionic dimeric iodixanol.[15-17] Nonionic iohexol and iodixanol are equivalent in reducing platelet aggregation.[18,19] In vitro platelet activation by thrombin is inhibited by ionic LOCM, whereas nonionic monomeric LOCM and dimeric iodixanol did not affect it.[20] Prior antiplatelet use of aspirin conferred neither clinical nor reperfusion benefit nor hemorrhagic risk in conjunction with IV rtPA in the National Institute of Neurological Disorders and Stroke trial, and none has previously been demonstrated in EVT.[21,22] While antiplatelet use in IMS III tended to be associated with increased ICH overall, its use was more common in the iodixanol group, yet ICH was decreased with iodixanol use.

Thrombin Activity Effects. The heparin dose used during EVT did not differ between the 2 treatment groups. Nonionic agents cause less direct inhibition of thrombin production compared with ionic IRCM, acting after the generation of thrombin at the step of fibrin monomer polymerization.[23] Both ionic and nonionic agents can prolong clotting time and may exaggerate the effects of anticoagulant and antiplatelet drugs.[24] Nonionic LOCM iopamidol and iohexol have an anticoagulant effect but permit thrombin generation in vitro.[25-27] The anticoagulant effect of iodixanol has been shown to be significantly less than that of iohexol.[16] LOCM iopamidol has been found to have a greater thrombotic effect than iodixanol.[28] One of 3 clinical studies of coronary intervention found a significant decrease in abrupt vessel occlusions with iodixanol, particularly in the absence of glycoprotein IIb/IIIa blockers, while the other 2 found no differences in major cardiac events.[29] No differences in mortality or length of stay were found among 107,994 coronary angiographies or interventions with 3 different LOCM.[29] Outcome differences in IRCM effects between procedures performed for acute occlusive EVT have been suggested for coronary intervention yet have also been inconclusive due to limited power.[30]

Fibrinolytic Effects. IRCM delay and impede fibrinolysis by recombinant tissue-type plasminogen activator. In vitro studies have shown that while iohexol delays the onset of lysis induced by all lytic agents, ioxaglate delayed the onset of lysis by rtPA and urokinase but not by streptokinase.[31] In vivo studies in dogs have shown that alteplase-induced fibrinolysis could be inhibited by iohexol. Reocclusion of coronary arteries following fibrinolysis was more common after IRCM administration, despite concomitant aspirin and heparin therapy.[32] Iohexol has been demonstrated to increase plasma levels of tPA plasminogen activator inhibitor type 1 in patients undergoing pulmonary angiography.[33] In an in vitro model of the sonographic effect on fibrinolysis, very limited data suggested that iodixanol may diminish the rate of sonography-assisted thrombus dissolution.[34] While a meta-analysis investigating the fibrinolysis effect of IRCM of any type or route of administration (IV or IA) has suggested no difference in recanalization rates,[35] the wide range of fibrinolytic practices makes the study only marginally relevant to the potential effects of individual IRCM types with EVT of M1 occlusion in IMS III. Dzialowski et al[3] reported reduced odds of favorable outcome in patients receiving IV contrast for CT angiography before IV thrombolysis.

Cytotoxic and Osmotic Effects. Cytotoxic effects on endothelial cells may contribute to thrombosis. While no clinically significant differences among nonionic IRCM are confirmed, buckling of endothelial cells with alteration of function is less conspicuous with iodixanol.[36,37] IRCM can also induce apoptosis of endothelial cells in vitro.[38] Significant in vitro differences between IRCM on red blood cell count morphology may also contribute to thrombosis in vivo, with iodixanol retaining a greater percentage of normal morphology compared with LOCM agents.[39]

Both IV and IA IRCM injection increase the permeability of the blood-brain barrier under normal conditions in animals.[40-42] Osmolality plays an important role in the BBB dysfunction, particularly after ischemic injury, even contributing to larger infarcts with hyperosmolal compared with iso-osmolal IRCM infusion.[12] Hypertension, which may reflexly occur with arterial occlusion, potentiates the effect of these BBB effects.[43] In humans, IRCM identification in the brain or subarachnoid space after aneurysm coiling procedures by using large IRCM volumes is usually asymptomatic.[44,45] Theoretically, it is possible that large IV or IA doses of IRCM (as used in nonischemia EVT procedures) may contribute to exaggerated BBB opening, edema, IRCM deposition, and ICH in ischemic stroke EVT as well.[46,47]

Following acute ischemia in rats, early leakage of MR imaging contrast agents across the BBB has been shown to predict and co-localize to subsequent hemorrhagic transformation.[48,49] In humans, contrast media deposition during MR imaging and CT perfusion in the acute ischemic setting is also a marker of subsequent hemorrhagic transformation.[50-52] Depositions confirmed on both post-EVT CT and MR imaging have also co-localized to MR imaging contrast enhancement and hemorrhagic transformation.[53] MR imaging contrast deposition during routine gadolinium-enhanced MR imaging following IV rtPA occurs in approximately 20% of infarcts and is predictive of subsequent ICH.[54,55] Lummul et al[56] connected CT-hyperattenuated cerebral lesions with IRCM deposition following both CTA/CTP and subsequent EVT. The high incidence of hyperattenuated lesions and the percentage of secondary ICH suggest that they both may be IRCM-volume related. It remains unclear whether contrast media deposition is both effect and cause, with IRCM leaking across the BBB contributing to additive cytotoxic effects on the interstitium and neuronal elements. However, in IMS III, the median iodixanol volume was numerically higher than that for LOCM, suggesting that either worse measured outcome differences were not merely LOCM-volume-related or greater iodixanol volume exerted a protective effect.

Complex mechanisms beyond osmolality-related toxicity and dysfunction may be operative.[57,58] Heinrich et al[59] compared the cytotoxic effects of dimeric iso-osmolal IRCM (iodixanol, iotrolan) and iso-osmolal formulations of monomeric IRCM on renal tubular cells in vitro and found that dimeric IRCM have stronger cytotoxic effects, postulating a mechanism beyond osmolality alone. Molecular chemotoxicity decreases as the number of carboxyl groups decreases and the number of hydroxyl groups increases, and IRCM with no carboxyl groups and a number of

hydroxyl groups evenly distributed around the main molecule have reduced neurotoxicity.[60,61] Iodixanol has an increased number of hydroxyl groups ($n = 9$) compared with LOCM (eg, 5 for iopamidol), but more carboxy groups (6 versus 3), theoretically disadvantageous in human use. Increasing the number of hydroxyl groups also increases solubility, thus reducing the tendency to bind to tissues and proteins, which may then lead to inhibition of enzyme systems, including acetylcholinesterase.[62,63] The net vector for the benefit of the complex structural arrangement of iodixanol is uncertain.

Hyperosmolality-toxicity injury may be offset, in part, by a beneficial osmotic tonicity effect of intravascular IRCM on the intravascular and extracellular spaces based on molecular size. Dimeric iodixanol (1000 Da) is approximately twice as large as monomeric iopamidol (550 Da). Five times larger than mannitol (182 Da), iodixanol may not only be less able to traverse early damage to the BBB to exert adverse direct toxic or osmotic effects beyond endothelial cell tight junctions in the basal lamina or in the extracellular space, but it also may offer a microvascular osmotic advantage.[64] Conversely, monomeric LOCM may ultimately more easily traverse the damaged membrane to promote increased edema by an osmotic tissue effect. While conflicting evidence regarding increased neurotoxicity once the IRCM has crossed the BBB in animals and humans exists, [12,14,65-68] an additive effect of IRCM traversing the damaged BBB into the interstitium, affecting cellular and neural elements, contributing to greater ICH potential and neural injury, is hypothesized.

Hydrostatic Effects. Viscosity differences (iodixanol 11.8 cP at 37° versus iopamidol 4.7 cP) may simultaneously lead to a reduced hydrostatic effect of viscous, dimeric iodixanol, with prolonged vascular retention at the injured BBB, and may contribute to the reduced infarct edema volume measured in rats.[69] Hydrolysis of iodixanol in vitro can produce a derivative of propylene glycol (2,3-dihydroxy-1-propylamine HOCH2-CH [OH]-CH2-NH2), which, when injected intra-arterially in a rat ischemia model, has been found to decrease BBB dysfunction by a "sealing" effect, with subsequent decreased permeability and infarct size.[70] Similar hydrostatic IA "sealing" effects on the BBB could even be possible under certain conditions.[71,72] Molecule size alone may present a relative microvascular seal, delaying not only early ionic edema but also diminishing later vasogenic edema associated with hemorrhagic transformation.

Relatively reduced asymptomatic ICH and SICH with iodixanol in IMS III, despite the possibility of better mTICI reperfusion and larger infarct volume, contradict the theoretic construct of reperfusion ICH effects, suggesting that iodixanol may somehow offer an unrelated protective effect against ICH.[73] The mechanism of hemorrhagic transformation, though linked to reperfusion, infarct volume, and edema, might have a separate and different pathophysiologic pathway after reperfusion of acute ischemic stroke in humans and animals.[74,75] Infarct size and ICH differences are greater in rats with temporary-versus-permanent MCA occlusion.[76] Reduced infarct edema volume as a measure of reduced reperfusion injury with both LOCM-versus-saline reperfusion and viscous iso-osmolal-versus-less viscous LOCM has been found in rats.[1,2] In humans, improved mTICI reperfusion following ischemia would be anticipated to increase levels of reactive oxygen species, including superoxide radical and nitric oxide.[77,78] Oxidative radicals trigger activation of metalloproteinases, which, in turn, potentiate injury to microvasculature and neural cells.[79,80] However, IRCM may decrease the endothelial production of nitric oxide by reducing the activity of the enzyme nitric oxide synthase, which is responsible for the endogenous synthesis of this vasodilator.[81,82] Variable vasoactive effects of IRCM have been identified in the renal vasculature, where both iopamidol and iodixanol caused a brief initial vasodilation, followed by increased resistance with iopamidol, but not iodixanol.[83] Increased CO_2 release from the rat hippocampus incubated with the iso-osmolar dimers iotrolan and iodixanol has been measured, a potentiator of vasodilation. Increased CO_2 production could involve an effect of the glucose metabolic pathway or be indirect via an unspecified mechanism that increases cell glucose use.[84] Potential glucose metabolism effects of IRCM have been identified in vitro and in vivo for metrizamide, but not for iohexol or iopamidol. Clinically significant vasomotor differences in the cerebral vasculature in humans are unknown.

Miscellaneous Effects. IRCM have been reported to adversely affect oxyhemoglobin dissociation.[85] Decreased pH or increased temperature in the hypoxic brain tissue can cause changes in the physicochemical properties of IRCM as well. Increased BBB disruption has been demonstrated in rabbits with IA injection of higher iodine-concentration IRCM (300 versus 150 mg/mL), at a lower temperature (24°C versus 37°C), during a briefer time (1 versus 30 seconds).[86] The role that these miscellaneous effects might play in EVT can only be theorized.

ICH has been previously linked to microcatheter IRCM injections during EVT.[67,87] Microcatheter IRCM injections push saline ahead at higher initial pressures and flow rates, which decrease as the catheter becomes IRCM-filled (D. Hansmann, EKOS, unpublished data, 2014). The viscosity of iodixanol may diminish such distal catheter pressure and flow effects compared with LOCM, and it offers a relative safety margin reflected in lower ICH and SICH rates. Microcatheter IRCM injection delivers a higher concentration of IRCM locally within the occlusion, which then may wash out more slowly from patent or partially obstructed microvasculature, thereby amplifying protective hydrostatic microvascular iodixanol effects. Local microcatheter saline injections, used to clear catheters of IRCM, with pressure and flow increasing through the act of clearance, may be equally responsible for any untoward effects of IRCM MCI.

There are limitations to our results, analysis, and hypotheses. First, the importance of an unrecognized baseline or treatment factor may be underestimated. Prior antiplatelet and iodixanol use may favor revascularization and clinical outcomes in a way not previously demonstrated in IV or EVT revascularization studies. The specifics of recording IA injections of IRCM in a revascularization procedure leave room for wide ranges of practice variables that theoretically may have a secondary effect on outcome. Injections such as hand or power, intracranial microcatheter or cervical guide, saline-diluted or full-strength, high- or low-pressure, large- or low-volume may all be performed during the same procedure. Differences among operators that almost assuredly exist in all these variables may become relatively reproducible

within a the practice of a single operator or center. Site variables, then, might affect outcomes.

LOCM use following IV rtPA may not have the same effects by comparison in the absence of IV rtPA. While the impact of any proved, actionable differences between IRCM may be diminished in the current EVT atmosphere of shorter procedures with reduced IRCM volume use with application of devices not studied in IMS III, the use of MCI with LOCM may still prove to be a relevant risk factor.

While this is an analysis of a homogeneous population of M1 occlusion, new emboli during treatment in previously uninvolved vessels occurred in 12.8% of subjects with M1 occlusion in IMS III, numerically more common in the iodixanol group (16.1% versus 11.8%). An estimated 13% difference in mRS 0–2 outcomes between subjects with and without new emboli in IMS III has been reported.[4] While new emboli may have contributed to nonsignificantly larger infarcts in the iodixanol group, it remains unclear how larger infarcts relate to better clinical outcome.

CONCLUSIONS

A potential protective effect of iodixanol use in the EVT of M1 occlusion is proposed in IMS III, but perhaps only in the setting of MCI. Iodixanol contributes less endothelial cytotoxic effect to the thrombotic process. Its lower anticoagulant effect may diminish hemorrhagic transformation, with numerically fewer SICHs and fewer asymptomatic ICHs despite greater prior antiplatelet use. Its passage across the BBB is less than that with LOCM, while retaining a favorable osmotic microvascular potential. It may also have beneficial hydrostatic and vasoactive activity. The hypothesis that a small difference in outcomes may indeed exist by using different IRCM remains unproven in a small study population with only 50% of subjects with major arterial occlusion predisposed to good outcome.[88] Further analysis of not only the magnitude of the clinical effect potential of isosmolal IRCM but also the mechanisms conferring such benefit is warranted.

Disclosures: Thomas A. Tomsick—*RELATED*: *Grant*: University of Cincinnati,* *Comments*: Co-Principal Investigator, Principal Interventionist, IMS III; Angiographic Core Laboratory IMS III; *Support for Travel to Meetings for the Study or Other Purposes*: Executive Committee Meeting, Scientific Meeting travel expenses reimbursed through an IMS III grant; *UNRELATED*: *Expert Testimony*: consult and give expert testimony on stroke imaging or treatment-related cases (multiple law offices). Lydia D. Foster—*RELATED*: *Grant*: National Institute of Neurological Disorders and Stroke.* Ruediger von Kummer—*RELATED*: *Support for Travel to Meetings for the Study or Other Purposes*: National Institutes of Health, *Comments*: travel to meetings of the IMS III executive committee; *Board Membership*: Lundbeck; *Consultancy*: Lundbeck, Penumbra, Covidien, Boehringer Ingelheim; *Payment for Lectures (including service on Speakers Bureaus)*: Penumbra. Mayank Goyal—*UNRELATED*: *Consultancy*: Covidien, *Comments*: for trial design and conduct of Solitaire With the Intention For Thrombectomy as PRIMary Endovascular Treatment trial and for teaching engagements; *Grants/Grants Pending*: Covidien,* *Comments*: institutional grant for partial funding for Evaluation Study of Congestive Heart Failure and Pulmonary Artery Catheterization Effectiveness trial; *Payment for Lectures (including service on Speakers Bureaus)*: Covidien, *Comments*: for speaking engagements and teaching. Imanuel Dzialowski—*RELATED*: *Support for Travel to Meetings for the Study or Other Purposes*: honoraria for physician scientific advisory activity for the IMS III study. Yuko Y. Palesch—*RELATED*: *Grant*: National Institutes of Health,* *Comments*: for the IMS III trial; *Support for Travel to Meetings for the Study or Other Purposes*: National Institutes of Health,* *Comments*: for travel related to the IMS III grant activities and presentations at conferences; *UNRELATED*: *Consultancy*: Brainsgate, Biogen, *Comments*: honorarium for Data Monitoring Committee statistical member; *Grants/Grants Pending*: National Institutes of Health,* *Comments*: U01 and R01 grants; *Travel/Accommodations/Meeting Expenses Unrelated to Activities Listed*: Brainsgate, *Comments*: travel reimbursement for a Data Monitoring Committee meeting. Pooja Khatri—*RELATED*: *Grant*: National Institutes of Health IMS III trial grant*; *UNRELATED*: *Other*: Genentech,* Penumbra,* Biogen,* *Comments*: Each pay my institutional department for my research roles in trials: Genentech/Study of Efficacy and Safety of Activase in Patients with Mild Stroke (PRISMS), Lead Principal Investigator, Penumbra/Assess the Penumbra System in the Treatment of Acute Stroke Trial, Neuro Principal Investigator, Biogen/Data Safety Monitoring Board member. Joseph Broderick—*RELATED*: *Grant*: Genentech,* *Comments*: For PRISMS study; *Other*: Genenetech,* Concentric,* EKOS,* Cordis Neurovascular,* *Comments*: study medication for IMS III, Concentric, EKOS, Cordis Neurovascular; catheters for study in early years of IMS III; *UNRELATED*: *Travel/Accommodations/Meeting Expenses Unrelated to Activities Listed*: Boehringer Ingelheim, *Comments*: paid for travel to International Meeting where I was keynote speaker. Sharon D. Yeatts—*RELATED*: *Grant*: National Institute of Neurological Disorders and Stroke,* *Comments*: grant support for unblinded statistical role on IMS III; *UNRELATED*: *Consultancy*: Genentech, *Comments*: statistician member of PRISMS Trial Steering Committee; *Expert Testimony*: National Institute of Neurological Disorders and Stroke,* *Comments*: statistical involvement in Albumin in Acute Stroke, Hi-dose Deferoxamine in Intracerebral Hemorrhage/Intracerebral Hemorrhage Deferoxamine clinical trials. Andrew M. Demchuk—*RELATED*: *Grant*: National Institutes of Health,* *Comments*: CT core laboratory funding for IMS III; *UNRELATED*: *Grants/Grants Pending*: Covidien,* *Comments*: unrestricted grant to support Evaluation Study of Congestive Heart Failure and Pulmonary Artery Catheterization Effectiveness trial; *Payment for Lectures (including service on Speakers Bureaus)*: Covidien, *Comments*: speaker fees for Continuing Medical Education events. Janice Carrozella—*RELATED*: *Grant*: National Institutes of Health/National Institute of Neurological Disorders and Stroke,* *Comments*: IMS III trial. Michael D. Hill—*UNRELATED*: *Board Membership*: Heart and Stroke Foundation of Alberta/NWT and Nunavut (Board Member: 2010–12; Vice-Chairman: 2012–2014; Chairman); Institute for Circulatory and Respiratory Health of Canadian Institutes of Health Research (Advisory Board: 2009–2013); Canadian Federation of Neurological Sciences (Advisory Board: 2013–2016); *Consultancy*: Vernalis Group (2009); Merck, Adjudication Committee for Diabetes clinical trials (2014-present); *Grants/Grants Pending*: Hoffmann-La Roche Canada (2011–2013, provided drug for clinical trial),* Covidien (2013–2014, grant for a clinical trial)*; *Payment for Lectures (including service on Speakers Bureaus)*: Hoffmann-LaRoche Canada (2009, consultancy and Continuing Medical Education lecture),* Servier Canada (2012 Continuing Medical Education lecture, funds donated to charity),* Bristol-Myers Squibb Canada (2012, consultancy, fund donated to charity); *Stock/Stock Options*: Calgary Scientific, *Comments*: technology software company in imaging; *Other*: Heart and Stroke Foundation of Alberta/NWT and Nunavut (salary award 2012–2015),* Albert Innovates–Health Solutions (salary award 2009–2014).* *Money paid to the institution.

REFERENCES

1. Kurosawa Y, Lu A, Khatri P, et al. **Intra-arterial iodinated radiographic contrast material injection administration in a rat middle cerebral artery occlusion and reperfusion model: possible effects on intracerebral hemorrhage.** *Stroke* 2010;41:1013–17 CrossRef Medline
2. Morales H, Lu A, Kurosawa Y, et al. **Decreased infarct volume and intracranial hemorrhage associated with intra-arterial nonionic iso-osmolar contrast material in an MCA occlusion/reperfusion model.** *AJNR Am J Neuroradiol* 2014;35:1885–91 CrossRef Medline
3. Dzialowski I, Puetz V, Buchan AM, et al; Calgary Stroke Program. **Does the application of x-ray contrast agents impair the clinical effect of intravenous recombinant tissue-type plasminogen activator in acute ischemic stroke patients?** *Stroke* 2012;43:1567–71 CrossRef Medline
4. Broderick JP, Palesch YY, Demchuk AM, et al; Interventional Management of Stroke (IMS) III Investigators. **Endovascular therapy after intravenous t-PA versus t-PA alone for stroke.** *N Engl J Med* 2013;368:893–903 CrossRef Medline
5. Khatri P, Hill M, Palesch Y, et al; Interventional Management of Stroke III Investigators. **Methodology of the Interventional Management of Stroke III Trial.** *Int J Stroke* 2008;3:130–37 CrossRef Medline
6. Tomsick T, Broderick J, Carrozella J, et al; IMS II Investigators. **Revascularization results in the Interventional Management of Stroke II trial.** *AJNR Am J Neuroradiol* 2008;29:582–87 CrossRef Medline
7. Smith WS, Sung G, Starkman S, et al; MERCI Trial Investigators. **Safety and efficacy of mechanical embolectomy in acute ischemic stroke: results of the MERCI trial.** *Stroke* 2005;36:1432–38 CrossRef Medline
8. Smith WS, Sung G, Saver J, et al. **Mechanical thrombectomy for**

acute ischemic stroke: final results of the Multi MERCI trial. *Stroke* 2008;39:1205–12 CrossRef Medline

9. Penumbra Pivotal Stroke Trial Investigators. **The Penumbra Pivotal Stroke Trial: safety and effectiveness of a new generation of mechanical devices for clot removal in intracranial large vessel occlusive disease.** *Stroke* 2009;40:2761–68 CrossRef Medline
10. Dávalos A, Pereira VM, Chapot R, et al; Solitaire Group. **Retrospective multicenter study of Solitaire FR for revascularization in the treatment of acute ischemic stroke.** *Stroke* 2012;43:2699–705 CrossRef Medline
11. Kendall BE, Pullicino P. **Intravascular contrast injection in ischaemic lesions, II: effect on prognosis.** *Neuroradiology* 1980;19: 241–43 Medline
12. Doerfler A, Engelhorn T, von Kummer R, et al. **Are iodinated contrast agents detrimental in acute cerebral ischemia? An experimental study in rats.** *Radiology* 1998;206:211–17 CrossRef Medline
13. Diedler J, Ahmed N, Sykora M, et al. **Safety of intravenous thrombolysis for acute ischemic stroke in patients receiving antiplatelet therapy at stroke onset.** *Stroke* 2010;41:288–94 CrossRef Medline
14. Hayman LA, Evans RA, Bastion FO, et al. **Delayed high dose contrast CT: identifying patients at risk of massive hemorrhagic infarction.** *AJR Am J Roentgenol* 1981;136:1151–59 CrossRef Medline
15. Chronos NA, Goodall AH, Wilson DJ, et al. **Profound platelet degranulation is an important side effect of some types of contrast media used in interventional cardiology.** *Circulation* 1993;88: 2035–44 CrossRef Medline
16. Corot C, Chronos N, Sabattier V. **In vitro comparison of the effects of contrast media on coagulation and platelet activation.** *Blood Coagul Fibrinolysis* 1996;7:602–08 CrossRef Medline
17. Jones CI, Goodall AH. **Differential effects of the iodinated contrast agents Ioxaglate, Iohexol and Iodixanol on thrombus formation and fibrinolysis.** *Thromb Res* 2003;112:65–71 CrossRef Medline
18. Dalby MC, Davidson SJ, Burman JF, et al. **Systemic platelet effects of contrast media: implications of cardiologic research and clinical practice.** *Am Heart J* 2002;143:E1 Medline
19. Markou CP, Chronos NA, Hanson SR. **Antithromotic effects of ionic and non-ionic contrast media in nonhuman primates.** *Thromb Haemost* 2001;85:488–93 Medline
20. Li X, Gabriel DA. **Differences between contrast media in the inhibition of platelet activation by specific platelet agonists.** *Acad Radiol* 1997;4:108–14 CrossRef Medline
21. NINDS t-PA Stroke Study Group. **Generalized efficacy of t-PA for acute stroke: subgroup analysis of the NINDS t-PA Stroke Trial.** *Stroke* 1997;28: 2119–25 CrossRef Medline
22. NINDS t-PA Stroke Study Group. **Intracerebral hemorrhage after intravenous t-PA therapy for ischemic stroke.** *Stroke* 1997;28: 2109–18 CrossRef Medline
23. Marcos SK, Thomsen HS, Exley CM; Members of Contrast Media Safety Committee of European Society of Urogenital Radiology (ESUR). **Contrast media: interactions with other drugs and clinical tests.** *Eur Radiol* 2005;15:1463–68 CrossRef Medline
24. Frohlich JM. **Systematic survey of interactions between contrast media and other drugs.** Special edition by Guerbet Switzerland; 2001
25. Corot C, Perrin JM, Belleville J, et al. **Effect of iodinated contrast media on blood clotting.** *Invest Radiol* 1989;24:390–93 CrossRef Medline
26. Ing JJ, Smith DC, Bull BS. **Differing mechanisms of clotting inhibition by ionic and nonionic contrast agents.** *Radiology* 1989;172: 345–48 CrossRef Medline
27. Kopko PM, Smith DC, Bull BS: **Thrombin generation in nonclottable mixtures of blood and nonionic contrast agents.** *Radiology* 1990;174:459–61 CrossRef Medline
28. Georgakis A, Ener RA, Jin J, et al. **Risk of thrombogenicity among nonionic radiocontrast agents.** *J Invasive Cardiol* 2008;20:349–53 Medline
29. LaBounty TM, Shah M, Raman SV, et al. **Within-hospital and 30-day outcomes in 107,994 patients undergoing invasive coronary angiography with different low-osmolar iodinated contrast media.** *Am J Cardiol* 2012;109:1594–99 CrossRef Medline
30. Sutton AG, Ashton VJ, Campbell PG, et al. **A randomized prospective trial of ioxaglate 320 (Hexabrix) vs. iodixanol 320 (Visipaque) in patients undergoing percutaneous coronary intervention.** *Catheter Cardiovasc Interv* 2002;57:346–52 CrossRef Medline
31. Dehmer GJ, Gresalfi N, Daly D, et al. **Impairment of fibrinolysis by streptokinase, urokinase and recombinant tissue-type plasminogen activator in the presence of radiographic contrast agents.** *J Am Coll Cardiol* 1995;25:1069–75 CrossRef Medline
32. Pislaru S, Pislaru C, Szilard M, et al. **In vivo effects of contrast media on coronary thrombolysis.** *Am Coll Cardiol* 1998;32:1102–08 CrossRef
33. Van Beek EJ, Levi M, Reekers JA, et al. **Increased plasma levels of PAI-1 after administration of nonionic contrast medium in patients undergoing pulmonary angiography.** *Radiology* 1994;193: 821–23 CrossRef Medline
34. Hill V, Meunier J, Shaw GJ, et al. **Effect of iodixanol on rt-PA thrombolysis in human clots**. In: *Proceedings of the Annual Meeting of the American Society of Neuroradiology and Neuroradiology Education and Research Foundation Symposium,* Boston, Massachusetts. May 16–20, 2010
35. Dani KA, Muir KW. **Do iodinated contrast agents impair fibrinolysis in acute stroke? A systematic review.** *AJNR Am J Neuroradiol* 2010;31:170–74 CrossRef Medline
36. Franke RP, Fuhrmann R, Hiebl B, et al. **Influence of various radiographic contrast media on the buckling of endothelial cells.** *Microvasc Res* 2008;76:110–13 CrossRef Medline
37. Franke RP, Fuhrmann R, Park JW, et al. **The effect of radiographic contrast media on the morphology of human venous endothelial cells.** *Clin Hemorheol Microcirc* 2007;37:329–38 Medline
38. Aspelin P, Stacul F, Thomsen HS, et al; Members of the Contrast Media Safety Committee of the European Society of Urogenital Radiology (ESUR). **Effects of iodinated contrast media on blood and endothelium.** *Eur Radiol* 2006;16:1041–49 CrossRef Medline
39. Jung F, Mrowietz C, Rickert D, et al. **The effect of radiographic contrast media on the morphology of human erythrocytes.** *Clin Hemorheol Microcirc* 2008;38:1–11 Medline
40. Aulie Michelet A. **Effects of intravascular contrast media on blood-brain barrier: comparison between iothalamate, iohexol, iopentol, and iodixanol.** *Acta Radiol* 1987;28:329–33 CrossRefMedline
41. Sage MR, Wilson AJ, Scroop R. **Contrast media and the brain: the basis of CT and MR imaging enhancement.** *Neuroimaging Clin N Am* 1998;8:695–707 Medline
42. Sage MR, Wilcox J, Evill CA, et al. **Comparison of blood-brain barrier disruption by intracarotid iopamidol and methylglucamine iothalamate.** *AJNR Am J Neuroradiol* 1983;4:893–95 Medline
43. Whisson CC, Wilson AJ, Evill CA, et al. **The effect of intracarotid nonionic contrast media on the blood-brain barrier in acute hypertension.** *AJNR Am J Neuroradiol* 1994;15:95–100 Medline
44. Lee KK, Kang DH, Kim YS, et al. **Serious blood brain disruption after coil embolization of unruptured intracranial aneurysm: report of two cases and role of immediate postembolization CT scan.** *J Korean Neurosurg Soc* 2011;50:45–47 CrossRef Medline
45. Ozturk A, Saatci I, Pamuk, et al. **Focal increased cortical density in immediate postembolization CT scans of patients with intracranial aneurysms.** *AJNR Am J Neuroradiol* 2006;27:1866–75 Medline
46. Hayakawa K, Morris TM, Katzberg RW. **Opening of the blood-brain barrier by intravenous contrast media in euvolemic and dehydrated rabbits.** *Acta Radiol* 1989;30:439–44 CrossRef Medline
47. Murphy A, Heran M, Smith A, et al. **Intra-arterial thrombolysis and parenchymal contrast staining: determining its meaning in the setting of acute stroke intervention.** In: *Proceedings of the Annual Meeting of the American Society of Neuroradiology and Neuroradiology Education and Research Foundation Symposium*, Vancouver, British Columbia, Canada. May 18–21, 2009:375
48. Knight RA, Barker PB, Fagan SC, et al. **Prediction of impending**

hemorrhagic transformation in ischemic stroke using magnetic resonance imaging in rats. *Stroke* 1998;29:144–51 CrossRef Medline
49. Neumann-Haefelin C, Brinker G, Uhlenküken U, et al. Prediction of hemorrhagic transformation after thrombolytic therapy of clot embolism: an MRI investigation in rat brain. *Stroke* 2002;33:1392–98 CrossRef Medline
50. Hom J, Dankbaar JW, Soares BP, et al. **Blood-brain barrier permeability assessed by perfusion CT predicts symptomatic hemorrhagic transformation and malignant edema in acute ischemic stroke.** *AJNR Am J Neuroradiol* 2011;32:41–48 CrossRef Medline
51. Aviv RI, d'Esterre CD, Murphy BD, et al. **Hemorrhagic transformation of ischemic stroke: prediction with CT perfusion.** *Radiology,* 2009;250:867–77 CrossRef Medline
52. Lin K, Kazmi KS, Law M, et al. **Measuring elevated microvascular permeability and predicting hemorrhagic transformation in acute ischemic stroke using first-pass dynamic perfusion CT imaging.** *AJNR Am J Neuroradiol*, 2007;28:1292–98 CrossRef Medline
53. Kim EY, Kim SS, Na DG, et al. **Sulcal hyperintensity on fluid-attenuated inversion recovery imaging in acute ischemic stroke patients treated with intra-arterial thrombolysis: iodinated contrast media as its possible cause and the association with hemorrhagic transformation.** *J Comput Assisted Tomogr* 2005;29:264–69 CrossRef Medline
54. Hjort N, Wu O, Ashkanian M, et al. **MRI detection of early blood brain barrier disruption: parenchymal enhancement predicts focal hemorrhagic transformation after thrombolysis.** *Stroke* 2008;39: 1025–28 CrossRef Medline
55. Latour LL, Kang DW, Ezzeddine MA, et al. **Early blood-brain barrier disruption in human focal brain ischemia.** *Ann Neurol* 2004;56: 468–77 CrossRef Medline
56. Lummul N, Schulte-Altedorneburg G, Bernau C, et al**. Hyperattenuated intracerebral lesions after mechanical revascularization in acute stroke.** *AJNR Am J Neuroradiol* 2014;35:345–51 CrossRef Medline
57. Pannu N, Wiebe N, Tonelli M. **Prophylaxis strategies for contrast-induced nephropathy.** *JAMA* 2006;295:2765–79 CrossRef Medline
58. Fountaine H, Harnish P, Andrew E, et al. **Safety, tolerance, and pharmacokinetics of iodixanol injection, a nonionic, isosmolar, hexaiodinated contrast agent.** *Acad Radiol* 1996;3(suppl 3):S475-84 CrossRef Medline
59. Heinrich MC, Kuhlmann MK, Grgic A, et al. **Cytotoxic effects of ionic high-osmolar, nonionic monomeric, and nonionic iso-osmolar dimeric iodinated contrast media on renal tubular cells in vitro.** *Radiology* 2005;235:843–49 CrossRef Medline
60. Dooley M, Jarvis B. **Iomeprol: a review of its use as a contrast medium.** *Drugs* 2000;59:1169–86 CrossRef Medline
61. McClennan BL, Stolberg HO. **Intravascular contrast media: ionic versus nonionic: current status.** *Radiol Clin North Am* 1991;29: 437–54 Medline
62. Lasser EC, Lang JH. **Inhibition of acetylcholinesterase by some organic contrast media: a preliminary communication.** *Invest Radiol* 1966;2:237–42
63. Gertz EW. **Thromboembolic events and non-ionic contrast.** *Diagn Imag* 1989;11:106–09
64. Paczynski RP, He YY, Diringer, et al. **Multiple-dose mannitol reduces brain water content in a rat model of cortical infarction.** *Stroke* 1997;28:1437–43; discussion 1444 Medline
65. Wilcox J, Wilson AJ, Evill CA, et al. **A comparison of blood-brain barrier disruption by intracarotid iohexol and iodixanol in the rabbit.** *AJNR Am J Neuroradiol* 1987;8:769–72 Medline
66. Macdougall NJ, McVerry F, Baird S, et al. **Iodinated contrast media and cerebral hemorrhage after intravenous thrombolysis.** *Stroke* 2011;42:2170–74 CrossRef Medline
67. Khatri P, Broderick JP, Khoury JC, et al; IMS I and II Investigators. **Microcatheter contrast injections during intra-arterial thrombolysis may increase intracranial hemorrhage risk.** *Stroke* 2008;39: 3283–87 CrossRef Medline
68. Leong S, Fanning NF. **Persistent neurological deficit from iodinated contrast encephalopathy following intracranial aneurysm coiling: a case report and review of the literature.** *Interv Neuroradiol* 2012; 18:33–41 Medline
69. Wilcox J, Sage MR. **Is viscosity important in the production of blood-brain barrier disruption by intracarotid contrast media?** *Neuroradiology* 1984;26:511–13 CrossRef Medline
70. Sood R, Taheri S, Estrada EY, et al. **Quantitative evaluation of the effect of propylene glycol on BBB permeability.** *J Magn Reson Imaging* 2007;25:39–47 CrossRef Medline
71. Jacobsen PB, Larsen A, Konarboland R, et al. **Biotransformation of nonionic x-ray contrast agents in vivo and in vitro.** *Drug Metab Dispos* 1999;27:1205–13 Medline
72. Spencer CM, Goa KL. **Iodixanol: a review of its pharmacodynamic and pharmacokinetic properties and diagnostic use as an x-ray contrast medium.** *Drugs* 1996;52:899–927 CrossRef Medline
73. Molina CA, Montaner J, Abilleira S, et al. **Timing of spontaneous recanalization and risk of hemorrhagic transformation in acute cardioembolic stroke.** *Stroke* 2001;32:1079–84 CrossRef Medline
74. Simard JM, Kent TA, Chen M, et al. **Brain oedema in focal ischaemia: molecular pathophysiology and theoretical implications.** *Lancet Neurol* 2007;6:258–68 CrossRef Medline
75. Zador Z, Stiver S, Wang V, et al. **Role of aquaporin-4 in cerebral edema and stroke.** *Handb Exp Pharmacol* 2009:159–70 CrossRef Medline
76. Lu A, Clark JF, Broderick JP, et al. **Mechanical reperfusion is associated with post-ischemic hemorrhage in rat brain.** *Exp Neurol* 2009; 216:407–12 CrossRef Medline
77. Dirnagl U, Lindauer U, Them A, et al. **Global cerebral ischemia in the rat: online monitoring of oxygen free radical production using chemiluminescence in vivo.** *J Cereb Blood Flow Metab* 1995;15: 929–40 CrossRef Medline
78. Kumura E, Yoshimine T, Iwatsuki KI, et al. **Generation of nitric oxide and superoxide during reperfusion after focal cerebral ischemia in rats.** *Am J Physiol* 1996;270(3 pt 1):C748-52 Medline
79. Lu A, Clark JF, Broderick JP, et al. **Reperfusion activates metalloproteinases that contribute to neurovascular injury.** *Exp Neurol* 2008; 210:549–59 CrossRef Medline
80. Rosell A, Foerch C, Murata Y, et al. **Mechanisms and markers for hemorrhagic transformation after stroke.** *Acta Neurochir Suppl* 2008;105:173–78 CrossRef Medline
81. Schwartz D, Blum M, Peer G, et al. **Role of nitric oxide (EDRF) in radiocontrast acute renal failure in rats.** *Am J Physiol* 1994;267: F374-79 Medline
82. Heyman SN, Goldfarb M, Carmeli F, et al. **Effect of radiocontrast agents on intrarenal nitric oxide (NO) and NO synthase activity.** *Exp Nephrol* 1998;6:557–62 CrossRef Medline
83. Treitl M, Rupprecht H, Wirth S, et al. **Assessment of renal vasoconstriction in vivo after intra-arterial administration of the isosmotic contrast medium iodixanol compared to the low-osmolar contrast medium iopamidol.** *Nephrol Dial Transplant* 2009;24:1478–85 CrossRef Medline
84. Morris TW, Ekholm SE, Prentice L, et al. **Iotrol, iodixanol, and 2-deoxy-D-glucose effects on neural tissue CO2 production.** *AJNR Am J Neuroradiol* 1989;10:1123–26 Medline
85. Kim SJ, Salem MR, Joseph NJ, et al. **Contrast media adversely affect oxyhemoglobin dissociation.** *Anesth Analg* 1990;71:73–76 Medline
86. Uchiyama Y, Abe T, Tanaka N, et al. **Factors contributing to blood-brain barrier disruption following intracarotid injection of nonionic iodinated contrast media for cerebral angiography: experimental study in rabbits.** *Radiat Med* 2006;24:321–26 CrossRef Medline
87. Khatri R, Khatri P, Khoury J, et al**. Microcatheter contrast injections during intra-arterial thrombolysis increase intracranial hemorrhage risk.** *J Neurointerv Surg* 2010;2:115–19 CrossRef Medline
88. Al-Ali F, Elias JJ, Tomsick TA, et al; IMS Study Groups. **Relative influence of capillary index score, revascularization, and time on stroke outcomes from the Interventional Management of Stroke III Trial.** *Stroke* 2015;46:1590–94 CrossRef Medline

Initial Experience with p64: A Novel Mechanically Detachable Flow Diverter for the Treatment of Intracranial Saccular Sidewall Aneurysms

S. Fischer, M. Aguilar-Pérez, E. Henkes, W. Kurre, O. Ganslandt, H. Bäzner, and H. Henkes

ABSTRACT

BACKGROUND AND PURPOSE: Flow diverters are important tools for the treatment of intracranial aneurysms. We report a retrospective evaluation of the safety and efficacy of p64, a fully resheathable, detachable flow diverter, in the endovascular treatment of intracranial sidewall aneurysms.

MATERIALS AND METHODS: Results of 121 patients with 130 aneurysms (median neck size, 3 mm; median fundus size, 4 mm), treated from April 2012 through October 2014, were analyzed. Aneurysms were unruptured or beyond the acute SAH phase. Thirteen aneurysms were located in the posterior circulation. Twenty-three aneurysms had previous saccular treatment but no previous parent vessel stent placement. In 19 aneurysms, a combination of coiling and flow diversion was performed.

RESULTS: Successful p64 deployment was achieved in 127/130 aneurysms. The average number of p64s used was 1.1 per aneurysm. The rates of transient and permanent morbidity and mortality were 5%, 1.7%, and 0.8%, respectively. Three-month DSA follow-up in 123/130 aneurysms showed complete occlusion in 58.5%. Nine-month DSA follow-up in 93/106 (87.7%) eligible aneurysms showed complete occlusion in 79.6%. Late follow-up (median, 496 days) has already been performed in 35 aneurysms, showing complete occlusion in 30 (85.7%).

CONCLUSIONS: p64 offers an efficacious treatment option for intracranial sidewall aneurysms with a high aneurysm occlusion and an acceptable complication rate. The possibility of repositioning or removing the device was an advantage. The higher attenuation may lead to fewer devices per case and early aneurysm occlusion. Long-term follow-up data are pending.

ABBREVIATIONS: LL = lumen loss; PED = Pipeline Embolization Device

Flow diversion has become an accepted endovascular treatment for selected intracranial aneurysms. Both the clinical and endovascular treatment data with follow-up results of several patient cohorts treated with different flow diverters have been published during the past 5 years.[1-6] In Europe, 6 flow diverters are currently available for clinical use (Silk+, Balt Extrusion, Montmorency, France; PED FLEX, Medtronic, Dublin, Ireland; FRED, MicroVention, Tustin, California; NeuroEndoGraft, Stryker Neurovascular, Fremont, California; Derivo, Acandis, Pforzheim, Germany; p64, phenox, Bochum, Germany). The principle of flow diversion is the redirection of blood flow away from the aneurysm along the longitudinal axis of the parent artery. This is accomplished by endoluminal placement of the device across the aneurysm neck. The hemodynamic effect depends mainly on the porosity of the mesh.[7] The occlusion of the aneurysm or the failure to occlude and potential complications follow device-specific patterns. An understanding of the technical features and functions of different flow diverters may help proper patient selection and procedure performance.

We report our experience in the treatment of intracranial saccular sidewall aneurysms with p64, a new mechanically detachable flow diverter.

MATERIALS AND METHODS

p64 Flow-Modulation Device

The p64 is a braided tubular implant consisting of 64 nitinol wires. It is available with nominal diameters from 2.5 to 5 mm with 0.5

Received November 13, 2014; accepted after revision March 17, 2015.

From the Neuroradiologische Klinik (S.F., M.A.-P., E.H., W.K., H.H.), Neurochirurgische Klinik (O.G.), and Neurologische Klinik (H.B.), Neurozentrum, Klinikum Stuttgart, Stuttgart, Germany; and the Institut für Diagnostische und Interventionelle Radiologie, Neuroradiologie und Nuklearmedizin (S.F.), Universitätsklinikum Knappschaftskrankenhaus, Bochum, Germany.

Preliminary data from this series was presented at: Annual Meeting of the American Society of Neuroradiology and the Foundation of the ASNR Symposium, May 17–22, 2014; Montreal, Quebec, Canada.

The Guidelines of the Declaration of Helsinki of the World Medical Association in its current version (WMA, 2004), the Guidelines of Good Clinical Practice (CPMP/ICH/135/95), and demands of the national medical and data protection laws were followed.

Please address correspondence to Hans Henkes, MD, Neuroradiologische Klinik, Neurozentrum, Klinikum Stuttgart, Katharinenhospital, Kriegsbergstr 60, D-70174 Stuttgart, Germany; e-mail: hhhenkes@aol.com

http://dx.doi.org/10.3174/ajnr.A4420

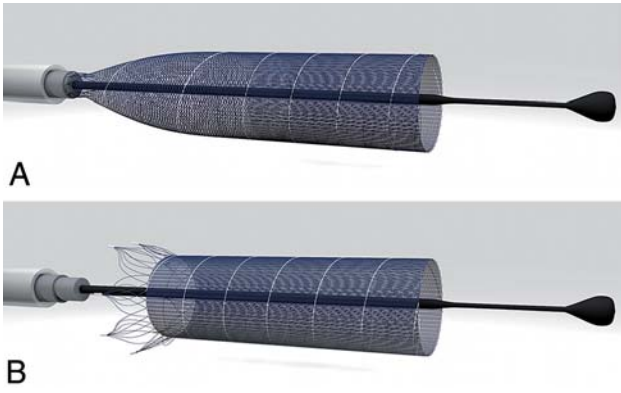

FIG 1. Detachment mechanism of the p64. Eight bundles, each containing 8 wires, are attached to a slotted crown (*A*) and released from there by pulling a polymer hypotube in the proximal direction (*B*). Image courtesy of phenox.

mm increments. The nominal length ranges from 9 to 30 mm with 3-mm increments. Visibility under x-ray fluoroscopy is possible by 2 platinum wires wrapped around opposing nitinol wires of the braided shaft. The 64 wires of the implant are grouped into 8 bundles proximally, each consisting of 8 individual wires. The ends of each bundle carry a radiopaque marker with a 0.5-mm length. The 8 bundles are mounted onto a slotted crown on the distal end of a stainless steel delivery wire. A polymer tube covers the crown, securing the 8 markers in the slotted crown and extends proximally for 180 cm over the delivery wire (Fig 1). A torque device is used to lock the polymer tube to the delivery wire to prevent premature detachment of the implant from the slotted crown. The p64 is available with and without a distal wire. In the model with a wire, the distal end of this wire has a radiopaque marker. The distal wire increases flexibility and support during navigation and deployment of the implant. Once deployed, the p64 can be fully recovered by advancing the microcatheter while pulling back on the delivery wire.

Detachment of p64 starts with repositioning of a torque device approximately 15 mm proximal to the end of the hypotube (Fig 2*A*, -*B*).Pulling the hypotube toward the torque device (Fig 2*C*) will result in movement of this tube in the proximal direction, thereby releasing the 8 markers from the slotted crown.

The porosity (defined as the proportion of the surface area without metal coverage over the total surface area) of the implanted device depends on the implant model size and the relationship between the diameter of the device and the target vessel. Under standardized conditions (ie, in a tube with a nominal diameter), the porosity of p64 varies from 51% to 60%; the coverage (defined as the proportion of the surface area with metal coverage over the total surface area) varies from 35% to 49%; and the area of an individual cell is largely dependent on the expansion status of the device. Undersizing increases and oversizing decreases the coverage. The radial force of the p64 at nominal diameters is similar to that of the PED FLEX (PED; Covidien, Irvine, California).

Patient Population and Aneurysm Characteristics

Given the high frequency of a fundus diameter of ≤6 mm in ruptured aneurysms, all treatment options are discussed and

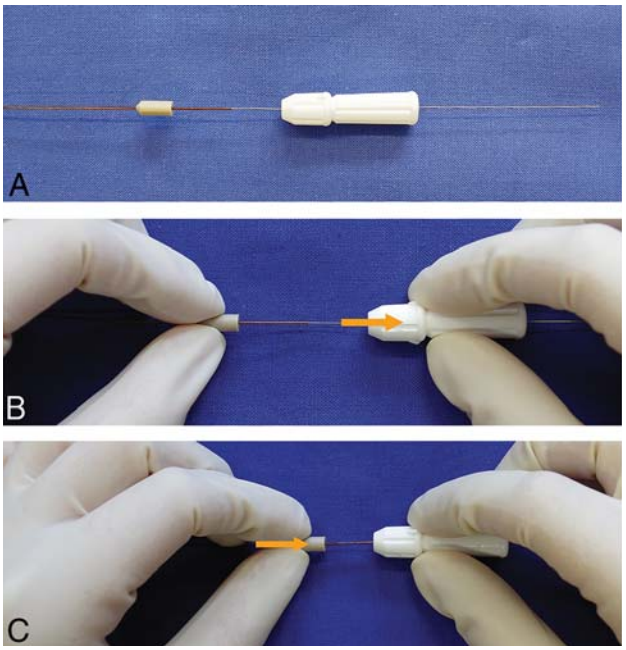

FIG 2. Manual detachment of the p64. The p64 comes with a torque device, which is locked over the hypotube to hold this hypotube in position (*A*). The detachment starts with unlocking the torquer, repositioning it, and again locking it approximately 15 mm proximally (*B*). A handle on the hypotube is then moved proximally (*C*).

offered to all patients with intradural aneurysms, unless individual aspects (eg, major comorbidity, older than 80 years of age, anticipated treatment difficulty, and so forth) are considered potential contraindications. A multidisciplinary neurovascular team, including vascular neurosurgeons and stroke neurologists, discussed the treatment concept for each patient in advance. All patients were informed about the nature of their disease and the intended treatment and potential alternatives, with informed consent obtained at least 24 hours before the procedure.

A retrospective review of all medical records and radiographic studies of patients treated with the p64 between April 2012 and October 15, 2014 was performed.

The selection criteria for the endovascular treatment with the p64 and inclusion in this retrospective analysis are summarized in Table 1.

According to these criteria, 121 patients (86 women; 35 men; median age 58 years (range, 26–79 years) with 130 intracranial aneurysms were included in this analysis.

The clinical pre- and postprocedural status of each patient was evaluated according to the modified Rankin Scale. Before the procedure, 88 patients were asymptomatic, 8 (6.6%) had an mRS score of 1 or 2 caused by a symptomatic target aneurysm, and 25 (20.7%) had an mRS score of ≥1 unrelated to the target aneurysm.

Of the 130 aneurysms treated, the p64 procedure was the first treatment in 107 aneurysms, whereas 23 aneurysms were remnants or recurrences after previous coil occlusion ($n = 20$) or microsurgical clipping ($n = 3$). Previous rupture was confirmed for 6 aneurysms. The locations of the 130 treated aneurysms were as follows: ICA, cavernous ($n = 8$); ICA, paraoph-

thalmic ($n = 32$); ICA, superior hypophyseal artery ($n = 25$); ICA, paraclinoid ($n = 10$); ICA, posterior communicating artery ($n = 18$); ICA, anterior choroidal artery ($n = 10$); anterior cerebral artery ($n = 10$); MCA ($n = 4$); vertebral artery/V4 ($n = 4$); posterior inferior cerebellar artery ($n = 1$); basilar artery ($n = 4$); superior cerebellar artery ($n = 2$); and posterior cerebral artery ($n = 2$).

The aneurysm fundus size was determined as the diameter of the perfused part of the aneurysm at the time of p64 implantation. The median size of the 130 treated aneurysms was 3 mm for the neck (range, 1–11 mm) and 4 mm for the fundus (range, 1–20 mm).

Endovascular Procedure

All procedures were performed in a single center with the patient under general anesthesia on biplane Axiom Artis DSA units (Siemens, Erlangen, Germany).

Either a 6F guide catheter alone or a triaxial access was used. A 0.027-inch-inner-diameter microcatheter was placed in a straight vessel segment of the parent artery distal to the aneurysm neck by using a 0.014- or 0.016-inch microguidewire.

After a suitable working projection was identified, the target-vessel diameter was measured, followed by device selection. The device matched the diameter of the healthy landing zone. Slight undersizing was possible because the diameter of the unconstrained implant is approximately 0.3 mm larger than the nominal diameter. This undersizing results in a denser coverage and shortening of the implant by a median length of 55% and was avoided if side branches were covered. Moderate oversizing was possible and resulted in a less attenuated coverage. The device was then prepared by pushing it out of and retracting it into the sheath, while submersed in saline. It was then advanced to the desired position via the microcatheter. Deployment was a combination of a slow withdrawal of the microcatheter, with a continuous counterpressure on the delivery wire. After the distal end of the device was anchored in the target vessel, the microcatheter was no longer pulled back. Pushing the delivery wire of the p64 resulted in a progressive deployment of the device with a passive proximal movement of the microcatheter. Once the proximal markers of the device were uncovered from the microcatheter, a single x-ray image or a flat panel CT was performed to confirm the complete opening of the device. In case of incomplete opening, resheathing and redeployment resulted in better device expansion. The fully-opened device was mechanically detached as previously described. If the wall apposition of the p64, once detached, was not satisfactory, a compliant balloon was inserted and gently inflated.

In this series, coil occlusion and p64 deployment in 1 session were performed in 19 (14.6%) aneurysms (Fig 3). The median fundus diameter of those partially coiled aneurysms was 8 mm (range, 4–20 mm); the median neck diameter was 5 mm (range, 2–8 mm).

In 13 selected aneurysms (10%), we implanted multiple p64s, concluding that 1 device might be insufficient (2 p64s, $n = 9$; 3 p64s, $n = 3$; 4 p64s, $n = 1$). The decision concerning additional coil occlusion or the deployment of multiple p64 devices was at the operator's discretion.

Table 1: Inclusion and exclusion criteria for the presented series of patients treated with p64

Criteria for the p64 Treatment and Analysis in this Series
Inclusion
Intracranial saccular sidewall aneurysm as treatment target
Aneurysms unruptured or at least not in the acute phase after rupture
Extra- or intradural symptomatic aneurysm
Asymptomatic intradural aneurysms, thus carrying a potential risk of intracranial rupture
Anticipated difficulty of coil or clip treatment (eg, complex aneurysm morphology, wide neck, dome-to-neck ratio of <1.2, small size, difficult surgical access)
No previous treatment or any previous treatment directed at the aneurysm sac without complete occlusion of the aneurysm from circulation
No previous treatment to the parent vessel
An ability and willingness of the patient to take the necessary medication for midterm dual platelet function inhibition
Exclusion
Bifurcation-type aneurysm or fusiform vessel dilation as a treatment target
Implants other than p64 used
Aneurysm rupture ≤30 days prior to the p64 treatment
Extradural asymptomatic aneurysm
Anticipated ease or sufficiency of clip or coil treatment
Previous implantation of stents or flow diverters to the target-vessel segment

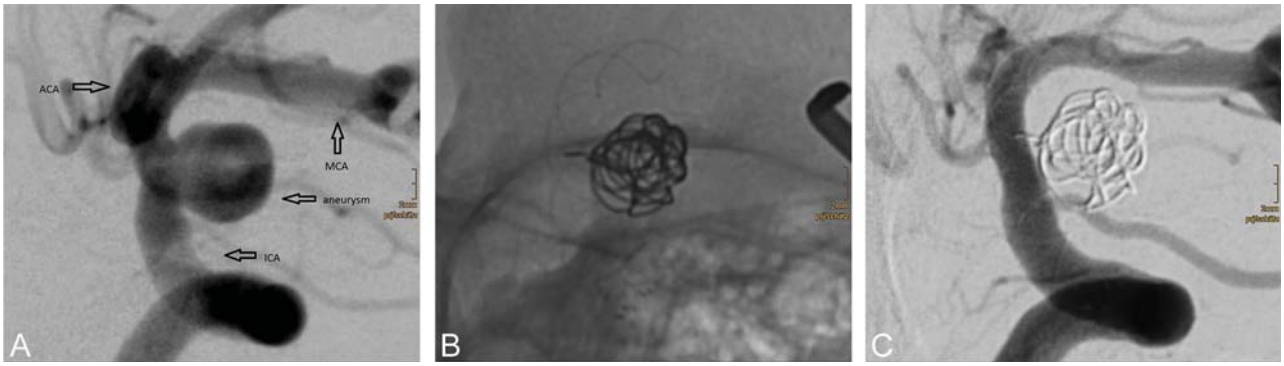

FIG 3. De novo unruptured paraclinoid aneurysm (7 × 5 mm) in a 63-year-old woman with a history of 2 spontaneous SAHs from 2 MCA bifurcation aneurysms, which had been clipped. The paraclinoid aneurysm was not considered ideal for coil occlusion alone (*A*), and the patient was reluctant to undergo surgery again. A single Morpheus 7 × 21 cm 3D coil (Medtronic, Dublin, Ireland) was inserted into the aneurysm. The aneurysm neck was then covered by a 4 × 18 mm p64 (*B*). DSA follow-up 93 days later reveals complete occlusion of the aneurysm (*C*).

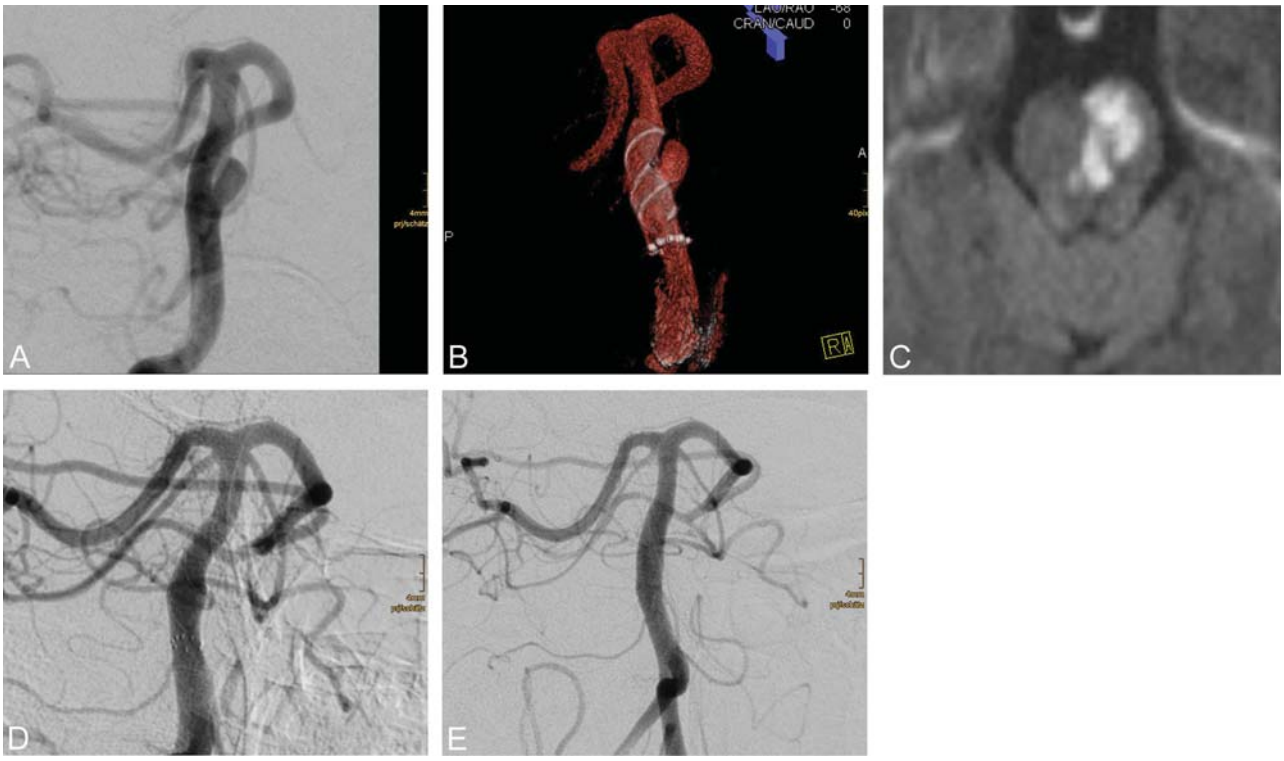

FIG 4. A small saccular aneurysm of the basilar trunk (4 × 3 mm) (*A*) in a 56-year-old woman. Both surgery and coil occlusion were not considered suitable treatment options. A 4.5 × 15 mm p64 was deployed in the basilar artery with complete coverage of the aneurysm (*B*). Although the procedure was well-tolerated, the patient developed a hemiparesis and dysarthria (mRS 3) 26 days later. MR imaging shows an ischemic pontine lesion (*C*); a Multiplate test (not shown) confirmed insufficient platelet function inhibition. Antiaggregation was switched to ticagrelor, and the patient subsequently recovered (mRS 1). Follow-up DSA after 28 days (*D*) and after 421 days (*E*) shows complete occlusion of the aneurysm.

Antiplatelet and Anticoagulation Regimen

Patients received a loading dose of 600 mg clopidogrel and 500 mg acetylsalicylic acid at least 1 day before the procedure and were then maintained on dual antiplatelet medication of 75 mg clopidogrel and 100 mg acetylsalicylic acid daily. Platelet aggregation inhibition was tested before the procedure and occasionally thereafter with the impedance aggregometry (Multiplate; Roche, Basel, Switzerland) in all patients. Patients with clopidogrel resistance were switched to ticagrelor (2× 90 mg daily) (Fig 4).[8,9] Dual antiplatelet aggregation was continued for 1 year and was thereafter reduced to a monomedication of acetylsalicylic acid. The periprocedural medication included systemic heparinization.

Follow-Up Schedule

Patients were scheduled for clinical and angiographic follow-up examinations after treatment as follows:

- Early follow-up (3 months ± 4 weeks)
- Intermediate follow-up (5–12 months)
- Late follow-up (>12 months).

A neurologist, a neurosurgeon, or a certified stroke nurse performed the clinical assessment by using the mRS. Clinical follow-up examinations compared the pretreatment and posttreatment clinical conditions of the patients.

Angiographic results were graded as follows: 1) complete occlusion, 2) neck remnant, 3) incomplete occlusion with residual sac filling, and 4) unchanged aneurysm perfusion.[10]

In-stent stenosis was graded as the following: 1, absent; 2, <50% lumen loss; 3, 50%–75% lumen loss; 4, >75% lumen loss. If in-stent stenosis was observed, the lumen loss (LL) on subsequent follow-up DSA examinations was separately qualified as unchanged, decreased, or increased.

Retreatment

Retreatment was considered after follow-up angiographies revealed an unchanged, incomplete aneurysm occlusion or device migration.

RESULTS

Procedural Technical Aspects and Difficulties

Insertion, deployment, and detachment of the p64 was possible as intended in 127/130 procedures (97.7%). Excessive friction was encountered in 2 aneurysms. In 1 case, a remnant of a previously coiled pericallosal artery could not be reached due to friction of the p64 at the level of the A1 segment. The aneurysm was treated in the same session with a PED with difficulty. In the second case, the target was an A1/A2 aneurysm. Serious friction was encountered during the attempted p64 insertion. In 2 subsequent sessions, an Enterprise self-expanding stent (Codman & Shurtleff, Raynham, Massachusetts) was deployed, followed by the insertion of a p64 inside this stent. Follow-up DSA confirmed the occlusion of the aneurysm. In patient 3, a basilar trunk aneurysm was reached and covered by a p64. The p64 was, however, withdrawn because a noncollateralized posterior cerebral artery would have been covered. The aneurysm was treated by Solitaire-assisted (Covidien) coil occlusion. In a subsequent session, a recurrence of this aneu-

Table 2: Breakdown of aneurysm occlusion rate and complication incidence according to the size of the aneurysm fundus

	Fundus Diameter			
	1–3 mm (*n* = 59)	4–6 mm (*n* = 42)	7–9 mm (*n* = 15)	>10 mm (*n* = 14)
Early follow-up	55/59 (93%)	42/42 (100%)	15/15 (100%)	12/14 (85.7%)
Complete occlusion	31 (56.4%)	28 (66.7%)	9 (60%)	4 (33.3%)
Neck remnant	13 (23.6%)	4 (9.5%)	2 (13%)	7 (58.3%)
Sac remnant	7 (12.7%)	5 (11.9%)	3 (20%)	1 (8.3%)
Unchanged	4 (7.3%)	4 (9.5%)	1 (6.7%)	0
Midterm follow-up	46/59 (78%)	34/42 (81%)	11/15 (73.3%)	8/14 (57.1%)
Complete occlusion	37 (80.4%)	26 (76.5%)	9 (81.8%)	4 (50%)
Neck remnant	3 (6.5)	5 (14.7%)	2 (18.2%)	3 (37.5%)
Sac remnant	4 (8.7%)	2 (5.9%)	0	1 (12.5%)
Unchanged	2 (4.3%)	1 (2.9%)	0	0
Complications	1 Pontine ischemia 1 CN VI palsy 1 Asymptomatic thrombosis	1 Pontine ischemia 1 TIA	1 TIA 1 Asymptomatic thrombosis	1 Death 1 Pulmonary artery occlusion

Note:—CN indicates cranial nerve.

rysm was treated with a p64. Follow-up DSA confirmed the complete occlusion of the aneurysm. Balloon expansion of the p64 after deployment was performed in 5 patients and was successful in all attempted cases.

Early Peri- and Postprocedural Complications

The peri- and postprocedural phases (24 hours) were clinically uneventful in 127/130 procedures (97.7%). One patient had a pulmonary artery embolism, and 2 patients had minor ischemic lesions with transient neurologic deficits.

The subacute phase (day 2 through 30) was within normal limits in 128/130 procedures (98.5%), and 2 patients experienced a pontine ischemic infarct. The clinical outcome of these patients was equivalent to mRS 1 ($n = 1$) as opposed to mRS 0 before the treatment. In 1 of these 2 patients, dual platelet inhibition was interrupted against medical advice.

Delayed Complications

Beyond 30 days, 1 patient died from pneumonia, which was indirectly related to the endovascular treatment. This patient had received steroids for severe cranial nerve palsy due to the mass effect of a large ICA aneurysm, which had been treated by coil occlusion and a different flow diverter. In 2 patients, asymptomatic thrombus formation after cessation of dual antiplatelet aggregation was observed. In 1 patient, an unrelated cranial nerve VI palsy occurred 10 months posttreatment.

In the entire series, 6/121 patients (5%) experienced a transient morbidity (1 pulmonary artery embolism, 2 postprocedural TIAs, 1 late transient cranial nerve palsy, 2 asymptomatic thromboses requiring hospitalization). Two of 121 patients (1.7%) developed a permanent morbidity, and 1/121 patients (0.8%) died. Neither aneurysm rupture nor parenchymal hemorrhage was observed after p64 treatment.

Angiographic Follow-Up

An early follow-up DSA examination was performed after a median of 92 days in 123/130 aneurysms (94.6%). The remaining 7 aneurysms included 3 failed treatment attempts, 1 patient who had died, 2 patients who refused follow-up examinations, and 1 pending DSA. Complete aneurysm occlusion was confirmed in 72 (58.5%), and a neck remnant, in 26 (21.1%) aneurysms. For 16 (13%) aneurysms, a sac remnant was found, and 9 (7.3%) aneurysms were unchanged.

An intermediate follow-up DSA was available in 93/106 eligible aneurysms (87.7%) treated until May 2014 after a median of 279 days, showing a complete aneurysm occlusion in 74 (79.6%) and a neck remnant in 13 (14%) aneurysms. For 4 (4.3%) aneurysms, a sac remnant was found, and 2 (2.2%) aneurysms were unchanged. The missing 13 aneurysms include 3 failed treatment attempts, 1 patient who died, 1 aneurysm that was retreated, 5 patients refusing follow-up DSA, and 3 pending examinations.

A late follow-up DSA (after 496 days, median) has been performed already in 35 aneurysms, revealing complete occlusion in 30 (85.7%) and neck remnant in 5 (14.3%) aneurysms, respectively.

Asymptomatic usually transient in-stent stenosis was identified in 24/123 (19.5%) patients during the early follow-up DSA (LL, <50%, $n = 11$; LL, 50%–75%, $n = 11$; LL, >75%, $n = 2$). The midterm follow-up DSA revealed in-stent stenosis in 11/93 (11.8%) patients (LL, <50%, $n = 9$; LL, 50%–75%, $n = 2$; LL, >75%, $n = 0$). The late follow-up DSA showed no in-stent stenosis with a LL of ≥50%.

Three patients underwent uneventful balloon angioplasty for asymptomatic in-stent stenoses. In 15 patients, in-stent stenosis significantly improved after the first follow-up DSA without any additional treatment.

Retreatment of the target lesion was performed in 5 patients. In 3 of these patients, the effect of the first implant was considered insufficient. In 2 patients, the first p64 had shortened from distal to proximal, leaving the aneurysm neck uncovered. All 5 patients were retreated by deploying another p64. All retreatments were performed and tolerated without any adverse events.

Clinical Follow-Up

The mRS score improved in 8 patients (6.6%) and remained unchanged in 110 patients (90.9%). Clinical deterioration was observed in 3 patients (2.5%). The rates of transient morbidity, permanent morbidity, and mortality in this series are 5%, 1.7%, and 0.8%, respectively.

Table 2 shows a breakdown of aneurysm occlusion rates and complication incidences according to the size of the aneurysm fundus. The cumulative numbers for complete occlusion and neck remnants are given. All complications are listed.

DISCUSSION

This retrospective study presents our experience in the treatment of intracranial saccular sidewall aneurysms with the p64, a mechanically detachable flow diverter. The technical success rate, clinical outcome, and angiographic results are in line with the findings of comparable series.[1,3-5,11-13] The device itself is being developed further, similar to modifications to the PED and NeuroEndoGraft.

Flow Diversion

Endovascular treatment of wide-neck and very small aneurysms can be challenging. The concept of redirecting the blood flow away from the aneurysm along the parent artery with subsequent intra-aneurysmal thrombosis resulted in the development of flow diverters. This effort led to numerous in vitro hemodynamic studies that identified porosity (defined as the percentage of open surface area relative to the entire surface area of the device) and pore and filament size as essential factors.[14,15] A porosity of approximately 70% was shown to be ideal for adequate hemodynamic efficiency without a relevant loss of flexibility and negligible effects on the parent artery and the side branches. Most of the currently available flow diverters, as well as the p64, are designed with a porosity of approximately 70% at nominal diameters. Compared with 48 wires for PED and Silk+, the p64 is a braid of 64 nitinol wires, which results in denser coverage across the aneurysm neck. It features a controlled mechanical detachment mechanism, which allows repositioning or withdrawal of the device even after complete deployment.

Issues after flow-diverting procedures are frequently the result of malpositioning or incomplete opening of the implant. In their initial presentation of 63 aneurysms treated with the PED, Lylyk et al[11] reported 2 cases with deployment issues. One was a dislocation of the proximal end of the device into the aneurysm, which was repositioned with a retrieval device. In the other case, the distal tip of the delivery wire fractured. These findings are similar to our own experience with the PED.[1]

The option to withdraw and redeploy the p64 helped avoid several of the previously encountered issues.

Berge et al[3] reported 7 malpositioned Silk flow diverters in their series of 77 aneurysms. Incomplete opening of the central part of the device with poor vessel wall apposition seems to occur more frequently in curved and elongated vessels and when a longer device is used and is associated with a higher rate of in-stent thrombosis.[16] The use of a compliant balloon to achieve complete wall apposition is technically straightforward and reduces the incidence of endoleaks. In our series, there were occasional instances of incomplete proximal opening of the p64 that were corrected by manipulation with the microguidewire or the microcatheter. Balloon angioplasty was performed in 5 procedures (3.8%). As a rule of thumb, shorter devices deploy better, show less twisting, and allow more consistent wall apposition. Mechanical detachment with the possibility of optimizing the final position of the device plays a key role in the abatement of device-related issues and might significantly improve long-term clinical and angiographic results.

Side branch occlusions may be avoided by using fewer devices. Kulcsár et al[17] discussed 2 potential mechanisms leading to side branch occlusions: mechanical blockade and a narrowing of the neck or conduction of embolic material from the surface of the flow diverter. They encountered 2 cases of side branch occlusions in their series of 12 basilar artery aneurysms treated with the Silk. In one of these patients, the flow diverter was placed in a previously implanted stent.[17] Other studies showed that side branch occlusions do not necessarily result in symptomatic ischemia in patients with adequate collateral circulation. Szikora et al[18] reported 19 wide-neck aneurysms treated with the PED and detected 3 clinically silent occlusions of the ophthalmic artery. In 2 patients, 3 and 4 PEDs, respectively, had been deployed.[18]

The fact that symptomatic side branch occlusion after flow diverter treatment occurs more frequently in the posterior circulation may be due to the vessel anatomy with pontine arteries originating from the basilar trunk. This is re-emphasized by our observation of 2 perforator strokes related to p64 implantation in the basilar artery. In the basilar artery and in the proximal MCA, undersizing the p64 should be avoided because increased coverage of perforating vessels may result. Slight oversizing is associated with less coverage, but increased chronic outward force might be a stimulus for in-stent stenosis, which might cause delayed perforator occlusion.

In our practice, the decision to implant multiple devices was at the operator's discretion. Arguments in favor of >1 device included unchanged aneurysm perfusion after implantation of the first device and segmental vessel disease with very wide-neck aneurysms. In this select series, >1 p64 was used in 13/127 successful procedures (10.2%), with an average of 1.1 p64 per procedure. This value is significantly lower than the respective number in our PED series, with >1 PED in 67 of 101 treated cases,[1] with an average of 3.2 PEDs per procedure, yet our initial follow-up results are comparable with or better than those published for the PED and Silk, respectively. The currently available data, however, do not yet allow a comparison of the aneurysm occlusion rate of the p64 versus other devices. A single-device strategy might result in a lower procedural complication rate, but there is nothing magical about a "one and done" approach to treatment with a flow diverter. Complete occlusion of an aneurysm occurs when braided filaments of the flow diverter are covered by neointima across the neck. In very wide, highly concave necks or fusiform segments, the amount of braid material available for neointima to grow on may not be sufficient to enable complete endothelial growth. A continuous blood/thrombus interface across the neck keeps the aneurysm alive. For rapid neointima coverage at the neck, multiple devices may be the only solution. While economic factors may impact operators' decisions, nevertheless, patients with such aneurysms must be adequately treated. All these theoretic arguments await reconsideration in significantly larger series and eventually in comparative trials.

The experience of our institution may be 1 reason for the low

rate of multiple-device complications in this series. By the time we used the first p64, >200 patients had already been treated with the PED.

Device Selection of the p64

Chalouhi et al[19] presented 5 selected patients with spontaneous delayed migration or shortening of the PED from a series of 155 patients. Two of these observations resulted in serious clinical issues (1 fatal SAH and 1 permanent disability due to a MCA occlusion). Correct device selection, based on precise measurements of healthy landing zones, is critical to proper deployment and treatment. A correlation between the diameter of the target vessel and the resulting length of the device is provided for each p64. A 4.5 × 21 mm device at minimum will expand to a diameter of 4.5 mm and a length of 21 mm but will lengthen to 28 mm when deployed into a 4 mm vessel, which results in a decrease of surface coverage. Moderate oversizing of the implant may be used intentionally to increase the porosity (eg, in perforator-rich territories). We observed delayed shortening of the p64 in 2 patients, requiring a second treatment.

Hemorrhagic Complications

Intracranial hemorrhages after flow-diversion procedures raised a major concern. This phenomenon is not common after endovascular coiling or microsurgical clipping.

Several reports of delayed aneurysm rupture after flow diversion have been published. The hemodynamic theory assumes a valve mechanism, induced by the flow diverter, which increases the wall stress to the aneurysm. The enzymatic theory, which appears more convincing, is based on the assumption that thrombus releases enzymes that cause lysis of the aneurysm wall.[20]

In a series of 295 intracranial aneurysms treated with PED or Silk in 25 Italian centers, the authors reported a high incidence of aneurysm ruptures after treatment of large and giant aneurysms, even though the flow diverters were used in combination with coils. The mortality in the subgroup of patients treated with additional coils was 35.7%. These data suggest that the use of coils does not prevent delayed aneurysm ruptures.[2] Kulcsár et al[21] reported that very large aneurysms containing a heavy thrombus burden were most prone to delayed rupture. We have not observed any case of delayed aneurysm rupture in our p64 series so far. One possible explanation is that aneurysms with a fundus diameter of ≥10 mm were at least partially coiled before flow-diversion treatment.

Parenchymal hemorrhages distal to the target vessel, occurring several days after flow-diverter treatment, may have different underlying causes. The incidence of delayed parenchymal hemorrhages in the Retrospective Analysis of Delayed Aneurysm Ruptures after Flow Diversion study was 1.9%. This retrospective multicenter study analyzed the incidence of hemorrhagic events after flow diversion.[21]

The underlying mechanism for remote parenchymal hemorrhages remains unclear. Periprocedural microguidewire perforations are an implausible explanation. Hemorrhagic transformation of clinically silent procedural embolic infarcts was proposed.[1] Hu et al[22] performed a histopathologic assessment of brain sections of 3 patients with fatal ipsilateral intracranial hemorrhages after uneventful treatment with the PED. They detected a nonbiologic material occluding the lumen of the vessels in the region of the hemorrhage. They suggested that a rise in venule pressure due to foreign body embolic occlusion was responsible for an increased microvascular permeability, resulting in the ipsilateral hemorrhagic infarction. The material was polyvinylpyrrolidone, which is part of the coating of many neurovascular devices. One explanation for the absence of delayed hemorrhages in the presented series might be found in the preparation of the p64 by complete submersion of the device in saline before the deployment to remove trapped air bubbles.

CONCLUSIONS

The p64 offers an effective treatment option for intracranial aneurysms with low complication rates, particularly due to the ability to reposition and/or remove the device in cases of poor deployment. It allows complete aneurysm occlusion within a few months, mostly achieved with a single device. Safety margins are within expected limits, with device-related complications being infrequent. A prospective study to confirm these findings is warranted.

Disclosures: Marta Aguilar-Pérez—*UNRELATED*: *Consultancy*: phenox. Wiebke Kurre—*UNRELATED*: *Consultancy*: phenox; *Grants/Grants Pending*: Covidien,* *Comments*: research grant for stroke research; *Payment for Lectures (including service on Speakers Bureaus)*: phenox. Hans Henkes—*RELATED*: *Consulting Fee or Honorarium*: phenox, *Comments*: I have a consulting contract and a proctoring contract with phenox, which includes compensation on a fee-for-service basis; *Support for Travel to Meetings for the Study or Other Purposes*: phenox, *Comments*: compensation for expenses related to the participation in meetings with presentation of p64 data; *Other*: phenox, *Comments*: I am cofounder and shareholder of phenox; *UNRELATED*: *Board Membership*: phenox, *Comments*: Expenses related to board meetings are compensated; *Grants/Grants Pending*: Siemens,* Covidien,* *Comments*: Siemens: DynaCT projects; Covidien: stroke research; *Payment for Lectures (including service on Speakers Bureaus)*: ev3/Covidien, *Comments*: presentations related to the Pipeline flow diverter; *Patents (planned, pending or issued)*: Dendron, phenox, *Comments*: participation in numerous patents filed by Dendron and phenox; *Royalties*: phenox; *Stock/Stock Options*: phenox; *Travel/Accommodations/Meeting Expenses Unrelated to Activities Listed*: AB Medica,* *Comments*: compensation for physician training. *Money paid to the institution.

REFERENCES

1. Fischer S, Vajda Z, Aguilar Perez M, et al. **Pipeline embolization device (PED) for neurovascular reconstruction: initial experience in the treatment of 101 intracranial aneurysms and dissections.** *Neuroradiology* 2012;54:369–82
2. Briganti F, Napoli M, Tortora, et al. **Italian multicenter experience with flow-diverter devices for intracranial unruptured aneurysm treatment with periprocedural complications: a retrospective data analysis.** *Neuroradiology* 2012;54:1145–52
3. Berge J, Biondi A, Machi P, et al. **Flow-diverter Silk stent for the treatment of intracranial aneurysms: 1-year follow-up in a multicenter study.** *AJNR Am J Neuroradiol* 2012;33:1150–55
4. De Vries J, Boogaarts J, Van Norden A, et al. **New generation of flow diverter (Surpass) for unruptured intracranial aneurysms: a prospective single-center study in 37 patients.** *Stroke* 2013;44:1567–77
5. Becske T, Kallmes DF, Saatci I, et al. **Pipeline for uncoilable or failed aneurysms: results from a multicenter clinical trial.** *Radiology* 2013;267:858–68
6. Mallik AS, Nuss K, Kronen PW, et al. **A new-generation, low-permeability flow diverting device for treatment of saccular aneurysms.** *Eur Radiol* 2014;24:12–18
7. Anzai H, Falcone JL, Chopard B, et al. **Optimization of strut place-**

ment in flow diverter stents for four different aneurysm configurations. *J Biomech Eng* 2014;136:061006
8. O I, M O, A AS, et al. **Evaluation of aspirin and clopidogrel resistance in patients with acute coronary syndrome using Adenosine Diphosphate Test and Aspirin Test.** *Pak J Med Sci* 2013;29:97–102
9. Del Castillo-Carnevali H, Barrios Alonso V, Zamorano Gomez JL. **Antiplatelet therapy: resistance to traditional antiaggregation drugs and role of new antiplatelet agents** [in Spanish]. *Med Clin (Barc)* 2014;143:222–29
10. Campi A, Ramzi N, Molyneux AJ, et al. **Retreatment of ruptured cerebral aneurysms in patients randomized by coiling or clipping in the International Subarachnoid Aneurysm Trial (ISAT).** *Stroke* 2007;38:1538–44
11. Lylyk P, Miranda C, Ceratto R, et al. **Curative endovascular reconstruction of cerebral aneurysms with the Pipeline embolization device: the Buenos Aires experience.** *Neurosurgery* 2009;64:632–42
12. D'Urso PI, Lanzino G, Cloft HJ, et al. **Flow diversion for intracranial aneurysms: a review.** *Stroke* 2011;42:2363–68
13. Zhou Y, Yang PF, Fang YB, et al. **A novel flow-diverting device (Tubridge) for the treatment of 28 large or giant intracranial aneurysms: a single-center experience.** *AJNR Am J Neuroradiol* 2014;35:2326–33
14. Augsburger L, Fahrhat M, Reymond P, et al. **Effect of flow diverter porosity an intraaneurysmal blood flow.** *Klin Neuroradiol* 2009;19:204–14
15. Seshadhri S, Janiga G, Beuing O, et al. **Impact of stents and flow diverters on hemodynamics in idealized aneurysm models.** *J Biomech Eng* 2011;133:071005
16. Wagner A, Cortsen M, Hauerberg J, et al. **Treatment of intracranial aneurysms: reconstruction of the parent artery with flow-diverting (Silk) stent.** *Neuroradiology* 2012;54:709–18
17. Kulcsár Z, Ernemann U, Wetzel SG, et al. **High-profile flow diverter (Silk) implantation in the basilar artery: efficacy in the treatment of aneurysms and the role of the perforators.** *Stroke* 2010;41:1690–96
18. Szikora I, Berentei Z, Kulcsar Z, et al. **Treatment of intracranial aneurysms by functional reconstruction of the parent artery: the Budapest experience with the Pipeline embolization device.** *AJNR Am J Neuroradiol* 2010;31:1139–47
19. Chalouhi N, Tjoumakaris SI, Gonzalez LF, et al. **Spontaneous delayed migration/shortening of the Pipeline embolization device: report of 5 cases.** *AJNR Am J Neuroradiol* 2013;34:2326–30
20. Turowski B, Macht S, Kulcsàr Z, et al. **Early fatal hemorrhage after endovascular cerebral aneurysm treatment with a flow diverter (SILK-Stent): do we need to rethink our concepts?** *Neuroradiology* 2011;53:37–41
21. Kulcsàr Z, Szikora I. **The ESMINT Retrospective Analysis of Delayed Aneurysm Ruptures after Flow Diversion (RADAR) study.** *The eJournal of the European Society of Minimally Invasive Neurological Therapy* 2012;1244000088. http://www.ejmint.org/sites/default/files/pdf/original_article_1244000088.pdf. Accessed October 29, 2012
22. Hu YC, Deshmukh VR, Albuquerque FC, et al. **Histopathological assessment of fatal ipsilateral intraparenchymal hemorrhages after the treatment of supraclinoid aneurysms with the Pipeline embolization device.** *J Neurosurg* 2014;120:365–74

Platelet Testing is Associated with Worse Clinical Outcomes for Patients Treated with the Pipeline Embolization Device

W. Brinjikji, G. Lanzino, H.J. Cloft, A.H. Siddiqui, R.A. Hanel, and D.F. Kallmes

ABSTRACT

BACKGROUND AND PURPOSE: The necessity for platelet-inhibition testing before aneurysm treatment in patients premedicated with antiplatelet agents is controversial. Using the International Retrospective Study of Pipeline Embolization Device registry, we studied complication rates in groups of patients who underwent platelet testing and those who did not undergo platelet testing to determine if these test results were associated with improved outcomes.

MATERIALS AND METHODS: Patients in the International Retrospective Study of Pipeline Embolization Device registry with an unruptured aneurysm were categorized as those who underwent platelet testing before Pipeline embolization device treatment or those who did not. Complication rates were compared by using the Fisher exact or Pearson χ^2 test. Multivariate analysis was performed to determine if platelet function testing was independently associated with poor outcomes after adjusting for age, number of devices and aneurysms, aneurysm location and size, and practitioner and center volume.

RESULTS: Compared with the patients who received a Pipeline embolization device without platelet testing, those who underwent platelet testing and Pipeline embolization device placement experienced higher rates of intracranial hemorrhage (0 of 187 [0.0%] vs 12 of 511 [2.3%], respectively; $P = .04$), neurologic morbidity (4 of 187 [2.1%] vs 42 of 511 [8.2%], respectively; $P < .01$), and combined neurologic morbidity and mortality (6 of 187 [3.2%] vs 45 of 511 [8.8%], respectively; $P = .01$). More patients in the platelet testing and Pipeline embolization device group were treated with multiple devices (227 [38.0%] vs 56 [27.8] patients, respectively; $P = .01$). On multivariate analysis, the group of patients who underwent platelet testing and Pipeline embolization device placement had higher odds of neurologic morbidity (OR, 3.25 [95% CI, 1.10–9.61]; $P = .03$).

CONCLUSIONS: Platelet testing in patients who undergo Pipeline embolization device placement is associated with higher rates of morbidity. Additional prospective studies are needed to determine if and when platelet testing in these patients is appropriate.

ABBREVIATION: PED = Pipeline embolization device

The Pipeline embolization device (PED; Covidien, Irvine, California) is increasingly used in the treatment of intracranial aneurysms.[1-4] The PED flow diverter is a bare-metal construct that serves as a scaffold for neointimal proliferation.[5,6] Because of the thrombogenic nature of the bare-metal component of the device, dual-antiplatelet therapy is required in both the preoperative and postoperative settings, and patients are required to take dual-antiplatelet therapy for several months after the procedure.

In addition to aspirin, clopidogrel is currently the most commonly prescribed antiplatelet drug for dual-antiplatelet therapy among patients who undergo PED placement. However, there exists wide variability in the activation of clopidogrel among individual patients.[7] As a result, platelet function testing is widely used among neurointerventionists to ensure proper function of the drug.[8,9] However, controversy exists as to whether platelet testing is necessary in patients who undergo PED placement, because the benefits have yet to be proved.[10] By using the International Retrospective Study of Pipeline Embolization Device (IntrePED) registry,[11] we compared the clinical outcomes of patients who underwent platelet testing and those who did not to determine whether this testing was associated with better outcomes among patients who undergo PED placement.

MATERIALS AND METHODS

Study Design and Participants

We retrospectively evaluated all patients with an unruptured intracranial aneurysm who were treated with the Pipeline embolization device between July 2008 and February 2013 in 1 of 17

Received January 29, 2015; accepted after revision March 24.

From the Departments of Radiology (W.B., G.L., H.J.C., D.F.K.) and Neurosurgery (G.L., H.J.C., D.F.K.), Mayo Clinic, Rochester, Minnesota; Department of Neurosurgery (A.H.S.), State University of New York, Buffalo, New York; and Department of Neurosurgery (R.A.H.), Baptist Neurological Institute, Jacksonville, Florida.

Please address correspondence to W. Brinjikji, MD, Mayo Clinic, 200 First St SW, OL1-112 SMH, Rochester, MN 55905; e-mail: kallmes.david@mayo.edu; @wbrinjikji

http://dx.doi.org/10.3174/ajnr.A4411

centers in 6 countries experienced in PED use. The local institutional review boards or ethics committees approved the study and granted waivers of informed consent for use of the patients' retrospective data. This postmarket observational registry was funded and supported by Covidien, which had scientific oversight of the study's steering committee members.

Patients were included if they underwent PED treatment for an intracranial aneurysm after the date of regulatory approval in that region or country. Patients were excluded if they had not undergone "meaningful" follow-up, defined as imaging and clinical evaluations after treatment during the window of time defined by each institutional review board/ethics committee approval. Seven hundred ninety-three patients with 906 aneurysms (76 [8.4%] ruptured, 824 [91%] unruptured, and 6 [0.7%] unknown) were included. Of the patients with an unruptured aneurysm, information on whether antecedent platelet testing was performed was available for 698 patients with 802 aneurysms. Any patient with a ruptured aneurysm was excluded from the analysis.

Procedures

Because this was a retrospective study, procedural details and periprocedural patient management varied across the centers. All the centers used a common study protocol. The steering committee defined neurologic "clinical safety events of interest" a priori, including spontaneous rupture of the target aneurysm causing subarachnoid hemorrhage or cavernous-carotid fistula, intraparenchymal hemorrhage, ischemic stroke, parent artery stenosis, and permanent cranial neuropathy. Site investigators identified events of interest according to the study protocol. All events of interest were reviewed in detail by an adverse events review committee, comprising 3 members of the steering committee, including the overall principal investigator. The adverse events review committee was independent of the sponsor. The committee determined the category of event and whether the event was major or minor. A major adverse event was defined as ongoing clinical deficit 7 days after the event. All major adverse events are included in the neurologic morbidity and mortality rates. The timing of every adverse event was recorded in relation to the timing of the PED procedure, not the timing of platelet testing. Information collected during the study included baseline characteristics of the patients and aneurysms, procedural information, and follow-up clinic visits or telephone calls. The use of platelet testing was indicated on the case report forms for each patient. Every patient who underwent platelet testing did so before the procedure.

Baseline Characteristics and Outcomes

Patients were categorized as those who underwent platelet testing before PED treatment (platelet testing/PED group) or those who underwent PED treatment only (PED alone group). No patient in the PED alone group underwent platelet testing, and every patient in the platelet testing/PED group underwent platelet testing before treatment. The decisions to perform platelet testing varied according to operator and center. The following baseline characteristics were compared between the groups: age, aneurysm size (in millimeters), aneurysm location (ICA, MCA, posterior nonbasilar, basilar, or other), number of PEDs used, aneurysm shape (dissecting, fusiform, saccular, or other), mean and median center volume of PED procedures during the study period, and the mean and median practitioner volume of PED procedures during the study period.

The primary outcome of this study was combined neurologic morbidity and neurologic mortality. The secondary outcomes were spontaneous rupture, intracranial hemorrhage, ischemic stroke, parent artery stenosis, cranial neuropathy, neurologic morbidity, neurologic mortality, and all-cause mortality. These outcomes were compared between the groups.

Statistical Analysis

Statistical analyses were performed by using SAS version 9.1 or higher (SAS Institute, Cary, North Carolina). Summary statistics are presented for all data available by using means and standard deviations for continuous variables and frequency tabulations for categoric variables. Comparisons between the groups for continuous variables were evaluated by using *t* tests or ANOVA and for binary categoric variables using the Fisher exact or Pearson χ^2 test. Most statistical analyses were performed across patient groups (ie, on a per-patient basis). Because some patients had >1 aneurysm, however, each patient's first aneurysm treated was used to classify him or her into the 4 anatomic/size subgroups, and the largest aneurysm was used to classify patients into 1 of the 3 aneurysm size categories. The first aneurysm treated was defined a priori.

A multivariate logistic regression analysis was performed to determine if platelet function testing was independently associated with the outcomes listed above. Adjusted variables in this model included age, aneurysm size, aneurysm location, number of aneurysms treated, number of PEDs, center volume (modeled as a continuous variable), and practitioner volume (modeled as a continuous variable). These variables were included in the model because they were associated with adverse outcomes in either the original International Retrospective Study of Pipeline Embolization Device study or subsequent subgroup analyses that are currently being performed. For complications with a low incidence rate (eg, spontaneous rupture, cranial neuropathy), the Firth penalized maximum-likelihood estimation was used to reduce bias in the parameter estimates caused by separability, as often occurs when the event is rare. Goodness-of-fit tests were performed for the multivariate models by using the Hosmer–Lemeshow models.

Role of the Funding Source

An academic principal investigator and an academic steering committee supervised the trial design and operations. The principal investigator, steering committee, and adverse events committee were independent of the sponsor. The steering committee interpreted the results, and the principal investigator wrote the report. The study sponsor was responsible for site management, data management, statistical analysis, and safety reporting. The corresponding author had full access to all study data and had final responsibility for the decision to submit for publication.

Table 1: Anatomic and clinical characteristics

Demographic Characteristic	Platelet Testing/PED Group	PED Alone Group	*P* Value
No. (%) of patients	511 (73.2)	187 (26.8)	
Age, y			
Mean ± SD	58.1 ± 14.1	55.7 ± 13.2	.022
Median (minimum, maximum)	59 (9, 86)	57 (13, 81)	
No. (%) male	98 (19.2)	40 (21.4)	.52
Follow-up duration, mo			
Mean ± SD	21.5 ± 8.0	23.5 ± 10.1	.20
Median (minimum, maximum)	20.8 (0.1, 48.0)	21.3 (0.2, 60.5)	
Total no. (%) of aneurysms	601 (74.8)	201 (25.2)	
No. (%) of patients with			
1 aneurysm	438 (85.7)	176 (94.1)	
2 aneurysms	61 (11.9)	9 (4.8)	.008
≥3 aneurysms	12 (2.4)	2 (1.1)	
Mean center volume ± SD, *n*	65 ± 45	63 ± 32	.06
Median center volume (minimum, maximum), *n*	47 (21, 149)	69 (19, 149)	
Mean practitioner volume ± SD, *n*	25 ± 15	21 ± 13	.004
Median practitioner volume (minimum, maximum), *n*	21 (1, 54)	21 (1, 54)	
Aneurysm size, mm			
Mean ± SD (*n*)	10.8 ± 7.7 (595)	12.0 ± 7.7 (200)	.01
Median (minimum, maximum)	8.8 (1.0, 55.0)	10.5 (1.0, 40.0)	
Aneurysm location, % (*n*/*N*)			
Internal carotid artery	78.0 (469/601)	77.1 (155/201)	
Middle cerebral artery	4.7 (28/601)	3.0 (6/201)	
Posterior cerebral artery	1.7 (10/601)	1.0 (2/201)	.11
Basilar artery	4.0 (24/601)	8.5 (17/201)	
Other	11.6 (70/601)	10.4 (21/201)	
Multiple PEDs used	38.0 (227/598)	27.9 (56/201)	.01
Aneurysm shape, % (*n*/*N*)			
Saccular	76.9 (462/601)	77.1 (155/201)	
Fusiform	13.1 (79/601)	13.4 (27/201)	.58
Dissecting	5.0 (30/601)	6.5 (13/201)	
Other	5.0 (30/601)	3.0 (6/201)	

Table 2: Complications

Complication	Platelet Testing/PED Group (*N* = 511) (% [*n*])	PED Alone Group (*N* = 187) (% [*n*])	*P* Value
Primary outcome: neurologic morbidity and neurologic mortality	8.8 (45)	3.2 (6)	.01
Secondary outcomes			
Spontaneous rupture	0.6 (3)	0.5 (1)	1
Intracranial hemorrhage	2.3 (12)	0.0 (0)	.04
Ischemic stroke	5.5 (28)	2.1 (4)	.07
Parent artery stenosis	0.2 (1)	0.5 (1)	.46
Cranial neuropathy	0.4 (2)	0.0 (0)	1
Neurologic morbidity	8.2 (42)	2.1 (4)	<.01
Neurologic mortality	3.5 (18)	1.1 (2)	.12
All-cause mortality	4.1 (21)	1.1 (2)	.05

RESULTS

Baseline Characteristics

A total of 698 patients with 802 treated unruptured aneurysms were included in this study; 511 (73.2%) patients with 601 aneurysms underwent platelet testing before PED placement, and 187 (26.8%) patients with 201 aneurysms underwent PED placement without platelet testing. Aneurysm sizes were significantly larger in the PED alone group than in the platelet testing/PED group (mean ± SD, 12.0 ± 7.7 vs 10.8 ± 7.7 mm, respectively; $P = .04$). More patients in the platelet testing/PED group were treated with multiple PEDs (227 [38.0%] vs 56 [27.9%] patients, respectively; $P = .01$). No differences in aneurysm shape ($P = .58$) or location ($P = .11$) were seen between the groups. More patients in the platelet testing/PED group were treated for multiple aneurysms than in the PED alone group (14.3% vs 5.9%, respectively; $P = .008$). The median follow-up time was 19.3 months. Patients in the platelet testing/PED group had a higher mean practitioner volume than those in the PED alone group (25 vs 21, respectively; $P = .004$). The mean center volumes were similar in both groups (65 [platelet testing/PED] vs 63 [PED alone]; $P = .06$). Ninety percent of the patients were followed up for >12 months. These data are summarized in Table 1.

Complication Rates According to Platelet-Testing Status

Bivariate Analysis. Among patients in the platelet testing/PED group, 12 of 511 (2.3%) patients suffered intracranial hemorrhage compared with 0 of 187 (0.0%) patients in the PED alone group ($P = .04$). There was a trend toward higher rates of ischemic stroke in the platelet testing/PED group; 28 (5.5%) patients in the platelet testing/PED group experienced ischemic stroke compared with 4 (2.1%) patients in the PED alone group ($P = .06$). The neurologic morbidity rate was higher in the platelet testing/PED group than in the PED alone group (42 [8.2%] vs 4 [2.1%] patients, respectively; $P = .01$). There was also a trend toward a higher neurologic mortality rate in the platelet testing/PED group than in the PED alone group (18 [3.5%] vs 2 [1.1] patients, respectively; $P = .12$). The combined neurologic morbidity and mortality rate was higher in the platelet testing/PED group than in the PED alone group (45 [8.8%] vs 6 [3.2%] patients, respectively; $P = .01$). The all-cause mortality rate was also higher in the platelet testing/PED group than in the PED alone group. There were 3 cases of nonneurologic mortality, 2 in the platelet testing/PED group and 1 in the PED alone group. Causes of nonneurologic mortality included extracranial hemorrhage, sudden death, and hepatic fibrosis with cirrhosis. All adverse events occurred after PED placement. The median and mean times for complications were 7 and 40 days after the procedure, respectively (range, 0–397 days). These data are summarized in Table 2.

Multivariate Analysis. On multivariate logistic regression analysis with adjustment for age, aneurysm size, aneurysm location, number of PEDs, center volume, practitioner volume, and number of aneurysms, the platelet testing/PED group had a higher odds of neurologic morbidity (OR, 3.25 [95% CI, 1.10–9.61]; $P =$

Table 3: Multivariate logistic regression analysis: odds of complications according to platelet-testing status

Complication	OR[a]	95% CI	*P* Value
Primary outcome: neurologic morbidity and neurologic mortality	2.37	0.95 to 5.93	.06
Secondary outcomes			
Spontaneous rupture	1.46	0.28 to 7.67	.65
Intracranial hemorrhage	6.56	0.50 to 85.80	.15
Ischemic stroke	2.03	0.67 to 6.20	.21
Parent artery stenosis	0.06	<0.001 to 24.51	.37
Cranial neuropathy	1.17	0.22 to 6.38	.85
Neurologic mortality	3.24	0.80 to 15.01	.13
Neurologic morbidity	3.25	1.10 to 9.61	.03
All-cause mortality	3.67	0.81 to 16.74	.09

[a] Shown are the odds in the platelet testing/PED group versus those in the PED alone group. For each of the complications, the OR is for the platelet testing/PED versus the PED alone group. The analysis was adjusted for age, gender, aneurysm size, number of aneurysms treated, use of multiple PEDs, practitioner's previous experience, and center volume.

.03). There was also a trend in the platelet testing/PED group toward higher odds of combined neurologic morbidity and mortality (OR, 2.37 [95% CI, 0.95–5.93]; $P = .064$) and all-cause mortality (OR, 3.67 [95% CI, 0.81–16.74]; $P = .09$) relative to those in the PED alone group. For all the models, *P* values from the Hosmer–Lemeshow goodness-of-fit test were nonsignificant ($P > .05$), indicating that there was no evidence of poor fit. These data are summarized in Table 3.

DISCUSSION

Our study of patients included in the International Retrospective Study of Pipeline Embolization Device registry found higher complication rates and higher rates of neurologic morbidity in the platelet testing/PED group than in the PED alone group. However, there were significant differences in the baseline characteristics of the 2 groups. Namely, patients in the PED alone group were younger and were less likely to be treated with multiple PEDs, and the group had a larger mean aneurysm size. In addition, patients in the platelet testing/PED group were more likely to be treated at high-volume centers and to be treated by higher-volume practitioners. In our analysis, which was adjusted for age, aneurysm size, aneurysm location, number of aneurysms, number of PEDs, center volume, and practitioner volume, platelet testing was associated with a significantly higher odds of neurologic morbidity. These findings are important, because they suggest that preoperative platelet testing does not result in improved outcomes of patients who undergo PED placement and is associated with higher odds of neurologic morbidity after PED treatment.

Previous studies have found variable associations between platelet response and ischemic and hemorrhagic complications after neurovascular stent placement and after PED placement. In a study of 96 patients who received a neurovascular (carotid or intracranial) stent, Fifi et al[9] found that clopidogrel-resistant patients had a significantly higher rate of thromboembolic events than those who were not resistant. In a study of 74 patients who underwent PED placement, Tan et al[12] found that having a level of >208 P2Y12 reaction units was associated with a non–statistically significant trend toward higher rates of symptomatic stroke on both univariate and multivariate analysis but no significant difference in infarcts as seen in diffusion-weighted MR imaging. Delgado Almandoz et al[13] found higher rates of stroke among patients with clopidogrel hyporesponse who underwent stent-assisted coiling and PED placement and higher rates of hemorrhage among patients with clopidogrel hyperresponse. Similarly, Goh et al found that hyperresponse to clopidogrel was associated with higher rates of hemorrhage.[14] Heller et al[15] studied the effect of antiplatelet therapy on thromboembolic events after flow diversion with the PED and found no difference in platelet reactivity between patients with and without infarcts found with MR imaging.

Although previous studies found an association between platelet-testing results and neurovascular complications after stent/PED placement, studies have yet to clearly demonstrate that altering antiplatelet regimens on the basis of platelet-testing results leads to improved clinical outcomes. Fifi et al[9] compared thromboembolic event rates among a group of patients who underwent changes in antiplatelet therapy regimens based on platelet-testing results and another group of patients who did not undergo any changes and found no difference in thromboembolic event rates. In a study that compared complication rates among patients who underwent platelet testing (68 patients) and those who did not (32 patients), Oran et al[16] found higher rates of morbidity and thrombotic complications in the group that did not undergo testing ($P = .03$). However, in a study of 81 patients who underwent flow-diverter placement, Nordeen et al[17] found that despite the fact that most clopidogrel-resistant patients received higher loading and maintenance doses of clopidogrel, the mortality rate was significantly higher in the clopidogrel-resistant group, and higher loading doses were associated with a trend toward higher complication rates ($P = .07$). The results of these studies range from demonstrating a mild benefit for platelet function testing to mild harm.

However, our study of >800 patients revealed that platelet function testing is associated with a significantly higher odds of morbidity in patients who undergo PED placement. Although it is unclear from this cohort exactly what the precise reasons might be for these findings, it is clear that testing by itself has no reason to affect outcome. We can speculate on the causes, but there are no available details in this dataset to indicate what actions were taken or not taken in response to the test results. We speculate that aggressive periprocedural manipulation of loading doses or other adjunctive drugs may be causal; however, there is no definitive evidence from this study to suggest that this is the case. It should be recognized, however, that there was a higher number of PEDs used in the platelet testing/PED group, which may have played a significant role in contributing to the morbidity related to the procedure. However, even when adjusting for this variable, the use of platelet testing was still associated with higher complication rates. Other unmeasured factors, such as the presence of comorbidities or baseline platelet dysfunction, may have contributed to the higher morbidity rate seen in the platelet testing/PED group. What may be recommended is that testing and any responses to the test results be performed days before the actual procedure to reduce the potential for overshooting targets and incurring potentially greater morbidity rates in the postprocedural period, as noted in this cohort of tested patients.

The effects of altering antiplatelet therapy to alter the rate of adverse thrombotic events have been studied extensively in the cardiology literature. The Gauging Responsiveness with a VerifyNow Assay-Impact on Thrombosis and Safety (GRAVITAS) trial compared the effects of high-dose and standard-dose clopidogrel with high on-treatment platelet reactivity after percutaneous coronary intervention; no differences in fatal cardiovascular events, stent thrombosis, or nonfatal myocardial infarction were seen between the standard- and high-dose-clopidogrel groups,[18] despite the fact that the high-dose group had significantly decreased platelet activity compared with that in the standard-dose group. Although the GRAVITAS study did not find a benefit with increased clopidogrel doses, it demonstrated an increased incidence of adverse events in the high-reactivity group compared with that of the clopidogrel responders. A meta-analysis of 10 randomized clinical trials in which an intensified antiplatelet protocol based on adenosine diphosphate–specific platelet-reactivity testing was used found that the intensified protocol was associated with lower mortality and myocardial infarction rates; however, the benefit of intensified antiplatelet therapy was highly dependent on the patient's initial risk of stent thrombosis.[19] In a recent position paper by the Working Group of the European Society of Cardiology, high platelet reactivity (resistance to clopidogrel) was recognized as a marker for a high event rate during coronary intervention, especially during acute myocardial infarct intervention.[20] The use of alternative second antiplatelet agents such as prasugrel and ticagrelor has been recommended in such cases. The significance and translation of these findings to neurointervention remain unclear.

Limitations

Our study had limitations. It was a retrospective study in which sites followed their own standard of practice for treating aneurysms with PED placement, and there was a wide range of treatment regimens (eg, antiplatelet therapy) between centers. Although we compared complication rates in the platelet testing/PED and PED alone groups, we do not have information regarding which patients in the testing group were nonresponders or hyperresponders. Thus, it is possible that more patients in the PED alone group had normal platelet function. We cannot report data on complication rates by antiplatelet-response status. We included only patients with an unruptured aneurysm, so the results of this study may not apply to patients with a ruptured aneurysm. Furthermore, we do not have information regarding which patients had changes to their antiplatelet regimens based on results from platelet-response testing. Last, outcomes were not ascertained while blinded to testing status. Overall, however, our study shows that platelet testing in and of itself does not lead to superior outcomes among patients who undergo PED placement.

CONCLUSIONS

Our study from a large retrospective registry shows that platelet testing of patients who underwent PED placement was not associated with improved outcomes. The underlying cause of this finding is unclear. Further prospective studies, similar to those published in the cardiology literature, are needed to determine if and when platelet testing and correction of antiplatelet therapies are appropriate in patients who undergo PED placement.

Disclosures: Giuseppe Lanzino—*UNRELATED*: *Consultancy*: ev3/Covidien.* Adnan Siddiqui—*RELATED*: *Consulting Fee or Honorarium*: Covidien, *Comments*: Consulting fees for Pipeline Proctoring and Scientific Advisory Board Membership, Member of the Covidien SWIFT PRIME National Steering Committee; *UNRELATED*: *Board Membership*: Codman and Shurtleff, ICAVL, and Medina Medical; *Consultancy*: Codman & Shurtleff, Guidepoint Global, Peneumbra, Stryker, Pulsar Vascular, MicroVention, Lazarus Effect, Blockade Medical, Reverse Medical, and Abbott Vascular; *Payment for Lectures (including service on speakers bureaus)*: Codman & Shurtleff; *Stock/Stock Options*: Hotspur, Intratech Medical, StimSox, Valor Medical, Blockade Medical, Lazarus Effect, Pulsar Vascular, and Medina Medical; *Other*: Penumbra and MicroVention, *Comments*: Member of Penumbra 3D Separator Trial National Steering Committee, Member of MicroVention FRED Trial National Steering Committee. Ricardo Hanel—*RELATED*: *Consulting Fee or Honorarium*: Covidien, Stryker, and Codman; *UNRELATED*: *Board Membership*: Medina; *Stock/Stock Options*: Blockade. David F. Kallmes—*RELATED*: *Grant:* ev3/Covidien,* *Comments*: Clinical trial implementation; *Consulting Fee or Honorarium*: ev3/Covidien,* *Comments*: Safety Monitoring Board and Steering Committee participation; *UNRELATED*: *Board Membership:* GE Healthcare, *Comments*: Cost-effectiveness board; *Consultancy*: ev3/Covidien,* *Comments*: Planning and implementing clinical trials; *Grants/Grants Pending*: MicroVention,* Codman,* SurModics,* Sequent,* NeuroSigma,* and ev3,* *Comments*: Preclinical and clinical research. *Money paid to institution.

REFERENCES

1. Arrese I, Sarabia R, Pintado R, et al. **Flow-diverter devices for intracranial aneurysms: systematic review and meta-analysis.** *Neurosurgery* 2013;73:193–99 ; discussion 199–200 CrossRef Medline
2. Briganti F, Napoli M, Tortora F, et al. **Italian multicenter experience with flow-diverter devices for intracranial unruptured aneurysm treatment with periprocedural complications—a retrospective data analysis.** *Neuroradiology* 2012;54:1145–52 CrossRef Medline
3. Brinjikji W, Murad MH, Lanzino G, et al. **Endovascular treatment of intracranial aneurysms with flow diverters: a meta-analysis.** *Stroke* 2013;44:442–47 CrossRef Medline
4. Yu SC, Kwok CK, Cheng PW, et al. **Intracranial aneurysms: mid-term outcome of Pipeline embolization device—a prospective study in 143 patients with 178 aneurysms.** *Radiology* 2012;265:893–901 CrossRef Medline
5. Kallmes DF, Ding YH, Dai D, et al. **A new endoluminal, flow-disrupting device for treatment of saccular aneurysms.** *Stroke* 2007;38:2346–52 CrossRef Medline
6. Kallmes DF, Ding YH, Dai D, et al. **A second-generation, endoluminal, flow-disrupting device for treatment of saccular aneurysms.** *AJNR Am J Neuroradiol* 2009;30:1153–58 CrossRef Medline
7. Karaźniewicz-Lada M, Danielak D, Burchardt P, et al. **Clinical pharmacokinetics of clopidogrel and its metabolites in patients with cardiovascular diseases.** *Clin Pharmacokinet* 2014;53:155–64 CrossRef Medline
8. Delgado Almandoz JE, Crandall BM, Scholz JM, et al. **Pre-procedure P2Y12 reaction units value predicts perioperative thromboembolic and hemorrhagic complications in patients with cerebral aneurysms treated with the Pipeline embolization device.** *J Neurointerv Surg* 2013;5(suppl 3):iii3-10 CrossRef Medline
9. Fifi JT, Brockington C, Narang J, et al. **Clopidogrel resistance is associated with thromboembolic complications in patients undergoing neurovascular stenting.** *AJNR Am J Neuroradiol* 2013;34:716–20 CrossRef Medline
10. Comin J, Kallmes DF. **Platelet-function testing in patients undergoing neurovascular procedures: caught between a rock and a hard place.** *AJNR Am J Neuroradiol* 2013;34:730–34 CrossRef Medline
11. Kallmes DF, Hanel R, Lopes D, et al. **International retrospective study of the Pipeline embolization device: a multicenter aneurysm treatment study.** *AJNR Am J Neuroradiol* 2015;36:108–15 CrossRef Medline
12. Tan LA, Keigher KM, Munich SA, et al. **Thromboembolic complications with Pipeline embolization device placement: impact of procedure time, number of stents and pre-procedure P2Y12 reaction**

unit (PRU) value. *J Neurointerv Surg* 2015;7:217–21 CrossRef Medline
13. Delgado Almandoz JE, Kadkhodayan Y, Crandall BM, et al. **Variability in initial response to standard clopidogrel therapy, delayed conversion to clopidogrel hyper-response, and associated thromboembolic and hemorrhagic complications in patients undergoing endovascular treatment of unruptured cerebral aneurysms.** *J Neurointerv Surg* 2014;6:767–73 CrossRef Medline
14. Goh C, Churilov L, Mitchell P, et al. **Clopidogrel hyper-response and bleeding risk in neurointerventional procedures.** *AJNR Am J Neuroradiol* 2013;34:721–26 CrossRef Medline
15. Heller RS, Dandamudi V, Lanfranchi M, et al. **Effect of antiplatelet therapy on thromboembolism after flow diversion with the Pipeline embolization device.** *J Neurosurg* 2013;119:1603–10 CrossRef Medline
16. Oran I, Cinar C, Bozkaya H, et al. **Tailoring platelet inhibition according to multiple electrode aggregometry decreases the rate of thrombotic complications after intracranial flow-diverting stent implantation.** *J Neurointerv Surg* 2015;7:357–62 CrossRef Medline
17. Nordeen JD, Patel AV, Darracott RM, et al. **Clopidogrel resistance by P2Y12 platelet function testing in patients undergoing neuroendovascular procedures: incidence of ischemic and hemorrhagic complications.** *J Vasc Interv Neurol* 2013;6:26–34 Medline
18. Price MJ, Berger PB, Teirstein PS, et al; GRAVITAS Investigators. **Standard- vs high-dose clopidogrel based on platelet function testing after percutaneous coronary intervention: the GRAVITAS randomized trial.** *JAMA* 2011;305:1097–105 CrossRef Medline
19. Aradi D, Komócsi A, Price MJ, et al; Tailored Antiplatelet Treatment Study Collaboration. **Efficacy and safety of intensified antiplatelet therapy on the basis of platelet reactivity testing in patients after percutaneous coronary intervention: systematic review and meta-analysis.** *Int J Cardiol* 2013;167:2140–48 CrossRef Medline
20. Aradi D, Storey RF, Komócsi A, et al; Working Group on Thrombosis of the European Society of Cardiology. **Expert position paper on the role of platelet function testing in patients undergoing percutaneous coronary intervention.** *Eur Heart J* 2014;35:209–15 CrossRef Medline

LEO Baby Stent Use following Balloon-Assisted Coiling: Single- and Dual-Stent Technique—Immediate and Midterm Results of 29 Consecutive Patients

P. Machi, V. Costalat, K. Lobotesis, C. Ruiz, Y.B. Cheikh, O. Eker, G. Gascou, F. Danière, C. Riquelme, and A. Bonafé

ABSTRACT

BACKGROUND AND PURPOSE: We report our preliminary results in terms of safety and efficacy in using the low-profile LEO Baby stent for the treatment of large-neck and complex intracranial aneurysms with balloon-then-stent-assisted coiling and single- or dual-stent-assisted coiling.

MATERIALS AND METHODS: Clinical and radiologic data of all consecutive patients treated at our institution from September 2012 to October 2013 for an intracranial aneurysm by using a LEO Baby stent were retrospectively analyzed. Immediate and midterm clinical and anatomic follow-up of each patient is reported.

RESULTS: Twenty-nine patients with 29 aneurysms were treated with LEO Baby stents at our institution. The mean age of patients was 48 years; 20 patients were women (71%). One patient was treated in the acute phase of a subarachnoid hemorrhage. In 8 procedures, a double-lumen-catheter balloon was used for balloon-then-stent-assisted coiling. In 3 cases, a LEO Baby stent was used in a Y-, T-, and telescopic dual-stent configuration. In 18 cases, a single LEO Baby stent was used. In 2 cases, technical failure to deploy the stent resulted in acute parent artery thrombosis. In 3 further cases, thromboembolic complications occurred intraoperatively. MR imaging and angiographic midterm follow-up showed complete aneurysm occlusion for 96% of the followed patients (27/29). Clinical outcome was favorable for all patients followed up.

CONCLUSIONS: Results obtained in our study by using the LEO Baby stent for balloon-then-stent and single- or dual-stent-assisted coiling of complex and distally located intracranial aneurysms are encouraging. Incomplete or inadequate opening of the device is a potential cause of laminar blood flow alteration and thrombus formation.

ABBREVIATIONS: ACA = anterior cerebral artery; AcomA = anterior communicating artery; LBS = LEO Baby stent

The results of endovascular treatment of wide-neck and complex intracranial aneurysms have improved following the introduction of balloon remodeling and stent-assisted coiling.[1-6] Theoretically, intracranial stents act as a scaffold to maintain the coil mass within the aneurysmal sac, allowing higher packing density. This leads to a reduction of the blood flow into the aneurysmal sac while diverting it toward the parent vessel and provides support for the neointima growth across the neck.[7,8] The LEO Baby stent (LBS; Balt Extrusion, Montmorency, France) is a new self-expandable stent with 16 nitinol wires (2 of which are radiopaque). This braided microstent can be delivered through a 0.0165-inch microcatheter or a dual-lumen balloon catheter system (Scepter XC; MicroVention, Tustin, California) and deployed within arteries with diameters ranging from 1.5 to 3.1 mm. In the present study, we report our preliminary results in terms of safety and efficacy by using the LBS for the treatment of large-neck and complex intracranial aneurysms with balloon-then-stent-assisted coiling and single- or dual-stent-assisted coiling.

MATERIALS AND METHODS

Patient Sample

Clinical and radiologic data of all consecutive patients treated at our institution from September 2012 to October 2013 for an intracranial aneurysm by stent-assisted coiling by using LBSs were retrospectively analyzed. This study followed institutional review board approval. Written informed consent was obtained from every patient before treatment.

Received December 2, 2014; accepted after revision March 19, 2015.

From the Centre Hospitalier Universitaire Gui de Chauliac (P.M., V.C., C.R., Y.B.C., O.E., G.G., F.D., C.R., A.B.), Montpellier, France; and Imperial College Healthcare (K.L.), London, UK.

Please address correspondence to Paolo Machi, MD, Centre Hospitalier Universitaire Gui de Chauliac, 80 Ave Augustine Fliche 34000 Montpellier, France; e-mail: paolo.machi@gmail.com

http://dx.doi.org/10.3174/ajnr.A4413

Patient findings

Pt	Aneurysm Location	Procedural Technique	Adverse Events	Clinical Outcome	Aneurysm Cure
1	AcomA	Single stent	Yes	Favorable	Yes
2	BA	Single stent	No	Favorable	Yes
3	MCA	Dual Y-stents	No	Favorable	No
4	ICA bifurcation	Single stent	Yes	Favorable	Yes
5	ACA (A1)	Single stent	No	Favorable	Yes
6	MCA	Single stent	No	Favorable	Yes
6bis[a]	MCA	Dual T-stents	No	Favorable	Yes
7	ACA (A1)	Telescopic	Yes	Unfavorable	
8	MCA	Balloon/stent	No	Favorable	Yes
9	MCA	Single stent	No	Favorable	Yes
10	MCA	Single stent	Yes	Favorable	Yes
11	Callosomarginal	Balloon/stent	No	Favorable	Yes
12	ACA (A1)	Dual T-stents	No	Favorable	Yes
13	MCA	Balloon/stent	No	Favorable	Yes
14	AcomA	Single stent	Yes	Unfavorable	
15	MCA	Balloon/stent	No	Favorable	Yes
16	MCA	Single stent	No	Favorable	Yes
17	AcomA	Single stent	No	Favorable	Yes
18	MCA	Single stent	No	Favorable	Yes
19	AcomA	Single stent	No	Favorable	Yes
20	AcomA	Single stent	No	Favorable	Yes
21	AcomA	Single stent	No	Favorable	Yes
22	PICA	Single stent	No	Favorable	Yes
23	AcomA	Single stent	No	Favorable	Yes
24	MCA	Balloon/stent	No	Favorable	Yes
25	BA	Single stent	No	Favorable	Yes
26	MCA	Balloon/stent	No	Favorable	Yes
27	AcomA	Balloon/tent	No	Favorable	Yes
28	MCA	Balloon/stent	No	Favorable	Yes
29	ACA (A1)	Single stent	No	Favorable	Yes

Note:—Pt indicates patient; BA, basilar artery.

[a] Retreatment of patient 6 for the second time with a LEO baby stent.

Medications

Patients treated for an unruptured aneurysm were premedicated the day before the procedure with a loading dose of 300 mg of clopidogrel. Resistance to clopidogrel was tested in the angiosuite by using a VerifyNow P2Y12 assay (Accumetrics, San Diego, California) just before the procedure. The day after the procedure, a dual-antiplatelet regimen was introduced for 3 months (75 mg clopidogrel and 75 mg aspirin, once daily); thereafter mono-antiplatelet therapy was maintained with aspirin for an additional 3 months. Patients treated in the acute phase of a subarachnoid hemorrhage were not premedicated and received an intravenous bolus of aspirin or anti-glycoprotein IIb/IIIa intraoperatively after LBS placement. All procedures were performed in patients on systemic anticoagulation with an activated clotting time maintained between 200 and 300 seconds. At the end of the procedure, the systemic anticoagulation was not continued.

Techniques

All procedures were performed with the patient under general anesthesia and by a senior interventional neuroradiologist with prior experience in intracranial stent placement. Depending on the technique of choice, a single or bilateral femoral artery approach was performed. A 6F or 7F guide catheter was placed proximally in the aneurysm parent artery (internal carotid or vertebral artery); a second guide catheter was placed in the contralateral corresponding artery; the contralateral catheter was not used systematically. Patients in this series were treated with different techniques: single-stent or dual-stent-assisted coiling or remodelling balloon-assisted coiling followed by parent artery stent placement. Moreover, in 1 case of a ruptured blister aneurysm, 2 LBSs were used in a telescopic configuration to produce a flow-diverting effect without adjunctive aneurysm coiling. In cases of dual-stent-assisted coiling, the LBSs were deployed in a Y- or T-configuration. In 3 cases of dual-stent placement, a Neuroform EZ stent system (Stryker Neurovascular, Fremont, California) was used in combination with an LBS.

Radiologic and Clinical Follow-Up

All patients were scheduled for an MR imaging/MRA follow-up at 6 months and conventional DSA at 12 months. The MR imaging follow-up consisted of structural imaging and time-of-flight MR angiography performed by using a 1.5T MR imaging scanner (Avanto; Siemens, Erlangen, Germany). Clinical outcomes were assessed at the time of the radiologic follow-up by using the modified Rankin Scale. An mRS of ≤ 2 was considered a good outcome.

RESULTS

Patient Sample

Between September 2012 and October 2013, 41 patients were treated at our institution endovascularly by stent-assisted coiling. Among them, 29 patients with 29 aneurysms were treated with LBSs (Table). Patients were selected for the specific treatment because of either the small parent vessel diameter or the need for

delivery of the stent via a "low-profile" microcatheter or balloon. One patient was treated twice for the same aneurysm (patient 6). The mean age of patients was 48 years (range, 23–68 years), and 20 patients were women (71%). One patient was treated in the acute phase of a subarachnoid hemorrhage due to a blister aneurysm. In 11 patients, an LBS was deployed for retreatment of an aneurysm previously treated endovascularly (10 cases) or surgically (1 case).

Aneurysm Location

Twelve aneurysms were located at the MCA bifurcation (1 treated twice), 8 were located at the anterior communicating artery (AcomA), 4 were located on the anterior cerebral artery (ACA, A1 segment), 1 was located at the pericallosal/callosomarginal artery bifurcation, 1 was located at the ICA bifurcation, 2 arose from the top of the basilar artery, and 1 was located on the proximal portion of the posterior inferior cerebellar artery.

Techniques

In 8 procedures, a double-lumen Scepter XC catheter balloon was used for balloon-then-stent-assisted coiling. In this setting, following balloon-assisted coiling, an LBS was navigated through the Scepter XC catheter balloon and deployed in the branch on which the aneurysm was implanted. In 3 cases, an LBS was used to perform dual-stent configurations. In 18 cases, an LBS was used via a single-stent-placement assisted-coiling technique. In all these cases, the LBS was navigated and deployed across the aneurysm neck via a 0.0165-inch microcatheter. The aneurysm coiling was performed through a 0.0165-inch microcatheter previously jailed in the aneurysmal sac.

Intraprocedural Adverse Events

Five intraprocedural adverse events occurred in our series. In 3 cases (patients 1, 4, and 10), a partial intrastent thrombosis was noted after stent deployment. All these patients were good responders to clopidogrel. In all cases, the complication was managed by intravenous injection of glycoprotein IIb/IIIa (abciximab) and patients had no clinical consequences. In 2 cases, the deployment of the stent was not adequate (patients 7 and 14). The first event happened during the treatment of a ruptured right A1 blister aneurysm for which telescopic deployment of 2 LBSs was planned. The apposition of the 2 devices was not optimal, and the distal portion of the proximal stent did not expand correctly (Fig 2). An angiographic examination at 24 hours demonstrated A1 thrombosis. The second technical complication occurred during the retreatment of an AcomA aneurysm (patient 14). Following stent detachment, the operator was not able to recover the delivery wire because it was locked through the stent struts. Further attempts resulted in migration of the LBS into the right A1. Following this, the operator managed to recover the delivery wire but the stent had partially collapsed and was left in the A1. Despite several attempts to retrieve the LBS with an Amplatz goose neck snare (Covidien, Irvine, California), the stent was not recovered and the artery thrombosed. Both patients developed right ACA territory ischemia and subsequently died because of diffuse cerebral vasospasm.

Immediate and Midterm Anatomic and Clinical Results

Angiography performed at the end of the procedure showed complete aneurysm occlusion in 16 of 29 patients (55%). Residual neck was recorded in 8 patients (27%), and residual aneurysms, in 3 patients (10%). In the remaining 2 patients, the aneurysm thrombosed with the parent artery intraprocedurally.

Twenty-seven patients of 29 (93%) had midterm radiologic and clinical follow-up, and 2 patients died. Eleven patients had MR imaging follow-up between 6 and 14 months (median, 7 months), and 16 patients had DSA follow-up between 3 and 25 months (median, 12 months) after the treatment (Fig 3). Radiologic follow-up demonstrated complete aneurysm occlusion for 26 of 27 patients (96%). In only 1 case (patient 3) did the 14-month MR imaging follow-up show a persisting residual aneurysm. All patients underwent clinical assessment at the time of the radiologic follow-up. Clinical outcome was assessed by a senior neurologist by using the mRS. In all patients followed up, an mRS $\leq$2 was recorded.

Flow-Diverter Effect

In 1 case of an AcomA residual aneurysm (patient 17), in which following the detachment of the first coil, there was premature expulsion of the jailed microcatheter, the 9-month angiogram showed complete aneurysm occlusion. In 2 cases of A1 fusiform aneurysms (patients 5 and 29), immediate contrast media stagnation was visualized before the coiling and just after stent deployment. In both of these cases, the final postoperative angiogram showed residual aneurysms. The radiologic follow-up of both patients (DSA at 13 months and MR imaging at 6 months, respectively) showed remodelling of the parent artery and complete healing of the aneurysm. In 1 patient (patient 2) presenting with mass effect symptoms due to a large, partially thrombosed, basilar tip aneurysm, an LBS was deployed across the aneurysm neck after complete aneurysm coiling. The 8-month DSA showed complete aneurysm exclusion, and the 15-month MR imaging follow-up showed aneurysm shrinkage with considerable mass effect reduction. Clinical outcome was favorable, with resolution of the mass-related symptoms.

In-Stent Neointimal Growth

In 3 cases, angiography demonstrated neointimal in-stent growth within the stented artery. In 1 case, this neointimal hyperplasia was associated with reduction of the caliber of the origin of a collateral branch covered by the LBS (patient 28, Fig 4). In 1 case of an MCA aneurysm in which both bifurcation branches were stented (patient 6), angiography showed complete occlusion of the inferior branch. None of these angiographic findings were associated with any documented clinical symptoms.

DISCUSSION

The endovascular treatment results of wide-neck and complex aneurysms improved following the introduction of the balloon- and stent-assisted coiling techniques.[1-6] Remodelling balloons act as a temporary scaffold for coils positioned in aneurysms with unfavorable dome-to-neck ratios. Intracranial stents act as a permanent scaffold, which, to facilitate coiling, leads to moderate diversion of the blood flow out of the aneurysm sac toward the

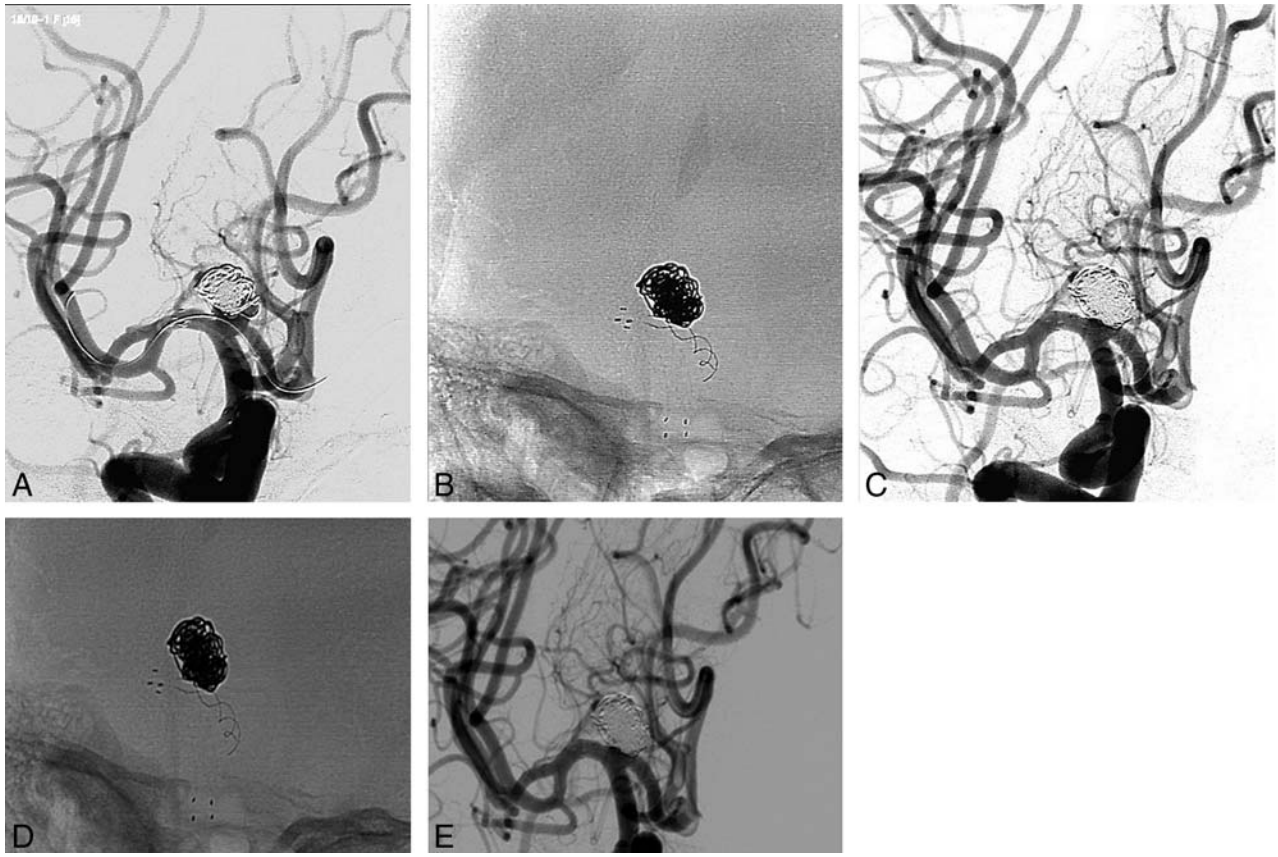

FIG 1. Patient 12. Retreatment of an ICA bifurcation aneurysm. *A*, A Neuroform EZ stent is initially deployed from the right MCA to the ipsilateral ICA then a 0.0165-inch microcatheter is navigated in the right MCA via the AcomA from the left ICA. *B* and *C*, An LBS is deployed within the right A1, and additional coils are released into the aneurysm sac. *D* and *E*, Postprocedural angiographic run.

vessel lumen and hence assists neck endothelialization due to neointima growth over the stent struts.[7-12] A major limitation of "conventional" intracranial stents is that they must be delivered through "large-profile" 0.021- or 0.027-inch microcatheters. These represent a technical drawback, especially for the treatment of lesions with complex angioarchitecture or distal locations. Moreover, conventional stents, especially laser-cut stents, are prone to kinking and do not adequately conform to the parent artery.[13] The LBS, with its technical features, represents an evolution in intracranial stents. The low profile of this device differentiates it from other conventional intracranial stents. The LBS can be navigated and delivered through standard-coiling 0.0165-inch microcatheters and dual-lumen balloon catheters. Consequently, it can be deployed in distal and tortuous vessel anatomy not achievable with conventional 0.021- or 0.027-inch stent-delivery microcatheters. Furthermore, it can be navigated through relatively small AcomAs, and this feature allows a contralateral approach for the treatment of aneurysms for which an ipsilateral approach is not feasible or effective. In addition, it can be easily navigated and deployed through another intracranial stent to perform dual-stent-assisted coiling, especially the open-cell type.

Nevertheless, the LBS can be deployed within arteries with a diameter of <2 mm, such as the posterior inferior cerebellar artery or callosomarginal artery. Finally, its 16 braided filaments aid the optimal artery wall apposition and conformability of the device to the arterial anatomy.[14] The LBS cell size is approximately 0.9 mm, and when it is released, the cells are usually compressed due to the advancement of the device, performed by the operator, over the delivery wire while the delivery catheter is maintained in a fixed position. The consequence of this delivery technique is that along the neck the cells size is reduced and the metal coverage increases.[15] Also, the hemodynamic deflection across the neck segment is higher in comparison with conventional laser-cut stents.[16] This feature probably explains the flow-diverter-like effect that we noted in some cases in our series, along with the extremely high rate of complete aneurysm occlusion reported at the midterm radiologic follow-up (26 of 27 patients, 96%).

Balloon-Then-Stent-Assisted Coiling Technique

Spiotta et al[17] first described the balloon-then-stent-assisted coiling technique. This procedure incorporates the use of a coaxial dual-lumen balloon catheter system (Scepter XC) through which a microstent, an LVIS Junior (MicroVention) in the original report, is advanced and delivered following aneurysm balloon-assisted coiling. This strategy is performed to add the benefits of the remodeling technique, such as better control of the microcatheter positioning and increasing packing density, to the benefits of the parent artery stent placement. The single-access technique for balloon-then-stent-assisted coiling was performed in 8 patients in our series by using the Scepter XC balloon first and then the LBS.

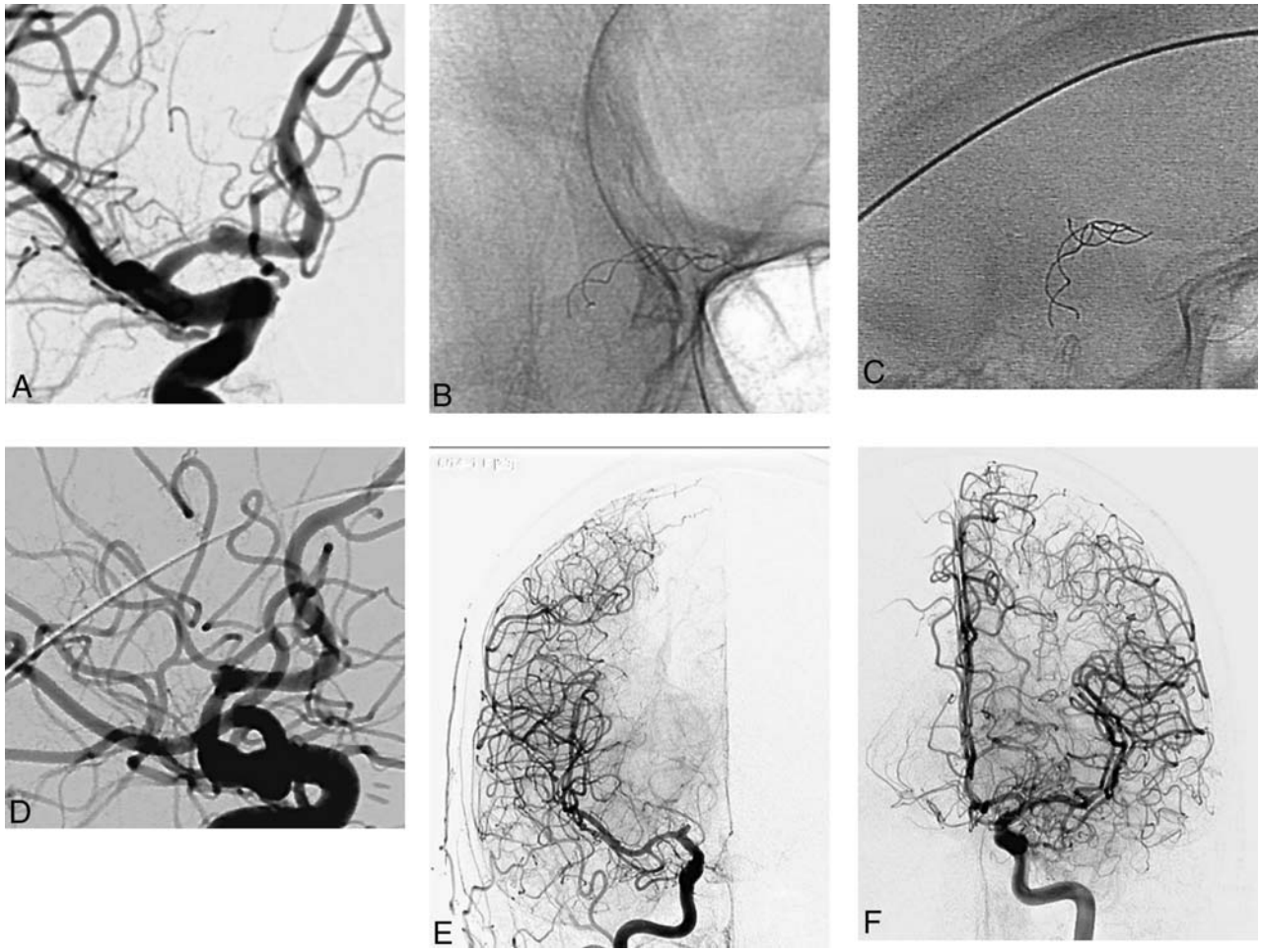

FIG 2. Patient 7. *A*, A ruptured A1 blister aneurysm. *B* and *C*, A nonoptimal apposition of telescoped LBSs (right oblique view). *D*, Postprocedural DSA. *E* and *F*, Angiograms obtained the day following the intervention show complete A1 occlusion.

No technical complications were recorded among these procedures, and the midterm radiologic follow-up showed complete aneurysm occlusion for all these aneurysms except for 1 for which a 3-mm residual neck was noted. To our knowledge, the use of the LBS single-access technique for balloon-then-stent-assisted coiling has not been reported in the literature.

LBS Used For Dual-Stent-Assisted Coiling

Akmangit et al[18] recently reported a series of 12 patients treated with the LBS used in a dual-stent configuration for the treatment of wide-neck, complex, and distal intracranial aneurysms. Nine patients from this series were treated with dual-stent-assisted coiling with 2 LBSs deployed in Y-, X-, and T-configurations, while 3 patients were treated with 2 telescoped LBSs without adjunctive coiling. Similar to findings in our series, good results in terms of technical feasibility and clinical and anatomic outcome were reported. In our series, 4 patients were treated with a dual-stent configuration. In 2 cases, an LBS was used in a dual-stent configuration with a Neuroform EZ stent. The Neuroform EZ stent is an open-cell laser-cut autoexpandable nitinol stent, which is delivered through a 0.027-inch microcatheter system. The Neuroform EZ stent was used with an LBS in 1 case of an MCA aneurysm for a Y-stent-assisted coiling and in 1 case of A1 T-stent-assisted coiling.

The rationale for the use of an open-cell stent is that when it is first placed in one of the bifurcation branches (in cases of bifurcation aneurysms), the catheterization of the other bifurcation branch through its open cells with a 0.0165-inch microcathter is relatively easy. Furthermore, the intersection between a low-profile stent and an open-cell stent reduces, theoretically, the risk of obstruction of the second stent at the point of intersection with the first one. In this setting, both stents provide a scaffold for aneurysm coiling and branch protection; moreover, the LBS provides a flow-diverter-like effect from the aneurysm toward the parent vessel. It could be argued that the intersection between 2 intracranial stents in a Y-configuration is suitable for intra-aneurysmal flow disruption and that it is not related to a higher rate of thromboembolic complications.[19-21] Nevertheless, long-term results of patients treated with such Y-intersecting stents are lacking, and our experience demonstrates that a novel nonintersecting dual-stent Y-configuration is feasible by using the LBS in combination with the Neuroform EZ stent. To our knowledge, this configuration has not been reported.

Intraprocedural Complications

Five intraoperative complications occurred in our series (5 of 29, 17%); in 3 cases, an intrastent thrombus formation was noted

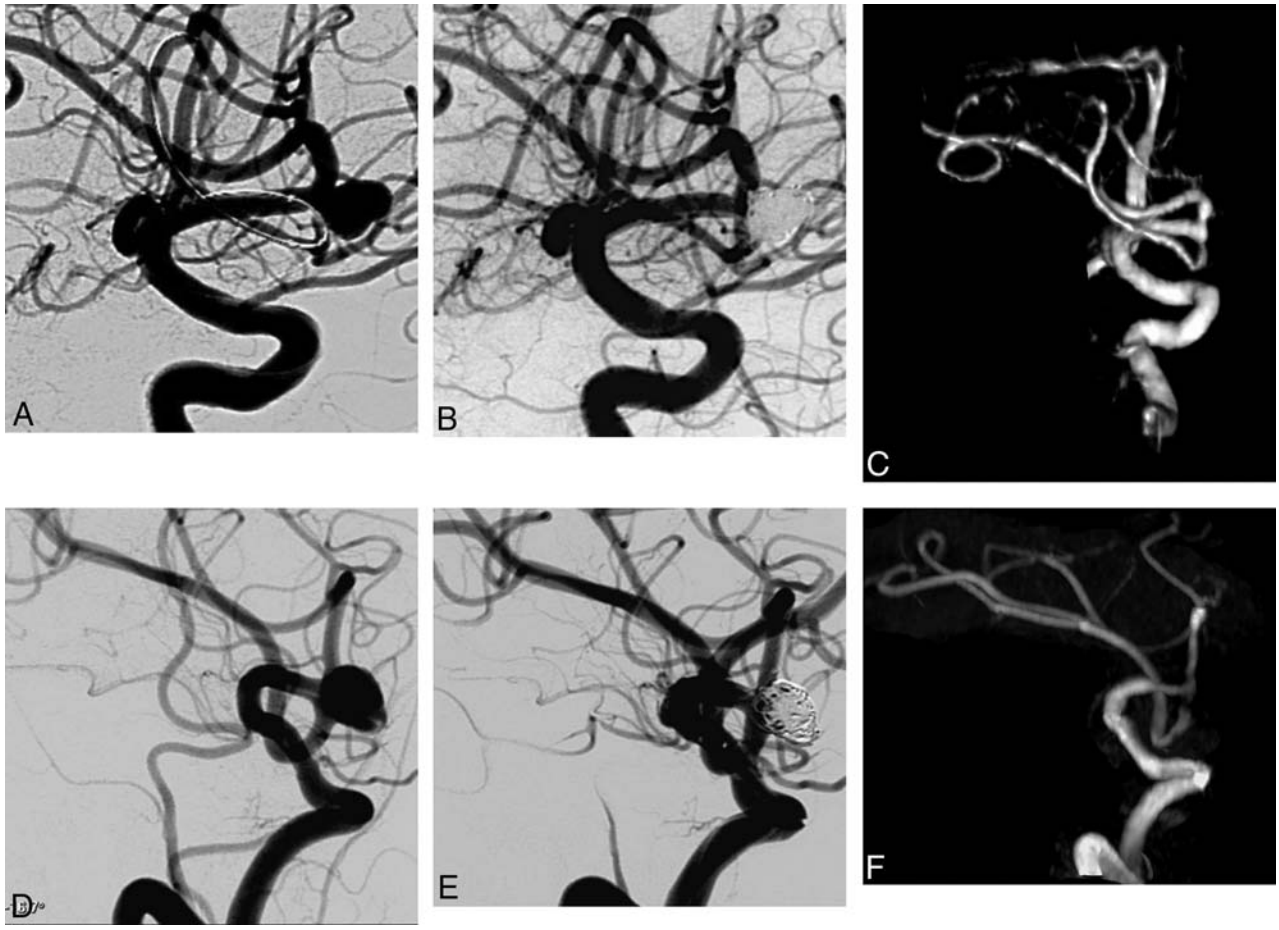

FIG 3. Two examples (*A–C*, *D–F*) of MCA aneurysms followed by MR imaging time-of-flight angiography.

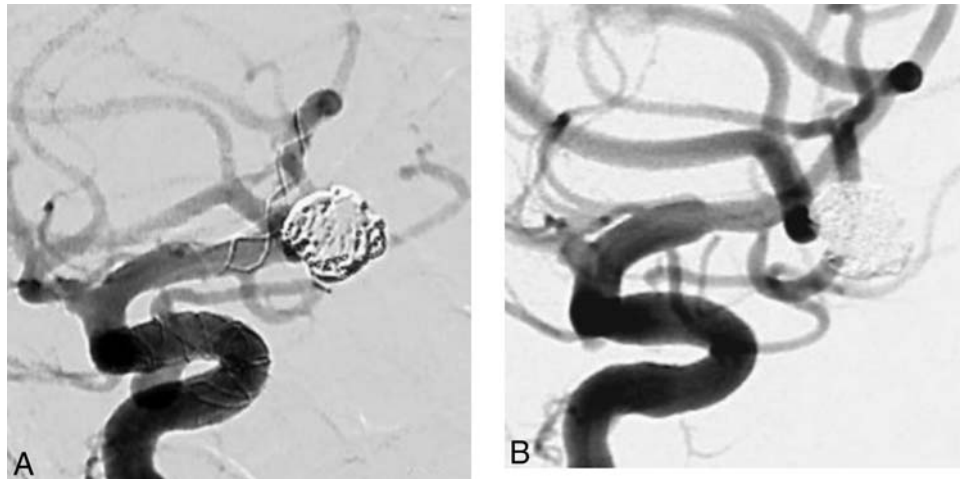

FIG 4. Patient 28. *A*, Postprocedural DSA of an MCA aneurysm treated with an LBS (in the same session the patient was treated for an ipsilateral carotid-cave aneurysm with a Silk flow-diverter [Balt Extrusion]). *B*, The DSA midterm follow-up shows shrinkage of the stented artery and of the origin of the MCA branch covered by the LBS.

after LBS deployment. The complication was managed with intravenous injection of glycoprotein IIb/IIIa (abciximab), and all patients had a good clinical outcome. In 2 of the transient thrombotic cases (patients 1 and 11), retrospective analysis of the nonsubtracted angiograms obtained after stent placement showed suboptimal deployment of the device. The radiopaque struts of the stents appeared elongated and not fully expanded. This noncomplete expansion of the stent probably led to turbulent blood flow within the device and subsequently platelet aggregation. In 2 cases, we recorded an intraprocedural technical complication: The first was a case of dual-telescopic stent configuration in which the apposition of the devices was not adequate and led to alteration of the laminar blood flow and to acute thrombosis of the parent vessel. The second was a case in which after LBS deploy-

ment, the operator was not able to recover the delivery wire because it was caught by the stent struts; additional attempts of delivery wire retrieval resulted in migration and collapse of the device. In these cases, the LBS was responsible for parent artery occlusion and IV abciximab was not effective in artery reopening. Both patients developed parenchymal ischemia in the territory of the stented artery and thereafter died because of diffuse cerebral vasospasm (these patients were in the acute and subacute phase of subarachnoid hemorrhage).

These deaths were taken into account for the mortality rate of our series (2/29, 6.8%). Therefore, the permanent morbidity and the mortality rates of our series were 0% and 6.8%, respectively. In 3 of 5 cases of complications in our series, the probable cause was related to the nonoptimal deployment of the device. It is unclear whether this was due to inappropriate maneuvering of the operator or the behavior of the stent itself. The LBS seems to have a moderate tendency to shorten after deployment. On the other hand, the higher "metal-to-artery" ratio of the braided stents in comparison with laser-cut stents, especially when placed in low-diameter arteries, might be related to a higher incidence of acute intrastent thrombus formations. Turk et al[22] reported a series of 8 distal aneurysms treated by stent-assisted coiling by using the Neuroform stent. The authors reported 2 intraprocedural thrombotic events, which were successfully treated by IV injection of abciximab. The incidence of intraprocedural thrombotic complications in this series (2 of 8, 25%) seems to be higher in comparison with our results.

LVIS Junior Stent

In a recent publication, Behme et al[23] reported their experience in using the LVIS Junior (MicroVention) stent for the treatment of 32 patients with 34 aneurysms. The LVIS Junior is an intracranial self-expandable stent made of 12 braided nitinol wires with technical features similar to those of the LBS. Similar to findings in our report, 5 complications occurred in this series, and 2 were related to intrastent periprocedural thrombosis. In both cases, patients were treated with intravenous eptifibatide and had a good clinical outcome. No information about stent deployment or opening is available in these patients. The anatomic results of this series are also similar to those in our study, with a rate of complete aneurysm occlusion at the midterm follow-up of >90%. Möhlenbruch et al[24] reported the results of a series of 22 patients treated with LVIS Junior–assisted coiling. In this cohort, 3 cases of partial, nonocclusive in-stent thrombosis occurred. All these complications completely resolved after intravenous injection of tirofiban. The authors reported no mortality or new neurologic deficits assessed in the periprocedural period or at the midterm follow-up in any patient in this series. Even for this cohort of patients, the midterm radiologic follow-up showed a rate of complete aneurysm occlusion of 90%.

Conventional Intracranial Stents and Thrombotic Complications

In our series, we recorded an extremely high radiologic rate of complete aneurysm cure at the midterm follow-up. Nevertheless, we experienced an intrastent thrombotic complication in 5 cases (of 29, 17%), and even if this led to the death of 2 patients (2 of 29, 6.8%), we have to compare these data with those reported in the literature on conventional stents. Bodily et al[25] reported a meta-analysis of 339 ruptured aneurysms treated by stent-assisted coiling with different types of laser-cut stents during the acute phase after rupture. The rate of clinically relevant thromboembolic complications in this series was 6%, while the incidence of clinically relevant hemorrhagic complications was 8%. The authors concluded that thromboembolic complications appeared reasonably well-controlled. Hetts et al[26] compared the results of a series of 361 patients treated for an unruptured aneurysm with stent-assisted coiling (performed with laser-cut stents) or simple coiling; 137 patients in this series (of 361, 38%) underwent stent placement. At 1 year, total significant adverse events, mortality and morbidity, were similar in both groups, but ischemic strokes were more common in patients with stent-assisted coiling than in those with simple coiling, 8.8% versus 2.2%. The authors concluded that patients in both groups had similar outcomes, and the increased ischemic events in stent-coiled aneurysms were attributable to baseline risk factors and aneurysm morphology.

Luo et al[11] reported results of a series of 15 patients with 17 aneurysms treated with LEO stents. Similar to findings in our series, the authors reported 2 cases of technical complications and 2 cases of periprocedural thromboembolic complications. Lv et al[27] reported a series of 28 patients treated with coiling assisted by LEO stents. The authors reported 3 (of 28, 10.7%) asymptomatic parent artery occlusions related to the deployment of the stent and 1 stent migration. Given the above results, the rate of thrombotic complications recorded with the LBS seems to be quite comparable with the rate reported in other conventional intracranial stents. Occurrence of thromboembolic complications after stent placement is the most frequent adverse event reported in the literature and in our series. In 3 of 4 thrombotic complications recorded in our series, an inadequate deployment of the stent was noted. In our opinion, the incidence of this type of complication is directly related, beyond the responsiveness of the patient to antiplatelet drugs, to the quality of the deployment of the device, hence its opening and apposition to the vessel wall. Incomplete or inadequate opening of the device is a potential cause of laminar blood flow alteration and thrombus formation.

CONCLUSIONS

The results obtained in our study by using the LBS for balloon-then-stent and single- or dual-stent-assisted coiling of complex and distally located intracranial aneurysms are encouraging. Due to its technical features, this device allows the treatment of lesions with complex angioarchitecture, not accessible with standard 0.021- or 0.027-inch microcatheters. Furthermore, we noted that the LBS may have some flow-diverter-like properties that can lead to aneurysm cure even after partial or incomplete coiling. The results of our study should be compared with those in larger series and long-term clinical outcome data.

Disclosures: Vincent Costalat—*UNRELATED*: *Consultancy*: Sequent Medical, Covidien, Stryker, Balt Extrusion; *Payment for Lectures (including service on Speakers Bureaus)*: Covidien, Stryker, Sequent Medical; *Payment for Development of Educational Presentations*: Covidien, Stryker. Alain Bonafé—*UNRELATED*: *Consultancy*: Covidien, Stryker.

REFERENCES

1. Moret J, Cognard C, Weill A, et al. **The "remodeling technique" in the treatment of wide neck intracranial aneurysms: angiographic results and clinical follow-up in 56 cases.** *Interv Neuroradiol* 1997;3: 21–35 Medline
2. Shapiro M, Babb J, Becske T, et al. **Safety and efficacy of adjunctive balloon remodeling during endovascular treatment of intracranial aneurysm: a literature review.** *AJNR Am J Neuroradiol* 2008;29: 1777–81 CrossRef Medline
3. Pierot L, Cognard C, Spelle L, et al. **Safety and efficacy of balloon remodelling technique during endovascular treatment of intracranial aneurysms: critical review of the literature.** *AJNR Am J Neuroradiol* 2012;33:12–15 CrossRef Medline
4. Piotin M, Blanc R, Spelle L, et al. **Stent-assisted coiling of intracranial aneurysms: clinical and angiographic results in 216 consecutive aneurysms.** *Stroke* 2010;41:110–15 CrossRef Medline
5. Vendrell JF, Costalat V, Brunel H, et al. **Stent-assisted coiling of complex middle cerebral artery aneurysms: initial and midterm results.** *AJNR Am J Neuroradiol* 2011;32:259–63 CrossRef Medline
6. Biondi A, Janardhan V, Katz JM, et al. **Neuroform stent-assisted coil embolization of wide-necked intracranial aneurysms: strategies in stent deployment and midterm follow-up.** *Neurosurgery* 2007;61: 460–68; discussion 468–69 Medline
7. Machi P, Lobotesis K, Vendrell JF, et al. **Endovascular therapeutic strategies in ruptured intracranial aneurysms.** *Eur J Radiol* 2013;82: 1646–52 CrossRef Medline
8. Fiorella D, Albuquerque FC, Deshmukh VR, et al. **Endovascular reconstruction with the Neuroform stent as monotherapy for the treatment of uncoilable intradural pseudoaneurysms.** *Neurosurgery* 2006;59:291–300; discussion 299–300 Medline
9. Kono K, Terada T. **Hemodynamics of 8 different configurations of stenting for bifurcation aneurysms.** *AJNR Am J Neuroradiol* 2013; 34:1980–86 CrossRef Medline
10. Lee YJ, Kim DJ, Suh SH, et al. **Stent-assisted coil embolization of intracranial wide-necked aneurysms.** *Neuroradiology* 2005;47: 680–89 CrossRef Medline
11. Luo J, Lv X, Jiang C, et al. **Preliminary use of the Leo stent in the endovascular treatment of wide-necked cerebral aneurysms.** *World Neurosurg* 2010;73:379–84 CrossRef Medline
12. Bendok BR, Parkinson RJ, Hage ZA, et al. **The effect of vascular reconstruction device-assisted coiling on packing density, effective neck coverage, and angiographic outcome: an in vitro study.** *Neurosurgery* 2007;61:835–40; discussion 840–41 Medline
13. Krischek O, Miloslavski E, Fischer S, et al. **A comparison of functional and physical properties of self-expanding intracranial stents [Neuroform3, Wingspan, Solitaire, Leo+, Enterprise].** *Minim Invasive Neurosurg* 2011;54:21–28 CrossRef Medline
14. Valdivia Y, Alvarado M, Ebrahimi N, et al. **Study of conformability of the new Leo plus stent to a curved vascular model using flat-panel detector computed tomography (DynaCT).** *Neurosurgery* 2009;64 (3 suppl):ons130–34; discussion ons134 Medline
15. Aenis M, Stancampiano AP, Wakhloo AK, et al. **Modeling of flow in a straight stented and nonstented side wall aneurysm model.** *J Biomech Eng* 1997;119:206–12 CrossRef Medline
16. Pumar JM, Lete I, Pardo MI, et al. **LEO stent monotherapy for the endovascular reconstruction of fusiform aneurysms of the middle cerebral artery.** *AJNR Am J Neuroradiol* 2008;29:1775–76 CrossRef Medline
17. Spiotta AM, Miranpuri A, Chaudry MI, et al. **Combined balloon stent technique with the Scepter C balloon and low-profile visualized intraluminal stent for the treatment of intracranial aneurysms.** *J Neurointerv Surg* 2013;5(suppl 3):iii79–82 CrossRef Medline
18. Akmangit I, Aydin K, Sencer S, et al. **Dual stenting using low profile LEO Baby stents for the endovascular management of challenging intracranial aneurysms.** *AJNR Am J Neuroradiol* 2015;36:323–29 CrossRef Medline
19. Spiotta AM, Gupta R, Fiorella D, et al. **Mid-term results of endovascular coiling of wide-necked aneurysms using double stents in a Y configuration.** *Neurosurgery* 2011;69:421–29 CrossRef Medline
20. Thorell WE, Chow MM, Woo HH, et al. **Y-configured dual intracranial stent-assisted coil embolization for the treatment of wide-necked basilar tip aneurysms.** *Neurosurgery* 2005;56:1035–40; discussion 1035–40 Medline
21. Fargen KM, Mocco J, Neal D, et al. **A multicenter study of stent-assisted coiling of cerebral aneurysms with a Y configuration.** *Neurosurgery* 2013;73:466–72 CrossRef Medline
22. Turk AS, Niemann DB, Ahmed A, et al. **Use of self-expanding stents in distal small cerebral vessels.** *AJNR Am J Neuroradiol.* 2007;28: 533–36 Medline
23. Behme D, Weber A, Kowoli A, et al. **Low-profile Visualized Intraluminal Support device (LVIS Jr) as a novel tool in the treatment of wide-necked intracranial aneurysms: initial experience in 32 cases.** *J Neurointerv Surg* 2015;7:281–85 CrossRef Medline
24. Möhlenbruch M, Herweh C, Behrens L, et al. **The LVIS Jr. microstent to assist coil embolization of wide-neck intracranial aneurysms: clinical study to assess safety and efficacy.** *Neuroradiology* 2014;56: 389–95 CrossRef Medline
25. Bodily KD, Cloft HJ, Lanzino G et Al. **Stent-assisted coiling in acutely ruptured intracranial aneurysms: a qualitative, systematic review of the literature.** *AJNR Am J Neuroradiol* 2011;32:1232–36 CrossRef Medline
26. Hetts SW, Turk A, English JD, et al; Matrix and Platinum Science Trial Investigators. **Stent-assisted coiling versus coiling alone in unruptured intracranial aneurysms in the Matrix and Platinum Science Trial: safety, efficacy, and mid-term outcomes.** *AJNR Am J Neuroradiol* 2014;35:698–705 CrossRef Medline
27. Lv X1, Li Y, Jiang C et al. **Potential advantages and limitations of the Leo stent in endovascular treatment of complex cerebral aneurysms.** *Eur J Radiol* 2011;79:317–22 CrossRef Medline

Could Statin Use Be Associated with Reduced Recurrence Rates following Coiling in Ruptured Intracranial Aneurysms?

W. Brinjikji, V. Shahi, H.J. Cloft, G. Lanzino, D.F. Kallmes, and R. Kadirvel

ABSTRACT

BACKGROUND AND PURPOSE: A number of studies have examined the role of matrix metalloproteinases in aneurysm healing following endovascular coiling. Because ruptured aneurysms are known to express higher levels of matrix metalloproteinases, we hypothesized that patients with subarachnoid hemorrhage who were on a statin at the time of coil embolization would have lower aneurysm recanalization and retreatment rates than patients not on statins.

MATERIALS AND METHODS: We performed a retrospective chart review of patients who underwent intrasaccular coil embolization of ruptured intracranial aneurysms of ≤10 mm with at least 6 months of imaging follow-up. Patients were separated into 2 groups: 1) those on an oral statin medication at the time of coiling, and 2) those who were not. Outcomes studied were aneurysm recurrence and aneurysm retreatment after endovascular coiling. Student *t* and χ^2 tests were used for statistical significance of differences between groups.

RESULTS: One hundred thirty-two patients with 132 ruptured aneurysms were included in our study. Sixteen were on statins (12.1%) and 116 were not (87.9%). The recurrence rate was 6.3% in the statin group (1/16) and 36.2% in the nonstatin group (42/107) ($P = .02$). Unplanned retreatment rates were 6.3% (1/16) for the statin group and 25.9% (30/116) for the nonstatin group ($P = .08$).

CONCLUSIONS: Statins were associated with a lower rate of aneurysm recurrence following endovascular coiling of small- and medium-sized ruptured aneurysms in this small retrospective study. Further studies are needed to confirm this finding to determine whether statins can be used to reduce recurrence rates in these aneurysms.

ABBREVIATION: MMP = matrix metalloproteinase

Approximately 20% of patients undergoing endovascular coiling of intracranial aneurysms have an aneurysm recurrence, and 10% require retreatment of the coiled aneurysm.[1] Given the risk of morbidity and mortality associated with retreatment, considerable research has been dedicated to determine methods to reduce the rate of aneurysm recurrence and retreatment. Statin medications are commonly prescribed and have been shown to have a number of beneficial health effects, including reducing the risk of cardiovascular disease and stroke. Statins have been found to stimulate production of extracellular matrix and chemotactic migration and mobilization of endothelial and mesenchymal progenitor cells and stromal osteoblasts, factors important to aneurysm healing.[2-5] Statins also inhibit chemotaxis of proinflammatory cells such as macrophages by inhibiting expression of adhesion molecules and decreasing macrophage expression of matrix metalloproteinases (MMPs).[6] MMPs are molecules that have been shown to promote recanalization of arteries and aneurysms following endovascular embolization.[7]

Because statins stimulate cellular and molecular pathways known to be helpful for aneurysm healing and inhibit the expression of MMPs, molecules thought to contribute to aneurysm recanalization following endovascular coiling, it would be interesting to study the effect of statins on aneurysm recanalization and retreatment rates. We retrospectively reviewed a large series of ruptured intracranial aneurysms treated with endovascular coiling and compared the rates of aneurysm recanalization and retreatment among patients who were taking statins at the time of treatment and those who were not. We chose to specifically study ruptured aneurysms because these aneurysms have high recanalization rates and have been shown

Received January 16, 2015; accepted after revision April 12.

From the Department of Radiology (W.B., H.J.C., D.F.K., R.K.), Mayo Medical School (V.S.), and Department of Neurosurgery (G.L.), Mayo Clinic, Rochester, Minnesota.

This work was supported by the National Institutes of Health (grant NS076491).

Please address correspondence to Waleed Brinjikji, MD, Department of Radiology, Mayo Clinic, OL 1-115, 200 SW First St, Rochester, MN 55905; e-mail: brinjikji.waleed@mayo.edu; @WBrinjikji

http://dx.doi.org/10.3174/ajnr.A4422

to highly express MMPs, molecules that are inhibited by statin medications.[8]

MATERIALS AND METHODS

Patient Selection

Following institutional review board approval, we conducted a retrospective chart review of all patients who underwent endovascular treatment of ruptured intracranial aneurysms from January 2005 to December 2013. Inclusion criteria were the following: 1) patients receiving intrasaccular coil embolization of an intracranial aneurysm with a maximum diameter of ≤10 mm, 2) having follow-up imaging with either digital subtraction angiography or MR angiography at least 6 months later, and 3) having a recording of a medical list from the time of presentation at aneurysm rupture. Patients who did not meet all 3 of these criteria were excluded from the analysis.

Baseline Characteristics

Patients were then stratified into 2 groups: 1) patients on statin medications, and 2) those not on statin medications. Use of statin medications was determined from the patient's medical chart from the time of admission for subarachnoid hemorrhage. Discharge notes were searched to ensure that the patient was not taken off the statin on hospital discharge. Thus, all patients in the statin group were on statins at the time of rupture and during the follow-up period. No patients were started on statins at the time of aneurysm rupture or at discharge. In addition to statin use, we obtained the following information: type and dose of statin, age, sex, comorbidities (hypertension, diabetes mellitus, and current smoking), aneurysm location, aneurysm maximum size, initial degree of occlusion, and use of balloon assistance. Current smokers were defined as patients who were smoking at the time of aneurysm rupture and continued to smoke on follow-up.

Outcomes

The 2 primary outcomes of this study were aneurysm recurrence and unplanned aneurysm retreatment following endovascular treatment. Initial aneurysm occlusion was categorized on the basis of the Raymond scale into the following groups: 1) residual aneurysm, 2) residual neck, and 3) complete occlusion. Follow-up aneurysm occlusion was categorized into 2 outcomes: 1) stable occlusion, and 2) aneurysm recurrence defined as coil compaction and/or recanalization. Retreatments were categorized as unplanned and planned-staged. A retreatment was considered planned-staged if the treating team mentioned in the operative note or follow-up clinical notes that further treatment was recommended to improve aneurysm occlusion (ie, planned coiling of an aneurysm followed by Pipeline Embolization Device [Covidien, Irvine, California] placement). Planned-staged retreatments were excluded from our analysis.

Statistical Analysis

Continuous variables were presented as mean (SD), and categorical variables, as frequency (percentage). Student t and χ^2 tests were used for statistical significance in aneurysm recurrence and/or retreatment in relation to patient statin use. We also performed a multivariate logistic regression analysis to determine whether statin use was independently associated with recanalization and retreatment. Any baseline variables that were significantly different between the 2 groups were included in this model.

RESULTS

Baseline Characteristics

When we considered patients with ruptured aneurysms of ≤10 mm, 16 patients were on statin medications at the time of treatment and 116 patients were not. The mean age of the statin group was higher than that of the nonstatin group (70.2 versus 57.0 years, $P < .0001$). Mean aneurysm size was similar between groups (5.4 versus 5.6 mm, $P = .63$). Baseline occlusion status ($P = .51$) and use of balloon assistance were similar between groups ($P = .31$). There were similar rates of hypertension ($P = .59$), diabetes mellitus ($P = .20$), and smoking ($P = .19$) between groups. Mean follow-up was 23.4 months for the statin group and 25.1 months for the nonstatin group ($P = .59$).

Among patients in the statin group, the most common statin medication used was simvastatin (6 patients; dose, 20–40 mg), followed by atorvastatin (5 patients; dose, 10–20 mg), rosuvastatin (3 patients; dose, 5–20 mg), and pravastatin (2 patients; dose, 20–80 mg). All patients were on statin therapy for the duration of their follow-up (25–96 months). The indication for statin therapy was hyperlipidemia in all cases.

Outcomes

Recurrence rates were significantly lower in the statin group than in the nonstatin group. Recurrence rates were 6.3% (1/16) for the statin group and 36.2% (41/116) for the nonstatin group ($P = .02$). There was a trend toward lower retreatment rates in the statin group. Unplanned retreatment rates were 6.3% (1/16) for the statin group and 25.9% (30/116) for the nonstatin group ($P = .08$). Among patients in the nonstatin group, 16 were recoiled, 5 underwent flow-diverter treatment, and 9 underwent clipping. One patient in the statin group was retreated with a flow diverter. These data are summarized in the Table.

The only baseline characteristic that differed between the statin and nonstatin groups was mean age. When we considered patients with ruptured aneurysms of ≤10 mm and adjusted for age, statin use was associated with significantly lower odds of recurrence (OR = 0.13; 95% CI, 0.01–0.72; $P = .016$) and a nonstatistically significant lower odds of retreatment (OR = 0.29; 95% CI, 0.01–1.55; $P = .16$).

DISCUSSION

Our small, retrospective study demonstrated that patients with ruptured aneurysms of ≤10 mm who were on a statin at the time of aneurysm treatment had lower rates of aneurysm recurrence and had a trend toward lower retreatment rates compared with those who were not on a statin. These findings are important because they suggest that statin use may represent a low-cost and efficacious therapy in reducing recurrence rates in some patients with ruptured aneurysms. However, these results need to be confirmed in future, larger studies before they can be applied in routine clinical practice.

We chose to specifically study the recanalization rates of ruptured aneurysms undergoing endovascular coiling because

Baseline characteristics and recurrence and retreatment rates: ruptured aneurysms of ≤10 mm

	Statin Group	Nonstatin Group	*P* Value
No.	16	116	–
Mean age (SD) (yr)	70.2 (9.0)	57.0 (11.7)	<.0001
No. (%) women	12 (75.0)	77 (66.4)	.58
No. (%) hypertension	10 (62.5)	61 (52.6)	.59
No. (%) diabetes	3 (18.8)	10 (8.6)	.20
No. (%) current smoker	3 (18.8)	41 (35.3)	.19
Aneurysm location			
ICA (No.) (%)	6	41	.88
ACA/AcomA (No.) (%)	9	50	
MCA (No.) (%)	0	7	
VBA (No.) (%)	1	16	
Other (No.) (%)	0	2	
Mean size (SD) (mm)	5.4 (1.8)	5.6 (2.0)	.63
Initial occlusion			
Complete	8 (5.0)	60 (51.7)	.51
Residual neck	6 (37.5)	50 (43.1)	
Residual aneurysm	2 (12.5)	6 (5.2)	
Balloon assistance	4 (25.0)	18 (15.5)	.31
Mean follow-up (months)	23.4 (14.4)	25.1 (25.4)	.59
No. (%) recurrence	1 (6.3)	42 (36.2)	.02
No. (%) retreatment	1 (6.3)	30 (25.9)	.08

Note:—ACA indicates anterior cerebral artery; AcomA, anterior communicating artery; VBA, vertebrobasilar arteries; –, no *P* value.

MMPs are expressed at significantly higher levels in ruptured compared with unruptured aneurysms.[8-10] MMPs, specifically MMP-2 and MMP-9, are proteases that are thought to play a role in aneurysm formation, growth, rupture, and recanalization.[11-14] Statins are potent inhibitors of MMP-2 and MMP-9 formation and expression.[15-18] We hypothesized that by inhibiting MMPs early in the healing process, statins can prevent any further growth of the aneurysm, thus reducing recurrence rates. This hypothesis is supported by work from Hasan et al,[19] who demonstrated that aneurysm sac growth, not coil compaction, is the primary mechanism associated with postcoiling aneurysm recurrence. In addition, statins likely enhance many other facets of the aneurysm healing process such as cellular infiltration of the aneurysm dome, deposition of extracellular matrix, and endothelialization of the aneurysm neck.[5,15,20] Statins upregulate expression of transforming growth factor β and bone morphogenetic protein 2, factors important in stimulating migration of osteoblasts and mesenchymal progenitor cells to the aneurysm dome.[21]

There are some other, previously reported preclinical data to suggest that statins could improve aneurysm healing following endovascular treatment of intracranial aneurysms. One previous study comparing statin-coated coils with bare metal coils in the coil embolization of rat aneurysms demonstrated that aneurysms treated with statin-covered coils had improved aneurysm occlusion due to increased tissue organization around the coils and increased collagen deposition in the aneurysm dome. In addition, this same previous study demonstrated increased endothelialization of the aneurysm neck in statin-covered-coil-treated aneurysms compared with non-statin-covered-coiled aneurysms.[22] A number of previous clinical studies of patients receiving endovascular aortic aneurysm repair have demonstrated that statin therapy can promote aneurysm sac regression and healing. A study by Raux et al[23] demonstrated that patients undergoing endovascular aortic aneurysm repair who were on statins had a significantly higher rate of aneurysm sac regression compared with their non-statin-using counterparts. These results were confirmed by a later study performed by Gray et al,[24] who demonstrated that statin use was independently associated with aneurysm sac regression following endovascular aortic aneurysm repair.

Limitations

Our study has limitations. First, we included only patients with aneurysms of ≤10 mm. We excluded patients with large and giant aneurysms because these patients had much higher recanalization rates than those with small- and medium-sized aneurysms due to difficulties in achieving high packing attenuation.[25] Thus, inclusion of large aneurysms may mask the benefit isolated to small- and medium-sized ones. Our study included only ruptured aneurysms because they have a different biology from unruptured aneurysms as evidenced by elevated recurrence rates in many series.[26] In our study, only 16 patients were on statin medication. This low number may have limited our ability to detect differences between the statin and nonstatin groups in aneurysm retreatment rates. In addition, the low number of statin-using patients in our study makes our conclusions unreliable because if only 1 additional patient had a recurrence in the statin group, statistical significance would be lost. Another limitation is that patients were on various statin agents and on various doses. There are differences in statin efficacy by type and dose.

Given the small size and limitations, our study should not serve to alter clinical management of patients with ruptured aneurysms. Ultimately, this study sought to determine whether systemic statin therapy warrants further study as a potential way to reduce aneurysm recanalization for patients with ruptured aneurysms. Future studies, including animal studies examining the effects of statins on the cellular response to endovascular coiling, large retrospective reviews combining data with multiple centers, and prospective clinical trials studying the impact of statins on angiographic outcomes of patients with ruptured intracranial aneurysms are needed to confirm these findings.

CONCLUSIONS

Our study found that patients with ruptured aneurysms of ≤10 mm who were on statins had significantly lower aneurysm recanalization rates than those who were not on statins. In addition, there was a trend toward lower retreatment rates in the statin group. These results suggest that the role of systemic statin therapy in reducing aneurysm recanalization rates in patients with ruptured aneurysms undergoing coiling should be further studied. More data from preclinical and retrospective and prospective clinical studies are needed to determine whether statins do, in fact, reduce aneurysm recanalization in the ruptured aneurysm population.

Disclosures: Waleed Brinjikji—*RELATED*: *Grant*: Brain Aneurysm Foundation,* *Comments*: Dr Brinjikji's effort was supported by a grant from the Brain Aneurysm Foundation. Giuseppe Lanzino—*UNRELATED*: *Consultancy*: ev3/Covidien.* David F. Kallmes—*UNRELATED*: *Board Membership*: GE Healthcare, *Comments*: Advisory Board, Cost Effectiveness; *Consultancy*: ev3,* *Comments*: planning and implementing clinical trials; *Grants/Grants Pending*: MicroVention,* Sequent,* Surmodics,* Codman,* Benvenue Medical,* University of Virginia,* NeuroSigma,* *Comments*: preclinical research and planning and implementing clinical trials; *Royalties*: University of Virginia Patent Foundation, *Comments*: spine fusion. Ramanathan Kadirvel—*RELATED*: *Grant*: National Institutes of Health NS076491.* *Money paid to the institution.

REFERENCES

1. Ferns SP, Sprengers ME, van Rooij WJ, et al. **Coiling of intracranial aneurysms: a systematic review on initial occlusion and reopening and retreatment rates.** *Stroke* 2009;40:e523–529 CrossRef Medline
2. Landmesser U, Engberding N, Bahlmann FH, et al. **Statin-induced improvement of endothelial progenitor cell mobilization, myocardial neovascularization, left ventricular function, and survival after experimental myocardial infarction requires endothelial nitric oxide synthase.** *Circulation* 2004;110:1933–39 CrossRef Medline
3. Song L, Yang YJ, Dong QT, et al. **Atorvastatin enhance efficacy of mesenchymal stem cells treatment for swine myocardial infarction via activation of nitric oxide synthase.** *PLoS One* 2013;8:e65702 CrossRef Medline
4. Sonobe M, Hattori K, Tomita N, et al. **Stimulatory effects of statins on bone marrow-derived mesenchymal stem cells: study of a new therapeutic agent for fracture.** *Biomed Mater Eng* 2005;15:261–67 Medline
5. Brinjikji W, Kallmes DF, Kadirvel R. **Mechanisms of healing in coiled intracranial aneurysms: a review of the literature.** *AJNR Am J Neuroradiol* 2015;36:1216–22 CrossRef Medline
6. Blanco-Colio LM, Tuñón J, Martin-Ventura JL, et al. **Anti-inflammatory and immunomodulatory effects of statins.** *Kidney Int* 2003; 63:12–23 CrossRef Medline
7. Bouzeghrane F, Darsaut T, Salazkin I, et al. **Matrix metalloproteinase-9 may play a role in recanalization and recurrence after therapeutic embolization of aneurysms or arteries.** *J Vasc Interv Radiol* 2007;18:1271–79 CrossRef Medline
8. Marchese E, Vignati A, Albanese A, et al. **Comparative evaluation of genome-wide gene expression profiles in ruptured and unruptured human intracranial aneurysms.** *J Biol Regul Homeost Agents* 2010;24: 185–95 Medline
9. Serra R, Volpentesta G, Gallelli L, et al. **Metalloproteinase-9 and neutrophil gelatinase-associated lipocalin plasma and tissue levels evaluation in middle cerebral artery aneurysms.** *Br J Neurosurg* 2014 May 5. [Epub ahead of print] CrossRef Medline
10. Jin D, Sheng J, Yang X, et al. **Matrix metalloproteinases and tissue inhibitors of metalloproteinases expression in human cerebral ruptured and unruptured aneurysm.** *Surg Neurol* 2007;68(suppl 2): S11–16; discussion S16 CrossRef Medline
11. Kim SC, Singh M, Huang J, et al. **Matrix metalloproteinase-9 in cerebral aneurysms.** *Neurosurgery* 1997;41:642–46; discussion 646–47 Medline
12. Razavian M, Zhang J, Nie L, et al. **Molecular imaging of matrix metalloproteinase activation to predict murine aneurysm expansion in vivo.** *J Nucl Med* 2010;51:1107–15 CrossRef Medline
13. Aoki T, Kataoka H, Morimoto M, et al. **Macrophage-derived matrix metalloproteinase-2 and -9 promote the progression of cerebral aneurysms in rats.** *Stroke* 2007;38:162–69 CrossRef Medline
14. Pannu H, Kim DH, Guo D, et al. **The role of MMP-2 and MMP-9 polymorphisms in sporadic intracranial aneurysms.** *J Neurosurg* 2006;105:418–23 CrossRef Medline
15. Bellosta S, Via D, Canavesi M, et al. **HMG-CoA reductase inhibitors reduce MMP-9 secretion by macrophages.** *Arterioscler Thromb Vasc Biol* 1998;18:1671–78 CrossRef Medline
16. Ganné F, Vasse M, Beaudeux JL, et al. **Cerivastatin, an inhibitor of HMG-CoA reductase, inhibits urokinase/urokinase-receptor expression and MMP-9 secretion by peripheral blood monocytes: a possible protective mechanism against atherothrombosis.** *Thromb Haemost* 2000;84:680–88 Medline
17. Guo H, Shi Y, Liu L, et al. **Rosuvastatin inhibits MMP-2 expression and limits the progression of atherosclerosis in LDLR-deficient mice.** *Arch Med Res* 2009;40:345–51 CrossRef Medline
18. Wong B, Lumma WC, Smith AM, et al. **Statins suppress THP-1 cell migration and secretion of matrix metalloproteinase 9 by inhibiting geranylgeranylation.** *J Leukoc Biol* 2001;69:959–62 Medline
19. Hasan DM, Nadareyshvili AI, Hoppe AL, et al. **Cerebral aneurysm sac growth as the etiology of recurrence after successful coil embolization.** *Stroke* 2012;43:866–68 CrossRef Medline
20. Luan Z, Chase AJ, Newby AC. **Statins inhibit secretion of metalloproteinases-1, -2, -3, and -9 from vascular smooth muscle cells and macrophages.** *Arterioscler Thromb Vasc Biol* 2003;23:769–75 CrossRef Medline
21. Nyan M, Miyahara T, Noritake K, et al. **Molecular and tissue responses in the healing of rat calvarial defects after local application of simvastatin combined with alpha tricalcium phosphate.** *J Biomed Mater Res B Appl Biomater* 2010;93:65–73 CrossRef Medline
22. Kodama T, Iwata H. **Comparison of bare metal and statin-coated coils on rates of intra-aneurysmal tissue organization in a rat model of aneurysm.** *J Biomed Mater Res B Appl Biomater* 2013;101:656–62 CrossRef Medline
23. Raux M, Cochennec F, Becquemin JP. **Statin therapy is associated with aneurysm sac regression after endovascular aortic repair.** *J Vasc Surg* 2012;55:1587–92 CrossRef Medline
24. Gray C, Goodman P, O'Malley MK, et al. **Statins promote residual aneurysm sac regression following endovascular aortic aneurysm repair.** *Vasc Endovasc Surg* 2014;48:111–15 CrossRef Medline
25. Chalouhi N, Tjoumakaris S, Gonzalez LF, et al. **Coiling of large and giant aneurysms: complications and long-term results of 334 cases.** *AJNR Am J Neuroradiol* 2014;35:546–52 CrossRef Medline
26. Crobeddu E, Lanzino G, Kallmes DF, et al. **Review of 2 decades of aneurysm-recurrence literature, part 1: reducing recurrence after endovascular coiling.** *AJNR Am J Neuroradiol* 2013;34:266–70 CrossRef Medline

Clinical and Imaging Follow-Up of Patients with Coiled Basilar Tip Aneurysms Up to 20 Years

M. van Eijck, R.S. Bechan, M. Sluzewski, J.P. Peluso, G. Roks, and W.J. van Rooij

ABSTRACT

BACKGROUND AND PURPOSE: Long-term follow-up data of coiled basilar tip aneurysms are scarce, and little is known about the risk of late aneurysm-related adverse events. We followed a cohort of 154 patients with basilar tip aneurysms coiled between 1995 and 2006.

MATERIALS AND METHODS: Imaging and clinical data were retrospectively reviewed. The incidence and timing of retreatment, rebleeds, and progressive mass effect by continuous aneurysm growth were recorded. Risk factors for retreatment were assessed.

RESULTS: Clinical follow-up of 144 of 154 patients who survived the admission period was a mean of 9.8 years (median, 10.2; range, 0.3–20.1 years). During this period, 37 basilar tip aneurysms (26%) were additionally coiled (annual incidence rate, 2.6%; 95% CI, 1.8%–3.6%). Aneurysm size of >15 mm was the most important independent predictor for retreatment (OR, 8.7; 95% CI, 3.4–22.5). The first additional coiling was performed in the first year of follow-up in 17 of 37 patients (46%) and in 20 patients (54%) at a later time up to 17.2 years. Nine rebleeds occurred in 9 of 106 patients who initially presented with SAH after a median follow-up of 8.3 years (range, 0.3–16.6 years). The annual incidence rate was 0.7% (95% CI, 0.4%–1.5%). Eight patients died of aneurysm-related adverse events: 3 of rebleed and 5 of progressive mass effect.

CONCLUSIONS: Retreatment of coiled basilar tip aneurysms was frequently needed during follow-up, also at long intervals. Most late mortality was from progressive mass effect, not from rebleeds. Life-long MRA follow-up at yearly intervals is recommended.

Approximately 20% of coiled of intracranial aneurysms show reopening at follow-up, of which half are retreated.[1] Risk factors for reopening with time are large aneurysm size, a wide neck, the presence of intraluminal thrombus, low packing attenuation, initial incomplete occlusion, duration of follow-up, and location in the posterior circulation.[2-17] In general, additional coiling is advocated in reopened aneurysms to prevent rebleeding. Most reopenings occur in the first year after coiling and become apparent at the first imaging follow-up after 6–12 months. A first time reopening beyond the 12-month follow-up is infrequent.[6,7,9,10,12,13]

Aneurysms at the basilar tip form a special subset of intracranial aneurysms. First, surgery is a less likely option in these aneurysms, and even aneurysms with unfavorable configuration are coiled, whereas unfavorable aneurysms in the anterior circulation can be clipped. Basilar tip aneurysms are located on a vascular bifurcation and often have a wide neck. Therefore, reopening in basilar tip aneurysms is more frequent than in aneurysms at other locations.[1,2,10,13,16,17] Second, some coiled basilar tip aneurysms show continuous growth with progressive mass effect on the brain stem.[17]

We followed a cohort of 154 patients with basilar tip aneurysms coiled between 1995 and 2006 for up to 20 years, to assess survival, frequency and timing of reopening, and retreatment. In addition, clinical events from the basilar tip aneurysm, such as rebleeds and progressive mass effect by continuous growth, were recorded.

MATERIALS AND METHODS

We retrospectively followed a cohort of 154 consecutive patients with basilar tip aneurysms coiled between January 1995 and August 2006. Details on the follow-up of a mean of 4.4 years of this patient cohort have been published previously.[18] We extended the clinical and MR angiographic follow-up time to obtain long-term clinical data and assess possible risk factors for late basilar tip aneurysm–related adverse events.

Study Population

The cohort of 154 patients with coiled basilar tip aneurysms included 42 men (27%) and 112 (73%) women, with a mean age of

Received February 24, 2015; accepted after revision March 24.

From the Departments of Neurology (M.v.E., G.R.) and Radiology (R.S.B., M.S., J.P.P., W.J.v.R.), Sint Elisabeth Ziekenhuis, Tilburg, the Netherlands.

Drs van Eijck and Bechan contributed equally to this article.

Please address correspondence to W.J. van Rooij, MD, Sint Elisabeth Ziekenhuis, Hilvarenbeekseweg 60, 5022GC Tilburg, the Netherlands; e-mail: wjjvanrooij@gmail.com

http://dx.doi.org/10.3174/ajnr.A4410

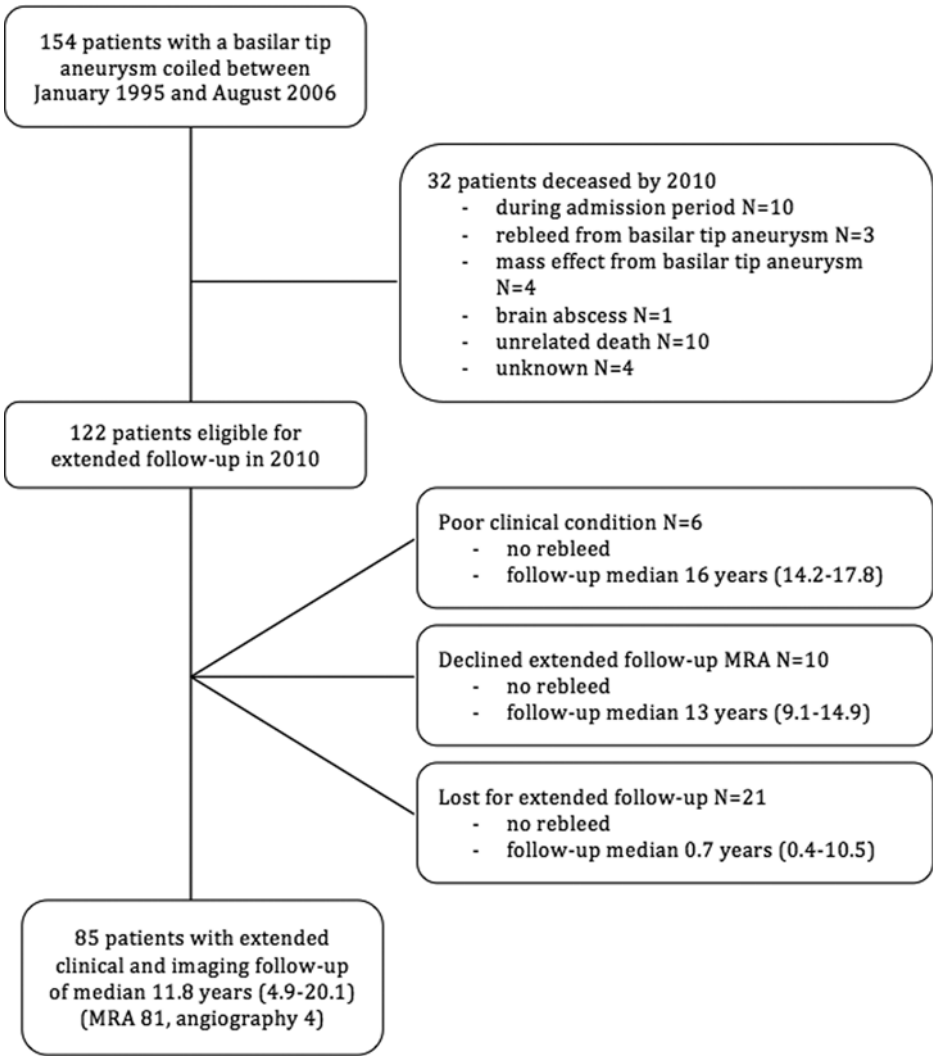

FIG 1. Follow-up scheme of 154 patients with a basilar tip aneurysm.

50.5 years at the time of coiling (median, 50 years; range, 25–73 years). There were 114 ruptured (74%) and 40 unruptured aneurysms (26%). The mean aneurysm size was 11.1 mm (median, 10 mm; range, 2–30 mm). There were 83 small aneurysms (<10 mm), 61 large aneurysms (11–24 mm), and 10 giant aneurysms (>25 mm). Demographics during follow-up of patients who survived the hospital admission period included sex, age, rupture status of the aneurysm, occlusion after coiling, use of supporting devices during coiling, procedural complications, and clinical and imaging outcomes. Additional coiling and its complications and timing during the years were documented. After we encountered several unexpected late adverse events in a short period in patients with coiled basilar tip aneurysms in 2012, we adapted our follow-up protocol and actively attempted to extend the MRA follow-up in as many patients as possible. Patients without imaging follow-up in the past 4 years were invited for follow-up MRA by letter. If there was no response, we contacted the general practitioner to find out whether the patient was still alive, and if not, we asked for the date and cause of death. Patients in poor clinical condition in nursing homes were excluded from extended imaging follow-up. Patients with a contraindication for MR imaging were invited for follow-up conventional angiography.

Follow-Up MR Imaging and Indications for Retreatment

MR imaging was performed on a 3T system (Intera R10; Philips Healthcare, Best, the Netherlands) by using a phased array head coil (MR Imaging Devices, Gainesville, Florida) with sensitivity encoding.

The MR imaging protocol included axial and coronal T2-weighted fast spin-echo, coronal T1-weighted spin-echo, and high-resolution multiple overlapping thin-slab acquisition 3D time-of-flight MRA sequences. The MRA protocol was validated in the follow-up of coiled intracranial aneurysms.[19]

Reopening was defined as flow on MRA at the base of the aneurysm, caused by either compaction of the coil mesh, aneurysm regrowth, or migration of coils into intra-aneurysmal thrombus. Results of follow-up MRA were evaluated by a multidisciplinary team. In general, any reopening was an indication for additional coiling. Only exceptionally, additional treatment was not performed or postponed for anatomic or clinical reasons.

Statistical Analysis

Putative risk factors for retreatment of the basilar tip aneurysm were assessed with univariate logistic regression analysis. Odds

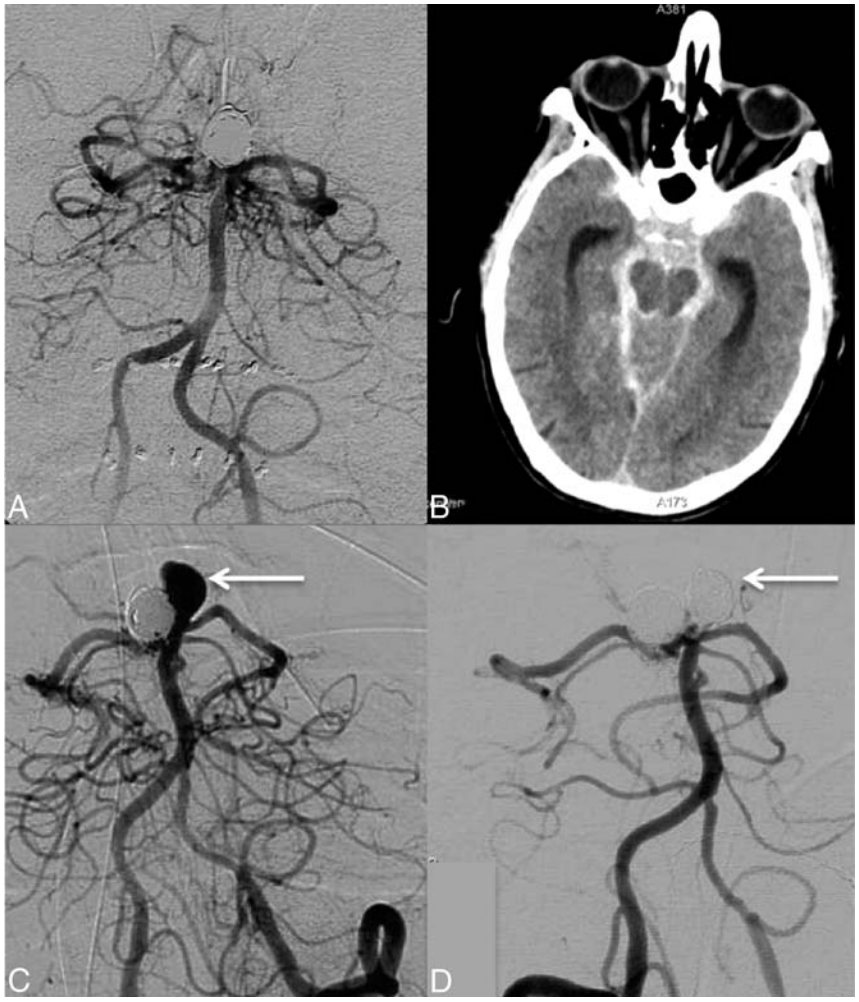

FIG 2. A 41-year-old man with a coiled ruptured basilar tip aneurysm in 1997 and a rebleed 15 years later. *A*, Angiography in 2006, 9 years after coiling in 1997, shows an adequately occluded basilar tip aneurysm. *B*, CT in 2012 demonstrates a rebleed from the basilar tip aneurysm. *C*, Angiography reveals regrowth of the aneurysm (*arrow*). *D*, After additional coiling, the aneurysm is completely occluded (*arrow*).

ratios were calculated for the following variables: median aneurysm size, rupture status, sex, age at first treatment, and duration of follow-up in years. Then, multivariate logistic regression analysis was performed with reopening of the basilar tip aneurysm as a dependent variable. Aneurysms that were additionally coiled were expressed as a proportion, and timing of the first retreatment was graphically displayed in a cumulative event plot.

For ruptured basilar tip aneurysms, rebleed was expressed as an annual incidence rate with corresponding 95% confidence intervals and was graphically displayed in a cumulative event plot.

The occurrence of progressive mass effect by the aneurysm was also calculated as an incidence rate.

The *t* test was used for continuous variables, and the Fisher exact test, for categoric data. A P value $< .05$ was considered statistically significant. Statistical analysis was performed with MedCalc Statistical Software, Version 14.12.0 (MedCalc Software, Mariakerke, Belgium).

RESULTS

Clinical and Imaging Follow-Up

Figure 1 is a follow-up scheme of the cohort. Of 154 patients, 32 had died by 2010.

Of 122 patients who were eligible for

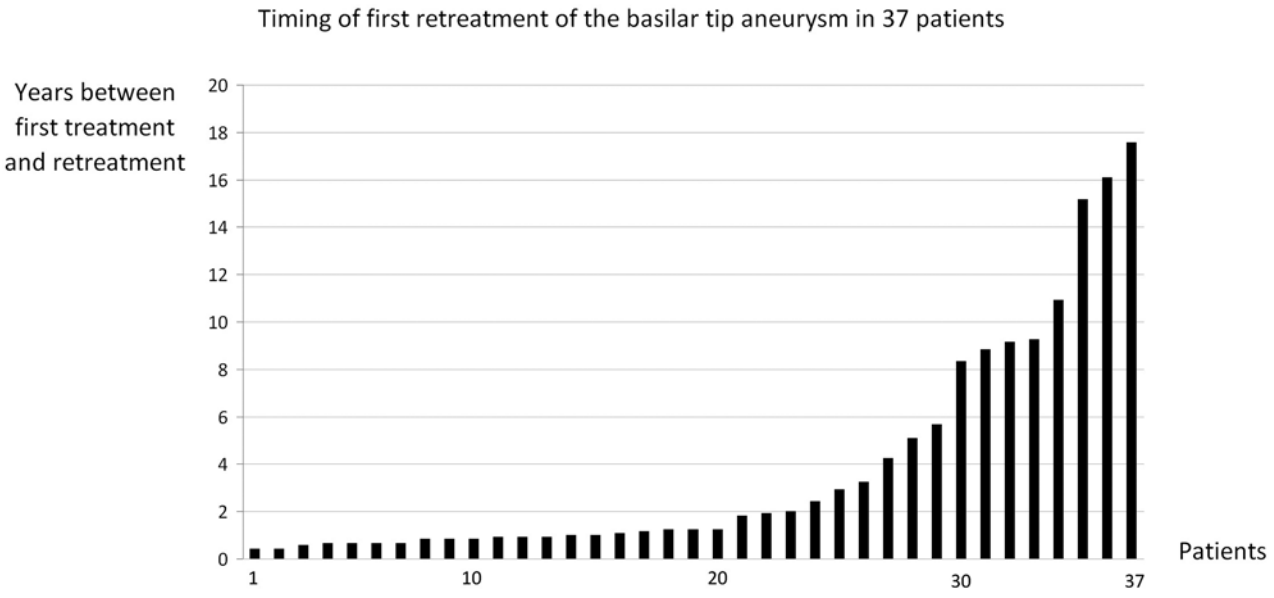

FIG 3. Timing of first retreatments in 37 patients with reopened basilar tip aneurysms.

extended follow-up in 2010, 85 (70%) had extended MRA (n = 81) or angiographic (n = 4) follow-up at a median of 11.8 years (range, 4.9–18.4 years). In 2 of these patients, angiography was performed after a rebleed from the basilar tip aneurysm at 16.6 and 15.2 years after coiling (Fig 2).

Incidence of Retreatment

Clinical follow-up of 144 patients who survived the admission period was for a mean of 9.8 years (median, 10.2 years; range, 0.3–20.1 years), totaling 1461 patient-years. During this period, 37 basilar tip aneurysms (26%) were additionally coiled. The annual incidence rate for retreatment was 2.5% (95% CI, 1.8%–3.5%).

The timing of the first additional coiling is graphically displayed in Fig 3. First additional coiling was performed in the first year of follow-up in 15 of 37 patients (41%) and in 22 patients (59%) later, up to 17.2 years after the first coiling. In 15 of 37 patients (41%), additional coiling was performed more than once and up to 5 times. The timing of additional treatments in these patients is displayed in Fig 4. In total, 68 additional coilings were performed during follow-up, all without complications (complication rate, 0%; 95% CI, 0%–5.7%).

Risk Factors for Retreatment

The results of logistic regression analysis are summarized in Table 1. In univariate analysis, age at first coiling, ruptured aneurysm status, and the mean period of follow-up were not different between patients with or without additional coiling during follow-up. Male sex and median aneurysm size were significantly associated with additional coiling (OR, 2.6 and 1.1). Because large aneurysm size is a well-known risk factor for aneurysm reopening, aneurysm size was further analyzed in quintiles. Aneurysms of 16–30 mm had a 9-fold higher chance of retreatment during follow-up than aneurysms of 2–6 mm (OR, 8.5; 95% CI, 2.5–29.3).

In multivariate analysis, aneurysm size of >15 mm was a strong independent predictor (OR, 8.7; 95% CI, 3.4–22.5). In addition, male sex was an independent risk factor for retreatment (OR, 2.7; 95% CI, 1.1–6.5). Age at first treatment, the mean period of follow-up, and ruptured aneurysm status were not independent risk factors.

Incidence of Rebleed

The mean follow-up of 38 of 40 patients who presented with unruptured basilar tip aneurysms and who survived the first treatment was 8.5 years (median, 9.1 years; range, 0.3–17 years). There were no first-time hemorrhages in these patients.

The clinical follow-up of 106 patients with a ruptured basilar tip aneurysm who survived the hospital admission period was a mean of 9.8 years (median, 10.2 years; range, 0.4–18.7 years), totaling 1158 patient-years. Nine episodes of rebleed were recorded in 9 patients. Three patients died of the rebleed (0.3, 7.2, and 16.1 years after first treatment). Rebleeds occurred after a median follow-up of 8.3 years (range, 0.3–16.6 years). The annual incidence rate for rebleed was 0.7% (95% CI, 0.4%–1.5%).

Progressive Mass Effect

Progressive compression on the brain stem by continuous growth of the basilar tip aneurysm occurred in 6 patients (Fig 5). Follow-up in these patients was a mean of 7.2 years (median, 5 years; range, 0.5–17.8 years), totaling 42.8 patient-years (Table 2). The annual incidence rate of progressive mass effect was 0.4% (95% CI, 0.2%–0.9%). In 5 deceased patients, this was the cause of death; in 4 patients, it was by progressive brain stem compression. In 1 patient, progressive growth of the aneurysm in an anterior direction caused compression of the chiasm with loss of vision 10.8 years after the first coiling. Despite partial surgical resection of the aneurysm, the patient died 1 month later.

Aneurysm-Related Mortality

During the follow-up period, 8 patients died of aneurysm-related adverse events: Three patients died of rebleed

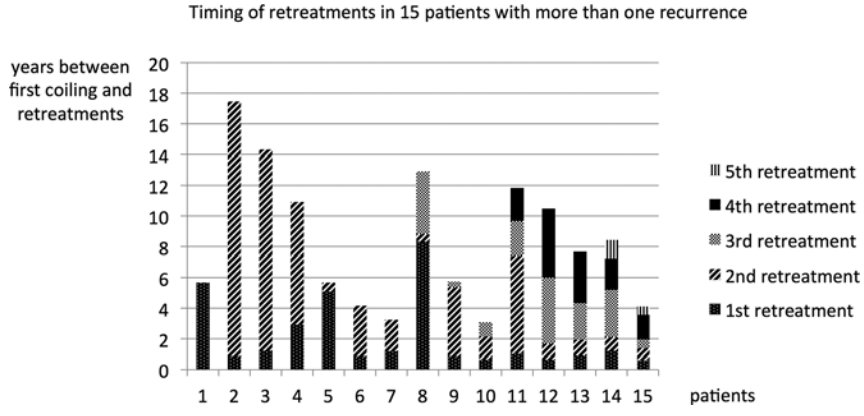

FIG 4. Timing of retreatments in 15 patients with coiled basilar tip aneurysms and >1 recurrence.

Table 1: Univariate analysis of risk factors for retreatment of coiled basilar tip aneurysms in 144 patients

	No Recurrence (n = 107)	Recurrence (n = 37)	OR (95% CI)	P Value
Median age at first treatment (yr)	54	46	0.97 (0.9–1.0)	.13
Male sex	25 (23%)	16 (43%)	2.6 (1.2–5.6)	.02
Median aneurysm size (mm)	9	15	1.1 (1.1–1.2)	<.001
Size of aneurysm in quintiles[a]				
Quintile 2 versus 1			0.9 (0.2–3.3)	
Quintile 3 versus 1			0.9 (0.2–3.3)	
Quintile 4 versus 1			1.6 (0.4–6.3)	
Quintile 5 versus 1			8.5 (2.5–29.3)	
Ruptured aneurysm	88 (82%)	14 (38%)	0.8 (0.3–1.9)	.62
Median follow-up (yr)	10.5	10	1.0 (0.98–1.14)	.20

[a] Size range in quintiles: quintile 1 = 2–5 mm; quintile 2 = 6–8 mm; quintile 3 = 9–12 mm; quintile 4 = 13–15 mm; quintile 5 = 16–30 mm.

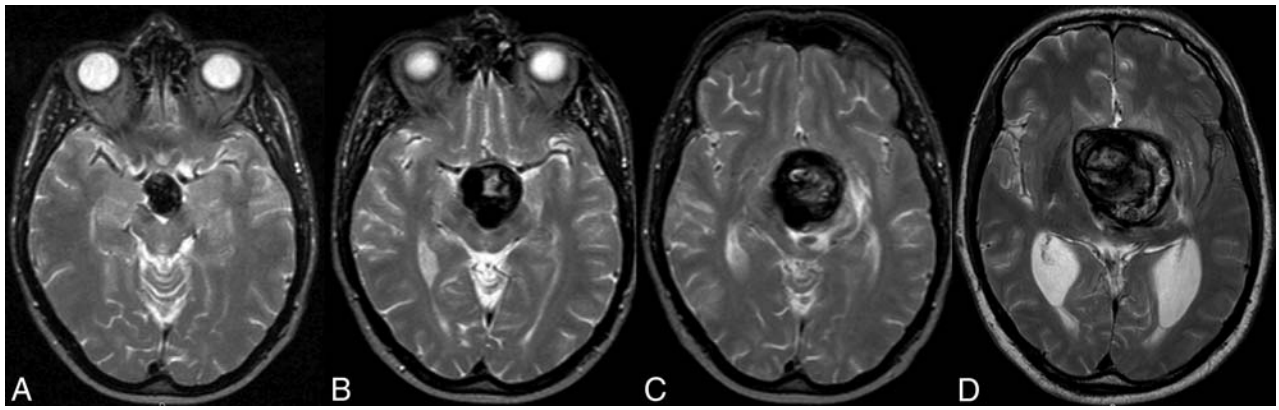

FIG 5. Serial MR images of a 40-year-old man with a coiled ruptured basilar tip aneurysm in 2003. *A*, Transversal T2-weighted MR image from December 2003 shows a basilar tip aneurysm 6 months after coiling. *B*, MR imaging in May 2008 shows enlargement of the aneurysm and compression of the brain stem. *C*, MR imaging in March 2009 shows further growth, now with edema in the brain stem. *D*, MR imaging in December 2009 shows a rapid increase in size with enormous compression of the brain stem. The patient died 1 month later.

Table 2: Characteristics of 6 patients with progressive mass effect by continuous growth of the basilar tip aneurysm despite (repeat) coiling

Date of First Treatment	Sex, Age (yr)	SAH	First Signs of Mass Effect	Compression Organ	No.of Coilings	Death	Follow-Up (yr)
Jan 10, 1996	M, 52	Yes	January 1996	Brain stem	1	Yes	0.5
June 5, 1996	M, 39	Yes	May 2008	Brain stem	5	No	11.8
June 18, 2001	F, 69	Yes	September 2004	Brain stem	1	Yes	3.3
July 27, 2001	M, 39	Yes	March 2009	Brain stem	5	Yes	8.4
November 5, 2001	M, 58	Yes	July 2012	Brain stem	5	Yes	12.5
May 30, 2002	M, 49	No	October 2002	Optic chiasm	2	Yes	0.5

and 5 died of progressive mass effect from the basilar tip aneurysm.

DISCUSSION

This long-term follow-up study of 154 coiled basilar tip aneurysms showed that retreatment during follow-up was performed in a quarter of patients. Almost half of retreatments were in the first year after coiling, but first retreatments were also performed up to 17 years after the first coiling. In 4 patients, the first retreatment was >10 years after coiling. A substantial proportion of retreated aneurysms were retreated more than once, up to 5 times. All retreatments were without complications. The incidence of retreatment of basilar tip aneurysms of 25% is significantly higher than that of aneurysms at other locations: In a meta-analysis by Ferns et al,[1] the overall retreatment rate was 10%, with aneurysm sizes of >10 mm and location in posterior circulation as risk factors. There are probably 3 reasons for this higher incidence of retreatment in aneurysms located on the basilar tip: First, in general, all basilar tip aneurysms are coiled; they are also aneurysms with unfavorable anatomy and an inherent higher chance of reopening. Surgical clipping is rarely considered an alternative for coiling. Second, almost half of the basilar tip aneurysms were of large or giant size. Third, our follow-up duration was extremely long, and various first retreatments were performed at very long follow-up intervals: In 8 of 37 patients, the first retreatment was >8 years after the first coiling.

The most important independent risk factor for retreatment was aneurysm size; increasing aneurysm size increases the chance of reopening and retreatment. Large aneurysm size as a risk factor for reopening and retreatment is a well-known and consistent finding in follow-up studies after coiling.[1-3,5-10,12-17] The second independent risk factor was male sex. We have no explanation for this finding. In 1 previous study, male sex was also found to be a risk factor for reopening after coiling.[7]

Rebleeds occurred in 9 of 106 patients with ruptured basilar tip aneurysms who survived the admission period at time intervals ranging from 4 months to 16.6 years after coiling. In 3 patients, the rebleed was fatal. The annual incidence rate for recurrent hemorrhage was a 0.7%, low but higher than approximately 0.3% in other studies comprising aneurysms at all locations.[20,21] This finding emphasizes the need for a regular and life-long follow-up scheme to detect reopening in a timely manner and prevent rebleeds by retreatment. Even after many years of stable aneurysm occlusion, reopening and rebleed may still occur.

Our study also demonstrated that most late mortality was due to continuous growth of some basilar tip aneurysms despite adequate first-time occlusion with coils and additional coiling when possible.[22,23] Why this phenomenon occurs in some aneurysms remains unclear. We were unable to identify risk factors for this infrequent event. Aneurysm growth may become apparent at any time during follow-up. The growth rate varies, and episodes of growth may alternate with stable periods. Patients with a growing basilar tip aneurysm can present with various clinical signs because of compression on the brain stem, such as cognitive dysfunction with apathy and loss of initiative, motor and gait difficulties, and cranial neuropathies with or without signs of hydrocephalus. In our population, most patients presented with gradually progressive cognitive decline; 1 patient presented with progressive loss of

vision from compression on the chiasm. The prognosis of a growing basilar tip aneurysm is poor, with variable times from onset of symptoms to death. Therapy can only be palliative, with steroids and treatment of hydrocephalus. Aneurysm debulking was performed in 1 patient but was not effective.

Our protocol for coiled aneurysms was fairly consistent during the follow-up period. Patients with large and giant basilar tip aneurysms and those who were coiled more than once had a tailored follow-up scheme, with MRA every 1–3 years. Patients with no regular follow-up scheme were actively contacted at different times to participate in various follow-up studies.[2,5,10,12,13,16,18] Despite this close monitoring, in 2012, we encountered several unexpected serious late clinical adverse events in a short time in patients with coiled basilar tip aneurysms. At that point, we decided to recall patients without follow-up imaging in the past 4 years for MR imaging and MRA, and 85 of 122 eligible patients responded positively. This response resulted in a very long clinical and imaging follow-up for the cohort. There are no other comparable studies with very long-term follow-up of basilar tip aneurysms, to our knowledge.

This retrospective study has several drawbacks. Clinical and imaging follow-up was not complete in all patients. Some patients had irregular or large intervals between follow-up imaging, and the assessment of the timing of reopening was thus inaccurate. In some patients, the cause of death remained unknown. Not all patients responded positively to an invitation for extended imaging follow-up.

The principal conclusion from this extended follow-up study of coiled basilar tip aneurysms is that serious adverse events may become apparent for the first time very long after a first or additional coiling. Aneurysms may be stable for long periods before or after reopening or rebleed. Coiled basilar tip aneurysms that increase in size despite adequate occlusion at first or repeated treatment have a poor prognosis. The growth rate is unpredictable; it can be slow or quick and gradual or alternating. When hydrocephalus occurs, it should be treated. When brain stem compression is accompanied by edema, steroids may be administered as palliation. With our follow-up scheme, most aneurysm-related mortality was from continuous aneurysm growth, not from rebleeds.

CONCLUSIONS

A regular and life-long clinical and imaging follow-up protocol is advisable in patients with both ruptured and unruptured basilar tip aneurysms that have been coiled. In our opinion, yearly MR imaging should be adequate to detect reopening needing additional treatment in a timely manner. Recurrent episodes of hemorrhage can thus be prevented.

REFERENCES

1. Ferns SP, Sprengers ME, van Rooij WJ, et al. **Coiling of intracranial aneurysms: a systematic review on initial occlusion and reopening and retreatment rates.** *Stroke* 2009;40:e523–29
2. Ferns SP, Sprengers ME, van Rooij WJ, et al; LOTUS Study Group. **Late reopening of adequately coiled intracranial aneurysms: frequency and risk factors in 400 patients with 440 aneurysms.** *Stroke* 2011;42:1331–37
3. Raymond J, Guilbert F, Weill A, et al. **Long-term angiographic recurrences after selective endovascular treatment of aneurysms with detachable coils.** *Stroke* 2003;34:1398–403
4. Schaafsma JD, Sprengers ME, van Rooij WJ, et al. **Long-term recurrent subarachnoid hemorrhage after adequate coiling versus clipping of ruptured intracranial aneurysms.** *Stroke* 2009;40:1758–63
5. Sluzewski M, van Rooij WJ, Rinkel GJ, et al. **Endovascular treatment of ruptured intracranial aneurysms with detachable coils: long-term clinical and serial angiographic results.** *Radiology* 2003;227:720–24
6. Cognard C, Weill A, Spelle L, et al. **Long-term angiographic follow-up of 169 intracranial berry aneurysms occluded with detachable coils.** *Radiology* 1999;212:348–56
7. Chalouhi N, Bovenzi CD, Thakkar V, et al. **Long-term catheter angiography after aneurysm coil therapy: results of 209 patients and predictors of delayed recurrence and retreatment.** *J Neurosurg* 2014;121:1102–06
8. Piotin M, Spelle L, Mounayer C, et al. **Intracranial aneurysms: treatment with bare platinum coils—aneurysm packing, complex coils, and angiographic recurrence.** *Radiology* 2007;243:500–08
9. Sluzewski M, van Rooij WJ, Slob MJ, et al. **Relation between aneurysm volume, packing, and compaction in 145 cerebral aneurysms treated with coils.** *Radiology* 2004;231:653–58
10. Sluzewski M, Menovsky T, van Rooij WJ, et al. **Coiling of very large or giant cerebral aneurysms: long-term clinical and serial angiographic results.** *AJNR Am J Neuroradiol* 2003;24:257–62
11. Slob MJ, Sluzewski M, van Rooij WJ, et al. **Additional coiling of previously coiled cerebral aneurysms: clinical and angiographic results.** *AJNR Am J Neuroradiol* 2004;25:1373–76
12. van Rooij WJ, Sprengers ME, Sluzewski M, et al. **Intracranial aneurysms that repeatedly reopen over time after coiling: imaging characteristics and treatment outcome.** *Neuroradiology* 2007;49:343–49
13. Sprengers ME, Schaafsma J, van Rooij WJ, et al. **Stability of intracranial aneurysms adequately occluded 6 months after coiling: a 3T MR angiography multicenter long-term follow-up study.** *AJNR Am J Neuroradiol* 2008;29:1768–74
14. Lozier AP, Connolly ES Jr, Lavine SD, et al. **Guglielmi detachable coil embolization of posterior circulation aneurysms: a systematic review of the literature.** *Stroke* 2002;33:2509–18
15. Henkes H, Fischer S, Mariushi W, et al. **Angiographic and clinical results in 316 coil-treated basilar artery bifurcation aneurysms.** *J Neurosurg* 2005;103:990–93
16. Ferns SP, Majoie CB, Sluzewski M, et al. **Late adverse events in coiled ruptured aneurysms with incomplete occlusion at 6-month angiographic follow-up.** *AJNR Am J Neuroradiol* 2010;31:464–69
17. van Rooij WJ, Sluzewski M. **Opinion: imaging follow-up after coiling of intracranial aneurysms.** *AJNR Am J Neuroradiol* 2009;30:1646–48
18. Peluso JP, van Rooij WJ, Sluzewski M, et al. **Coiling of basilar tip aneurysms: results in 154 consecutive patients with emphasis on recurrent haemorrhage and re-treatment during mid- and long-term follow-up.** *J Neurol Neurosurg Psychiatry* 2008;79:706–11
19. Sprengers ME, Schaafsma JD, van Rooij WJ, et al. **Evaluation of the occlusion status of coiled intracranial aneurysms with MR angiography at 3T: is contrast enhancement necessary?** *AJNR Am J Neuroradiol* 2009;30:1665–71
20. Molyneux AJ, Kerr RS, Birks J, et al; ISAT Collaborators. **Risk of recurrent subarachnoid haemorrhage, death, or dependence and standardised mortality ratios after clipping or coiling of an intracranial aneurysm in the International Subarachnoid Aneurysm Trial (ISAT): long-term follow-up.** *Lancet Neurol* 2009;8:427–33
21. Sluzewski M, van Rooij WJ, Beute GN, et al. **Late rebleeding of ruptured intracranial aneurysms treated with detachable coils.** *AJNR Am J Neuroradiol* 2005;26:2542–49
22. Krings T, Alvarez H, Reinacher P, et al. **Growth and rupture mechanism of partially thrombosed aneurysms.** *Interv Neuroradiol* 2007;13:117–26
23. Hasan DM, Nadareyshvili AI, Hoppe AL, et al. **Cerebral aneurysm sac growth as the etiology of recurrence after successful coil embolization.** *Stroke* 2012;43:866–68

Combined Selective Cerebral Hypothermia and Mechanical Artery Recanalization in Acute Ischemic Stroke: In Vitro Study of Cooling Performance

G. Cattaneo, M. Schumacher, J. Wolfertz, T. Jost, and S. Meckel

ABSTRACT

BACKGROUND AND PURPOSE: Therapeutic hypothermia represents a promising neuroprotective treatment for patients with ischemic stroke. Selective, intracarotid blood cooling may initiate rapid and early brain hypothermia, reduce systemic effects, and allow combined endovascular mechanical thrombectomy. For this approach, a balloon cooling catheter system was designed and studied in vitro to optimize its cooling performance.

MATERIALS AND METHODS: Computational fluid dynamics of blood cooling was performed within the common carotid artery lumen by using 3 different catheter designs (1-, 2-, and 4-balloon array). On the basis of these results, a first catheter prototype was manufactured, and its heat-exchange performance was tested in an artificial in vitro circulation simulating the common carotid artery lumen at different flow rates (inflow temperature of 37°C).

RESULTS: In the computational fluid dynamics model, the catheter with the 4-balloon array achieved the highest cooling rate of −1.6°C, which may be attributed to disruption of the thermal boundary layers. In the in vitro study, cooling of the blood substitute at flow rates of 400 mL/min (normal common carotid artery flow) and 250 mL/min (reduced common carotid artery flow due to distal MCA occlusion) achieved a temperature drop inside the blood substitute along the cooling balloons of −1.6°C and −2.2°C, respectively.

CONCLUSIONS: The feasibility of intracarotid blood cooling using a new catheter system was demonstrated in vitro. A serial 4-balloon array led to an optimized cooling capacity approaching optimum target temperatures of mild therapeutic hypothermia. To determine the therapeutic efficacy of combined selective therapeutic hypothermia and mechanical thrombectomy, further in vivo studies by using a model of temporary ischemia with large-vessel occlusion and recanalization are required.

ABBREVIATIONS: CCA = common carotid artery; MT = mechanical thrombectomy; TH = therapeutic hypothermia

Therapeutic hypothermia (TH) has become a clinical standard in patients with successful resuscitation after cardiac arrest and in neonates with severe asphyxia, to increase the rate of favorable neurologic outcome and reduce mortality.[1-4] Neuroprotection provided by TH affects multiple aspects of brain physiology during all stages of ischemia (eg, excitotoxicity, apoptosis, inflammation, free radical production, blood flow, metabolism, and blood-brain barrier integrity).[5] Recently, the feasibility and safety of TH in patients with acute ischemic stroke was proved in controlled studies,[6-9] and 2 multicenter, randomized clinical trials (European Stroke Research Network for Hypothermia-1 and Intravenous Thrombolysis plus Hypothermia for Acute Treatment of Ischemic Stroke 2/3)[10,11] are currently underway to study its efficacy. Until now, TH in patients with acute stroke has been applied only systematically by surface cooling, intravenous cooling, or cold saline infusions.

In patients with acute ischemic stroke related to large-artery occlusions, rapid treatment with mechanical thrombectomy (MT) by using stent retrievers for vessel recanalization reduces mortality and improves functional outcome according to the recent release of landmark randomized controlled trials.[12-14] However, reperfusion of ischemic brain tissue may also induce additional tissue damage and hemorrhagic trans-

Received February 6, 2015; accepted after revision March 31.

From Acandis GmbH & Co. KG (G.C., J.W., T.J.), Pforzheim, Germany; and Department of Neuroradiology (M.S., S.M.), University Hospital Freiburg, Freiburg, Germany.

This work was sponsored by Federal Ministry of Education and Research, Germany (Federal Ministry of Education and Research grant 13GW0015B).

Please address correspondence to Stephan Meckel, MD, Department of Neuroradiology, Neurocenter, University Hospital Freiburg, Breisacher Str 64, D-79106 Freiburg, Germany; e-mail: stephanmeckel@gmail.com

http://dx.doi.org/10.3174/ajnr.A4434

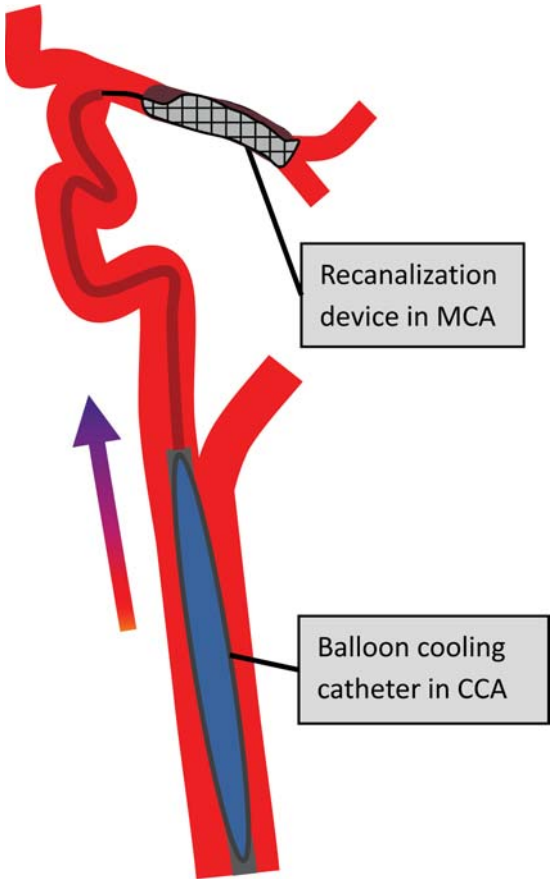

FIG 1. Schematic illustration of combined simultaneous intracarotid blood cooling in CCA and MT procedures by using a stent retriever device for the treatment of acute MCA occlusion. The *colored arrow* indicates transfer of cooled blood to ischemic brain and penumbra via collateral arteries before the MT procedure with the stent retriever device placed across MCA occlusion.

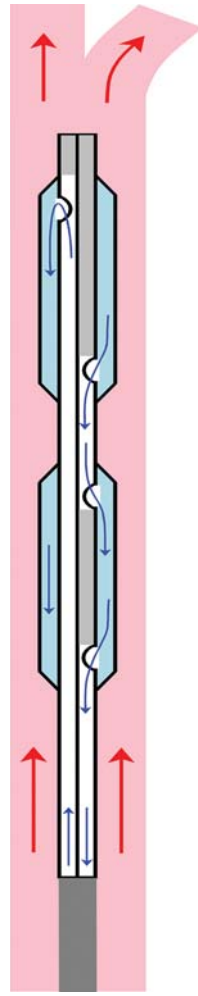

FIG 2. Schematic of the cooling catheter system as a heat exchanger between streaming blood and closed-loop circulation of cooling fluid inside the catheter. *Blue arrows* represent flow pathways of cooling fluid inside the inlet and outlet catheter lumen, with diversion from distal to proximal into 2 adjacent balloons. *Red arrows* represent the blood flow direction from the CCA into the ICA and external carotid artery.

formation, which potentially limit the benefits of such recanalization therapies.[15] Although the neuroprotective effects of TH may positively modulate mechanisms responsible for reperfusion injury, current systemic cooling approaches involve long induction times so that the therapeutic window may still be missed for many patients.[16]

We aimed to develop a combined approach of selective cerebral TH and MT within a single procedure by using a cooling catheter system that will be positioned in the common carotid artery (CCA) and proximal ICA and simultaneously serve as access for the intracranial MT procedure (Fig 1). Thus, cooled blood may first reach the ischemic penumbra via collaterals before recanalization and then further provide a "cold reperfusion" of the ischemic core during and after recanalization treatment of the occluded cerebral arteries. Moreover, this approach of selective TH may enable an earlier and faster induction of brain cooling and the reduction of systemic adverse effects of TH (ie, pneumonia) compared with systemic cooling techniques. In particular, early initiation of TH before or during vessel recanalization therapy is expected to be a critical determinant of clinical outcome.[10]

Before in vivo testing, the goal of this numeric and experimental in vitro study was to assess the feasibility and optimize the blood cooling performance of the newly developed balloon cooling catheter system for TH within the CCA lumen.

MATERIALS AND METHODS

Concept of Heat Exchange with the Balloon Cooling Catheter System

The balloons at the tip of the catheter system act as a heat exchanger between the bypassing blood stream and the separated cooling fluid circuit inside the cooling catheter, which is schematically depicted in Fig 2. The cooling fluid is circulated from the inlet lumen up to the distal catheter tip and then diverted within the outlet lumen, where openings to the balloons are provided that allow heat exchange with the bypassing blood via thin balloon surface membranes. In case of a multiple balloon array at the catheter tip, the balloons are serially connected with the direction of cooling fluid flow from distal to proximal. Thus, the catheter outlet lumen is interrupted between the openings of each balloon to prevent cooling fluid flow from bypassing the balloons. The third central lumen designed for delivery of catheter systems for MT is not depicted in the schematic.

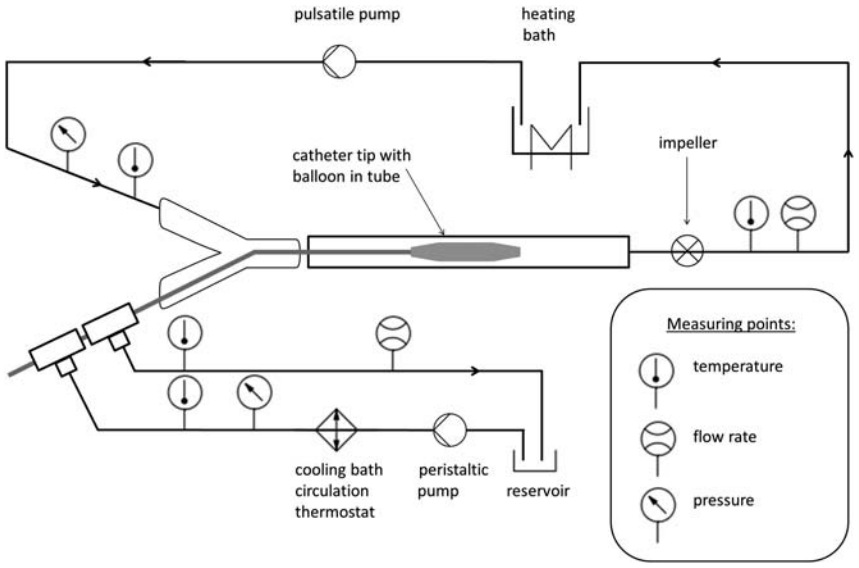

FIG 3. Schematic illustration of a bench test array for in vitro analysis of balloon cooling catheter system performance.

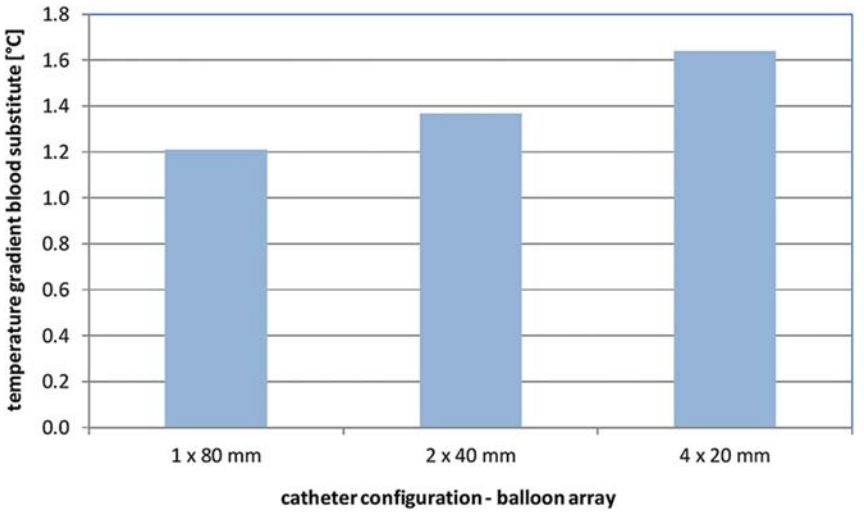

FIG 4. Temperature gradient across heat exchange balloons with 3 different balloon arrays.

Numeric Simulation

A numeric calculation of the fluid flow and heat transfer was performed by using the computational fluid dynamics software SolidWorks Flow Simulation 2013 SP3.0 (Dassault Systèmes SolidWorks, Waltham, Massachusetts) by using a simplified steady-state model without consideration of pulsatile flow behavior. We simulated 3 cooling catheter configurations with different balloon arrays: 1) 1 balloon with an 80-mm length, 2) 2 balloons with 40-mm lengths, and 3) 4 balloons with 20-mm lengths, all of which had a similar total surface area for heat exchange. Balloon wall thickness was 15 μm.

The computational mesh grid consisted of rectangular parallel-pipe-shaped fluid, solid, and partial cells, whose boundaries were orthogonal to the axes of the Cartesian global coordinate system. The meshing of the fluid domain presented approximately 2 million cells with mesh refinement near the balloon wall, where the heat transfer takes place. For simulation, the distal catheter tip with the heat exchanging balloons was immobile and centered in a rigid vessel that represented a simplified geometry of the CCA (7-mm diameter). An adiabatic behavior of the vessel wall was assumed; hence, heat transfer with the surrounding tissues was not considered. The rheology of the human blood was depicted through the Power Law model, by using the blood fluid parameters provided in the SolidWorks data base.

Closed-loop circulation of the cooling fluid (normal saline) inside the balloon catheter was provided by a simplified symmetric 2-lumen catheter, as shown in Fig 2. We set the cooling fluid temperature to 10°C at the inlet of the computational domain, considering an estimated heat loss of 4°C along the whole catheter length. The blood inlet temperature was set to 37°C. Blood and cooling fluid flow rates were set to 400 and 100 mL/min, respectively. Flow was steady for both fluids.

The bulk-average blood temperature (area- and flow-rate-weighted average) was calculated proximal and distal to the balloon array at the cooling catheter tip. Because of steady-state flow conditions, the temperature calculation was performed time-independently.

In Vitro Artificial "Blood Circuit" Testing

An artificial "blood circuit" was constructed with an internal diameter of 7 mm, compatible with the human CCA (mean diameter, 7.4 mm[17]); the artificial blood circuit was made of PVC tubes (Guttasyn Kunststoff, Witten, Germany). The complete installation of the in vitro bench test is illustrated in Fig 3.

This circuit was filled with a blood substitute consisting of a water-glycerine mixture (56% glycerin, 44% bi-distilled water), which approximated the rheologic properties of human blood (dynamic viscosity of 3.6 cP at 37°C). Constant warming to a temperature of 37°C proximal to the cooling catheter inlet was provided by a heating circulator bath (Haake DC10-B3; Thermo Haake, Karlsruhe, Germany). Pulsatile circulation of the blood substitute was achieved by a gear pump (Optima 1000 PD12; Diener Precision Pumps, Embrach, Switzerland). The distal part of the cooling catheter system with the heat-exchange balloons was inserted into the circuit via a hemostatic valve.

The coolant (0.9% sodium chloride) was circulated inside the cooling catheter circuit by means of a roller pump (Behrotest PLP 220 with pump head PPH 303; Behr Labor-Technik, Düsseldorf, Germany) at a flow rate of 100 mL/min. The cool-

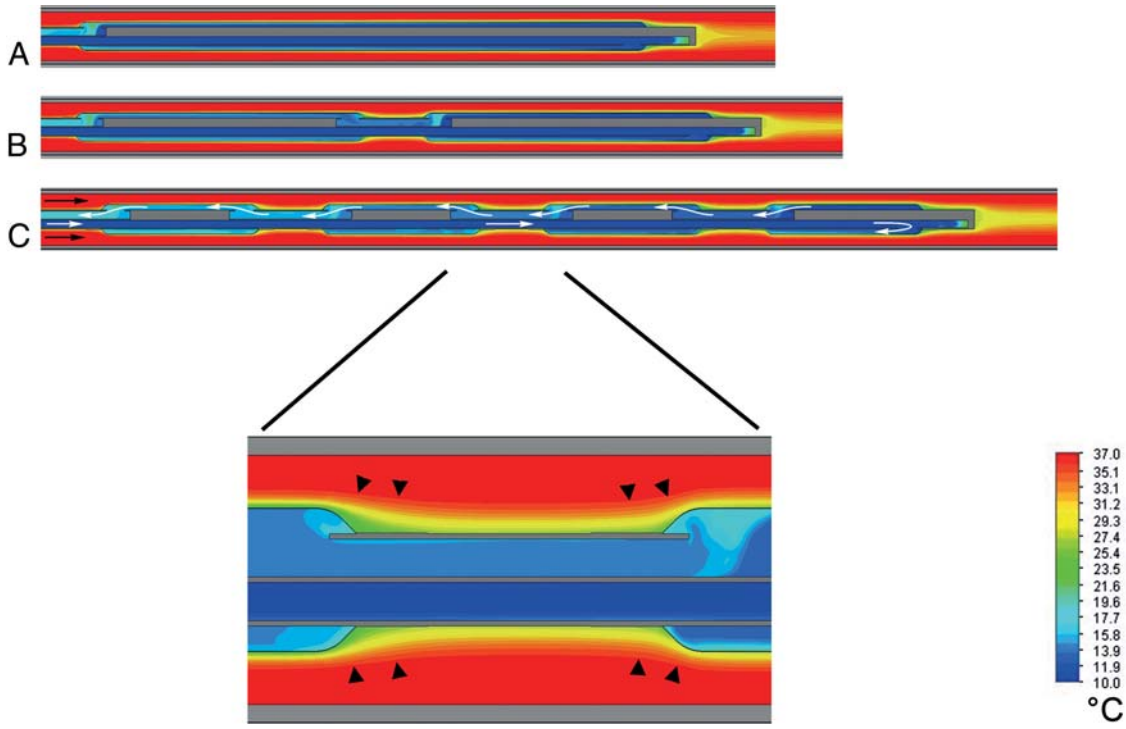

FIG 5. Temperature profiles derived from numeric simulation are illustrated along the cooling catheters with different serial balloon arrays (all 4-mm diameters): 1 × 80 mm (*A*); 2 × 40 mm (*B*); and 4 × 20 mm (*C*). *C*, The direction of blood flow is indicated by *small black arrows*, and the direction of coolant flow inside the catheter lumina is indicated by *small white arrows*. Temperatures are not visualized on solid catheter material (gray); larger rectangular gray areas represent blocked endoluminal portions, which enable serial coolant flow through respective balloons. The magnified inlet image shows the junction between adjacent balloons: Disruption of thermal boundary layers is depicted at both junction zones (*small black arrowheads*). Color coding corresponds to respective fluid temperature (10°C–37°C range; see scale).

ant temperature was kept constant at ~6°C provided by a circulation thermostat (Ministat 125; Peter Huber Kältemaschinenbau, Offenburg, Germany). Flow rates of both circuits were constantly measured by ultrasonic flow meters (M-2111; Malema Engineering, Boca Raton, Florida). Pressures were measured inside the cooling catheter circuit proximal to the catheter inlet (HPSA-B10DVAB-020-G; Althen, Kelkheim, Germany) and inside the "blood circuit" proximal to the cooling balloons (HPSA-B10DVAC-0,4BG; Althen). The coolant temperature was measured at the catheter inlet and outlet hub with precision fine-wire thermocouples (5TC-KK-KI-24–2 m; Omega Engineering, Stamford, Connecticut). Temperatures inside the blood circuit were measured by customized 1-mm mineral-insulated thermocouples (NiCr-Ni; Temperatur Messelemente Hettstedt, Maintal, Germany) proximal and distal to the cooling catheter system. To compensate for temperature stream layering of cooled and noncooled fluid distal to the balloon cooling catheter, we positioned the distal point of temperature measurement behind a flow indicator (CheMobil PMP; Bürkle, Bad Bellingen, Germany), which had an integrated impeller function for mixing of different temperature fluid layers.

Three similar prototypes of the cooling catheter were tested inside the blood circuit. We performed measurements separately at 2 predefined flow rates of the blood circuit: 400 mL/min, which is compatible with the mean blood flow rate of a human CCA (389 ± 73 and 381 ± 79 mL/min; left and right CCA, respectively[18]), and 250 mL/min, which aims to simulate the CCA flow reduction caused by an MCA occlusion (150 ± 31 and 145 ± 27 mL/min; normal left and right MCA flow rate, respectively[18]), neglecting potential autoregulatory flow changes. All temperature, fluid pressure, and flow data were continuously recorded and processed with an in-house-programmed software (LabVIEW 2013; National Instruments Corporation, Austin, Texas). After the start of the blood substitute and coolant pumps and a brief transient time of 2 minutes to allow steady-state flow conditions, recording of temperature data was performed for 2 minutes (100 temperature measurements per second). The temperature data were time-averaged over the 3 catheter prototypes.

RESULTS

The results of the numeric simulation are depicted in Fig 4, showing the temperature gradient across the cooling catheter for the 3 tested balloon arrays. The increasing number of balloons correlated with a higher blood-cooling performance, though the total heat-exchange surface area remained the same for all balloon arrays. This improved heat exchange for serial balloon alignments may be attributed to a disruption of the thermal boundary layer and increase of flow convection between the adjacent balloons (Fig 5). The highest temperature decrease across the catheter was −1.63°C by using a serial array of 4 × 20 mm balloons, while a single 1 × 80 mm balloon provided a temperature decrease of only −1.21°C.

On the basis of these results, the first prototype of the balloon cooling catheter was manufactured, which consisted of 4

polyamide balloons (Bavaria Medizin Technologie, Wessling, Germany) with a diameter of 4 mm, a length of 20 mm, and a wall thickness of 15 μm each. These were serially arranged at the catheter tip communicating with 2 separate catheter lumina that constituted the closed-loop cooling circuit. The third central "working lumen" with a diameter of 1 mm had an end-hole at the catheter tip allowing passage of a 2.5F microcatheter and thus distal access for MT treatment with a stent retriever device (Fig 6).

The in vitro experiments in the artificial blood circuit revealed a mean temperature gradient induced by the cooling catheter system (time-averaged over 3 similar catheter prototypes) of 2.17 ± 0.07°C and 1.55 ± 0.06°C at "blood" flow rates of 250 and 400 mL/min, respectively (Fig 7). During cooling, the temperature of the coolant inside the balloon catheter circuit increased by 5.46 ± .55°C and 5.95 ± 0.76°C at 250 and 400 mL/min, respectively. The mean pressure drop of the coolant within the cooling catheter system was 4.33 bar.

DISCUSSION

In this in vitro feasibility study, the blood-cooling performance of a newly developed balloon cooling catheter system designed for combined selective intracarotid TH and MT in acute stroke due to large-artery occlusion was investigated. Intra-CCA blood cooling was feasible with a mean temperature drop of 1.55°C. This result was closely matched by the numeric simulation (temperature drop of 1.63°C), which underlines the value of numeric simulation as a developmental tool.

These measured temperature drops imply an in vivo blood outlet temperature of ≈35.5°C (based on a physiologic temperature of 37°). Clinical trials evaluating mild TH aim for optimum target temperatures between 33°C and 35°C.[11] In both the numeric and in vitro models, however, temperatures were kept constant to 37°C proximal to the inlet of the balloon catheter system, which neglects the in vivo recirculation effect of already cooled blood. The latter may add to a further decrease in blood temperature distal to the balloon catheter system in an in vivo application. The latter effects should be dependent on the duration of cooling. Moreover, at a lowered "blood" flow rate of 250 mL/min reproducing the reduction of CCA blood flow because of distal MCA occlusion, cooling reached −2.17°C, which more closely approached the target of mild TH. This effect of heat exchange improvement may likely be explained by the longer contact time between balloons and blood substitute at lower flow rates.

It can be assumed that the blood temperature distal to the balloon does not necessarily represent the parenchymal brain temperature due to further heat loss through the arterial walls. However, heat transfer with surrounding tissues is limited in larger vessels and occurs predominantly in smaller arteries and capillaries, suggesting that cooling is mostly transferred to the region of perfused brain tissue: first, the ischemic penumbra; then, following successful MT treatment, the ischemic core.

With regard to the cooling catheter design, numeric simulation helped to improve the heat exchange performance by >30% by using the serial balloon array at the catheter tip (4 × 20 mm). The observed disruption of thermal boundary layers and increase of flow convection between the adjacent balloons appear crucial

FIG 6. Photograph of the cooling catheter tip with 4 sequentially arrayed balloons.

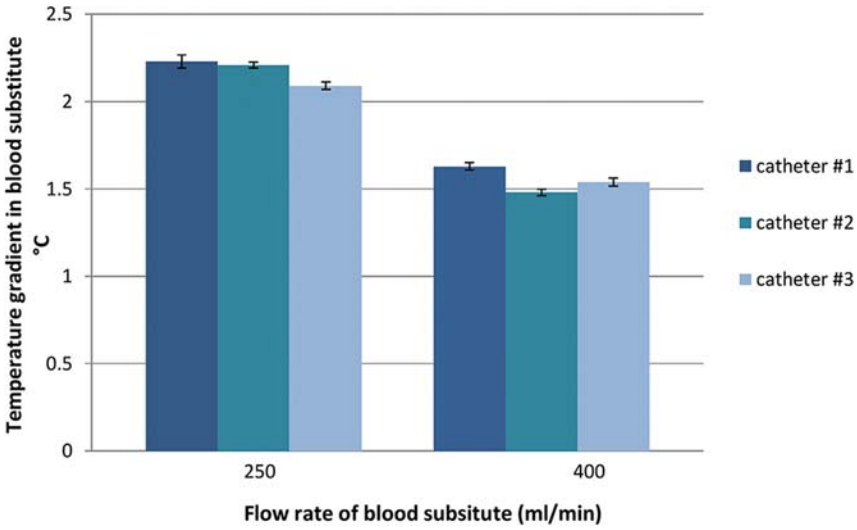

FIG 7. Mean temperature gradients (SD) measured inside the in vitro blood circuit, which are induced by 3 tested cooling catheter prototypes (balloon array; 4 × 20 mm) at 2 predefined flow rates of blood substitute.

for optimization of cooling performance in view of the limited volume within the CCA lumen and in a limited time window.

Our in vitro model has several limitations: Straight plastic tubing has different thermal conductivity than arterial walls, and the artificial blood substitute has different thermal conductivity than blood. Further assumptions were made relative to a constant pulsatile blood flow and straight vessel anatomy with constant diameters, which is not like individual human in vivo variations. Moreover, the following assumptions are limitations to the computational fluid dynamics model: the rigid and adiabatic behavior of vessel walls, an immobile centered balloon catheter tip with a simplified symmetric 2-lumen catheter model, data base–derived values of human rheology, estimated heat loss along whole catheter length, and a simplified steady-state flow model with nonpulsatile flow.

Intracarotid cold saline infusions have been investigated as an alternative approach to selective brain hypothermia for the treatment of acute ischemic stroke. Thus, a rapid induction of moderate brain hypothermia was achieved in theoretic models of selective brain cooling.[19-22] However, the in vivo experiments with infusion of cold isotonic saline (4°C–17°C; 33 mL/min for 10 minutes) into the ICA could only demonstrate a temperature drop of 0.84°C within the jugular venous bulb; these experiments were performed in patients undergoing diagnostic cerebral angiography.[23] Moreover, hemodilution effects and volume overload may be other limiting factors for longer application of this technique in patients with acute stroke.

As the next step, we will perform an in vivo study of intracarotid blood cooling that will aim to evaluate the safety and efficacy of the presented balloon catheter system in a large animal model of temporary MCA ischemia and reperfusion.

CONCLUSIONS

In this in vitro study, the feasibility of intracarotid (CCA) blood cooling was demonstrated by using a new 3-lumen balloon catheter system, which was designed for combined selective TH and MT in acute stroke due to large cerebral artery occlusion. This approach appears particularly promising due to rapid and early induction of cooling before vessel recanalization within a single procedure. An optimized balloon catheter design with a serial array of 4 balloons improved the cooling capacity of the system by >30%, reaching the target of mild TH with a blood temperature decrease of 1.6°C–2.2°C.

Disclosures: Giorgio Cattaneo—*RELATED*: *Grant*: German Federal Ministry of Research and Education*; *UNRELATED*: *Employment*: Acandis GmbH & Co. KG (Pforzheim, Germany); *Grants/Grants Pending*: German Federal Ministry of Research and Education.* Martin Schumacher, Julia Wolfertz, Tobias Jost—*RELATED*: *Grant*: Federal Ministry of Education and Research,* *Comments*: national grant; *Support for Travel to Meetings for the Study or Other Purposes*: Federal Ministry of Education and Research; *Fees for Participation in Review Activities such as Data Monitoring Boards, Statistical Analysis, Endpoint Committees, and the Like*: Federal Ministry of Education and Research*; *UNRELATED*: *Board Membership*: Acandis GmbH & Co. KG. Stephan Meckel—*RELATED*: *Grant*: Federal Ministry of Education and Research, Germany (Federal Ministry of Education and Research grant 13GW0015B)*; *Consulting Fee or Honorarium*: Acandis GmbH & Co. KG, *Comments*: member of Scientific Advisory Board; *Support for Travel to Meetings for the Study or Other Purposes*: Acandis GmbH & Co. KG; *UNRELATED*: *Travel/Accommodations/Meeting Expenses Unrelated to Activities Listed*: Covidien, MicroVention, Stryker. *Money paid to the institution.

REFERENCES

1. Bernard SA, Gray TW, Buist MD, et al. **Treatment of comatose survivors of out-of-hospital cardiac arrest with induced hypothermia.** *N Engl J Med* 2002;346:557–63 CrossRef Medline
2. Hypothermia after Cardiac Arrest Study Group. **Mild therapeutic hypothermia to improve the neurologic outcome after cardiac arrest.** *N Engl J Med* 2002;346:549–56 CrossRef Medline
3. Shankaran S, Laptook AR, Ehrenkranz RA, et al; National Institute of Child Health and Human Development Neonatal Research Network. **Whole-body hypothermia for neonates with hypoxic-ischemic encephalopathy.** *N Engl J Med* 2005;353:1574–84 CrossRef Medline
4. Azzopardi DV, Strohm B, Edwards AD, et al; TOBY Study Group. **Moderate hypothermia to treat perinatal asphyxial encephalopathy.** *N Engl J Med* 2009;361:1349–58 CrossRef Medline
5. Yenari MA, Han HS. **Neuroprotective mechanisms of hypothermia in brain ischaemia.** *Nat Rev Neurosci* 2012;13:267–78 CrossRefMedline
6. Piironen K, Tiainen M, Mustanoja S, et al. **Mild hypothermia after intravenous thrombolysis in patients with acute stroke: a randomized controlled trial.** *Stroke* 2014;45:486–91 CrossRef Medline
7. De Georgia MA, Krieger DW, Abou-Chebl A, et al. **Cooling for Acute Ischemic Brain Damage (COOL AID): a feasibility trial of endovascular cooling.** *Neurology* 2004;63:312–17 CrossRef Medline
8. Hemmen TM, Raman R, Guluma KZ, et al; ICTuS-L Investigators. **Intravenous thrombolysis plus hypothermia for acute treatment of ischemic stroke (ICTuS-L): final results.** *Stroke* 2010;41:2265–70 CrossRef Medline
9. Kammersgaard LP, Rasmussen BH, Jørgensen HS, et al. **Feasibility and safety of inducing modest hypothermia in awake patients with acute stroke through surface cooling: a case-control study—the Copenhagen Stroke Study.** *Stroke* 2000;31:2251–56 CrossRef Medline
10. van der Worp HB, Macleod MR, Kollmar R; European Stroke Research Network for Hypothermia (EuroHYP). **Therapeutic hypothermia for acute ischemic stroke: ready to start large randomized trials?** *J Cereb Blood Flow Metab* 2010;30:1079–93 CrossRef Medline

11. Wu TC, Grotta JC. **Hypothermia for acute ischaemic stroke.** *Lancet Neurol* 2013;12:275–84 CrossRef Medline
12. Berkhemer OA, Fransen PS, Beumer D, et al. **A randomized trial of intraarterial treatment for acute ischemic stroke.** *N Engl J Med* 2015; 372:11–20 CrossRef Medline
13. Campbell BC, Mitchell PJ, Kleinig TJ, et al; EXTEND-IA Investigators. **Endovascular therapy for ischemic stroke with perfusion-imaging selection.** *N Engl J Med* 2015;372:1009–18 CrossRef Medline
14. Goyal M, Demchuk AM, Menon BK, et al; ESCAPE Trial Investigators. **Randomized assessment of rapid endovascular treatment of ischemic stroke.** *N Engl J Med* 2015;372:1019–30 CrossRef Medline
15. Khatri R, McKinney AM, Swenson B, et al. **Blood-brain barrier, reperfusion injury, and hemorrhagic transformation in acute ischemic stroke.** *Neurology* 2012;79:S52-57 CrossRef Medline
16. Pan J, Konstas AA, Bateman B, et al. **Reperfusion injury following cerebral ischemia: pathophysiology, MR imaging, and potential therapies.** *Neuroradiology* 2007;49:93–102 CrossRef Medline
17. Avolio AP. **Multi-branched model of the human arterial system.** *Med Biol Eng Comput* 1980;18:709–18 CrossRef Medline
18. Zhao M, Amin-Hanjani S, Ruland S, et al. **Regional cerebral blood flow using quantitative MR angiography.** *AJNR Am J Neuroradiol* 2007;28:1470–73 CrossRef Medline
19. Konstas AA, Neimark MA, Laine AF, et al. **A theoretical model of selective cooling using intracarotid cold saline infusion in the human brain.** *J Appl Physiol (1985)* 2007;102:1329–40 Medline
20. Neimark MA, Konstas AA, Choi JH, et al. **The role of intracarotid cold saline infusion on a theoretical brain model incorporating the circle of Willis and cerebral venous return.** *Conf Proc IEEE Eng Med Biol Soc* 2007;2007:1140–43 Medline
21. Neimark MA, Konstas AA, Laine AF, et al. **Heat transfer model of hyporthermic intracarotid infusion of cold saline for stroke therapy.** *Conf Proc IEEE Eng Med Biol Soc* 2006;1:363–66 Medline
22. Neimark MA, Konstas AA, Laine AF, et al. **Integration of jugular venous return and circle of Willis in a theoretical human model of selective brain cooling.** *J Appl Physiol (1985)* 2007;103:1837–47 CrossRef Medline
23. Choi JH, Marshall RS, Neimark MA, et al. **Selective brain cooling with endovascular intracarotid infusion of cold saline: a pilot feasibility study.** *AJNR Am J Neuroradiol* 2010;31:928–34 CrossRef Medline

Foreign Body Emboli following Cerebrovascular Interventions: Clinical, Radiographic, and Histopathologic Features

M. Shapiro, M.D. Ollenschleger, C. Baccin, T. Becske, G.R. Spiegel, Y. Wang, X. Song, E. Raz, D. Zumofen, M.B. Potts, and P.K. Nelson

ABSTRACT

SUMMARY: Foreign material emboli following cerebral, cardiac, and peripheral catheterizations have been reported since the mid-1990s. Catheter coatings have been frequently implicated. The most recent surge of interest in this phenomenon within the neurointerventional community is associated with procedures using flow-diversion devices for the treatment of cerebral aneurysms. Following coil-supported Pipeline embolization in 4 cases and stent-supported coiling in 1, 5 patients developed multiple subcentimeter enhancing lesions, usually with surrounding edema and variable magnetic susceptibility in the vascular territories of the treated aneurysms. Conventional angiography findings were unrevealing. Laboratory work-up showed mild CSF protein elevation with no leukocytosis. Brain biopsy in 2 cases revealed granulomatous angiitis encasing foreign material, identical in stain appearance to a polyvinylpyrrolidone catheter coating. Corticosteroid administration typically produced clinical improvement. A heterogeneous radiographic and clinical course was noted, with rise and fall in the number of enhancing lesions in 2 patients and persistence in others. The etiology may be related to widespread adoption of increasingly sophisticated catheterization techniques.

ABBREVIATIONS: PRU = P2Y12 reaction units; PVP = polyvinylpyrrolidone

Foreign material embolization into the cerebral arteries during neurointerventional procedures has emerged as 1 potential cause of periprocedural ischemic stroke and ipsilateral parenchymal hemorrhage. A histopathologic study by Hu et al[1] described 3 patients dying from intracerebral hemorrhage shortly after embolization with the Pipeline Embolization Device (Covidien, Irvine, California). Postmortem examination showed polyvinylpyrrolidone (PVP), a hydrophilic material coating the outer surface of many catheters,[2] within cerebral vessels surrounding parenchymal hematomas. Cruz et al[3] described 7 patients with subacute development of nonlethal enhancing lesions in the territory of prior catheter intervention, with extensive surrounding vasogenic edema and variable susceptibility. No biopsy was reported; the authors concluded that foreign body emboli were likely responsible.

Received December 27, 2014; accepted after revision March 24, 2015.

From the Departments of Radiology (M.S., M.D.O., T.B., E.R., D.Z., M.B.P., P.K.N.), Bernard and Irene Schwartz Neurointerventional Radiology Section, Neurology (M.S., T.B.), and Neurosurgery (D.Z. M.B.P., P.K.N.), New York University Langone Medical Center, New York University School of Medicine, New York, New York; Departments of Radiology (G.R.S.) and Pathology (X.S.), Hartford Hospital, Hartford, Connecticut; Department of Interventional Neuroradiology (C.B.), São Paulo, Brazil; and Department of Rheumatology (Y.W.), Grove Hill Medical Center and The Hospital of Central Connecticut, New Britain, Connecticut.

Please address correspondence to Maksim Shapiro, MD, Departments of Radiology and Neurology, Bernard and Irene Schwartz Neurointerventional Radiology Section, NYU Langone Medical Center, 660 First Ave, 7th floor, New York, NY 10016; e-mail: neuroangio@neuroangio.org

http://dx.doi.org/10.3174/ajnr.A4415

Occurrence of foreign body embolization has been previously described in the neurointerventional literature following thrombolysis, tumor embolization, and coiling.[4-6] Development of subcutaneous foreign body granulomas after coated sheath radial artery access is well-documented in the cardiac literature.[7-9] Foreign body pulmonary emboli producing angiocentric granulomas have also been observed.[10] Another source is a histopathologic review by Mehta et al.[11]

Case Series

Patient 1 (Figs 1 and 2) underwent unremarkable coil-supported Pipeline embolization of an incidental right trigeminal aneurysm using dual-groin access; the Pipeline deployment axis consisted of 5F Shuttle (Cook, Bloomington, Indiana), 058 Navien (Covidien), and Marksman (Covidien) catheters. The patient felt persistently tired during the subsequent 8 weeks, followed by development of left-sided weakness and left homonymous quadrantanopsia. CT showed multifocal right-hemisphere edema. MR imaging demonstrated multiple subcentimeter lesions, predominantly within the subcortical white matter and at the gray-white junctions. Most lesions showed both magnetic susceptibility and enhancement. None had restricted diffusion, and all were surrounded by extensive vasogenic edema. Empiric 6-week antibiotic treatment was undertaken concurrently with a 2-month course of dexamethasone. All neurologic symptoms resolved in 4 weeks. Serial MR imaging showed near-resolution of the edema. All

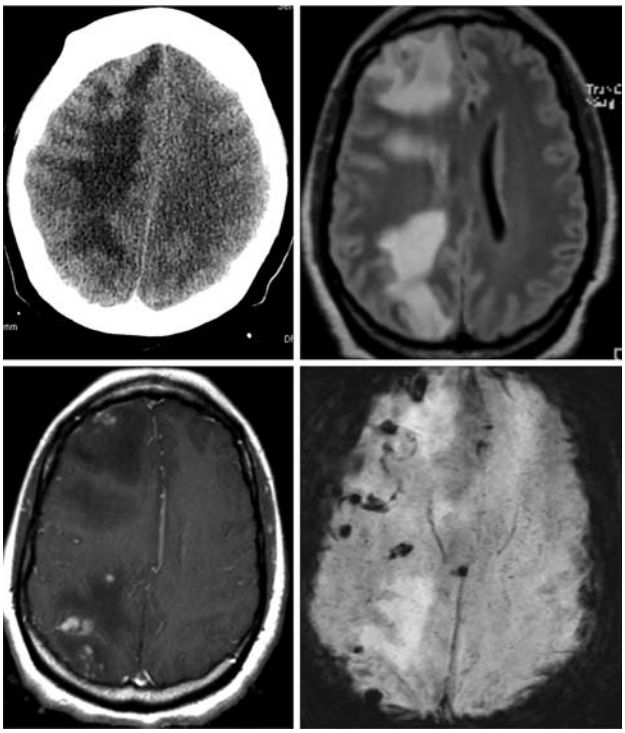

FIG 1. CT and MR images of patient 1.

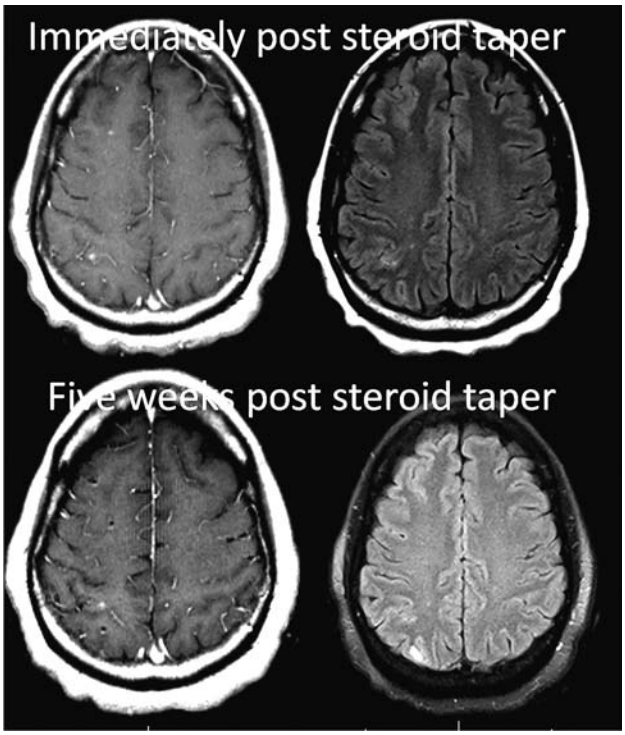

FIG 2. Patient 1, following a 2-month course of oral dexamethasone treatment.

lesions continue to enhance. Currently, the extent of magnetic susceptibility is unchanged, and no new lesions have developed.

Patient 2 (Fig 3) underwent uneventful coil-supported Pipeline embolization of a right paraophthalmic aneurysm,[12] also using dual-groin access, with the Pipeline deployed through a triaxial system of 5F Arrow Sheath (Teleflex, Limerick, Pennsylvania), 5F Navien, and Marksman catheters. This patient also was tired during the next 2 months. On week 8 postembolization, she developed sudden headache and neck pain while watching a foreign movie and noticed difficulty reading the subtitles. Neurologic examination revealed left inferior homonymous quadrantanopsia. CT and MR imaging demonstrated a 2 × 3 cm right parieto-occipital hematoma, with multiple subcortical enhancing lesions scattered throughout the ipsilateral hemisphere. The clopidogrel dosage was titrated to an empiric range of 100–200 P2Y12 reaction units (PRU). After an 8-week course of dexamethasone, MR imaging showed near-complete resolution of perilesional edema and decreased lesion enhancement, with no new lesions.

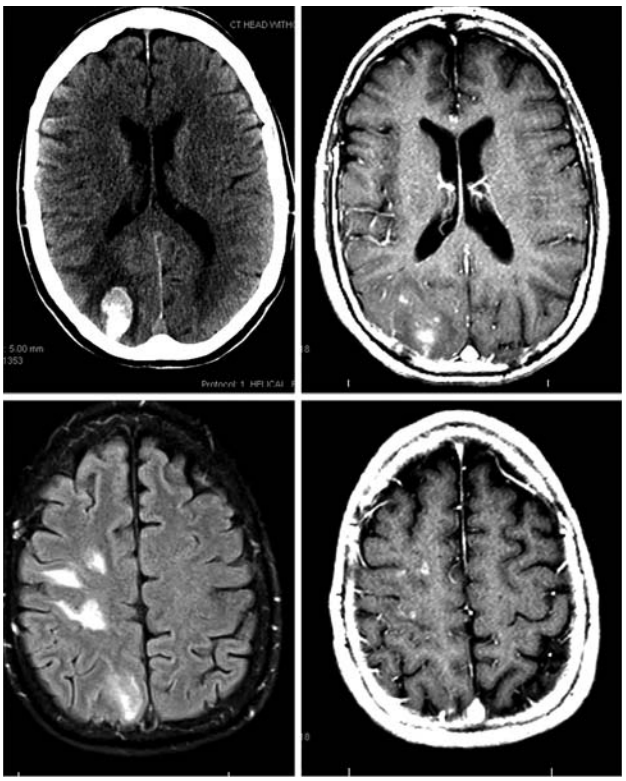

FIG 3. MR images of patient 2 on initial presentation.

Patient 3 (Figs 4 and 5) presented with incidental bilateral paraophthalmic aneurysms, treated 4 weeks apart by coil-supported Pipeline embolization using single-groin access, with sequential deployment of coils and the Pipeline device, the latter through a triaxial system of 6F Shuttle, DAC 057 (Stryker, Kalamazoo, Michigan) and Marksman catheters. Persistent daily headaches developed 2 weeks later; MR imaging performed 2 months postembolization showed bilateral predominantly subcortical enhancing lesions, in this case with little edema and no susceptibility artifacts. Findings of extensive rheumatologic and infectious evaluations were negative. No treatment was undertaken. Two follow-up MRIs during 18 months showed an increase in the number and size of the lesions. A six-week course of corticosteroids had minimal effect on baseline mild edema or daily headaches. Biopsy of the left frontal lobe showed giant cell granulomas and reactive gliosis surrounding foreign body material with staining characteristics identical to those of a PVP coating. A

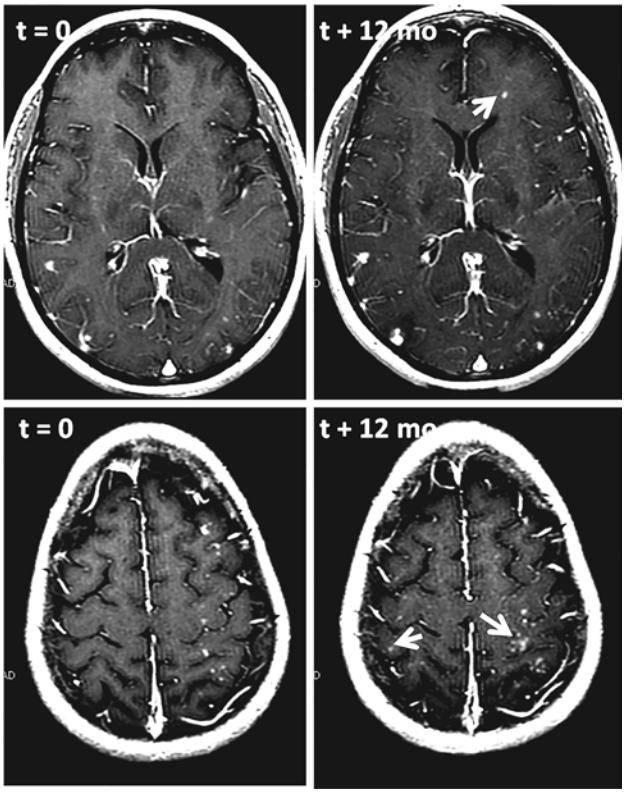

FIG 4. T1 postcontrast images of patient 3, demonstrating an increase in the size and development of new enhancing lesions after 12 months of follow-up. Some new lesions are marked by *arrows*.

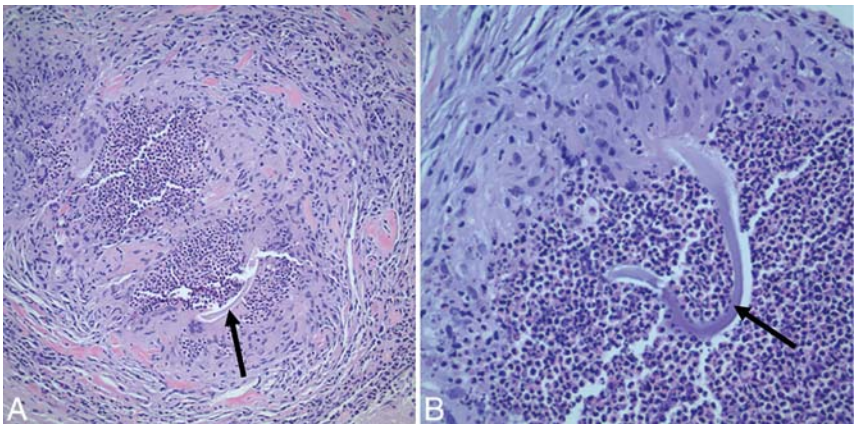

FIG 5. Patient 3. Right frontal lobe biopsy. Hematoxylin-eosin stain at ×200 (*A*) and ×400 (*B*) magnification demonstrates granulomatous angiitis with central blue-gray nonpolarizable foreign material, some with "cotton thread-like" appearance (*arrows*).

more delayed MR imaging 3 months post-steroid taper showed a decrease in the number and size of enhancing nodules. Surveillance is ongoing.

Patient 4 underwent Pipeline-supported coiling of an incidentally discovered right paraophthalmic aneurysm using single-groin access, with Pipeline deployment through 6F Shuttle, 058 Navien, and Marksman catheters. She developed transient mild left hemiparesis 1 day postprocedure. MR imaging showed several diffusion-positive lesions. A catheter angiogram at this time showed complete patency of the Pipeline; however, at 6 months, the internal carotid artery was closed with asymptomatic complete hemisphere reconstitution via the anterior communicating artery. She developed periodic involuntary movements of the left upper extremity and left eyelid 3 months postembolization, increasing in duration and frequency; mild hemiparesis followed. CT and MR imaging showed right-hemisphere edema, with multiple subcortical enhancing lesions, many demonstrating susceptibility. Electroencephalography demonstrated focal slowing in the right parietal region with no epileptiform discharges. Right frontal biopsy showed granulomatous angiitis surrounding amorphous foreign material, identical in staining characteristics to the coating of the Shuttle guide catheter (Fig 6). Abnormal movements resolved after treatment with antiepileptics and dexamethasone. Follow-up MR imaging showed near-complete disappearance of enhancing nodules, with areas of persistent white matter T2 hyperintensity. Several weeks after completion of the taper, symptoms recurred and steroid treatment was reinstated; the patient is being considered for alternative immunomodulating regimens due to steroid-related side effects.

Patient 5 underwent Y-stent-assisted coiling of a left middle cerebral artery aneurysm with single-groin access consisting of 6F Shuttle, Navien 070, Excelsior XT-27 (Stryker), and Echelon-10 (Covidien) catheters. Embolization was notable for intraprocedural occlusion of 2 superior division frontal branches, with no immediate clinical sequelae. Transient episodes of right upper extremity paresthesia and spasm developed 2 weeks postembolization. Conventional angiography demonstrated recanalization of the aforementioned frontal branches. MR imaging and MR spectroscopy showed multiple enhancing lesions throughout the left MCA territory, the largest involving areas subserved by initially occluded branches. A course of oral corticosteroids was administered. MR imaging 3 months after the event showed decreased perilesional edema and reduced enhancement.

DISCUSSION

This article reports 2 biopsy-proved and 3 suspected cases of foreign body emboli after endovascular interventions. An incidence of ~0.6% is estimated on the basis of the total number of aneurysm embolizations (~720) performed at our 6 institutions during the 2-year period, during which 5 cases came to attention. Because asymptomatic patients are not routinely subjected to cross-sectional imaging, additional clinically silent cases may exist. The embolic material appears to be a PVP catheter coating. Presumably the same substance was found on postmortem examination of patients dying after Pipeline embolization from ipsilateral parenchymal hemorrhage, as reported by Hu et al.[1] Thus, both clinical and histopathologic evidence suggest that PVP embolization may have a spectrum of presentations, with the conditions of survivors of the initial event evolving into a subacute granulomatous angiitis. Although most patients present with symptoms related to perilesional edema, the frequently observed intralesional susceptibility signal and subacute development of nonlethal hematoma

in patient 2 attest to a continued hemorrhagic potential beyond the periprocedural window. In our case, the catheter coating was identified by histopathologic staining techniques, whereas Hu et al[1] used mass spectroscopy for what is likely a more definitive analysis. PVP-coated catheters were used in all 5 cases; however, coating methods, including other substances in the coating, may vary among manufacturers.

Foreign body granulomatous reaction seen in our cohort adds to previously documented instances in the neurointerventional, cardiology, and peripheral interventional literature.[8,10,11] Both clinical and radiographic courses were similar to those in the case series of Cruz et al.[3] Our management relies on corticosteroid modulation of the inflammatory response and empiric titration of antiplatelets to balance the risks of hemorrhagic conversion and thromboembolism. Most patients report headache and/or malaise throughout the postoperative period. Focal symptoms typically appear after ~2 months, often reflecting the consequences of corticosteroid-responsive vasogenic edema. A radiographically heterogeneous course is notable—for example, the initial rise in the number and size of lesions followed by a decline in patients 3 and 4 versus a more static picture in patient 1. Contributing factors may include the nature, extent, and effectiveness of individual immune reactions; phases of response to possible PVP breakdown products; and the role of corticosteroids.

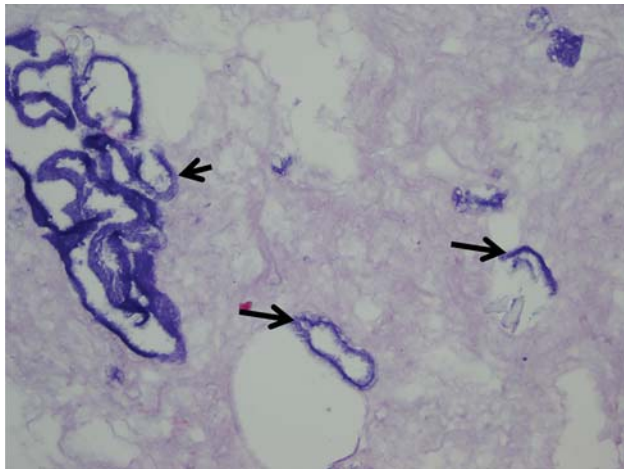

FIG 6. Hematoxylin-eosin stain of the outer coating (*arrows*) from the Flexor Shuttle guide catheter (Cook Medical, Bloomington, Indiana).

Case 3 is unique in demonstrating bilateral lesions following 2 separate procedures performed 4 weeks apart. Coincidental bilateral embolization is possible. However, a cell-mediated allergic-type reaction may be an intriguing alternative explanation, whereby only a subset of patients experiencing PVP embolization develop clinicopathologic manifestations based on individual reactions to the emboli. Allergies to food/medication/contrast material were reported in 4 of 5 patients (Table 1). The prevalence of allergy to any food in the US population is 10%–15%,[13,14] while medication allergies and adverse reactions are at 5%–15%.[15] Thus, a 30% estimate of combined food and medication allergy in the US population is substantially lower than the 80% seen in our cohort.

Allergic reactions to PVP have been reported.[16-18] Aside from its use in catheter technology, PVP has many applications—for example, as a thickening and emulsifying agent in toothpastes, shampoos, contact lens solutions, and gel and tablet formulations. In combination with iodine, it forms the polyvinylpyrrolidone-iodine solution better known as Betadine (Betadine Microbicides, Stamford, Connecticut). Two instances of anaphylaxis to Betadine were traced to its PVP, rather than iodine, component.[17,18] An anaphylactic reaction to an acetaminophen tablet was traced to its PVP ingredient.[16] However, our cases would be more consistent with a type IV, cell-mediated response, rather than a type I, an anaphylactic one. Materials other than PVP are also present in the hydrophilic coating. Further investigation may be warranted.

From a technical standpoint, all our procedures were associated with the use of potentially tight-fitting catheter combinations

Table 1: Case details

Parameter	Case 1	Case 2	Case 3	Case 4	Case 5
Allergy	Iodinated contrast	Peanuts; sesame oil	Carisoprodol; NSAIDs	No known allergies	Iodinated contrast
Length of clinical follow-up to date (mo)	15	13	33	4.5	3.5
ESR (mm/h)	56	12	8	11	46, then 21
CRP (mg/dL)	<5	<7	<0.2	0.25	1.3 then 3.7
Periprocedural antiplatelet monitoring	PRU = 97	PRU = 96	PRU = 38	PRU = 120	ADP = 35%
Antiplatelet monitoring at readmission	PRU = 101	PRU = 2	Not done	PRU = 215	Not done
WBC (K/μL)	7	11.4	8.8	11.6	9.7
Platelets (K/μL)	297	345	254	184	314
Blood culture	Negative	Negative	Negative	Negative	Not done
CSF appearance	Clear, colorless	Clear, colorless	Clear, colorless	Clear, pale yellow	Clear, colorless
CSF opening pressure (cm H_2O)	17	15	NA	NA	20
CSF RBC (No./HPF)	0	6	0	273	3
CSF WBC (No./HPF)	4	1	1	2	25
CSF % lymphocytes	90%	NA	62%	80%	78%
CSF protein (mg/dL)	96	71	35	92	66
CSF Gram stain	Negative	Negative	Negative	Negative	Negative
CSF culture	Negative	Negative	Negative	Negative	Negative

Note:—ESR indicates erythrocyte sedimentation rate; CRP, C-reactive protein; WBC, white blood cell count; RBC, red blood cell count; HPF, high-power field.; NSAID, nonsteroidal anti-inflammatory drug; ADP, adenosine diphosphate; NA, not applicable.

Table 2: Equipment

Tools	Case 1	Case 2	Case 3	Case 4	Case 5
Diagnostic catheter	5F VER[a]	5F VER[a]	4F Glidecath[b]	4F Glidecath[b]	5F VER[a]
Diagnostic wire	038[b]	038[b]	038[b]	038[b]	J&J 035[c]
Exchange wire	Wholey Exchange[d]	Wholey Exchange[d]	Amplatz SuperStiff[e]	Amplatz SuperStiff[e]	Amplatz SuperStiff[e]
Sheath	Shuttle 5F	Arrow 5F	Shuttle 6F × 2	Shuttle 6F	Shuttle 6F
Second catheter	Envoy 5F[f]	Envoy 5F[f]	None	None	None
Distal support catheter	Navien 058	Navien 058	Neuron-053,[g] DAC-057	Navien 058	Neuron 070[g]
Microcatheter	Marksman-150	Marksman-150	Marksman-150 × 2	Marksman-150	Excelsior XT-27
Microcatheter, other	Echelon-10	Excelsior SL-10[j]	Echelon 10, PX-400,[h] Prowler Select Plus[f]	PX-Slim[g]	Echelon-10
Microwire	Transend 014[j] Platinum[i]	Transend 014[j] Platinum[i]	Fathom-16,[e] X-Celerator-14[d]	Synchro2 Std,[e] X-Celerator-14[d]	SilverSpeed-14[d]
Devices	Pipeline 4.5 × 14	Pipeline 3.75 × 12	Pipeline 3.5 × 20, 3.5 × 18, 4.0 × 20	Pipeline 4.0 × 18	Neuroform EZ,[j] LEO Baby[k]
Coils	Target[j]	Target[j]	Cosmos,[l] Penumbra 400[g]	Penumbra 400[g]	Axium[d]
Other			Alligator,[m] Amplatz goose neck snare[d]	ScepterC 4 × 15 mm[l]	

[a] Cordis, Miami Lakes, Florida.
[b] Terumo, Tokyo, Japan.
[c] Cordis, Fremont, California.
[d] Covidien.
[e] Boston Scientific, Natick, Massachusetts.
[f] Codman & Shurtleff, Raynham, Massachusetts.
[g] Penumbra, Alameda, California.
[h] biyodenge, Ankara, Turkey.
[i] Eagle Eye Platinum; Volcano Corporation, Rancho Cordova, California.
[j] Stryker Neurovascular, Kalamazoo, Michigan.
[k] Balt Extrusion, Montmorency, France.
[l] MicroVention, Tustin, California.
[m] Chestnut Medical Technologies, Menlo Park, California.

(Table 2). PVP embolization could be related to intercatheter friction, made increasingly common by the adoption of triaxial configurations for deployment of present day devices. We modified our protocols to avoid marginally accommodated access components and favor 2-groin access for coil-supported Pipeline embolization. No new case has yet emerged after these changes. Our series does not suggest that the Pipeline device is the source of emboli, nor is the Shuttle guide catheter the sole culprit as highlighted by case 2, in which an Arrow guide catheter was used. In another instance, we have aspirated coating from a 4.3 DAC catheter used in combination with a Marksman microcatheter, another very tight coupling we have abandoned. Notably, this patient did not develop evidence of foreign body emboli, lending further support to the allergic mechanism hypothesis.

Although the numeric incidence of symptomatic catheter-coating embolization appears to be low, it is disturbing to see that having been identified as a concern in the cerebrovascular and other fields >15 years ago, the issue seems to be on the rise rather than declining, creating lethal and long-term nonlethal damage. We hope that highlighting such cases will result in prompt attention from catheter and coating manufacturers so that this chapter in the book of neurointerventional complications may finally be completed.

CONCLUSIONS

Catheter-coating embolization is well-documented in peripheral, cardiology, and neurointerventional literature. While some patients with CNS emboli develop catastrophic hemorrhage shortly after the procedure,[1] this and other series[3] confirm that foreign body emboli elicit a spectrum of manifestations. Survivors of the initial insult may develop a granulomatous angiitis characterized by enhancement, perilesional edema, and local microhemorrhage. The PVP coating appears to be responsible for the current generation of cases. We propose the possibility of an allergic-type response, with emboli possibly remaining asymptomatic in some or most cases or reactions developing after the breakdown of PVP into more biologically active components. From the technical standpoint, embolization may be related to the use of sophisticated catheter-support systems, increasing the possibility of intercatheter friction. Symptoms may be successfully managed with corticosteroids and antiplatelet monitoring. One should consider the following recommendations:

- Avoid tight-fitting catheter-intermediate catheter-microcatheter combinations; consider 2-groin access for multicatheter scenarios, especially those involving larger sized microcatheters required for the delivery of many currently implanted devices.
- Focal symptoms emerging several months after embolization in a background of nonspecific symptoms, such as headache and malaise, are typical, especially in patients with food or drug allergies.
- An MR imaging pattern of multiple enhancing lesions with surrounding edema and susceptibility, in the vascular territory of an index lesion, is highly characteristic.
- A corticosteroid regimen of 4- to 8-week duration is typically effective in controlling perilesional edema, which is often responsible for focal symptoms. A decrease in the size and/or number of enhancing lesions may not be evident for several weeks after completion of the taper. This should be taken into account when assessing the effectiveness and contemplating alternative regimens.

• Adjustment of the antiplatelet regimen to avoid overinhibition may be beneficial.

Disclosures: Maksim Shapiro—*UNRELATED*: *Consultancy*: Covidien, *Comments*: I am a proctor and consultant with Covidien, manufacturer of the Pipeline device; *Grants/Grants Pending*: I have a grant, for Pipeline devices only, from Covidien, manufacturer of the Pipeline device. The purpose of the grant is to study the properties of the Pipeline device; *Payment for Development of Educational Presentations*: I am a proctor and consultant with Covidien, manufacturer of the Pipeline device. Tibor Becske—*UNRELATED*: *Consultancy*: Covidien, *Comments*: proctoring and consulting; *Payment for Lectures (including service on Speakers Bureaus)*: Covidien; *Payment for Development of Educational Presentations*: none in the past 36 months. Daniel Zumofen—*UNRELATED*: *Grants/Grants Pending*: Helmut Hartweg Fund, Swiss Academy of Medical Science, *Comments*: personal scholarship not related to the submitted publication. Peter K. Nelson—*UNRELATED*: *Consultancy*: Covidien, *Comments*: consultant and Pipeline proctor.

REFERENCES

1. Hu YC, Deshmukh VR, Albuquerque FC, et al. **Histopathological assessment of fatal ipsilateral intraparenchymal hemorrhages after the treatment of supraclinoid aneurysms with the Pipeline Embolization Device.** *J Neurosurg* 2014;120:365–74 CrossRef Medline
2. Francois P, Vaudaux P, Nurdin N, et al. **Physical and biological effects of a surface coating procedure on polyurethane catheters.** *Biomaterials* 1996;17:667–78 CrossRef Medline
3. Cruz JP, Marotta T, O'Kelly C, et al. **Enhancing brain lesions after endovascular treatment of aneurysms.** *AJNR Am J Neuroradiol* 2014;35:1954–58 CrossRef Medline
4. Barnwell SL, D'Agostino AN, Shapiro SL, et al. **Foreign bodies in small arteries after use of an infusion microcatheter.** *AJNR Am J Neuroradiol* 1997;18:1886–89 Medline
5. Fealey ME, Edwards WD, Giannini C, et al. **Complications of endovascular polymers associated with vascular introducer sheaths and metallic coils in 3 patients, with literature review.** *Am J Surg Pathol* 2008;32:1310–16 CrossRef Medline
6. Mehta RI, Mehta RI, Fishbein MC, et al. **Intravascular polymer material after coil embolization of a giant cerebral aneurysm.** *Hum Pathol* 2009;40:1803–07 CrossRef Medline
7. Kozak M, Adams DR, Ioffreda MD, et al. **Sterile inflammation associated with transradial catheterization and hydrophilic sheaths.** *Catheter Cardiovasc Interv* 2003;59:207–13 CrossRef Medline
8. Sado D, Witherow F. **Sterile granuloma formation following radial artery facilitated coronary catheterization.** *Catheter Cardiovasc Interv* 2009;74:606 CrossRef Medline
9. Saririan M, Pyne CT. **Sterile granuloma formation following radial artery catheterization: too many cooks?** *Catheter Cardiovasc Interv* 2010;76:907–08; author reply 909–10 CrossRef Medline
10. Allan RW, Alnuaimat H, Edwards WD, et al. **Embolization of hydrophilic catheter coating to the lungs: report of a case mimicking granulomatous vasculitis.** *Am J Clin Pathol* 2009;132:794–97 CrossRef Medline
11. Mehta RI, Mehta RI, Solis OE, et al. **Hydrophilic polymer emboli: an under-recognized iatrogenic cause of ischemia and infarct.** *Mod Pathol* 2010;23:921–30 CrossRef Medline
12. Shapiro M, Becske T, Riina HA, et al. **Toward an endovascular internal carotid artery classification system.** *AJNR Am J Neuroradiol* 2014;35:230–36 CrossRef Medline
13. McGowan EC, Keet CA. **Prevalence of self-reported food allergy in the National Health and Nutrition Examination Survey (NHANES) 2007–2010.** *J Allergy Clin Immunol* 2013;132:1216–19.e5 CrossRef Medline
14. Vierk KA, Koehler KM, Fein SB, et al. **Prevalence of self-reported food allergy in American adults and use of food labels.** *J Allergy Clin Immunol* 2007;119:1504–10 CrossRef Medline
15. Thong BY, Tan TC. **Epidemiology and risk factors for drug allergy.** *Br J Clin Pharmacol* 2011;71:684–700 CrossRef Medline
16. Rönnau AC, Wulferink M, Gleichmann E, et al. **Anaphylaxis to polyvinylpyrrolidone in an analgesic preparation.** *Br J Dermatol* 2000; 143:1055–58 CrossRef Medline
17. Yoshida K, Sakurai Y, Kawahara S, et al. **Anaphylaxis to polyvinylpyrrolidone in povidone-iodine for impetigo contagiosum in a boy with atopic dermatitis.** *Int Arch Allergy Immunol* 2008;146: 169–73 CrossRef Medline
18. Adachi A, Fukunaga A, Hayashi K, et al. **Anaphylaxis to polyvinylpyrrolidone after vaginal application of povidone-iodine.** *Contact Dermatitis* 2003;48:133–36 CrossRef Medline

Intraplaque Hemorrhage and the Plaque Surface in Carotid Atherosclerosis: The Plaque At RISK Study (PARISK)

A.C. van Dijk, M.T.B. Truijman, B. Hussain, T. Zadi, G. Saiedie, A.A.J. de Rotte, M.I. Liem, A.F.W. van der Steen, M.J.A.P. Daemen, P.J. Koudstaal, P.J. Nederkoorn, J. Hendrikse, M.E. Kooi, and A. van der Lugt

ABSTRACT

BACKGROUND AND PURPOSE: An important characteristic of vulnerable plaque, intraplaque hemorrhage, may predict plaque rupture. Plaque rupture can be visible on noninvasive imaging as a disruption of the plaque surface. We investigated the association between intraplaque hemorrhage and disruption of the plaque surface.

MATERIALS AND METHODS: We selected the first 100 patients of the Plaque At RISK study, an ongoing prospective noninvasive plaque imaging study in patients with mild-to-moderate atherosclerotic lesions in the carotid artery. In carotid artery plaques, disruption of the plaque surface (defined as ulcerated plaques and/or fissured fibrous cap) and intraplaque hemorrhage were assessed by using MDCTA and 3T MR imaging, respectively. We used a χ^2 test and multivariable logistic regression to assess the association between intraplaque hemorrhage and disrupted plaque surface.

RESULTS: One hundred forty-nine carotid arteries in 78 patients could be used for the current analyses. Intraplaque hemorrhage and plaque ulcerations were more prevalent in symptomatic compared with contralateral vessels (hemorrhage, 38% versus 11%; $P < .001$; and ulcerations, 27% versus 7%; $P = .001$). Fissured fibrous cap was more prevalent in symptomatic compared with contralateral vessels (13% versus 4%; $P = .06$). After adjustment for age, sex, diabetes mellitus, and degree of stenosis, intraplaque hemorrhage was associated with disrupted plaque surface (OR, 3.13; 95% CI, 1.25–7.84) in all vessels.

CONCLUSIONS: Intraplaque hemorrhage is associated with disruption of the plaque surface in patients with a carotid artery stenosis of <70%. Serial studies are needed to investigate whether intraplaque hemorrhage indeed increases the risk of plaque rupture and subsequent ischemic stroke during follow-up.

ABBREVIATIONS: ECST = European Carotid Surgery Trial; PARISK = Plaque At RISK

The need to identify patients with mild-to-moderate carotid artery stenosis and an increased stroke risk who might benefit from surgical treatment has shifted research interest from assessment of the degree of carotid stenosis to assessment of vulnerable plaque characteristics.[1] Vulnerable plaques are atherosclerotic plaques more prone to rupture and are associated with a higher risk for thromboembolism and ischemic stroke.[2,3] Intraplaque hemorrhage is an important characteristic of the vulnerable plaque.[4] Prevalence of intraplaque hemorrhage has been shown to be higher in symptomatic than in asymptomatic lesions.[5] Moreover, the presence of intraplaque hemorrhage in carotid artery disease is associated with an increased risk of cerebral ischemic events.[6-8]

The pathophysiologic mechanism leading to intraplaque hemorrhage is a topic of debate. However, a common viewpoint is that small leaky neovessels in the atherosclerotic plaques are a likely

Received December 23, 2014; accepted after revision March 14, 2015.

From the Departments of Radiology (A.C.v.D., B.H., T.Z.,G.S., A.v.d.L.), Neurology (A.C.v.D., P.J.K.), and Biomedical Engineering (A.F.W.v.d.S.), Erasmus Medical Center, Rotterdam, the Netherlands; Departments of Radiology (M.T.B.T., M.E.K.) and Clinical Neurophysiology (M.T.B.T.) and Cardiovascular Research Institute Maastricht School for Cardiovascular Diseases (M.T.B.T., M.E.K.), Maastricht University Medical Center, Maastricht, the Netherlands; Department of Radiology (A.A.J.d.R., J.H.), University Medical Center Utrecht, Utrecht, the Netherlands; and Departments of Neurology (M.I.L., P.J.N.) and Pathology (M.J.A.P.D.), Amsterdam Medical Center, Amsterdam, the Netherlands.

This work was performed within the framework of the Center for Translational Molecular Medicine (www.ctmm.nl), project PARISK (grant 01C-202), and was supported by the Dutch Heart Foundation.

Paper previously presented in part at: Annual Meetings of the European Congress of Radiology, May 28–31, 2013, Vienna, Austria; the European Stroke Conference, May 28–31, 2013, London, UK; and the European Society for Magnetic Resonance in Medicine and Biology, October 3–5, 2013, Toulouse, France.

Please address correspondence to Aad van der Lugt, MD, PhD, Erasmus MC–University Medical Center Rotterdam, Department of Radiology, 's Gravendijkwal 230, 3015 CE Rotterdam, the Netherlands; e-mail: a.vanderlugt@erasmusmc.nl

Indicates article with supplemental on-line tables.

http://dx.doi.org/10.3174/ajnr.A4414

source of intraplaque hemorrhage.[5,9,10] The presence of intraplaque hemorrhage is thought to initiate several biologic processes like phagocytosis and local inflammation, leading to the release of proteolytic enzymes, deposition of free cholesterol and subsequently plaque growth, plaque destabilization, and possible plaque rupture.[5,9-12] Plaque rupture can be visible on imaging as a disruption of the atherosclerotic plaque surface (plaque ulceration and/or a fissured fibrous cap).[13,14] A previous study reported that plaque ulceration on CTA was useful for the prediction of intraplaque hemorrhage on MR imaging in a broad group of symptomatic patients referred for carotid artery imaging.[15] Ulcerated plaques themselves are independently associated with an increased risk of ipsilateral ischemic events as well.[16,17]

The aim of the current study was to investigate the association between intraplaque hemorrhage, as assessed on MR imaging, and disruption of the plaque surface, assessed on MDCTA, in symptomatic patients with a carotid artery stenosis of <70%.

MATERIALS AND METHODS

Study Population

Patients were derived from the Plaque At RISK (PARISK) study (clinical trials.gov, NCT01208025). Details of the PARISK study are previously described.[18] The PARISK study is an ongoing prospective multicenter cohort study focusing on the identification of patients with mild-to-moderate carotid artery stenosis with an increased risk of recurrent stroke by using noninvasive plaque imaging. Eligible for inclusion are patients with a TIA, including amaurosis fugax, or minor stroke in the carotid artery territory and a mild-to-moderate stenosis (30%–69%) of the ipsilateral internal carotid artery. "TIA" was defined as an episode of temporary and focal cerebral dysfunction of vascular origin, lasting for a maximum 24 hours, leaving no persistent neurologic deficits. "Minor stroke" was defined as an episode of temporary and focal cerebral dysfunction of vascular origin, lasting for >24 hours or a nondisabling stroke with a modified Rankin Scale score of ≤3. "Amaurosis fugax" was defined as a sudden loss of vision of presumed vascular origin and confined to 1 eye. The degree of stenosis was determined with clinically obtained Doppler sonography or MDCTA. The upper cutoff value of 70% was based on the NASCET criteria. The lower cutoff value was an atherosclerotic plaque with a thickness of at least 2–3 mm, which corresponds to a European Carotid Surgery Trial (ECST) stenosis of 30%.[19] Exclusion criteria were a probable cardiac source of embolism, a clotting disorder, severe comorbidity, standard contraindications for MR imaging, a documented allergy to MR imaging or CT contrast agents, or a renal clearance of <30 mL/min. Institutional review board approval was obtained in all university hospitals, and all patients gave written informed consent. For the current analyses, we selected the first 100 included patients.

Cardiovascular Risk Factors

"Hypercholesterolemia" was defined as fasting total cholesterol of >5 mmol/L or the use of cholesterol-lowering medication at the time of the TIA or ischemic stroke. We defined "hypertension" as systolic blood pressure of >140 mm Hg or a diastolic blood pressure of >90 mm Hg during 2 episodes of at least 15 minutes of continuous noninvasive blood pressure measurement or treatment with antihypertensive medication. "Diabetes mellitus" was defined as a fasting serum glucose level of >6.9 mmol/L, 2-hour postload glucose level of >11.0 mmol/L, or the use of antidiabetic medication. We assessed smoking status at the time of the TIA or ischemic stroke and dichotomized it into current smoker or no current smoker. In addition, we recorded body mass index, the use of cardiovascular medications, and medical history.

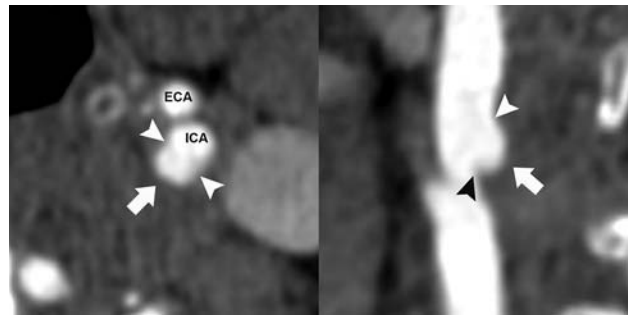

FIG 1. Plaque ulceration on MDCTA. Transversal (*left*) and longitudinal (*right*) MDCTA images of the carotid bifurcation. A "plaque ulceration," defined as the extension of contrast material in the atherosclerotic plaque, is visible on both planes (*arrows*; *arrowheads* indicate the edges of the plaque ulceration). ECA indicates external carotid artery.

MDCTA Data Acquisition and Analysis

We performed image acquisition by using a standardized protocol, as discussed in the study design article.[18] All MDCTA studies were evaluated by trained readers blinded to clinical data and other imaging tests. The MDCTA images were transferred to a workstation equipped with dedicated 3D analysis software (Leonardo and syngo.via; Siemens, Erlangen, Germany). The multiplanar reformatting application allowed analysis of both carotid arteries in oblique, coronal, and sagittal planes. Image quality was rated on a 3-point scale: 1) poor, defined as low contrast and major artifacts and not eligible for analysis; 2) moderate, defined as moderate artifacts and eligible for analysis; and 3) good, defined as few or no artifacts and eligible for analysis.

First, we evaluated the presence of an atherosclerotic plaque in both carotid arteries, defined as the presence of calcifications and/or thickening of the vessel wall (≥~1 mm). If present, disruption of the plaque surface was assessed in both arteries at the same time. "Disruption of the plaque surface," defined as the presence of plaque ulceration and/or a fissured fibrous cap, was assessed by 2 independent observers (B.H., 12 months, and A.C.v.D., 4 years of experience); discrepancies were solved by consensus and/or an experienced third observer (A.v.d.L, 10 years of experience). We defined "plaque ulceration" as an extension of contrast material of >1 mm into the atherosclerotic plaque on at least 2 orthogonal planes (Fig 1).[13,20] We defined "fissured fibrous cap" according to the criteria of Saba and Mallarini,[21] extension of contrast material of <1 mm into the atherosclerotic plaque and an angle of ≥230° with the lumen (Fig 2).

Interobserver variability for the initial review was moderate ($\kappa = 0.41$) for the detection of disruption of the plaque surface (plaque ulceration and/or fissured fibrous cap), moderate ($\kappa = 0.46$) for the detection of plaque ulceration, and fair ($\kappa = 0.24$) for the detection of fissured fibrous cap. Moreover, the most severe

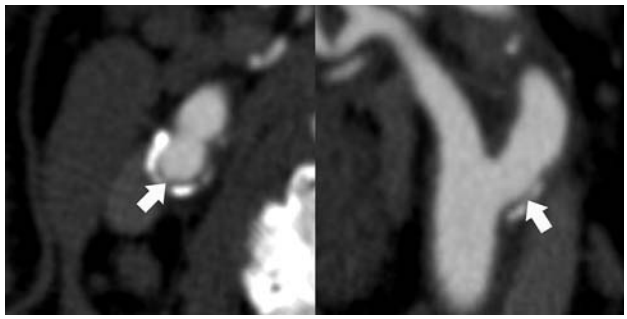

FIG 2. Fissured fibrous cap on MDCTA. Transversal (*left*) and longitudinal (*right*) MDCTA images of the carotid bifurcation. A "fissured fibrous cap," defined as an extension of contrast material of <1 mm into the atherosclerotic plaque and an angle of ≥230° with the lumen, is visible only on the transversal plane (*arrows*).

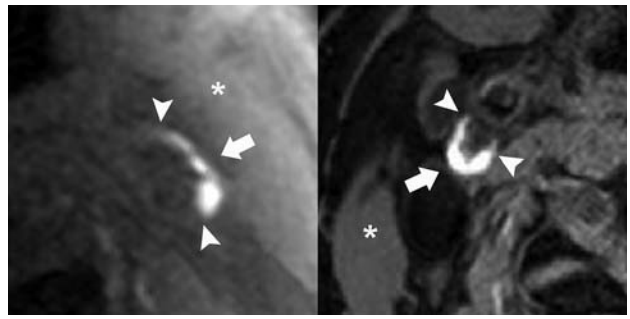

FIG 3. Intraplaque hemorrhage on MR imaging. Carotid bifurcations of 2 patients: *left*, the 3D-T1W fat suppressed spoiled gradient echo sequence (Discovery MR 750; GE Healthcare), and *right,* the 2D-T1W inversion recovery turbo field echo sequence (Achieva; Philips Healthcare). In both patients, intraplaque hemorrhage is present (*arrows*; *arrowheads* indicate the edges of the intraplaque hemorrhage), defined as a hyperintense signal in the atherosclerotic plaque compared with the sternocleidomastoid muscle (*asterisk*).

stenosis in the carotid bifurcations and internal carotid arteries was measured according to the ECST and NASCET criteria, perpendicular to the central lumen line.[19,22] A custom-made plug-in for the freely available ImageJ software (National Institutes of Health, Bethesda, Maryland) was used to quantify calcifications in both carotid arteries within 3 cm proximal and distal to the bifurcation. We used a threshold of 600 HU to differentiate calcifications from contrast material in the lumen; calcification volume was expressed in cubic millimeters. A detailed description of the measurements is provided elsewhere.[23]

MR Imaging Data Acquisition and Analysis

Image acquisition was performed on a 3T MR imaging system (Achieva; Philips Healthcare, Best, the Netherlands; or Discovery MR 750; GE Healthcare, Milwaukee, Wisconsin). A multisequence contrast-enhanced protocol was used; a detailed description of this protocol is provided in the study design article.[18] For this study, we used the 3D-T1W fat suppressed spoiled gradient echo sequence (GE Healthcare) or the 2D-T1W inversion recovery turbo field echo sequence (Philips Healthcare). A 3D volume of the extracranial carotid artery (GE Healthcare) or 15 transverse adjoining sections of 2 mm each covering the entire plaque (Philips Healthcare) were imaged.

All MR imaging studies were evaluated by a trained reader (M.T.B.T., 4 years of experience) blinded to clinical data and other imaging tests. MR images were reviewed by using a standard DICOM viewer. Image quality was rated on a 5-point scale: 1) low SNR, limits use, arterial wall and vessel margins unidentifiable; 2) marginal SNR, arterial wall visible, with the substructure, lumen, and outer boundaries indistinct; 3) marginal SNR, wall structures identifiable with the lumen and outer boundaries partially obscured; 4) high SNR with minimal artifacts; vessel wall, lumen, and adventitial margins well-defined; and 5) high SNR without artifacts, wall architecture depicted in detail, lumen and adventitial boundary clearly defined.[24] Intraplaque hemorrhage was scored in both arteries at the same time and was defined as a hyperintense signal in the plaque compared with the adjacent sternocleidomastoid muscle (Fig 3).[24] In 47 vessels, the presence of intraplaque hemorrhage was assessed by a second independent observer (A.C.v.D, 4 years of experience; the minimum interval between MDCTA and MR imaging scores was 8 months) to assess interobserver variability, and an excellent agreement was found ($\kappa = 0.95$; 95% CI, 0.86–1.00).

Statistical Analysis

Baseline characteristics are shown for all patients; vessel characteristics are shown for all vessels and for symptomatic and contralateral vessels separately. Data are presented as mean ± SD, median (25th–75th percentile), or number of patients (percentage). Differences between symptomatic and contralateral vessels were evaluated by using a χ^2 test for categoric data and a Student *t* test or Mann-Whitney *U* test for continuous data. For the analysis of calcification volume, we used natural log-transformed values and added 1.0 mm^3 to the nontransformed values to deal with participants with a calcification volume of zero. First, we used a χ^2 test to assess the association between intraplaque hemorrhage and disrupted plaque surface (ulcerated plaques and/or a fissured fibrous cap) in all vessels. We used all vessels because we assumed that the underlying pathophysiologic mechanism would be similar in symptomatic and contralateral vessels. Additionally, a logistic regression was used to further investigate the association between intraplaque hemorrhage, other plaque characteristics, and cardiovascular risk factors on the one hand and disrupted plaque surface on the other. We used a generalized estimation equation approach with an unstructured correlation matrix to adjust for the correlation between both carotid arteries in each patient. Adjustments were made for age and sex (model 1) supplemented with all variables with a *P* value < .10 in model 1 (model 2, included the degree of stenosis according to the ECST criteria to correct for differences in stenosis).

Analyses were repeated to assess the association between intraplaque hemorrhage and ulcerated plaques alone. In addition, analyses were repeated for the symptomatic artery. The location of intraplaque hemorrhage and disrupted plaque surface was visually correlated by 2 independent observers after manual alignment of the MR imaging and MDCTA scans based on vessel geometry and the location of the plaque. Statistical analyses were performed by using STATA software (Version 13.1; StataCorp, College Station, Texas). $P < .05$ was considered statistically significant.

RESULTS

Patient Characteristics

In 20 of the 100 patients, MDCTA ($n = 18$) or MR imaging ($n = 2$) of the carotid arteries had not been performed due to contraindications. Two patients were excluded due to inferior image quality of the MDCTA. Of the remaining 78 patients, 149 vessels could be used for the current analyses. Seven contralateral vessels were excluded from analysis due to the absence of plaque ($n = 5$) or occlusion of the carotid artery ($n = 2$). Baseline characteristics are shown in Table 1. Forty-one of the 78 patients (53%) had an ischemic stroke; 37 (47%) patients had a TIA, including 7 with amaurosis fugax.

Vessel Characteristics

The median interval between the neurologic event and MDCTA was 32 days (25th to 75th percentile, 14–56 days); the median interval between the event and MR imaging was 44 days (25th to 75th percentile, 27–62 days). Characteristics of all vessels and symptomatic and contralateral vessels separately are shown in Table 2. The mean severity of stenosis was 51% ± 17% (ECST). The prevalence of intraplaque hemorrhage in the symptomatic and contralateral vessels was 38% and 11%, respectively. Twenty-six of the 149 vessels (17%) showed plaque ulceration; the prevalence in the symptomatic vessels and the contralateral vessels was 27% and 7%, respectively. In 13 of the 149 vessels (9%), a fissured fibrous cap was present; most were found in the symptomatic vessels ($n = 10$), but the difference was not significant ($P = .06$).

Intraplaque Hemorrhage and Disrupted Plaque Surface

In Table 3, the association between the presence of intraplaque hemorrhage and disrupted plaque surface (ulcerated plaque and/or fissured fibrous cap) is shown. In vessels with intraplaque hemorrhage, a disrupted plaque surface was significantly more prevalent compared with vessels without intraplaque hemorrhage (45% versus 15%; $P < .001$). Table 4 shows the results of the multivariable logistic regression. After correction for age and sex, the presence of intraplaque hemorrhage was associated with a disrupted plaque surface (OR, 3.98; 95% CI, 1.73–9.16; $P = .001$). Additionally, we found an association between the degree of stenosis and disrupted plaque surface (OR per 10% increase 1.42; 95% CI, 1.09–1.84; $P = .009$). After correction for age, sex, and all variables with $P < .10$, intraplaque hemorrhage was still significantly associated with disrupted plaque surface (OR, 3.13; 95% CI, 1.25–7.84; $P = .02$). Diabetes mellitus was inversely associated with disrupted plaque surface (OR, 0.31; 95% CI, 0.11–0.94; $P = .04$). Similar results were found when the analyses were repeated to assess the association between intraplaque hemorrhage and ulcerated plaque alone. The association between intraplaque hemorrhage and disrupted plaque surface was attenuated when the analyses were repeated in only the symptomatic arteries (Online Tables 1–3). The location of the plaque ulceration and/or fissured fibrous cap was the same as that of the intraplaque hemorrhage in 16 of the 21 lesions (76%); an example is shown in Fig 4.

Table 1: Clinical characteristics of patients ($n = 78$)[a]

Clinical Characteristic	
Age (yr)	67 ± 9
Male sex	57 (73%)
Classification event	
TIA	30 (38%)
Stroke	41 (53%)
Amaurosis fugax	7 (9%)
Hypercholesterolemia	43 (55%)
Hypertension	56 (72%)
Diabetes mellitus	19 (24%)
Current smoking	
No	58 (74%)
Yes	20 (26%)
Body mass index	25.2 (24.3–28.4)
Current use	
Antiplatelet therapy	36 (46%)
Oral anticoagulants	0 (0%)
Statins	36 (46%)
Antihypertensive medication	50 (64%)
Antidiabetic medication	13 (17%)
History	
Ischemic stroke or TIA	13 (17%)
Ischemic heart disease	16 (21%)
Peripheral arterial disease	15 (19%)

[a] Data are mean ± SD, absolute numbers of patients (%), or median (25th–75th percentile).

Table 3: Association of intraplaque hemorrhage and disrupted plaque surface in all vessels[a]

	Disrupted Plaque[b]	Intact Plaque Surface	Total
Intraplaque hemorrhage present ($n = 38$)	17 (45%)	21 (55%)	38
Intraplaque hemorrhage absent ($n = 111$)	17 (15%)	94 (85%)	111
Total	34	115	149

[a] $P < .001$.

[b] Defined as ulcerated plaque and/or fissured fibrous cap.

Table 2: Vessel characteristics[a]

Vessel Characteristic	All Vessels	Symptomatic Vessels	Contralateral Vessels	*P* Value, Symptomatic versus Contralateral Vessels
No.	149	78	71	
Plaque ulceration	26 (17%)	21 (27%)	5 (7%)	.001[b]
Fissured fibrous cap	13 (9%)	10 (13%)	3 (4%)	.06
Calcium volume (mm^3)	21.0 (3.6–56.2)	24.2 (6.2–71.8)	17.2 (1.9–53.1)	.09
Degree of stenosis (ECST) (%)	51 ± 17	55 ± 17	47 ± 16	.004[b]
Degree of stenosis (NASCET) (%)	8 (0–32)	14 (0–35)	2 (0–26)	.03[b]
Intraplaque hemorrhage	38 (26%)	30 (38%)	8 (11%)	<.001[b]

[a] Data are absolute numbers of vessels (%), median (25th–75th percentile), or mean ± SD.

[b] $P < .05$.

Table 4: Multivariable OR for the association among clinical characteristics, vessel characteristics, and disrupted plaque surface in all vessels

Characteristic	Multivariable (Age, Sex)		Multivariable[a] (Age, Sex, Factors *P* < .10)	
	OR (95% CI)	*P* Value	OR (95% CI)	*P* Value
Age	1.05 (1.00–1.10)	.07	1.05 (1.00–1.10)	.07
Sex	0.42 (0.15–1.12)	.08	0.50 (0.17–1.42)	.19
Hypertension	1.98 (0.73–5.35)	.18		
Diabetes mellitus	0.40 (0.14–1.10)	.08	0.31 (0.11–0.94)	.04[b]
Hypercholesterolemia	1.41 (0.63–3.15)	.40		
Current smoking	0.48 (0.16–1.46)	.20		
Intraplaque hemorrhage	3.98 (1.73–9.16)	.001[b]	3.13 (1.25–7.84)	.02[b]
Degree of stenosis (ECST, per 10%)	1.42 (1.09–1.84)	.009[b]	1.30 (1.00–1.69)	.07
Calcification volume	0.86 (0.69–1.08)	.21		

[a] We corrected for age, sex, diabetes mellitus, and degree of stenosis (ECST).
[b] $P < .05$.

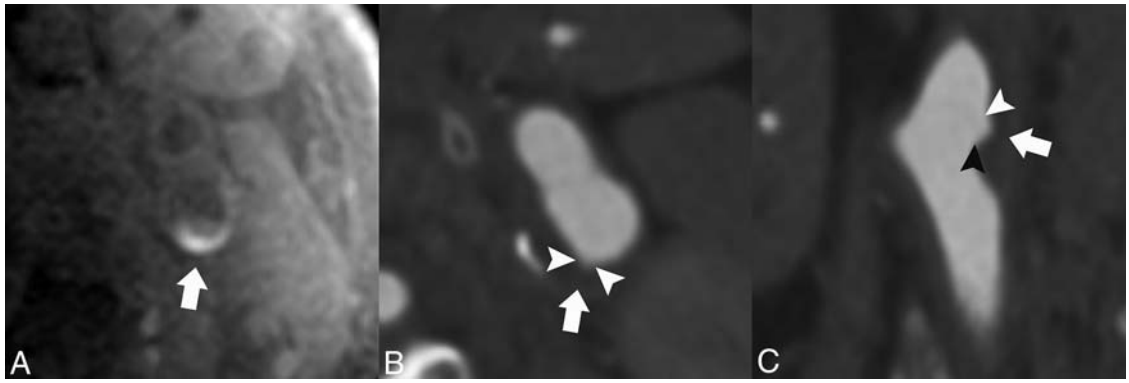

FIG 4. Correlated intraplaque hemorrhage on MR imaging and plaque ulceration on MDCTA. An example of MR imaging and MDCTA images of the left carotid bifurcation. On the 3D-TIW fat suppressed echo-spoiled gradient echo MR imaging sequence, intraplaque hemorrhage is visible in the atherosclerotic plaque (*A*, *arrow*). MDCTA images show a small ulceration on both the transversal and longitudinal plane at the site of the intraplaque hemorrhage (*B* and *C*, *arrows*; *arrowheads* indicate the edges of the plaque ulceration).

DISCUSSION

This study shows that intraplaque hemorrhage is associated with a disrupted plaque surface (plaque ulceration and/or fissured fibrous cap) and plaque ulceration alone. In 76% of the vessels with both intraplaque hemorrhage and a disrupted plaque surface, intraplaque hemorrhage and plaque ulceration or fissured fibrous cap shared the same location. The association between these 2 vulnerable plaque characteristics may support the notion that intraplaque hemorrhage increases the risk of plaque rupture. However, because of the cross-sectional study design, serial studies are needed to further investigate the role of intraplaque hemorrhage in plaque rupture.

Some methodologic issues need to be discussed first. A strength of our prospective study is that most vessels showed a mild stenosis. Most previous studies focused on patients with a moderate or severe carotid artery stenosis. However, plaque imaging in this patient group is less relevant for clinical decision-making because patients with a moderate (male patients) or severe (all patients) symptomatic carotid artery stenosis are already eligible for carotid endarterectomy.[16] Moreover, the amount of calcification will probably be higher in patients with a moderate or severe carotid artery stenosis, complicating the detection of plaque surface morphology. Second, we reviewed MDCTA and MR images of all patients with a disrupted plaque surface and intraplaque hemorrhage to investigate whether the intraplaque hemorrhage and plaque disruption were at the same location. The finding that the location was indeed similar in 76% strengthens the association between the 2 vulnerable plaque characteristics.

A limitation of our multicenter study is that we used different MDCTA and MR imaging scanners. MDCTA scanning protocols, however, were similar. We used the 3D-T1W fat suppresssed spoiled gradient echo or the 2D-T1W inversion recovery turbo field echo MR imaging sequence to detect intraplaque hemorrhage. Bitar et al[25] and Cappendijk et al[26] used sequences like ours and found a good sensitivity, specificity, and interobserver agreement for the detection of intraplaque hemorrhage in both sequences. They also found good agreement between MR imaging–depicted intraplaque hemorrhage and histologic sections. In addition, our overall prevalence of intraplaque hemorrhage of 26% is in accordance with that in the literature.[4,5,15] Correction for MR imaging protocol used in the multivariate model did not change our results. A second limitation is the lack of histology. We used MDCTA instead of MR imaging for the evaluation of the plaque surface, because MDCTA has been shown to have a high sensitivity and specificity for the detection of plaque ulceration and has fewer limitations such as partial volume effects and flow artifacts that mimic plaques.[27,28] In addition, when we reviewed the MR images and MDCTA images side by side, plaque ulcerations were hardly visible on the MR images. Saba et al[27] showed a good sensitivity and specificity for the detection of plaque ulceration by using MDCTA and multiplanar reconstruction (sensitivity,

75.8%; specificity, 90.8%). We found an overall prevalence of plaque ulceration of 17%. Similar prevalence of plaque ulceration was found in other studies, ranging from 13% to 22%.[15,20,29,30] Detection of the presence of a fissured fibrous cap has been studied less intensively. We found an overall prevalence of the presence of a fissured fibrous cap of 9%, in agreement with the 11% found by Saba and Mallarini.[20] Rupture of the fissured fibrous cap was significantly associated with cerebrovascular symptoms ($P = .003$).[20] Based on the good sensitivity and specificity of MDCTA for plaque ulcerations and the good agreement between MR imaging–depicted intraplaque hemorrhage and histology, we therefore conclude that it is legitimate to use imaging techniques such as MDCTA and MR imaging to study the relationship between intraplaque hemorrhage and the disruption of the plaque surface.[25,26] Moreover, the use of MDCTA and MR imaging provides the opportunity to investigate the relationship in a specific category of patients—that is, those with a mild-to-moderate carotid artery stenosis, patients who are treated medically and thus have no available histology. The final limitation of our study is that it is cross-sectional. Our results should therefore be confirmed in a serial study.

Rupture of an atherosclerotic carotid artery plaque is an important cause of ischemic stroke. Therefore, understanding the pathophysiology of plaque rupture is very important. Infiltration of macrophages in pathologic intima thickening plays a key role in the development of atherosclerotic plaques. The combination of macrophage infiltration, apoptosis, and hypoxia-induced necrosis leads to the development of more advanced atherosclerotic plaques with a lipid-rich necrotic core. Previous studies already showed an association between lipid-rich necrotic core volumes and plaque ulceration.[29-31] In these larger plaques, hypoxia and the inflammatory response are assumed to promote neovascularization. As stated previously, the common viewpoint is that these small leaky neovessels are responsible for the occurrence of intraplaque hemorrhage and subsequently the development of an unstable rupture-prone plaque.[5,9-12,32] Our results—if confirmed in serial studies—can support the pathophysiologic relation between intraplaque hemorrhage and disrupted plaque surface. An alternative viewpoint to explain this relationship is that repeated fissuring of the plaque and associated formation of nonocclusive luminal thrombus incorporated in the plaque could be the cause of intraplaque hemorrhage.[5] Nevertheless, observations that intraplaque hemorrhage is related to high attenuation of plaque neovessels, in the absence of plaque fissuring, supports the more common view of small leaky neovessels as the cause of intraplaque hemorrhage.[5,10]

CONCLUSIONS

We showed that intraplaque hemorrhage is associated with a disrupted plaque surface (plaque ulceration and/or fissured fibrous cap) in patients with a <70% carotid artery stenosis. Our findings suggest a strong association between these 2 vulnerable plaque characteristics. Nevertheless, because of the cross-sectional study design, additional serial studies are needed to evaluate whether intraplaque hemorrhage indeed increases the risk for plaque rupture and subsequent TIA or ischemic stroke.

APPENDIX

Participating centers: Academic Medical Center, Amsterdam (P.J. Nederkoorn); Atrium Medisch Centrum, Heerlen (A.H.C.M.L. Schreuder); Erasmus Medical Center, Rotterdam (A. van der Lugt, P.J. Koudstaal); Flevoziekenhuis, Almere (M. Limburg); Kennemer Gasthuis, Haarlem (M. Weisfelt); Laurentius Ziekenhuis, Roermond (A.G. Korten); Maasstad Ziekenhuis, Rotterdam (R. Saxena); Maastricht University Medical Center (M.E. Kooi, R.J. van Oostenbrugge, W.H. Mess); Orbis Medisch Centrum, Sittard (N.P. van Orshoven); Sint Antonius Ziekenhuis, Nieuwegein (S.C. Tromp); Sint Franciscus Gasthuis, Rotterdam (S.L.M. Bakker); Slotervaartziekenhuis, Amsterdam (N.D. Kruyt); Tergooi Ziekenhuizen, Hilversum/Blaricum (J.R. de Kruijk); University Medical Center Utrecht (J. Hendrikse, G.J. de Borst); Viecuri Medisch Centrum, Venlo (B.J. Meems); Vlietland Ziekenhuis, Schiedam (J.C.B. Verhey); IJsselland Ziekenhuis, Capelle a/d IJsel (A.D. Wijnhoud).

Disclosures: Anouk C. van Dijk—*RELATED*: *Grant*: Center for Translational Molecular Medicine and supported by the Dutch Heart Foundation,* *Comments*: Project PARISK (grant 01C-202). Antonius F.W. van der Steen—*RELATED*: *Grant*: Center for Translational Molecular Medicine, project PARISK,* *Comments*: This work is part of a public-private partnership by the Center for Translational Molecular Medicine and the Dutch Heart Foundation; I am Co-Principal Investigator of this grant. Mat J.A.P. Daemen—*RELATED*: *Grant*: Center for Translational Molecular Medicine,* *Comments*: The Center for Translational Molecular Medicine provided the grant for the PARISK research program. Peter J. Koudstaal—*UNRELATED*: editor and author, *Comments*: *Textbook of Neurology*, Reed Elsevier. Paul J. Nederkoorn—*UNRELATED*: *Grants/Grants Pending*: 1) Preventive Antibiotics in Stroke Study, the Netherlands Organization for Health Research and Development (no. 171002302) and the Netherlands Heart Foundation (no. 2009B095); 2) The ThRombolysis in UnconTrolled Hypertension study: Fonds NutsOhra, grant No. 1302–026. Marianne Eline Kooi—*RELATED*: *Grant*: Center for Translational Molecular Medicine.* Aad van der Lugt—*RELATED*: *Grant*: Center for Translational Molecular Medicine,* Dutch Heart Foundation*; *UNRELATED*: *Grants/Grants Pending*: GE Healthcare,* *Comments*: MRI vendor; *Payment for Lectures (including service on Speakers Bureaus)*: GE Healthcare,* *Comments*: MRI vendor. *Money paid to the institution.

REFERENCES

1. Yuan C, Mitsumori LM, Beach KW, et al. **Carotid atherosclerotic plaque: noninvasive MR characterization and identification of vulnerable lesions.** *Radiology* 2001;221:285–99
2. Naghavi M, Libby P, Falk E, et al. **From vulnerable plaque to vulnerable patient: a call for new definitions and risk assessment strategies, part II.** *Circulation* 2003;108:1772–78
3. Naghavi M, Libby P, Falk E, et al. **From vulnerable plaque to vulnerable patient: a call for new definitions and risk assessment strategies, part I.** *Circulation* 2003;108:1664–72
4. Saam T, Hetterich H, Hoffmann V, et al. **Meta-analysis and systematic review of the predictive value of carotid plaque hemorrhage on cerebrovascular events by magnetic resonance imaging.** *J Am Coll Cardiol* 2013;62:1081–91
5. Teng Z, Sadat U, Brown AJ, et al. **Plaque hemorrhage in carotid artery disease: pathogenesis, clinical and biomechanical considerations.** *J Biomech* 2014;47:847–58
6. Altaf N, Daniels L, Morgan PS, et al. **Detection of intraplaque hemorrhage by magnetic resonance imaging in symptomatic patients with mild to moderate carotid stenosis predicts recurrent neurological events.** *J Vasc Surg* 2008;47:337–42
7. Kwee RM, van Oostenbrugge RJ, Mess WH, et al. **MRI of carotid atherosclerosis to identify TIA and stroke patients who are at risk of a recurrence.** *J Magn Reson Imaging* 2013;37:1189–94
8. Takaya N, Yuan C, Chu B, et al. **Association between carotid plaque characteristics and subsequent ischemic cerebrovascular events: a prospective assessment with MRI—initial results.** *Stroke* 2006; 37:818–23

9. Michel JB, Virmani R, Arbustini E, et al. **Intraplaque haemorrhages as the trigger of plaque vulnerability.** *Eur Heart J* 2011;32:1977–85, 85a, 85b, 85c
10. Virmani R, Kolodgie FD, Burke AP, et al. **Atherosclerotic plaque progression and vulnerability to rupture: angiogenesis as a source of intraplaque hemorrhage.** *Arterioscler Thromb Vasc Biol* 2005; 25:2054–61
11. Michel JB, Delbosc S, Ho-Tin-Noé B, et al. **From intraplaque haemorrhages to plaque vulnerability: biological consequences of intraplaque haemorrhages.** *J Cardiovasc Med (Hagerstown)* 2012;13: 628–34
12. Takaya N, Yuan C, Chu B, et al. **Presence of intraplaque hemorrhage stimulates progression of carotid atherosclerotic plaques: a high-resolution magnetic resonance imaging study.** *Circulation* 2005; 111:2768–75
13. Lovett JK, Gallagher PJ, Hands LJ, et al. **Histological correlates of carotid plaque surface morphology on lumen contrast imaging.** *Circulation* 2004;110:2190–97
14. Saba L, Sanfilippo R, Pirisi R, et al. **Multidetector-row CT angiography in the study of atherosclerotic carotid arteries.** *Neuroradiology* 2007;49:623–37
15. U-King-Im JM, Fox AJ, Aviv RI, et al. **Characterization of carotid plaque hemorrhage: a CT angiography and MR intraplaque hemorrhage study.** *Stroke* 2010;41:1623–29
16. Rothwell PM, Eliasziw M, Gutnikov SA, et al; Carotid Endarterectomy Trialists Collaboration. **Endarterectomy for symptomatic carotid stenosis in relation to clinical subgroups and timing of surgery.** *Lancet* 2004;363:915–24
17. Rothwell PM, Gibson R, Warlow CP; European Carotid Surgery Trialists' Collaborative Group. **Interrelation between plaque surface morphology and degree of stenosis on carotid angiograms and the risk of ischemic stroke in patients with symptomatic carotid stenosis.** *Stroke* 2000;31:615–21
18. Truijman MT, Kooi ME, van Dijk AC, et al. **Plaque At RISK (PARISK): prospective multicenter study to improve diagnosis of high-risk carotid plaques.** *Int J Stroke* 2014;9:747–54
19. **Randomised trial of endarterectomy for recently symptomatic carotid stenosis: final results of the MRC European Carotid Surgery Trial (ECST).** *Lancet* 1998;351:1379–87
20. de Weert TT, Cretier S, Groen HC, et al. **Atherosclerotic plaque surface morphology in the carotid bifurcation assessed with multidetector computed tomography angiography.** *Stroke* 2009;40:1334–40
21. Saba L, Mallarini G. **Fissured fibrous cap of vulnerable carotid plaques and symptomaticity: are they correlated? Preliminary results by using multi-detector-row CT angiography.** *Cerebrovasc Dis* 2009;27:322–27
22. North American Symptomatic Carotid Endarterectomy Trial Collaborators. **Beneficial effect of carotid endarterectomy in symptomatic patients with high-grade carotid stenosis.** *N Engl J Med* 1991;325:445–53
23. de Weert TT, Cakir H, Rozie S, et al. **Intracranial internal carotid artery calcifications: association with vascular risk factors and ischemic cerebrovascular disease.** *AJNR Am J Neuroradiol* 2009;30:177–84
24. Yuan C, Mitsumori LM, Ferguson MS, et al. **In vivo accuracy of multispectral magnetic resonance imaging for identifying lipid-rich necrotic cores and intraplaque hemorrhage in advanced human carotid plaques.** *Circulation* 2001;104:2051–56
25. Bitar R, Moody AR, Leung G, et al. **In vivo 3D high-spatial-resolution MR imaging of intraplaque hemorrhage.** *Radiology* 2008;249:259–67
26. Cappendijk VC, Cleutjens KB, Heeneman S, et al. **In vivo detection of hemorrhage in human atherosclerotic plaques with magnetic resonance imaging.** *J Magn Reson Imaging* 2004;20:105–10
27. Saba L, Caddeo G, Sanfilippo R, et al. **Efficacy and sensitivity of axial scans and different reconstruction methods in the study of the ulcerated carotid plaque using multidetector-row CT angiography: comparison with surgical results.** *AJNR Am J Neuroradiol* 2007; 28:716–23
28. Yu W, Underhill HR, Ferguson MS, et al. **The added value of longitudinal black-blood cardiovascular magnetic resonance angiography in the cross sectional identification of carotid atherosclerotic ulceration.** *J Cardiovasc Magn Reson* 2009;11:31
29. Homburg PJ, Rozie S, van Gils MJ, et al. **Association between carotid artery plaque ulceration and plaque composition evaluated with multidetector CT angiography.** *Stroke* 2011;42:367–72
30. Saba L, Sanfilippo R, Sannia S, et al. **Association between carotid artery plaque volume, composition, and ulceration: a retrospective assessment with MDCT.** *AJR Am J Roentgenol* 2012;199:151–56
31. Underhill HR, Yuan C, Yarnykh VL, et al. **Predictors of surface disruption with MR imaging in asymptomatic carotid artery stenosis.** *AJNR Am J Neuroradiol* 2010;31:487–93
32. DeMarco JK, Huston J 3rd. **Imaging of high-risk carotid artery plaques: current status and future directions.** *Neurosurg Focus* 2014; 36:E1

Carotid Webs and Recurrent Ischemic Strokes in the Era of CT Angiography

P.M.C. Choi, D. Singh, A. Trivedi, E. Qazi, D. George, J. Wong, A.M. Demchuk, M. Goyal, M.D. Hill, and B.K. Menon

ABSTRACT

BACKGROUND AND PURPOSE: Carotid webs may cause recurrent ischemic stroke. We describe the prevalence, demographics, clinical presentation, imaging features, histopathology, and stroke risk associated with this under-recognized lesion.

MATERIALS AND METHODS: A carotid web was defined on CTA as a thin intraluminal filling defect along the posterior wall of the carotid bulb just beyond the carotid bifurcation on oblique sagittal section CTA that was seen as a septum on axial CTA. Using a prospective case series from April 2013 to April 2014, we describe the demographics, spectrum of imaging features on CTA, and histopathology of these carotid webs. From a retrospective analysis of patients at our center from May 2012 to April 2013 who had a baseline head and neck CTA followed by a brain MR imaging within 1–2 days of the CTA, we determine the period prevalence of carotid webs and the prevalence of ipsilateral stroke on imaging.

RESULTS: In the prospective series, the mean age was 50 years (range, 41–55 years); 5/7 patients were women. Recurrent stroke was seen in 5/7 (71.4%) patients with the carotid web; time to recurrence ranged from 1 to 97 months. Histopathology suggested a high probability of fibromuscular dysplasia. In the retrospective series, carotid webs were seen in 7/576 patients for a hospital-based-period prevalence of 1.2% (95% CI, 0.4%–2.5%). Two of these 7 patients had acute stroke in the vascular territory of the carotid web.

CONCLUSIONS: A carotid web may contribute to recurrent ischemic stroke in patients with no other determined stroke mechanism. Intimal variant fibromuscular dysplasia is the pathologic diagnosis in most cases. The prevalence of carotid web is low, while the optimal management strategy remains unknown.

ABBREVIATIONS: ASA = acetylsalicylic acid; FMD = fibromuscular dysplasia

For >50 years, a shelf-like projection within the lumen of the carotid bulb on vascular imaging has been referred to as a web in the carotid artery. Momose and New[1] first used the term "web" in 1973 to describe this entity on carotid angiography in 4 patients in a series of 7000 patients during 8 years at Massachusetts General Hospital. The authors distinguished this entity from fibromuscular dysplasia (FMD) and postulated that carotid webs were developmental in origin. In 1977, Osborn and Anderson[2] described a patient with an isolated, smooth, well-defined web at the origin of the internal carotid artery on conventional angiography in a case series of patients with FMD. The radiologic features were very similar to those in a histologically proved case of FMD of the carotid artery described by Rainer et al[3] in 1968.

Apart from 1 isolated case report,[4] in which "intraluminal web" was used to described multiple membranous strands within the carotid artery lumen, the terms "carotid web" and "pseudovalvular fold" have been used to refer to an imaging entity that appears as a small, shelf-like linear filling defect projecting superiorly into the arterial lumen and arising from the posterior aspect of the proximal internal carotid artery on conventional angiography.[5] Here, we report 12 cases of carotid web from a combined prospective and retrospective series. We describe in detail the prevalence, demographics, clinical presentation, imaging features, histopathology, and stroke risk associated with carotid webs.

MATERIALS AND METHODS

All patients included in this study are part of the Calgary CT angiography data base, an ongoing imaging registry of patients

Received January 2, 2015; accepted after revision March 19.

From the Calgary Stroke Program, Department of Clinical Neuroscience (P.M.C.C., D.S., A.T., E.Q., J.W., A.M.D., M.G., M.D.H., B.K.M.), and Departments of Pathology and Laboratory Medicine (D.G.), Radiology (J.W., A.M.D., M.G., M.D.H., B.K.M.), and Medicine and Community Health Science (M.D.H.), University of Calgary, Calgary, Alberta, Canada; and Hotchkiss Brain Institute (A.M.D., M.G., M.D.H., B.K.M.), Calgary, Alberta, Canada.

Please address correspondence to Bijoy K. Menon, MD, 1079 A, 29th St NW, Calgary, AB, Canada T3H4J2; e-mail: Bijoy.Menon@Albertahealthservices.ca

Indicates article with supplemental on-line tables.

http://dx.doi.org/10.3174/ajnr.A4431

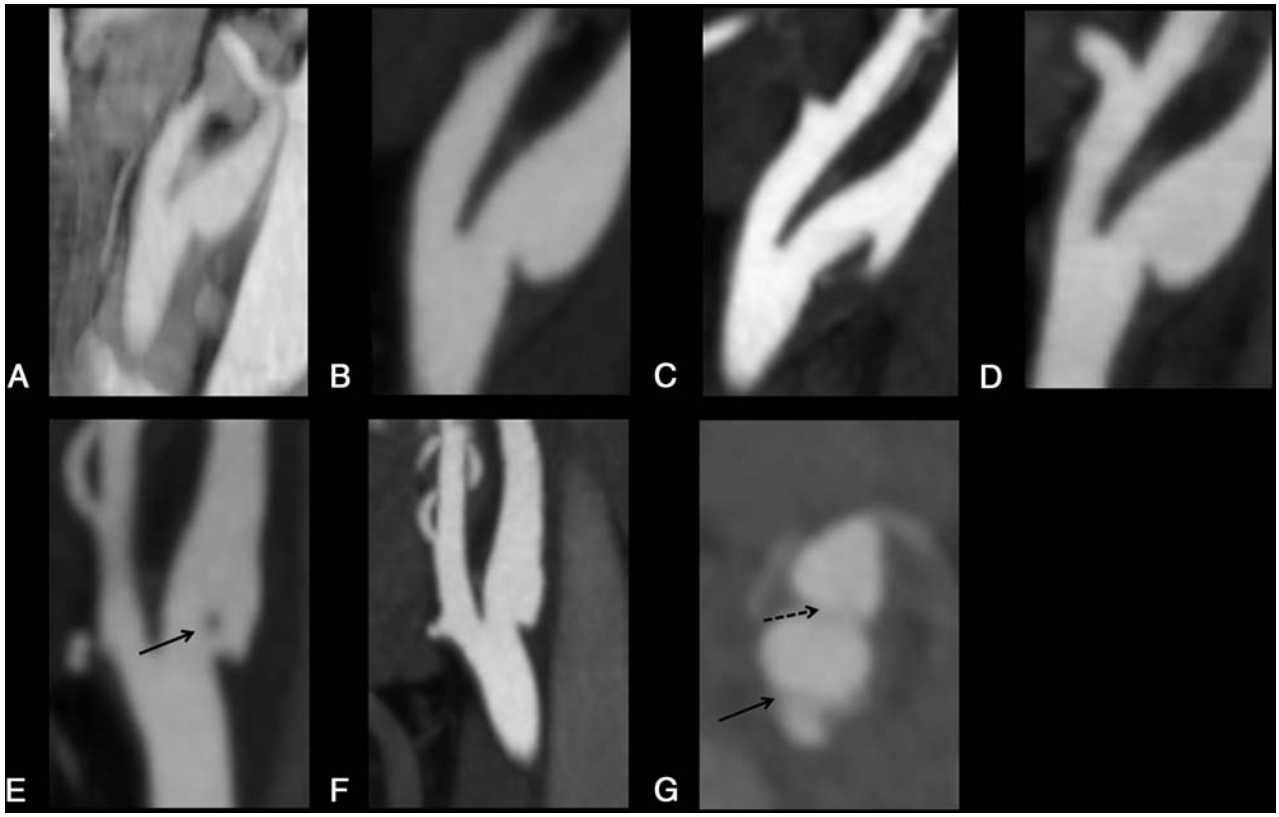

FIG 1. Sagittal and axial images of carotid webs. The top panel shows serial sagittal-view CTAs in patient A. *A* and *B*, Carotid webs 8 years apart. *C*, Changing morphology of the right carotid web within days with possible thrombus formation in the setting of dual antiplatelet therapy. *D*, A return to baseline morphology with the use of unfractionated heparin. The bottom panel shows serial CTAs in patient B. *E*, A carotid web with possible thrombus in the lumen (*arrow*). *F*, The same carotid web 1 month later with no thrombus. *G*, An axial-view CTA with the same carotid web appearing as a septum (*arrow*). The *broken arrow* indicates the carotid bifurcation.

with acute ischemic stroke. Details of this registry have been previously described.[6]

Prospective Case Series

From April 2013, when we first identified a patient with a carotid web and ipsilesional ischemic stroke on head and neck CTA, we have identified 7 such patients prospectively until April 2014. The diagnosis of stroke was based on clinical grounds, supported by positive MR imaging findings in all cases. We defined a carotid web on CTA as follows: a thin intraluminal filling defect along the posterior wall of the carotid bulb just beyond the carotid bifurcation on oblique sagittal section CTA and seen as a septum on axial CTA (Fig 1*A*–*F*). We collected information on demographics, clinical characteristics, drugs, and treatment offered at baseline and during hospital stays in these patients. Stroke severity was assessed by using the NIHSS at baseline, at discharge, and at 90 days. Functional status was assessed by using the mRS at similar time points. Four of 7 patients underwent carotid endarterectomy at the discretion of the treating physician. The endarterectomy specimens were sectioned in the axial plane, fixed in formalin, and embedded in paraffin. Sections were stained for light microscopy with the following: hematoxylin-eosin, Masson trichrome, and Musto (elastin).

Retrospective Series

We also identified consecutive patients who presented to our center from May 2012 to April 2013 and had a baseline head and neck CTA followed by a follow-up brain MR imaging at 24–48 hours. Baseline neck CTA was assessed for the presence or absence of a carotid web. Follow-up brain MR imaging (DWI and/or FLAIR) was assessed for the presence of any ischemic stroke. The side of the carotid web (left versus right) and ischemic stroke (left versus right versus posterior) was identified on baseline CTA. All images were read by consensus by 3 experienced raters (P.M.C.C., D.S., and A.T.). The readers were blinded to baseline scans while reading follow-up MR imaging.

We describe, by using standard summary statistics, the demographics and clinical characteristics of all patients (in both prospective and retrospective series). The Conjoint Health Research Board of the University of Calgary has approved the use of the CTA data base for imaging-related studies.

RESULTS

Demographics

During a 12-month period, ipsilateral carotid webs were identified prospectively in 7 patients with acute ischemic stroke (Online Table 1). The mean age of these patients was 50 years (range, 41–55 years); 5 of the 7 patients were women. Five of the 7 patients had recurrent stroke in the ipsilateral vascular territory; 1 of those 5 had 4 recurrent strokes in the same vascular territory. These patients, in total, experienced 14 ischemic strokes during 8.5 years with time to recurrence ranging from 1 to 97 months. In 2 patients, thrombus-like material was seen at the site of the carotid web, with changing morphology on serial CTAs, despite concur-

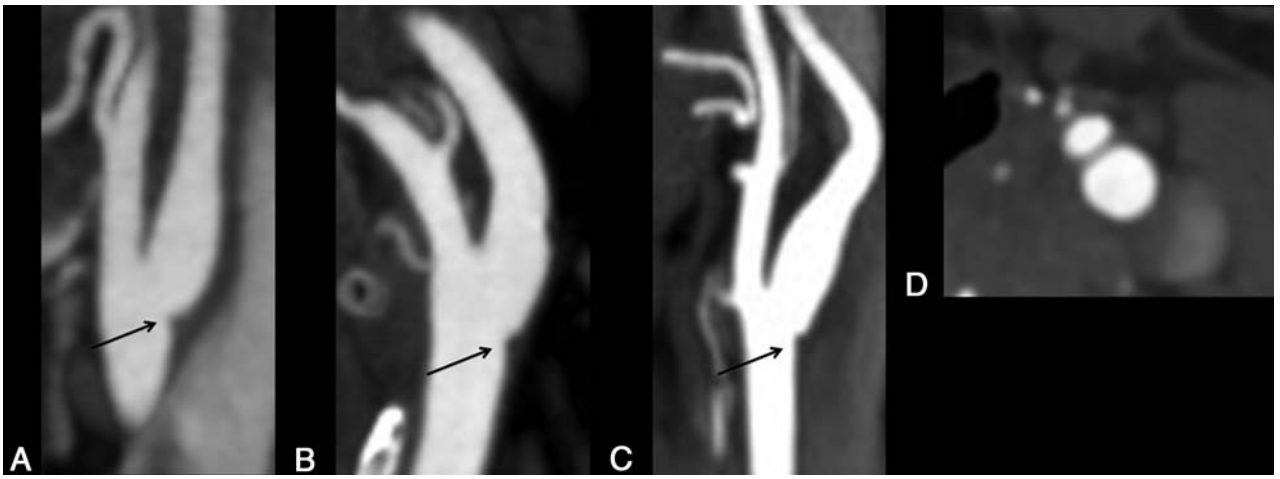

FIG 2. Small protruding lesions that are distinct from carotid webs in 3 different patients on sagittal and axial CTA (*A–C*, *arrow*). Axial CTA shows no septum with this lesion, unlike in carotid webs.

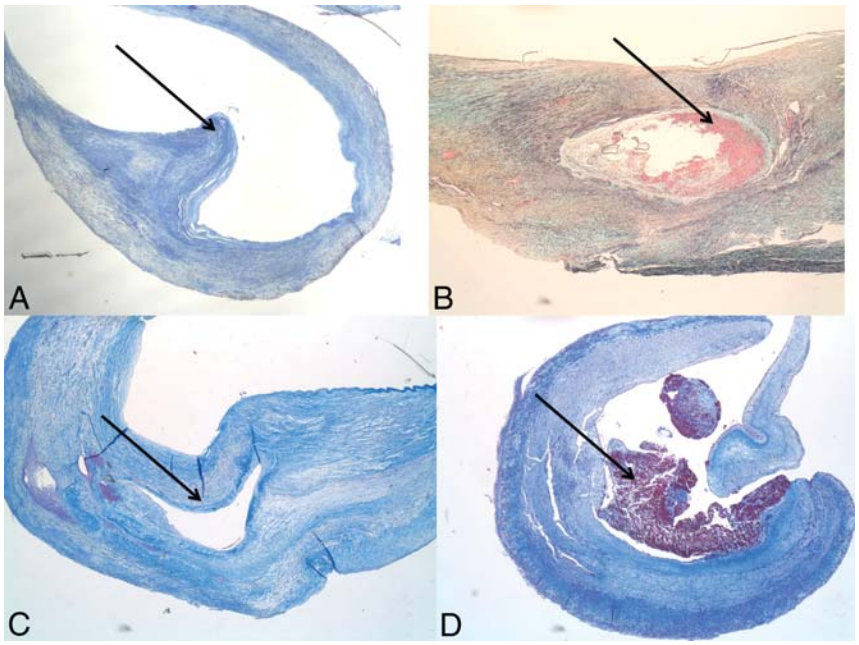

FIG 3. Figures show the histopathology of carotid webs. *A*, A shelf-like projection of abnormal intimal fibrous tissue. *B*, Focal hemorrhagic dissection with early organization. *C*, Fibrous intimal thickening with focal dissection into the fibrotic intima. *D*, Focal fibrous intimal thickening with adherent thrombus.

rent antiplatelet therapy. Four of 5 patients with recurrent strokes underwent carotid endarterectomy and remained stroke-free at last follow-up (range, 3–7 months). All our patients had no other identified cause of stroke after standard work-up. Patient characteristics and other details are described in On-line Table 1.

Prevalence

Estimating the period prevalence of the carotid web would need a population-based imaging study. This was not practical. We therefore attempted to study period prevalence in a hospital-based sample of convenience. CTAs from 576 patients who presented to our center from May 2012 to April 2013 with suspected stroke were reviewed. These patients had a brain MR imaging performed within 1–2 days of presenting symptoms. Seven carotid webs were identified in 576 individual patients: 4 on the left and 3 on the right (On-line Table 2). Thus, the prevalence of carotid webs in a hospital-based series is estimated at 1.2% (95% CI, 0.4%–2.5%). The mean age of these patients was 63 years (range, 47–78 years). Four of the 7 patients were women. Two of 7 patients had acute stroke in the vascular territory of the carotid web.

In our retrospective series, we also identified patients with single, small, protruding lesions in the proximal ICA. In contrast to carotid webs, these lesions were smaller and not seen on the axial sections (Fig 2). None of the patients in our prospective series had this appearance on CTA. These small protruding lesions were identified in 14/576 patients: 7 on the left and 7 on the right (On-line Table 2) for an estimated prevalence of 2.43% (95% CI, 1.3%–4.0%). The mean age of these patients was also 63 years (range, 39–90 years). Six of the 14 patients were woman. Three of 14 patients had acute stroke in the vascular territory of the small protruding lesion.

Pathology

Each of the endarterectomy specimens was characterized by foci of marked fibroelastic thickening of the intima. None contained the necrotic, cholesterol-rich core of a classic atheroma. In 1 specimen, there was a shelf of intimal fibrous tissue that projected into the lumen (Fig 3*A*). In 2 cases, the fibrous intimal cushion was split by a dissection: One showed an organizing hemorrhage within (Fig 3*B*), while another formed an open endothelial-lined cavity (Fig 3*C*). Specimens from another case contained a thick fibrous intimal cushion with a recent mural thrombus (Fig 3*D*). As is characteristic of endarterectomy specimens, each specimen had an attenuated rim of elastin-

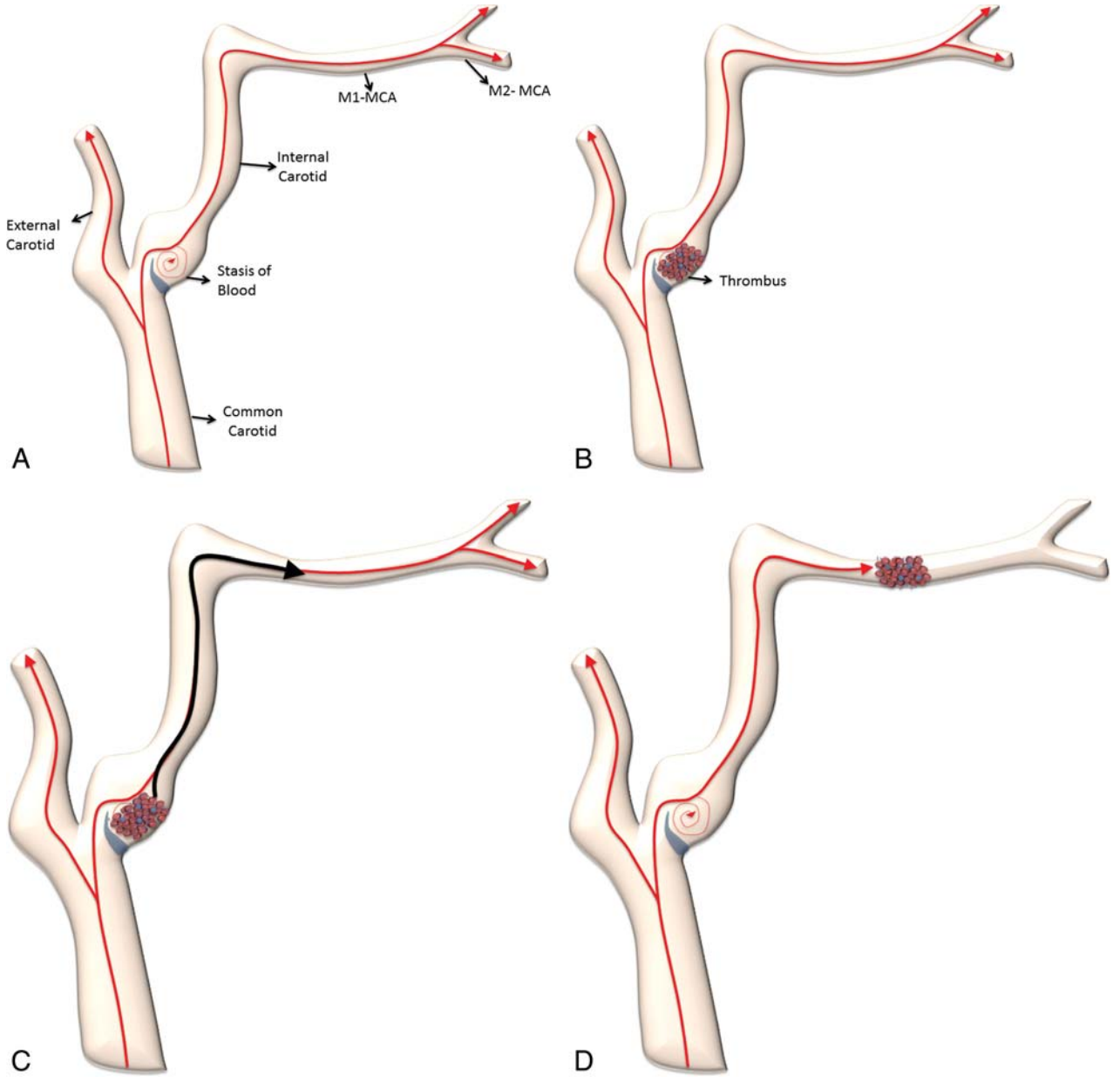

FIG 4. Animated figures depict thrombogenicity in the internal carotid artery due to the presence of a carotid web. *A*, Stasis of blood flow developing distal to the carotid web results in thrombus formation (*B*). This thrombus, when of sufficient size, dislodges and embolizes intracranially (*C* and *D*).

rich medial tissue, but in none was a full-thickness medial section available.

Below we describe the clinical history and imaging findings of 2 patients in detail.

Patient A

A 54-year-old man (patient 1, On-line Table 1) was found slumped on the sofa with left-sided hemiparesis. He was last seen healthy 45 minutes prior. Medical history was unremarkable apart from a remote episode of transient left-arm weakness and numbness. On arrival, he had moderate left hemiplegia, neglect, and sensory loss; the National Institutes of Health Stroke Scale score was 11. Noncontrast brain CT showed early ischemic changes in the lentiform nucleus and the lateral MCA territory (ASPECTS = 8). CT angiography showed a mid-M1 occlusion on the right. Intravenous tPA was given followed by intra-arterial tPA combined with primary thrombus angioplasty. At 4 hours poststroke, his NIHSS score was zero. A shelf-like narrowing at the proximal right internal carotid artery with no ulceration was noted both on CTA (Fig 1*A*) and at the time of the catheter angiography. Investigations were negative for diabetes or hyperlipidemia; 24-hour Holter monitoring and transthoracic echocardiogram findings were normal. The patient made a full recovery and was treated with dual antiplatelet therapy for 3 months, followed by acetylsalicylic acid (ASA) and simvastatin, 40 mg long term.

Eight years later, the patient woke up with acute mild left hemiparesis with an NIHSS score of 4. He had stopped ASA 7 days prior for excision of a basal cell carcinoma on his left ear and

restarted ASA the night before his presentation. NCCT showed no new ischemic change; CTA showed a new proximal right M1 occlusion and the same shelf-like narrowing in the right ICA (Fig 1*B*). Because he was last seen healthy >12 hours prior, no thrombolysis was administered. He received a loading dose of clopidogrel. MR imaging showed a new striatocapsular infarct with persistent occlusion of the M1 MCA 2 days later. Repeat CTA 4 days later showed changing morphology of the right carotid web (shelf-like narrowing), suggestive of thrombus formation in the setting of dual antiplatelet therapy (Fig 1*C*). Transcranial Doppler studies on 2 occasions were negative for microembolic signals. Clopidogrel was stopped, and he was treated with intravenous unfractionated heparin and ASA for 3 days with resolution of the thrombus on repeat CTA 5 days later (Fig 1*D*). Carotid endarterectomy was performed 12 days poststroke. Pathology from carotid endarterectomy showed a focal shelf-like projection of the fibrotic intima into the lumen without any changes typical of atherosclerosis (Fig 3*A*).

Patient B

A 59-year-old woman (patient 2, On-line Table 1) presented with sudden onset of left hemiparesis. There was a history of recurrent right hemispheric strokes 2 and 7 years prior for which she was treated with ASA and had no residual symptoms. On arrival, she had an NIHSS score of 11. NCCT of the brain showed an old right basal ganglia infarct with early ischemic changes in the right insula and right M2 region; her ASPECTS was 8. CTA revealed a right M1 MCA occlusion and a carotid web just distal to the ICA bifurcation with probable thrombus-like material attached (Fig 1*E*). She received IV tPA followed by endovascular therapy. Recanalization (TICI 2b/3) was achieved postprocedure with an NIHSS score of 2. She was discharged on dual antiplatelet therapy.

One month later, the patient was found hemiplegic on the left side. On arrival, her NIHSS score was 12. NCCT showed early ischemic changes in the right temporal cortex; CTA again showed a right M1 occlusion. The carotid web in the right ICA was again noted (Fig 1*F*). She was treated with endovascular therapy, and the right MCA recanalized. Her NIHSS score was 1 postprocedure. This time, right carotid endarterectomy was performed 8 days poststroke, with pathology showing fibrous intimal thickening with focal hemorrhagic dissection (Fig 3*B*). There was no history to suggest medication noncompliance before her recent stroke.

DISCUSSION

A carotid web, as an imaging entity, can be observed on both oblique sagittal reformats and axial sections of CTA. An operational definition is a thin intraluminal filling defect along the posterior wall of the carotid bulb in oblique sagittal reformats and, most important, a septum evident on axial section CTA. We demonstrate that carotid webs, though rare, are associated with recurrent ipsilateral strokes, possibly because they serve as a nidus for thrombus formation. CTA provides a reliable representation of gross structures protruding into the ICA lumen and should therefore be the imaging method of choice in noninvasive detection of carotid webs. Carotid webs may be detected by carotid sonography, but sensitivity is limited by their size and non-flow-limiting nature.[5,7] With a few exceptions,[5,7-10] previous reports of carotid web descriptions relied on conventional angiography.[1,3,11-15] The MRA appearance of the carotid web is expected to be similar to that on CTA, though this needs to be studied.

Endarterectomy performed for atherosclerotic carotid stenosis typically produces a specimen with a classic atheroma, characterized by a large necrotic lipid-rich core covered by a fibrous cap. A thin rim of atrophic media is often adherent to the outer aspect of the atheroma. The endarterectomy specimen in each of our cases, in contrast, was characterized by thick fibrous intimal cushions associated with a shelf in 1 (Fig 3*A*), dissections in 2 (Fig 3*B*,-*C*), and a mural thrombus in 1 (Fig 3*D*). Fibrous intimal thickening noted in our specimens may be a feature of the intimal variant of fibromuscular dysplasia in the internal carotid artery.[12,13,15,16] The intimal shelf observed in 1 of our patients has been previously described as an intimal variant of FMD.[16] It is also possible that the various forms of asymmetric fibrous intimal cushions observed in the other 3 patients in our study represent part of the spectrum of intimal FMD in the internal carotid artery. Our ability to comment on medial variants of FMD is hampered by a lack of full-thickness medial sampling in our endarterectomy specimens. Medial fibroplasia,[3] medial hyperplasia,[11] and medial dysplasia[10] have all been reported previously, the first 2 from full-segment resection of the carotid artery, while the latter was said to be from an endarterectomy specimen. Carotid webs containing fibroelastic-with-muscular tissue[14] and fibroelastic tissue with areas of myxoid degeneration[8] have also been reported. Most interesting, none of our cases had an abnormal enlargement of the carotid bulb (megacarotid) previously described with carotid webs.[5,17] None of our patients had evidence of FMD in any other vascular bed.

It is likely that the carotid web played an integral part in the stroke mechanism in all our patients. Even a short period of antiplatelet discontinuation appeared to be associated with increased thrombogenicity. In 1 patient, thrombus evolved during antiplatelet therapy, eventually responding to anticoagulant therapy. Regardless of the actual pathology, we postulate that it is the morphology rather than the histology of the web that is important in determining thrombogenicity. We postulate the existence of turbulence and stasis in a cul-de-sac upstream to the web that could potentially create a thrombogenic milieu (Fig 4). Like the left atrial appendage, this thrombogenic milieu may potentially respond best to anticoagulants. It is possible that unlike carotid webs, the small protruding lesions we describe in our retrospective series (Fig 2) may not be as thrombogenic. Although a recent case series seems to suggest that these lesions may have the same pathology as carotid webs, we cannot confirm this.[5] Moreover, 3 of 14 patients with these lesions in our retrospective series had ipsilateral stroke. None of the patients in our prospective case series who had recurrent strokes had this imaging appearance though.

CONCLUSIONS

The carotid web may be an important cause of ischemic stroke in patients with otherwise no determined mechanism of stroke and may present a high risk of recurrent stroke. Intimal variant FMD may be the pathologic diagnosis in most cases. The prevalence of a carotid web in both the general and stroke population is low, and

the optimal management strategy remains unknown. Future effort should be directed at further understanding the epidemiology, etiology, and factors associated with thrombogenicity of these lesions.

ACKNOWLEDGMENTS

We acknowledge the Calgary Stroke Program fellows, nurses, and staff including the research office for helping with the conduct, data collection, and execution of the study. We acknowledge the Seaman Family MR Research Centre and the Hotchkiss Brain Institute for their support.

Disclosures: Andrew M. Demchuk—*UNRELATED*: *Payment for Lectures (including service on Speakers Bureaus)*: Covidien (modest). Mayank Goyal—*UNRELATED*: *Consultancy*: Covidien/ev3, *Comments*: for teaching engagements; *Grants/Grants Pending*: Covidien/ev3,* *Comments*: partial funding for the Evaluation Study of Congestive Heart Failure and Pulmonary Artery Catheterization Effectiveness trial; *Payment for Lectures (including service on Speakers Bureaus)*: Covidien/ev3, *Comments*: for teaching, designing trials. Michael D. Hill—*UNRELATED*: *Stock/Stock Options*: Calgary Scientific Inc, *Comments*: Stock ownership. Calgary Scientific Inc is an image software company. *Money paid to the institution.

REFERENCES

1. Momose KJ, New PF. **Non-atheromatous stenosis and occlusion of the internal carotid artery and its main branches.** *Am J Roentgenol Radium Ther Nucl Med* 1973;118:550–66 CrossRef Medline
2. Osborn AG, Anderson RE. **Angiographic spectrum of cervical and intracranial fibromuscular dysplasia.** *Stroke* 1977;8:617–26 CrossRef Medline
3. Rainer WG, Cramer GG, Newby JP, et al. **Fibromuscular hyperplasia of the carotid artery causing positional cerebral ischemia.** *Ann Surg* 1968;167:444–46 CrossRef Medline
4. Karlson KJ, Wolf B, Neptune WB. **Symptomatic carotid stenosis secondary to an intraluminal web: a case report.** *Vasc Endovascular Surg* 1987;21:422–26 CrossRef
5. Joux J, Chausson N, Jeannin S, et al. **Carotid-bulb atypical fibromuscular dysplasia in young Afro-Caribbean patients with stroke.** *Stroke* 2014;45:3711–13 CrossRef Medline
6. Menon BK, Smith EE, Modi J, et al. **Regional leptomeningeal score on CT angiography predicts clinical and imaging outcomes in patients with acute anterior circulation occlusions.** *AJNR Am J Neuroradiol* 2011;32:1640–45 CrossRef Medline
7. Kliewer MA, Carroll BA. **Ultrasound case of the day: internal carotid artery web (atypical fibromuscular dysplasia).** *Radiographics* 1991;11:504–05 CrossRef Medline
8. Gironell A, Martí-Fàbregas J, de Juan-Delago M, et al. **Carotid pseudo-valvular fold: a probable cause of ischaemic stroke.** *J Neurol* 1995;242:351–53 CrossRef Medline
9. Cordoliani MA, Lucas C, Durieu I, et al. **Carotid pseudovalvular fold: a case diagnosed by angiography and helical cervical tomography.** *Stroke* 1996;27:1010 Medline
10. Perren F, Urbano L, Rossetti AO, et al. **Ultrasound image of a single symptomatic carotid stenosis disclosed as fibromuscular dysplasia.** *Neurology* 2004;62:1023–24 CrossRef Medline
11. Gee W, Burton R, Stoney RJ. **Atypical fibromuscular hyperplasia involving the carotid artery.** *Ann Surg* 1974;180:136–38 CrossRef Medline
12. So EL, Toole JF, Moody DM, et al. **Cerebral embolism from septal fibromuscular dysplasia of the common carotid artery.** *Ann Neurol* 1979;6:75–78 CrossRef Medline
13. Wirth FP, Miller WA, Russell AP. **Atypical fibromuscular hyperplasia. Report of two cases.** *J Neurosurg* 1981;54:685–89 CrossRef Medline
14. McNamara MF. **The carotid web: a developmental anomaly of the brachiocephalic system.** *Ann Vasc Surg* 1987;1:595–97 CrossRef Medline
15. Morgenlander JC, Goldstein LB. **Recurrent transient ischemic attacks and stroke in association with an internal carotid artery web.** *Stroke* 1991;22:94–98 CrossRef Medline
16. Touzé E, Oppenheim C, Trystram D, et al. **Fibromuscular dysplasia of cervical and intracranial arteries.** *Int J Stroke* 2010;5:296–305 CrossRef Medline
17. Kubis N, Von Langsdorff D, Petitjean C, et al. **Thrombotic carotid megabulb: fibromuscular dysplasia, septae, and ischemic stroke.** *Neurology* 1999;52:883–86 CrossRef Medline

Morphologic Features of Carotid Plaque Rupture Assessed by Optical Coherence Tomography

S. Shindo, K. Fujii, M. Shirakawa, K. Uchida, Y. Enomoto, T. Iwama, M. Kawasaki, Y. Ando, and S. Yoshimura

ABSTRACT

BACKGROUND AND PURPOSE: Rupture of the plaque fibrous cap and subsequent thrombosis are the major causes of stroke. This study evaluated morphologic features of plaque rupture in the carotid artery by using optical coherence tomography in vivo.

MATERIALS AND METHODS: Thirty-six carotid plaques with high-grade stenosis were prospectively imaged by optical coherence tomography. "Plaque rupture" was defined as a plaque containing a cavity that had overlying residual fibrous caps. The fibrous cap thickness was measured at its thinnest part for both ruptured and nonruptured plaques. The distance between the minimum fibrous cap thickness site and the bifurcation point was also measured. Optical coherence tomography identified 24 ruptured and 12 nonruptured plaques.

RESULTS: Multiple ruptures were observed in 9 (38%) patients: Six patients had 2 ruptures in the same plaque, 2 patients had 3 ruptures in the same plaque, and 1 patient had 5 ruptures in the same plaque. Most (84%) of the fibrous cap disruptions were identified at the plaque shoulder and near the bifurcation point (within a 4.2-mm distance). The median thinnest cap thickness was 80 μm (interquartile range, 70–100 μm), and 95% of ruptured plaques had fibrous caps of $<$130 μm. Receiver operating characteristic analysis revealed that a fibrous cap thickness of $<$130 μm was the critical threshold value for plaque rupture in the carotid artery.

CONCLUSIONS: Plaque rupture was common in high-grade stenosis and was located at the shoulder of the carotid plaque close to the bifurcation. A cap thickness of $<$130 μm was the threshold for plaque rupture in the carotid artery.

ABBREVIATION: OCT = optical coherence tomography

Rupture of the fibrous cap and subsequent thrombosis are the major causes of cardiovascular events such as heart attack and stroke.[1-3] In a previous study of sudden coronary death, a fibrous cap thickness of 65 μm was chosen as a criterion of instability because for a cap to rupture, the average cap thickness was 23 $\pm$ 19 μm; 95% of caps measured $<$65 μm within a limit of only 2 SDs.[1] Therefore, the fibrous cap thickness of $<$65 μm is now widely accepted as the definition of in vivo coronary vulnerable plaque that is prone to rupture. Disruption of the fibrous cap is frequently observed in symptomatic carotid plaques[4,5] and is strongly associated with an ulceration appearance on angiography,[6] which is considered an independent predictor of stroke on long-term follow-up in patients with symptomatic severe carotid stenosis.[7] Redgrave et al[8] examined the cross-sections of plaques with high-grade carotid stenosis and found that the optimum fibrous cap thickness for discriminating ruptured and nonruptured plaques was 200 μm; thus, it appears that there is no clear threshold for classifying plaques that are prone to rupture in vivo.

Intravascular sonography, which is a widely used imaging method in the field of carotid artery intervention, has an axial resolution of 100–200 μm and a lateral resolution of 250 μm.[9] Although it can visualize deep structures, intravascular sonography is not a suitable imaging technique for the detection of thin fibrous caps because its resolution is too low. Optical coherence tomography (OCT) has been introduced recently as a high-resolution imaging method.[10,11] The typical OCT image has an axial resolution of 10 μm, approximately 10 times higher than that of any other clinically available diagnostic imaging technique, such as intravascular sonography. OCT provides an accurate representation of the thickness of the

Received January 6, 2015; accepted after revision March 23.

From the Department of Neurology (S.S., Y.A.), Graduate School of Medical Science, Kumamoto University, Kumamoto, Japan; Department of Neurosurgery (S.S., M.S., K.U., S.Y.) and Cardiovascular Division (K.F.), Hyogo College of Medicine, Nishinomiya, Japan; and Departments of Neurosurgery (Y.E., T.I.) and Cardiology (M.K.), Gifu University Graduate School of Medicine, Gifu, Japan.

Please address correspondence to Shinichi Yoshimura, MD, PhD, Hyogo College of Medicine, Department of Neurosurgery, Mukogawa-cho, Nishinomiya, Hyogo, 6638501, Japan; e-mail: shinyoshi523@me.com

http://dx.doi.org/10.3174/ajnr.A4404

fibrous cap that could not be measured by other imaging modalities.[12] In the present study, we evaluated the morphologic features of ruptured plaques in the carotid artery by using OCT.

MATERIALS AND METHODS

Study Population

Between March 2012 and November 2013, a prospective but nonconsecutive series of 38 carotid arteries in 36 patients who were scheduled for carotid artery stenting to treat a high-grade stenosis in previously untreated carotid arteries underwent diagnostic OCT examinations to evaluate plaque morphology. OCT was performed only when carotid artery stenting was planned under proximal protection methods, due to the need for continuous injection of saline and contrast through the guiding catheter to remove blood from the FOV. Patients with a moderate stenosis at the proximal common carotid artery, a very tight stenosis at the target lesion, and intramural thrombus suspected on the basis of other modalities were not enrolled in this study because of the potential difficulty in acquiring and interpreting OCT images with such conditions. OCT examinations were performed for 38 carotid arteries in 36 patients, with 2 patients undergoing bilateral carotid artery stenting. Two patients were excluded because of poor OCT images. Finally, 36 carotid arteries in 34 patients were considered eligible for performing OCT image assessments. The grade of carotid stenosis was assessed by using angiography,[13] and indications for carotid artery stenting were based on the Stenting and Angioplasty with Protection in Patients at High Risk for Endarterectomy trial.[14] Because OCT is approved only for coronary arteries, its use in human carotid arteries was approved by our institutional ethics committee (No. 21–108), and the study protocol was submitted to an open-access data base (University Hospital Medical Information Network, trial number UMIN 000002808; http://www.umin.ac.jp/english/). Informed consent was obtained from all patients before participation.

OCT Procedure

Frequency domain OCT imaging was performed by using a C7-XR OCT imaging system (St. Jude Medical, St. Paul, Minnesota). A 9F guiding catheter with an occlusion balloon was inserted into the common carotid artery, and a guidewire with an occlusion balloon (GuardWire; Medtronic, Minneapolis, Minnesota) was introduced into the external carotid artery; or a 9F Mo.Ma system (Medtronic), which has 2 compliant balloons, was inserted where the distal balloon was located in the external carotid artery and the proximal balloon was located in the common carotid artery. Following a Z offset adjustment, an OCT imaging catheter (Dragonfly; St. Jude Medical) was advanced into the carotid artery beyond the stenotic site over a 0.014-inch microguidewire. After the OCT catheter placement, a carefully debubbled mixture of saline and contrast (1:1 dilution) (iomeprol, Iomeron 300; Bracco, Milan, Italy) at 37°C was flushed through the guiding catheter at a rate of 6 mL/s for a 5-second period by using a motor-driven injector. When a blood-free image was observed, the OCT imaging core was withdrawn by using a stand-alone electronic control of the pullback motor. We stored OCT images digitally for subsequent analysis.

OCT Imaging Analysis

All images were recorded digitally and analyzed by 2 independent investigators who were blinded to the clinical presentations and angiographic findings. Qualitative OCT assessment was performed for each artery by using previously published criteria.[15] Plaques were classified as the following: 1) fibrous (homogeneous with high backscatter regions), 2) lipid-rich (low-signal region with diffuse border), or 3) calcified (low backscattering signal with a sharp border inside a plaque). For all nonruptured plaques that were determined lipid-rich with OCT, the fibrous cap thickness was measured at its thinnest part. The cap thicknesses were measured 3 times, and the average value was calculated. The distance between the minimum fibrous cap thickness site and the carotid bifurcation point was measured. "Plaque rupture" was defined as a plaque containing a cavity that was in contact with the lumen that had any overlying residual fibrous cap fragment.[16] Rupture sites separated by a length of artery containing smooth lumen contours and no cavity were considered to represent different plaque ruptures. The thinnest cap thickness was measured at the thinnest part of the remnant of the disrupted fibrous cap. The distance between the plaque rupture site and the carotid bifurcation point was also measured. The largest intraplaque cavity was measured and extrapolated to the ruptured capsule area. Representative measurements of the thinnest part of ruptured and nonruptured caps are shown in Fig 1. "Thrombus" was defined as a backscattering protrusion into the carotid lumen with signal-intensity-free shadowing.[17] "Neovascularization" was defined as a microchannel structure with no signal intensity without a connection to the vessel lumen that was present in ≥3 continuous cross-sections of the OCT images.[18]

Identification of 2 separate plaques in the same artery (ie, infarct-related versus non–infarct-related lesion) required a 5-mm reference segment between them; if not, they were considered to be part of 1 long lesion.

Statistical Analysis

JMP, Version 10.0 (SAS Institute, Cary, North Carolina) was used for all statistical analyses. Categoric data were expressed as absolute frequencies and percentages and were compared by using the χ^2 or Fisher exact test, as appropriate. Continuous variables were expressed as either mean ± SD for normally distributed variables or median (interquartile range, 25th to 75th percentiles) for non-normally distributed variables and were compared by using either an unpaired Student *t* test or a Mann-Whitney *U* test, respectively. Receiver operating characteristic analysis was used to determine the best cutoff cap thickness values for discriminating ruptured and nonruptured plaques. The κ statistic was used to define the level of intra- and interobserver agreement in the identification of plaque rupture. The interobserver variability for measuring the fibrous cap thickness was assessed by linear regression analysis. $P < .05$ was regarded as a statistically significant difference.

RESULTS

The average time required for the OCT examination was 5.6 ± 1.3 minutes. No technical or neurologic complications were encountered during OCT procedures, though transient carotid artery occlusion and continuous infusion of saline and contrast media were nec-

essary during the time required for imaging. The average pullback length imaged by OCT was 54 mm. Among all of the 36 arteries examined, OCT identified 24 ruptured (67%) and 12 nonruptured (33%) plaques.

Patient Characteristics

Patient characteristics and angiographic findings are presented in Table 1. There were no statistically significant differences in terms of age, sex, or other important stroke risk factors between patients with plaque rupture and those without plaque rupture.

Fibrous Cap Thicknesses between Ruptured and Nonruptured Plaques

Thirty-eight plaque ruptures in 24 arteries were identified by OCT. Of the 24 arteries with plaque ruptures, multiple ruptures were observed in 9 arteries (38%): Six patients had 2 OCT ruptures in the same artery, 2 patients had 3 ruptures each in the same artery, and 1 patient had 5 ruptures in the same artery. In the remaining 12 arteries without plaque ruptures, OCT identified 12 nonruptured lipid-rich plaques in which the fibrous cap thickness could be reliably measured. OCT findings are summarized in Table 2. Among the findings presented, neovascularization was frequently identified in ruptured plaques compared with nonruptured plaques (54% versus 17%, $P < .03$). The median cap thickness at the thinnest part of the cap was significantly thinner in ruptured fibrous caps than in nonruptured fibrous caps (80 μm [interquartile range, 70–100 μm] versus 175 μm [155–238 μm]; $P < .001$) The fibrous cap thickness was thinner than 130 μm in 95% of ruptured plaques and thicker than 130 μm in 85% of nonruptured plaques. Figure 2 shows the frequency distribution of ruptured and nonruptured plaques according to the cap thickness measured at the thinnest part. On the basis of the receiver operating characteristic analysis, the optimal cap thickness for predicting plaque rupture was <130 μm (Fig 3).

The κ statistic for intraobserver and interobserver variability for plaque rupture imaging was 1.00 and 1.00, respec-

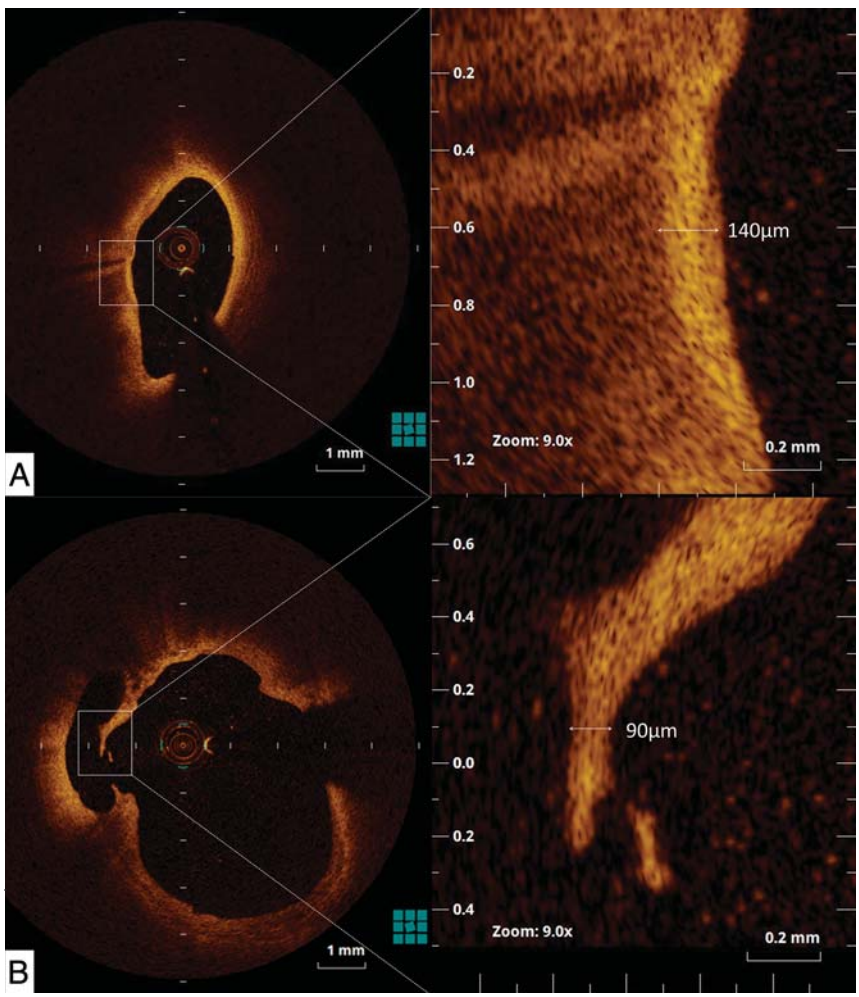

FIG 1. Representative measurements of nonruptured (*A*) and ruptured (*B*) fibrous cap thickness at the thinnest part. In these specimens, the thickness of the fibrous cap measured 140 μm for a nonruptured lipid-rich plaque (*A*), and 90 μm for a ruptured plaque (*B*)

Table 1: Patient and angiographic characteristics[a]

	Ruptured Plaques (*n* = 24)	Nonruptured Plaques (*n* = 12)	*P* Value
Age (yr)	72 ± 9	72 ± 6	.85
Male sex (%)	22 (92)	10 (83)	.47
Imaged artery			.64
Right	12 (50)	10 (83)	
Left	12 (50)	2 (17)	
Symptomatic (%)	11 (46)	5 (42)	.8
Hypertension (%)	17 (71)	11 (92)	.13
Diabetes mellitus (%)	14 (58)	5 (42)	.34
Dyslipidemia (%)	16 (67)	9 (75)	.61
Degree of stenosis (%)	79 ± 12	75 ± 14	.48
Aspirin (%)	19 (79)	11 (92)	.32
Clopidogrel (%)	22 (92%)	11 (92)	1.00
Cilostazol (%)	10 (42)	4 (33)	.63

[a] Data are given as mean ± SD or No. (%).

Table 2: Qualitative OCT analysis[a]

	Ruptured Plaques (*n* = 24)	Nonruptured Plaques (*n* = 12)	*P* Value
Plaque morphology			.19
Fibrous	2 (8)	0 (0)	
Lipid-rich	22 (92)	12 (100)	
Calcified	0 (0)	0 (0)	
Thrombus (%)	9 (38)	3 (25)	.45
Neovascularization (%)	13 (54)	2 (17)	.03

[a] Data are given as No. (%).

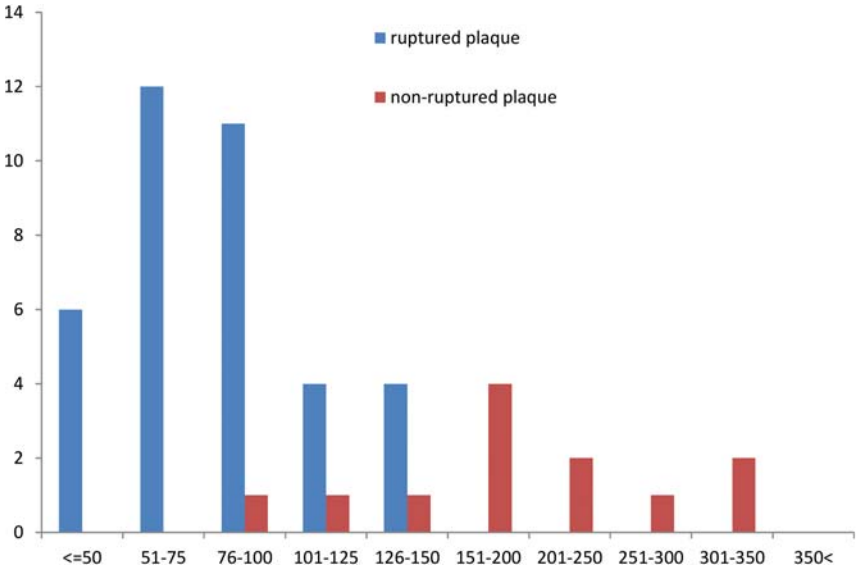

FIG 2. The frequency distribution of ruptured and nonruptured plaques according to the cap thickness at the thinnest part. Although the thinnest fibrous cap of ruptured plaques was <150 μm for all plaques, most nonruptured plaques had thicker fibrous caps.

tively. The measurement of fibrous cap thickness by OCT showed excellent interobserver reproducibility ($r = 0.73$, $P < .01$).

Spatial Distribution and the Largest Ulcer Areas of Ruptured Plaques

Eight ruptured sites (21%) were located in the common carotid artery, and 30 (79%), in the internal carotid artery. The median area of the ruptured plaque cavity measured 1.38 mm^2 (interquartile range, 0.35–3.03 mm^2). In all plaque ruptures, the site of the original tear in the fibrous cap could be identified; 26% (10/38) of tears appeared to have occurred in the center of the plaque, and the rest (74%), at the shoulder of the plaque. The image section with plaque rupture was located at the narrowest lumen site in only 6 (16%) plaques. A representative case that has plaque ruptures at the shoulder of the plaque is shown in Fig 4. The rupture site was proximal to the narrowest lumen site in 22 plaques (58%) and distal to the narrowest lumen site in 10 plaques (26%). In all plaques, the image section with the narrowest lumen area was near the bifurcation point. The median distance between the narrowest lumen site and the bifurcation point measured 4.2 mm (interquartile range, 2.2–13.8 mm) in ruptured plaques and 6.7 mm (interquartile range, 3.0–8.8 mm) in nonruptured plaques ($P = .67$). Similarly, the median distance between the fibrous cap thickness at the thinnest part and the bifurcation point was 4.6 mm (interquartile range, 0–12.0 mm) in ruptured plaques and 5.0 mm (interquartile range, 1.3–10.5 mm) in nonruptured plaques ($P = .82$).

DISCUSSION

The main findings of the present study were the following: Plaque ruptures were frequently observed within carotid arteries with a high-grade stenosis; plaque ruptures may be multiple; fibrous cap thickness of <130 μm was the critical threshold for plaque rupture in the carotid artery; and most of the rupture tears were located at the shoulder of the carotid plaque but close to a side branch.

Fibrous Cap Thicknesses between Ruptured and Nonruptured Plaques

Carotid plaque composition has been proposed as an important risk factor for thromboembolic events, such as stroke, giving rise to the concept of "vulnerable plaque."[19] It has been suggested that thromboembolic phenomena are associated with thinning and subsequent rupture of the fibrous cap on the surface of atherosclerotic plaques, resulting in the release into the parent vessel of necrotic debris from the plaque substance. Several studies have established a correlation between plaque rupture and irregularity with clinical presentation and prognosis.[4,20] Therefore, the identification of the fibrous cap is especially important because its thickness is a major determinant of plaque vulnerability in a lipid-rich carotid plaque.[8] Therefore, the ability to measure the thickness of the fibrous cap accurately in vivo would help identify the carotid vulnerable plaque that is prone to rupture. OCT is a novel intravascular imaging technique, based on infrared light emission, that enables high-resolution arterial wall imaging, in the range of 10–20 μm. OCT penetration through a superficial lipidic component is less than that through fibrous tissue. Although the assessment of necrotic thickness would be an important piece of information, in most lesions, necrotic thickness cannot be measured because of insufficient OCT imaging penetration. In clinical practice, it may not be necessary to visualize the entire wall of a resection cavity; however, OCT analysis of entire suspicious areas of the resection cavity may have some benefit when choosing an optimal treatment strategy. However, the thickness of the fibrous cap is also a major determinant in the vulnerability of atherosclerotic plaque.[21] OCT is the only imaging technique that can resolve intracoronary features on the scale of the thickness of a rupture-prone cap. Kume et al[12] reported that OCT provides an accurate rep-

resentation of the thickness of the fibrous cap that could not be measured by other imaging modalities.

Virmani et al[1] defined plaque vulnerability on the basis of the actual thickness of the histologic section from measurements made of coronary plaque ruptures. A thickness of 65 μm was considered a criterion of plaque instability in the coronary arteries because the average cap thickness was 23 $\pm$ 19 μm in ruptured plaques and 95% of the disrupted caps were <65-μm-thick. Thus, the fibrous cap thickness of <65 μm has been widely used as the definition of in vivo coronary vulnerable plaque that is prone to rupture. Recently, Yonetsu et al[22] evaluated the critical threshold of fibrous cap thickness for coronary plaque rupture by using OCT. They reported that the fibrous cap thickness was <80 μm in 95% of ruptured coronary plaques and the median fibrous cap thickness of ruptured plaques was 54 μm. Although the values of the critical threshold for the disruption of the fibrous cap in coronary plaques are similar regardless of the methodology, there are large discrepancies in the values of the critical threshold for carotid plaques. The critical cap thickness of carotid plaques might be thicker than that of coronary plaques because the hemodynamic forces acting at the carotid bifurcation are greater in the carotid artery.

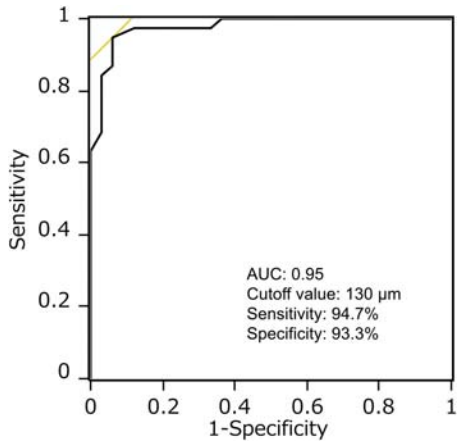

FIG 3. Receiver operating characteristic curves for measurements of fibrous cap thickness for the prediction of fibrous cap rupture. The optimal cap thickness value for predicting rupture was a cap thickness of <130 μm (area under the curve, 0.95; sensitivity, 94.7%; and specificity, 93.3%).

Redgrave et al[8] conducted a histologic evaluation of 526 carotid plaques from patients undergoing endarterectomy for symptomatic severe stenosis. They reported that the median cap thickness was 150 μm in ruptured plaques, and the optimum cutoff for discriminating ruptured and nonruptured plaques was a minimum cap thickness of <200 μm. On the contrary, a previous in vivo study by using sonography found that the critical cap thickness in carotid plaques was 460 μm.[23] In the current OCT study, the median thickness of a fibrous cap at the thinnest part was 80 μm and 95% of ruptured plaques had a fibrous cap thickness that was thinner than 130 μm. Possible reasons for the large discrepancy between the current OCT study and the previous sonography and postmortem studies are not entirely clear; however, possible points of difference may include study population variations and a small sample size of ruptured plaques in these studies. However, detection of plaques with complex morphology, such as a thin-cap fibroatheroma, may be more precise with OCT than with sonography because the higher resolution of OCT permits accurate measurement of the thin fibrous cap.

Spatial Distribution of Ruptured Plaques

From postmortem studies, it is known that fibrous caps vary widely in thickness, cellularity, matrix, strength, and stiffness, but they are often thinnest (and macrophage infiltration is greatest) at their shoulder regions where disruption most frequently occurs.[24] The current study revealed that plaque ruptures were distinct

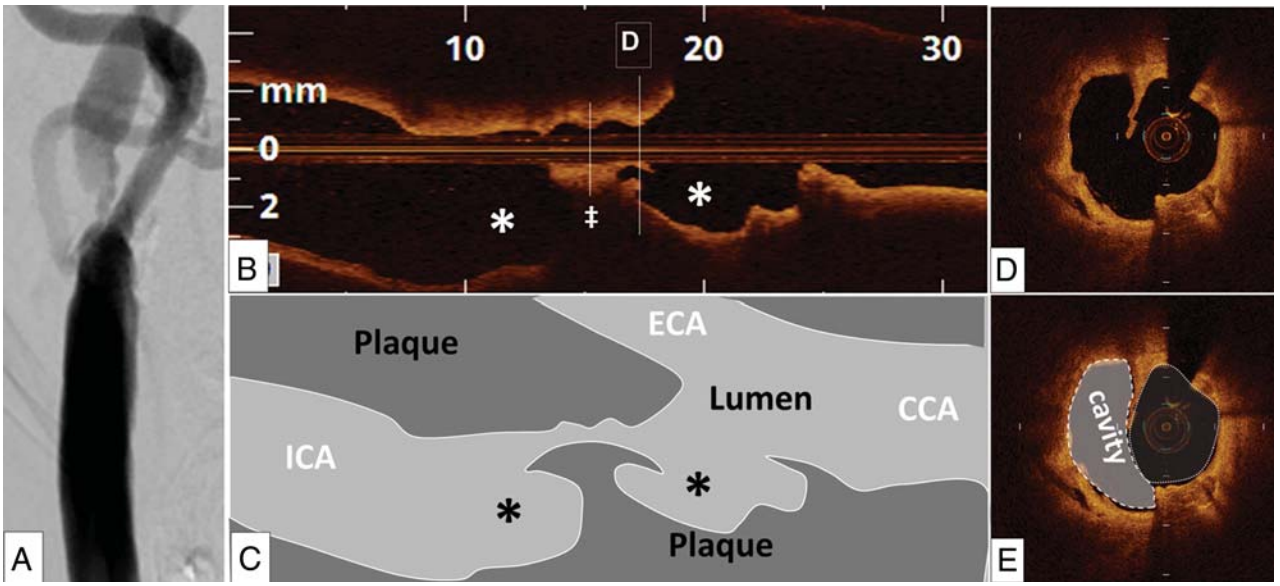

FIG 4. A representative patient (64-year-old man) with a 90% stenosis in the right internal carotid artery. A high-grade stenosis in the internal carotid artery was identified on the angiogram (*A*). The disruptions of the plaques (*asterisks*) were identified near the bifurcation, but not at the narrowest lumen site (*double dagger*) in the optical coherence tomography longitudinal view (*B* and *C*). A ruptured plaque contains a cavity that communicates with the lumen with an overlying residual fibrous cap fragment (*D* and *E*).

from minimum lumen sites in 74%. These data confirm previous reports showing that plaque rupture occurs most often at the shoulder of the plaque.[25] A previous histopathologic study demonstrated that inflammation of the atherosclerotic cap and shoulder of the plaque was a common and locally observed phenomenon in coronary arteries, similar to our findings.[26] Activated metalloproteinases may be expressed more commonly at the shoulder of the vulnerable plaque.[27-29] In the current study, 58% of ruptured plaques were located in the proximal shoulder of the site with the most stenosis; the distance between the location of the minimum cap thickness and the bifurcation point measured 4.6 mm for ruptured plaques and 5.0 mm for nonruptured plaques. Severe stenoses produce flow turbulence that may increase stress on the nearby segment. In addition, endothelial cells near branches of a vessel have a reduced ability to repair wounds compared with cells from nonbifurcation regions.[30]

Study Limitations

Several limitations of the present study should be considered. First, this study was a single-center study with a relatively small study population. Further multicenter studies are required to reconfirm the results in a larger number of patients. Second, because the proximal segments of the target carotid arteries had to be occluded to remove blood from the imaging field during OCT image acquisition, some patients were not enrolled in this study if there was a potential difficulty in performing the proximal segment occlusion. Third, we also excluded patients who received emergent carotid artery stent placement because such patients must be treated as soon as possible. This selection bias might affect the results. Fourth, the penetration depth of OCT imaging is limited almost entirely by basic tissue optical properties and is the chief limitation of the technique, providing between 0.5 and 1.5 mm of imaging depth in most tissue types. Therefore, some ruptured plaques might be missed, especially when the cavity was filled by a lipidic component. Fifth, qualitative assessment of plaque composition by OCT may limit its diagnostic accuracy. However, this study confirmed that OCT demonstrated excellent reproducibility for the identification of plaque rupture. Finally, there are no data showing that OCT provides an accurate representation of the thickness of the fibrous cap in carotid plaques.

CONCLUSIONS

OCT showed that plaque rupture was common in carotid arteries with high-grade stenosis and was located at the shoulder of the carotid plaque close to a side branch. A fibrous cap thickness of <130 μm was the critical threshold for plaque rupture in the carotid artery. Future prospective large-scale in vivo studies are required to validate whether the fibrous cap thickness of <130 μm predicts plaque rupture and subsequent thromboembolic events for patients with carotid artery disease.

REFERENCES

1. Virmani R, Kolodgie FD, Burke AP, et al. **Lessons from sudden coronary death: a comprehensive morphological classification scheme for atherosclerotic lesions.** *Arterioscler Thromb Vasc Biol* 2000;20:1262–75 CrossRef Medline
2. Burke AP, Farb A, Malcom GT, et al. **Coronary risk factors and plaque morphology in men with coronary disease who died suddenly.** *N Engl J Med* 1997;336:1276–82 CrossRef Medline
3. Farb A, Tang AL, Burke AP, et al. **Sudden coronary death: frequency of active coronary lesions, inactive coronary lesions, and myocardial infarction.** *Circulation* 1995;92:1701–09 CrossRef Medline
4. Carr S, Farb A, Pearce WH, et al. **Atherosclerotic plaque rupture in symptomatic carotid artery stenosis.** *J Vasc Surg* 1996;23:755–65; discussion 765–66 Medline
5. Saam T, Cai J, Ma L, et al. **Comparison of symptomatic and asymptomatic atherosclerotic carotid plaque features with in vivo MR imaging.** *Radiology* 2006;240:464–72 CrossRef Medline
6. Lovett JK, Gallagher PJ, Hands LJ, et al. **Histological correlates of carotid plaque surface morphology on lumen contrast imaging.** *Circulation* 2004;110:2190–97 CrossRef Medline
7. Rothwell PM, Villagra R, Gibson R, et al. **Evidence of a chronic systemic cause of instability of atherosclerotic plaques.** *Lancet* 2000;355:19–24 CrossRef Medline
8. Redgrave JN, Gallagher P, Lovett JK, et al. **Critical cap thickness and rupture in symptomatic carotid plaques: the Oxford plaque study.** *Stroke* 2008;39:1722–29 CrossRef Medline
9. Nissen SE, Yock P. **Intravascular ultrasound: novel pathophysiological insights and current clinical applications.** *Circulation* 2001;103:604–16 CrossRef Medline
10. Fujii K, Masutani M, Okumura T, et al. **Frequency and predictor of coronary thin-cap fibroatheroma in patients with acute myocardial infarction and stable angina pectoris a 3-vessel optical coherence tomography study.** *J Am Coll Cardiol* 2008;52:787–88 CrossRef Medline
11. Yoshimura S, Kawasaki M, Yamada K, et al. **OCT of human carotid arterial plaques.** *JACC Cardiovasc Imaging* 2011;4:432–36 CrossRef Medline
12. Kume T, Akasaka T, Kawamoto T, et al. **Measurement of the thickness of the fibrous cap by optical coherence tomography.** *Am Heart J* 2006;152.755.e1-4Medline
13. North American Symptomatic Carotid Endarterectomy Trial Collaborators. **Beneficial effect of carotid endarterectomy in symptomatic patients with high-grade carotid stenosis**. *N Engl J Med* 1991;325:445–53 CrossRef Medline
14. Yadav JS, Wholey MH, Kuntz RE, et al; Stenting and Angioplasty with Protection in Patients at High Risk for Endarterectomy Investigators. **Protected carotid-artery stenting versus endarterectomy in high-risk patients.** *N Engl J Med* 2004;351:1493–501 CrossRef Medline
15. Tearney GJ, Regar E, Akasaka T, et al. **Consensus standards for acquisition, measurement, and reporting of intravascular optical coherence tomography studies: a report from the International Working Group for Intravascular Optical Coherence Tomography Standardization and Validation.** *J Am Coll Cardiol* 2012;59:1058–72 CrossRef Medline
16. Fukunaga M, Fujii K, Nakata T, et al. **Multiple complex coronary atherosclerosis in diabetic patients with acute myocardial infarction: a three-vessel optical coherence tomography study.** *Eurointervention* 2012;8:955–61 CrossRef Medline
17. Kume T, Akasaka T, Kawamoto T, et al. **Assessment of coronary arterial thrombus by optical coherence tomography.** *Am J Cardiol* 2006;97:1713–17 CrossRef Medline
18. Kitabata H, Tanaka A, Kubo T, et al. **Relation of microchannel structure identified by optical coherence tomography to plaque vulnerability in patients with coronary artery disease.** *Am J Cardiol* 2010;105:1673–78 CrossRef Medline
19. Streifler JY, Eliasziw M, Fox AJ, et al. **Angiographic detection of carotid plaque ulceration: comparison with surgical observations in a multicenter study—North American Symptomatic Carotid Endarterectomy Trial.** *Stroke* 1994;25:1130–32 CrossRef Medline

20. Toussaint JF, LaMuraglia GM, Southern JF, et al. **Magnetic resonance images lipid, fibrous, calcified, hemorrhagic, and thrombotic components of human atherosclerosis in vivo.** *Circulation* 1996;94: 932–38 CrossRef Medline
21. Naghavi M, Libby P, Falk E, et al. **From vulnerable plaque to vulnerable patient: a call for new definitions and risk assessment strategies: Part I.** *Circulation* 2003;108:1664–72 CrossRef Medline
22. Yonetsu T, Kakuta T, Lee T, et al. **In vivo critical fibrous cap thickness for rupture-prone coronary plaques assessed by optical coherence tomography.** *Eur Heart J* 2011;32:1251–59 CrossRef Medline
23. Devuyst G, Karapanayiotides T, Ruchat P, et al. **Ultrasound measurement of the fibrous cap in symptomatic and asymptomatic atheromatous carotid plaques.** *Circulation* 2005;111:2776–82 CrossRef Medline
24. Richardson PD, Davies MJ, Born GV. **Influence of plaque configuration and stress distribution on fissuring of coronary atherosclerotic plaques.** *Lancet* 1989;2:941–44 Medline
25. Galis ZS, Sukhova GK, Lark MW, et al. **Increased expression of matrix metalloproteinases and matrix degrading activity in vulnerable regions of human atherosclerotic plaques.** *J Clin Invest* 1994;94: 2493–503 CrossRef Medline
26. Pasterkamp G, Schoneveld AH, van der Wal AC, et al. **Inflammation of the atherosclerotic cap and shoulder of the plaque is a common and locally observed feature in unruptured plaques of femoral and coronary arteries.** *Arterioscler Thromb Vasc Biol* 1999;19:54–58 CrossRef Medline
27. Brown DL, Hibbs MS, Kearney M, et al. **Identification of 92-kD gelatinase in human coronary atherosclerotic lesions: association of active enzyme synthesis with unstable angina.** *Circulation* 1995;91: 2125–31 CrossRef Medline
28. de Kleijn DP, Sluijter JP, Smit J, et al. **Furin and membrane type-1 metalloproteinase mRNA levels and activation of metalloproteinase-2 are associated with arterial remodeling.** *FEBS Lett* 2001;501: 37–41 CrossRef Medline
29. Tang D, Teng Z, Canton G, et al. **Sites of rupture in human atherosclerotic carotid plaques are associated with high structural stresses: an in vivo MRI-based 3d fluid-structure interaction study.** *Stroke* 2009;40:3258–63 CrossRef Medline
30. Akong TA, Gotlieb AI. **Reduced in vitro repair in endothelial cells harvested from the intercostal ostia of porcine thoracic aorta.** *Arterioscler Thromb Vasc Biol* 1999;19:665–71 CrossRef Medline

Dynamic 4D MRI for Characterization of Parathyroid Adenomas: Multiparametric Analysis

K. Nael, J. Hur, A. Bauer, R. Khan, A. Sepahdari, R. Inampudi, and M. Guerrero

ABSTRACT

BACKGROUND AND PURPOSE: The hypervascular nature of parathyroid adenomas can be explored by proper dynamic imaging to narrow the target lesions for surgical exploration. The purpose of this study was to establish MR perfusion characteristics of parathyroid adenomas to differentiate them from their mimics, such as subjacent thyroid tissue and cervical lymph nodes.

MATERIALS AND METHODS: Preoperative high-spatial and -temporal resolution dynamic 4D contrast-enhanced MR imaging in 30 patients with surgically proved parathyroid adenomas was evaluated retrospectively. Using coregistered images, we placed ROIs over the parathyroid adenoma, thyroid gland, and a cervical lymph node (jugulodigastric) to obtain peak enhancement, time-to-peak, wash-in, and washout in each patient. Data were analyzed by logistic regression and analysis of variance. Receiver operating characteristic analysis was performed to determine the optimal parameters for determination of parathyroid adenomas versus thyroid tissue and cervical lymph nodes.

RESULTS: Parathyroid adenomas showed significantly ($P < .05$) faster time-to-peak, higher wash-in, and higher washout compared with cervical lymph nodes and significantly ($P < .05$) higher peak enhancement, faster time-to-peak, higher wash-in, and higher washout compared with thyroid tissue. Logistic regression analysis indicated significant contribution from time-to-peak ($P = .02$), wash-in ($P = .03$), and washout ($P = .008$) for differentiation of parathyroid adenomas from thyroid and cervical lymph nodes. Using receiver operating characteristic analysis, we obtained the best diagnostic accuracy from a combination of time-to-peak/wash-in/washout in the differentiation of parathyroid adenomas versus lymph nodes (area under the curve, 0.96; sensitivity/specificity, 88%/90%) and in distinguishing parathyroid adenomas versus thyroid tissue (area under the curve, 0.96; sensitivity/specificity, 91%/95%).

CONCLUSIONS: Dynamic 4D contrast-enhanced MR imaging can be used to exploit the hypervascular nature of parathyroid adenomas. Multiparametric MR perfusion can distinguish parathyroid adenomas from subjacent thyroid tissue or lymph nodes with diagnostic accuracies of 96%.

ABBREVIATIONS: AUC = area under the curve; CAIPIRINHA = controlled aliasing in parallel imaging results in higher acceleration; PTA = parathyroid adenoma; ROC = receiver operating characteristic; TTP = time-to-peak; TWIST = time-resolved imaging with stochastic trajectories

Single parathyroid adenoma (PTA) is the most common cause of primary hyperparathyroidism, accounting for approximately 80%–90% of all cases.[1] Definitive treatment requires surgical excision, and preoperative localization with imaging is commonly used to decrease the size of surgical incisions and complication rates.[2]

Imaging has been increasingly used for preoperative detection of parathyroid adenomas. While sonography and technetium Tc99m sestamibi scintigraphy have often been used as first-line imaging to localize PTA, these tests are often inconclusive. This situation has led to the development of multiphasic CT (4D CT), which identifies PTAs through their hypervascular perfusion pattern compared with lymph nodes and the thyroid gland. 4D CT has shown superior accuracy compared with scintigraphy,[3] though the radiation dose remains as high as 5.56–10.4 mSv.[4-6]

MR imaging is an attractive alternative to both scintigraphy and 4D CT due to the lack of radiation and has been used for the evaluation of PTAs with some success,[7-9] though not with

Received February 13, 2015; accepted after revision April 12.

From the Departments of Medical Imaging (K.N., J.H., A.B., R.K., R.I.) and Surgery (M.G.), University of Arizona, Tucson, Arizona; Department of Radiology (K.N.), Neuroradiology Section, Icahn School of Medicine at Mount Sinai, New York, New York; and Department of Radiological Sciences (A.S.), University of California, Los Angeles, Los Angeles, California.

Please address correspondence to Kambiz Nael, MD, Department of Radiology, Neuroradiology Section, Mount Sinai Hospital, 1176 5th Ave, Box 1235, New York, NY 10029; e-mail: Kambiznael@gmail.com; @kambiznael

Indicates open access to non-subscribers at www.ajnr.org

Indicates article with supplemental on-line table.

http://dx.doi.org/10.3174/ajnr.A4425

the same effectiveness as 4D CT. Traditional technical limitations to localizing PTAs with MR imaging have recently been addressed with modern MR imaging technology. These include limited spatial and temporal resolution for multiphase dynamic contrast-enhanced MR imaging over a large FOV required for parathyroid imaging. This limitation can be addressed by the use of fast imaging tools such as time-resolved imaging with stochastic trajectories (TWIST)[10] and improved parallel imaging techniques such as controlled aliasing in parallel imaging results in higher acceleration (CAIPIRINHA).[11] The second limitation is inhomogeneity of fat suppression in the neck required for detection of small parathyroid adenomas. The Dixon fat-suppression technique[12] can dramatically improve this shortcoming.[13]

In this study by using a modified dynamic contrast-enhanced sequence with incorporation of a TWIST-CAIPIRINHA combination and the Dixon fat saturation technique, we sought to describe MR perfusion characteristics of PTAs in a cohort of patients with pathology-proved PTA. We hypothesized that MR perfusion biomarkers can differentiate PTA from PTA mimics, such as subjacent thyroid gland and cervical lymph nodes.

MATERIALS AND METHODS

Informed consent was waived by the institutional review board for this retrospective single-institution study. Inclusion criteria were the following: 1) a patient with a known single PTA (confirmed by surgical pathology); and 2) preoperative dynamic 4D contrast-enhanced MR imaging available. Preoperative serum Ca^{2+} and parathyroid hormone levels were also documented for each patient.

Imaging Protocol

All patients underwent MR imaging on a 3T Skyra MR imaging system (Siemens, Erlangen, Germany). A combination of 12-element head and neck coil was used for radiofrequency signal reception. Dynamic 4D contrast-enhanced MR imaging was performed by using a 3D volumetric interpolated examination sequence with the following parameters: TR = 4.06 ms, first TE = 1.31 ms, second TE = 2.54 ms, flip angle = 9°, matrix = 160 mm, FOV = 200 mm, 60 sections × 2 mm thick. To improve inhomogeneity of fat suppression in the neck, we used the Dixon fat-suppression technique as described in prior reports.[12,13] The TWIST view-sharing and Dixon fat/water separation were merged into 1 pulse sequence.[14] Bipolar readout gradients were used to produce 2 partial echoes at the first in-phase (TE = 1.31 ms) and the second opposed-phase (TE = 2.54 ms). Bipolar gradients allowed a shorter TR and less echo asymmetry. Integration of TWIST as an echo-sharing technique with a sampling density of 33% resulted in ×2 acceleration. In addition, CAIPIRINHA with an acceleration factor of 4 was incorporated as a parallel-acquisition technique. This combination resulted in a net acceleration of 8, which was used to acquire a 3D dataset with a voxel size of 1.3 × 1.3 × 2 mm^3 and a temporal resolution of 6 seconds over a craniocaudal coverage of 120 mm, spanning the inferior mandibular rim to the carina. Twenty-four temporal frames were obtained during 140 seconds of acquisition time, 4 before contrast injection to establish a baseline. A total of 0.1 mmol/kg of gadolinium was injected at 4 mL/s.

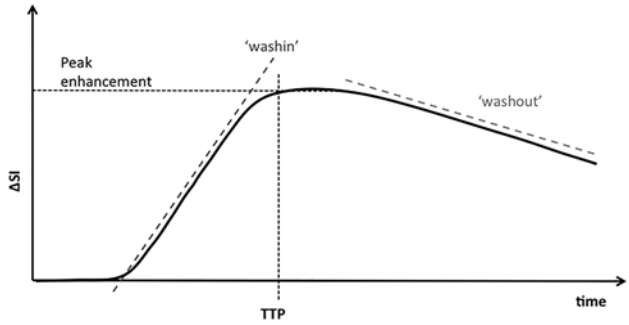

FIG 1. Concentration-time curve. Peak enhancement: maximal concentration of contrast agent with time: $Peak = \max_t C(t)$. Time-to-peak enhancement: the time needed for the contrast agent to reach its maximum concentration: $TTP = \arg\max_t C(t)$. Wash-in: initial upslope of the concentration-time curve (slope from the end of the baseline to the peak of the curve). Washout: down-slope of the concentration time curve (negative slope from the peak to the last acquisition time point). ΔSI indicates change in signal intensity.

Image Analysis

The perfusion datasets were processed by using commercially available US Food and Drug Administration–approved software (Olea Sphere; Olea Medical SAS, La Ciotat, France). Motion correction was implemented automatically by the software. Signal-to-concentration conversion was performed [$C(t) = S(t) - S0$], with *S0* being the baseline signal. The arterial input function was selected automatically to deconvolute the concentration-time curve, assuming a multicompartmental model.[15] The concentration-time curve was then reconstructed from this analysis to obtain a noise-free signal.

Multiparametric quantitative perfusion parameters, including peak enhancement, time-to-peak (TTP), wash-in, and washout, were then computed from the reconvolved concentration-time curve. The wash-in and washout were defined by the initial upslope and downslope of the concentration-time curve, respectively. The definition of these parameters and how they are calculated from the concentration time curves are shown in Fig 1.

Image coregistration was performed by using a 6-*df* transformation and a mutual-information cost function. This was followed by visual inspection to ensure adequate alignment. PTAs were identified by a fellowship-trained neuroradiologist in conjunction with the endocrine surgeon who performed all the surgeries. Using coregistered images, we placed ROIs over the known PTA, thyroid gland, and cervical lymph node (jugulodigastric station). Using the same ROIs, we also calculated the percentage of internal fat content of each PTA on precontrast T1 images before and after Dixon fat saturation.

Statistical Analysis

Statistical analysis was performed by using MedCalc for Windows, Version 14.12.0 (MedCalc Software, Mariakerke, Belgium). The semiquantitative data, including the peak enhancement, TTP, wash-in, and washout values of the PTA, thyroid gland, and cervical lymph node were plotted as mean and SD and tested for

Table 1: Multivariate analysis of MR perfusion parameters for PTA, thyroid gland, and cervical lymph node[a]

	PTA	Thyroid Gland	Lymph Node	ANOVA (*P* Value)
Peak enhancement, AU	360.9 ± 87	214 ± 47	305.3 ± 153	PTA vs thyroid: <.001[b] PTA vs LN: .38
Time-to-peak (seconds)	35.2 ± 12.8	48.7 ± 22.6	64.4 ± 35	PTA vs thyroid: .001[b] PTA vs LN: <.001[b]
Wash-in, AU	7.5 ± 2.6	3.9 ± 1.2	4.4 ± 1.9	PTA vs thyroid: <.001[b] PTA vs LN: <.001[b]
Washout, AU	0.80 ± 0.24	0.43 ± 0.17	0.58 ± 0.31	PTA vs thyroid: <.001[b] PTA vs LN: .016[b]

Note:—LN indicates lymph node; AU, arbitrary units.
[a] Data are means ± SD.
[b] Significant.

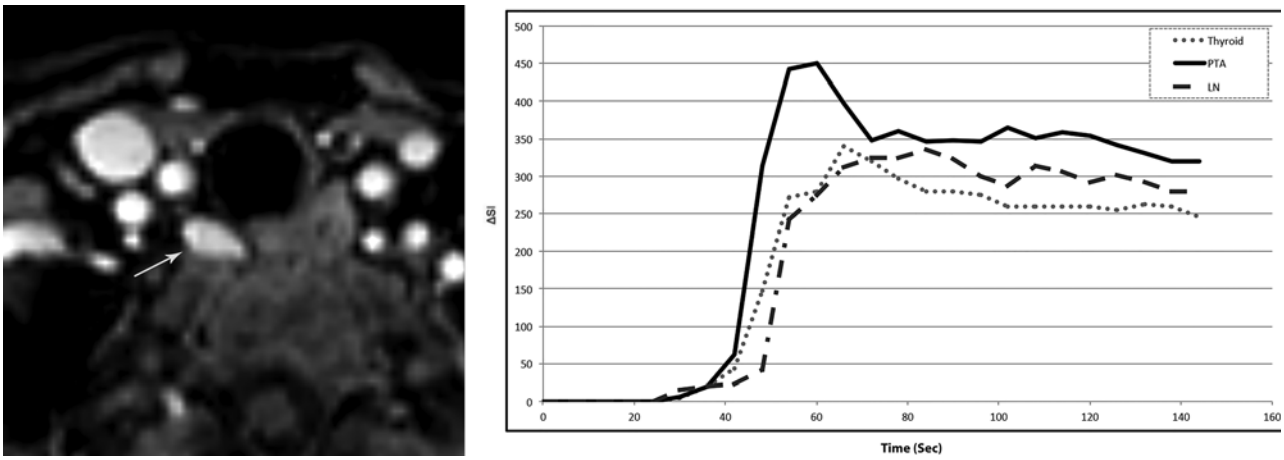

FIG 2. A 68-year-old woman with primary hyperparathyroidism (parathyroid hormone =120 pg/mL, Ca^{2+} = 11.2 mg/dL). Axial arterial phase contrast-enhanced image from MR perfusion demonstrates a PTA (*arrow*) in the right tracheoesophageal groove. Contrast-time curve analysis from ROIs placed over the PTA (*arrow*), thyroid gland, and a jugulodigastric lymph node shows significantly faster TTP and higher wash-in and washout values in the PTA compared with the thyroid gland and cervical lymph node. PTA: TTP, 37 seconds; wash-in, 7.8; washout, 0.58. Thyroid: TTP, 42 seconds; wash-in, 5.4 washout, 0.46. Lymph node: TTP, 60 seconds; wash-in, 4.8; washout, 0.29.

statistical significance by using a repeated-measures ANOVA with protected least-squares-difference post hoc tests. Logistic regression analysis was performed to identify the contribution of each perfusion parameter to the model. Receiver operating characteristic (ROC) analysis was performed to ascertain the optimal parameters and threshold for determination of PTA versus cervical lymph node and thyroid gland.

We calculated optimal thresholds for each ROC curve to maximize both sensitivity and specificity using the Youden statistic. Subsequently, an ROC curve for the combination of parameters was calculated, extrapolating from the maximum-likelihood-estimation model of combining classifiers.[16] The area under the curve was calculated for the ROC curve of each individual classifier and for the combined ROC curves. Correlation coefficients of perfusion parameters in PTA were calculated against the internal fat content of the PTA with 95% confidence intervals. The significance level was defined as $P < .05$.

RESULTS

Thirty patients (20 women, 10 men) with a mean age of 60 years (range, 27–79 years) were included. The preoperative serum Ca^{2+} ranged from 9.9 to 12 mg/dL (mean, 10.92 mg/dL; interquartile range, 10.6–11.2 mg/dL). The preoperative serum parathyroid hormone ranged from 52 to 246 pg/mL (mean, 115.3 pg/mL; interquartile range, 78–147 pg/mL). The percentage of fat content of PTAs ranged from 7.2% to 71% (mean, 38.7%; interquartile range, 21.3%–59.5%). Patient demographic data and the size, weight, and location of parathyroid adenomas are listed in the On-line Table.

Despite using motion correction, we found that in 7 patients (23%), 1–2 temporal frames were affected by motion artifacts. These frames were excluded from perfusion analysis. The mean ± SD of MR perfusion parameters for PTA, thyroid gland, and cervical lymph node and the corresponding *P* values by using ANOVA analysis are summarized in Table 1.

PTA versus Cervical Lymph Node

Three perfusion parameters, including TTP, wash-in, and washout, were significantly different between PTAs and cervical lymph nodes (Table 1). PTAs showed significantly faster arterial enhancement with a mean TTP enhancement of 29 seconds earlier than that in lymph nodes ($P < .001$). PTAs also showed significantly higher ($P < .001$) wash-in and higher ($P < .001$) washout values in comparison with lymph nodes (Fig 2). The peak enhancement was not significantly different between PTAs and cervical lymph nodes ($P = .38$).

ROC curve analyses for differentiation of PTAs versus cervical lymph nodes and PTAs versus thyroid glands are shown in Fig 3. Optimal threshold values, area under the curve (AUC), and corresponding sensitivity and specificity for each perfusion parameter for the differentiation of PTA versus lymph node are summarized in Table 2. With multiparametric

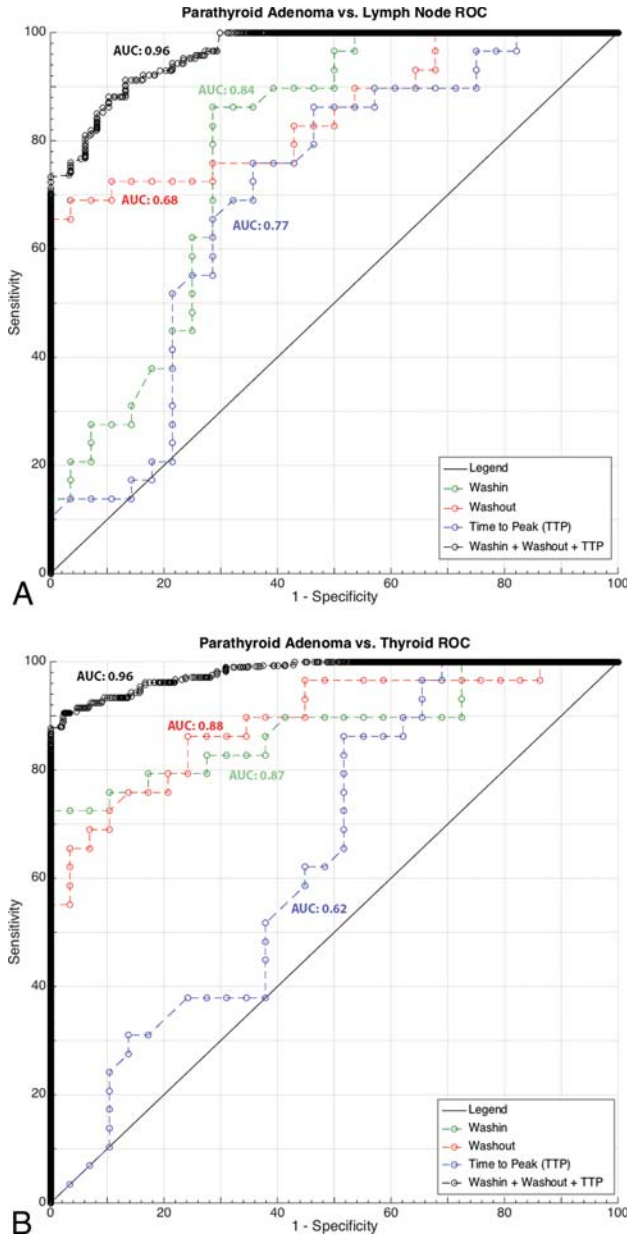

FIG 3. ROC analysis with the AUC for each imaging biomarker and best combined AUC for PTA-versus-lymph node and PTA-versus-thyroid gland is shown.

MR perfusion analysis, a combination of TTP (threshold of <40 seconds), wash-in (threshold of >6.3), and washout (threshold of >0.62) improved the diagnostic power, resulting in an AUC of 0.96 with sensitivity/specificity of 88%/90% for differentiating PTAs (Fig 3).

PTA versus Thyroid Gland

All 4 perfusion parameters were significantly different between PTAs and thyroid glands (Table 1). Again PTAs showed significantly faster arterial enhancement with a mean TTP enhancement difference of 13 seconds earlier than that in thyroid glands ($P = .001$). There was significantly higher peak enhancement ($P < .001$), wash-in ($P < .001$), and washout ($P = .016$) in PTAs compared with thyroid glands (Fig 4).

Optimal threshold values, AUC, and corresponding sensitivity and specificity for each perfusion parameter for the differentiation of PTA versus thyroid gland are summarized in Table 2. The best sensitivity (86%) to differentiate PTA from thyroid gland was obtained by using the TTP value at a threshold of >37 seconds. Wash-in showed the highest specificity (90%) for differentiating PTA versus thyroid gland at a threshold value of >5.27. With multiparametric MR perfusion analysis, a combination of TTP (threshold of >30 seconds), wash-in (threshold of >5.86), and washout (threshold of >0.67) improved the diagnostic power resulting in an AUC of 0.96 with sensitivity/specificity of 91%/95% (Fig 3).

Logistic regression analysis indicated significant contribution from TTP ($P = .02$; 95% CI, 0.88-.99), wash-in ($P = .03$; 95% CI, 1.04–3.06), and washout ($P = .008$; 95% CI, 3.28–37.15) for the differentiation of PTA from thyroid and cervical lymph nodes. There was no contribution from peak enhancement to differentiate PTA from thyroid and cervical lymph nodes ($P = .56$; 95% CI, 0.98–1.00).

Correlation analysis between the percentage of internal fat content and multiparametric perfusion values of PTAs showed only a significant ($P = .019$) negative correlation ($r = -0.632$) with washout values of PTAs. The correlation coefficients between the percentage of internal fat content of PTAs with peak enhancement, time-to-peak, and wash-in values were 0.150, 0.004, and −0.007, respectively.

DISCUSSION

In this study by using a modified MR imaging sequence with incorporation of fast imaging tools, for the first time, we describe MR perfusion characteristics of PTAs. We performed a multiparametric quantitative analysis and showed significant differences between perfusion biomarkers in PTAs versus cervical lymph nodes and thyroid gland. We note 3 findings:

First, the described MR imaging technique has significantly improved the traditional drawbacks of MR imaging, including limited spatial and temporal resolution. Using a modified MR image that incorporates fast imaging tools such as TWIST[10] and CAIPIRINHA[11] has allowed acquisition of multiphase contrast-enhanced MR imaging with high spatial ($1.3 \times 1.3 \times 2$ mm^3) and temporal (6 seconds) resolution.

Fast image acquisition and high spatial resolution have long been major advantages of CT; hence, significant attention has been given to 4D CT for the detection of PTAs. However, the main disadvantage of CT that can be addressed by the described MR imaging technique is radiation.

There is significant ongoing discussion in the literature as to which 4D CT protocol has a better diagnostic accuracy, whether a noncontrast scan is required, and how many postcontrast phases are required for optimal results without the added and unnecessary radiation dose. This discussion is beyond the scope of this article; however, effective radiation doses ranging from 5.56 to 10.4 mSv[4-6] have been reported, depending on the acquisition scheme used.

Our second finding is that the described MR perfusion technique can successfully exploit the hypervascular nature of PTAs, a feature that can be used to differentiate them from PTA candidates such as subjacent cervical lymph node and thyroid tissue.

Table 2: ROC analysis of multiparametric MR perfusion for differentiation of PTA from cervical lymph nodes and thyroid gland

	PTA vs Lymph Node				PTA vs Thyroid Gland			
	AUC	Threshold	Sensitivity	Specificity	AUC	Threshold	Sensitivity	Specificity
Peak enhancement	0.62	>340	65%	64%	0.94	>270	83%	93%
Time-to-peak (seconds)	0.77	<49	66%	71%	0.62	<37	86%	48%
Wash-in	0.84	>5.52	72%	89%	0.87	>5.27	76%	90%
Washout	0.68	>0.62	76%	64%	0.88	>0.63	76%	86%

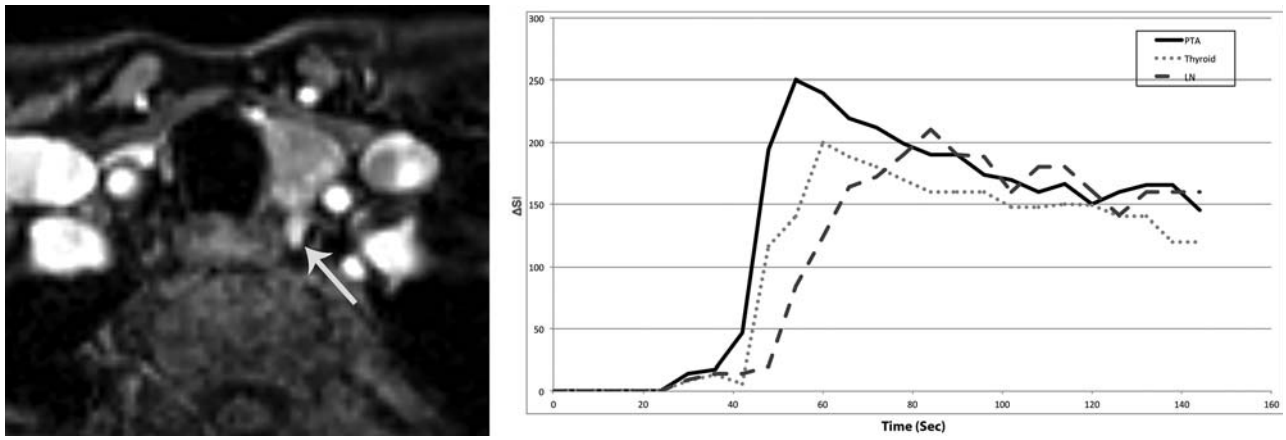

FIG 4. A 47-year-old woman with primary hyperparathyroidism (parathyroid hormone = 164 pg/mL, Ca^{2+} = 10.8 mg/dL). Axial arterial phase contrast-enhanced image from MR perfusion data demonstrates a PTA (*arrow*) in the left tracheoesophageal groove. Contrast-time curve analysis from ROIs placed over the PTA, thyroid gland, and a cervical lymph node shows significantly faster TTP and higher wash-in and significant washout values in the PTA compared with the thyroid gland and cervical lymph node. PTA: TTP, 30 seconds; wash-in, 5.6; washout, 0.64 Thyroid: TTP, 38 seconds; wash-in, 3.8 seconds; washout, 0.43 seconds. Lymph node: TTP, 62 seconds; wash-in, 2.9; washout, 0.23.

The hypervascular nature of PTAs was shown in the 1970s by the use of arterial conventional angiography, demonstrating arterial blush as an indication of PTA against normal thyroid and parathyroid glands.[17,18] Similar principles have been applied to dynamic contrast-enhanced CT and can be applied to MR imaging as shown in our results for the detection of PTAs.

Because continuous CT acquisition during the entire dynamic course of contrast through the parathyroid glands is restricted due to radiation concerns, 4D CT provides only snapshots of contrast dynamics at certain time points (depending on the number of acquisitions). There is no consensus on the number and time-interval between CT acquisitions for an optimal 4D CT.

Therefore investigators have tried to identify acquisition schemes by using a combination of unenhanced and multiple postcontrast phases including 2 phases,[19-21] 2.5 phases,[22,23] 3 phases,[4,24] or 4 phases,[25-27] with the time interval ranging from 30 to 90 seconds, each with strengths and limitations.

Compared with CT, the unique ability of MR imaging to sample many points on the contrast-versus-time curve allowed us to obtain perfusion characteristics such as TTP, peak-enhancement, wash-in, and washout. In our study, TTP and wash-in, 2 characteristics of arterial enhancement, were significantly higher in PTAs, indicative of their hypervascular nature in comparison with cervical lymph nodes and thyroid tissue. PTAs showed significant early arterial enhancement with a mean TTP of 13 and 29 seconds earlier than thyroid tissue and normal cervical lymph nodes, respectively. Logistic regression analysis indicated significant contribution from TTP, wash-in, and washout for the differentiation of PTA from thyroid and cervical lymph nodes but not from peak enhancement.

In addition, we showed the added value of multiparametric quantitative perfusion analysis to improve diagnostic accuracy over a single perfusion classifier to differentiate PTA among PTA candidates such as subjacent thyroid gland and cervical lymph nodes. Using multiparametric MR perfusion and combined ROC analysis, we found that the best overall model to distinguish PTA from cervical lymph node or subjacent thyroid tissue consisted of a combination of TTP, wash-in, and washout, yielding an AUC of 0.96, superior to any individual or combination of other classifiers.

Finally, we found a significant ($P = .019$) negative correlation ($r = -0.632$) between fat content percentage and washout values of PTAs. The clinical significance of this observation is rather unclear at this point. We assume that while TTP and wash-in are indicators of hypervascularity, the washout may be a reflection of the cellular content of PTAs. In other words, there is delayed clearance and contrast washout in lipid-rich adenomas with less cellularity. This finding should be interpreted with caution and within the 2-minute imaging window used in our study because some of these adenomas may further washout later, outside our imaging window.

This study has several limitations, including a relatively small sample size drawn from a single institution, possibly introducing a sample bias. In addition, inclusion of patients with known PTAs can further introduce selection bias. Another limitation is the retrospective nature of the study, possibly introducing unknown bias. The diagnostic accuracy of this MR imaging technique for the localization of PTA should be evaluated prospectively in a larger cohort. The last limitation is the insufficient availability and technical demands due to the 3T MR imaging scanners and mul-

ticoil technology required for parallel imaging and the echo-sharing technique. Although all of these technologies are now commercially available, broad accessibility across imaging centers is still limited.

CONCLUSIONS

Dynamic 4D contrast-enhanced MR imaging can be obtained and used to exploit the hypervascular nature of PTAs. Multiparametric MR perfusion can distinguish PTAs from subjacent thyroid tissue or lymph nodes with a diagnostic accuracy of 96%.

ACKNOWLEDGMENTS

We thank Elizabeth A. Krupinski, PhD, for help with statistical analysis.

Disclosures: Kambiz Nael—*UNRELATED*: *Consultancy*: Olea Medical.* *Money paid to the institution.

REFERENCES

1. Heath H 3rd, Hodgson SF, Kennedy MA. **Primary hyperparathyroidism: incidence, morbidity, and potential economic impact in a community.** *N Engl J Med* 1980;302:189–93 CrossRef Medline
2. Chen H, Mack E, Starling JR. **A comprehensive evaluation of perioperative adjuncts during minimally invasive parathyroidectomy: which is most reliable?** *Ann Surg* 2005;242:375–80; discussion 380–83 Medline
3. Mortenson MM, Evans DB, Lee JE, et al. **Parathyroid exploration in the reoperative neck: improved preoperative localization with 4D-computed tomography.** *J Am Coll Surg* 2008;206:888–95; discussion 895–96 CrossRef Medline
4. Kelly HR, Hamberg LM, Hunter GJ. **4D-CT for preoperative localization of abnormal parathyroid glands in patients with hyperparathyroidism: accuracy and ability to stratify patients by unilateral versus bilateral disease in surgery-naive and re-exploration patients.** *AJNR Am J Neuroradiol* 2014;35:176–81 CrossRef Medline
5. Mahajan A, Starker LF, Ghita M, et al. **Parathyroid four-dimensional computed tomography: evaluation of radiation dose exposure during preoperative localization of parathyroid tumors in primary hyperparathyroidism.** *World J Surg* 2012;36:1335–39 CrossRef Medline
6. Madorin CA, Owen R, Coakley B, et al. **Comparison of radiation exposure and cost between dynamic computed tomography and sestamibi scintigraphy for preoperative localization of parathyroid lesions.** *JAMA Surg* 2013;148:500–03 CrossRef Medline
7. Gotway MB, Reddy GP, Webb WR, et al. **Comparison between MR imaging and 99mTc MIBI scintigraphy in the evaluation of recurrent of persistent hyperparathyroidism.** *Radiology* 2001;218:783–90 CrossRef Medline
8. Lee VS, Spritzer CE, Coleman RE, et al. **The complementary roles of fast spin-echo MR imaging and double-phase 99m Tc-sestamibi scintigraphy for localization of hyperfunctioning parathyroid glands.** *AJR Am J Roentgenol* 1996;167:1555–62 CrossRef Medline
9. Grayev AM, Gentry LR, Hartman MJ, et al. **Presurgical localization of parathyroid adenomas with magnetic resonance imaging at 3.0 T: an adjunct method to supplement traditional imaging.** *Ann Surg Oncol* 2012;19:981–89 CrossRef Medline
10. Song T, Laine AF, Chen Q, et al. **Optimal k-space sampling for dynamic contrast-enhanced MRI with an application to MR renography.** *Magn Reson Med* 2009;61:1242–48 CrossRef Medline
11. Breuer FA, Blaimer M, Heidemann RM, et al. **Controlled aliasing in parallel imaging results in higher acceleration (CAIPIRINHA) for multi-slice imaging.** *Magn Reson Med* 2005;53:684–91 CrossRef Medline
12. Dixon WT. **Simple proton spectroscopic imaging.** *Radiology* 1984; 153:189–94 CrossRef Medline
13. Barger AV, DeLone DR, Bernstein MA, et al. **Fat signal suppression in head and neck imaging using fast spin-echo-IDEAL technique.** *AJNR Am J Neuroradiol* 2006;27:1292–94 Medline
14. Le Y, Kroeker R, Kipfer HD, et al. **Development and evaluation of TWIST Dixon for dynamic contrast-enhanced (DCE) MRI with improved acquisition efficiency and fat suppression.** *J Magn Reson Imaging* 2012; 36:483–91 CrossRef Medline
15. Tofts PS. **Modeling tracer kinetics in dynamic Gd-DTPA MR imaging.** *J Magn Reson Imaging* 1997;7:91–101 CrossRef Medline
16. Haker S, Wells WM 3rd, Warfield SK, et al. **Combining classifiers using their receiver operating characteristics and maximum likelihood estimation.** *Med Image Comput Comput Assist Interv* 2005;8(pt 1):506–14 Medline
17. Doppman JL. **Parathyroid localization: arteriography and venous sampling.** *Radiol Clin North Am* 1976;14:163–88 Medline
18. Miller DL, Doppman JL. **Parathyroid angiography.** *Ann Intern Med* 1987;107:942–43 CrossRef Medline
19. Linda DD, Ng B, Rebello R, et al. **The utility of multidetector computed tomography for detection of parathyroid disease in the setting of primary hyperparathyroidism.** *Can Assoc Radiol J* 2012;63: 100–08 CrossRef Medline
20. Gafton AR, Glastonbury CM, Eastwood JD, et al. **Parathyroid lesions: characterization with dual-phase arterial and venous enhanced CT of the neck.** *AJNR Am J Neuroradiol* 2012;33:949–52 CrossRef Medline
21. Noureldine SI, Aygun N, Walden MJ, et al. **Multiphase computed tomography for localization of parathyroid disease in patients with primary hyperparathyroidism: how many phases do we really need?** *Surgery* 2014;156:1300–06; discussion 1306–07 CrossRef Medline
22. Kutler DI, Moquete R, Kazam E, et al. **Parathyroid localization with modified 4D-computed tomography and ultrasonography for patients with primary hyperparathyroidism.** *Laryngoscope* 2011;121: 1219–24 CrossRef Medline
23. Harari A, Zarnegar R, Lee J, et al. **Computed tomography can guide focused exploration in select patients with primary hyperparathyroidism and negative sestamibi scanning.** *Surgery* 2008;144:970–76; discussion 976–79 CrossRef Medline
24. Chazen JL, Gupta A, Dunning A, et al. **Diagnostic accuracy of 4D-CT for parathyroid adenomas and hyperplasia.** *AJNR Am J Neuroradiol* 2012;33:429–33 CrossRef Medline
25. Starker LF, Mahajan A, Björklund P, et al. **4D parathyroid CT as the initial localization study for patients with de novo primary hyperparathyroidism.** *Ann Surg Oncol* 2011;18:1723–28 CrossRef Medline
26. Beland MD, Mayo-Smith WW, Grand DJ, et al. **Dynamic MDCT for localization of occult parathyroid adenomas in 26 patients with primary hyperparathyroidism.** *AJR Am J Roentgenol* 2011;196:61–65 CrossRef Medline
27. Rodgers SE, Hunter GJ, Hamberg LM, et al. **Improved preoperative planning for directed parathyroidectomy with 4-dimensional computed tomography.** *Surgery* 2006;140:932–40; discussion 940–41 CrossRef Medline

Fusion of Freehand SPECT and Ultrasound to Perform Ultrasound-Guided Fine-Needle Aspiration Cytology of Sentinel Nodes in Head and Neck Cancer

R. de Bree, B. Pouw, D.A. Heuveling, and J.A. Castelijns

ABSTRACT

BACKGROUND AND PURPOSE: Criteria for ultrasound-guided fine-needle aspiration cytology (USgFNAC) for the detection of occult lymph node metastasis in patients with clinically negative head and neck cancer are based on the morphology of cervical lymph nodes. To improve the selection of lymph nodes for USgFNAC, we examined the feasibility of fused freehand single-photon emission tomography ultrasound-guided fine-needle cytology (freehand SPECT-USgFNAC) of sentinel nodes in patients with early stage oral and head and neck skin cancer.

MATERIALS AND METHODS: Six patients with early-stage head and neck cancer (4 oral and 2 head and neck skin cancers) and a clinically negative neck who were scheduled for transoral or local excision and a sentinel node procedure underwent USgFNAC and freehand SPECT-USgFNAC preoperatively.

RESULTS: All freehand SPECT sonographic examinations were technically successful in terms of identifying sentinel nodes. All aspirates of sentinel nodes obtained by freehand SPECT-USgFNAC contained substantial radioactivity, confirming puncture of the sentinel nodes. USgFNAC evaluated 13 lymph nodes; freehand SPECT-USgFNAC, 19 nodes; and sentinel node biopsy, 13 nodes. Three sentinel nodes were histopathologically positive and were selected for aspiration cytology by freehand SPECT-USgFNAC, but not by conventional ultrasound. The cytologic examination findings of the aspirations were negative or inconclusive.

CONCLUSIONS: Freehand SPECT ultrasound can identify sentinel nodes and could potentially improve USgFNAC in patients with head and neck cancer by better selection of lymph nodes at highest risk of having metastases (sentinel nodes), but its sensitivity is limited by sampling error and insufficient aspirated material for cytology.

ABBREVIATIONS: cN0 = clinically node-negative; OSCC = oral squamous cell carcinoma; SN = sentinel node; SNB = sentinel node biopsy; US = ultrasound; USgFNAC = ultrasound-guided fine-needle aspiration cytology

Head and neck cancer has a high propensity for metastasizing through the lymphatics to regional lymph nodes rather than spreading hematogenously. It is universally accepted that the neck has to be treated by either surgery with or without adjuvant radiation or chemoradiation or by primary radiation or chemoradiation when lymph node metastases are present.

In patients with clinically node-negative (cN0) tumors, occult metastases or micrometastases are still present in approximately 30% of cases. Clinical staging by palpation is typically followed by imaging with CT, MR imaging, positron-emission tomography, ultrasound (US), and/or ultrasound-guided fine-needle aspiration cytology (USgFNAC).[1,2] USgFNAC is the most reliable of these diagnostic techniques, with a sensitivity of 48%–73% and a specificity approaching 100%.[2]

In an attempt to select the lymph nodes most likely to contain metastases, the sentinel node (SN) concept has been introduced. Sentinel node biopsy (SNB) is a diagnostic staging procedure that is applied in a variety of tumor types, including head and neck skin cancers and oral squamous cell carcinoma (OSCC). The procedure aims to identify the first draining lymph nodes, the SNs that are most likely to have metastases. The histopathologic status of the SN should reflect that of the rest of the nodal basin, and additional treatment of the nodal basin (eg, lymph node dissection) should only be performed in case of metastatic involvement of the SN.[3]

Received February 14, 2015; accepted after revision April 14.

From the Departments of Otolaryngology-Head and Neck Surgery (R.d.B., D.A.H.) and Radiology and Nuclear Medicine (J.A.C.), VU University Medical Center, Amsterdam, the Netherlands; Department of Head and Neck Surgical Oncology (R.d.B.), UMC Utrecht Cancer Center, Utrecht, the Netherlands; and Department of Nuclear Medicine (B.P.), Netherlands Cancer Institute-Antoni van Leeuwenhoek Hospital, Amsterdam, the Netherlands.

This work was supported by VUmc Cancer Center Amsterdam.

Please address correspondence to Remco de Bree, MD PhD, Department of Head and Neck Surgical Oncology, UMC Utrecht Cancer Center, UMCU Utrecht, Heidelberglaan 1000, 3584 CX Utrecht, the Netherlands, PO Box 85500,3508 GA Utrecht, the Netherlands; e-mail: r.debree@umcutrecht.nl

http://dx.doi.org/10.3174/ajnr.A4426

SNB is a reliable diagnostic procedure for staging of the cN0 neck and identifying patients with occult nodal metastatic disease. A recent meta-analysis on SNB in early OSCC showed a pooled sensitivity of 92% and a negative predictive value of 88%–100%.[4] More recently, a retrospective study of 90 previously untreated patients with early OSCC with a cN0 neck who underwent SNB (only neck dissection after positive findings on SNB) was performed: A lymphoscintigraphic identification rate of 98%, a surgical detection rate of 99%, and an upstaging rate of 30% were found.[5] SNB has been extensively used in skin cancer, particularly melanoma.[6]

Although less invasive compared with elective neck dissection, SNB is still a surgical procedure. Moreover, SNB is more complex and costly than USgFNAC. Therefore, in most centers in which SNB is used, patients are selected for SNB after negative findings of USgFNAC. USgFNAC may thus avoid unnecessary SNB but would also decrease the risk of false-negative SNB when gross metastatic involvement of the node prohibits tracer uptake. If the sensitivity of USgFNAC can be improved, the better yield of this procedure as a first-line technique may reduce the number of SNBs without jeopardizing oncologic outcome. Additionally, SNB may result in fibrosis, making subsequent neck dissection more difficult. Finally, patients can be scheduled immediately for neck dissection and do not have to wait for the results of the time-consuming and labor-intensive SN procedure.

Criteria for USgFNAC in patients with cN0 OSCC are based on the morphology of the cervical lymph nodes. Lymph nodes with a minimal axial diameter of >4 mm in level II of the neck and 3 mm in other levels of the neck are selected for USgFNAC to obtain a high sensitivity.[7] Inaccurate results of USgFNAC are attributed to an absence of enlarged lymph nodes, aspiration of the wrong lymph node, failure of cytologic analysis due to insufficient material for cytopathologic diagnosis, or the presence of micrometastases in parts of the lymph nodes not aspirated (sampling error). Whereas the conventional selection is based on standard drainage patterns and lymph node size and morphology, lymphatic mapping identifying the SN may improve selection of the lymph nodes with the highest risk of having metastases to be aspirated.

Freehand single-photon emission tomography is an innovative technique aiming to guide the physician to the exact localization of the radioactive area of interest (eg, the SN). Freehand SPECT is a 3D tomographic technique based on the imaging concepts of SPECT, but with the major difference being that it is based on data acquisition by hand-held detectors instead of gantry-based gamma cameras. The technology is designed to use a conventional gamma probe or hand-held gamma camera for the detection of radiation and positioning systems to determine the position of the detector relative to the patient. On the basis of the integration of the acquired set of detector readouts and their position and orientation, the system is capable of generating 3D nuclear images similar to a SPECT image, thus providing visualization of the SN at any time.[8,9] Freehand SPECT can be integrated with video or other imaging modalities.[10] Recently, the fusion of these 3D nuclear images with US, making SN visualization on US possible, was introduced.[11,12] In this setup, functional (fully 3D freehand SPECT) and anatomic (2D ultrasound) information are combined in real-time.

We performed a pilot study to examine the feasibility of freehand SPECT-USgFNAC of SNs in patients with early OSCC and head and neck skin cancer.

MATERIALS AND METHODS

Patient Selection

Six patients with early-stage head and neck cancer (4 OSCCs and 2 head and neck skin cancers) with a cN0 neck who were scheduled for transoral or local excision and an SN procedure underwent USgFNAC and freehand SPECT-USgFNAC preoperatively. This study was approved by the institutional review board.

USgFNAC

In routine USgFNAC, lymph nodes with a minimal axial diameter of >4 mm in level II of the neck and 3 mm in other levels of the neck, absence of an echogenic hilus, presence of coagulation necrosis, and presence of eccentric cortical hypertrophy or hypoechoic sonomorphology were selected for puncture. USgFNAC was obtained by using a syringe holder (Cameco, Täby, Sweden) and a 22-ga needle (Terumo, Sommerset, New Jersey). Lymph nodes were punctured twice. The radiologist performing this procedure had 25 years' experience, and the cytopathologist, >15 years.

Lymphoscintigraphy

The SN procedure was performed according the guidelines of the European Association of Nuclear Medicine and the European Sentinel Node Trial group,[3] within 1 week following USgFNAC. In the 24-hour period before surgery 100 MBq (divided over 4 aliquots of 0.15–0.20 mL each) of technetium Tc99m–labeled nanocolloid (NanoColl; GE Healthcare, Eindhoven, the Netherlands) was injected peritumorally. Directly following injection, dynamic and planar lymphoscintigraphic images were acquired followed by SPECT-CT imaging.

Freehand SPECT-USgFNAC

After complete lymphoscintigraphy (including SPECT-CT), patients underwent freehand SPECT-USgFNAC. The freehand SPECT system (declipse SPECT; SurgicEye, Munich, Germany) combines a hand-held gamma probe system (Crystal Probe; Crystal Photonics, Berlin, Germany; first patient) or a hand-held gamma camera system (CrystalCam; Crystal Photonics; patients 2–6) with an infrared optical tracking system and an integrated data processing unit. To reference a common coordinate system, we taped a configuration of optical and magnetic markers on the sternum or head and used it to determine the position of the patient (see below). The gamma detectors were calibrated to include the 140 keV(peak) of technetium Tc99m with an energy window of 40 keV for the probe and 10 keV for the camera. The collimator opening of the probe was approximately 40°. The gamma camera used a hand-held, semiconductor solid-state scintillator and a solid-state detector-based handheld gamma camera parallel collimator with 16 × 16 holes with dimensions of 2.16 × 2.16 mm^2, resulting in an FOV of 40 × 40 mm^2. See Fig 1 for the clinical setup.

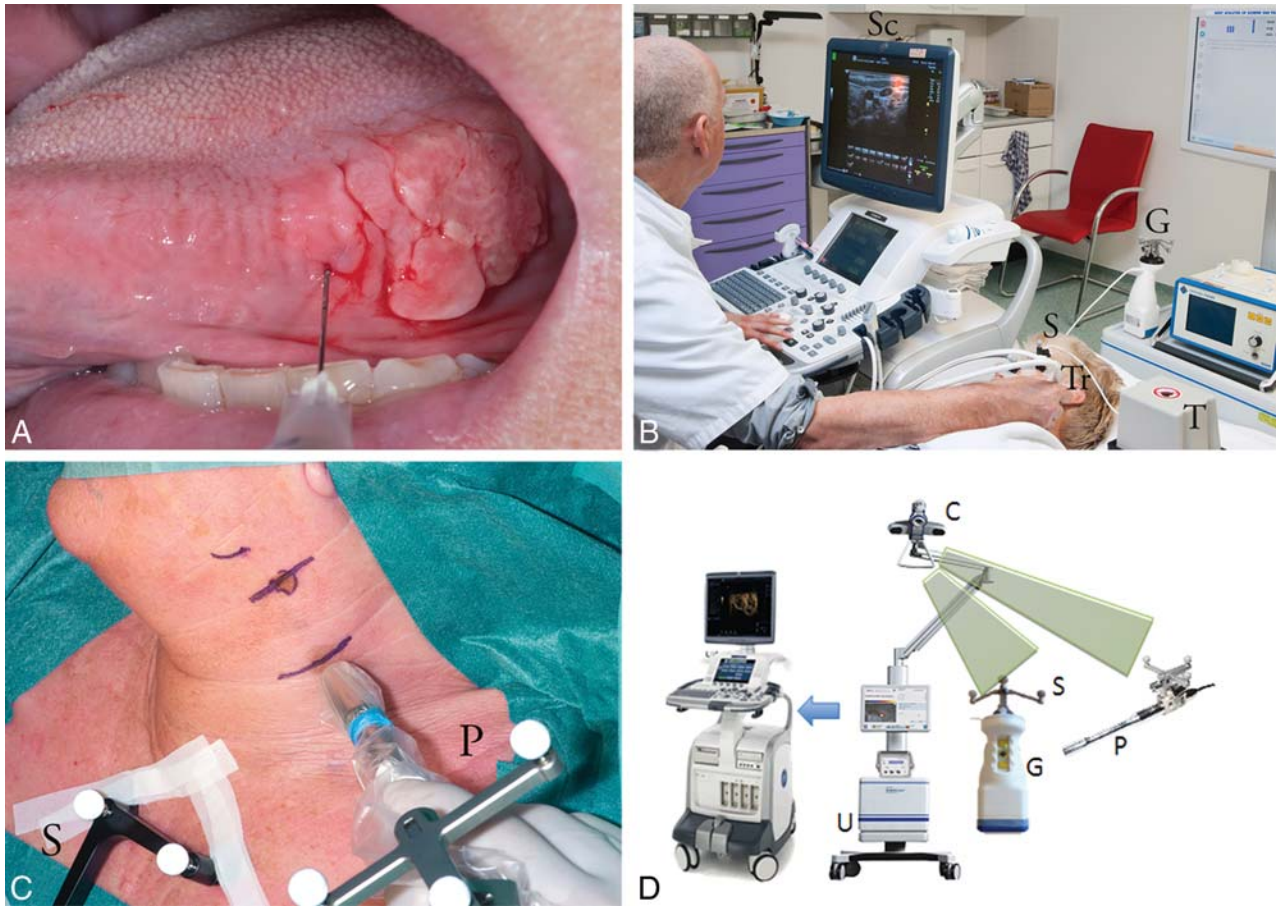

FIG 1. Patient 2 with a T2 lateral tongue carcinoma. *A*, Peritumoral injection of technetium Tc99m labeled–nanocolloid. *B*, Freehand SPECT-US. Note the optical markers on the freehand gamma camera (G), the transmitter generating the magnetic field (T), the electromagnetic sensor attached to the US transducer (Tr), and the shared optical and electromagnetic sensor (S) affixed to the head of the patient. The optical camera is not shown in this image. A fused SPECT-US image is on the screen (Sc) after SPECT data have been loaded onto the US machine in DICOM format by using a USB stick. *C*, Use of freehand SPECT during surgery. Note the optical sensors on the probe (P) and the sternum of the patient (S). *D*, Freehand SPECT and US system with infrared optical tracking system (camera [*C*], detectors [G+P], and sensors [S]) and a data processing unit (U).

To obtain 3D images, we separately scanned each area of preoperatively identified SN by moving the gamma probe or camera in different directions over the skin. Scanning was stopped when the complete volume reached a sufficient information attenuation (as indicated by the system; commonly 1 minute) and thus a sufficient image quality.

US was performed by using a commercially available US system (LOGIQ E9; GE Healthcare, Milwaukee, Wisconsin) configured with Volume Navigation and an ML6–15 US transducer. An electromagnetic transmitter was placed near the imaging area, and a pair of electromagnetic sensors was attached to a bracket that connects to the US transducer. The position-sensing equipment allowed the US device to track the position of the transducer, and therefore the image position, within the electromagnetic field.

To ensure the correct positioning and alignment of both tracking systems, we used the merged common optical/electromagnetic patient reference as mentioned above. The combination of 2 independent tracking systems allowed automatic coregistration of SPECT and US images without the need of user-interaction-like point-based registration (eg, by using anatomic landmarks or surface scanners) as used in commercial surgical navigation suites. As the US image is moved, the freehand SPECT image follows its movement in real-time. The images are displayed side by side or in blended, overlapping format.

Specific attention was paid to avoid movement of the head and neck during the procedure to minimize deviations in the fused images. The head of the patient lay in a holder normally used in the operating room for patients undergoing head and neck surgery.

USgFNAC was performed on the SN visualized on the fused images. The radiologist who performed freehand SPECT-USgFNAC was blinded to the results of planar lymphoscintigraphy and SPECT-CT. Freehand SPECT-US-guided aspirations were performed by using a syringe holder (Cameco) and a 0.6 × 25 mm needle (Terumo). After visualization of the needle inside the lymph node, we started aspiration and continued it by moving the needle gently up and down. Aspirates were checked for radioactivity by counting 60 seconds in a well-counter (1282 Compugamma; LBK Wallac, Turku, Finland) and sent for cytopathologic examination.

Sentinel Node Biopsy

At the start of surgery, 1 mL of Patent Blue V dye diluted 1:3 (volume to volume) in water was injected at 4 equally spaced points to completely surround the tumor. Subsequently, the po-

Primary tumors and results of USgFNAC, aspiration cytology guided by fused images of freehand SPECT-USgFNAC, and SNB of 6 patients with early-stage head and neck cancer

		USgFNAC			Freehand SPECT-USgFNAC			SNB		
Patient	Primary Tumor	Level	Size (mm)	Cytopath	Level	Size (mm)[a]	Counts[b]	Cytopath		Histopath
1	T1 tongue L SCC				II L	2.5	52710	−	II L	−
					II L	1.5	555	−	II L	−
					II L	1.5	35340	−	II L	−
									III R	−
2	T2 tongue L SCC	II L	6.2	−	II L	4.8	3051	−	II L	−
		III L	7.4	−	III L	7.1	40151	−		
		IV L	5.1	−	IV L	4.8	36354	−	IV L	−
3	T2 ala nasi R Merkel cell carcinoma				I R	4.0	2847	0	I R	+ (i+)
					I R	4.3	208	−		
		II R	6.4	−	II R	6.6	204	0		
					I L	4.9	409	0		
4	T1 auricle R melanoma	P R	2.8	−	P R	2.3	74944	−	P R	+ (mi)
					II R	2.4	241233	−	II R	−
5	T2 floor of mouth L SCC	I R	4.5	−	I R	2.8	2782	−	I R	−
					I R	5.8	6707	−		
		I L	4.9	−	I L	3.9	2080	−	I L	−
		I L	4.4	−	I L	3.9	3124	−		
					I L	4.5	553	−		
6	T1 tongue L SCC	R II	4.8	−						
		L I	4.5	−	L I	4.2	207518	−	L I	−
		L I	4.5	−						
		L I	4.5	−						
		L II	5.9	−						
					L II	2.8	45942	−	L II	+ (mi)

Note:—SCC indicates squamous cell carcinoma; Cytopath, cytopathologic examination; Histopath, histopathologic examination; L, left; R, right; P, in parotid gland; i+, isolated tumor cells; mi, micrometastasis; −, tumor negative; 0, inconclusive; + tumor positive.

[a] Size in minimal axial diameter.

[b] Counts per 60 seconds.

sition of the SN was verified by using the freehand SPECT system before the skin incision was made. The 3D navigation modus provides information about the direction and distance of the SN in relation to the tip of the gamma probe and could be displayed in real-time during the procedure. After excision of the SN, the same area was scanned once more and compared with the primary scan on-screen before excision to confirm removal of all SNs.

Histopathologic examination of SNs consisted of step-serial sectioning with an interval of 150–250 μm of the entire lymph node. Of each level, staining with hematoxylin-eosin and pan Cytokeratin Antibody (AE 1/3) was performed. Occult metastases were differentiated into isolated tumor cells (<0.2 mm), micrometastasis (>0.2 mm and ≤2 mm), or macrometastasis (>2 mm). If a nodal tumor deposit was proved by SNB, subsequent neck dissection was performed during a second surgical procedure.

For topographic evaluation, the lymph nodes were scored according to the universally used neck level classification.[13]

RESULTS

All freehand SPECT-US examinations were technically successful in terms of identifying SNs. Deviations of the fused freehand SPECT and US images were limited to a few millimeters, not precluding selection of lymph nodes for freehand SPECT-USgFNAC. All aspirates obtained by freehand SPECT-USgFNAC contained substantial radioactivity, confirming the puncture of the SNs. The results of the USgFNAC, freehand SPECT-USgFNAC, and SNB are summarized in the Table.

Overall 13 lymph nodes were detected as suspicious and sampled on the basis of US alone, and no tumor deposits were found in these nodes. Four of these 13 nodes (all in the last patient) were not SNs as determined by freehand SPECT-US or SNB. Freehand SPECT-US selected 10 (sentinel) lymph nodes for aspiration, which had not been selected by US-only, mainly because the diameter of these nodes was below the selection limit (see, for example, Figs 2 and 3). Freehand SPECT-US also enabled sampling of 7 nodes not resected during the surgical SNB. One negative SN that was not identified by freehand SPECT-US was resected during SNB. Although none of the freehand SPECT-USgFNAC aspirates were positive for lymph node metastases, all 3 positive SNs were selected for puncture by freehand SPECT-US and not by US-only. One SN contained isolated tumor cells, and the other 2 positive SNs contained micrometastasis (0.2 and 0.3 mm). Patients 3 and 4 had no additional lymph node metastases,

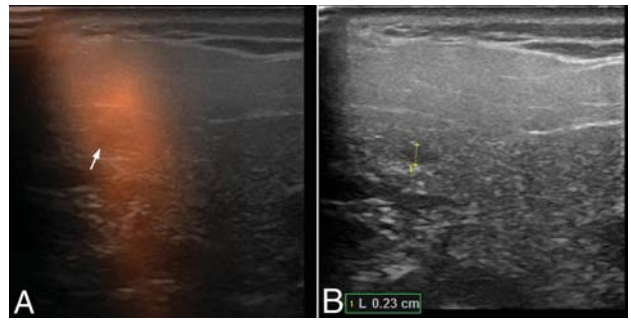

FIG 2. Freehand SPECT-US (*A*) and US-only image (*B*) of a sonographically unremarkable (nonsuspicious) sentinel lymph node of 2.3 mm with micrometastasis in the right parotid gland in patient 4.

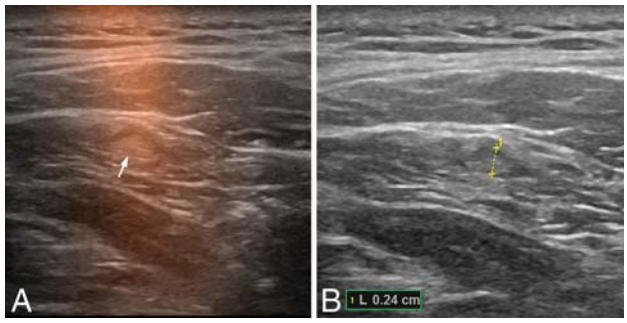

FIG 3. Freehand SPECT-US (*A*) and US-only image (*B*) of a sonographically unremarkable (nonsuspicious) pathologically tumor-negative sentinel lymph node of 2.4 mm in level II on the right side in patient 4.

while patient 6 had 2 additional micrometastatic (nonsentinel) lymph nodes in the neck dissection specimen. During follow-up (including USgFNAC every 3 months) of at least 6 months, none of the patients developed a recurrence in the neck.

DISCUSSION

The present study is the first to report on freehand SPECT-USgFNAC in patients with head and neck cancer, to our knowledge. Freehand SPECT-US mapping of SNs is feasible in patients with early head and neck cancer. Although freehand SPECT-USgFNAC revealed no metastasis, freehand SPECT-US selected the metastatic lymph nodes correctly, whereas US-only did not select these lymph nodes. Moreover, freehand SPECT-USgFNAC allowed evaluation of SNs not identified during SNB (eg, due to blocked drainage by tumor deposits or shinethrough of the injection site, which could reduce the false-negative rate of SNB).

Findings of freehand SPECT-USgFNAC were false-negative in 3 patients, probably due to sampling error and the limited amount of aspirated material (insufficient material for diagnosis) because these 3 lymph nodes contained only isolated tumor cells or micrometastasis. Although polymerase chain reaction techniques may decrease the number of inconclusive diagnoses,[14] sampling error will be inherent in aspiration instead of excisional biopsy of the SN.

A few studies reported on USgFNAC of SNs in early oral cancer. Colnot et al[15] reported in 2001 the initial experiences of VU University Medical Center in 12 patients with oral and oropharyngeal cancer and a cN0 neck. After visualization of the SN, the position was marked on the overlying skin with the use of a point-of-source ^{57}Co marker and was confirmed with a gamma probe. After preparation of the cytologic smears, they counted residues of the aspirates from SNs in a liquid scintillation counter to confirm correct aspiration. Cytologic examination of the aspirated SNs revealed lymph node metastases in 6 patients who underwent neck dissection. In the remaining patients who underwent only transoral excision, 1 false-negative result was observed. They concluded that this combined approach is expected to improve the detection of occult lymph node metastases.[15]

In a further study, Nieuwenhuis et al[16] reported in 2002 that in 39 patients with early oral and oropharyngeal squamous cell carcinoma undergoing conventional and SN-guided USgFNAC, 11 additional lymph nodes were aspirated because of the SN procedure. Because these lymph nodes were all tumor-negative or contained insufficient material at cytologic examination, no additional value of SN aspiration could be demonstrated at that time.[16] In the aforementioned studies, aspiration of radioactivity-only does not prove that the real SN has been aspirated because second-echelon nodes can become radioactive. In the last decade, SN identification has been improved. In the aforementioned studies, no SPECT-CT has been used. SPECT-CT may be especially helpful in the identification and localization of SNs close to the injection site and in differentiation of SNs and second-echelon nodes. Moreover, in the study of Nieuwenhuis et al,[16] late images were only obtained in 9 of 39 patients, potentially missing SNs in oral cavity tumors other than the lateral tongue and floor of mouth and contralateral SNs in or near midline tumors.[17]

Höft et al[18] reported on 16 patients diagnosed with oral, oropharyngeal, or dermal squamous cell carcinoma who had been staged as N0 and who underwent lymphoscintigraphy to localize SNs and USgFNAC on SNs before elective neck dissection. In 14 of 16 patients, an SN could be visualized. Seventeen ipsilateral and 4 contralateral nodes were identified as SNs. No gamma probe was used. In 9 of these 21 SNs, it was difficult to differentiate the SN from other lymph nodes in close proximity by US. In 6 of these 14 patients, lymph node metastases were found in the neck dissection specimen, and all patients had at least macrometastases. In only 1 of these 6 patients was metastasis detected by USgFNAC of the SN.[18] In this study, it is debatable whether without the use of the gamma probe and confirmation of radioactivity in the aspirate, the real SNs were sampled.

Improvement of USgFNAC by aspiration of the real SN can probably increase the sensitivity of the detection of occult lymph node metastasis, but it cannot address the problem of lymph nodes too small for aspiration, insufficient aspirated material, and sampling error. However, any yield in the detection of occult lymph node metastasis by USgFNAC will reduce the number of SNBs needed to give patients with early OSCC the best prognosis without unnecessary extensive diagnostic procedures.

The first clinical results of freehand SPECT have been reported in patients with breast cancer.[19] In head and neck cancer, initial studies described the feasibility of this technique.[20-23] A recent study in 66 patients with early OSCC confirmed that the use of the freehand SPECT system is feasible in the intraoperative detection of sentinel nodes in early-stage oral cancer. Moreover, freehand SPECT provides helpful information facilitating the SN biopsy procedure in a quarter of cases.[24] Freehand SPECT has also been used successfully in malignant melanoma to facilitate the detection and resection of SNs.[25]

Freehand SPECT-US fusion combines the advantages of functional and anatomic information. Freesmeyer et al[11,12] showed that freehand SPECT-US was feasible and technically successful in patients with breast cancer, melanoma, and thyroid disease. However, some technical limitations were shown in freehand SPECT quality and fusion precision.[23,24] The use of a hand-held gamma camera instead of a gamma probe and proper stabilization of the neck as shown in this preliminary study seem to overcome these difficulties. Recently, it has been shown that freehand SPECT-US-guided needle biopsy of sentinel lymph nodes in the axilla is feasible.[26] In the present study, we present the first results of free-

hand SPECT-USgFNAC in 6 patients with early-stage head and neck cancer.

Limitations of this study are the small number of patients included and the lack of pathologically positive freehand SPECT-USgFNAC findings, but the concept and feasibility of sentinel node identification and aspiration by freehand SPECT-USgFNAC are shown. Larger studies are needed to determine the accuracy of this new technique. As a potential pitfall, because the neck is nonrigid, extra attention must be paid to perform the different examinations in positions as similar as possible. A holder for fixation of the head would be helpful.

CONCLUSIONS

Freehand SPECT-US can identify SNs and could improve USgFNAC in patients with head and neck cancer by better selection of lymph nodes at the highest risk of having metastases, but its sensitivity is limited by sampling error and insufficient aspirated material for cytology. Nevertheless, it can potentially reduce the need for SNB, currently the most sensitive technique for the detection of occult lymph node metastases, in patients with head and neck cancer by selecting patients directly for therapeutic neck dissection. Larger studies are needed to assess the additional value of freehand SPECT-USgFNAC.

ACKNOWLEDGMENTS

The authors thank SurgicEye GmbH and GE Healthcare for contributing the hardware and training needed to perform these studies.

REFERENCES

1. Liao LJ, Lo WC, Hsu WL, et al. **Detection of cervical lymph node metastasis in head and neck cancer patients with clinically N0 neck—a meta-analysis comparing different imaging modalities.** *BMC Cancer* 2012;12:236 CrossRef Medline
2. De Bree R, Takes RP, Castelijns JA, et al. **Advances in diagnostic modalities to detect occult lymph node metastases in head and neck squamous cell carcinoma.** *Head Neck* 2014 Jun 21. [Epub ahead of print] CrossRef Medline
3. Alkureishi LW, Burak Z, Alvarez JA, et al; European Association of Nuclear Medicine Oncology Committee, European Sentinel Node Biopsy Trial Committee. **Joint practice guidelines for radionuclide lymphoscintigraphy for sentinel node localization in oral/oropharyngeal squamous cell carcinoma.** *Eur J Nucl Med Mol Imaging* 2009; 36:1915–36 CrossRef Medline
4. Govers TM, Hannink G, Merkx MA, et al. **Sentinel node biopsy for squamous cell carcinoma of the oral cavity and oropharynx: a diagnostic meta-analysis.** *Oral Oncol* 2013;49:726–32 CrossRef Medline
5. Den Toom IJ, Heuveling DA, Flach GB, et al. **Sentinel node biopsy for early-stage oral cavity cancer: the VU University Medical Center experience.** *Head Neck* 2015;37:573–78 CrossRef Medline
6. Morton DL, Thompson JF, Cochran AJ, et al; MSLT Group. **Final trial report of sentinel-node biopsy versus nodal observation in melanoma.** *N Engl J Med* 2014;370:599–609 CrossRef Medline
7. van den Brekel MW, Castelijns JA, Snow GB. **The size of lymph nodes in the neck on sonograms as a radiologic criterion for metastasis: how reliable is it?** *AJNR Am J Neuroradiol* 1998;19:695–700 Medline
8. Wendler T, Hartl A, Lasser T, et al. **Towards intra-operative 3D nuclear imaging: reconstruction of 3D radioactive distributions using tracked gamma probes.** *Med Image Comput Comput Assist Interv* 2007;10(pt 2):909–17 Medline
9. Matthies P, Gardiazabal J, Okur A, et al. **Mini gamma cameras for intra-operative nuclear tomographic reconstruction.** *Med Image Anal* 2014;18:1329–36 CrossRef Medline
10. Matthies P, Okur A, Wendler T, et al. **Combination of intra-operative freehand SPECT imaging with MR images for guidance and navigation.** *Conf Proc IEEE Eng Med Biol Soc* 2013;2013:3383–86 CrossRef Medline
11. Freesmeyer M, Winkens T, Opfermann T, et al. **Real-time ultrasound and freehand-SPECT: experiences with sentinel lymph node mapping.** *Nuklearmedizin* 2014;53:259–64 CrossRef Medline
12. Freesmeyer M, Opfermann T, Winkens T. **Hybrid integration of real-time US and freehand SPECT: proof of concept in patients with thyroid diseases.** *Radiology* 2014;271:856–61 CrossRef Medline
13. Robbins KT, Medina JE, Wolfe GT, et al. **Standardizing neck dissection terminology: Official Report of the Academy's Committee for Head and Neck Surgery and Oncology.** *Arch Otolaryngol Head Neck Surg* 1991;117:601–05 CrossRef Medline
14. Nieuwenhuis EJ, Jaspars LH, Castelijns JA, et al. **Quantitative molecular detection of minimal residual head and neck cancer in lymph node aspirates.** *Clin Cancer Res* 2003;9:755–61 Medline
15. Colnot DR, Nieuwenhuis EJ, van den Brekel MW, et al. **Head and neck squamous cell carcinoma: US-guided fine-needle aspiration of sentinel lymph nodes for improved staging—initial experience.** *Radiology* 2001;218:289–93 CrossRef Medline
16. Nieuwenhuis EJ, Castelijns JA, Pijpers R, et al. **Wait-and-see policy for the N0 neck in early-stage oral and oropharyngeal squamous cell carcinoma using ultrasonography-guided cytology: is there a role for identification of the sentinel node?** *Head Neck* 2002;24: 282–89 CrossRef Medline
17. Heuveling DA, Flach GB, van Schie A, et al. **Visualization of the sentinel node in early-stage oral cancer: limited value of late static lymphoscintigraphy.** *Nucl Med Commun* 2012;33:1065–69 CrossRef Medline
18. Höft S, Muhle C, Brenner W, et al. **Fine-needle aspiration cytology of the sentinel lymph node in head and neck cancer.** *J Nucl Med* 2002; 43:1585–90 Medline
19. Wendler T, Hermann K, Schnelzer A, et al. **First demonstration of 3-D lymphatic mapping in breast cancer using freehand SPECT.** *Eur J Nucl Med Mol Imaging* 2010;37:1452–61 CrossRef Medline
20. Heuveling DA, Karagozoglu KH, van Schie A, et al. **Sentinel node biopsy using 3D lymphatic mapping by freehand SPECT in early stage oral cancer: a new technique.** *Clin Otolaryngol* 2012;37:89–90 CrossRef Medline
21. Mandapathil M, Teymoortash A, Heinis J, et al. **Freehand SPECT for sentinel lymph node detection in patients with head and neck cancer: first experiences.** *Acta Otolaryngol* 2014;134:100–04 CrossRef Medline
22. Bluemel C, Herrmann K, Müller-Richter U, et al. **Freehand SPECT-guided sentinel lymph node biopsy in early oral squamous cell carcinoma.** *Head Neck* 2014;36:E112–16 CrossRef Medline
23. Bluemel C, Herrmann, Kübler A, et al. **Intraoperative 3-D imaging improves sentinel lymph node biopsy in oral cancer.** *Eur J Nucl Med Mol Imaging* 2014;41:2257–64 CrossRef Medline
24. Heuveling DA, van Weert S, Karagozoglu KH, et al. **Evaluation of the use of freehand SPECT for sentinel node biopsy in early stage oral carcinoma.** *Oral Oncol* 2015;51:287–90 CrossRef Medline
25. Mihaljevic AL, Rieger A, Belloni B, et al. **Transferring innovative freehand SPECT to the operating room: first experiences with sentinel lymph node biopsy in malignant melanoma.** *Eur J Surg Oncol* 2014;40:42–48 CrossRef Medline
26. Okur A, Hennersperger C, Runyan B, et al. **FhSPECT-US guided needle biopsy of sentinel lymph nodes in the axilla: is it feasible?** *Med Image Comput Comput Assist Interv* 2014;17(pt 1): 577–84 Medline

Enlargement of the Internal Auditory Canal and Associated Posterior Fossa Anomalies in PHACES Association

D.E. Meltzer, C.D. Robson, F. Blei, and R.A. Holliday

SUMMARY: We noted enlargement of the internal auditory canal in several of our patients with posterior fossa malformations, hemangiomas, arterial anomalies, cardiac defects, eye abnormalities, and sternal or supraumbilical defects (PHACES) association and hence evaluated children with PHACES for the presence of an enlarged internal auditory canal and potential associated findings, including infantile hemangioma within the internal auditory canal, to understand the genesis of this enlargement. We reviewed our records to identify children with PHACES association who had been evaluated with MR imaging at our institutions. Imaging was reviewed for abnormal enhancement in the internal auditory canal, internal auditory canal enlargement, cerebellar hypoplasia, prominence of the petrous ridge, and deformity of the calvarium. We raise the possibility of an association between enlargement of the internal auditory canal in PHACES and a generalized malformation of the posterior fossa with cerebellar and calvarial hypoplasia.

ABBREVIATIONS: IAC = internal auditory canal; PHACES = posterior fossa malformations, hemangiomas, arterial anomalies, cardiac defects, eye abnormalities, and sternal or supraumbilical defects

Posterior fossa malformations, hemangiomas, arterial anomalies, cardiac defects, eye abnormalities, and sternal or supraumbilical defects compose the PHACES association.[1,2] The regional facial infantile hemangiomas of PHACES association are frequently associated with ipsilateral cerebellar hypoplasia and ipsilateral anomalies of the intracranial internal carotid artery.[3,4] More recently, attention has been drawn to the incidence of intracranial hemangiomas, especially in the internal auditory canal (IAC) and cerebellopontine angle cistern.[5-8] The purpose of this study was to document the incidence and imaging appearance of anomalies of the IAC and the potential for associated posterior fossa anomalies in patients with PHACES association.

CASE SERIES

The index patient was a 25-year-old woman who presented with chronic hearing loss and a history of a facial hemangioma in infancy. Initial temporal bone CT revealed a funnel-shaped configuration of the prominent left IAC, prominence of the left posterior petrous ridge, hypoplasia of the left occipital bone, and findings consistent with a persistent left stapedial artery (Fig 1). Subsequent MR imaging demonstrated left cerebellar hypoplasia, enlargement of the left IAC, and an asymmetrically prominent left retrocerebellar CSF space (Fig 2). No abnormal enhancement was observed in the IAC or posterior fossa.

Subsequent review of clinical data bases at 2 institutions identified 44 patients (37 male, 7 female) diagnosed with PHACES association who underwent diagnostic MR imaging of the brain between 2003 and 2012. Institutional review board approval was obtained from the 2 participating institutions for this retrospective review. A neuroradiologist with 9 years of experience and a pediatric neuroradiologist with 20 years of experience performed a consensus review of MR imaging examinations of the brain from pediatric patients with an established diagnosis of PHACES association based on accepted clinical criteria.

MR imaging techniques varied slightly among the patients, depending on the location of their scans and whether the brain examinations were modified for inclusion of imaging of the face to evaluate facial hemangiomas. Typically, axial T2-weighted images were obtained by using an FSE or TSE technique at section thicknesses ranging from 2.5 to 5 mm, with a 0- or 1-mm gap. Multiplanar postgadolinium T1-weighted images were acquired at a 3- to 5-mm section thickness with a 0- or 1-mm gap, with or without a fat-saturation technique. All MR imaging studies were evaluated for asymmetric caliber or contour of the IAC, intracanalicular enhancement, cerebellar asymmetry, and asymmetric

Received December 31, 2013; accepted after revision March 17, 2015.

From the Department of Radiology (D.E.M., F.B.), St. Luke's-Roosevelt Hospital Center, New York, New York; Department of Radiology (C.D.R.), Boston Children's Hospital/Harvard Medical School, Boston, Massachusetts; Vascular Birthmark Institute of New York (F.B.), New York, New York; and New York Eye and Ear Infirmary (R.A.H.), New York, New York.

Paper previously presented as an electronic poster at: American Society of Neuroradiology Annual Meeting and the Foundation of the ASNR Symposium, May 18–23, 2013; San Diego, California.

Please address correspondence to Daniel E. Meltzer, MD, Roosevelt Hospital, 1000 Tenth Ave, Suite 4C-12, New York, NY 10019; e-mail: dmeltzer@chpnet.org

http://dx.doi.org/10.3174/ajnr.A4395

size or morphology of the petrous and occipital bones (Fig 3). All abnormal findings were classified as ipsilateral or contralateral to the patients' facial hemangiomas (Fig 4).

Nineteen of 44 (43%) cases demonstrated unilateral funnel-

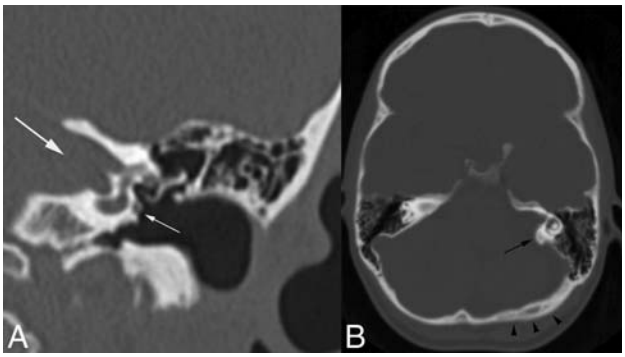

FIG 1. Coronal CT image of the left temporal bone (*A*) shows a prominent IAC (*large white arrow*) and a persistent stapedial artery (*small white arrow*). Axial CT image of the head (*B*) shows prominence of the left posterior petrous ridge (*black arrow*) and a relatively flattened, slightly thickened ipsilateral occipital calvarium (*arrowheads*).

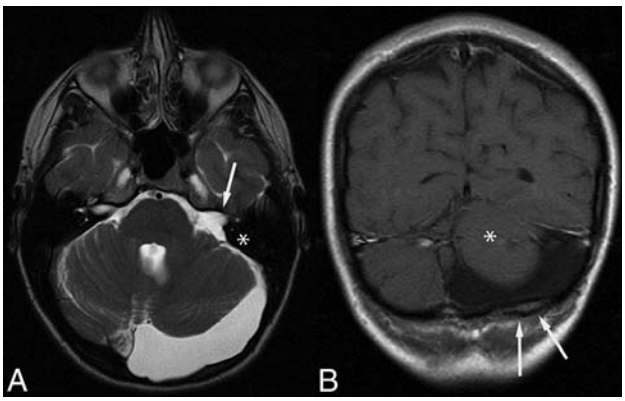

FIG 2. MR imaging of the same adult patient as in Fig 1. Axial T2-weighted image (*A*) shows prominent CSF in the left posterior fossa, enlarged left IAC (*white arrow*), and prominence of the posterior petrous ridge (*asterisk* in *A*). *B*, Coronal postcontrast T1-weighted image. The left cerebellum is hypoplastic (*asterisk* in *B*), and there is subtle calvarial deformity with focal thickening of the diploic space (*arrows* in *B*).

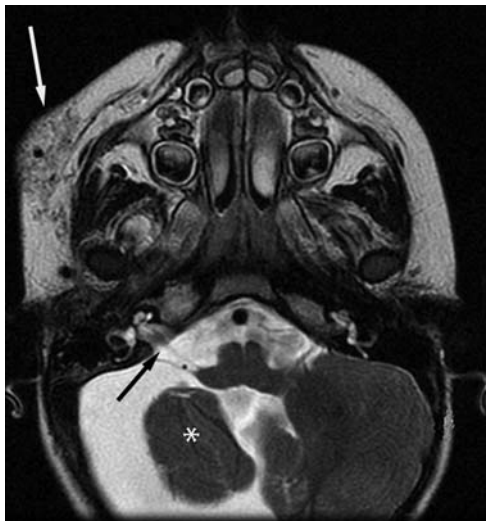

FIG 4. A 26-month-old girl. Axial T2-weighted image shows a right facial hemangioma (*white arrow*), ipsilateral to the enlarged right IAC (*black arrow*), and cerebellar hypoplasia (*asterisk*).

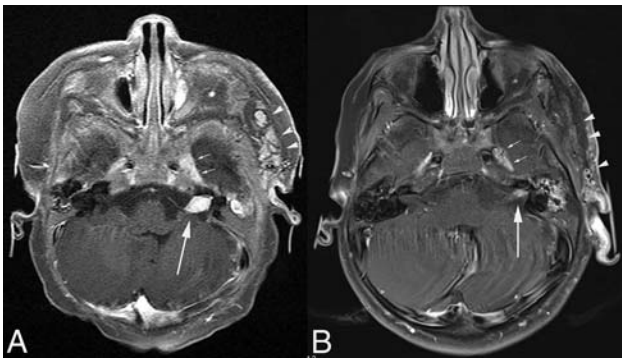

FIG 5. A 4-month-old girl. Axial postcontrast fat-suppressed T1-weighted images show an enhancing mass in the left IAC (*arrow* in *A*), which markedly diminishes in size on follow-up imaging at 3 years of age (*arrow* in *B*). Note the ipsilateral left facial and preauricular hemangioma, which similarly involutes (*arrowheads* in *A* and *B*). Note also mild prominence of the left cavernous sinus, thought to harbor an additional small hemangioma (*small arrows* in *A* and *B*). Minimal left cerebellar hypoplasia was better demonstrated on T2-weighted images (not shown).

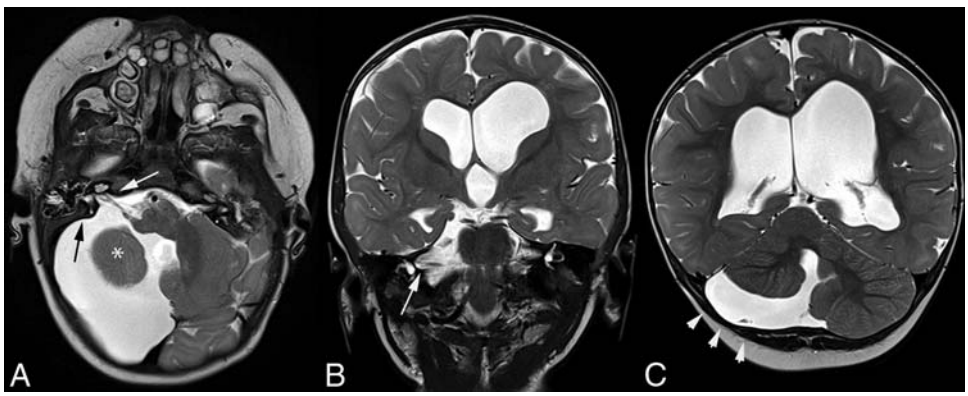

FIG 3. A 6-month-old girl. Axial (*A*) and coronal (*B*) T2-weighted images show unilateral enlargement and downsloping of the right IAC (*white arrows*). Note ipsilateral cerebellar hypoplasia (*asterisk* in *A*) and prominence of the posterior petrous ridge (*black arrow*). Additional coronal T2-weighted image (*C*) shows mild occipital calvarial flattening (*arrowheads*) ipsilateral to the cerebellar hypoplasia.

shaped IAC enlargement; this group of 19 patients included 16 female and 3 male patients between 8 days and 18 years of age (average age, 40 months) at the time of initial MR imaging. IAC enlargement was ipsilateral to the facial hemangioma in 17/19 patients and contralateral in 1/19. One patient with enlargement of the left IAC had bilateral facial hemangiomas.

Fifteen of 19 patients with unilateral IAC enlargement underwent contrast-enhanced thin-section imaging through the posterior fossa during the first 3 years of life. Of the remaining 4 patients, 3 were initially imaged with intravenous contrast at ages 8, 17, and 18 years. One neonate did not receive intravenous contrast.

Of the 15 patients in whom MR imaging was performed with contrast during the first 3 years of life, 6 had avidly enhancing IAC masses consistent with hemangiomas. Asymmetric IAC enhancement without a discrete mass was identified in 1 patient. Follow-up studies were available on 4 of these 7 patients, all of which demonstrated resolution of enhancement or reduction in lesion size (Fig 5). IAC enhancement was ipsilateral to the facial hemangioma in 7/7 patients. Resolution of IAC enhancement appeared to parallel resolution of the facial hemangiomas.

In 2 of the 7 patients with IAC enhancement, there was also abnormal enhancement within the fourth ventricle, consistent with an additional intracranial hemangioma. Involution of this enhancement also paralleled the involution of the facial hemangioma (Fig 6).

Of the 7 patients with IAC enhancement, 6 demonstrated prominence of the ipsilateral posterior petrous ridge, 5 had ipsilateral cerebellar hypoplasia, and 5 had a deformity of the ipsilateral occipital bone.

Of the 12 patients without documented IAC enhancement, 10 demonstrated prominence of the ipsilateral posterior petrous ridge, 11 had ipsilateral cerebellar hypoplasia, and 11 had a deformity of the ipsilateral occipital bone.

Overall, 13/19 patients demonstrated a combination of enlargement of the IAC, ipsilateral cerebellar hypoplasia, prominence of the ipsilateral posterior petrous ridge, and deformity of the ipsilateral occipital bone.

The findings discussed above are summarized in the Table.

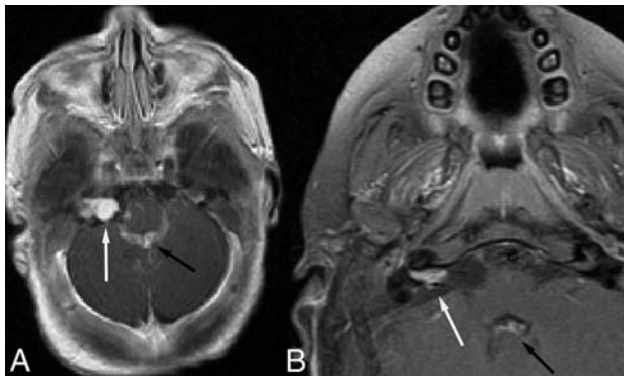

FIG 6. A 3-month-old boy. *A*, Axial postcontrast T1-weighted image shows an enhancing mass in the right IAC (*white arrow*). There is also abnormal enhancement in the fourth ventricle (*black arrow*), suspicious for an additional hemangioma. *B*, Fifteen-month follow-up imaging of the same patient. Fat-suppressed T1-weighted image shows diminished enhancement in the right IAC (*white arrow*). The previously seen enhancement in the fourth ventricle is also less conspicuous, beginning to resemble normal choroidal enhancement (*black arrow*). The cerebellum appears normal.

DISCUSSION

Approximately 36% of the pediatric patients with enlarged IACs imaged with contrast-enhanced MR imaging during the first 3 years of life had abnormal IAC enhancement indicating the presence of an ipsilateral IAC hemangioma. The percentage increased to 70% of patients when imaging was performed during the first year of life.

One limitation to the detection of IAC hemangioma is the requirement of MR imaging during infancy with intravenous contrast and thin-section, high-resolution T1-weighted images through the IAC. In 1 patient, the examination during infancy was performed without sedation, following feeding and swaddling, and contrast was not administered. In another, the initial facial lesion was mistaken for a port-wine stain, and imaging before 2 years of age was performed for evaluation of possible Sturge-Weber syndrome. Eight patients underwent initial imaging beyond infancy, at which time any intracranial hemangioma would presumably have involuted.

Eighty-four percent of patients with IAC enlargement had ipsilateral prominence of the petrous ridge, 79% had ipsilateral cerebellar hypoplasia, and 79% had ipsilateral abnormality of the over-

Posterior fossa anomalies in 19 patients with PHACES with IAC enlargement

Age at Initial MRI	Sex	IAC Enhancing	Posterior Petrous Prominence	Cerebellar Hypoplasia	Occipital Bone	Side of Facial Hemangioma
3 mo	F	Yes[a]	Yes	Yes	Smaller	Ipsilateral
1 mo	F	Yes[a]	Yes	No	No	Ipsilateral
2 mo	F	Yes[a]	Yes	No	No	Ipsilateral
4 mo	F	Yes[a]	Yes	Yes	Smaller	Ipsilateral
38 d	M	Yes	No	Yes	Larger	Ipsilateral
9 mo	F	Yes	Yes	Yes	Smaller	Ipsilateral[b]
29 mo	M	Yes	Yes	Yes	Smaller	Ipsilateral
24 mo	F	No	Yes	Yes	Smaller	Ipsilateral
18 mo	M	No	Yes	Yes	Smaller	Ipsilateral
15 mo	F	No	Yes	Yes	Deformed	Contralateral
4 mo	F	No	Yes	Yes	Smaller	Ipsilateral
24 mo	F	No	Yes	Yes	Smaller	Ipsilateral
21 d	F	No	Yes	Yes	Larger	Ipsilateral
32 d	F	No	Yes	Yes	Larger	Ipsilateral
18 y	F	No	Yes	Yes	Smaller	Ipsilateral
8 y	F	NA	No	Yes	Smaller	Ipsilateral
13 y	F	NA	Yes	Yes	Deformed	Ipsilateral
17 y	F	NA	No	No	No	Ipsilateral
8 d	F	NA	Yes	Yes	Larger	Ipsilateral

Note:—NA indicates that the patient did not receive intravenous contrast.
[a] Enhancement involuted on subsequent study.
[b] Facial hemangioma was bilateral.

lying calvarium. Sixty-eight percent of the patients with IAC enlargement had all 3 of these findings. This result would suggest that the enlarged IAC may be part of a spectrum of related posterior fossa abnormalities in a subset of patients with PHACES association, possibly due to abnormal embryogenesis, but 28% of patients with IAC enhancement did not have cerebellar hypoplasia or occipital deformities.

All 19 patients with IAC enlargement had segmental facial hemangiomas as expected in PHACES association. All except 1 of the facial hemangiomas were ipsilateral to their posterior fossa anomalies, consistent with the prevailing theories regarding the underlying pathogenesis of conditions such as PHACES association. PHACES is an example of a metameric association, similar to other entities such as cerebrofacial venous metameric syndromes and cerebrofacial arteriovenous metameric syndromes. These syndromes share an underlying etiology related to the cephalic migration of neural crest cells.[9-11]

Cerebrofacial venous metameric syndromes and cerebrofacial arteriovenous metameric syndromes tend to have an axial, segmentally arranged distribution of lesions, with lesions in a single metamere. In contrast, the anomalies in PHACES (sternal, aortic, arterial, ocular, and posterior fossa) suggest a longitudinal dysfunction in the migration of the cephalic neural crest cells. Krings et al[9] suggested that the association between hemangiomas of the cerebellopontine angle and ipsilateral agenesis of the ICA indicates links between migrational aberrations affecting the third aortic arch, the third branchial arch, and the rhombencephalon.

Although the presence or absence of a hemangioma in the IAC or cerebellopontine angle cistern could be incidental to the other posterior fossa findings described, a hemangioma in this region occurs with a frequency that suggests, at least in some cases, a causal relationship. In addition, the demonstration of unilateral cerebellar hypoplasia with ipsilateral funnel-shaped IAC enlargement later in childhood or in adulthood may be helpful in suggesting a diagnosis of PHACES association. This finding is useful in distinguishing PHACES association from other causes of cerebellar hypoplasia. Detection of fetal cerebellar hypoplasia, particularly when unilateral, should prompt consideration of PHACES association in the differential diagnosis. A diagnosis of PHACES association should prompt questioning about a history of prior regional infantile hemangioma and a critical assessment with MR imaging and MRA for associated intracranial arterial anomalies and/or steno-occlusive disease.

CONCLUSIONS

We demonstrate a high incidence of funnel-shaped IAC enlargement in patients with PHACES association, and many of these patients were found to have hemangiomas within the enlarged IAC, particularly when scanned with contrast-enhanced MR imaging during the first year of life. Those patients with IAC enlargement, in the presence or absence of an enhancing mass, have a high incidence of abnormalities of the petrous bone, occipital bone, or cerebellum The results raise the possibility that the enlarged IAC in PHACES is related to a generalized malformation of the osseous components of the posterior fossa, in association with cerebellar hypoplasia and sometimes with IAC hemangioma. Unilateral enlargement of the IAC in an adult patient without an apparent mass in the IAC should prompt questioning and evaluation for possible PHACES association.

Disclosures: Caroline D. Robson—*UNRELATED*: *Royalties*: Amirsys, *Comments*: Editor and content author. Francine Blei—*UNRELATED*: *Consultancy*: Pierre Fabre, *Comment*: Medical Advisory Board; *Grants/Grants Pending*: Pierre Fabre,* *Comments*: Burden of Disease (Infantile Hemangiomas) Study. *Money paid to the institution.

REFERENCES

1. Frieden IJ, Reese V, Cohen D. **PHACE syndrome: the association of posterior fossa brain malformations, hemangiomas, arterial anomalies, coarctation of the aorta and cardiac defects, and eye abnormalities.** *Arch Dermatol* 1996;132:307–11
2. Metry D, Heyer G, Hess C, et al; PHACE Syndrome Research Conference. **Consensus statement on diagnostic criteria for PHACE syndrome.** *Pediatrics* 2009;124:1447–56
3. Oza VS, Wang E, Berenstein A, et al. **PHACES association: a neuroradiologic review of 17 patients.** *AJNR Am J Neuroradiol* 2008; 29:807–13
4. Hess CP, Fullerton HJ, Metry DW, et al. **Cervical and intracranial arterial anomalies in 70 patients with PHACE syndrome.** *AJNR Am J Neuroradiol* 2010;31:1980–86
5. Judd CD, Chapman PR, Koch B, et al. **Intracranial infantile hemangiomas associated with PHACE syndrome.** *AJNR Am J Neuroradiol* 2007;28:25–29
6. Poetke M, Frommeld T, Berlien HP. **PHACE syndrome: new views on diagnostic criteria.** *Eur J Pediatr Surg* 2002;12:366–74
7. Kim DH, Choi JH, Lee JH, et al. **PHACE association with intracranial, oropharyngeal hemangiomas, and an atypical patent ductus arteriosus arising from the tortuous left subclavian artery in a premature infant.** *Korean J Pediatr* 2012;55:29–33
8. Duffy KJ, Runge-Samuelson C, Bayer ML, et al. **Association of hearing loss with PHACE syndrome.** *Arch Dermatol* 2010;146:1391–96
9. Krings T, Geibprasert S, Luo CB, et al. **Segmental neurovascular syndromes in children.** *Neuroimaging Clin N Am* 2007;17:245–58
10. Bhattacharya JJ, Luo CB, Suh DC, et al. **Wyburn-Mason or Bonnet-Dechaume-Blanc as cerebrofacial arteriovenous metameric syndromes (CAMS): a new concept and a new classification.** *Interv Neuroradiol* 2001;7:5–17
11. Ramli N, Sachet M, Bao C, et al. **Cerebrofacial venous metameric syndrome (CVMS) 3: Sturge-Weber syndrome with bilateral lymphatic/venous malformations of the mandible.** *Neuroradiology* 2003;45:687–90

White Matter Development is Potentially Influenced in Adolescents with Vertically Transmitted HIV Infections: A Tract-Based Spatial Statistics Study

J. Li, G. Wu, Z. Wen, J. Zhang, H. Lei, X. Gui, and F. Lin

ABSTRACT

BACKGROUND AND PURPOSE: Convergent evidence indicates that HIV is associated with abnormal WM microstructure in adults. However, little is known about whether HIV affects WM development in adolescents. In this study, we used DTI to investigate the integrity of WM microstructure in adolescents with vertically transmitted HIV infections.

MATERIALS AND METHODS: Fifteen HIV-positive adolescents with vertically transmitted infections and 26 HIV-negative controls participated in this study. Whole-brain analysis of fractional anisotropy was performed by Tract-Based Spatial Statistics to localize abnormal WM regions between groups. VOI analysis was further performed to explore the changes in diffusivity indices in the regions with fractional anisotropy alterations. Correlation analyses were used to assess the relationship between fractional anisotropy alterations and clinical measures within the HIV-positive group.

RESULTS: Relative to HIV-negative controls, HIV-positive adolescents demonstrated significantly reduced fractional anisotropy in the corpus callosum, superior and posterior corona radiata, frontal and parietal WM, pre-/postcentral gyrus, and superior longitudinal fasciculus. In the affected regions, fractional anisotropy reductions were caused by an increase in radial diffusivity, and no changes were observed in axial diffusivity. Moreover, fractional anisotropy values in the bilateral frontal WM were negatively correlated with the duration of highly active antiretroviral therapy and were positively associated with the age at onset of highly active antiretroviral therapy.

CONCLUSIONS: These findings suggest that early HIV infections may affect WM development, especially in the frontal WM, corpus callosum, and corona radiata in adolescents, which may be associated with hypomyelination and demyelination. Moreover, WM integrity may serve as a potential new treatment target.

ABBREVIATIONS: AD = axial diffusivity; FA = fractional anisotropy; HAART = highly active antiretroviral therapy; MD = mean diffusivity; RD = radial diffusivity; TBSS = Tract-Based Spatial Statistics

HIV infections around the world are increasing constantly.[1] HIV is a neurotrophic virus affecting the cellular immune system through the infection and destruction of CD4 lymphocytes, which causes multiple organs, such as the respiratory system,[2] digestive system,[3] and CNS, to have relevant illnesses.[4] Cognitive impairment, HIV-associated dementia, and AIDS dementia complex are commonly observed.[5]

DTI is capable of examining the WM and providing objective parameters that measure the microstructural features nondestructively and noninvasively.[6] Recent DTI studies have identified abnormalities in the subcortical WM and corpus callosum, despite appearing normal on conventional MRI in HIV-infected adults.[7] Abnormal WM integrity, such as reduced fractional anisotropy (FA) or increased mean diffusivity (MD), was found in the splenium,[8] superior longitudinal fasciculus,[9] anterior and superior corona radiata,[10,11] and frontal and parietal WM[12] in HIV-infected adults.

Similarly, neuroimaging studies have also demonstrated vast WM abnormalities in adolescents with vertically transmitted HIV infection. For example, a voxel-based morphometry study reported WM atrophy in the posterior part of corpus callosum,

Received January 24, 2015; accepted after revision February 25.

From the Departments of Magnetic Resonance Imaging (J.L., G.W., Z.W., J.Z.) and Infectious Diseases (X.G.), Zhongnan Hospital of Wuhan University, Wuhan, China; and National Center for Magnetic Resonance in Wuhan (H.L., F.L.), State Key Laboratory of Magnetic Resonance and Atomic and Molecular Physics, Wuhan Institute of Physics and Mathematics, Chinese Academy of Sciences, Wuhan, China.

Please address correspondence to Guangyao Wu, MD, PhD, Zhongnan Hospital of Wuhan University, No. 169 Donghu Rd, Wuhan 430071, China; e-mail: wuguangy2002@163.com; and Fuchun Lin, PhD, Wuhan Institute of Physics and Mathematics, Chinese Academy of Sciences., West No. 30 Xiao Hong Shan, Wuhan 430071, China; e-mail: fclin@wipm.ac.cn

This work was partially supported by the Natural Science Foundation of China (Nos. 81171315, 81227902 and 21221064), and National Basic Research Program of China (973 Program) Grant No. 2011CB707802.

Indicates open access to non-subscribers at www.ajnr.org

Evidence-Based Medicine Level 2.

http://dx.doi.org/10.3174/ajnr.A4417

Table 1: Demographic information for subjects in each group

	HIV(+)	HIV(-)	*P* Value
Age (yr)	15.3 ± 1.3	15.0 ± 1.6	.54
Sex (male/female)	8:7	13:13	.84
Education level (yr)	7.5 ± 1.2	8.7 ± 1.9	.05
Current CD4 (cells/mL)	605.8 ± 345.0	NA	NA
Age at first HIV treatment (yr)	9.5 ± 3.4	NA	NA
HIV treatment duration (mo)	68.3 ± 39.5	NA	NA
% Treated at younger than 2 yr	13.3 (n = 2)	NA	NA
Plasma viral load (copies/mL)	0–50	NA	NA
MoCA total score	25.7 ± 3.8	27.1 ± 3.1	.21
MMSE total score	25.8 ± 2.1	27.3 ± 2.4	.05

Note:—NA indicates not applicable or available; MoCa, Montreal Cognitive Assessment; MMSE, Mini-Mental State Examination.

external capsule, and ventral temporal lobe in vertically infected youths (age range, 13–25 years).[13] Hoare et al[14] found that vertically HIV-infected children (age range, 8–12 years) had lower FA and higher MD and radial diffusivity (RD) in the corpus callosum and increased MD in the superior longitudinal fasciculus. Taken together, these findings suggest that abnormal WM integrity may also be present in adolescents (age range, 12–18 years) with vertically transmitted HIV infections. However, previous studies have focused mainly on adults or younger children, and few studies have focused on adolescents with HIV infections. In addition, highly active antiretroviral therapy (HAART) appears to have a positive impact on the WM in the temporal lobe[15] but with some toxicity.[16] The effects of HAART in adolescents are also uncertain; this uncertainty may be attributed to high rates of nonadherence[17] and loss to follow-up.[18]

Therefore, in this study, we used DTI combined with Tract-Based Spatial Statistics (TBSS; http://fsl.fmrib.ox.ac.uk/fsl/fslwiki/TBSS) analysis to investigate the integrity of WM microstructure in adolescents with vertically transmitted HIV infections undergoing current HAART.

MATERIALS AND METHODS

Subjects

We recruited 15 HIV-positive adolescents undergoing combination HAART (mean age, 15.3 ± 1.3 years; range, 13–17 years). The HIV was confirmed by an enzyme-linked immunosorbent assay and western blot. We also recruited 26 age- and sex-matched HIV-negative subjects (mean age, 15.0 ± 1.6 years; range, 12–18 years). All of the HIV-positive adolescents were infected through mother-to-child transmission during pregnancy, delivery, or breastfeeding, and the HIV-negative subjects' fathers or mothers (or both) also had HIV infections. The socioeconomic statuses of the groups and the cultural and ethnic backgrounds of their families were similar. The detailed demographic information and clinical measures are listed in Table 1. All subjects were recruited from the Center of AIDS Prevention and Cure of Zhongnan Hospital, Wuhan University. The inclusion criteria for HIV-infected subjects were HIV acquisition during the fetal or neonatal period, current treatment with HAART, and right-handedness. For the control subjects, the inclusion criteria were the confirmation of HIV-negative status by enzyme-linked immunosorbent assay and right-handedness.

The exclusion criteria for all the subjects included age younger than 12 years or older than 18 years, acute medical illnesses, current or past medical or neurologic disorders, psychiatric diseases, mental retardation, current alcohol or substance abuse, HIV encephalopathy and opportunistic infections, MR imaging contraindications, claustrophobia, and metabolic disturbances or other brain diseases (not HIV-related). For control subjects, the exclusion criteria also included severe school difficulties and any chronic medication other than asthma medication. Most of the HIV-infected participants underwent laboratory evaluations, such as plasma CD4 T-cell counts. The CD4 counts ranged from 12 to 1014 cells/mL (average, 605.8 cells/mL). In this study, the patients who were HIV-positive were all undergoing HAART. Thus, all of the plasma viral loads were undetectable (0–50 copies/mL). The Montreal Cognitive Assessment and the Mini-Mental State Examination were used to assess the subjects' cognitive abilities.

The study was approved by the Medical Ethics Committee of Zhongnan Hospital of Wuhan University, and written informed consent was obtained from all participants or their guardians after a complete description of the measurements required for the study.

Image Acquisition

All subjects were scanned by a 3T MR imaging scanner (Tim Trio; Siemens, Erlangen, Germany). An 8-channel phased array head coil was used with restraining foam pads to minimize head motion and diminish the sounds of the scanner. A single-shot, spin-echo EPI technique with alignment of the anterior/posterior commissure plane was performed with the following parameters: TR = 6000 ms, TE = 87 ms, FOV = 24 × 24 cm^2, acquisition matrix = 128 × 128 zero-filled to 256 × 256, section thickness = 3 mm without gap, sections = 45, number of repetitions = 4, parallel acceleration factor = 2. The diffusion sensitizing gradients were applied along 20 noncollinear gradient encoding directions with b=1000 s/mm^2 with an acquisition without diffusion-weighting (b=0 s/mm^2).

Data Processing

DTI data analysis was performed by the FMRIB Diffusion Toolbox http://www.fmrib.ox.ac.uk/fsl/fdt/index.html). The diffusion-weighted volumes were first aligned to their corresponding non-diffusion-weighted images to minimize image distortion and reduce simple head motion. The diffusion tensor for each voxel was then assessed, and the diffusion tensor was diagonalized to obtain its 3 pairs of eigenvalues (λ_1, λ_2, λ_3) and eigenvectors. Four diffusion indices, including FA, MD, axial diffusivity (AD = λ_1), and RD [RD = (λ_2 + λ_3) / 2] were calculated. These measurements are associated with the microstructural integrity of the WM and are often applied to infer the structural characteristics of the local tissue environment.[19]

Voxelwise, observer-independent, whole-brain analysis of FA images was performed by TBSS.[20] In brief, the FA volumes for all subjects were first normalized to the Montreal Neurological Institute space. The registered FA images were then averaged to

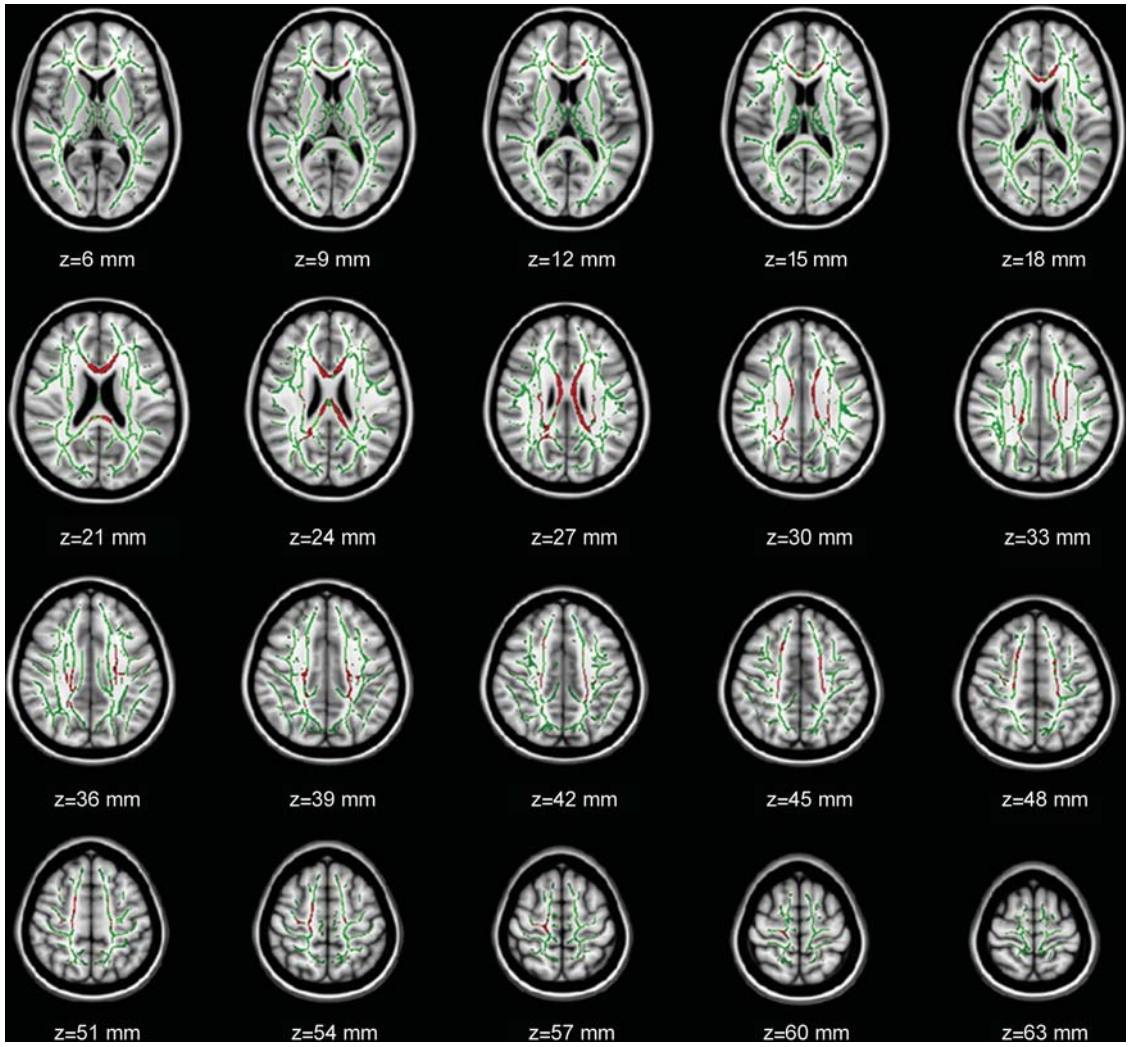

FIG 1. TBSS analysis of fractional anisotropy maps. Areas in red are brain regions where FA is significantly reduced ($P < .05$, corrected by multiple comparison) in HIV-positive subjects relative to HIV-negative controls. The results are shown overlaid on the Montreal Neurological Institute 152-T1 template and the mean FA skeleton (green). The *left* side of the image corresponds to the right hemisphere of the brain. FA changes occur in the region with Montreal Neurological Institute coordinates in the z-direction between z = 6 and z = 63.

obtain a mean FA image, and the mean FA image was applied to create a mean FA skeleton, which represents the main fiber tracts. The mean FA skeleton was further thresholded to exclude gray matter and CSF by a value of 0.2. Following this step, the aligned FA data for each subject were projected onto the mean skeleton to create a skeletonized FA map. To identify FA differences between groups, we fed the skeletonized FA data into the voxel-by-voxel, nonparametric statistical analysis with age, sex, and educational levels as covariates. Threshold-free cluster enhancement was used to obtain the significant differences between 2 groups at $P < .05$ after accounting for multiple comparisons by controlling for the family-wise error rate. The significant results were located with the JHU-ICBM-DTI-81 WM label atlas (http://cmrm.med.jhmi.edu/) in the Montreal Neurological Institute space.

To explore mechanisms related to the FA changes, we further performed VOI analysis to investigate alterations in diffusivity indices (AD, RD, and MD) in the regions with FA alterations. The VOI mask was first extracted on the basis of the clusters with intergroup FA differences and were then inversely transformed to the original images of each subject. The mean values of the diffusivity indices were calculated. A 1-way analysis of covariance with the group as the independent variable and diffusivity indices as the dependent variables was performed (controlling for age, sex, and education levels). A significance level of $P < .05$ (Bonferroni correction for multiple comparisons) was used.

Multiple linear regression analysis was performed to investigate whether there were relationships between the clinical variables and FA changes in the affected regions with WM abnormalities. A $P < .05$ (uncorrected) was considered significant.

RESULTS

Demographic Information

Table 1 lists the detailed demographic and clinical information for the HIV-positive adolescents and HIV-negative controls. The HIV-positive subjects demonstrated no significant differences in age, sex, or education level (in years). There were no differences in the Montreal Cognitive Assessment or Mini-

Mental State Examination total scores between these 2 study groups. The average CD4 count in HIV-positive subjects was 605.8 ± 345.0 cells/mL.

TBSS Results

The spatial distribution of the brain regions demonstrating decreased FA in the HIV-positive adolescents is presented in Fig 1 and Table 2. Compared with the controls, the HIV-positive adolescents demonstrated significantly reduced FA in the bilateral corpus callosum (including the genu, body, and splenium), bilateral superior and posterior corona radiata, bilateral frontal and parietal WM, bilateral pre-/postcentral gyrus, and left superior longitudinal fasciculus. In no regions did HIV-positive adolescents demonstrate higher FA than controls.

VOI Results

To investigate the mechanisms related to the FA changes, the brain regions with significantly decreased FA were extracted for VOI-based analyses of other diffusion indices. Twelve of the 14 VOIs demonstrated significantly increased RD ($P < .05$ after Bonferroni correction). The other 2 VOIs trended toward increased RD. No significant differences were detected in AD in any of the VOIs. Only 3 VOIs had significantly increased MD ($P < .05$ after Bonferroni correction). The results are listed in Table 3.

Correlation Results

Using a multiple linear regression analysis, we found that in HIV-infected adolescents, the FA values of the bilateral WM were negatively correlated with the duration of HAART (right frontal WM: $r = -0.634$, $P = .011$, Fig 2*A*; left frontal WM: $r = -0.623$, $P = .013$, Fig 2*B*), and the FA values of the bilateral WM were positively correlated with the age at onset of HAART (right frontal WM: $r = 0.615$, $P = .015$, Fig 2*C*; left frontal WM: $r = 0.553$, $P = .032$, Fig 2*D*).

DISCUSSION

In this study, we used DTI to explore the integrity of WM microstructure in adolescents with vertically transmitted HIV infections by voxelwise TBSS analysis. HIV-positive adolescents showed decreased FA in the bilateral corpus callosum, bilateral superior and posterior corona radiata, bilateral frontal and parietal WM, bilateral pre-/postcentral gyrus, and left superior longitudinal fasciculus. These results reflect a disruption in the microstructure of the WM in HIV-infected adolescents. VOI analysis demonstrated that decreased FA in the HIV-positive subjects was mainly a result of increased RD but no changes in AD; these findings were perhaps a manifestation of the disrupted integrity of myelin. Moreover, a multiple regression analysis demonstrated that the FA values in the bilateral frontal WM were negatively correlated with the duration of HAART and positively correlated with the age at onset of HAART.

The findings that FA values within

Table 2: Neuroanatomic regions with decreased FA in HIV-positive subjects relative to HIV-negative controls[a]

Anatomic Region	Hemisphere	MNI Coordinates (mm)			Cluster Size (mm^3)
		X	Y	Z	
Genu of corpus callosum	Bilateral	−13	20	24	530
Body of corpus callosum	Bilateral	−11	16	24	2228
Splenium	Bilateral	−11	−35	24	564
Superior corona radiata	Left	−20	−25	39	497
Superior corona radiata	Right	20	−24	37	386
Posterior corona radiata	Left	−21	−28	34	262
Posterior corona radiata	Right	25	−27	33	249
Frontal WM	Left	−18	5	43	164
Frontal WM	Right	17	19	44	399
Pre-/postcentral gyrus WM	Left	−21	−25	42	269
Pre-/postcentral gyrus WM	Right	21	−24	42	524
Parietal WM	Left	−22	−31	40	149
Parietal WM	Right	17	−54	28	437
SLF	Left	−30	−17	34	85

Note:—MNI indicates Montreal Neurological Institute; SLF, superior longitudinal fasciculus.
[a] $P < .05$, threshold-free cluster enhancement multiple comparison–corrected. Coordinates for the peak voxels are displayed.

Table 3: Group differences in diffusivity indices from VOIs

Anatomic Region	Hemisphere	AD (×$10^{-3}$$mm^2$/s) (Mean)			RD (×$10^{-3}$$mm^2$/s) (Mean)			MD (×$10^{-3}$$mm^2$/s) (Mean)		
		HIV−	HIV+	*P* Value	HIV−	HIV+	*P* Value	HIV−	HIV+	*P* Value
Genu of corpus callosum	Bilateral	1.62 ± 0.08	1.58 ± 0.08	.16	0.36 ± 0.03	0.40 ± 0.06	.004	0.78 ± 0.03	0.79 ± 0.05	.22
Body of corpus callosum	Bilateral	1.78 ± 0.06	1.78 ± 0.06	.99	0.41 ± 0.05	0.49 ± 0.07	.0003[a]	0.87 ± 0.04	0.92 ± 0.05	.002[a]
Splenium	Bilateral	1.66 ± 0.06	1.67 ± 0.05	.41	0.33 ± 0.03	0.37 ± 0.04	.0003[a]	0.77 ± 0.02	0.80 ± 0.03	.001[a]
Superior corona radiata	Left	1.21 ± 0.04	1.20 ± 0.03	.33	0.53 ± 0.02	0.56 ± 0.04	.0003[a]	0.76 ± 0.02	0.78 ± 0.03	.01
Superior corona radiata	Right	1.26 ± 0.05	1.26 ± 0.04	.78	0.49 ± 0.02	0.53 ± 0.03	.00009[a]	0.74 ± 0.02	0.77 ± 0.02	.001[a]
Posterior corona radiata	Left	1.23 ± 0.06	1.23 ± 0.03	.81	0.59 ± 0.03	0.62 ± 0.03	.002[a]	0.80 ± 0.03	0.82 ± 0.02	.02
Posterior corona radiata	Right	1.26 ± 0.04	1.25 ± 0.03	.32	0.57 ± 0.03	0.61 ± 0.04	.002[a]	0.80 ± 0.03	0.82 ± 0.04	.05
Frontal WM	Left	1.35 ± 0.07	1.32 ± 0.05	.22	0.44 ± 0.03	0.48 ± 0.04	.001[a]	0.74 ± 0.03	0.76 ± 0.03	.09
Frontal WM	Right	1.37 ± 0.06	1.32 ± 0.07	.02	0.40 ± 0.03	0.48 ± 0.03	.0003[a]	0.72 ± 0.03	0.73 ± 0.03	.21
Pre-/postcentral gyrus WM	Left	1.32 ± 0.06	1.29 ± 0.06	.14	0.47 ± 0.03	0.50 ± 0.03	.0007[a]	0.75 ± 0.02	0.76 ± 0.02	.06
Pre-/postcentral gyrus WM	Right	1.30 ± 0.04	1.27 ± 0.04	.01	0.44 ± 0.02	0.48 ± 0.03	.00009[a]	0.73 ± 0.02	0.74 ± 0.02	.08
Parietal WM	Left	1.31 ± 0.05	1.31 ± 0.05	.94	0.57 ± 0.04	0.61 ± 0.03	.001[a]	0.82 ± 0.03	0.84 ± 0.03	.02
Parietal WM	Right	1.29 ± 0.06	1.27 ± 0.04	.28	0.58 ± 0.03	0.62 ± 0.05	.002[a]	0.81 ± 0.03	0.84 ± 0.04	.07
SLF	Left	1.11 ± 0.04	1.09 ± 0.03	.13	0.54 ± 0.03	0.57 ± 0.04	.004	0.73 ± 0.02	0.75 ± 0.03	.05

Note:—HIV− indicates HIV-negative controls; HIV+, HIV-positive subjects.
[a] $P < .05/14 \approx .0035$ (Bonferroni-corrected for multiple comparisons).

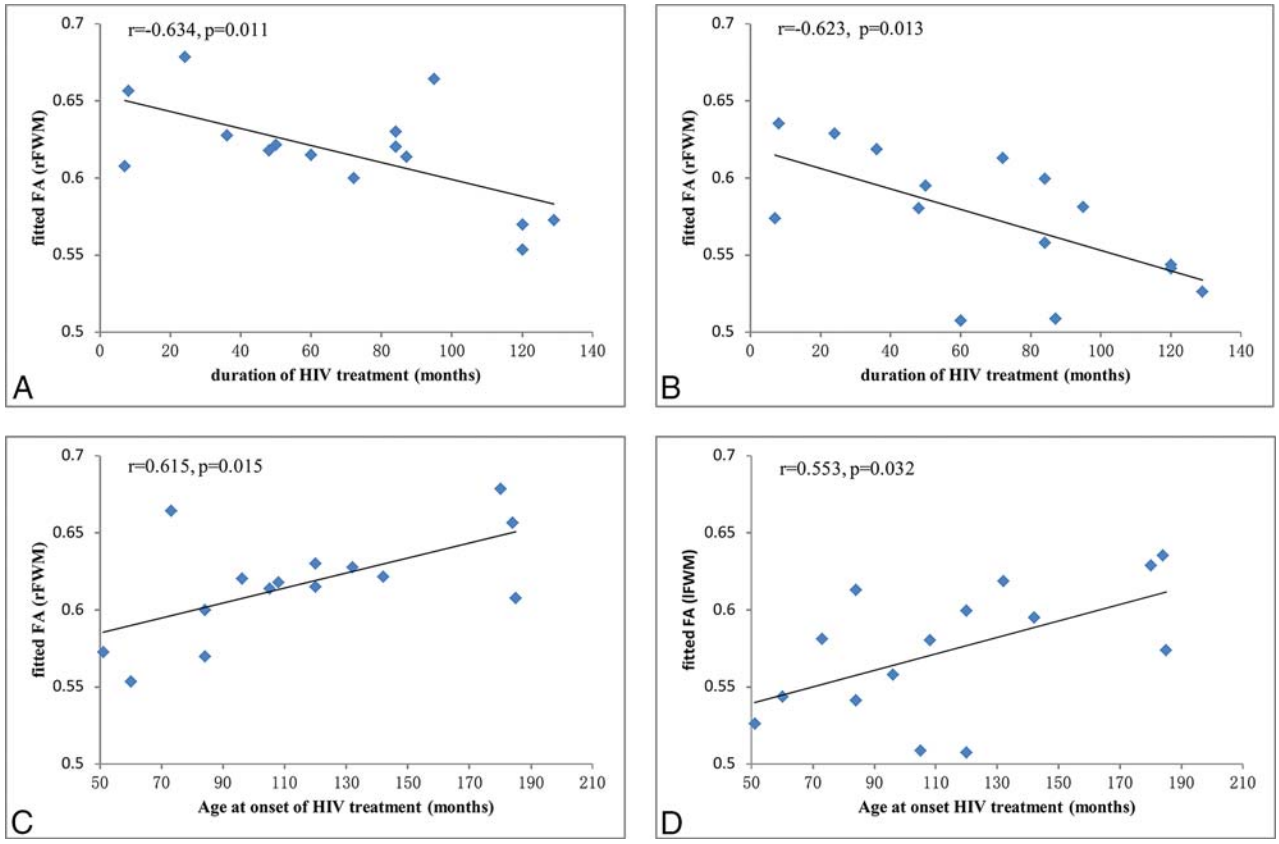

FIG 2. Correlation results between FA alterations and clinical measures in the HIV-positive subjects. *A*, FA values in the right frontal WM (rFWM) are negatively correlated with the duration of HAART ($r = -0.634$, $P = .011$). *B*, FA values in the left frontal WM (lFWM) are negatively correlated with the duration of HAART ($r = -0.623$, $P = .013$). *C*, FA values in the rFWM are positively correlated with the age at onset of HAART ($r = 0.615$, $P = .015$). *D*, FA values in the lFWM are positively correlated with the age at onset of HAART ($r = 0.553$, $P = .032$).

the genu, body, and splenium of the corpus callosum were reduced in HIV-positive adolescents are consistent with findings in previous studies on HIV-infected children and adults. For example, FA values for the genu,[10] body,[21] and splenium[8] of the corpus callosum[11,22] are significantly reduced in HIV-infected adults. Decreased FA of the body of corpus callosum is also reported in HIV-infected children.[14] In addition, a lower FA in the genu of corpus callosum is demonstrated in a macaque model of neuroAIDS.[23] Greater callosal maturation is associated with greater motor function.[24] The corpus callosum is also involved with memory and executive function.[25] Moreover, deceased FA is also found in the anterior and superior corona radiata in HIV-infected participants.[10,11] The anterior corona radiata is associated with functions of the executive network.[26] Previous studies have focused on HIV-infected children and found that the subjects displayed visual-spatial memory and motor developmental deficits and executive function disorders.[27,28] Taken together, it can be concluded that a decline in the microstructural integrity of WM fibers may account for cognitive decline in HIV-positive adolescents.

In addition, patients with asymptomatic HIV have an abnormal WM microstructure. Xuan et al[29] reported that the mean FA values were significantly lower and the mean AIDS dementia complex values were significantly higher in the corpus callosum and periventricular, frontal, and parietal WM in the asymptomatic group. A similar result has been found in the study by Hoare et al.[14] These results imply that patients with HIV may have alterations in the diffusion of water molecules in their brain WM, whether they have symptoms or not. In our study, most of the subjects were also asymptomatic, and there were no significant differences in the Montreal Cognitive Assessment and Mini-Mental State Examination scores between the 2 groups.

The genu and splenium of the corpus callosum reach 90% of the maximum FA value by 11 years of age and demonstrate the earliest and most rapid FA changes with age, while the corona radiata demonstrates no FA changes with age from 5 to 30 years of age.[30] Age-related FA increases in the adolescent group, including the body of the corpus callosum and right superior corona radiata. In contrast, in the young adult group, the FA changes are much less prominent.[31] By 8–9 months, the corpus callosum appears identical to that of an adult.[32] All these results indicate that early HIV infection may affect WM development, especially in the corpus callosum and corona radiata.

Reduced FA is a well-established biomarker for the impaired integrity of WM. FA may be affected by many factors, including myelination, axon size and attenuation, path geometry, and extracellular water space between fibers.[19] In our study, FA reduction in HIV-positive adolescents was mainly driven by an increase in RD (no changes in AD). It is generally believed that RD mainly reflects the integrity and thickness of the myelin sheets covering the axons.[33] Although the mechanism of this interesting phenomenon is not yet clear, we presume that it may be related to a manifestation of disrupted integrity of myelin or even hypomyelina-

tion in the affected brain regions and the axonal injury cannot be identified. Related studies have demonstrated the predominant pathologic features, including pericapillary multinucleated giant cells, myelin loss, reactive astrocytosis, and microglial activation with microglial nodules.[34] These factors may influence myelination and myelin development. The above findings indicate that the WM integrity may serve as a potential new treatment target for HIV-positive patients, and FA may be used as a qualified biomarker to understand the underlying mechanisms of injury or to evaluate the effectiveness of early interventions in adolescents with vertically transmitted HIV infections.

In this study, we found that the FA values in the bilateral frontal WM were negatively correlated with the duration of HAART and positively correlated with the age at onset of HAART. Although HAART can effectively suppress the HIV systemic burden, poor penetration into the CNS provides incomplete protection. Increasing evidence has also suggested that certain HAARTs may cause mitochondrial toxicity and lead to neuronal loss.[16,35] This finding suggests that a longer HIV treatment may be associated with possible neurotoxicity in the WM of HIV-infected adolescents. However, the HIV treatment is offered to patients with $<$350 CD4+ T cells/mm^3 or plasma HIV ribonucleic acid levels of $>$55,000 copies/mL,[36] so the earlier and longer HIV treatment may have been due to more virulent strains, thus accounting for direct viral effects on the WM by a very heterogeneous viral population. The early formation of myelin integrity may be disrupted irreversibly. In general, we infer that the cerebral WM development and myelination of HIV-infected adolescents might be affected by the HIV treatment and direct viral effects, especially in the frontal lobe.

In addition, the bilateral frontal white matter appears to be more involved according to the significant correlation results. Pomara et al[37] found that subjects with HIV who were receiving HAART had significantly decreased FA compared with the healthy controls only in the frontal lobes. This is possibly because the frontal WM myelination may be more vulnerable during brain maturation.

There are several limitations in this study. First, cross-sectional and longitudinal studies on HIV-infected adolescents are needed to confirm the correlation between DTI alterations and neurocognitive performance, and more detailed neurocognitive tests should be performed. Furthermore, all of our subjects were receiving HAART during the DTI examination. Thus, we could not compare the potential differences between treated and untreated patients in the DTI analysis.

CONCLUSIONS

Adolescents with vertically transmitted HIV infections demonstrated microstructural WM damage as measured by reduced FA values in some brain regions, which may be caused by disrupted myelin integrity associated with increased RD. Our results have the potential to improve our understanding of the pathogenesis of brain WM changes in adolescents with vertically transmitted HIV infections and indicate that early HIV infection may affect WM development, especially in the frontal WM, corpus callosum, and corona radiata of adolescents. New neuroprotective regimens should be developed and performed earlier for children and adolescents with vertically transmitted HIV infections. The effectiveness of specific, early interventions can be confirmed by DTI, and FA values may be qualified biomarkers.

REFERENCES

1. Sullivan PS, Jones JS, Baral SD. **The global north: HIV epidemiology in high-income countries.** *Curr Opin HIV AIDS* 2014;9:199–205
2. Platzker AC, Colin AA, Chen XC, et al. **Thoracoabdominal compression and respiratory system compliance in HIV-infected infants.** *Am J Respir Crit Care Med* 2000;161:1567–71
3. Winter H. **Gastrointestinal tract function and malnutrition in HIV-infected children.** *J Nutr* 1996;126:2620S–22S
4. Price RW, Brew B, Sidtis J, et al. **The brain in AIDS: central nervous system HIV-1 infection and AIDS dementia complex.** *Science* 1988;239:586–92
5. Ragin AB, Storey P, Cohen BA, et al. **Disease burden in HIV-associated cognitive impairment: a study of whole-brain imaging measures.** *Neurology* 2004;63:2293–97
6. Basser PJ, Pierpaoli C. **Microstructural and physiological features of tissues elucidated by quantitative-diffusion-tensor MRI.** *J Magn Reson B* 1996;111:209–19
7. Filippi CG, Ulug AM, Ryan E, et al. **Diffusion tensor imaging of patients with HIV and normal-appearing white matter on MR images of the brain.** *AJNR Am J Neuroradiol* 2001;22:277–83
8. Wu Y, Storey P, Cohen BA, et al. **Diffusion alterations in corpus callosum of patients with HIV.** *AJNR Am J Neuroradiol* 2006;27:656–60
9. Hoare J, Fouche JP, Spottiswoode B, et al. **White-matter damage in Clade C HIV-positive subjects: a diffusion tensor imaging study.** *J Neuropsychiatry Clin Neurosci* 2011;23:308–15
10. Zhu T, Zhong J, Hu R, et al. **Patterns of white matter injury in HIV infection after partial immune reconstitution: a DTI tract-based spatial statistics study.** *J Neurovirol* 2013;19:10–23
11. Nir TM, Jahanshad N, Busovaca E, et al. **Mapping white matter integrity in elderly people with HIV.** *Hum Brain Mapp* 2014;35:975–92
12. Chang L, Wong V, Nakama H, et al. **Greater than age-related changes in brain diffusion of HIV patients after 1 year.** *J Neuroimmune Pharmacol* 2008;3:265–74
13. Sarma MK, Nagarajan R, Keller MA, et al. **Regional brain gray and white matter changes in perinatally HIV-infected adolescents.** *Neuroimage Clin* 2014;4:29–34
14. Hoare J, Fouche JP, Spottiswoode B, et al. **A diffusion tensor imaging and neurocognitive study of HIV-positive children who are HAART- naïve "slow progressors."** *J Neurovirol* 2012;18:205–12
15. Gongvatana A, Cohen RA, Correia S, et al. **Clinical contributors to cerebral white matter integrity in HIV-infected individuals.** *J Neurovirol* 2011;17:477–86
16. Robertson KR, Su Z, Margolis DM, et al. **Neurocognitive effects of treatment interruption in stable HIV-positive patients in an observational cohort.** *Neurology* 2010;74:1260–66
17. Murphy DA, Sarr M, Durako SJ, et al. **Barriers to HAART adherence among human immunodeficiency virus-infected adolescents.** *Arch Pediatr Adolesc Med* 2003;157:249–55
18. Auld AF, Agolory SG, Shiraishi RW, et al. **Antiretroviral therapy enrollment characteristics and outcomes among HIV-infected adolescents and young adults compared with older adults: seven African countries, 2004–2013.** *MMWR Morb Mortal Wkly Rep* 2014;63:1097–103
19. Le Bihan D. **Looking into the functional architecture of the brain with diffusion MRI.** *Nat Rev Neurosci* 2003;4:469–80
20. Smith SM, Jenkinson M, Johansen-Berg H, et al. **Tract-based spatial statistics: voxelwise analysis of multi-subject diffusion data.** *Neuroimage* 2006;31:1487–505
21. Leite SC, Corrêa DG, Doring TM, et al. **Diffusion tensor MRI evaluation of the corona radiata, cingulate gyri, and corpus callosum in HIV patients.** *J Magn Reson Imaging* 2013;38:1488–93
22. Chen Y, An H, Zhu H, et al. **White matter abnormalities revealed by**

diffusion tensor imaging in non-demented and demented HIV+ patients. *Neuroimage* 2009;47:1154–62
23. Li C, Zhang X, Komery A, et al. **Longitudinal diffusion tensor imaging and perfusion MRI investigation in a macaque model of neuro-AIDS: a preliminary study.** *Neuroimage* 2011;58:286–92
24. Mathew P, Pannek K, Snow P, et al. **Maturation of corpus callosum anterior midbody is associated with neonatal motor function in eight preterm-born infants.** *Neural Plast* 2013;2013:359532
25. Voineskos AN, Rajji TK, Lobaugh NJ, et al. **Age-related decline in white matter tract integrity and cognitive performance: a DTI tractography and structural equation modeling study.** *Neurobiol Aging* 2012;33:21–34
26. Yin X, Han Y, Ge H, et al. **Inferior frontal white matter asymmetry correlates with executive control of attention.** *Hum Brain Mapp* 2013;34:796–813
27. Boivin MJ, Green SD, Davies AG, et al. **A preliminary evaluation of the cognitive and motor effects of pediatric HIV infection in Zairian children.** *Health Psychol* 1995;14:13–21
28. Nozyce ML, Lee SS, Wiznia A, et al. **A behavioral and cognitive profile of clinically stable HIV-infected children.** *Pediatrics* 2006;117:763–70
29. Xuan A, Wang GB, Shi DP, et al. **Initial study of magnetic resonance diffusion tensor imaging in brain white matter of early AIDS patients.** *Chin Med J (Engl)* 2013;126:2720–24
30. Lebel C, Walker L, Leemans A, et al. **Microstructural maturation of the human brain from childhood to adulthood.** *Neuroimage* 2008;40:1044–55
31. Giorgio A, Watkins KE, Douaud G, et al. **Changes in white matter microstructure during adolescence.** *Neuroimage* 2008;39:52–61
32. Barkovich AJ, Kjos BO. **Normal postnatal development of the corpus callosum as demonstrated by MR imaging.** *AJNR Am J Neuroradiol* 1988;9:487–91
33. Song SK, Sun SW, Ramsbottom MJ, et al. **Dysmyelination revealed through MRI as increased radial (but unchanged axial) diffusion of water.** *Neuroimage* 2002;17:1429–36
34. Smith AB, Smirniotopoulos JG, Rushing EJ. **From the archives of the AFIP: central nervous system infections associated with human immunodeficiency virus infection: radiologic-pathologic correlation.** *Radiographics* 2008;28:2033–58
35. Marra CM, Zhao Y, Clifford DB, et al; AIDS Clinical Trials Group 736 Study Team. **Impact of combination antiretroviral therapy on cerebrospinal fluid HIV RNA and neurocognitive performance.** *AIDS* 2009;23:1359–66
36. Dybul M, Fauci AS, Bartlett JG, et al; Panel on Clinical Practices for Treatment of HIV. **Guidelines for using antiretroviral agents among HIV-infected adults and adolescents.** *Ann Intern Med* 2002;137:381–433
37. Pomara N, Crandall DT, Choi SJ, et al. **White matter abnormalities in HIV-1 infection: a diffusion tensor imaging study.** *Psychiatry Res* 2001;106:15–24

Parametric Response Mapping of Apparent Diffusion Coefficient as an Imaging Biomarker to Distinguish Pseudoprogression from True Tumor Progression in Peptide-Based Vaccine Therapy for Pediatric Diffuse Intrinsic Pontine Glioma

R. Ceschin, B.F. Kurland, S.R. Abberbock, B.M. Ellingson, H. Okada, R.I. Jakacki, I.F. Pollack, and A. Panigrahy

ABSTRACT

BACKGROUND AND PURPOSE: Immune response to cancer therapy may result in pseudoprogression, which can only be identified retrospectively and may disrupt an effective therapy. This study assesses whether serial parametric response mapping (a voxel-by-voxel method of image analysis also known as functional diffusion mapping) analysis of ADC measurements following peptide-based vaccination may help prospectively distinguish progression from pseudoprogression in pediatric patients with diffuse intrinsic pontine gliomas.

MATERIALS AND METHODS: From 2009 to 2012, 21 children, 4–18 years of age, with diffuse intrinsic pontine gliomas were enrolled in a serial peptide-based vaccination protocol following radiation therapy. DWI was acquired before immunotherapy and at 6-week intervals during vaccine treatment. Pseudoprogression was identified retrospectively on the basis of clinical and radiographic findings, excluding DWI. Parametric response mapping was used to analyze 96 scans, comparing ADC measures at multiple time points (from the first vaccine to up to 12 weeks after the vaccine was halted) with prevaccine baseline values. Log-transformed fractional increased ADC, fractional decreased ADC, and parametric response mapping ratio (fractional increased ADC/fractional decreased ADC) were compared between patients with and without pseudoprogression, by using generalized estimating equations with inverse weighting by cluster size.

RESULTS: Median survival was 13.1 months from diagnosis (range, 6.4–24.9 months). Four of 21 children (19%) were assessed as experiencing pseudoprogression. Patients with pseudoprogression had higher fitted average log-transformed parametric response mapping ratios ($P = .01$) and fractional decreased ADCs ($P = .0004$), compared with patients without pseudoprogression.

CONCLUSIONS: Serial parametric response mapping of ADC, performed at multiple time points of therapy, may distinguish pseudoprogression from true progression in patients with diffuse intrinsic pontine gliomas treated with peptide-based vaccination.

ABBREVIATIONS: DIPG = diffuse intrinsic pontine gliomas; fdADC = fractional decreased ADC; fiADC = fractional increased ADC; PRM = parametric response mapping; PRMratio = ratio of fiADC to fdADC; WGEE = weighted generalized estimating equations

Diffuse intrinsic pontine gliomas (DIPG) are highly malignant brain stem tumors affecting primarily children.[1] One-year progression-free survival is <25%, with a median overall survival of 9–10 months.[2] Despite multiple clinical trials, irradiation is the only therapy that is of proved clinical benefit. Cancer peptide vaccines work by administering epitopes from antigens that are overexpressed in tumor cells to trigger the patient's immune response. The results of a pilot clinical trial targeting 3 glioma-associated antigens, interleukin-13 receptor α 2, EphA2, and survivin, in children with newly diagnosed malignant brain stem

Received February 24, 2015; accepted after revision April 5.

From the Departments of Radiology (R.C., A.P.), Pediatrics (R.I.J.), Surgery (H.O.), Neurosurgery (H.O., I.F.P.), Immunology (H.O.), and Biomedical Informatics (R.C., A.P.), University of Pittsburgh School of Medicine, Pittsburgh, Pennsylvania; Departments of Radiology (R.C., A.P.), Pediatrics (R.I.J.), and Neurosurgery (I.F.P.), Children's Hospital of Pittsburgh, University of Pittsburgh Cancer Institute (B.F.K., S.R.A., H.O., R.I.J., I.F.P., A.P.), and Department of Biostatistics, Graduate School of Public Health (B.F.K.), University of Pittsburgh, Pittsburgh, Pennsylvania; and Department of Radiological Sciences (B.M.E.), University of California, Los Angeles, Los Angeles, California.

This clinical trial was supported by National Institutes of Health grants R21CA149872 and P01NS40923 and the University of Pittsburgh Cancer Institute Immunological Monitoring Core and Biostatistics shared resource facility, supported in part by National Institutes of Health award P30CA47904; grants from the Pediatric Low-Grade Glioma Initiative via the National Brain Tumor Society and the Ellie Kavalieros Fund of the Children's Hospital of Pittsburgh Foundation; and the Pediatric Clinical and Translational Research Center, supported by the National Institutes of Health through grants UL1 RR024153 and UL1TR000005. The imaging postprocessing was supported by the Ian's (Ian Yagoda) Friends Foundation grant, the Society of Pediatric Radiology Pilot Award, and a National Library of Medicine grant 5T15LM007059-27.

Paper previously presented at: Annual Meeting of the American Society of Neuroradiology and the Foundation of the ASNR Symposium, May 18–23, 2013; San Diego, California.

Please address correspondence to Ashok Panigrahy, MD, Department of Pediatric Radiology, Children's Hospital of Pittsburgh of UPMC, 4401 Penn Ave, Pittsburgh, PA 15224; e-mail: panigrahya@upmc.edu

Indicates open access to non-subscribers at www.ajnr.org

Indicates article with supplemental on-line appendix and table.

Indicates article with supplemental on-line photos.

http://dx.doi.org/10.3174/ajnr.A4428

gliomas have been recently published.[3] Pseudoprogression was observed in parallel to immunologic responses.[3] Pseudoprogression, defined radiologically as a transient increase in the size of contrast-enhancing tumor on structural MR imaging, is thought to result from local tissue inflammation due to vasogenic edema and abnormal vessel permeability. Thus, assessment of pseudoprogression in peptide-based immunotherapy of pediatric brain stem gliomas presents a challenge for clinical management. Pseudoprogression can currently only be determined retrospectively after a period during which treatment is potentially halted, thus creating the evident problem of stopping treatment at a time when it is possibly at its highest efficacy.

Because structural MR imaging cannot reliably differentiate inflammation from recurrent tumor,[4] advanced neuroimaging techniques such as DWI have been evaluated to assess brain tumor therapeutic response,[5-12] including discriminating between pseudoprogression and true progression. We evaluated DWI as a potential tool to discriminate tumor response and true tumor progression, by using information available close to the time of suspected progression. The apparent diffusion coefficient is a quantitative measure reflecting the observed net movement of water calculated from DWI and has been shown to correlate with tissue cellularity in tumors,[5-12] likely due to restriction of extracellular water motion in tightly packed tumor cells. Modulation of diffusion measurements has been previously observed in both preclinical and human studies of immunotherapy.[13-15] While mean tissue ADC may be a useful measure for distinguishing tumor from other masses, it may be problematic for quantifying change with time. Opposing heterogeneous responses (ie, different areas of tumor with increasing and decreasing diffusion) may neutralize each other with no change in overall mean ADC.[16] To overcome this limitation, we applied parametric response mapping (PRM),[6,17-19] formerly known as functional diffusion mapping, to evaluate the response to immunotherapy with time by quantifying voxelwise changes in ADC.[20] Our study differs from prior studies by evaluating immunotherapy, by its exclusive focus on pediatric brain tumors, and by using information from >2 time points in PRM. We hypothesized that serial PRMs calculated at multiple time points during immunotherapy could differentiate pseudoprogression from true progression in pediatric brain stem gliomas.

MATERIALS AND METHODS

Demographics, Clinical Characteristics, and Study Design

The cohort consisted of the 21 children (9 males) with DIPG enrolled in our institutional glioma vaccine trial (ClinicalTrials.gov No. NCT01130077).[3] Before enrollment, patients had completed 5000- to 6000-cGy involved field fractionated radiation therapy, with or without concurrent chemotherapy; postirradiation chemotherapy precluded enrollment. Adequate organ function, absolute lymphocyte count of ≥500, performance status of ≥60, and human leukocyte antigen–A2+ status were required for vaccine treatment initiation. Patients with increased edema or mass effect after irradiation did not start the vaccination until this had resolved (up to 12 weeks after completion of irradiation).

Signed institutional review board–approved informed consent was required for human leukocyte antigen screening and initiation of therapy. Patients received subcutaneous injections of glioma-associated antigen–derived human leukocyte antigen–A*0201–restricted peptides and a tetanus toxoid peptide (TetA830) emulsified in Montanide ISA-51 (Seppic, Puteaux, France) and concurrent intramuscular injections of 30 μg/kg of the toll-like receptor ligand, Hiltonol (poly-ICLC; Oncovir, Washington, DC), every 3 weeks × 8 followed by a maintenance phase, every 6 weeks.[3]

Participants were evaluated with neurologic examinations and laboratory testing as previously described.[3] MR imaging (including DWI) was performed before initiating vaccine therapy (week 0) and at weeks 6, 15, 21, after initiating vaccine therapy, and 12-week intervals thereafter. More frequent scans were obtained if clinically warranted. Between May 2009 and October 2012, we enrolled 21 newly diagnosed patients: 15 with DIPG treated with irradiation alone and 6 with DIPG treated with irradiation and concurrent chemotherapy (On-line Table). Patients received 2–11 doses of vaccine (median, 7). The mean age at diagnosis was 9 ± 4.0 years, and median survival was 56.3 weeks (range, 6.4–24.9 months).

Pseudoprogression

Because the development of pseudoprogression is an area of concern in immunotherapy studies, the trial incorporated detailed guidelines for managing possible pseudoprogression.[3] If tumor enlargement or increased enhancement or both were noted on structural MR imaging and the patient was neurologically worse, sufficient to warrant initiation of corticosteroid administration or an increase in corticosteroid dose, subsequent doses of vaccine and poly-ICLC were withheld. Imaging and clinical assessments were performed at 4-week intervals thereafter, until it was determined whether the clinical and imaging changes reflected pseudoprogression or true progression. If the subject improved clinically on declining corticosteroid doses that could be weaned to ≤0.1-mg/kg/day dexamethasone for ≥1 week and the MR imaging changes improved or resolved, the patient was presumed to have had pseudoprogression and could restart vaccine treatment with 67% of the poly-ICLC dose (ie, 20 μg/kg). Conversely, if the repeat MR imaging findings were unchanged or worse and the patient's clinical status had not improved despite increased corticosteroid doses, the patient was removed from the study due to presumed true tumor progression.

MR Imaging and Diffusion-Weighted Imaging

Imaging was conducted on 1.5T MR imaging systems with most of the studies performed on a 1.5T HDx system (GE Healthcare, Milwaukee, Wisconsin). Diffusion-weighted images were acquired at section thicknesses of 4–5 mm (1-mm gap), a TR ranging from 6000 to 8000 ms, and b=0 and 1000 s/mm^2 per clinical protocol. To register every time point onto a common space for subsequent analysis, we chose the earliest time point available with volumetric imaging (T1- or T2-weighted, which in most cases was a 3D T2-Cube; GE Healthcare) after completion of radiation therapy and before vaccine therapy as a structural reference. A minimum of 3 diffusion imaging time points (pre- or post-initial vaccine) were required for analysis. Gradient-

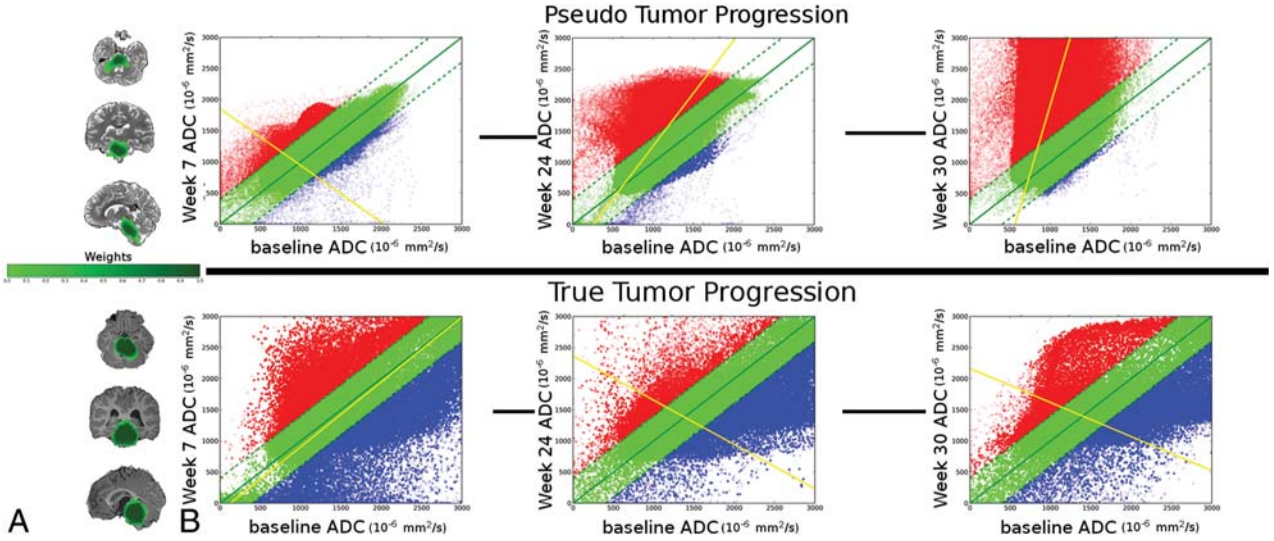

FIG 1. *A*, Tumor ROI for a patient with confirmed pseudoprogression (*top*) and a patient with true tumor progression without pseudoprogression (*bottom*). The color scale indicates the proportion of scans in which each voxel was classified as tumor tissue (voxel weights). *B*, Sample serial PRM maps at weeks 7, 24, and 30 compared with the baseline scan before vaccine therapy. Plots show coregistered voxels at baseline compared with the indicated time point. Green voxels indicate no significant change above or below the predefined threshold of ±0.4 mm^2/ms. Red voxels show a significant increase in ADC, and blue voxels, a decrease in ADC with time. Point opacity is proportional to the voxel weight (ie, how much does the voxel contribute to the PRM metric calculation in the weighted model).

echo or susceptibility-weighted imaging was also available for assessment of blood products.

Image Registration

A semiautomated processing pipeline[21]was developed by using Nipype (http://nipy.sourceforge.net/nipype).[22] Tumor area was manually delineated for each patient at each time point. We excluded regions with blood product that might cause EPI distortion. Tumor volume delineation was consistently performed for every patient in diffusion space, by using the B0 and ADC images to avoid any bias related to variations in institutional protocol. FLAIR imaging was also used to confirm the margin of the tumor. We performed a 2-step registration method to minimize potential registration errors: First the diffusion-weighted images were brain extracted and preregistered to a medium-resolution T2-weighted image acquired at the same time point by using a 6-*df* rigid-body registration. The medium-resolution images were then registered to the chosen high-resolution structural image, and the resulting registration matrix was applied to the preregistered diffusion images. Linear registration was performed with FLIRT (FMRIB Linear Image Registration Tool; http://www.fmrib.ox.ac.uk/)[23] by using an affine registration algorithm, followed by affine Fourier registration with Analysis of Functional Neuro Images software (ANFI; http://afni.nimh.nih.gov/afni/).[24] We generated an aggregate-tumor ROI by adding all registered delineated tumor areas in common space and only including regions present in at least 10% of all time points.

Serial PRM Postprocessing

Parametric response maps were generated by an operator blinded to pseudoprogression diagnosis for every time point in reference to the baseline scan by calculating the voxelwise difference in the apparent diffusion coefficient within the aggregate tumor ROI

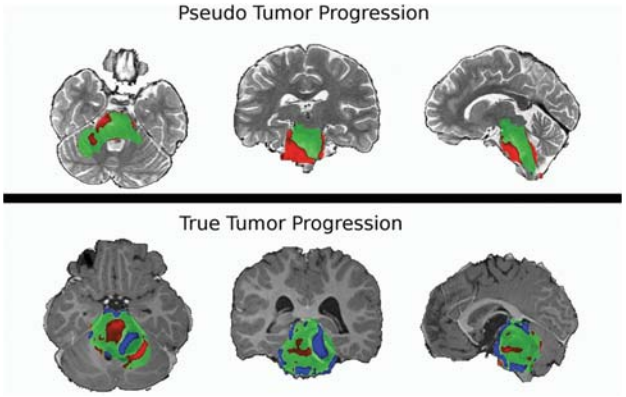

FIG 2. Sample PRM snapshots for a patient with confirmed pseudoprogression (*top*) and a patient with true tumor progression without pseudoprogression (*bottom*) give a spatiotemporal reference to tumor characterization. ADC maps are coregistered onto a common space, and voxelwise subtraction is calculated between each subsequent time point and the baseline scan. Green voxels indicate no significant change above or below the predefined threshold of ±0.4 mm^2/s. Red voxels show a significant increase in ADC, and blue voxels, a decrease in ADC compared with the baseline. There is evidence of spatial heterogeneity of diffusion within the brain stem tumor of both patients.

(Figs 1 and 2). We chose a significant change threshold of ±0.4 mm^2/s, as empirically determined by Ellingson et al,[6] to represent the 95% confidence interval of temporal ADC variation in normal brain tissue. Patient-level summary measures were created following generation of PRMs. Fractional increased ADC (fiADC) measured by the percentage of voxels above this threshold reflects a decrease in cellularity and potentially indicates an inflammatory response or necrotic tissue.[19,25] Fractional decreased ADC (fdADC) reflects the relative degree of hypercellularity and potentially indicates true tumor progression. We also looked at the ratio of fiADC to fdADC (PRMratio), calculated as fiADC / (fdADC + 0.01)[26] (to account for instances in which fdADC = 0), as a po-

tential marker for the overall trend of tissue progression. Whole-tumor volume and mean ADC were also extracted from the same ROI as that used for PRM analysis.

Statistical Analysis

At the time of analysis, all patients in this study were deceased and can therefore be presumed to have had true tumor progression as an overall disease outcome. We therefore categorized patients without confirmed pseudoprogression as experiencing true progression (in contrast to patients whose eventual tumor progression was preceded by pseudoprogression). We tested for average differences in fiADC, fdADC, and PRMratio values between these 2 groups, with log-transformation of each to limit the influence of large values. The analysis was restricted to PRM values measured from scans performed no later than 12 weeks following a subject's final vaccination, because later scans are relevant only for retrospective assessment of pseudoprogression. Associations between each measure and pseudoprogression status were modeled by using weighted generalized estimating equations (WGEE) with independence working correlation. Because patients with rapid disease progression undergo fewer scans, the cluster size (number of scans per person) is informative. Regression analysis used inverse weighting by cluster size and an adjusted inference to "typical" PRM results for each patient rather than the full set of PRM results (which would implicitly contain information about prognosis).[25,27] Statistical analyses were performed by using SAS/STAT statistical software, Version 9.4 (SAS Institute, Cary, North Carolina) and R, Version 3.0.1 (http://www.r-project.org/).

RESULTS

Pseudoprogression Cases and Overall Survival Time

Four children (19%) developed acute neurologic worsening associated with increased tumor size and/or enhancement several months after beginning the vaccination, with subsequent clinical and radiographic improvement on corticosteroids, consistent with pseudoprogression (On-line Fig 1). One of these patients experienced a prolonged objective response, maintained until 19.5 months postdiagnosis as previously reported.[3] Median survival from the time of diagnosis among patients with DIPG with pseudoprogression was 19.1 months, compared with 12.5 months in those without pseudoprogression.

Differences in Serial PRM Metrics and Standard Measures (Mean ADC and Tumor Volume) between Patients with Pseudoprogression and True Progression

A total of 151 MR imaging time points for 21 patients had ADC maps available, with 3 scans excluded due to image-registration failure and an additional 2, due to artifacts in the diffusion imaging. Although the patients were on a treatment trial with scheduled follow-up, imaging time points varied due to scheduling windows and use of DWI. Serial PRM metrics for each patient are shown in Fig 3, with colored lines connecting PRM results for each subject's nonbaseline time points. The 3 rows display 3 PRM metrics (fiADC, fdADC, and the fiADC/fdADC or PRMratio) as the y-axis for each plot. The x-axis for each plot is the number of weeks after the first vaccine treatment (in contrast to the time from diagnosis, which is used for survival analysis). The 3 columns are panels created for ease of presentation, with patients sorted by increasing survival time. Each patient appears in all 3 rows, but in only 1 column. There is 1 pseudoprogression case in the second column and 3 in the third column (dashed lines), reflecting the longer survival for patients with pseudoprogression. Figure 3 suggests that patients with pseudoprogression (dashed lines) had a higher fiADC and higher PRMratio compared with patients whose vaccine therapy was halted due to true progression (solid lines) for most postbaseline scans. These trends are examined further in Fig 4, which shows the same PRM metrics for the same patients (with the same color coding across both Figs 3 and 4) for pseudoprogression and true progression but without information about scan timing.

To compare PRM metrics assessed earlier than the current (retrospective) standards for pseudoprogression, Fig 4 shows only the serial diffusion data used for statistical modeling, which is limited to time points from baseline until 12 weeks after the vaccine was halted (96 scans; 2–8 scans per patient; median, 4 scans per patient). Assessed by using WGEE models accounting for informative clustering, patients with pseudoprogression, on average, had higher log-transformed PRMratios ($P = .01$) and fiADCs ($P = .0004$) and no statistically significant difference for lower log-transformed fdADCs ($P = .12$) than patients without pseudoprogression. The fitted average fiADC/fdADC or PRMratio for a scan compared with baseline was 0.4 for patients without pseudoprogression (95% CI, 0.3–0.6) and 3.7 for patients with pseudoprogression (95% CI, 0.8–18.0).

There was no significant difference in mean ADC or tumor volume between patients with pseudoprogression and true progression. In the 4 patients with pseudoprogression, the greatest percentage change in mean ADC from the baseline measurement ranged from a 24% decrease to an 86% increase (median, 33% increase), compared with −25% to 36% (median, 5%) for the 17 remaining patients. Raw data for change in both mean ADC and tumor volume are found in the On-line Table. Using the same timeframe (postvaccine scans until 12 weeks after the last vaccine dose) and the same analysis approach (WGEE), we explored the association between mean ADC and tumor volume with pseudoprogression, controlling for baseline values. Neither mean ADC ($P = .55$) nor tumor volume ($P = .44$) was associated with pseudoprogression.

For a post hoc sensitivity analysis, we examined PRM, comparing baseline measures only to the time points most proximal to decisions about continuing vaccine therapy when progression (or pseudoprogression) was suspected. We defined these time points as up to 6 weeks before the last vaccine and up to 3 weeks after the last vaccine (allowing for no missed vaccines if pseudoprogression was identified). Twenty-seven scans with DWI met these criteria, 1–2 scans in 18 patients. Again the magnitude and direction of effects for fiADC and fdADC were maintained (and statistical significance strengthened) comparing pseudoprogression versus true progression; however, 2 of the 4 patients with pseudoprogression did not have scans within this timeframe. Other explor-

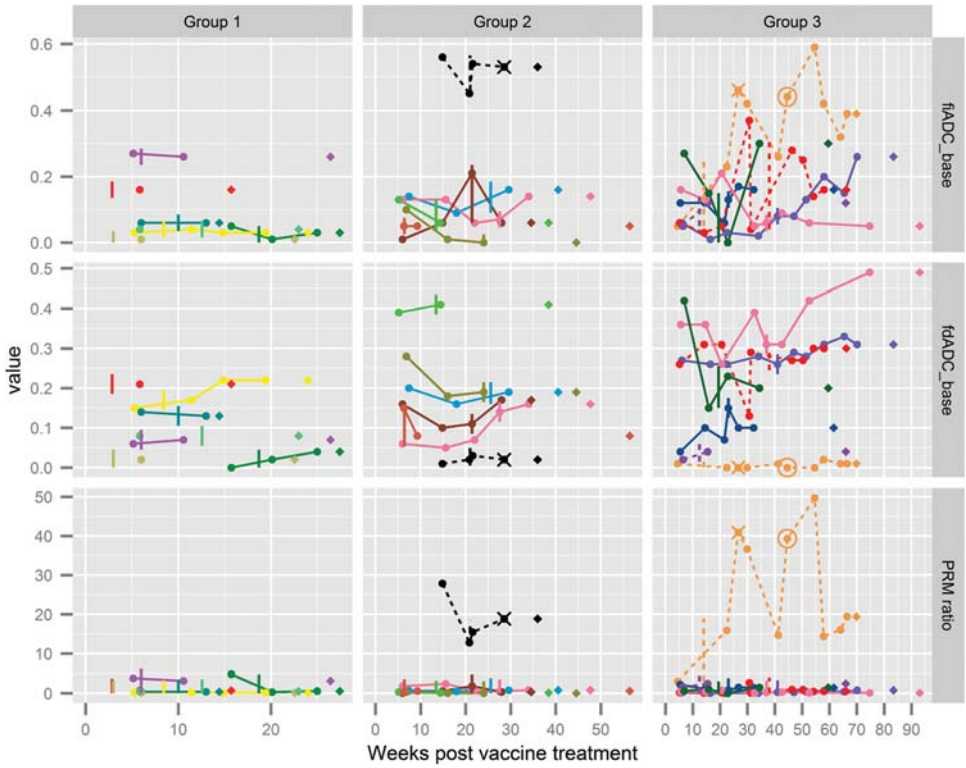

FIG 3. Serial PRM metric and disease trajectories for 21 pediatric patients with brain stem gliomas. Although the patients were on a treatment trial with scheduled follow-up, imaging time points varied due to scheduling windows and use of DWI. Serial PRM metrics for each patient are shown, with colored lines connecting PRM results for each subject's nonbaseline time points. Columns divide patients into groups by increasing overall survival from the start of vaccine therapy (14–27 weeks, 28–56 weeks, 57–93 weeks). Rows display fractional increased ADC, fractional decreased ADC, and PRMratio compared with the baseline (prevaccine) scan. Each PRM measurement is indicated by a *circle*, connected by *solid lines* for patients without pseudoprogression and *dashed lines* for patients with eventual diagnosis of pseudoprogression. *Vertical lines* indicate the date of the last vaccine for each patient. For 2 patients with psuedoprogression, vaccine treatment was restarted (date shown as X) 8 and 13 weeks after the initial halt. One of these patients underwent a second treatment stoppage (date shown as a *circle*). If one examined the time from the last vaccine dose (*vertical line* or *circle* for the patient who restarted therapy) to death (◇), patients survived 4–56 weeks after halting vaccine therapy.

atory analyses examined the robustness of our results to select tumor ROIs and exclude patients treated with bevacizumab (On-line Appendix and On-line Fig 2).

DISCUSSION

This study, to our knowledge, is the first demonstration of the use of serial diffusion-weighted imaging and parametric response mapping in distinguishing pseudoprogression and true progression in immunotherapy trials for pediatric brain tumors. Childhood brain stem tumors treated with peptide-based vaccination had a notable rate of pseudoprogression, all with transient increases in tumor size or enhancement, with new or worsening neurologic deficits, and subsequent clinical improvement and MR imaging stabilization or improvement after administration of corticosteroids and suspension of vaccine therapy.[3] Accurately identifying and managing such patients are essential to avoid both premature termination of therapy and unacceptable neurologic decline, a particular concern in children with DIPG who may develop significant neurologic deterioration with changes in mass effect. Our results suggest that PRM used to characterize temporal diffusion profiles is better able to distinguish pseudoprogression from true progression than mean ADC measurement or tumor volume. This outcome is likely related to treatment-related heterogeneity, in which there may be a mix of viable tumor (low ADC), necrosis (high ADC), and vasogenic edema (high ADC) within the tumor ROI. When measuring change in the mean ADC value of the tumor ROI, the potentially lower ADC values of active tumor foci likely blended with the higher ADC values found in areas of edema and necrosis.[9]

While these results are promising clinically, further study is required for greater understanding of the mechanisms underlying advanced MR imaging manifestations of immunotherapy-induced inflammatory response in the brain.[14,28,29] One hypothesis is that immunotherapy effects on the tumor microenvironment lead to transient vasodilation, increased vessel permeability, and local inflammation, with a resultant increase in contrast enhancement and edema that mimics early tumor progression. An increase in ADC may correspond with tissue hypocellularity due to either treatment-related inflammation and/or tumor reduction.[30] Animal models have demonstrated fractional increase in ADC by PRM as early as 24 hours following introduction of 1,3-bis(2-chloroethyl)-1-nitrosourea[15] and a detectable increase in ADC within 2 days following interleukin-13 receptor α 2 T-cell injection.[13] Progressive separation observed in long-term diffusion profiles between some patients with confirmed pseudoprogression versus true tumor progression in our study supports the use of parametric response maps as supplementary imaging biomarkers for monitoring tumor response in the setting of

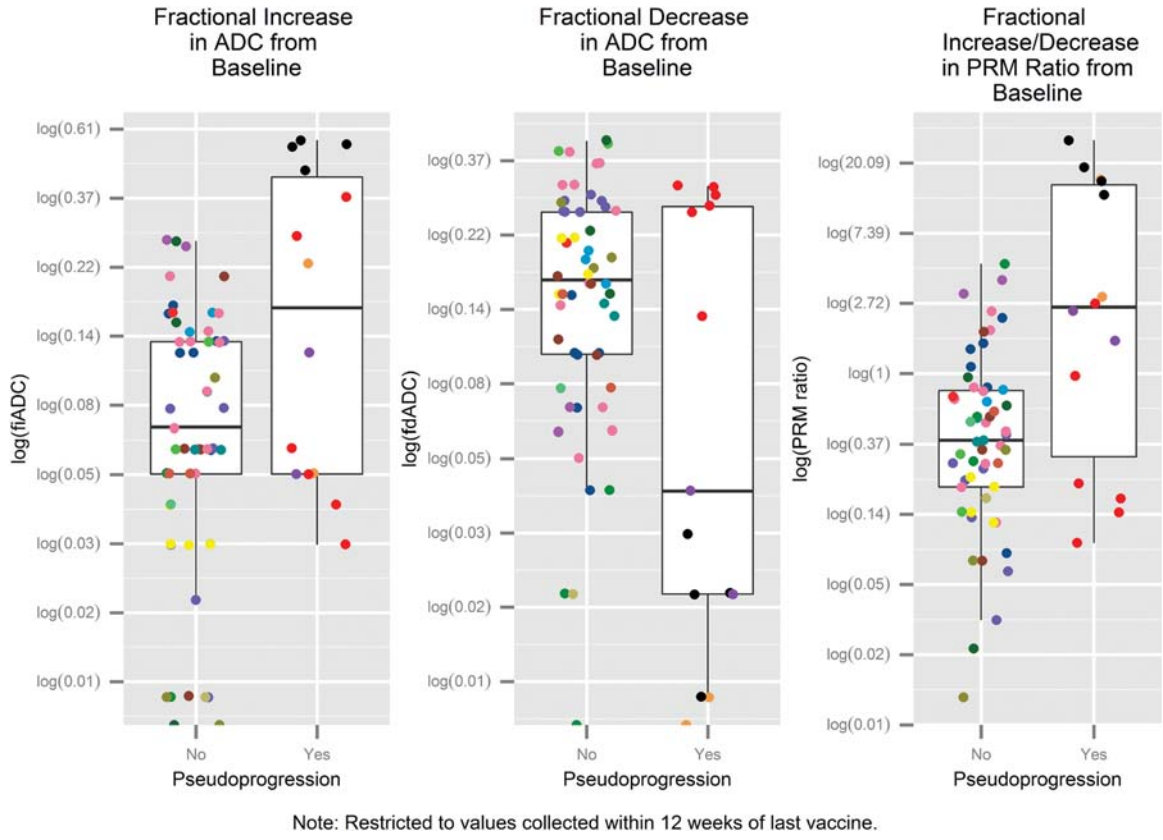

FIG 4. Boxplots of log-fractional increased ADC [log(fiADC)], log-fractional decreased ADC [log(fdADC)], and log-ratio of fiADC/fdADC [log (PRMratio)]. Values are obtained from PRMs from 75 postbaseline scans no more than 12 weeks after the last vaccine date, each compared with the patient's baseline scan. Cohorts are confirmed pseudoprogression ($n = 4$ patients) and true tumor progression (no pseudoprogression, $n = 17$ patients). Data points of the same color are the same patient's PRM metrics for multiple scans, each compared with the baseline. Figure 3 uses the same coloring scheme (but includes time points >12 weeks after last vaccine date).

peptide-based immunotherapy. In particular, fiADC and the PRMratio appear to be the strongest candidates as potential early biomarkers for determining pseudoprogression.

PRMs have been shown to predict treatment response and survival in the setting of adult glioblastoma multiforme.[17,18] However, these studies used only 2 imaging time points, in contrast to our study, in which multiple PRMs were analyzed per patient. Some limitations of the use of PRM in adult tumors are related to poor image registration of lesions resulting from changes in mass effect and tumor contour, which was less of an issue in our pediatric brain stem gliomas. Given that PRM measurements can be confounded by normal tissue,[31] we used weighted-PRM techniques to control for changes in tumor size from each time point, without substantive changes in study results.

Study limitations include a small number of pseudoprogression cases and lack of biopsy confirmation for pseudoprogression. (Biopsy is a high-risk procedure for DIPG lesions.) The peak period of pseudoprogression following radiation therapy for DIPG is generally within the first 3 months.[3] Anything after that time is presumed to be true tumor progression, unless the patient has received vaccine-related immunotherapy, as in our study. The peak period of pseudoprogression related to radiation therapy had likely passed before initiation of vaccine therapy, and the observed cases of pseudoprogression occurred after several doses of vaccine. Furthermore, patients with increased edema or mass effect after irradiation did not start vaccination until this had resolved (up to 12 weeks after completion of irradiation). Regardless, the objective of our study was not to elucidate mechanisms for pseudoprogression by using PRM but to explore its utility in the characterization of pseudoprogression in pediatric DIPG.

CONCLUSIONS

Our study is the first to suggest that serial PRM may be useful to identify pseudoprogression in children with DIPG receiving peptide-based immunotherapy. The valuable properties of diffusion imaging with PRM analysis as an in vivo imaging biomarker include its translatability to the clinical arena, its quantitative nature, and its ease of use and cost effectiveness. The accurate identification of pseudoprogression versus true tumor progression is crucial in determining the optimal management of this novel treatment. We have 3 strong candidates (fiADC, fdADC, and PRMratio) for the development of a predictive model of pseudoprogression, in conjunction with other types of biomarkers that may assist in the treatment of children undergoing immunotherapy. We believe that combining diffusion imaging metrics with clinical information and standard MR imaging will allow timely discrimination of pseudoprogression and true progression, enabling optimal use of immunotherapy. Our preliminary observations, which analyzed 96 scans in 21 patients, should be validated in a planned multi-institutional clinical trial before being used to guide clinical management.

ACKNOWLEDGMENTS

We thank University of Pittsburgh Cancer Institute Clinical Research Services for regulatory management; Andres Salazar, Oncovir, for provision of poly-ICLC; physicians who referred their patients; and the patients and families who participated in this trial. We also thank Angela K. Connelly, Sharon Dibridge, Fern Wasco, and Melanie Gieraltowski for research coordination.

Disclosures: Hideho Okada—*RELATED*: *Grant*: National Institutes of Health*; *UNRELATED*: *Patents (planned, pending, or issued)*: Stemline Therapeutics,* *Comments*: The peptides used for vaccines in the current study are my invention (with other coinventors) and have been exclusively licensed to Stemline Therapeutics for further development; *Royalties*: Stemline Therapeutics,* *Comments*: The same as above. Stemline pays royalties to the University of Pittsburgh; *OTHER*: Hideho Okada is an inventor in the US Patent Application No. 60,611, 797 (Utility Patent Application) "Identification of An IL-13 Receptor Alpha2 Peptide Analogue Capable of Enhancing Stimulation of Glioma-Specific CTL Response." An exclusive licensing agreement has been completed on this application between University of Pittsburgh and Stemline. Due to the potential conflicts of interest, Hideho Okada did not solely interpret any data in the current study. *Money paid to the institution.

REFERENCES

1. Poussaint TY, Rossi A. **Imaging of pediatric brain and spinal cord tumors.** In: Hodler J, Schulthess GK. *Diseases of the Brain, Head & Neck, Spine 2012–2015*: *Diagnostic Imaging and Interventional Techniques*. New York: Springer-Verlag; 2012:203–14
2. Jennings MT, Freeman ML, Murray MJ. **Strategies in the treatment of diffuse pontine gliomas: the therapeutic role of hyperfractionated radiotherapy and chemotherapy.** *J Neurooncol* 1996;28:207–22 Medline
3. Pollack IF, Jakacki RI, Butterfield LH, et al. **Antigen-specific immune responses and clinical outcome after vaccination with glioma-associated antigen peptides and polyinosinic-polycytidylic acid stabilized by lysine and carboxymethylcellulose in children with newly diagnosed malignant brainstem and nonbrainstem gliomas.** *J Clin Oncol* 2014;32:2050–58 CrossRef Medline
4. Hygino da Cruz LC Jr, Rodriguez I, Domingues RC, et al. **Pseudoprogression and pseudoresponse: imaging challenges in the assessment of posttreatment glioma.** *AJNR Am J Neuroradiol* 2011;32:1978–85 CrossRef Medline
5. Bode MK, Ruohonen J, Nieminen MT, et al. **Potential of diffusion imaging in brain tumors: a review.** *Acta Radiol* 2006;47:585–94 CrossRef Medline
6. Ellingson BM, Malkin MG, Rand SD, et al. **Validation of functional diffusion maps (fDMs) as a biomarker for human glioma cellularity.** *J Magn Reson Imaging* 2010;31:538–48 CrossRef Medline
7. Sugahara T, Korogi Y, Kochi M, et al. **Usefulness of diffusion-weighted MRI with echo-planar technique in the evaluation of cellularity in gliomas.** *J Magn Reson Imaging* 1999;9:53–60 CrossRef Medline
8. Lyng H, Haraldseth O, Rofstad EK. **Measurement of cell density and necrotic fraction in human melanoma xenografts by diffusion weighted magnetic resonance imaging.** *Magn Reson Med* 2000;43:828–36 CrossRef Medline
9. Chenevert TL, Stegman LD, Taylor JM, et al. **Diffusion magnetic resonance imaging: an early surrogate marker of therapeutic efficacy in brain tumors.** *J Natl Cancer Inst* 2000;92:2029–36 CrossRef Medline
10. Guo AC, Cummings TJ, Dash RC, et al. **Lymphomas and high-grade astrocytomas: comparison of water diffusibility and histologic characteristics.** *Radiology* 2002;224:177–83 CrossRef Medline
11. Hayashida Y, Hirai T, Morishita S, et al. **Diffusion-weighted imaging of metastatic brain tumors: comparison with histologic type and tumor cellularity.** *AJNR Am J Neuroradiol* 2006;27:1419–25 Medline
12. Kinoshita M, Hashimoto N, Goto T, et al. **Fractional anisotropy and tumor cell density of the tumor core show positive correlation in diffusion tensor magnetic resonance imaging of malignant brain tumors.** *Neuroimage* 2008;43:29–35 CrossRef Medline
13. Lazovic J, Jensen MC, Ferkassian E, et al. **Imaging immune response in vivo: cytolytic action of genetically altered T cells directed to glioblastoma multiforme imaging immune response in vivo: cytolytic action of genetically altered T cells directed to glioblastoma multiforme.** *Clin Cancer Res* 2008;14:3832–39 CrossRef Medline
14. Vrabec M, Van Cauter S, Himmelreich U, et al. **MR perfusion and diffusion imaging in the follow-up of recurrent glioblastoma treated with dendritic cell immunotherapy: a pilot study.** *Neuroradiology* 2011;53:721–31 CrossRef Medline
15. Moffat B, Chenevert TL, Meyer CR, et al. **The functional diffusion map: an imaging biomarker for the early prediction of cancer treatment outcome.** *Neoplasia* 2006;8:259–67 CrossRef Medline
16. LaViolette PS, Mickevicius NJ, Cochran EJ, et al. **Precise ex vivo histological validation of heightened cellularity and diffusion-restricted necrosis in regions of dark apparent diffusion coefficient in 7 cases of high-grade glioma.** *Neuro Oncol* 2014;16:1599–606 CrossRef Medline
17. Hamstra DA, Chenevert TL, Moffat BA, et al. **Evaluation of the functional diffusion map as an early biomarker of time-to-progression and overall survival in high-grade glioma.** *Proc Natl Acad Sci U S A* 2005;102:16759–64 CrossRef Medline
18. Moffat BA, Chenevert TL, Lawrence TS, et al. **Functional diffusion map: a noninvasive MRI biomarker for early stratification of clinical brain tumor response.** *Proc Natl Acad Sci U S A* 2005;102:5524–29 CrossRef Medline
19. Ellingson BM, Cloughesy TF, Zaw T, et al. **Functional diffusion maps (fDMs) evaluated before and after radiochemotherapy predict progression-free and overall survival in newly diagnosed glioblastoma.** *Neuro Oncol* 2012;14:333–43 CrossRef Medline
20. Ellingson BM, Malkin MG, Rand SD, et al. **Volumetric analysis of functional diffusion maps is a predictive imaging biomarker for cytotoxic and anti-angiogenic treatments in malignant gliomas.** *J Neurooncol* 2011;102:95–103 CrossRef Medline
21. Ceschin R, Panigrahy A, Gopalakrishnan V. **sfDM: open-source software for temporal analysis and visualization of brain tumor diffusion MR using serial functional diffusion mapping.** *Cancer Inform* 2015;14(suppl 2):1–9 CrossRef Medline
22. Gorgolewski K, Burns CD, Madison C, et al. **Nipype: a flexible, lightweight and extensible neuroimaging data processing framework in python.** *Front Neuroinform* 2011;5:13 CrossRef Medline
23. Jenkinson M, Beckmann CF, Behrens TE, et al. **FSL.** *Neuroimage* 2012;62:782–90 CrossRef Medline
24. Cox RW. **AFNI: software for analysis and visualization of functional magnetic resonance neuroimages.** *Comput Biomed Res* 1996;29:162–73 CrossRef Medline
25. Pavlou M. **Analysis of clustered data when the cluster size is informative.** University College London, 2012. http://discovery.ucl.ac.uk/1357842/1/mpavlou_thesis.pdf.
26. Rodriguez Gutierrez D, Manita M, Jaspan T, et al. **Serial MR diffusion to predict treatment response in high-grade pediatric brain tumors: a comparison of regional and voxel-based diffusion change metrics.** *Neuro Oncol* 2013;15:981–89 CrossRef Medline
27. Williamson JM, Datta S, Satten G. **Marginal analyses of clustered data when cluster size is informative.** *Biometrics* 2003;59:36–42 CrossRef Medline
28. Yang I, Huh NG, Smith ZA, et al. **Distinguishing glioma recurrence from treatment effect after radiochemotherapy and immunotherapy.** *Neurosurg Clin N Am* 2010;21:181–86 CrossRef Medline
29. Okada H, Pollack IF. **Do we need novel radiologic response criteria for brain tumor immunotherapy?** *Expert Rev Neurother* 2011;11:619–22 CrossRef Medline
30. Wieduwilt MJ, Valles F, Issa S, et al. **Immunochemotherapy with intensive consolidation for primary CNS lymphoma: a pilot study and prognostic assessment by diffusion-weighted MRI.** *Clin Cancer Res* 2012;18:1146–55 CrossRef Medline
31. Grech-Sollars M, Saunders DE, Phipps KP, et al. **Challenges for the functional diffusion map in pediatric brain tumors.** *Neuro Oncol* 2014;16:449–56 CrossRef Medline

Prospective Hemorrhage Rates of Cerebral Cavernous Malformations in Children and Adolescents Based on MRI Appearance

O. Nikoubashman, F. Di Rocco, I. Davagnanam, K. Mankad, M. Zerah, and M. Wiesmann

ABSTRACT

BACKGROUND AND PURPOSE: Current classifications of cerebral cavernous malformations focus solely on morphologic aspects. Our aim was to provide a morphologic classification that reflects hemorrhage rates.

MATERIALS AND METHODS: We retrospectively categorized 355 cavernous malformations of 70 children and adolescents according to their morphologic appearance on MR imaging and calculated prospective hemorrhage rates on the basis of survival functions for 255 lesions in 25 patients with a radiologic observation period of >180 days.

RESULTS: Overall, there were 199 MR imaging examinations with 1558 distinct cavernous malformation observations during a cumulative observation period of 1094.2 lesion-years. The mean hemorrhage rate of all 355 cavernous malformations was 4.5% per lesion-year. According to Kaplan-Meier survival models, Zabramski type I and II cavernous malformations had a significantly higher hemorrhage rate than type III and IV lesions. The presence of acute or subacute blood-degradation products was the strongest indicator for an increased hemorrhage risk ($P = .036$, Cox regression): The mean annual hemorrhage rate and mean hemorrhage-free interval for cavernous malformations with and without signs of acute or subacute blood degradation products were 23.4% and 22.6 months and 3.4% and 27.9 months, respectively. Dot-sized cavernous malformations, visible in T2* and not or barely visible in T1WI and T2WI sequences, had a mean annual hemorrhage rate of 1.3% and a mean hemorrhage-free interval of 37.8 months.

CONCLUSIONS: It is possible to predict hemorrhage rates based on the Zabramski classification. Our findings imply a tripartite classification distinguishing lesions with and without acute or subacute blood degradation products and dot-sized cavernous malformations.

ABBREVIATIONS: CCM = cerebral cavernous malformation; GRE = gradient-echo

Cerebral cavernous malformations (CCMs) are common vascular malformations with a prevalence of 0.2%–0.5%.[1] CCMs may have a considerable clinical impact due to their high annual hemorrhage rates of up to 60%.[2]

The appearance of CCMs on MR imaging is manifold, and knowledge of specific imaging features and how these relate to hemorrhage rates can influence surgical treatment considerations and the frequency of radiologic follow-up. Zabramski et al[3] (Table 1 and Fig 1) and Mottolese et al[4] (On-line Table 1) presented MR imaging classifications characterizing the varied appearances of CCMs. However, neither classification elucidates the relationship between morphologic CCM type and clinical risk. Therefore, these classifications are rarely used in clinical practice. Recently, Jeon et al[5] investigated hemorrhage rates of Zabramski types I–III in an adult population and found that nonhemorrhagic type III CCMs were associated with a significantly lower hemorrhage rate than hemorrhagic type I and II CCMs. Unfortunately, the authors excluded children and adolescents and did not analyze dot-sized type IV CCMs, thus leaving out an important type of CCM frequently encountered in hereditary forms of the disease.[6]

Other authors identified prior hemorrhage as an important risk factor for subsequent hemorrhage by comparing hemorrhage rates of CCMs with and without prior hemorrhage.[1,2,5,7-9] According to these studies, hemorrhage rates ranged from 0%–6% and 4.5%–60%, depending on whether prior hemorrhage was or was not present, respectively.[1,2,5,7-9] However, these articles have

Received February 17, 2015; accepted after revision March 17.

From the Department of Neuroradiology (O.N., M.W.), University Hospital Aachen, Aachen, Germany; Institute for Neuroscience and Medicine 4 (O.N.), Science Centre Jülich, Jülich, Germany; Service de Neurochirurgie Pédiatrique (F.D.R., M.Z.), Hôpital Necker–Enfants Malades, Paris, France; Department of Neuroradiology (I.D.), National Hospital for Neurology and Neurosurgery, London, UK; Brain Repair & Rehabilitation Unit (I.D.), UCL Institute of Neurology, London, UK; and Department of Paediatric Neuroradiology (K.M.), Great Ormond Street Hospital, London, UK.

Please address correspondence to Martin Wiesmann, MD, PhD, Department of Neuroradiology, University Hospital Aachen, Pauwelsstrasse 30, 52074 Aachen, Germany; e-mail: mwiesmann@ukaachen.de

Indicates article with supplemental on-line tables

http://dx.doi.org/10.3174/ajnr.A4427

Table 1: Original MRI classification of CCMs according to Zabramski et al[3]

Lesion Type	MRI Signal Characteristics	Pathologic Characteristics
Type I	T1: hyperintense core T2: hyper- or hypointense core with surrounding hypointense rim	Subacute hemorrhage, surrounded by a rim of hemosiderin-stained macrophages and gliotic brain
Type II	T1: reticulated mixed-signal core T2: reticulated mixed-signal core with surrounding hypointense rim	Loculated areas of hemorrhage and thrombosis of varying ages, surrounded by gliotic, hemosiderin-stained brain; in large lesions, areas of calcification may be seen
Type III	T1: iso- or hypointense core T2: hypointense with a hypointense rim that magnifies the size of the lesion GE: hypointense with greater magnification than T2	Chronic resolved hemorrhage, with hemosiderin staining within and around the lesion
Type IV	T1: poorly seen or not visualized at all T2: poorly seen or not visualized at all GE: punctate hypointense lesions	Two lesions in the category were pathologically documented as telangiectasias

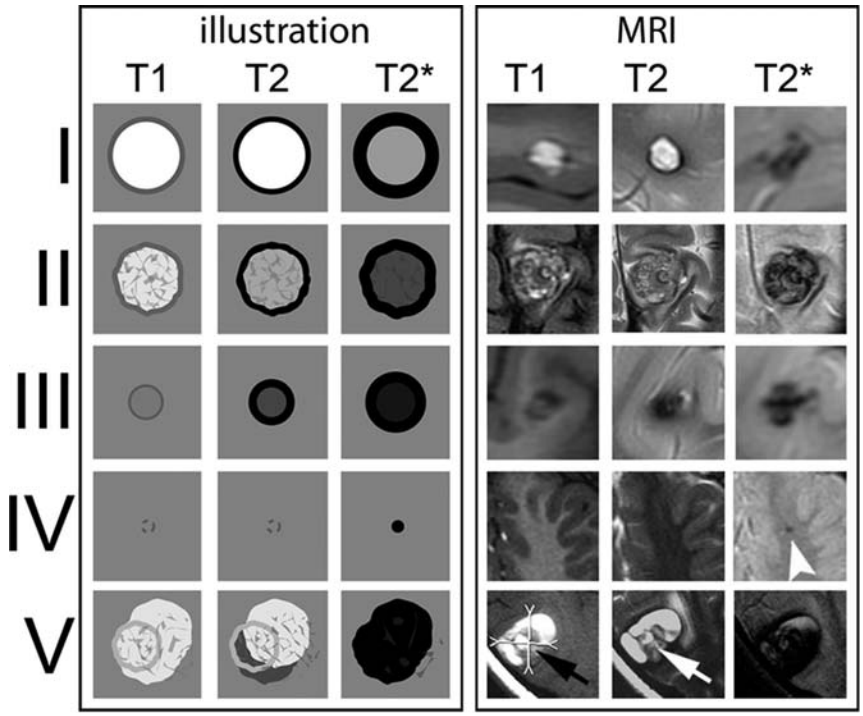

FIG 1. CCM types according to the Zabramski classification. Graphic illustration (*left 3 rows*) and corresponding MR images (*right 3 rows*) of CCMs according to the MR imaging classification of Zabramski et al.[3] Type IV CCM: *arrowhead* indicates a small T2* lesion. Type V: *arrows* indicate parts of the actual CCMs that are visible in the center of the hemorrhage; however, the CCM is not fully distinguishable from hemorrhage.

a lack of comparability because of differing hemorrhage definitions.[10] Hence, our aim was to evaluate whether the different CCM types according to the Zabramski classification, including dot-sized type IV lesions, are associated with different hemorrhage rates and to provide a simple, yet comprehensive morphologic classification that reflects hemorrhage rates best.

MATERIALS AND METHODS

Patients

After approval from the local institutional ethics board, we retrospectively reviewed data from the medical files from the department of Pediatric Neurosurgery of Hôpital Necker Enfants Malades, Paris, France, between January 1, 1993, and December 31, 2009. We identified 74 patients younger than 18 years of age with clear radiologic and/or pathologic criteria of CCMs, of whom 4 were excluded from the study due to a history of radiation. The remaining 70 patients had 356 CCMs. One small histologically proved CCM was found to be adjacent to a larger CCM during an operation and was removed. It was excluded from our analysis because it was not visible in previous imaging. In the end, we included 355 CCMs in 70 patients in this study. In addition to neuroimaging features, we assessed clinical and demographic information, such as age, sex, medical history, treatment, family history, and histologic findings by chart review. Two neuroradiologists, blinded to all clinical data, analyzed the imaging data. Unblinded consensus readings were performed to obtain a reference standard for statistical analyses.

Definitions

All lesions were radiologically defined according to the Zabramski classification.[3] An additional category (type V) accounting for CCMs presenting with gross extralesional hemorrhage was added to take these lesions into account (Fig 1).

Only MR imaging studies performed at 1.5T were included, to minimize variation through magnetic field strength on susceptibility artifacts. All examinations were evaluated on T1WI and T2WI sequences with gradient-echo (GRE) imaging considered when present.

CCM diameters on T1WI and T2WI were averaged in all cases except in dot-sized CCMs (Zabramski type IV). The diameter of these lesions, which are only visible on T2*, was arbitrarily defined as 1 mm, because measuring lesion diameters on the basis of susceptibility artifacts alone will result in different results depending on the amount of hemosiderin depositions, section thickness, and section orientation. Overall hemorrhage size was assessed if the discrimination of a distinct lesion within the hemorrhage was not possible. Lesion growth was defined as a visually distinct increase of lesion diameter of at least 1 mm.

Hemorrhage Definition

To differentiate hemorrhage and simple intralesional thrombosis of blood, we postulated a radiologic hemorrhagic event if there was extralesional hemorrhage (acute or subacute blood-degradation products) or if there was intralesional hemorrhage (acute or subacute blood-degradation products) accompanied by lesion growth, mass effect, or edema. In accordance with criteria proposed by Al-Shahi Salman et al,[10] neither lesion growth without signal changes nor the presence of hemosiderin without signs of recent hemorrhage was considered a hemorrhagic event. In addition, the appearance of subacute blood-degradation products without lesion growth or edema was not considered a hemorrhagic event. Because assessment of lesion growth is, by definition, not possible for supposedly hemorrhagic lesions at first imaging, intralesional hemorrhage at first imaging accompanied by corresponding clinical symptoms was also regarded as hemorrhage.[3] A hemorrhagic event was considered symptomatic if there was a relation between clinical symptoms and hemorrhage age, anatomic location, or electrophysiologic examination findings. Lesions were regarded as de novo only when their new appearance could be shown in 2 comparable (ie, section thickness and orientation) consecutive series.

Hemorrhage Rate Calculations

Hemorrhage rates were calculated by 2 methods:

1) Lifetime hemorrhage rates were calculated as hemorrhagic events per time. The observation period of de novo lesions was defined as the period between radiologic diagnosis and last imaging. The observation period of lesions that were present at first imaging (presumably congenital lesions) was defined as the period between birth and last imaging. The lifetime hemorrhage rate was calculated as the average of hemorrhage rates of de novo and presumably congenital lesions. All 355 lesions were included in these calculations.

2) Prospective hemorrhage rates were calculated on the basis of Kaplan-Meier survival models and were analyzed with the Breslow test, log-rank test, and Cox regression. Because CCMs are dynamic lesions that may change in appearance with time, we analyzed prospective hemorrhage rates depending on the lesion appearance at any given observation point.[6,11] Only lesions with a radiologic follow-up of >180 days were included in these calculations.

Statistical Analysis

Standard statistical tests (Student *t* test, Fisher exact test, Pearson χ^2 test, Breslow test, log-rank test, Cox regression) were performed when applicable. *P* values under the α level of .05 were defined as significant. All statistical analyses were performed with SPSS software (Version 20; IBM, Armonk, New York).

RESULTS

Demographics and Genetics

There were 355 CCMs in 48 male and 22 female patients. Twenty of 70 patients had multiple CCMs. The mean age of all 70 patients at first radiologic diagnosis of a CCM was 8.9 ± 4.5 years, ranging from 6.7 months to 17.3 years (median 9.5 years).

If one considered only lesions with a radiologic observation period of at least 180 days, there were 255 lesions in 10 female and 15 male patients. Of these 255 lesions, 248 were observed in 18 patients with multiple lesions. Six of these 18 children were tested for *CCM1*, *CCM2*, and *CCM3* mutations. Three patients had a *CCM1* mutation, and 3 children had a *CCM3* mutation.

Lesion Characteristics

In initial imaging, there were 33 type I, 15 type II, 74 type III, 190 type IV, and 30 type V CCMs. In addition, there was 1 hemorrhagic, predominantly cystic CCM. Initial lesion type could not be classified in 12 cases because of a lack of adequate MR imaging examinations at the date of the finding. Overall, there were 91 frontal, 72 parietal, 64 temporal, 59 occipital, and 5 subependymal CCMs. Twenty-five CCMs were located in deep brain structures, 19 in the brain stem, and 20 in the cerebellum. Sixteen of 355 CCMs were associated with developmental venous anomalies. The initial average diameter of all CCMs excluding dot-sized CCMs was 12.0 ± 12.3 mm, ranging from 1 to 50 mm (median 5 mm). The diameter of lesions with extralesional hemorrhage (mean, 22.5 ± 11.8 mm; median, 20 mm; range, 5–50 mm) was greater than that of lesions with intralesional hemorrhage (mean, 9.4 ± 8.8 mm; median, 5 mm; range, 1–35 mm) and that of nonhemorrhagic type III lesions (mean, 3.4 ± 3 mm; median, 2 mm; range, 1–15 mm) ($P < .001$, Student *t* test).

Clinical Findings

Overall, 63 of 70 patients were symptomatic during a mean clinical observation period of 4.0 years. Seizures, signs of raised intracranial pressure, focal neurologic deficits, and isolated headache were observed in 24, 22, 20, and 2 patients, respectively. A cross-tabulation illustrating the co-occurrence of initial symptoms can be found in On-line Table 2. Infratentorial lesions were more likely to present with symptoms related to mass effect (ie, intracranial pressure and focal neurologic deficits), while supratentorial lesions were more likely to present with seizures ($P < .001$, Pearson χ^2 test). Seven patients with 36 CCMs were symptom-free at diagnosis. All 7 patients remained symptom-free during the entire clinical observation period (mean, 5.1 ± 4.5 years; median, 3.9 years; range, 7 months to 13.0 years).

Radiologic Events

If one considered all 355 CCMs, there were 131 radiologic hemorrhagic events. Seventy-four of 131 hemorrhagic events were clinically symptomatic, while the remaining 57 hemorrhagic events were clinically silent. In addition to the 74 clinically symptomatic cases, there were 10 further reported clinical events in which an association between a clinical event and hemorrhage was not determinable due to a lack of adequate MR imaging examinations. Clinical symptoms were likely to be caused by hemorrhage ($P = .004$, Fisher exact test). Hemorrhage was more likely to be clinically symptomatic if the CCM was located in the brain stem ($P = .004$, Fisher exact test).

Intralesional signal changes without fulfillment of our hemorrhage criteria were present in 97 cases. These intralesional signal changes were likely to be asymptomatic ($P < .001$, Pearson χ^2 test).

Three cases of recurring seizures were associated with nonhemorrhagic type III lesions. All dot-sized CCMs (Zabramski type IV) in our series were asymptomatic.

Conventional Hemorrhage Rate Calculations

Overall, 199 MR imaging studies were performed (mean: 4.4 studies per child; range, 1–12 MR imaging studies per child). There were 1558 distinct observations of 355 CCMs with a cumulative radiologic observation period of 1094.2 lesion-years. The lifetime hemorrhage risk with regard to all 355 lesions was 4.5% per lesion-year on average, based on 20 hemorrhagic events in 95 de novo lesions during a mean observation period of 3.8 years (5.5% per lesion-year) and 111 hemorrhagic events in 260 presumed congenital CCMs during a mean observation period of 12.3 years (3.5% per lesion-year).

Prospective Hemorrhage Rate Calculations

The mean radiologic observation period of 255 CCMs with a radiologic observation period of at least 180 days was 4.2 ± 2.9 lesion-years, ranging from 217 days to 13.0 years (median 3.2 years). There were 1398 radiologic observations of 255 lesions. The mean time between imaging was 8.8 months, ranging from 2 days to 29.9 ± 7.7 months (median 5.6 months). Table 2, On-line Table 3, and Figs 2 and 3 provide an overview of hemorrhage rates based on survival functions.

Table 2: Hemorrhage-free survival[a]

CCM Type	Mean Hemorrhage-Free Survival			
	Estimator	Standard Error	95% CI Lower	95% CI Upper
I	18.82	1.52	15.84	21.80
II	24.92	2.91	19.21	30.63
III	27.88	0.38	27.13	28.63
IV	37.78	0.40	37.00	38.57
V	21.34	2.67	16.10	26.59
I, II, V	22.63	1.50	19.68	25.57
All	36.06	0.59	34.91	37.21

[a] Demonstrating mean hemorrhage-free survival in months depending on the extended CCM type of Zabramski et al.[3]

Sixty-one of 131 radiologic hemorrhagic events occurred in the excluded 100 lesions. Fifty-three of these 61 hemorrhagic events corresponded to CCMs that were hemorrhagic at first imaging. Only 8 of 61 excluded hemorrhagic events corresponded to consecutive hemorrhagic events of lesions that eventually were resected within 180 days.

Prospective Hemorrhage Rates Based on Zabramski Type

The annual hemorrhage rate was 29.8% for Zabramski type I, 20.1% for type II, 3.4% for type III CCMs, and 1.3% for type IV CCMs. The hemorrhage rate was 23.1% for our proposed new type V CCM and 23.4% for combined type I, II, and V CCMs.

Hemorrhage rates of type III and IV CCMs differed significantly (Breslow test: $P = .015$; log-rank test: $P = .014$). There was no significant difference between hemorrhage rates of type I, II, and V CCMs (Breslow test: $P \geq .133$; log-rank test: $P \geq .247$; On-line Table 3). Mean event-free intervals of type I, II, and V lesions were significantly shorter compared with type III and IV CCMs (Breslow test: $P \leq .006$; log-rank test: $P \leq .044$; On-line Table 3).

Prospective Hemorrhage Rates Based on Other Factors

Univariate analyses revealed that solitary CCMs had a higher hemorrhage risk in the long term than CCMs in the context of multiple CCMs (Breslow test: $P = .082$; log-rank test: $P = .002$). In addition, CCMs located in the brain stem had an increased hemorrhage rate (Breslow test: $P = .007$; log-rank test: $P = .044$).

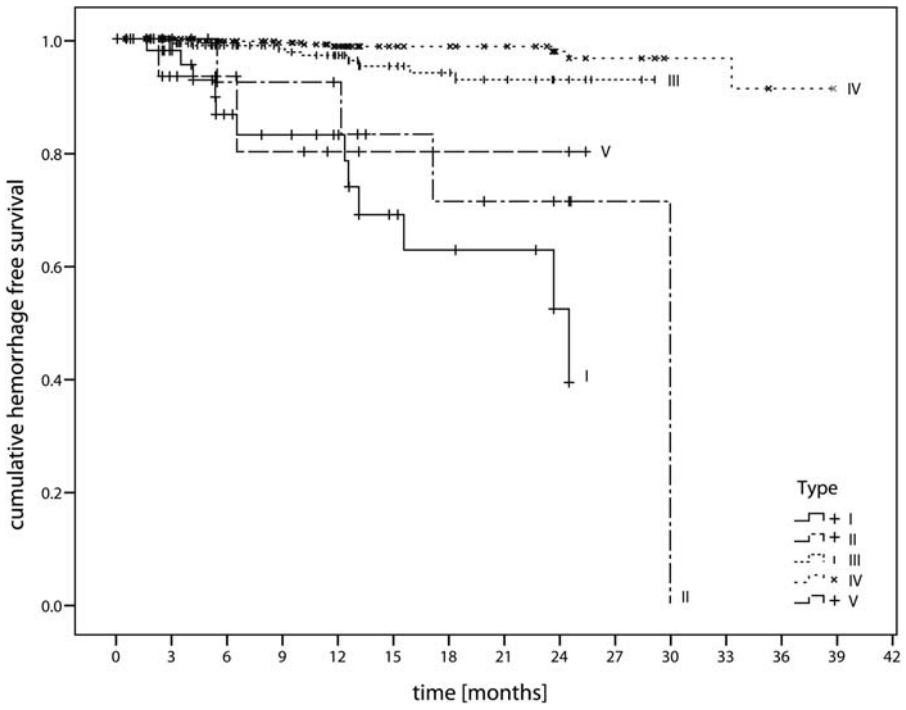

FIG 2. Hemorrhage-free survival. Kaplan-Meier diagram illustrates hemorrhage-free survival depending on the Zabramski CCM type.

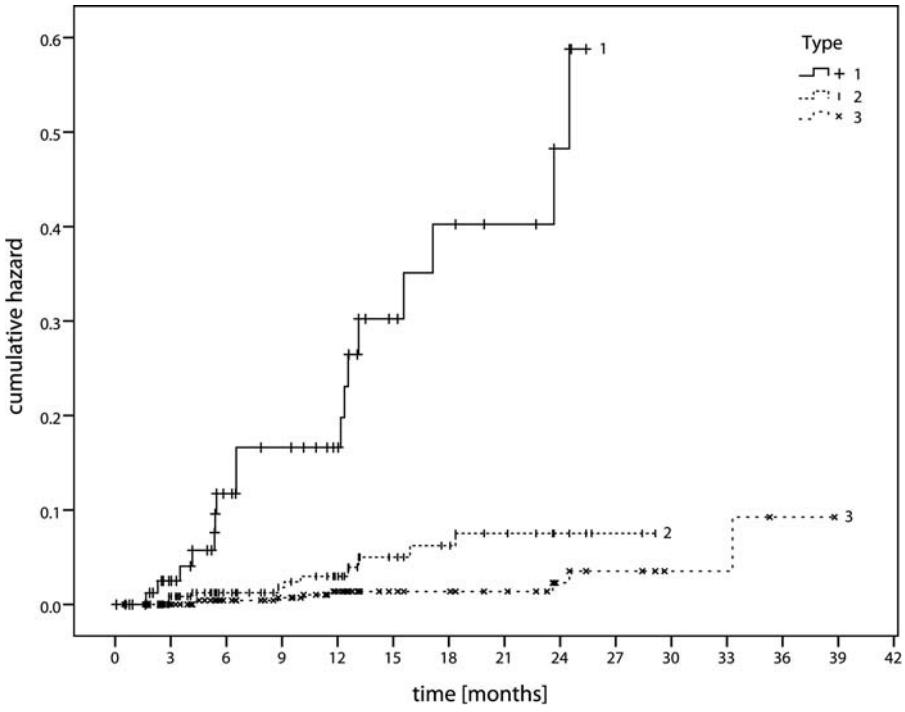

FIG 3. Cumulative hazard. Diagram illustrates the cumulative hazard for hemorrhage according to our proposed CCM classification, 1) CCM with signs of acute or subacute hemorrhage, 2) CCM without signs of acute or subacute hemorrhage, and 3) dot-sized CCMs.

Table 3: Prospective hemorrhage rates in the literature[a]

Study	No. of Patients	No. of Lesions	Hemorrhage Assessment	Hemorrhage Rate without Prior Hemorrhage	Hemorrhage Rate with Prior Hemorrhage
Al-Shahi Salman et al[1]	134	NI	MRI/clinical	2.4%	29.5%
Kondziolka et al[8]	122	NI	MRI/clinical	0.6%	4.5%
Moriarity et al[15]	68	228	MRI/clinical	3.1%[b]	NI
Porter et al[16]	173	NI	MRI/clinical	1.6%[b]	NI
Robinson et al[17]	57	66	MRI/clinical	0.7%[b,c]	NI

Note:—NI indicates not indicated.

[a] Hemorrhage rates of supratentorial and infratentorial CCMs found in prospective registry studies. Hemorrhage rates are in patient-years.

[b] Overall hemorrhage rate.

[c] Hemorrhage rates in lesion-years.

CCMs associated with a developmental venous anomaly had a higher hemorrhage risk in the shortterm (Breslow test: $P = .032$; log-rank test: $P = .213$).

CCM size (cutoffs: 1.5, 2, 2.5, 3 cm) had no significant impact on hemorrhage rates, when dot-sized CCMs were excluded from analysis (Breslow test: $P \geq .352$; log-rank test: $P \geq .299$). CCMs located close to gray matter had no increased hemorrhage rate (Breslow test: $P = .723$; log-rank test: $P = .759$). Neither sex nor mutation type (*CCM1* versus *CCM3*) had a significant influence on hemorrhage rates (Breslow test: $P = .203$; log-rank test: $P = .071$; and Breslow test: $P = .173$; log-rank test: $P = .232$, respectively).

Eventually, multivariate analyses (Cox regression) revealed that the presence of acute or subacute blood-degradation products had a significant impact on hemorrhage rates ($P = .036$), whereas mass effect ($P = .161$), the presence of extralesional hemorrhage ($P = .307$), CCMs in the context of multiplicity ($P = .139$), the presence of a developmental venous anomaly ($P = .511$), and localization in the brain stem ($P = .761$) had no significant influence on hemorrhage rates.

DISCUSSION

Prospective Hemorrhage Rates Based on the Zabramski Classification

When a CCM is diagnosed, the most important issue is to predict the risk for future hemorrhage and clinical symptoms. Thus, the aim of any classification should be to predict hemorrhage (and consequently clinical) risks. Prior hemorrhage has already been described as an important risk factor for subsequent hemorrhage.[1,2,7-9] However, the term "hemorrhage" is used to describe both cerebral bleeding and a clinical symptom in the published literature, making accurate comparisons of hemorrhage rates difficult, with some authors calculating hemorrhage rates per patient and indicating clinical event rates instead of radiologic event rates (Table 3).[10] While the assessment of clinical events appears practical, there is a distinct risk of false generalization: The same CCM will lead to different clinical event rates depending on whether it is located in the precentral or the middle frontal gyrus. Accordingly, hemorrhage of brain stem CCMs was more likely to be symptomatic than other CCMs in our series. Therefore, we advocate the assessment of lesion-based radiologic hemorrhage rates because the occurrence of clinical events (with the exception of seizures) depends primarily on lesion location and the extent of hemorrhage.[12,13] Clinical event rates can then be deduced when the localization and hemorrhage rate of a given CCM are known.[11]

We analyzed hemorrhage rates on the basis of the most common CCM classification by Zabramski et al[3] and found that it is

possible to predict radiologic hemorrhage rates on the basis of this classification. Even though Zabramski type I, II, and (proposed) V CCMs have distinctive morphologic features, these lesions share statistically similar high annual hemorrhage rates of 20.1%–29.8%. Annual hemorrhage rates of type III and dot-sized CCM are significantly lower (3.4% and 1.3%, respectively). Our results imply that the presence of acute or subacute blood-degradation products, present in Zabramski type I, II, and V CCMs, is the strongest predictor of hemorrhage. These findings are highly in accordance with results provided by Jeon et al,[5] who performed a comparable analysis on 410 mostly solitary-type I, II, and III CCMs in a population older than 18 years of age: The authors reported an increased annual hemorrhage risk of type I and II lesions (27.6% and 15.4%, respectively) compared with type III lesions (5.4%) ($P < .001$).[5] Additionally, the authors found that female sex, age, infratentorial localization, multiplicity, size, and the presence of venous angioma were no risk factors for hemorrhage, which is also in accordance with our results.[5] The outstanding role of signs of prior hemorrhage is also supported by previous published results, in which an increased risk for hemorrhagic CCM has been reported despite different definitions of hemorrhage (Table 3).[1,2,7-9] A possible explanation might be the destruction of microstructural integrity after a first hemorrhagic event.[14]

Our findings and data from the literature imply that a simple tripartite classification might be more useful in clinical practice:

1) CCMs with acute or subacute blood-degradation products (Zabramski I, II, V). High hemorrhage risk of 23.4% (literature: 4.5%–60%).[1,2,5,8] Mean hemorrhage-free interval: 22.63 months. Association with acute or subacute clinical symptoms.
2) CCMs without acute or subacute blood-degradation products (Zabramski III). Intermediate annual hemorrhage risk of 3.4% (literature: 0%–6%).[1,2,5,8,15-17] Mean hemorrhage-free interval: 27.88 months. They may be symptomatic particularly in the context of seizures: Ten percent of seizures in our series were associated with these CCMs.
3) Dot-sized lesions, visible in T2* and not or barely visible in T1WI and T2WI (Zabramski IV). The lowest hemorrhage rate of 1.3%. Mean hemorrhage-free interval: 37.78 months. Appear to be asymptomatic unless they are hemorrhagic.[6]

Other Possible Risk Factors

Whereas univariate analyses implied that brain stem localization, the presence of a developmental venous anomaly, and a solitary CCM are associated with an increased hemorrhage risk, these factors did not prove significant in our multivariate analyses. In fact, data from various authors imply that an apparent increased hemorrhage risk of brain stem lesions is likely to be caused by a selection bias: Brain stem hemorrhage is more likely to be symptomatic than supratentorial hemorrhage and is therefore more likely to lead to MR imaging.[9,12,18,19] Furthermore, while the relationship between developmental venous anomalies and CCMs is not fully understood yet, neither Flemming et al[20] nor Jeon et al,[5] who performed analyses comparable with ours found that the presence of developmental venous anomalies was associated with an increased hemorrhage risk. Finally, it has been reported that patients with multiple CCMs and patients with *CCM3* mutations have a more aggressive clinical course. Flemming et al,[20] for example, indicated an odds ratio of 2.65 for hemorrhage in patients with multiple lesions. However, a more aggressive clinical course does not necessarily imply an increased hemorrhage risk. Current evidence suggests that a more aggressive clinical course is possibly caused by an increased cumulative hemorrhage rate rather than an increased hemorrhage rate of each CCM.[5,21,22] Paradoxically, our data demonstrated an increased long-term hemorrhage rate of solitary lesions. However, this result may have been biased because most of the solitary lesions were more likely to be resected early on and thus were absent from long-term radiologic follow-up analyses. Although there were limited patient data with mutations in our analyzed population, our results did not suggest that hemorrhage rates of each CCM type depended on a specific mutation type. Results in the literature suggest that those carrying the *CCM3* mutation are likely to present with an increased number of CCMs at an early age.[6,22] Again, a more aggressive clinical course in patients with *CCM3* mutations may be caused by an increased cumulative risk due to a high number of CCMs.[6,21,22]

Limitations

Our retrospective approach involves a degree of selection bias. An ideal study dealing with hemorrhage rates should be prospective and standardized. However, examining a considerable number of patients with CCMs on a regular basis—ideally monthly to reliably diagnose new hemorrhage—can be a tedious task, which is reflected by the fact that all published prospective studies dealing with the natural history of CCMs are registry studies.[1,8,15-17]

Furthermore, it has been discussed controversially whether CCMs in children bear an increased hemorrhage risk.[23] Mottolese et al,[4] for instance, reported that CCMs in children are more likely to be symptomatic. In the end, the sometimes reported lower proportion of asymptomatic incidental CCMs in children is likely to be caused by a selection bias because routine examinations of the brain are more common in adults than in children. Additionally, hemorrhage rates in the literature are commonly calculated under the assumption that CCMs are congenital, despite the proof of de novo lesions.[7-9,15-17] Consequently, hemorrhage rates calculated under this assumption are always inversely proportional to the mean age of a patient population, leading to a higher hemorrhage rate in younger populations. In fact, Jeon et al,[5] who performed a prospective hemorrhage rate calculation similar to ours, reported comparable hemorrhage rates for a population older than 18 years of age.

A further limitation of our study is a diagnostic uncertainty concerning dot-sized lesions.[6] The size and signal of dot-sized lesions depend strongly on technical MR imaging parameters such as magnetic field strength and section thickness. It is conceivable that dot-sized CCMs simply correspond to small nonhemorrhagic CCMs.[6] Nonetheless, our data suggest that these different CCM types have statistically significant distinctive clinical and radiologic features that justify differentiation of these lesions.

In summary, we believe that analyzing CCMs in children and adolescents with multiple CCMs is a practical approach in the

absence of prospective studies with serial MR imaging examinations; examining CCMs in the context of multiple lesions allows a longitudinal analysis of different CCMs of varying types, sizes, and locations at the same time and underlying the same possible influence factors. Furthermore, differential diagnosis of dot-sized T2* lesions in adults comprises microangiopathic, amyloid angiopathic, or drug-induced (eg, anticoagulant therapy) microbleeds, which are rare in children and adolescents.

CONCLUSIONS

This study has shown that it is possible to predict hemorrhage rates of CCMs on the basis of the most common morphologic CCM classification proposed by Zabramski et al[3] when a further category accounting for CCMs with gross extralesional hemorrhage is added. Our findings and data from the literature imply that a simpler tripartite classification predicts hemorrhage risks best. Nevertheless, further prospective research needs to be done to establish whether our results prove correct and practical in daily clinical work.

Disclosures: Indran Davagnanam—*RELATED*: *Grant*: University College London Biomedical Research Centre,* *Comments*: University College London Biomedical Research Centre funding for 1 consultant session in 2014–2016. Martin Wiesmann—*UNRELATED*: *Consultancy*: Stryker Neurovascular; *Grants/Grants Pending*: Covidien*; *Payment for Lectures (including service on Speakers Bureaus)*: Siemens, Stryker Neurovascular, Bracco. *Money paid to the institution.

REFERENCES

1. Al-Shahi Salman R, Hall JM, Horne MA, et al; Scottish Audit of Intracranial Vascular Malformations (SAIVMs) collaborators. **Untreated clinical course of cerebral cavernous malformations: a prospective, population-based cohort study.** *Lancet Neurol* 2012;11:217–24 CrossRef Medline
2. Wang CC, Liu A, Zhang JT, et al. **Surgical management of brainstem cavernous malformations: report of 137 cases.** *Surg Neurol* 2003;59:444–54; discussion 454 CrossRef Medline
3. Zabramski JM, Wascher TM, Spetzler RF, et al. **The natural history of familial cavernous malformations: results of an ongoing study.** *J Neurosurg* 1994;80:422–32 CrossRef Medline
4. Mottolese C, Hermier M, Stan H, et al. **Central nervous system cavernomas in the pediatric age group.** *Neurosurg Rev* 2001;24:55–71 CrossRef Medline
5. Jeon JS, Kim JE, Chung YS, et al. **A risk factor analysis of prospective symptomatic haemorrhage in adult patients with cerebral cavernous malformation.** *J Neurol Neurosurg Psychiatry* 2014;85:1366–70 CrossRef Medline
6. Nikoubashman O, Wiesmann M, Tournier-Lasserve E, et al. **Natural history of cerebral dot-like cavernomas.** *Clin Radiol* 2013;68:e453-59 CrossRef Medline
7. Aiba T, Tanaka R, Koike T, et al. **Natural history of intracranial cavernous malformations.** *J Neurosurg* 1995;83:56–59 CrossRef Medline
8. Kondziolka D, Monaco EA 3rd, Lunsford LD. **Cavernous malformations and hemorrhage risk.** *Prog Neurol Surg* 2013;27:141–46 CrossRef Medline
9. Li D, Yang Y, Hao SY, et al. **Hemorrhage risk, surgical management, and functional outcome of brainstem cavernous malformations.** *J Neurosurg* 2013;119:996–1008 CrossRef Medline
10. Al-Shahi Salman R, Berg MJ, Morrison L; Angioma Alliance Scientific Advisory Board. **Hemorrhage from cavernous malformations of the brain: definition and reporting standards.** *Stroke* 2008;39:3222–30 CrossRef Medline
11. Clatterbuck RE, Moriarity JL, Elmaci I, et al. **Dynamic nature of cavernous malformations: a prospective magnetic resonance imaging study with volumetric analysis.** *J Neurosurg* 2000;93:981–86 CrossRef Medline
12. Gross BA, Batjer HH, Awad IA, et al. **Brainstem cavernous malformations: 1390 surgical cases from the literature.** *World Neurosurg* 2013;80:89–93 CrossRef Medline
13. Rosenow F, Alonso-Vanegas MA, Baumgartner C, et al; Surgical Task Force, Commission on Therapeutic Strategies of the ILAE. **Cavernoma-related epilepsy: review and recommendations for management—report of the Surgical Task Force of the ILAE Commission on Therapeutic Strategies.** *Epilepsia* 2013;54:2025–35 CrossRef Medline
14. Tu J, Stoodley MA, Morgan MK, et al. **Ultrastructural characteristics of hemorrhagic, nonhemorrhagic, and recurrent cavernous malformations.** *J Neurosurg* 2005;103:903–09 CrossRef Medline
15. Moriarity JL, Wetzel M, Clatterbuck RE, et al. **The natural history of cavernous malformations: a prospective study of 68 patients.** *Neurosurgery* 1999;44:1166–71; discussion 1172–73 CrossRef Medline
16. Porter PJ, Willinsky RA, Harper W, et al. **Cerebral cavernous malformations: natural history and prognosis after clinical deterioration with or without hemorrhage.** *J Neurosurg* 1997;87:190–97 CrossRef Medline
17. Robinson JR, Awad IA, Little JR. **Natural history of the cavernous angioma.** *J Neurosurg* 1991;75:709–14 CrossRef Medline
18. Maraire JN, and Awad IA. **Intracranial cavernous malformations: lesion behavior and management strategies.** *Neurosurgery* 1995;37:591–605 CrossRef Medline
19. Hauck EF, Barnett SL, White JA, et al. **Symptomatic brainstem cavernomas.** *Neurosurgery* 2009;64:61–70; discussion 70–71 CrossRef Medline
20. Flemming KD, Link MJ, Christianson TJ, et al. **Prospective hemorrhage risk of intracerebral cavernous malformations.** *Neurology* 2012;78:632–36 CrossRef Medline
21. Schneble HM, Soumare A, Hervé D, et al. **Antithrombotic therapy and bleeding risk in a prospective cohort study of patients with cerebral cavernous malformations.** *Stroke* 2012;43:3196–99 CrossRef Medline
22. Spiegler S, Najm J, Liu J, et al. **High mutation detection rates in cerebral cavernous malformation upon stringent inclusion criteria: one-third of probands are minors.** *Mol Genet Genomic Med* 2014;2:176–85 CrossRef Medline
23. Al-Holou WN, O'Lynnger TM, Pandey AS, et al. **Natural history and imaging prevalence of cavernous malformations in children and young adults.** *J Neurosurg Pediatr* 2012;9:198–205 CrossRef Medline

CT Metal Artifact Reduction in the Spine: Can an Iterative Reconstruction Technique Improve Visualization?

A.L. Kotsenas, G.J. Michalak, D.R. DeLone, F.E. Diehn, K. Grant, A.F. Halaweish, A. Krauss, R. Raupach, B. Schmidt, C.H. McCollough, and J.G. Fletcher

ABSTRACT

BACKGROUND AND PURPOSE: Metal-related artifacts from spine instrumentation can obscure relevant anatomy and pathology. We evaluated the ability of CT images reconstructed with and without iterative metal artifact reduction to visualize critical anatomic structures in postoperative spines and assessed the potential for implementation into clinical practice.

MATERIALS AND METHODS: We archived CT projection data in patients with instrumented spinal fusion. CT images were reconstructed by using weighted filtered back-projection and iterative metal artifact reduction. Two neuroradiologists evaluated images in the region of spinal hardware and assigned a score for the visualization of critical anatomic structures by using soft-tissue and bone windows (critical structures totally obscured, $n = 0$; anatomic recognition with high diagnostic confidence, $n = 5$). Using bone windows, we measured the length of the most pronounced linear artifacts. For each patient, neuroradiologists made recommendations regarding the optimal use of iterative metal artifact reduction and its impact on diagnostic confidence.

RESULTS: Sixty-eight patients met the inclusion criteria. Visualization of critical soft-tissue anatomic structures was significantly improved by using iterative metal artifact reduction compared with weighted filtered back-projection (median, 1 ± 1.5 versus 3 ± 1.3, $P < .001$), with improvement in the worst visualized anatomic structure in 88% (60/68) of patients. There was not significant improvement in visualization of critical osseous structures. Linear metal artifacts were reduced from 29 to 11 mm ($P < .001$). In 87% of patients, neuroradiologists recommended reconstructing iterative metal artifact reduction images instead of weighted filtered back-projection images, with definite improvement in diagnostic confidence in 32% (22/68).

CONCLUSIONS: Iterative metal artifact reduction improves visualization of critical soft-tissue structures in patients with spinal hardware. Routine generation of these images in addition to routine weighted filtered back-projection is recommended.

ABBREVIATIONS: IMAR = iterative metal artifact reduction; wFBP = weighted filtered back-projection; HU = Hounsfield units

Spinal fusion is commonly performed to treat pain and/or minimize abnormal vertebral motion. In 2011, 488,000 spinal fusion procedures were performed in the United States, a nearly 3-fold increase since 1998.[1,2] However, despite advances in surgical technique and a proliferation of novel fusion devices and hardware, the rates of the so-called failed back surgery syndrome have not declined, and patients undergoing these procedures often require follow-up imaging.[3,4] MR imaging and CT are both useful in the evaluation of patients after spinal fusion, but both are limited by artifacts related to metallic spinal implants. Misregistration artifacts on MR imaging and beam-hardening artifacts on CT degrade image quality, obscure relevant postoperative anatomy and pathology, and reduce the overall diagnostic confidence in distinguishing normal structures and pathologic findings.[5,6]

On CT, beam-hardening and photon starvation artifacts from metallic fusion hardware frequently compromise visualization of critical anatomic structures and pathologic findings, particularly in the ROI near implanted hardware. Recent publications have presented several postprocessing methods for decreasing the severity of metal implant artifacts in CT.[7-11] These works describe unique challenges to minimizing metal-related artifacts in different body regions due to differences in local anatomy and in implant composition.[12] However, only a few of these works focused on the unique challenges of the postoperative spine,[12,13] and none assessed visualization of the critical anatomic structures that the neuroradiologist must evaluate in the postoperative

Received January 6, 2015; accepted after revision March 11.

From the Department of Radiology (A.L.K., G.J.M., D.R.D., F.E.D., C.H.M., J.G.F.), Mayo Clinic, Rochester, Minnesota; Siemens Medical Solutions (K.G., A.F.H.), Malvern, Pennsylvania; and Siemens Healthcare (A.K., R.R., B.S.), Forchheim, Germany.

Please address correspondence to Amy L. Kotsenas, MD, Department of Radiology, Mayo Clinic, Rochester, MN 55905; e-mail: Kotsenas.amy@mayo.edu; @AmyKotsenas

http://dx.doi.org/10.3174/ajnr.A4416

setting. Additionally, prior studies have not systematically assessed how metal artifact reduction images should be incorporated into clinical practice (eg, instead of or in addition to routine images).

In this study, we performed clinical assessment of a prototype iterative metal artifact reduction (IMAR) algorithm (Siemens, Erlangen, Germany) applied to CT data in patients with spinal fusion. The prototype IMAR algorithm makes image-based corrections that aim to minimize artifacts tangential to high-contrast regions on the basis of spatial frequency and recover detail close to the metallic implants, thus theoretically retaining important anatomic information from the original images. Image improvements are refined by using iterative normalization of metal artifact reduction specifically tailored to the postoperative spine.[8,14] We evaluated the ability of CT images reconstructed with and without IMAR to visualize critical anatomic structures in the postoperative spine and assessed the potential for routine implementation of IMAR into clinical practice.

MATERIALS AND METHODS

Data Collection and CT Acquisition

Institutional review board approval was obtained, and informed consent was waived for this retrospective study. Imaging data were collected from July 25, 2012, to August 23, 2013. Inclusion criteria were the following; 1) prior instrumented spine fusion, 2) noncontrast CT imaging of the spine performed at the level of spine fusion, 3) use of a 128-section CT system (Definition Flash; Siemens), and 4) archived CT projection data. All CT imaging was performed by using the routine acquisition parameters of our institution in clinical practice at the time for cervical, thoracic, and lumbar spine CT by using collimation of 128 × 0.6 mm, pitch of 0.9, gantry rotation time of 1 second, automatic exposure control tube current setting of 280 or 260 quality reference milliampere-second (for cervical and thoracolumbar protocols, respectively), and a 50-cm scan FOV. Cervical spine scans were performed by using 140 kV(peak), while scans of the lumbar and thoracic spine were performed with 120 kVp.

Image Reconstruction

CT images were reconstructed by a senior research technologist (G.J.M.) from archived projection data by using an off-line computer workstation, with images reconstructed by using a conventional weighted filtered back-projection (wFBP) kernel (B35) and the prototype IMAR algorithm (spine parameters). IMAR was performed by using a vendor-specified "spine" setting, which entails predetermined IMAR reconstruction parameters appropriate for spinal anatomy and hardware. Briefly, for IMAR reconstruction, images are produced by first reconstructing an uncorrected wFBP image, which is segmented into the metal and nonmetal pixels by thresholding. The nonmetal pixels are used to produce a prior image, while the metal pixels are used to generate a metal image. The images are projected back into the sinogram space and are used to normalize and identify the metal projections in the original uncorrected sinogram data. Metal projections data are interpolated, and the sinogram is then denormalized. High- and low-pass-filtered versions of corrected images are then generated. The final images are produced by a weighted combination of the high-pass-filtered images (corrected and uncorrected) with the low-pass-filtered corrected images. This filtering and mixing step is performed iteratively and reduces the blurring of the anatomic structures near the metal object. For both, images of 0.6-mm thickness at 0.6-mm increments were produced with a reconstruction FOV of 50 cm. For the purposes of this retrospective research project, images were displayed to include the entire FOV to assess the whole image for potential artifacts and to delineate their full extent if present.

Image Analysis

After reconstruction, images were loaded onto an Advantage Windows Workstation (GE Healthcare, Milwaukee, Wisconsin) for viewing. Two Certificate of Added Qualification–certified neuroradiologists (A.L.K., D.R.D.), each with 14 years of experience, performed image evaluation in consensus. Location and type of hardware were identified. Each study was evaluated by viewing axial wFBP and IMAR images side-by-side, first with soft-tissue window settings (window width, 3700 Hounsfield units [HU]; window level, 600 HU) and then subsequently with bone window settings (window width, 300 HU; window level, 40 HU). Images were only evaluated in the axial plane without scanogram images or multiplanar reformations.

Visualization of Critical Anatomic Structures. Critical structures were defined as the central canal, the spinal cord, neural foramina, and prevertebral soft tissues. Separate evaluations were performed for evaluation of soft-tissue and osseous structures by using the appropriate window/level display settings. Neuroradiologists evaluated wFBP and IMAR images in a side-by-side fashion for each patient. For both evaluations, a 6-point diagnostic image-quality scale was used (0 = critical structures totally obscured, no structures identifiable; 1 = marked artifacts, questionable anatomic recognition of critical structures; 2 = faint anatomic recognition, no confidence in the ability to identify pathology; 3 = anatomic recognition with low confidence in diagnosis; 4 = anatomic recognition with medium confidence in diagnosis; 5 = anatomic recognition with high confidence in diagnosis).

For evaluation of soft-tissue structures, the neuroradiologists assigned the overall score on the basis of their impression of soft-tissue planes and structures. In addition, the neuroradiologists identified the critical anatomic structure that had the worst visualization (ie, greatest anatomic obscuration due to metal or IMAR-related artifacts) and assigned a separate soft-tissue visualization score for this structure by using the same scale. Improvement or worsening in soft-tissue visualization scores was calculated by subtracting the score of the wFBP images from that for the IMAR images so that positive values reflected improvement and negative values reflected degradation.

For evaluation of cortical bone structures, the neuroradiologists examined cortical bone visualization around the region of metal hardware by using the wFBP and IMAR bone window images in a similar fashion and by using the same 6-point scale. Improvement or worsening in visualization of osseous structures between wFBP and IMAR was calculated, as described above.

Objective Artifact Measures. Two objective measures were used to further describe the severity of metal-related artifacts. Verte-

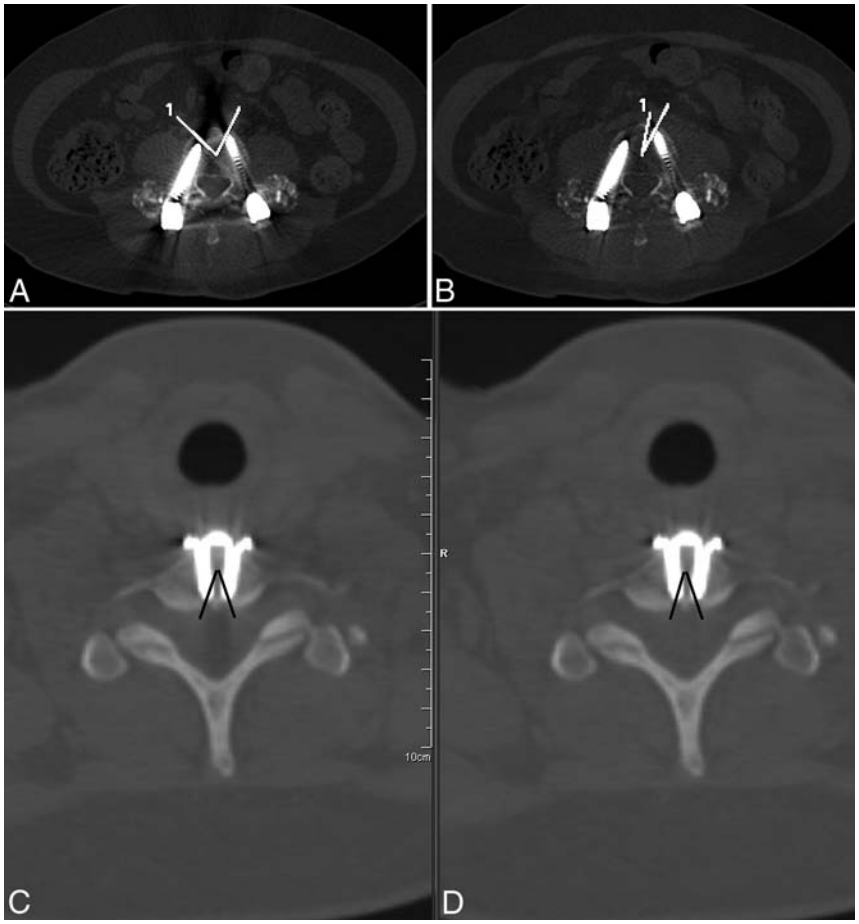

FIG 1. Quantitative measurement describing the maximum extent of vertebral body cortex that was obscured by metal beam-hardening artifacts in 2 patients. The central angle of an angle measurement tool was placed in the middle of the vertebral body, with its rays circumscribing the portions of the vertebral body cortex that were obscured by metal artifacts. The process was repeated for wFBP (*A* and *C*) and IMAR (*B* and *D*) images. In 1 patient with bilateral screw/rod fixation in the lumbar spine, artifacts from both screws cross at the anterior margin of the vertebral body cortex, resulting in obscuration of a large portion of the anterior cortex (*A*). There is marked improvement with IMAR in the degree of anterior vertebral body cortical obscuration caused by metal artifacts (*B*) because only artifacts from the left-sided screw extend to the cortical surface. In another patient with anterior cervical discectomy and fusion (*C* and *D*), there is no change in the degree of vertebral body cortical obscuration as measured by the circumscribed angle.

bral body cortical obscuration was first measured at the level with the greatest beam-hardening artifacts in each patient, by using the same level for each of 2 objective measures. For estimation of vertebral body cortical obscuration, an angle measurement tool was used, with the central angle placed in the middle of the vertebral body as the reference point. The 2 rays forming the angle were drawn so that they circumscribed the portions of vertebral body cortex that were obscured by metal artifacts (Fig 1). This circumscribed angle (or arc, in degrees) was measured for both the wFBP and IMAR images. The improvement in the angular cortical obscuration was calculated by subtracting the angles calculated in the IMAR images from the wFBP images.

A "flame" artifact, reflecting the length of severe beam-hardening parallel to the orientation of spinal hardware (usually a pedicle screw), was also measured. For this measurement, the linear dark band that emanates from the tip of a metal object along its long axis in the imaging plane was measured by first selecting the level of most severe beam-hardening artifacts in each patient. The extent of the flame artifact was then quantified by measuring the distance (in millimeters) from the tip of the metal object to the end of the linear dark band at the same level on both wFBP and IMAR images (Fig 2). The improvement (decrease) in flame artifact severity was calculated by subtracting the length of the flame artifact on the IMAR images from the length on the wFBP images at the same level so that positive values reflected improvement and negative values reflected degradation.

Recommendation for Clinical Practice. Finally, the neuroradiologist readers assigned recommendations for clinical use of IMAR images and their estimated impact on diagnostic confidence. Impact on diagnostic confidence was a synthesis of the ability to see both critical and other soft-tissue structures, visualization of osseous structures, and introduction of artifacts. These recommendations were made after viewing wFBP and IMAR images in a side-by-side comparison by using both soft-tissue and bone window images for each case. Radiologists were asked to determine their recommendation regarding clinical use of IMAR images with similar future cases as follows: 1 = always generated instead of routine wFBP images; 2 = always generated in addition to routine wFBP; 3 = only reconstructed when requested; or 4 = not reconstructed at all. A categoric score was also given for the estimated impact on diagnostic confidence (0 = unclear impact, 1 = probable increase in confidence, 2 = definite increase in confidence, −1 = probable decrease in diagnostic confidence, −2 = definite decrease in diagnostic confidence).

To ensure that IMAR did not degrade clinically relevant diagnostic information, we retrospectively examined all cases with a description of potential hardware complications at the level of spinal fusion in the clinical radiology reports. In these cases, we compared the visualization of the hardware complication between the wFBP and IMAR images.

Statistical Analysis

Statistical analysis was performed comparing the soft-tissue and bone visualization scores for critical anatomic structures by using wFBP and IMAR and for similar comparisons of vertebral body cortical obscuration, by using the 2-tailed Wilcoxon signed rank test. For comparison of flame artifacts between wFBP and IMAR, we used a paired *t* test because data were normally distributed. A *P* value $\leq$ .05 was considered statistically significant for both sets of comparisons. Descriptive statistics were used to classify spinal hard-

ware in our cohort, rank improvements in visualization of anatomic structures, and objective measures of artifact severity and to assess recommendations for use of IMAR images in clinical practice.

RESULTS

Sixty-eight patients with spinal hardware met the inclusion criteria (38 females [56%]; age range, 17–87 years). Thirty-nine (57%) had imaging of the lumbar spine; 21 (31%), of the cervical spine; and 8 (12%), of the thoracic spine. The radiation dose ranged from 5.9 to 40.7 mGy, with a mean dose of 19.6 mGy. Thirty-seven patients had posterior rods and pedicle screws, 16 had an anterior fixation plate and screws, 3 had interbody fusion cages, and 12 had other more complex hardware fixation.

Visualization of Critical Anatomic Structures

The results from the subjective and objective analyses comparing IMAR and wFBP are shown in the Table. The overall soft-tissue visualization scores for critical anatomic structures (median) were 1 ± 1.5 for wFBP and 3 ± 1.3 for IMAR images ($P < .001$). The spinal canal was the worst visualized structure in a large majority of patients (56/68; 82%), followed by the prevertebral soft tissues in 7/68 (10%) and other structures in 5/68 (7%). The median soft-tissue visualization scores for these worst visualized structures were 0 ± 1.3 for wFBP (with a score of zero indicating that the structure is totally obscured), which improved to 3 ± 1.2 for IMAR ($P < .001$; a score of 3 indicating anatomic recognition with a low level of confidence in diagnosis). The mean improvement in overall soft-tissue visualization scores was 1.0 ± 1.0, with an improvement of ≥1 point in 55/68 (81%) patients. The mean improvement in the worst visualized anatomic structure was 1.5 ± 1.1, with an improvement of ≥1 point in 60/68 (88%) patients (Fig 3). In 11 patients (16%; 11/68), the worst visualized anatomic structure improved by at least 3 points. In 4 patients (6%; 4/68), the worst structure improved from a rank of ≤2 with wFBP (no structures identifiable; no confidence in ability to identify pathology) to ≥4 with IMAR (medium-to-high confidence in diagnosis).

The overall bone visualization scores (median) were similar for wFBP and IMAR: 5 ± 0.5 and 5 ± 0.9, respectively (Fig 4). Only 1 patient (1.5%) had worsening of the bone-visualization score. In this patient, complex hardware was present in the thoracic spine causing severe artifacts on both wFBP and IMAR.

In 3/68 (4.4%) patients, we observed shadowing at the image periphery somewhere within the reconstructed image stack. None of the images with the shading artifacts contained anatomy evaluated in the study; hence, the artifacts did not affect the study results.

Objective Artifact Measures

For objective measures of metal-related artifacts, the mean estimate of vertebral body cortical obscuration for wFBP and IMAR images was 7° and 3°, respectively ($P = .004$). In 54 of the 68 (79%) patients, the vertebral body cortex was visualized in its entirety on both wFBP and IMAR images. In the 14 patients in whom there was a nonzero value for estimation of vertebral body cortical obscuration, mean angular obscuration was 34° for wFBP and 15° for IMAR ($P = .001$).

Flame-related linear metal artifacts were present in 66/68 (97%). The mean flame artifact lengths for the wFBP and IMAR images were 29 and 11 mm, respectively ($P < .001$).

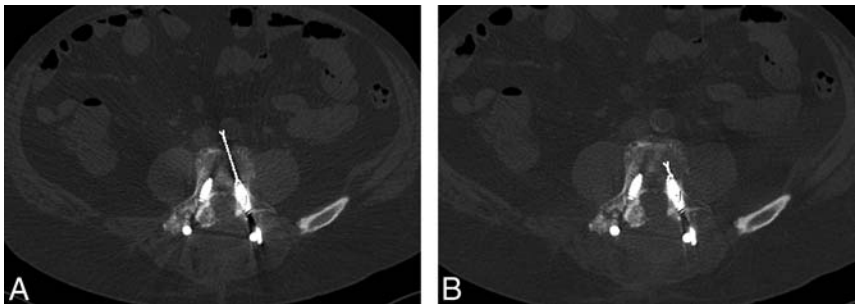

FIG 2. Extent of the flame artifact was quantified by measuring the distance (millimeters) from the tip of the metal object to the end of the linear dark band at the same level on both wFBP (*A*) and IMAR images (*B*). Improvement in artifact severity is demonstrated on the IMAR image.

Results from the subjective and objective analyses comparing IMAR and wFBP

Neuroradiologist Evaluation	wFBP (Median)	IMAR (Median)	Test	*P* Value
Subjective				
Overall soft-tissue visualization score[a]	1 ± 1.50	3 ± 1.27	WSR	<.001
Cervical ($n = 21$)	2 ± 1.54	4 ± 1.06	WSR	.001
Thoracic ($n = 8$)			NA[b]	NA[b]
Lumbar ($n = 39$)	1 ± 1.24	3 ± 1.15	WSR	<.001
Soft-tissue structure with worst artifacts, visualization score[a]	0 ± 1.34	3 ± 1.19	WSR	<.001
Cervical ($n = 21$)	1 ± 1.53	3 ± 1.20	WSR	.001
Thoracic ($n = 8$)			NA[b]	NA[b]
Lumbar ($n = 39$)	0 ± 1.18	2 ± 1.04	WSR	<.001
Bone (cortex) visualization score	5 ± 0.49	5 ± 0.87	WSR	.02
Cervical ($n = 21$)	5 ± 0.36	5 ± 0.30	WSR	.16
Thoracic ($n = 8$)			NA[b]	NA[b]
Lumbar ($n = 39$)	5 ± 0.54	5 ± 0.16	WSR	<.001
Objective				
Vertebral body cortical obscuration (in degrees)	7 ± 17	3 ± 12	PTT	<.001
Vertebral body cortical obscuration, when present ($n = 15$) (degrees)	34 ± 22	13 ± 24	PTT	<.001
Length of flame artifacts (mm)	29 ± 18	11 ± 7	PTT	<.001

Note:—NA indicates not applicable; PTT, 2-tailed paired *t* test; WSR, Wilcoxon signed rank test.

[a] Structures evaluated in the region of metal fixation hardware included the central canal, spinal cord, neural foramina, and prevertebral soft tissues.

[b] A subgroup analysis of thoracic spine cases was not performed due to the few cases in this group.

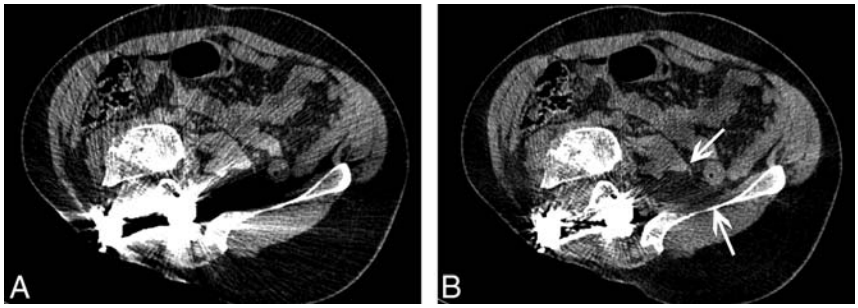

FIG 3. wFBP (*A*) and IMAR (*B*) images in a 33-year-old man status post right hemipelvectomy for resection of a fibrosarcoma. IMAR improves visualization of the psoas and iliacus muscles (*arrows*), the retroperitoneal fat, and the spinal canal to exclude tumor recurrence.

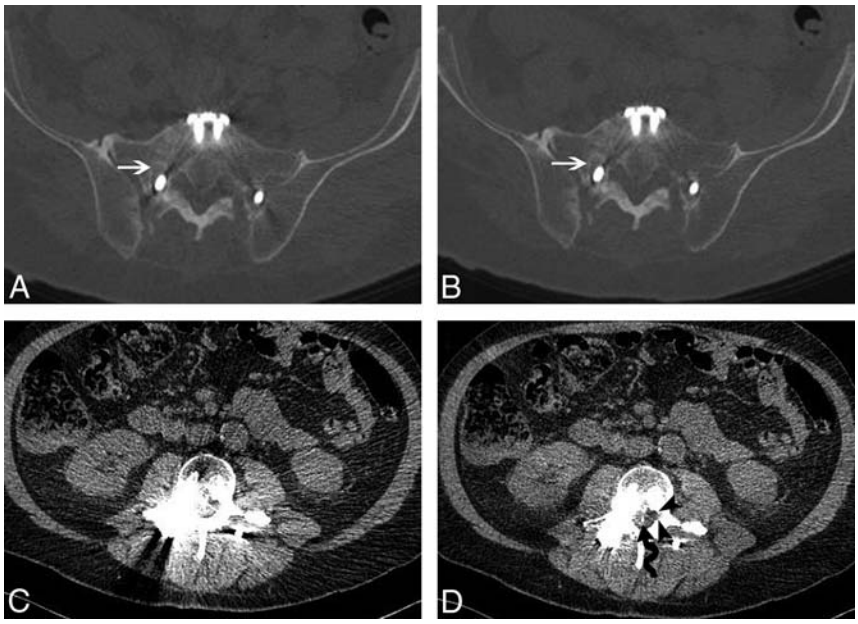

FIG 4. A 65-year-old man status post L3-to-S1 pedicle screw and rod fixation. wFBP (*A*) and IMAR (*B*) images at the S1 level using bone window settings demonstrate lucency about the right S1 screw, consistent with hardware loosening (*white arrows*). At the L3 level, the central canal and lateral recesses are obscured by artifacts on wFBP (*C*) image with soft-tissue window settings. IMAR (*D*) image with soft-tissue window settings at the same level demonstrates a retained wire from a prior spinal cord stimulator (*wavy arrow*) and improved visualization of the left lateral recess (*black arrowheads*).

Recommendation for Clinical Practice

In most patients (87%; 59/68), the neuroradiologists wanted IMAR images instead of wFBP images; in an additional 10% (7/68), IMAR images were requested in addition to wFBP images. These cases included those in which soft-tissue artifacts remote from the spine were identified. In 3% (2/68) of patients, IMAR images were deemed necessary only if specifically requested. Both of these patients had complex, multilevel fusions. When asked about the impact of IMAR images on diagnostic confidence, the readers estimated a definite increase in confidence in clinical diagnosis in 22/68 (32%) patients, a probable increase in 25/68 (37%) patients, unclear impact on diagnostic confidence in 21/68 (31%) patients, and probable or definite decrease in none (0%).

Seven percent (5/68) of patients had a hardware complication at the level of the spinal fusion based on retrospective review of clinical radiology reports (3 with hardware loosening, 1 with a pedicle screw extending beyond the medial pedicle margin, and 1 with migration of an interbody fusion cage). In these 5 patients, IMAR images were thought to display the hardware complications as well as the FBP images (Fig 4).

DISCUSSION

The presence of metallic structures such as screws, rods, and dental fillings in CT images may cause severe artifacts due to beam-hardening, photon starvation, and the presence of sharp gradients in the sinogram data. Metal objects can generate streaks or dark areas in the image and obscure low-contrast neural structures of interest in the spinal canal or in adjacent paravertebral soft tissues. Our pilot study demonstrated significant improvement in visualization of critical anatomic structures such as the spinal canal and adjacent paravertebral soft tissues by using a prototype IMAR reconstruction technique. Additionally, IMAR reduced the extent of linear "flame" artifacts. In those cases in which the vertebral body cortex was obscured, IMAR improved cortical visualization. Neuroradiologist readers recommended reconstruction of IMAR images routinely in clinical practice in >90% of cases (and in >80%, they recommended reconstruction of IMAR without wFBP images). Neuroradiologists thought that the use of IMAR images definitely improved diagnostic confidence in 32% of patients. These results are important because they demonstrate that this technology may be a useful method for reducing metal artifacts on CT images in the ever-growing population of patients with spinal fixation hardware, improving the diagnostic benefit of wFBP images, particularly in the evaluation of critical soft-tissue anatomic structures.

Most studies evaluating metal artifact reduction algorithms have evaluated orthopedic hardware in phantoms or in a heterogeneous mix of patients (often with none having spinal-fixation hardware). Similar to our study, however, Wang et al[13] evaluated 18 patients with spinal fusion and metal hardware, using dual-energy, virtual monochromatic kiloelectron volt images and metal artifact reduction algorithms. They used subjective 5-point image-quality and diagnostic interpretability scales in addition to measuring the width of pedicle screws as an objective measure of metal artifacts. These investigators found that their approach resulted in improved image quality and diagnostic interpretability but that metal artifact reduction degraded pedicle screw shape. In contrast, we imaged a larger number of patients with different types of spinal fixation hardware and performed a visual analysis

of critical anatomic structures that may be affected by postoperative complications. Furthermore, we performed a side-by-side assessment of wFBP and IMAR images across our cohort to determine how such algorithms should be integrated into routine clinical practice. We submit that while IMAR images are sufficient to replace wFBP images in >80% of patients, both wFBP and IMAR images should be routinely reconstructed for the minority of patients in whom unusual artifacts can be caused by postprocessing with the IMAR algorithm itself (Fig 4). Routine reconstruction of IMAR images is warranted, given the definite or probable increase in diagnostic confidence in more than half of patients, usually on the basis of improved visualization of soft-tissue structures.

Several recent proposals for metal artifact reduction have used dual-energy CT with virtual monochromatic kiloelectron volt images in addition to metal artifact reduction algorithms.[7,14] However, the effectiveness of artifact reduction by using monoenergetic imaging appears to be dependent on implant material and size.[7,9,12,13] Our work used a method for metal artifact reduction that can be employed using conventional single-energy CT acquisition with thresholds and other settings potentially altered to adjust for different types and location of metal implants. Others have previously described a 1D linear interpolation to improve CT sinogram data,[15,16] but such approaches have not been put into clinical practice until recently, primarily due to the high computational time requirements.[17] Recently, the linear interpolation approach was improved by adding a normalization process (ie, "normalized metal artifact" reduction) that can be performed quickly and efficiently.[10] The IMAR prototype used in this study is yet a further improvement to these existing algorithms. We herein test this new approach for the first time in a large set of patients with spinal hardware by using an off-line computer workstation.

Some limitations of our study should be acknowledged. First, as described above, in this study, the projection data gathered during each patient's examination were exported to an off-line station where the reconstruction with the prototype IMAR algorithm was performed. This delay in workflow would not likely be clinically acceptable on a routine basis. We did not record the off-line image reconstruction time for each case because CT scanner image reconstruction systems are much more powerful than the off-line workstation. We anticipate that IMAR implementation in a scanner image reconstruction system will reconstruct several IMAR images per second. Second, evaluation of wFBP and IMAR images was performed in a side-by-side fashion, so the readers could readily ascertain which image set was created by using the IMAR algorithm. This methodology was required to allow detection of subtle differences in visualization of soft-tissue structures between the 2 techniques and quantification of the most severe artifacts at the same anatomic level and to understand the nature and frequency of artifacts caused by the IMAR algorithm itself. Our CT system can reconstruct images by using sinogram-affirmed iterative reconstruction, another vendor-specific iterative reconstruction technique, but we did not generate a third set of images by using sinogram-affirmed iterative reconstruction for this analysis because sinogram-affirmed iterative reconstruction itself may cause artifacts and the goal in this study was not to reduce noise but to reduce metal artifacts. Additionally, we only evaluated noncontrast images.

The implications of using IMAR for examinations in which intravenous or intrathecal contrast (ie, myelography) is administered will require further investigation. Finally, we used visualization of critical anatomic structures and estimation of diagnostic confidence as a surrogate for detection of postoperative pathology; an increase in diagnostic confidence may not translate into clinical relevance. We only assessed axial images and did not view scanogram images or multiplanar reformats as would be routine for our clinical practice. While our results suggest that abnormalities such as nerve root or spinal cord compromise or the presence/absence of soft-tissue tumor recurrence may be determined with higher confidence by using IMAR, we did not design our study to address this hypothesis. Given that IMAR reconstruction may take time to perform, the true clinical utility of IMAR remains uncertain despite our findings. Prospective assessment of the ability of IMAR to identify clinical findings will be a focus of future work.

CONCLUSIONS

The IMAR prototype improves anatomic visualization of critical soft-tissue structures in the postoperative spine and reduces metal artifacts by both subjective and objective measurement, resulting in improved diagnostic confidence in the large majority of patients with spinal fusion hardware.

Disclosures: Amy L. Kotsenas—*RELATED*: *Grant*: Siemens,* *Comments*: Siemens created the prototype iterative metal artifact reduction technique under study. David R. DeLone—*RELATED*: *Grant*: Siemens,* *Comments*: Mayo Clinic receives a grant from Siemens, creator of the metal artifact reduction prototype under study; *Travel/Accommodations/Meeting Expenses Unrelated to Activities Listed*: Siemens, *Comments*: Mayo Clinic–Siemens Collaboration Summit 2014. Katharine Grant—*RELATED*: *Other*: Siemens, *Comments*: I am a full-time employee of Siemens USA (includes stock/stock options). Ahmed F. Halaweish—*UNRELATED*: *Employment*: Siemens. Andreas Krauss—*OTHER RELATIONSHIP*: employee of Siemens. Rainer Raupach—*UNRELATED*: *Employment*: Siemens; *Patents (planned, pending, or issued)*: Siemens; *Stock/Stock Options*: Siemens. Bernhard Schmidt—*UNRELATED*: *Employment*: Siemens. Cynthia H. McCollough—*RELATED*: *Grant*: Siemens,* *Comments*: This work was part of a larger sponsored research grant to evaluate new CT technology. I am the Principal Investigator of this grant. During the course of the study, I had no direct access to any study data or results; *Support for Travel to Meetings for the Study or Other Purposes*: Siemens,* *Comments*: Travel support was provided for me to report to Siemens the results of the overall technology research grant that I have with them; *Provision of Writing Assistance, Medicines, Equipment, or Administrative Support*: Siemens, *Comments*: I am the Principal Investigator of a technology research grant with Siemens. A portion of the funds are for administrative support; *UNRELATED*: *Patents (planned, pending or issued)*: Siemens,* *Comments*: Mayo Clinic and I have intellectual property rights for technology outside the work performed here for which Siemens has purchased licensing rights; *Royalties*: Siemens,* *Comments*: Mayo Clinic and I have intellectual property rights for technology outside the work performed here for which Siemens has purchased licensing rights. Joel G. Fletcher—*UNRELATED*: *Grants/Grants Pending*: Siemens,* *Comments*: I am co-investigator on a grant from Siemens, which provided the prototype metal artifact reduction software for this study. *Money paid to the institution.

REFERENCES

1. Rajaee SS, Bae HW, Kanim LE, et al. **Spinal fusion in the United States: analysis of trends from 1998 to 2008.** *Spine (Phila Pa 1976)* 2012;37:67–76 CrossRef Medline
2. Weiss AJ, Elixhauser A, Andrews RM. *Characteristics of Operating Room Procedures in U.S. Hospitals, 2011: Healthcare Cost and Utilization Project Statistical Brief #170.* Rockville: Agency for Healthcare Research and Quality; 2014

3. Chan CW, Peng P. **Failed back surgery syndrome.** *Pain Med* 2011; 12:577–606 CrossRef Medline
4. Young PM, Berquist TH, Bancroft LW, et al. **Complications of spinal instrumentation.** *Radiographics* 2007;27:775–89 CrossRef Medline
5. Stradiotti P, Curti A, Castellazzi G, et al. **Metal-related artifacts in instrumented spine: techniques for reducing artifacts in CT and MRI—state of the art.** *Eur Spine J* 2009;18(suppl 1):102–08 CrossRef Medline
6. White LM, Buckwalter KA. **Technical considerations: CT and MR imaging in the postoperative orthopedic patient.** *Semin Musculoskelet Radiol* 2002;6:5–17 CrossRef Medline
7. Lee YH, Park KK, Song HT, et al. **Metal artefact reduction in gemstone spectral imaging dual-energy CT with and without metal artefact reduction software.** *Eur Radiol* 2012;22:1331–40 CrossRef Medline
8. Lell MM, Meyer E, Schmid M, et al. **Frequency split metal artefact reduction in pelvic computed tomography.** *Eur Radiol* 2013;23: 2137–45 CrossRef Medline
9. Meinel FG, Bischoff B, Zhang Q, et al. **Metal artifact reduction by dual-energy computed tomography using energetic extrapolation: a systematically optimized protocol.** *Invest Radiol* 2012;47:406–14 CrossRef Medline
10. Meyer E, Raupach R, Lell M, et al. **Normalized metal artifact reduction (NMAR) in computed tomography.** *Med Phys* 2010;37:5482–93 CrossRef Medline
11. Meyer E, Raupach R, Lell M, et al. **Frequency split metal artifact reduction (FSMAR) in computed tomography.** *Med Phys* 2012;39: 1904–16 CrossRef Medline
12. Guggenberger R, Winklhofer S, Osterhoff G, et al. **Metallic artefact reduction with monoenergetic dual-energy CT: systematic ex vivo evaluation of posterior spinal fusion implants from various vendors and different spine levels.** *Eur Radiol* 2012;22:2357–64 CrossRef Medline
13. Wang Y, Qian B, Li B, et al. **Metal artifacts reduction using monochromatic images from spectral CT: evaluation of pedicle screws in patients with scoliosis.** *Eur J Radiol* 2013;82:e360-366 CrossRef Medline
14. Morsbach F, Wurnig M, Kunz DM, et al. **Metal artefact reduction from dental hardware in carotid CT angiography using iterative reconstructions.** *Eur Radiol* 2013;23:2687–94 CrossRef Medline
15. Kalender WA, Hebel R, Ebersberger J. **Reduction of CT artifacts caused by metallic implants.** *Radiology* 1987;164:576–77 CrossRef Medline
16. Mahnken AH, Raupach R, Wildberger JE, et al. **A new algorithm for metal artifact reduction in computed tomography: in vitro and in vivo evaluation after total hip replacement.** *Invest Radiol* 2003;38: 769–75 CrossRef Medline
17. Beister M, Kolditz D, Kalender WA. **Iterative reconstruction methods in X-ray CT.** *Phys Med* 2012;28:94–108 CrossRef Medline

Celebrating 35 Years of the AJNR

November 1980 edition

521

Brainstem Evaluation with CT Cisternography

J. Richard Steele[1]
James C. Hoffman[1]

Seventy-eight positive contrast computed tomography (CT) cisternograms were reviewed to assess the normal anatomy of the brainstem and its surrounding cisterns. Normal brainstem and cisternal anatomy was found to be constant and symmetrical. The review included six patients with brainstem gliomas and five patients with extraaxial masses. In these patients CT cisternography accurately identified mass formation and permitted the confident distinction of extraaxial from intra-axial masses. CT cisternography is a safe and accurate method for evaluating the anterior compartment of the posterior fossa. This procedure is particularly applicable to those cases where conventional CT yields insufficient diagnostic information.

Before the advent of computed tomography (CT), patients suspected of harboring a brainstem glioma were subjected to angiography and pneumoencephalography. In most instances CT is now capable of identifying a brainstem mass [1, 2], although angiography and pneumoencephalography are frequently considered necessary to support the diagnosis [1–4]. The reports of early investigators concerning the potential value of positive contrast CT cisternography encouraged us to use this technique for brainstem evaluation [5–7]. This report discusses our experience with CT cisternography as it relates to the normal and abnormal brainstem, and the application of this technique to those cases in which conventional CT of the brainstem is negative or insufficiently diagnostic for patient management.

Materials and Methods

CT cisternography is performed by the lumbar subarachnoid instillation of 6 ml of metrizamide in a concentration of 190 mg I/ml under fluoroscopic control. A proportionately smaller volume is administered to infants and children [5]. With the patient still prone, the fluoroscopic table is tilted into a 45° Trendelenburg position with the head flexed (chin tucked) for about 2 min to allow passage of the contrast agent into the intracranial cisterns. The patient remains in a prone hanging-head position during transport to a General Electric 8800 CT scanner. CT scanning is then carried out in the supine position, parallel to the canthomeatal line. Adjacent 10 mm thick slices are obtained. When greater detail is sought, 5 mm slices are used. The use of coronal scanning varies with the individual circumstance. No attempt is made to return the contrast to the lumbar sac at the end of the examination.

During a 2 year period, 78 CT cisternograms were obtained in our radiology department for a variety of indications (table 1). All cisternograms were reviewed in order to determine the appearance of the normal and abnormal brainstem. Symmetry of the brainstem and its surrounding cisterns was noted. Where possible, the transverse diameters of the medulla, pons, and cerebral peduncles, as well as the distance from the anterior pons to the fourth ventricle, were determined from axial images. Our experience includes six intraaxial and five extraaxial masses (arachnoid cyst, cholesteatoma, chordoma, hypoglossal neuroma, and metastasis). The cisternographic distinction between these two groups was sought. In addition, a chart review was conducted for all patients who underwent CT cisternography to determine the incidence and severity of adverse symptoms attributable to the examination.

Received April 11, 1980; accepted after revision June 24, 1980.

[1]Department of Radiology, Emory University Clinic, 1365 Clifton Rd. N.E., Atlanta, GA 30322. Address reprint requests to J. R. Steele.

This article appears in November/December 1980 AJNR and February 1981 AJR.

AJNR 1:521–526, November/December 1980
0195–6108/80/0016–0521 $00.00

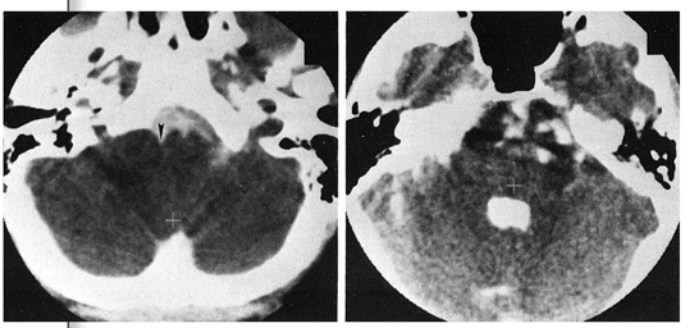

551

CT of the Lumbosacral Spine: Importance of Tomographic Planes Parallel to Vertebral End Plate

James C. Hirschy[1]
William M. Leue[2]
Walter H. Berninger[2]
Richard H. Hamilton[3]
Gerald F. Abbott[1]

An experimental computer program capable of reformatting stored display data from a CT scanner into true cross-sectional images of the spine has been clinically tested over a 1 year period. With this program, tomographic planes exactly parallel to the vertebral end plate can be imaged at the lumbosacral level even in patients who are markedly rotated or have scoliotic deformities. The reformatted image planes are tilted in the dorsoventral and mediolateral directions to compensate for lordosis or scoliosis. The reformatting can also produce images in coronal and sagittal planes on axes other than true horizontal or vertical. The program has been used in the examination of 269 spines and has been found to be valuable in demonstrating the spinal canal and the intervertebral foramina.

The computed axial tomogram should be the ideal instrument for the examination of the spine, particularly for the evaluation of the size and shape of the spinal canal and the intervertebral disc. However, several technical limitations have hindered its completely successful application and, in a recent report by Mankin and Teng [1], preoperative evaluation of the spinal canal by CT was described as unreliable compared with the myelogram.

One of the problems with CT examination of the spine has been the inability to determine the exact position of an axial image within the spine. The placement of radiopaque catheters of graduated length on the patient's skin and correlating the number of catheters seen in the cross section on the CT image with the number of catheters at a specific level seen on the preliminary radiograph provided a useful but somewhat awkward solution to the problem of localization [2–4].

A better solution is the digital projection radiograph (GE-Scout View) that can be viewed on the CT monitor. An electronically generated line can be precisely located on the digital radiograph and the CT scanner can be programmed to obtain an axial image at that level [5].

Excessive thickness of the tomographic section has also been a problem, since small abnormalities become lost in the summation of data from a thick slice [6–8]. The recent availability of 1.5–2.0 mm scan collimation has surmounted this obstacle.

A further problem has been the inability to align the plane of the cross section at right angles to the long axis of the spinal canal or parallel to the vertebral end plate [9]. This problem is overcome in the upper four-fifths of the lumbar spine by tilting the gantry. The digital radiograph can then be used to determine the desired angle of gantry tilt for each axial slice. Unfortunately, the tilt has been insufficient to enable the plane to become parallel to the lumbosacral disc (L5–S1) in more than 96% of the patients in this series. Many patients also have lateral curvatures (scoliosis) and there is no mechanical means of making the scan plane parallel to the laterally tilted vertebrae.

These problems of tilt have been addressed by a computer program that allows

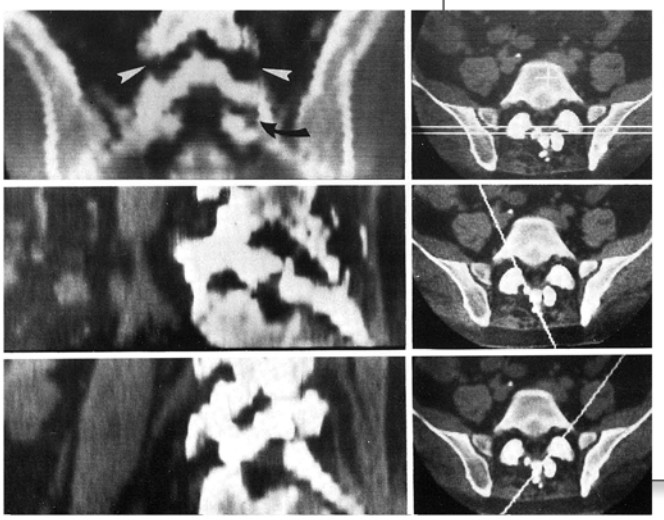

In the author listing for the article "Evaluating CT Perfusion Deficits in Global Cerebral Edema after Aneurysmal Subarachnoid Hemorrhage" (*AJNR Am J Neuroradiol* 2015;36:1431–35, originally published on-line on May 14, 2015, doi:10.3174/ajnr.A4328) the name of the fourth author was spelled incorrectly. The correct author list appears below. The Journal regrets this error.

Baradaran H, Fodera V, Mir D, Kesavabhotla K, Ivanidze J, Ozbek U, Gupta A, Claassen J, Sanelli PC.

http://dx.doi.org/10.3174/ajnr.A4565